Static and Modal Analysis of Wind Turbine Towers

Mark Johnston

March 2, 1999

Disclaimer

I declare that no material contained in this thesis has been used in any other submission for an academic award.

I declare that while registered as a candidate for the University research degree I have not been a registered candidate or enrolled student for another award of the University or any other academic or professional institution.

The information reported in the following document results from my own work except where specific references are cited. To the best of my knowledge, it represents original research.

AUTHOR:
Mark Johnston,
Garrad Hassan and Partners Ltd.
The Coach House, Folleigh Lane,
Long Ashton, Bristol.
BS41 9JB
johnston@garradhassan.co.uk
+44 1275 394360

DIRECTOR OF STUDIES:
John Twidell,
Bridgeford House,
Horninghold,
Leicestershire,
LE16 8DH
amset@compuserve.com
+44 1858 555204

SECOND SUPERVISOR:
Graham Chapman,
International Centre,
Trinity House,
De Montfort University,
Leicester.
gmc@dmu.ac.uk
+44 116 2506086

Summary

As wind turbines become more advanced, mass and cost are being reduced. A new generation of *lightweight* designs has emerged. The Carter 300 kW wind turbine was an early example.

Structural analysis of all components is important so that the designer can be confident that the machine will:-

- resist fatigue damage during its design life;
- withstand the extreme loads it will experience;
- not be subject to loads critical for buckling;
- only be subject to harmonic loads near one of its natural frequencies for short periods of time.

Accurate analysis of lightweight structures is even more important than for older, more conservative designs as structural stiffness is less. Deflections are larger and care has to be taken that the turbine blades do not collide with the tower. Natural frequencies of vibration are lower and it must be ensured that the operating frequency of rotation is not close to a tower resonance. The operating frequency of most wind turbines is fixed by the electrical grid frequency but more and more prototypes are appearing which operate at variable speeds in order to increase energy capture and noise at low windspeeds. Reliable structural analysis of variable machines is even more important.

Many modelling approaches exist. For analysis of an existing design, Finite Element Analysis is the most flexible and accurate, allowing almost any degree of complexity to be incorporated into the numerical model. For a design tool, a simpler approach may be useful as it may produce results faster and offer greater transparency, showing the connections between a small number of critical design parameters and the desired performance indicators. Tubular, steel wind turbine towers are well suited to simple structural models as stresses and deflections depend most significantly on the vertical distance up the tower.

For modal analysis, the Rayleigh/ Stodola method has been implimented here. It has not been used in this form before. It incorporates a novel model of static deflections from which inertia loads are calculated. The static model uses cubic splines stretched over a course array of nodal points distributed up the tower. Longitudinal loads are included in the model of lateral deflections allowing the calculation of loads critical for tower buckling. This is necessary for the analysis of the Carter 300 kW wind turbine which is guyed to reduce mass and to reduce loads at the tower base. The opportunity also arises to analyse the vibrations

of turbine blades which are stiffened during constant speed operation by centrifugal forces. True variations of geometric and material parameters can be modelled.

This method of modal analysis relies on the principle of conservation of energy so no account can be taken of structural or aerodynamic damping or gross discontinuities. Transparency is attained because the design parameter representing each structural component contributes to one term for kinetic or potential energy in the Rayleigh energy balance equation. The method is also fast enough to allow many different sets of design parameters to be compared sequentially.

Good agreement has been obtained between the theoretical methods presented here and the exact solutions of the equations of motion or static equilibrium for the simplest structures. Finite element analysis of more complex systems also confirms the validity of the methods.

Experimental methods have been developed which do not disrupt normal operation of the wind turbines to the extent of shutting the machine down for many hours while sensors are attached. Video recordings of lateral vibrations have yielded some detailed descriptions of the tower static deflection and fundamental frequency and mode shape. These measurements agree well with predictions.

Using accelerometers attached to the tower and analysing the power spectral density of the measured signal has not produced strong indications of the fundamental lateral mode of vibration. Improvements in the measurement and analysis techniques are possible.

The models can be applied to investigate novel design approaches. The effect of increasing the guy tension is to lower the lateral stiffness of the tower and consequently the natural frequencies of vibration. The distribution of stress in the tower in response to normal operating loads indicates the position of the maximum stress. This is normally near the base for free-standing, cylindrical towers. This position rises for conical towers with increases in base diameter. At the same time, the minimum mass of a tower which will withstand these loads falls. Using an automatic search algorithm, the tower shape for which the stress is constant with tower height can be found. Attaching guy cables allows the mass of the tower to be reduced still further and still be able to withstand these normal operating loads.

The methods presented here could form the basis of future developments to enable non-linear, damped vibrations to be analysed. With some alterations, the important field of rotor dynamics could also be analysed. Using more comprehensive, multi-variate search methods, all design parameters could be optimised with respect to particular design requirements. The experimental methods could also form the basis for non-disruptive machine surveys.

Preface

The Anthony Marmont Sustainable Energy Technology Centre (AMSET) was set up with an endowment from Leicestershire businessman, Tony Marmont in 1993. Advanced research and development was initiated in three areas, each with equipment of mainstream, commercial standard.

- drive cycle monitoring of electric vehicles
- domestic-scale combined heat and power
- wind turbines

The wind turbine research centered on two Carter 300 kW machines purchased by AMSET and planned for sites at or near De Montfort University Campuses. The original plan for the research of this thesis would have involved both theoretical and practical investigations based on these machines. Planning applications were already advanced and I performed a detailed resource assessment [1] at the proposed site using the Wind Atlas Analysis Application Program, WA^{S}P [2]. I also began monitoring the wind resource at the site. Objections were made during the planning process and the final decision went against the first site. Several others were then considered. For the next site, planning permission and NFFO (Non-Fossil Fuel Obligation) support was obtained, but problems with supply of the wind turbines, changes at De Montfort University with the management of the Marmont endowment and finally the bancruptcy of Carter Technology Limited in the Autumn of 1996 prevented any comprehensive testing of this AMSET Carter machine.

Because of the lack of a dedicated test facility, the bulk of the work for this thesis has been simulation of lightweight wind turbine towers. In order to relate analysis to actual performance, several series of measurements were collected on a range of operating wind turbines and I am grateful for the cooperation of Tony Marmont (West Beacon Energy Ltd.) and Mick Ploughwright (Dudley Bower Ltd.) for access to two 25 kW Carter machines at West Beacon Farm, Julian Harbottle and the management of Faccombe Estates Ltd. where there is a 300 kW Carter machine on a short 38 m tower and Dave Pinsky who operates the 10 Carter 300 kW machines at Great Orton Airfield. Mike Wastling (formerly of Carter Technology Ltd.) has been very helpful providing information about the Carter 300 kW design. Jung Tao Wei, Dave Quarton and colleagues at Garrad Hassan and Partners Ltd. have offered helpful advice and guidance along the way as well as results from a comprehensive monitoring program on the Carter 300 kW. Many others at Carter Technology

Ltd. and Garrad Hassan and Partners Ltd. have helped me. David Sharpe has offered detailed advice about some of the modelling techniques and his other colleagues at the Centre for Renewable Energy Systems Technology at Loughborough University have also been generous with their time. David Corbet of Viridis Ltd. has provided a useful real life application for the software.

I acknowledge the support of my director of studies, John Twidell and second supervisor. Graham Chapman as well as Martin Crane from the School of Maths and Computing. Andy Rylott and Matthew Forman have been invaluable, facillitating my use of all the UNIX software running on the SUN workstations. My colleagues Mark Hsieh, Iain Fraser, Martin Smith and Matthew Forman among many others have offered frequent help with technical and research-related problems throughout the last four and a half years.

Contents

Chapter 1

Introduction - Light or Heavy Structures

1.1 Commercial Wind Turbines

With the advance of commercial wind power, it is now necessary to optimise all components. The research described here focuses on support towers which are essential and often expensive parts of machines.

Wind turbine support structures have been given less attention than rotors and drive-trains. Recent research has aimed to improve the efficiency of energy capture with lighter, more responsive and robust designs. Examples of this in 1997 are the Wind Energy Group MS4-600 wind turbine [3], the Atlantic Orient AOC 35/400 [4] and papers giving design guidelines for steel towers such as that by Reuter and Bormann [5].

There are three main categories of tower (see Figure 1.1). Following the standard notation (for example, Martin Kühn's paper on optimisation of towers for offshore applications [6]):

1. soft-soft towers (fundamental natural frequency is below the frequency of rotation, P):

2. soft-stiff towers (fundamental natural frequency is between the frequency of rotation and the blade passing frequency, nP where n is the number of blades);

3. stiff-stiff towers (fundamental natural frequency is above nP).

Mass is approximately proportional to cost so reducing the mass of the tower is important. Soft-soft towers are generally lighter than stiffer towers. Martin Kühn [6] alludes to analysis that shows that aerodynamic damping is approximately inversely proportional both to tower mass and tower first lateral frequency. To obtain maximum structural damping. towers should therefore be both light and soft.

At first, wind turbines were supported on towers constructed from a lattice of steel girders much like electricity pylons in Great Britain. Such constructions are stiff and light. cheap to transport and can potentially be assembled on a relatively inexpensive ring foundation. Now. many large wind turbines (greater than 1 MW rated power) are supported on hollow reinforced concrete towers. They are free-standing. stiff and heavy. The latest designs have been of steel. By tapering and guying towers. they can be made strongest where the highest

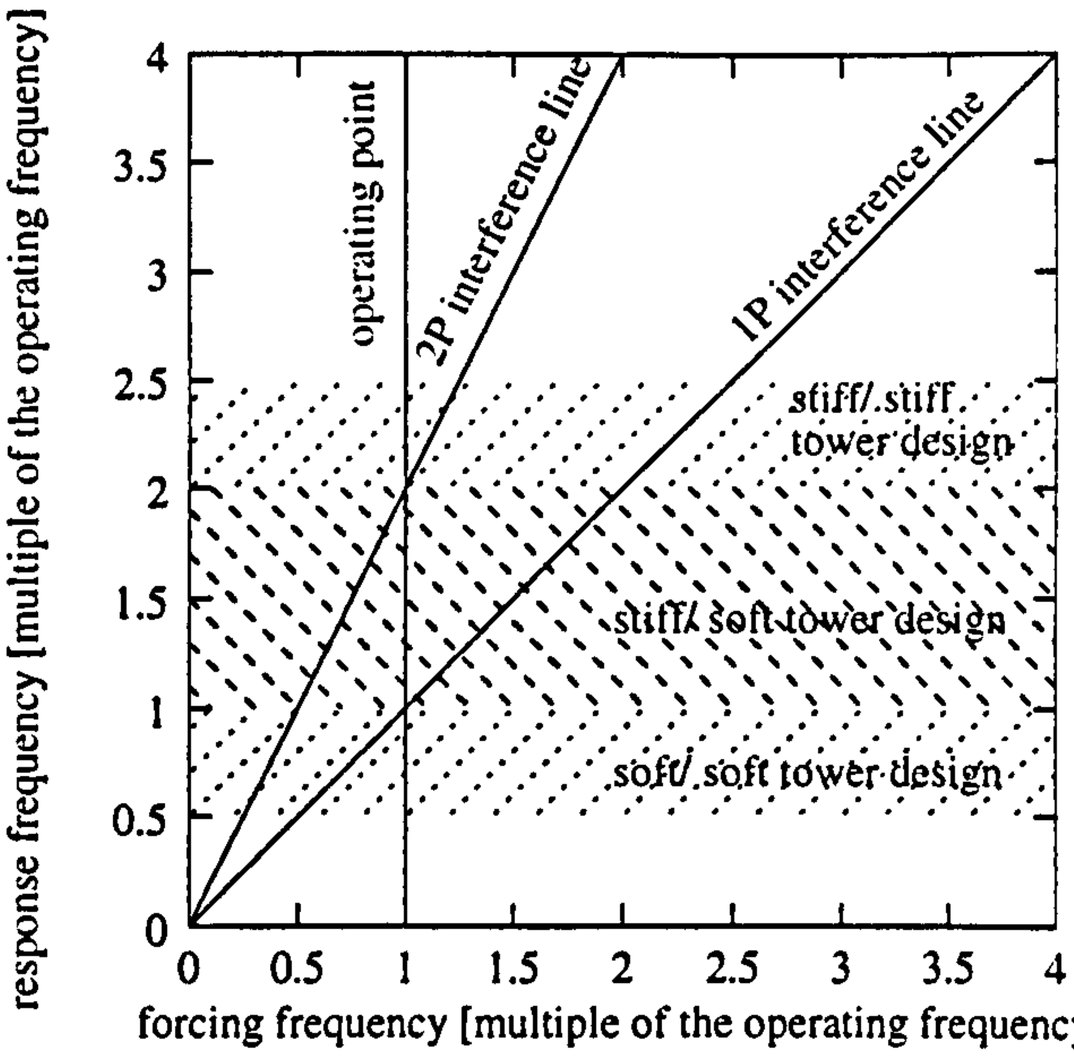

Figure 1.1: A general Campbell diagram for a 2 bladed wind turbine showing the ranges of values for the fundamental frequency of towers in three different categories (soft/ soft, stiff/ soft and stiff/ stiff). All frequencies are scaled with respect to the operating frequency.

loads must be carried. This means that the overall weight can be reduced. Table 1.1 shows examples of towers which are steel lattice, tubular steel or tubular concrete.

Table 1.1 shows that the lightest towers are generally those that are guyed. Exceptions are the small Carter machine which is relatively expensive and the larger Nordex with a lattice tower which is relatively cheap. As expected, the heaviest towers are the concrete towers. The column in Table 1.1 giving specific tower mass is probably proportional to tower cost. The Carter 300 kW design is more recent than the 25 kW design and so some significant reduction in specific tower mass has been possible.

The Carter designs have the smallest specific nacelle mass because of the integrated design in which the housing for the transmission carries the weight of the whole assembly. In contrast, the nacelles of many wind turbines are built onto a bedplate on which the gearbox and generator are independently supported.

Comparing the overall machine cost per unit rated power, the Carter designs are both relatively expensive. Conclusions about technical optimisation are difficult to draw from cost alone because of the differences in size and success of the manufacturing companies and the numbers of machines produced and methods of production. For example, when *Windkraftanlagen* [7] was compiled, Carter Technology was a small company with very little manufacturing experience.

Figure 1.2 shows a linear relationship between the specific cost of steel towers and the specific mass. The data include steel lattice and steel tubular towers. Data come from a 1997 wind turbine market survey [7]. Because they are narrower and less strong, the towers necessary for smaller wind turbines are lighter and also cheaper per unit height than for larger wind turbines. However, Figure 1.3 shows that the cost per unit height per unit rated power production is higher for small wind turbines. This may be because less attention

Table 1.1: A comparison of some examples of different types of towers. The data comes from a 1997 wind turbine market survey [7]. Costs are quoted with an exchange rate of 2.97 Deutsch marks to one pound and include delivery within Germany and assembly. Two exceptions are the Flowind and Südwind machines for which data was taken from a 1996 wind turbine market survey [8].

type of tower	wind turbine	hub height (m)	rated power (kW)	tower mass per unit height per unit rated power ($kg\ m^{-1}\ kW^{-1}$)	nacelle mass per unit rated power ($kg\ kW^{-1}$)	cost per unit rated power ($£\ kW^{-1}$)
steel, lattice	Nordex N29	50	250	1.84	60.0	580
steel, lattice	Nordex N43	77	600	0.995	36.7	548
concrete, conical	Lagerwey LW18/80	52	80	12.5	37.5	800
concrete, conical	Enercon E40	50	500	4.68	57.0	570
hollow, stepped, cylindrical steel	Lagerwey LW18/80	40	80	42.2	37.5	713
steel, conical	Enercon E40	50	500	1.74	57.0	638
steel, conical	Nordex N29	50	250	2.64	60.0	604
steel, conical	Nordex N43	50	600	1.94	36.7	495
guyed, steel, tubular	Flowind AWT-26	44	275	1.41	19.5	545
guyed, steel, tubular	Südwind 1200	30.5	45	1.45	33.3	911
guyed, steel, conical	Carter 25	23.25	25	2.3	11.2	1200
guyed, steel, double-tapered	Carter 300	49	300	0.668	10.3	667

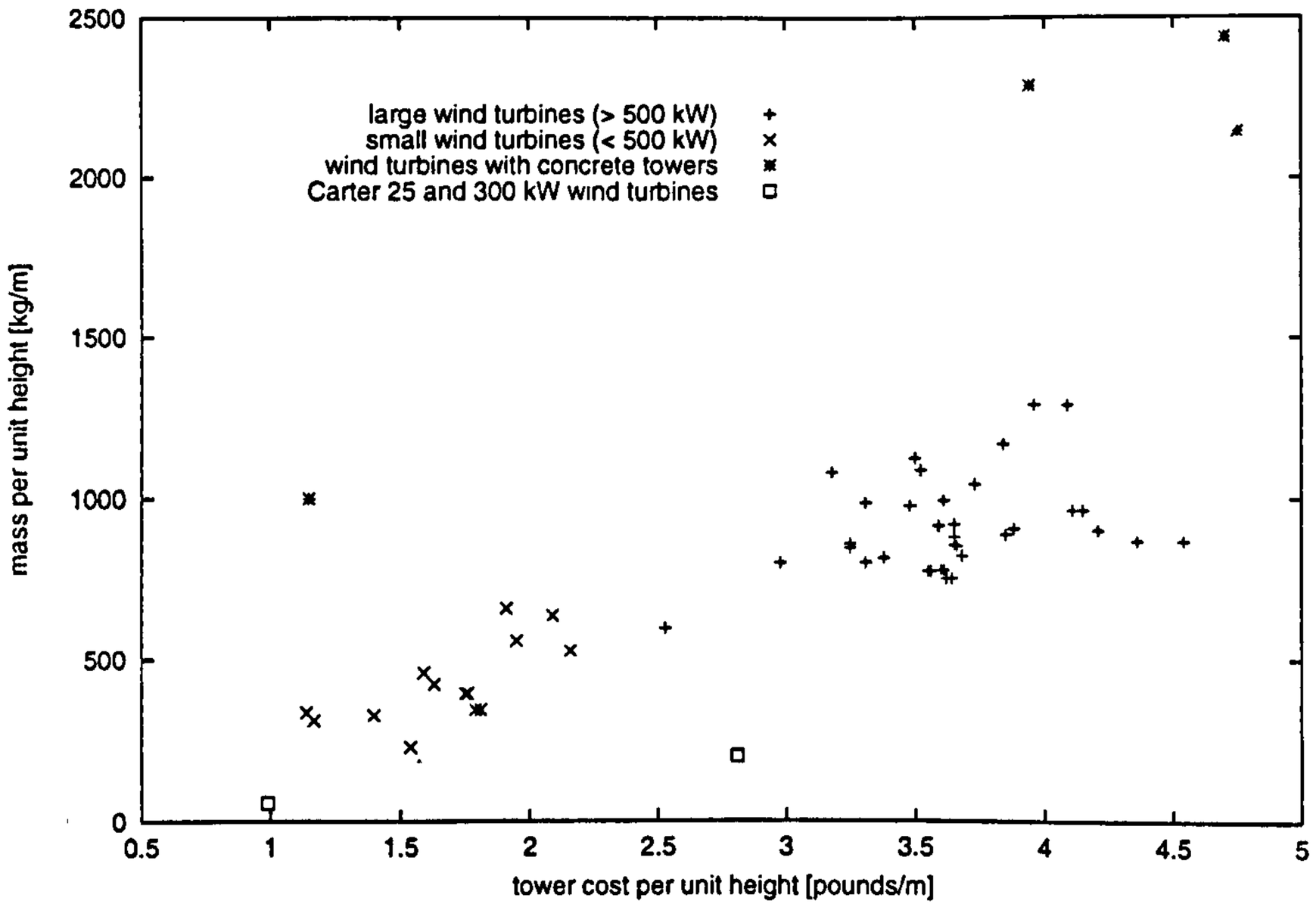

Figure 1.2: Estimates of the cost of the tower of various wind turbines per unit height against the mass of the tower per unit height. Data is from a 1997 wind turbine market survey [7]. 53 different wind turbines manufactured by 16 different companies are compared.

is paid to tower optimisation for smaller wind turbines or because the increased yield from larger machines justifies more expensive control systems which reduce the loads on the tower. Manufacturing and transportation costs are likely to be lower for a small number of larger machines than for a large number of smaller machines generating the same power. Costs of connection to an electrical grid and losses in transformers are both likely to be lower if larger single units are used in a commercial wind farm. These factors have driven manufacturers towards very large wind turbines with power production rated greater than 1 MW. Because specific tower mass is so much greater for towers of larger diameter, more emphasis will be placed on optimising tower mass.

From Figure 1.2, both Carter machines can be seen to be considerably lighter than wind turbines of an equivalent specific cost. From Figure 1.3, the 25 kW can be seen to be underdesigned and relatively expensive although the 300 kW machine is comparable in cost to other machines of a similar height.

The wind turbine market survey covered only three windfarm-scale guyed wind turbines. It is unusual for wind farm machines with power production rated above 100 kW to be guyed. This may be because of the increasing importance of aesthetic appearance to the choice of wind turbines. This is particularly the case in densely populated European countries where machines are likely to overlook nearby communities. Lattice towers, although cheaper are widely taken to be less attractive [9]. Some people also consider guyed towers to be less aesthetically pleasing. They also take up more land although it is often possible for normal agricultural practices to carry on underneath the turbines with minimal disturbance. The

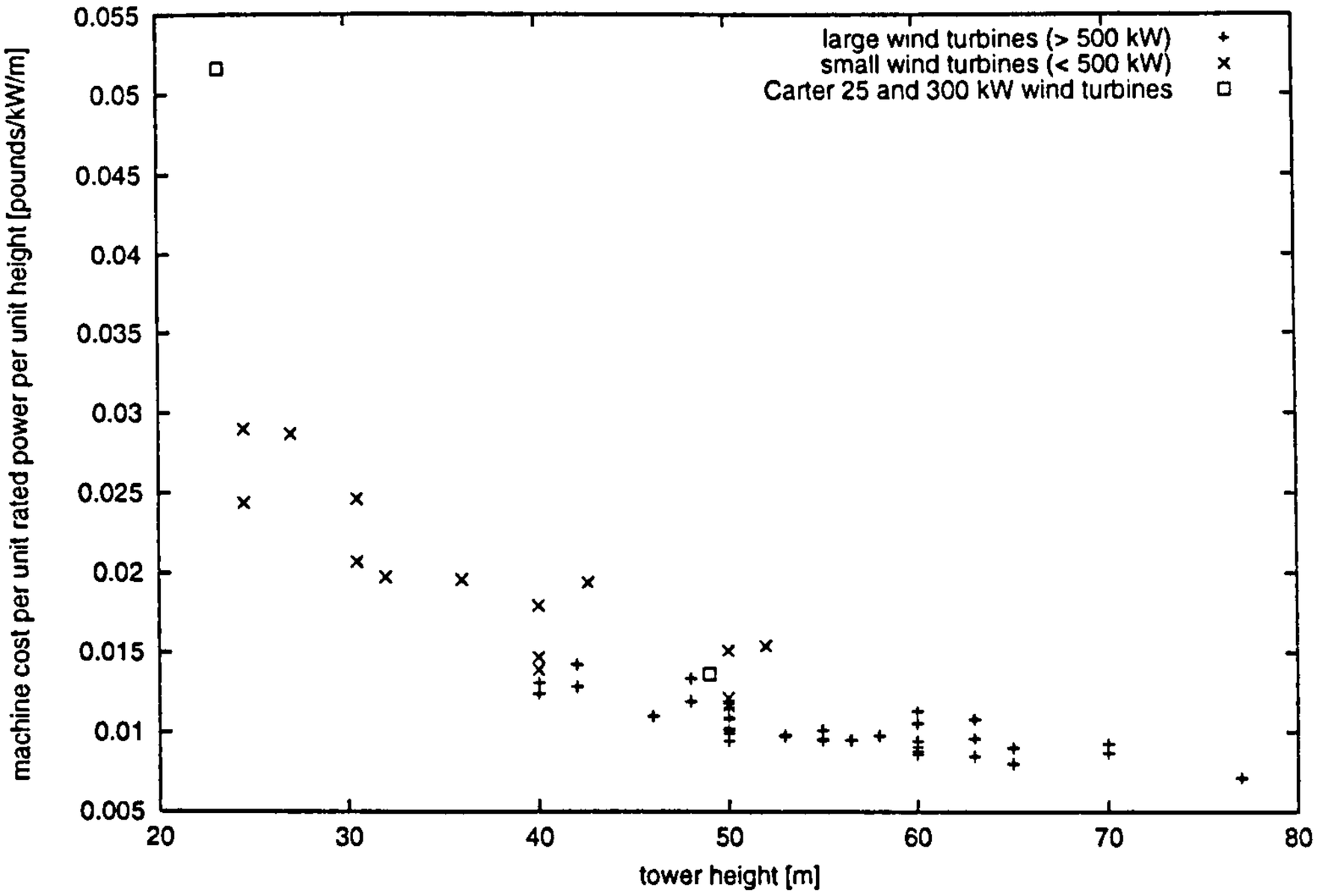

Figure 1.3: Estimates of the cost of the tower of various wind turbines against the hub height. Data is from a 1997 wind turbine market survey [7].

potential for vandalism of a guyed tower is worse than for a free-standing one. However. guying a tower allows its weight to be decreased as the tower alone will not be required to be as stiff nor as strong. Lightweight towers are cheaper to produce and install. As well as being light, guyed structures allow the complete machine to be tilted downwards for installation and maintenance. Thus, the expense of cranes and access roads can be reduced.

David Corbet [10] shows that the Carter 300 kW machine is considerably lighter, taller and has a smaller rotor diameter for the same energy captured than other contemporaries.

Peter Jamieson [11] warns of the dangers of comparing lightweight American wind turbines with heavier European designs because the design loads and safety margins are different on the two continents. He also points out that the standards for noise emissions are often more strict for the densely populated localities of European wind farms. American designs therefore often operate at higher tip speed ratios which reduces the drive train torque and therefore the required strength of the structure.

1.2 The Importance of Structural Analysis

1.2.1 The Importance of Static Analysis

The main load on the tower is a horizontal thrust at the top due to the rotor which extracts energy from the moving airstream. The larger the energy capture. the stronger and more expensive the tower needs to be. The energy capture and hence the thrust can be increased by increasing either:

swept area increased by greater rotor diameter (energy $\propto \rho_{\text{air}} A_{\text{swept}} u_{\text{wind}}^3$) where ρ_{air} is the air density, A_{swept} is the area swept by the rotor and u_{wind} is the free-stream wind speed;

tower height because of 'wind shear' which describes the increase in wind speed at greater heights (wind speed at height z, $u_z = V \ln\left(\frac{z-d}{z_0}\right)$ in which the *zero plane displacement*, d and the *roughness length* z_0 relate to the tendency of surface features and local obstacles to induce turbulence and reduce the windspeed near to ground level).

Other loads on the tower are due to aerodynamic drag, torque from the rotor and gyroscopic torques during situations of nacelle yaw. High loads may be experienced during coupled resonance of the tower and other components such as the rotor.

As well as increasing energy capture, building a wind turbine taller pushes the rotors clear of the turbulence caused by surface roughness and nearby obstacles such as buildings, trees and topographical features [2]. This reduces the fatigue loads to which the machine will be subject during its expected lifetime.

If the tower is required to be stiff, its weight and cost will increase considerably. The Wind Energy Group's LS-1 on Burgar Hill in Orkney is rated at 3 MW electricity generation. It is 45 m high and the tower is a tapered concrete tube which weighs 4 550 000 kg. The hollow, steel rotors weigh 50 000 kg and the rest of the nacelle weighs 103 000 kg. The structure is *stiff-stiff* with tower bending frequencies of 3.6 Hz and 15.1 Hz [12] and forcing from the two-bladed rotor at 0.56 Hz (P) and 1.13 Hz ($2P$). It was recently recommissioned by AMSET and is still generating electricity.

As knowledge of the static response and stress distributions in towers gets more complete, safety factors can be reduced. For early designs, safety factors probably turned out to be greater than 5. Current machines are routinely designed with safety factors of 1.5 or lower. The consequence of this decline in margins of safety is that machines have been made taller and more energy has been captured from the wind without proportional increases in tower mass and thus cost. The Carter 300 kW wind turbine is an example of such a lightweight design.

1.2.2 Tower Buckling

A significant load on a guyed tower is the axial compression from the guy cables. This will result in lower frequencies of lateral vibration of the structure and also introduces the risk of tower buckling. It is important that analysis techniques do not overlook the possibility of tower buckling during operation and also during installation when the machine is tilted up by passing one of the guy cables over a gin pole (see Figure 2.8). The danger of overlooking this possibility is illustrated by the Oussant disaster shown in Figure 3.1.

Calculation of ultimate axial loads for buckling is possible using a reasonably elaborate static model of the structure and an ordered search technique (see Chapter 3).

1.2.3 The Importance of Modal Analysis

The operating frequency must not coincide with a natural frequency or resonance will be excited (see Figure 1.1). The operating frequency is the dominant harmonic input. It is usually fixed but contemporary machines are being designed to operate at variable speed in order to increase energy capture and reduce noise below rated power. As safety margins have decreased and towers have become less stiff, their resonant frequencies have also fallen (see Figure 1.1). If the forcing frequency is not fixed, it is even more important to know the resonant frequencies of all parts of the structure.

It is usual to display operating frequencies and natural (response) frequencies on an interference diagram in which the forcing frequencies are shown as straight lines of gradient 1 and n for a wind turbine with n blades. For fixed speed machines, the dominant forcing occurs at two frequencies which are the rotational frequency and the rotational frequency multiplied by the number of blades (the points (1,1) and (1,2) on the cartesian axes in Figure 1.1). However, as the machine speeds up or slows down the forcing passes through all frequencies below the normal operating frequency.

The fact that there are likely to be many sinusoidal excitation loads at frequencies of nP is because the rotors are symmetrical. For example, in a 2-bladed machine, low speed shaft torque and blade bending moments will vary at a frequency of $2P$. These periodic loads arise because one of the blades passes through a particular mass of air which is smaller than the rotor disk twice per revolution. That mass of air may be moving faster or slower than the air around it thus changing the force on the blade as it moves through the air. Gravity loads willalso vary at $2P$. Downwind machines also have a $2P$ forcing due to the 'tower shadow'. As each blade passes the tower, lift is lost momentarily in the turbulent wake behind the tower. $1P$ forcing will only be due to assymmetry such as different mass or aerodynamic characteristics of the blades (lift and drag).

Tower natural frequencies do not vary much with rotor speed. On the Campbell diagram (Figure 1.1), they are straight, horizontal lines. By contrast, rotor natural frequencies usually increase with rotor speed because centrifugal forces on the blades increase their stiffness.

As a consequence of the large safety factors for ultimate stresses, early wind turbine support structures were stiff/ stiff. In contrast, the guyed tower of the Carter 300 kW machine is soft-soft. This means that the fundamental resonant frequency of the tower is less than $1P$ for normal operation. Both $1P$ and $2P$ excite this mode momentarily whilst the rotor speeds up. Provided damping (aerodynamic and mechanical) is sufficient, these modes will not cause damage when briefly excited in this way. A stiff-stiff tower is not expected to resonate in response to the predominant excitations, deflections are expected to be small and buckling is insignificant. Although softer towers may be lighter and cheaper. more precise predictions about the machine's static and dynamic performance are required.

The results of the analysis presented in Section 4.7.4. Figure 4.23 show that the tower of the Carter 300 kW wind turbine is soft-soft and also that the fundamental frequencies of flatwise and edgewise vibration of the blades increase with increasing rotor speed.

1.3 Analysis of Guyed Towers

The design of guyed towers which carry radio antennae or tethered offshore platforms has been much documented. Such structures usually include very long cables and in the case of radio masts very long, slender columns. The wind or hydrodynamic loads on both the cables and mast are therefore significant. Deflections and rotations of the structure contribute to both longitudinal and lateral deflections of the top. The structure is often prescribed to be stiff. In the case of radio antennae, the rotation at the head must be less than 1° [13]. The sag of the guy cables is significant. Often, parabolic approximations are made for the shape of a sagging guy cable (for example Poskitt in 1963 [13]). More general models have also been described (for example Rosenthal and Skop in 1980 [14]).

The modal response of such structures has also attracted some research. McCaffrey and Hartmann reported in 1972 [15] that there was significant dependence of the natural frequencies on the ambient temperature.

In contrast a wind turbine can tolerate relatively large head deflections and rotations. The predominant load is due to the thrust on the powertrain rather than aerodynamic drag on the structure. Tower and cables will both be wider and stronger than for radio antennae to support the large head load. Unlike a radio antenna of an equivalent height, cable tensions are likely to be high enough to avoid significant sag. Models of guy cables are compared in Section 8.1.

1.4 Modelling Approaches

Conventional methods of analysis of wind turbine towers involve building complex finite element models of the structure. The methods presented here allow many designs to be compared in rapid succession while still incorporating all the necessary complexity described in the previous section. The relationship between various design parameters and the resulting static loads, resonant frequencies or ultimate buckling loads can be see relatively clearly either because of the simplicity of the model or because parameters can be incremented through many different values and the effects on the desired performance indicators quantified.

The simplicity of the techniques adopted is illustrated by the Rayleigh method [16] in which each structural component such as the tower, guys, nacelle and foundation contributes one energy term either to the denominator or the numerator (or both) in the expression (Equation 4.8) for the resonant frequency. The combination of Rayleigh's and Stodola's [17] method developed for this thesis is thought to be unique.

Static analysis involves solution of the differential equations of equilibrium but in order to speed up the analysis, the tower deflection is smoothed using cubic splines stretched over a relatively course set of nodal points. Equilibrium of lateral and axial forces, applied torques and bending moments is only calculated at the nodes. No other references have been found to the implimentation of this technique for static analysis.

Throughout this thesis, the models described in the first three chapters will be referred to as *general, numerical models.* They are general because they enable the structural analysis of a general wind turbine tower which may be free-standing or have any number of guys attached at different heights. Any tower shape may be prescribed and the mass and moments of inertia

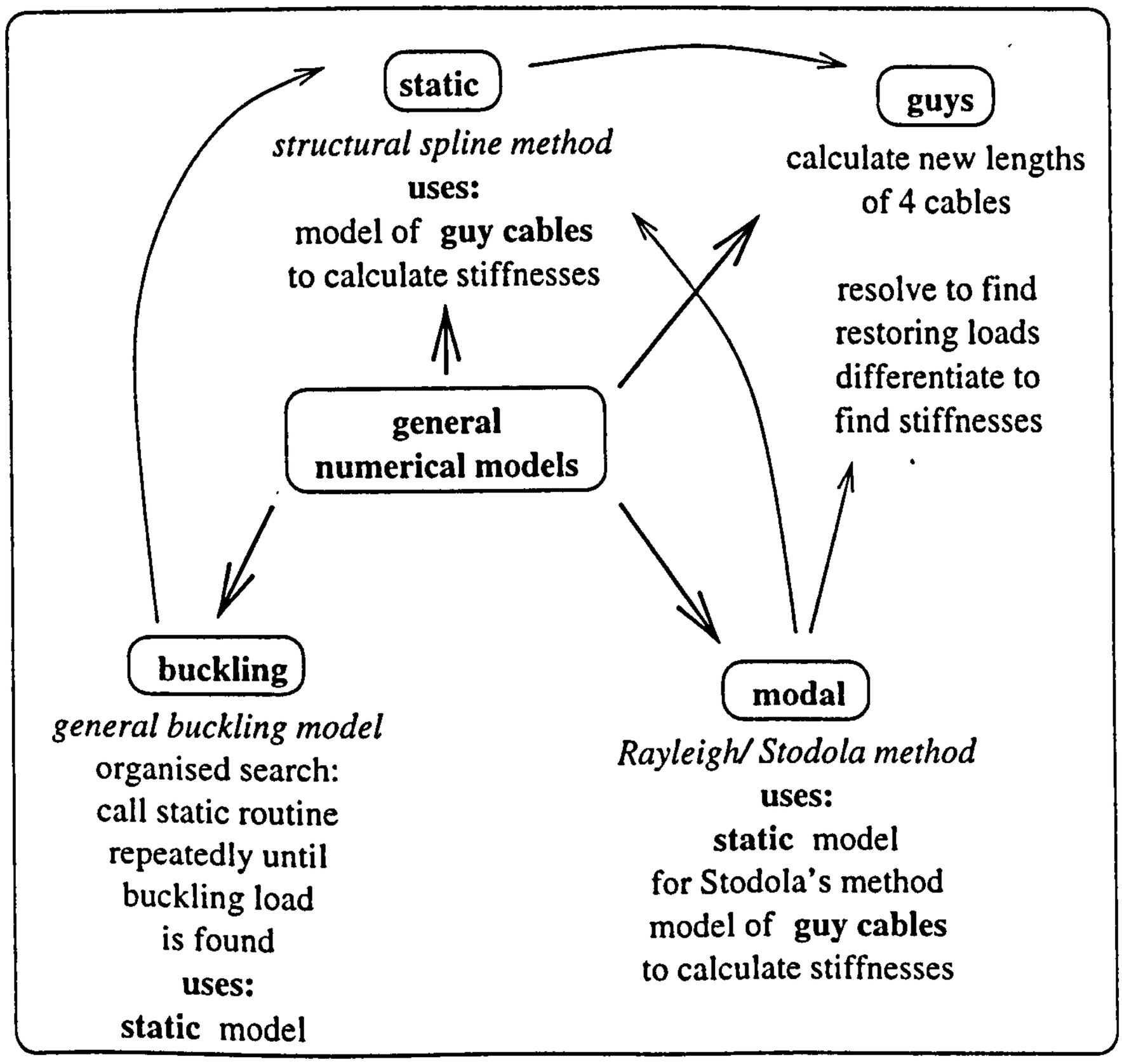

Figure 1.4: The structure of and interconnections between the analysis techniques presented in this thesis.

of the nacelle can be varied. The elastic properties of the tower base fixing are also variable. Even more general is the Finite Element method for which *any geometric model* may be defined. When discussing static analysis, the model will be referred to, more specifically, as the *structural spline model* and for modal analysis, the *Rayleigh/ Stodola model.*

1.4.1 Direct, Classical, Analytical Methods

In a slender tower with a concentrated head mass, shear forces, axial forces and bending moments vary predominantly with one dimension (vertical distance). This suggests that direct solutions of the equations of static equilibrium for a beam may predict bending moments and deflections to the required accuracy. Euler's biharmonic wave equation might be accurate enough to predict lateral vibrations. However, many features such as guy cables and the massive nacelle give rise to discontinuities. Small geometric variations greatly increase the complexity of the problem. For a more general approach, the theory of the conservation of energy is often implimented as is the case with the Rayleigh/ Stodola method.

In 1980, an evaluation of the MOSTAS [18] code was undertaken for the DOE/ NASA 100 kW Mod-0 wind turbine by Kaza and Janetzke [19]. This solves the differential equations of motion of the blades and support. The tower is modelled by differential equations in generalised coordinates.

The software `Bladed for Windows` used and sold by Garrad Hassan is based on the equations of motion of the whole structure. Each time a new structural element is to be modelled, the equations of motion must be derived. This is automated using a symbolic processor called `REDUCE` . These equations of motion are derived only once before being enshrined in the computer code. Direct solution of the equations is very fast. The strategy is illustrated in a paper by Andrew Garrad and David Quarton [20].

Simplified models for which the equations of motion can be solved directly have been described in two parts of this thesis:

1. Sections 5.1.1, 5.1.2 and 5.1.3 in which the *general numerical methods* are validated:

2. Chapter 7 in which it is shown that certain, simple tower designs can be analysed accurately using such classical methods but often more general methods must be employed.

1.4.2 General Numerical Models

For this thesis, *general, numerical models* have been developed for the analysis of guyed or free-standing towers of any prescribed shape. Three analysis types have been included:

1. Static analysis to obtain distributions of stress and deformation (Chapter 2).

2. Buckling of towers under axial loads (Chapter 3).

3. Modal analysis of tower vibrations (Chapter 4).

The modular structure of the software is illustrated in Figure 1.4 in which the modal analysis routine calls a static analysis routine once per iteration. This corresponds to implimenting

the theory of the conservation of energy every cycle of the vibrations. The stiffness of the guy cables is calculated just once before static or modal analysis. For more complex structures, this could easily be replaced by more frequent calculations of guy cable geometry and stiffness.

Unlike conventional finite element techniques, the eigenvalues and eigenfunctions of some linear combination of stiffness, mass and damping matrices are not explicitly calculated.

Being modular, the combination of Rayleigh's and Stodola's methods have allowed the model to evolve, incorporating more and more elements of the structure (the tower, the nacelle, the guys and also different conditions at the base).

In the models, the rotation of the blades and aerodynamic damping has been excluded. No coupling between blade and tower vibrations is considered. Several justifications can be given for this simplification.

- A two bladed rotor often has a teetered hub which passes no bending moments from rotor to tower head. The rotor therefore 'looks like' a lumped mass from the point of view of the tower.

- The rotor modal frequency is typically more than three times tower modal frequency as assumed by Kaiser and Gasch in their finite element analysis of wind turbine towers [21]. Although this is clearly not the case for the Carter machine for which rotor frequencies are very low (see Section 4.7.4, Figure 4.23), as blade designs get lighter, it may be that their fundamental frequencies of vibration get higher.

Three classes of vibration have been analysed independently as shown in Figure 1.5.

1.4.3 Finite Element Methods

Finite Element methods have also been used to validate the *general numerical models.* The results are reviewed in Sections 5.2.1, 5.2.2 and 5.2.3.

1.4.4 Summary of Modelling Techniques Used

The nine combinations of analysis and modelling types are illustrated in Figure 1.6 and Table 1.2.

The research is directed towards the analysis of three Carter wind turbines. Hence descriptions of these designs have been used as examples of commercial wind turbine configurations and real response data has been collected to validate the modelling techniques. Being soft-soft, guyed structures, the support structures are more complex than for most other wind-farm-sized machines.

1.5 Validating the Models

To ensure the predictions from the various modelling approches described above can be relied upon. comparisons between these and predictions from direct solutions of the equations of static equilibrium or the equations of motion have been made. The simple situations

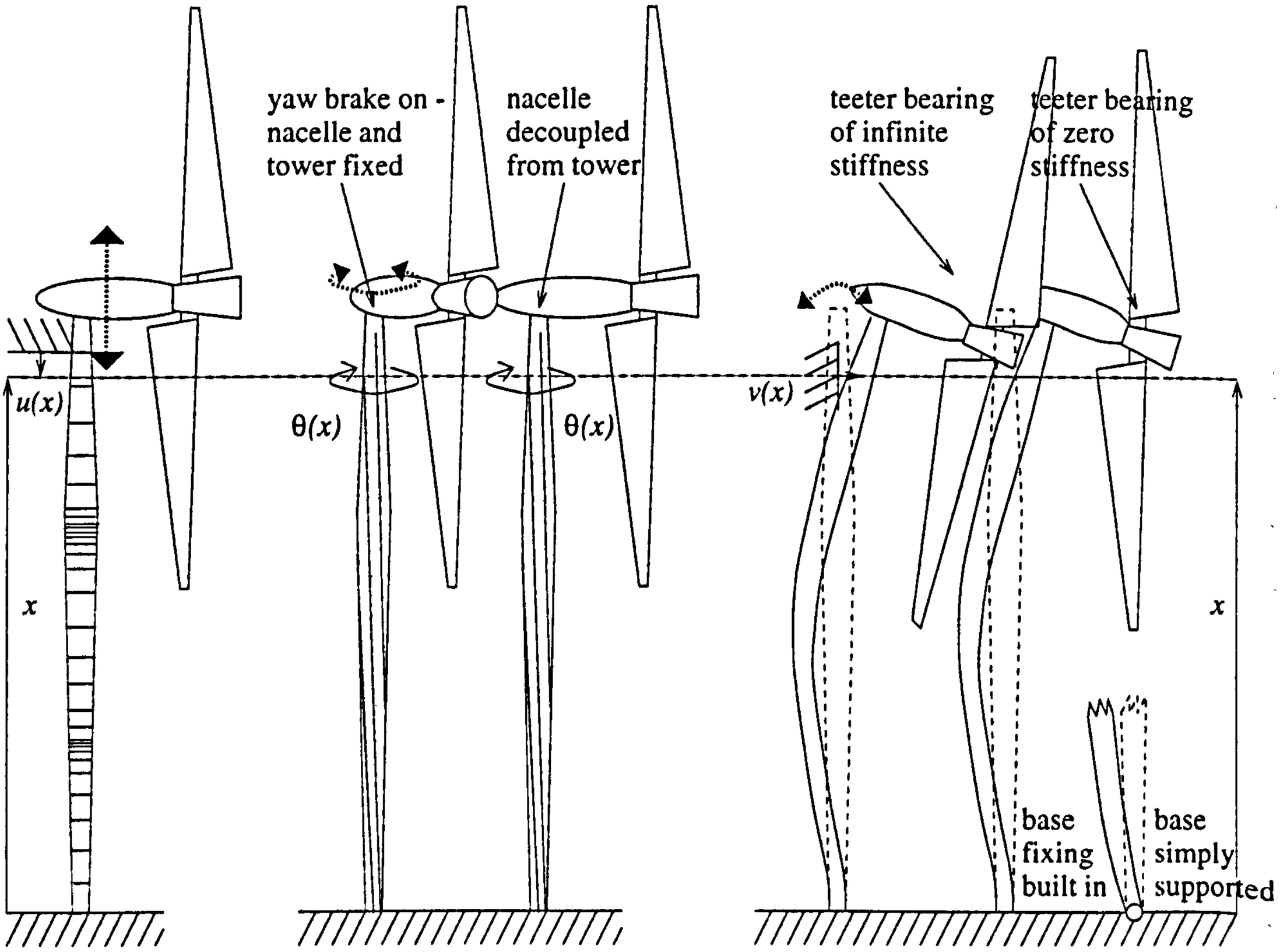

Figure 1.5: The three classes of static deflection and vibration. For this analysis they are assumed to be decoupled. The nacelle may be coupled to or decoupled from the tower top in terms of yaw. The rotor is decoupled from the low speed shaft in terms of shaft bending by the teeter bearing. A parameter for the torsional stiffness of the tower base can be used to define all types of connection from an ideal hinge to an ideal built in or encastré *support. Only planar lateral deflections are considered.*

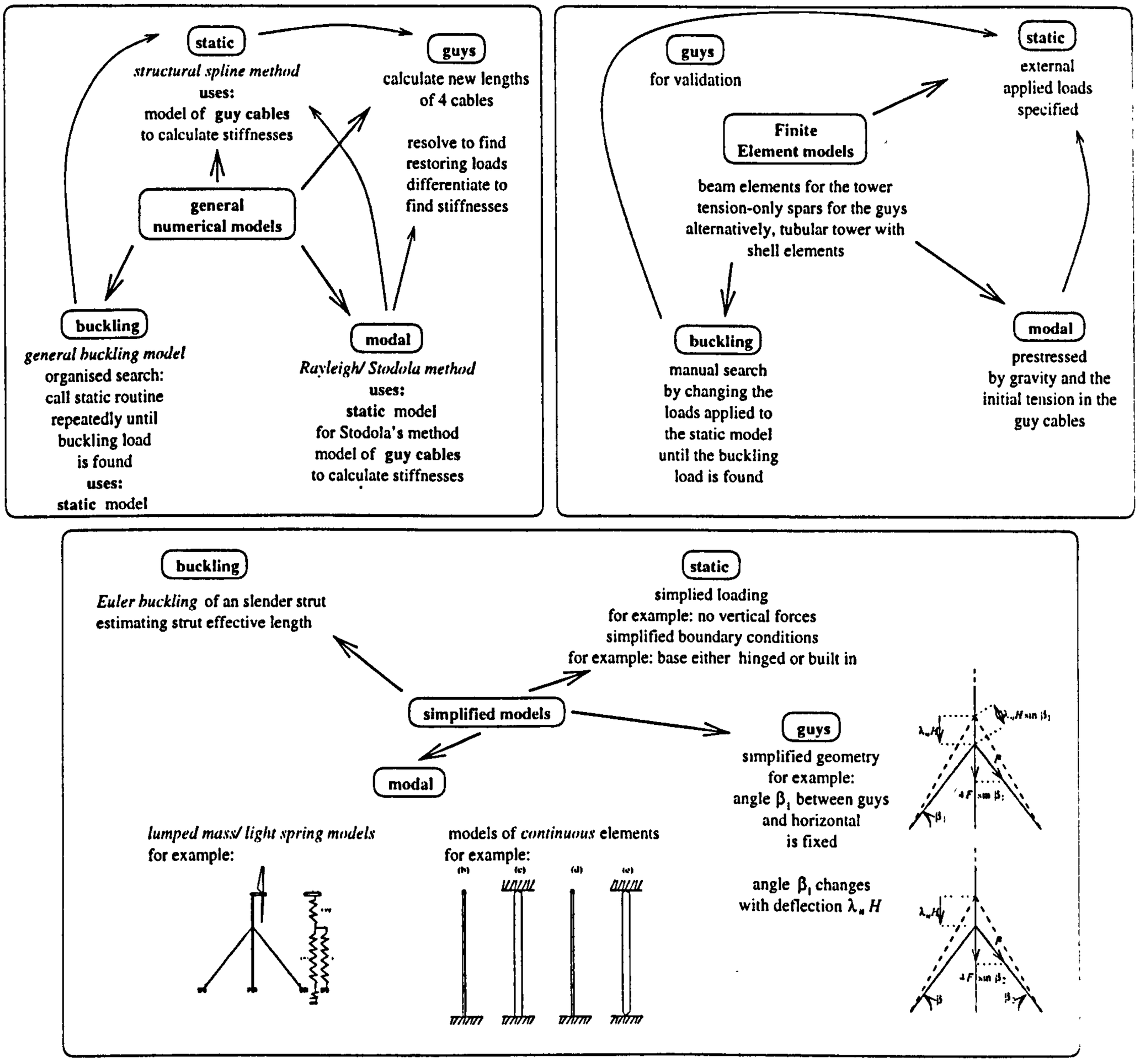

Figure 1.6: The combinations of analysis types and models described in this thesis.

Table 1.2: The occurrance in this thesis of the models and analysis types listed.

1. *general numerical models*
   (a) *structural spline model*
   (b) buckling
   (c) *Rayleigh/ Stodola method*
2. simplified models
   (a) static models
   (b) Euler buckling
   (c) modal analysis
3. Finite Element models
   (a) static analysis
   (b) buckling under axial loads
   (c) modal analysis

Chapter	Section	Model
2		1(a)
3		1(b)
4		1(c)
5	5.1.1	2(a)
	5.1.2	2(b)
	5.1.3	2(c)
	5.2.1	3(a)
	5.2.2	3(b)
	5.2.3	3(c)
7		1 and 2
8		1
9		extending 1

for which such comparisons can be made often do not correspond well to real structural systems, but show that the more general models behave accurately. These tests are reported in Chapter 5 along with comparisons with predictions from finite element models.

It is also important that predictions from any model agree with measurements from wind turbines. This is difficult because of the difficulty of obtaining accurate measurements and also of obtaining accurate estimates of the parameters used in the models to define the physical components. Given these limitations, results from experimental observations are close to predictions from theoretical models.

1.5.1 Experimental Methods

Using a video camera, lateral vibrations of the tower were recorded and later analysed by taking measurements directly off the screen from consecutive still pictures. This method has not been used before for monitoring vibrations of structures. Methods in current use include attaching strain gauges which require either access to the machine prior to installation or considerable disruption of the machine's operation. Strain gauges frequently deteriorate with time. They can become increasingly poorly attached to the surface whose strain they are measuring. They can also yield eroneous readings because of differential heating of the structure. Accelerometers can be used to measure vibrations but they are expensive and also need to be attached to different parts of the machine requiring access to the machine when not generating electricity.

Using just two accelerometers and attaching them to the tower during operation required no disruption of machine operation and so measurements were obtained from three different

variants of the Carter design at sites in Hampshire, Leicestershire and Cumbria. Because the measurements were made during normal operation of the machines, there was no particular excitation of the natural modes of vibration of the tower which had been predicted. Validation of the predictions was attempted by comparison with the spectral response of a point on the tower approximately two meters above the ground.

The experimental methods developed to validate the theoretical predictions are described in Chapter 6 and Appendix G.

1.6 Applications of Analytical Models

Different design approaches affect the various natural frequencies and maximum stresses in different ways. Having validated these models for slender towers, a range of different designs within that class can be compared. Straight, tubular towers may be cheapest to manufacture and even be bought 'off the shelf' but conical towers are lighter for the same load-bearing capability. The towers used for the Carter 300 kW machine are double-tapered which improves performance still further. Increasing the tension in the guys does not normally increase the natural frequencies of the structure because of the close proximity of the cable anchor points to the tower base. The predominant effect is that the increased axial compressive load on the tower *decreases* the overall stiffness of the system and hence its natural frequencies despite the increased lateral stiffness of the system of guy cables. Ultimately, the stiffness of the system falls to zero and buckling of the tower occurs.

The opposite effect to the decrease of tower stiffness due to the axial compression from the guys is the increase in stiffness of the blades caused by centrifugal forces due to blade rotation. The models of lateral vibrations have illustrated this effect and agree closely with conventional *floquet* methods which simplify the differential equations of motion of rotating systems. The results of the survey of the Carter 300 kW wind turbine by Garrad Hassan and Partners [22] are used for comparison.

By changing various parameters such as those which define nacelle mass or tower density, the general models have been shown to map the gradual transition between direct solutions which are available for the pure mathematical approaches at the extremes (Chapter 7).

1.6.1 Optimising Tower Mass

Subject to static design loads, the mass of a wind turbine tower can be optimised using search methods to move through the design space defined by the values of all the design parameters. This is described in Chapter 8. It is important to note that the cost of a whole wind power project cannot be optimised by stress-limited optimisation alone. Alexander Bormann's study of wind turbine costs [23] shows that although the tower material costs comprise over half (56%) of the material costs of the support structure, they account for only about one third of the material and finishing costs of the structure (37%). Although it is not possible to optimise the costs of the project with stress-limited optimisation alone. stress analysis is a necessary *component* of any optimisation.

For instance, the overall structual mass can be minimised by changing parameters affecting the tower geometry. Significant mass reduction can be achieved by curving the sides of

the tower towards the top where the bending moments are lowest. Adding guy cables allows further reduction in tower mass. Not only do the guys carry some of the applied loads, but the base can be hinged reducing bending moments there as compared with a cantilever. The benefits of guy cables are seen most clearly for straight towers. Conical towers may be more efficient if free-standing but are significantly less efficient if guyed because the extra material in the lower portion of the tower becomes unnecessary and under-stressed.

Chapter 2

Static Deformation of Wind Turbine Towers

Static analysis is important to allow the designer of wind turbine support structures to estimate maximum *stresses* carried by various parts of the structure when loads are applied. The largest stresses may be due to static loads such as the thrust or torque on the powertrain when the turbine is generating peak power.

Deflections of the structure may also be of interest. For instance, it is necessary to ensure the blades will not collide with the tower or cables.

The *modal analysis* technique described in Chapter 4 involves static analysis to calculate deflections due to inertia loads. It is possible that *stresses* occurring momentarily during vibration of some part of the structure will be larger than stresses occurring due to loads which last relatively longer. *Fatigue analysis* also requires detailed knowledge of modal vibrations.

The tower may *buckle* under excessive vertical loads applied where either the guys or nacelle are attached. This is considered in Chapter 3. The external load at which part of the structure buckles is estimated by successive static analysis of the structure.

A mathematical model of a structure requires various assumptions. Some are standard for classical structural analysis. Others have been adopted here to ensure that mathematical solutions are possible.

The complete *numerical method* for calculating static deflections has been tested in several ways, as described in Chapter 5.

- The simplest structural systems are analysed and results compared with standard solutions to the differential equations of equilibrium.

- More lifelike and complex structural systems are analysed using both Finite Element Methods and the *general, numerical model.*

- *General, numerical models* of real systems are analysed and results compared with data collected from three operating wind turbines.

The three operating wind turbines from which data have been collected about their dynamic behaviour illustrate design configurations that have been implemented. Parameters necessary to model these designs have been measured or obtained from drawings.

Photographs of the three machines studied are shown in Figure 2.1.

Figure 2.1: The three wind turbines studied: the Carter 300 kW machine at Great Orton Airfield (50 m tower), the Carter 300 kW machine at Faccombe Estate (39 m tower) and the Carter 25 kW machine at West Beacon Farm (15 m tower).

2.1 Assumptions About Static Structural Response

In this section are listed the assumptions which underpin the *general, numerical model* of static deformations of wind turbine towers described in the rest of this thesis.

The deflection of a wind turbine tower under various loads can be calculated using *small deflection theory* [24], which assumes that:

- the strain in the material does not exceed the yield strain,
- plane cross-sections remain plane (without warping),
- the tower deforms in response to bending moments only, no shear deformation is considered,
- small angle approximations to trigonometric functions and calculus are accurate (for example, $\sin(\theta) \approx \theta$ and chord subtended by angle differential element $\approx r\delta\theta$).
- 'nominal stress' and 'nominal strain' [25] are acceptable approximations to true stress and strain.

The static analysis techniques do not include coupling between lateral, longitudinal and torsional deformations. Because the same techniques are used for modal analysis, there is therefore also no coupling between modes (see later, Figure 4.2 in Section 4.2). The only coupling modelled is between longitudinal deflections and lateral deflections. If the tower design includes guy cables, the longitudinal deflection of the tower changes the length of the

cables and hence their elastic stiffness. As described in Section 2.2.3.1, this modification is small and so is deliberately neglected for modal analysis.

In the models described, it is possible to specify the torsional stiffness, k_{Bf} of the foundation for analysis of tower bending. However, it has not been possible to measure this parameter for any of the machines studied. This thesis reports comparisons between the two extreme cases in which the base is either 'hinged' or 'built in' (see Glossary for definitions). Lateral deflections in the two orthogonal planes are considered uncoupled (see Figure 2.2). The two extreme cases of boundary conditions at the base are considered separately (see Section 2.2.2). On real machines, the two planes are not identical. As well as the base, the guys are not identical. On the Carter family of machines, one guy carries a winch at one end so that the whole structure may be raised or lowered for maintenance. Although no coupling between the two planes is modelled, in real life, there may be the possibility of material inhomogeneities or slight geometric imperfections in the tower which transfer forces between the two planes. Lateral deflection of the structure in planes other than those including the guy cables are not considered here.

Lateral deflections are estimated assuming pure bending. No shear deformation is considered. For modal analysis using the *Rayleigh/ Stodola* method proposed here, it is necessary to calculate strain potential energy having calculated tower deflections (see Section 4.3 later). If the deflection has been calculated by the superposition of shear and bending deflections, it is impossible to calculate the strain potential energy accurately because the relative magnitudes of the two components cannot later be deduced in order to calculate the two strain potential energy terms. It can be shown [24] that shear deflections are only significant in short or wide structures.

Three classes of deformation are considered independently. Lateral deflections will be described first and in most detail. Calculating longitudinal deflections is similar to calculating torsional deflections, but, unlike for lateral deflections, there are no loads which are proportional to height.

2.2 Parametric Models of Structural Components

2.2.1 The Tower

Carter wind turbines have towers which are either eight- or twelve-sided, tapered. galvanised steel tubes. Additionally, the tubes are fabricated in several pieces. Assembly is by slotting adjoining pieces together. Friction at the sliding surfaces and the weight of the structure above the joint stops the pieces sliding apart. On each side of each junction between tower pieces. there is a hole to fasten a winch which forces the pieces together compressing the junctions (see Figure 2.4).

For this research, the cross-section is modelled as circular to simplify the analysis. It is therefore possible to use the same basic parameters to represent many similar designs all of which are approximately circular in cross section. Where a particular tower is not circular. there may be some coupling. for instance between torsional and bending deflections. This effect. called *flutter* occurs sometimes in aircraft wings and was the cause of the collapse of the Tacoma Narrows suspension bridge. Approximating the cross section as circular as is

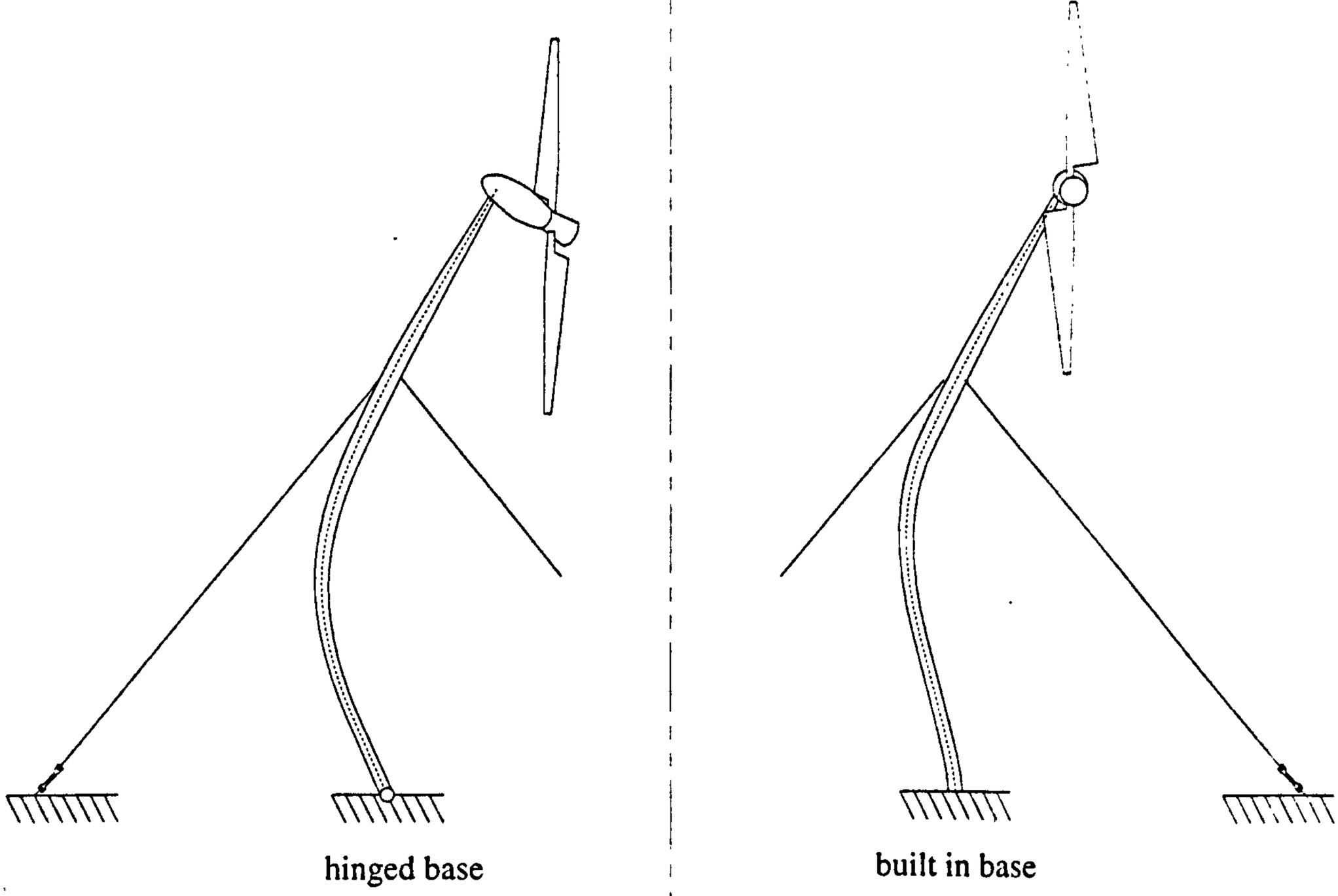

Figure 2.2: The two orthogonal planes considered for lateral deflections. Flexibility in the mechanical hinge at the base of assembled machines leads to less rigidity in the plane of lateral deflections parallel to the axis of the hinge than if the base had been ideally built in *(see the Glossary, for an explanation of beam boundary conditions). The designers of the Carter 300 kW machine give assurances however, that the tower can be treated as pin-jointed in both planes. The layouts of the base hinges of Carter 25 kW and 300 kW machines are different and are illustrated in Figure 2.8. In this figure, the nacelle and rotors are shown both aligned normal to the tower base hinge axis.*

Figure 2.3: When lowered to the ground, the nacelle of the Carter 300 kW wind turbine at Great Orton Airfield rests on its two 12m rotors.

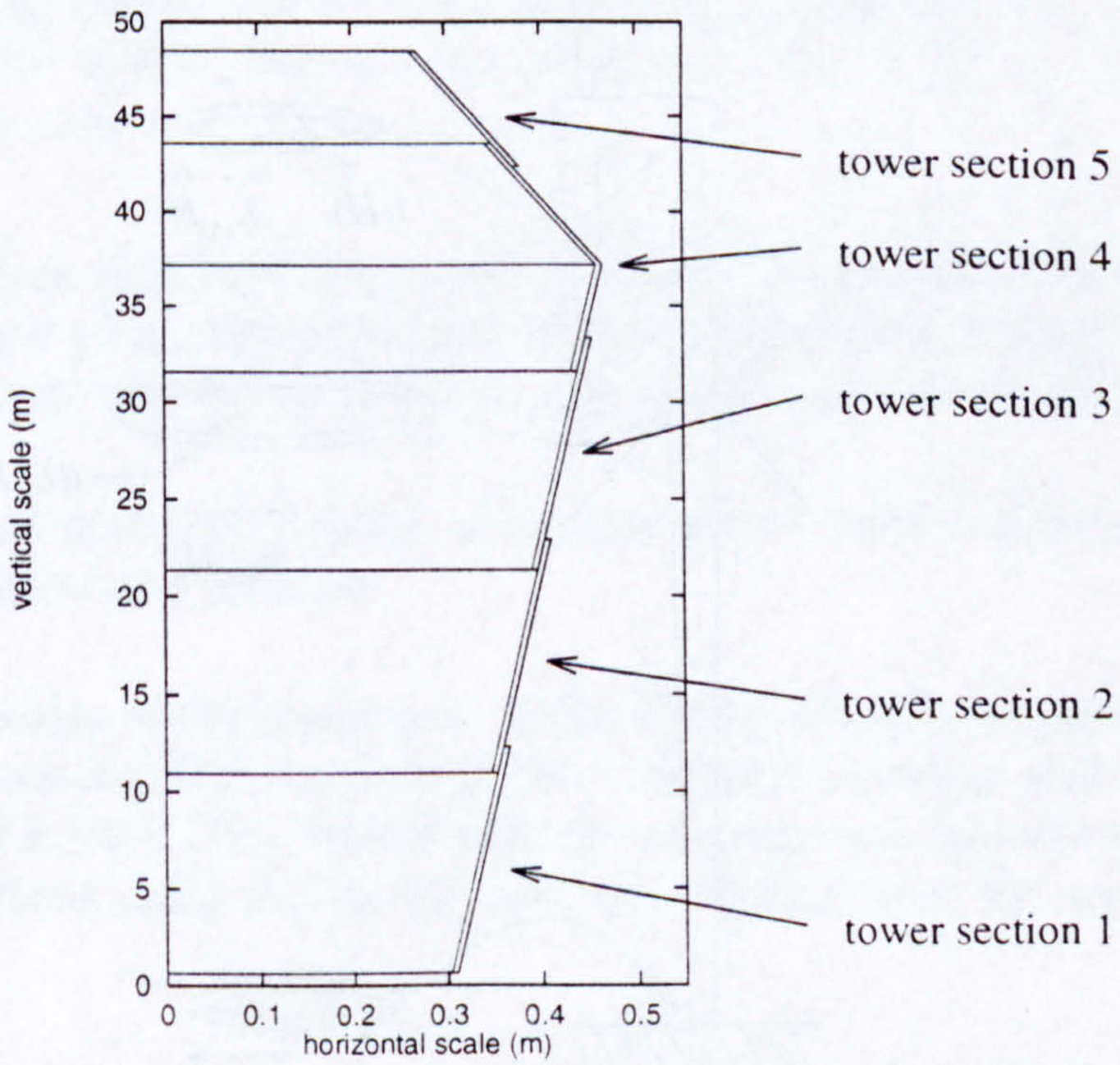

Figure 2.4: A vertical cross-section through the tower showing the variation of outside radius and wall thickness with height.

done here, may yield misleading results. This is particularly the case when modelling blade vibrations (see Section 4.7.4).

It is straightforward to use the techniques described in Chapters 2, 3 and 4 to analyse any general tower for which the radius of the cross section is defined at many points up the tower. However, Carter wind turbines use towers which are conical or double-tapered and so may be described more succinctly by just three radii (see Figure 2.5). The rate of change of the tower radius with height changes at the point of attachment of the guy cables. All geometric properties of the tower depend on the wall thickness and external radius. In the Carter tower, steel plate of two different tower wall thicknesses is used: 6.35 mm for sections 1, 2 and 3 and 7.14 mm for sections 4 and 5. In this model, the average thickness is used throughout to eliminate discontinuities which make integration unnecessarily complicated.

Other properties such as elastic modulus and density have been considered constant. All these properties are defined as functions for which the only argument is dimensionless tower height. This means that, to make the *numerical methods* more general, it is possible to specify properties as new functions of height. This gives complete control over the precise way these quantities vary with height. Section 8.3.1 suggests uses of software described in this thesis to optimise the tower design by seeking optimum values of the design parameters such as tower outside radius and wall thickness.

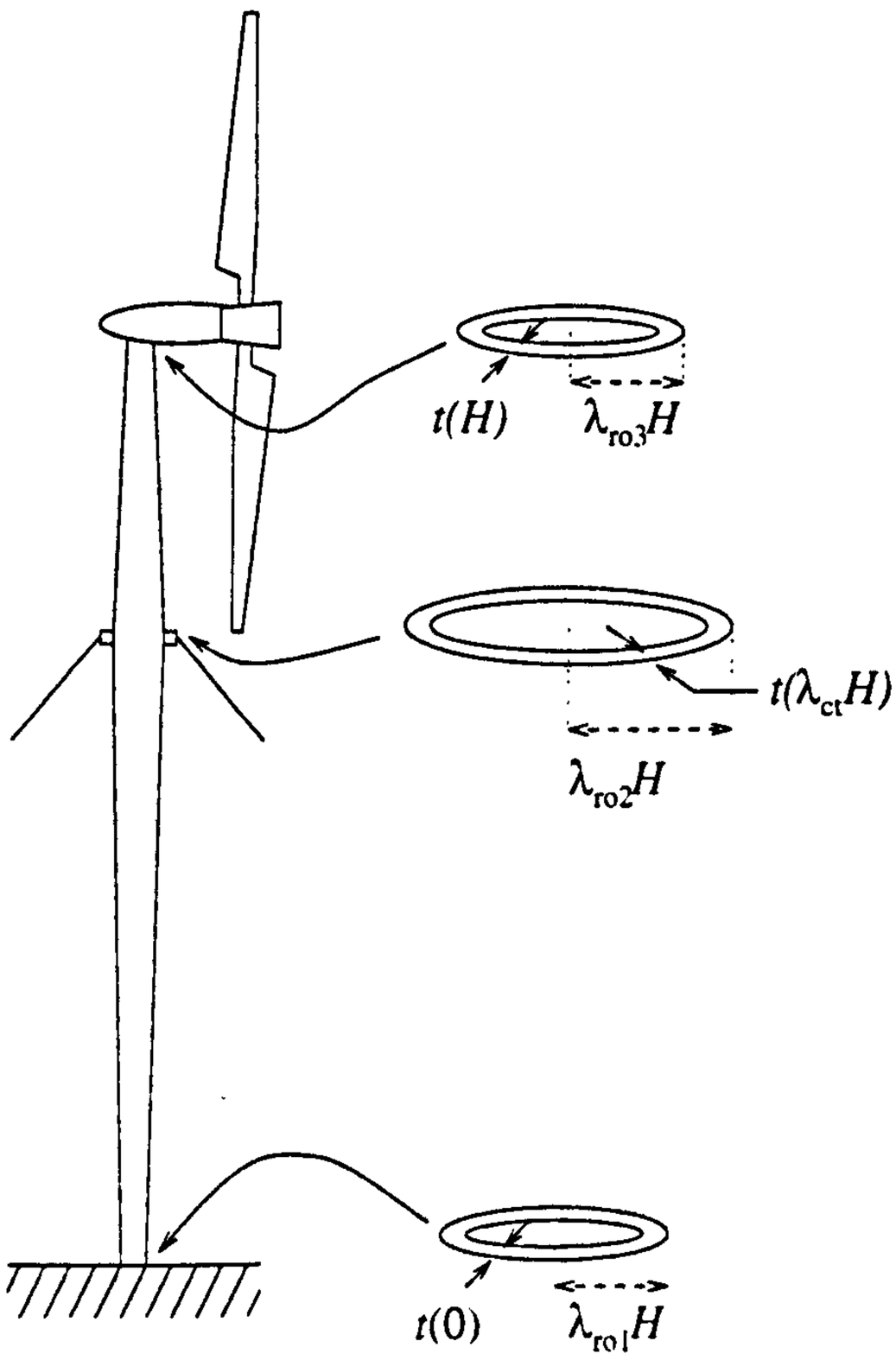

Figure 2.5: The double-tapered tower used for the Carter 300 kW wind turbine. The key positions at which the tower cross section is defined are shown.

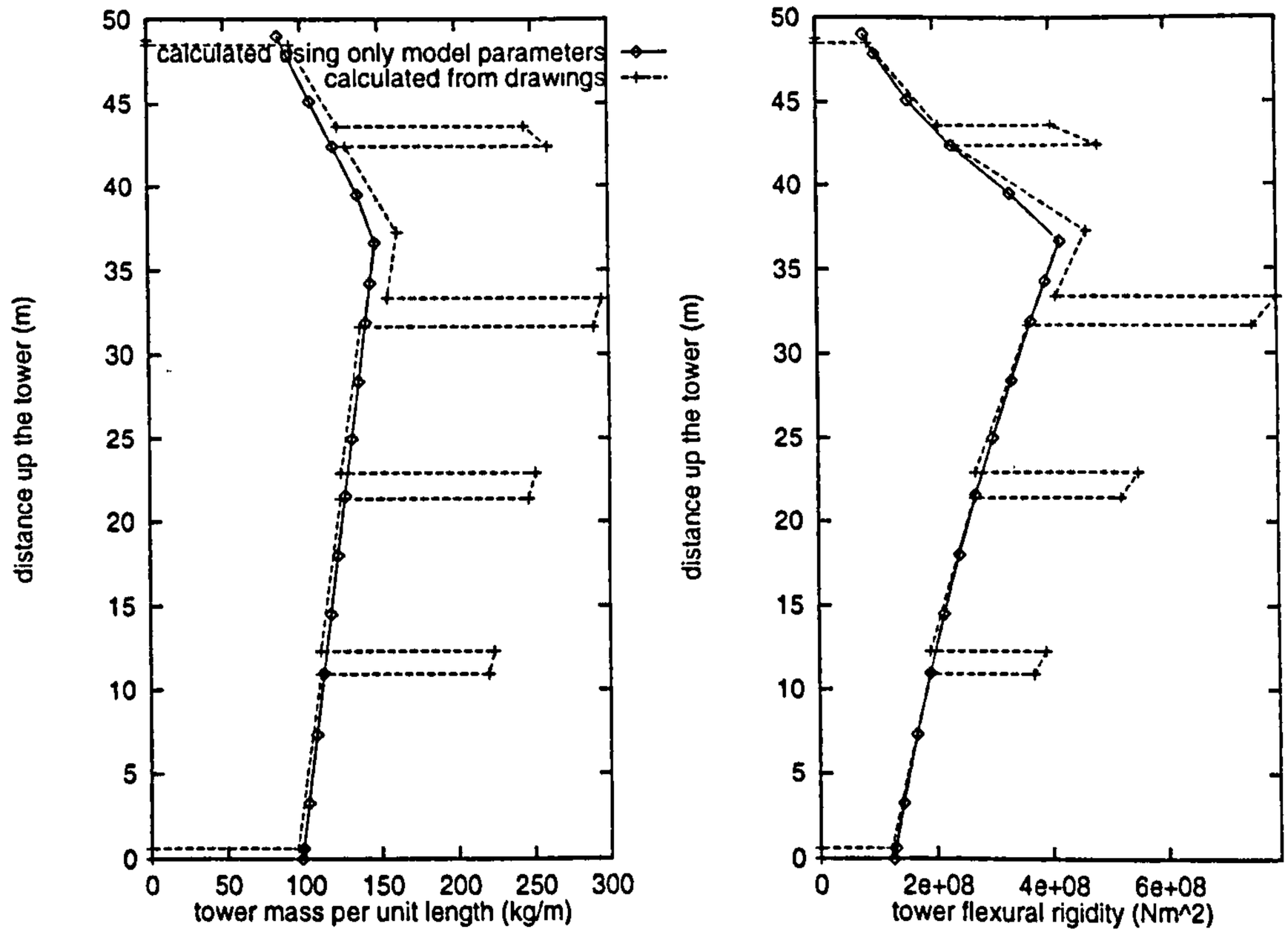

Figure 2.6: The real variations of tower mass and stiffness. The doublings occur because the tower is assembled by sliding one section inside the adjacent section and compressing the junction. On each set of axes, two graphs are drawn. The first represents values of the mass or stiffness of the real tower calculated using diameters and thicknesses taken from drawings. The second represents the mass or stiffness calculated using only the parameters used by the numerical model *(diameters used have been taken off the drawings but average thickness values are used).*

The tower thickness is modelled as constant with height despite the fact that tower pieces slide one into another giving rise to local doublings in thickness (Figure 2.6). In Figure 2.6, there are three differences between the data used for the numerical model and the real data:

1. The tower wall thickness doubles in regions where tower sections overlap leading to doublings in mass and stiffness.

2. The wall thickness of the tower used in the Carter 300 kW machine is different for the top two sections than for the bottom three sections. Average wall thickness is used in the numerical model. This means that the average area and average second moment of area calculated using the model data are different from the average values for the real tower.

3. The tower base is 24" above the ground because of the base hinge mechanism and the nacelle centre of gravity is 20" above the top of the tower. In the model. the tower extends. unbroken, between the ground and the nacelle centre of gravity.

2.2.2 Tower Base and Foundation

Where end conditions are described, the terms *base* and *base fixing* include the connection at the tower base (for Carter machines, a mechanical hinge welded to the tower, Figure 2.8), the reinforced concrete foundation and the surrounding ground. Mathematical symbols incorporate the subscript f to denote this tower foundation boundary. To model this *base fixing*, elastic stiffness parameters are defined. In practice, it is difficult for the designer either to implement these parameters in a new design or to measure them once the wind turbine has been installed. Often, extreme limits must be used to obtain upper and lower bounds for the analysis solutions sought (for instance, $k_{Bf} = 0$ or $k_{Bf} = \infty$).

For use in the static analysis of compression, torsion and bending of the tower, the four equivalent stiffness parameters (k_{Cf}, k_{Tf}, k_{Bf} and k_{Lf}) are calculated. Figure 2.7 shows all these stiffness parameters defined for the *base fixing*.

In general, forces are proportional to linear deflection (Equation 2.1) and torques are proportional to angular deflections (Equation 2.2).

$$F = k_{lin} v \tag{2.1}$$

$$Q = k_{tor} \theta \tag{2.2}$$

$$\tag{2.3}$$

For small angles, θ (lateral deflections, v for example) the angle is approximately equal to the gradient of the deflection.

$$Q \approx k_{tor} \frac{dv}{dx} \tag{2.4}$$

Wind turbine tilt-down towers are secured to a concrete foundation block via a hinge which is designed to tilt smoothly about one axis to raise or lower the wind turbine. In terms of tower vibrations, this mechanism probably does not constrain the base of the tower much about the other axis either. This is the claim of the manufacturer. However. there probably is some difference between the base torsional stiffnesses for bending, k_{Bf} in the two orthogonal planes (see Figure 2.7), depending on other properties of the structure. The base bending stiffness parameter of the base is zero if the base is a frictionless hinge and infinite if the tower is rigidly joined to the ground (as many free-standing towers are). Setting these two extremes results in upper and lower bounds for the lateral deformation or the lateral modal frequency of vibration. It is also possible to compare frequencies of transverse tower vibration in two perpendicular planes with slightly different base stiffnesses (Figure 5.2 shows the effect on the static deflection of values of k_{Bf} between 0 and 1×10^{12}).

In order to tilt down the entire tower the Carter wind turbine has a 'gin pole' which is attached to the tower base. On small machines such as the 25 kW machine studied. the gin pole is welded directly to the tower and so affects its static and dynamic response (see Figure 2.8). For larger machines, the gin pole is freely hinged on the same hinge shaft as the tower. It is also likely that k_{Bf} is different in the two planes of lateral deflection in the case of the 25 kW machine because the base plate pin connects to the tower via closed holes. The 300 kW machines use slots.

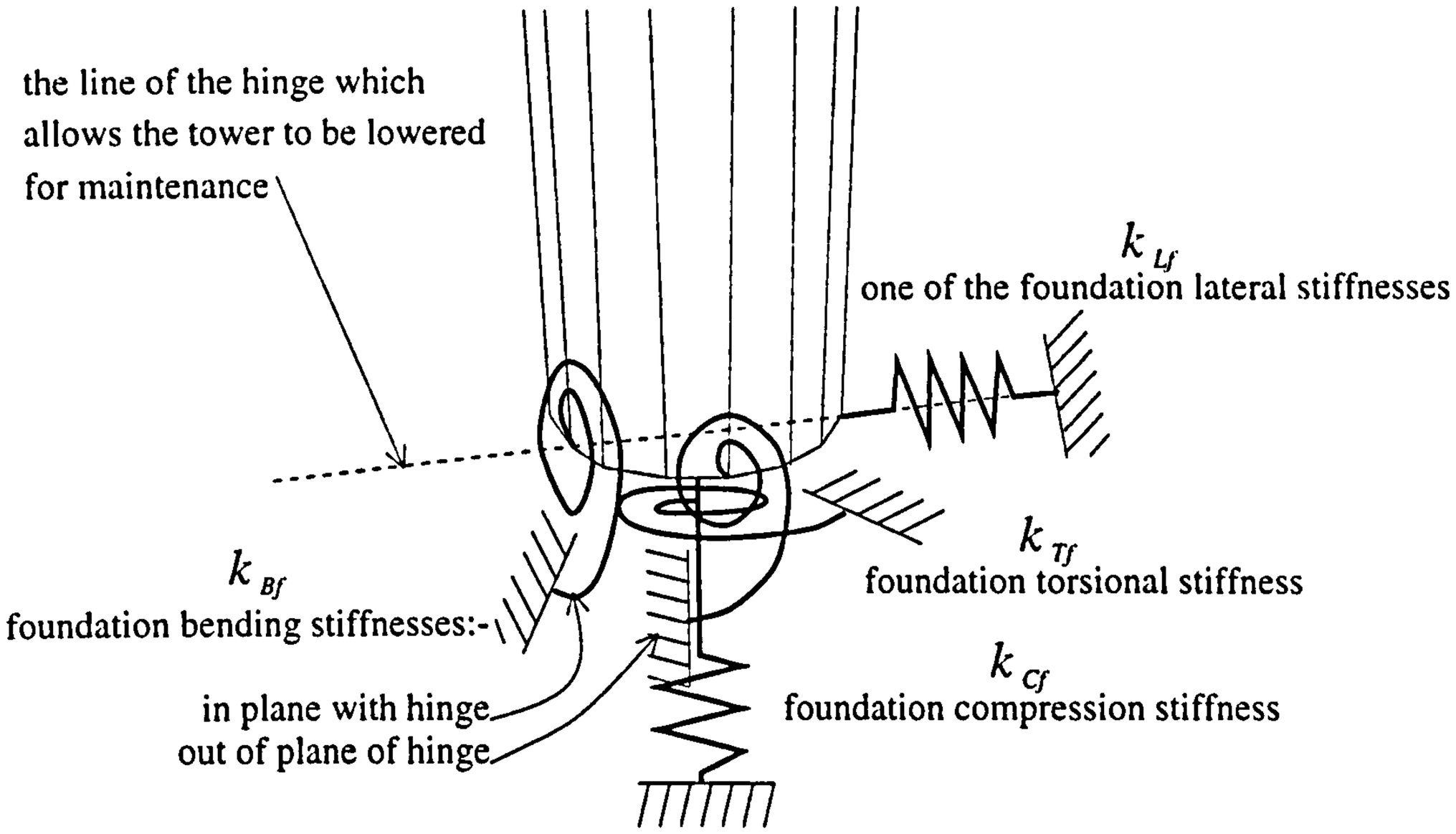

Figure 2.7: Parameters defining the rigidity of the base fixing. *Since lateral tower vibrations in orthogonal planes are modelled as uncoupled, an independent set of stiffness parameters (k_{Lf} and k_{Bf}) can be defined for each plane. In order to simplify the figure, only one lateral stiffness parameter, k_{Lf} is shown although both base bending parameters are shown.*

2.2.3 The Guy Cables

The cables are treated as linear elastic stiffness elements modelled by the equivalent stiffness parameters (k_{Bc}, k_{Cc} and k_{Tc}). It is assumed that they are always taut. This is essential if vibrations are to be treated as linear. These are the same assumptions made by Thresher et al in 1981 [26]. Both Thresher and Skop in 1979 [27] calculate cable stiffness parameters by vector algebra and linearisation near to equilibrium. In this thesis, stiffness parameters are calculated by numerical differentiation of restoring forces with respect to deflections of the point of attachment of the guy cables. The advantage of this method is that the method for calculating restoring forces can easily be changed without modifying the code for calculating cable parameters.

Methods for modelling guy cables so as to include both the elastic properties of the cables and the gravity and aerodynamic loads were proposed by Skop and O'Hara in 1970 [28] and by Peyrot and Goulois in 1979 [29]. Peyrot and Goulois' method has been used to obtain a force/ deflection curve. Given a set of end loads and distributed loads, the positions of the ends and the shape of the cable may be calculated. The iterative technique proposed by Peyrot and Goulois for finding which end loads are necessary to close the gap between the prescribed coordinates of the anchor points and the ends of the cable worked well in situations in which the cable was taut or slack. However, convergence was not achieved in situations close to slackening of the cable. Skop and O'Hara's 'Method of Imaginary Reactions' [28] has not been attempted during the course of this research. It has been found that once the cable has gone slack, the relative drop in the restoring force from a single cable

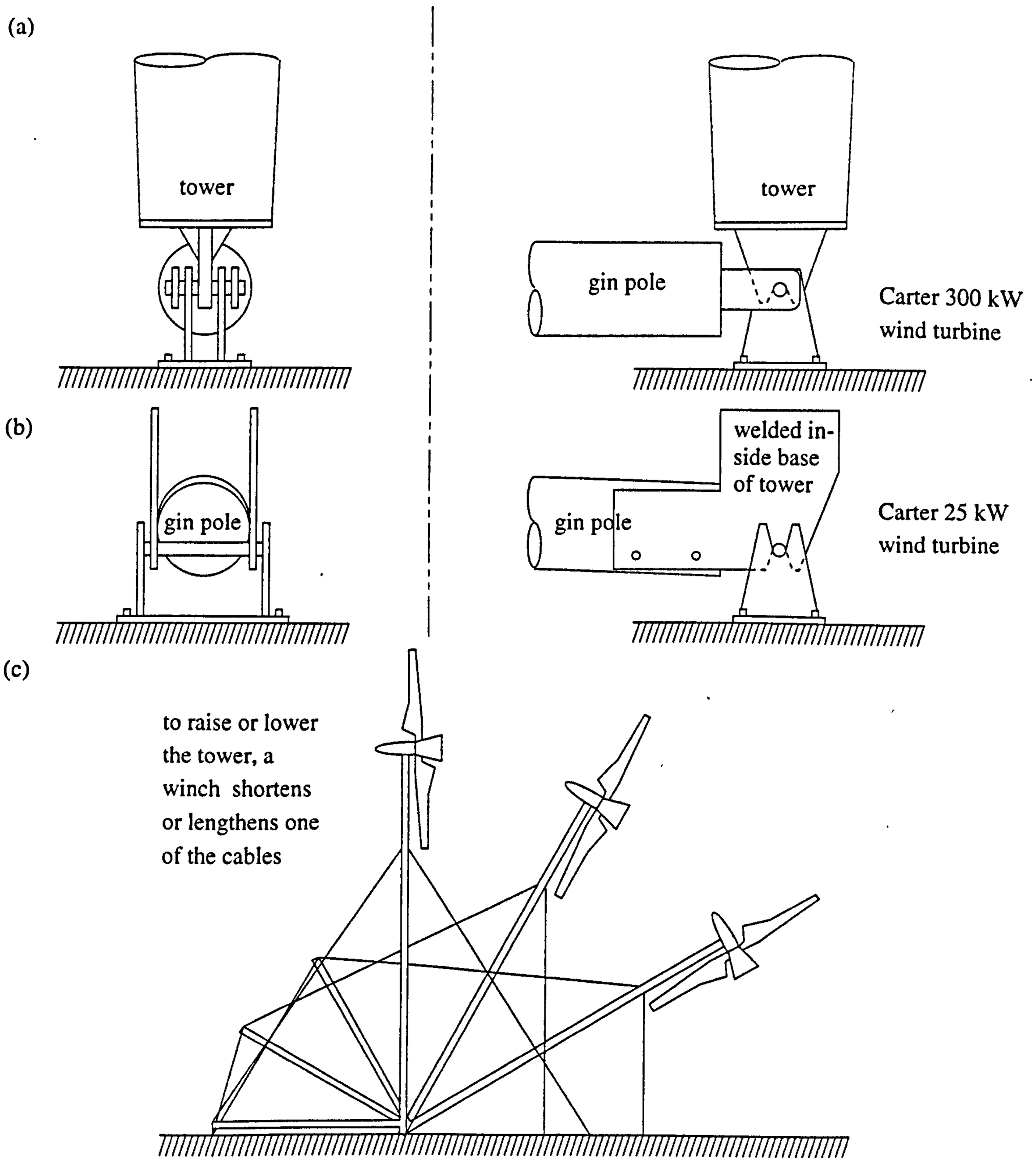

Figure 2.8: The layout of the base hinge showing where the gin pole joins the tower. (a) Carter 300 kW machine, (b) Carter 25 kW machine. (c) When the tower is raised or lowered, this pole carries the guy cable connected to the winch.

is so great that it was decided that a linear model would be adequate. A numerical method for the dynamic analysis of such a cable model which can be subjected to aerodynamic loads was proposed by N. Ben Kahla in 1995 [30]. The mass of the cable is lumped at discrete points along its length.

To calculate the guy cable stiffness parameters for this research, the tension in the cables was calculated for different deflections of the point of attachment of the cables to the tower. Given the tension in each cable, the reaction of the set of cables can be calculated aligned to the axes of the tower coordinates system. Reaction loads considered are a vertical force F_{cv}, a horizontal force F_{ch} and a torque, Q_{cv}. The torque, Q_{ch} about a horizontal axis is assumed negligible. By calculating an array of reaction loads for an array of deflections, three stiffness parameters ($k_{Bc} = \frac{dF_{ch}}{dv}$, $k_{Cc} = \frac{dF_{cv}}{du}$ and $k_{Tc} = \frac{dQ_c}{d\theta_c}$) are calculated for use in static analysis of tower compression, bending and torsion. Equations B.4 to B.18 define the method by which these reaction loads are calculated. Because the reactions are calculated afresh for each deflection, the non-linear variations of restoring loads and stiffness parameters with deflection can be illustrated (see Appendix B). Also in Appendix B, the numerically derived stiffness parameters are compared with parameters derived by algebraic analysis of a simplified system. The more general numerical methods show non-linear behaviours such as deflections at which one or more of the cables goes slack.

The parameter defining guy cable pretension in both the Finite Element software and algorithms described in this thesis is the initial strain ϵ_{ic}. It is the strain in the cables at assembly before any tower deformation and is defined by Equation 2.5 which is a simplification of the equation for the true (logarithmic) strain in the guy cables. The geometry of a single guy cable attached to the tower is shown in Figure 2.9.

$$\begin{aligned} \epsilon_{ic} &= \log\left(\frac{\sqrt{\lambda_{ct}^2 + (\lambda_{cg} - \lambda_{ro2})^2}}{\lambda_{cn}}\right) \\ &\approx \frac{\sqrt{\lambda_{ct}^2 + (\lambda_{cg} - \lambda_{ro2})^2} - \lambda_{cn}}{\lambda_{cn}} \end{aligned} \tag{2.5}$$

Once assembled, the combination of the gravity forces on the tower and the axial compression due to the guys compress the lower section of the tower which deflects vertically a little, relieving the stress in the cables. Before any further analysis, the vertical deflection at which the stresses in the tower and the guy cables are in equilibrium is sought using the iterative process shown schematically in Figure 2.10.

The iterative method has been chosen because of its generality. An alternative approximation would be to calculate an equivalent vertical stiffness for the tower and find the intersection of the two approximately straight lines shown in Figure 2.11.

Three factors give rise to slight non-linearities of the lines in Figure 2.11.

1. the variation of vertical forces on the tower with height:
2. the variation of tower geometry with height;
3. the non-linearity of the cables.

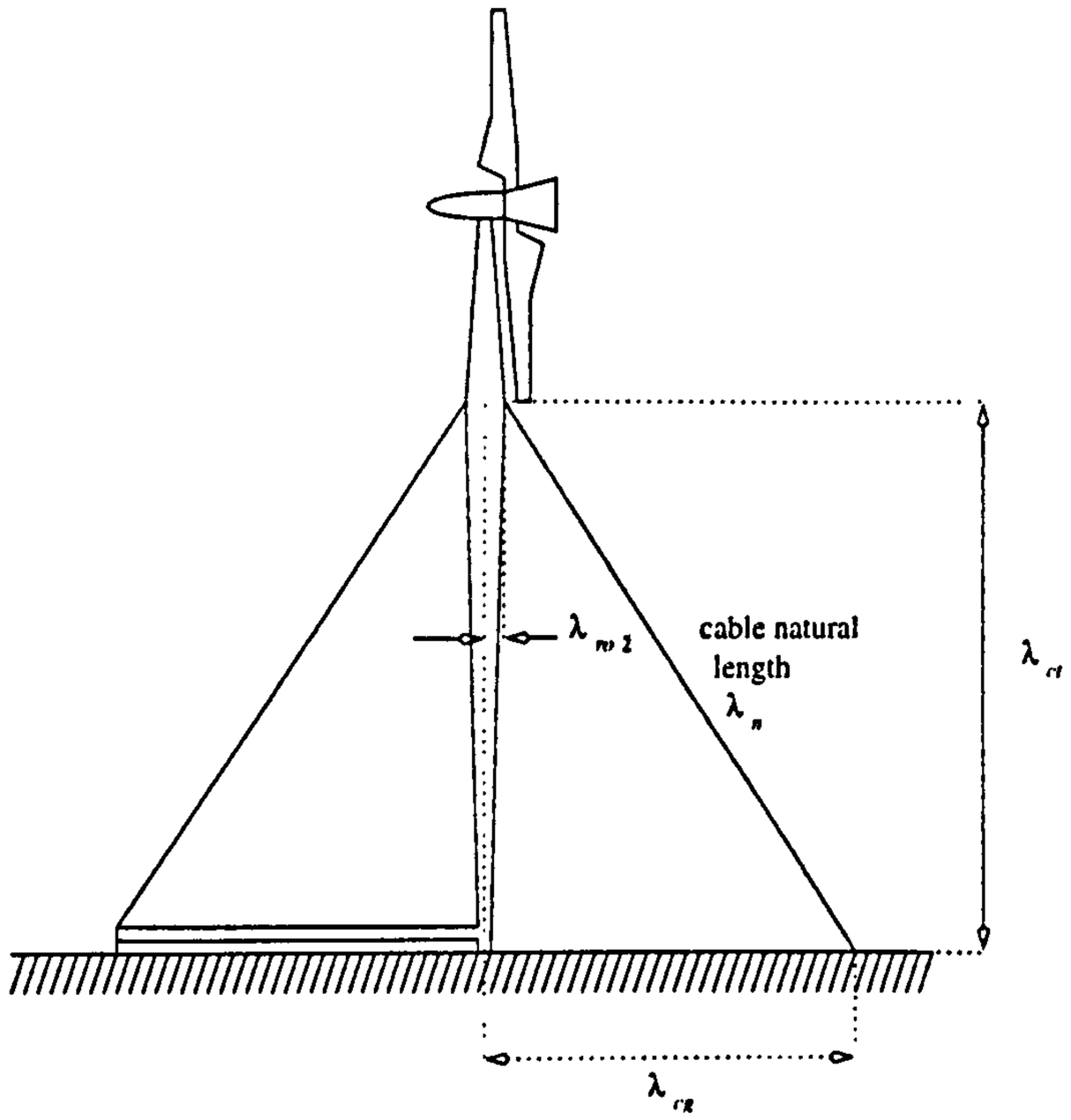

Figure 2.9: The geometry of a single guy cable attached to a tower of the kind used for the Carter 300 kW wind turbine. The parameters shown enable the initial strain parameter ϵ_{ic} to be calculated using Equation 2.5.

Because the only vertical force on the tower which varies with height is due to gravity and this is small compared to the compressiveforce from the guy cables, (1) is negligible. Because for the Carter 300 kW wind turbine, the taper in the tower is only slight, (2) is negligible. Because the cables are made of steel and initial strains are small and positive, (3) is negligible provided the cables do not go slack. For these reasons, it would be reasonable to linearise the initial straining of the system in this particular case. In practice, the result of this nearly linear situation is that two iterations round the central loop shown in Figure 2.10 are adequate for convergence. The final stage is to calculate the particular stiffness parameter required for the analysis (either k_{Bc}, k_{Cc} or k_{Tc}). The axial compression in the tower (F_{cv}) is also obtained from this procedure. It too is assumed constant for small lateral and torsional tower deflections.

For example using data for the tower used in the Carter 300 kW wind turbine of the type used at Great Orton airfield and initial strain parameter ϵ_{ic} of 0.0005 the equilibrium calculation reveals that this falls to 0.000430 after assembly because of a vertical tower deflection of 0.00328 m at the point of attachment of the guy cables (see Figure 2.11).

Figure 2.11 shows that deformation of both the guys and the tower must occur for the structure to be in equilibrium. To generate the two curves on the illustration, models described in this thesis were used. The curve for tower deflections was obtained by changing the force. F_{cv} applied to the tower and using the static model of the tower (Section 2.3) to calculate the vertical deflection. The curve for vertical deflections of the point of attachment of the guy cables was obtained by changing the vertical deflection of this point and calculating

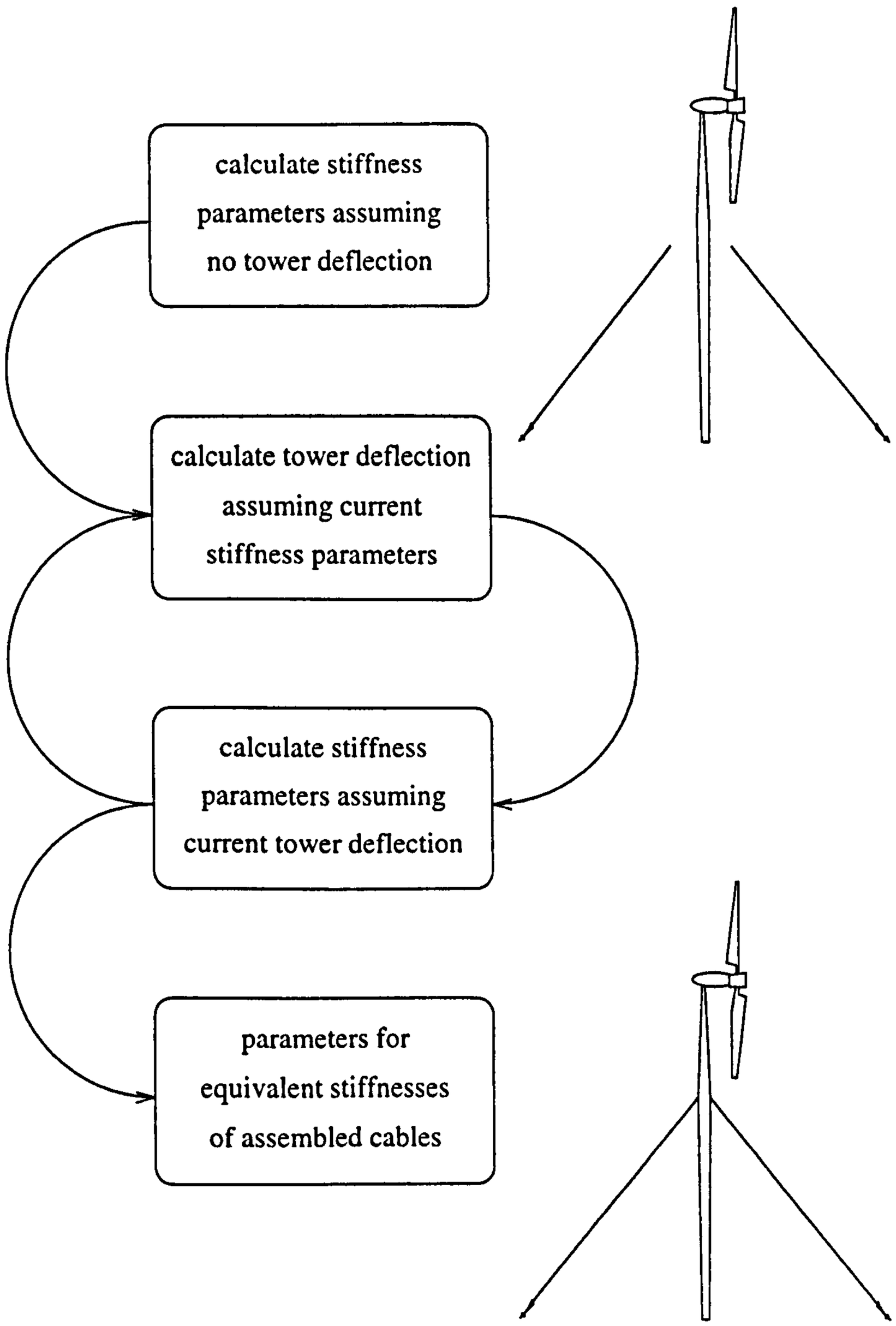

Figure 2.10: Iterative loops to find the equivalent stiffness parameters and axial compression in the tower due to the guys.

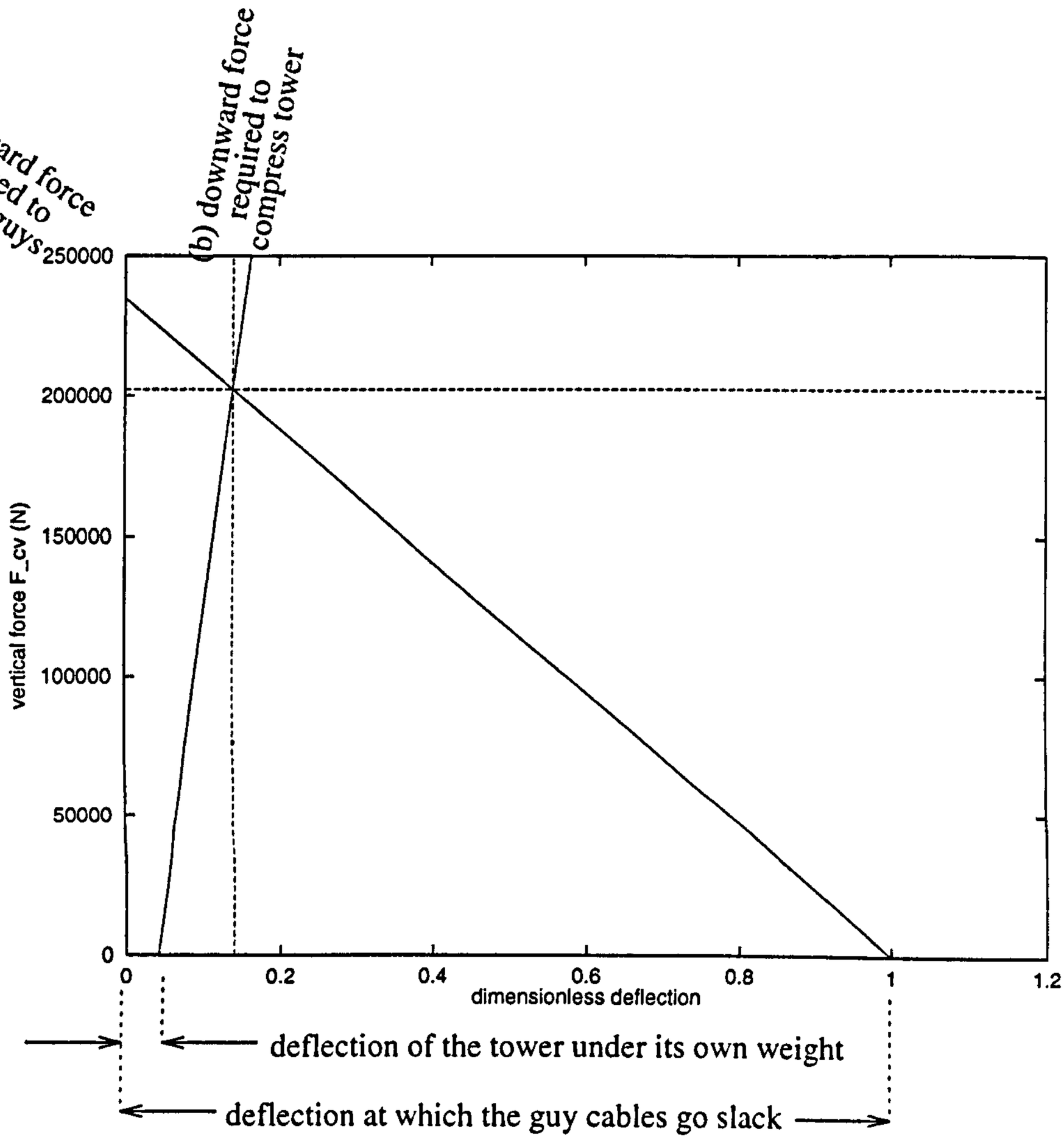

Figure 2.11: The variation of the vertical force F_{cv} with vertical deflections of either (a) the shared point where the four guy cables meet or (b) the point on the tower to which the cables will be joined. In the curve of tower deflections (b), F_{cv} is the force applied to the tower (downwards is positive). It is the deflection, u which is the dependent variable. The weight of the tower is a load which always acts on the tower, so the deflection of the tower is not zero when $F_{cv} = 0$. In the curve of guy cable deflections (a), F_{cv} is the dependent variable and is the force necessary to extend the cables (upwards positive). Horizontal deflections are measured relative to a point on the tower before assembly and are scaled by the deflection necessary to slacken the cables (0.0235 m). The initial strain in the guy cables ϵ_{ic} is 0.0005. In addition to the elastic curves for the tower and guy cables, horizontal and vertical lines are plotted which cross at the equilibrium point calculated using the iterative method illustrated in Figure 2.10.

the vertical force by resolving the four cable tensions along a vertical axis (Section 2.2.3 and Appendix B). The curve for tower deflections is almost linear.

The stiffness parameters, k_{Cc}, k_{Bc} and k_{Tc} are assumed constant for all small deflections. In Appendix B, Figures B.4, B.7 and B.10, show that this assumption is reasonable. However. for torsional deflections of the tower used in the Carter 300 kW machine, it is shown that deflections greater than $\pm 0.058\pi$ rad ($\pm 10.8°$) increase the stiffness parameter by 50% of its equilibrium value. Linearisation of the force/ deflection relationship therefore seems tenuous. However, the potential energy stored in the guy cables is typically small compared to other potential energy terms for the vibrations. Also, provided vibrations are small in amplitude and the initial strain in the guy cables is small but adequate to ensure that the cables do not go slack, the approximation is valid.

Lateral deflections of the tower depend on both horizontal and vertical forces as well as torques. For small lateral deflections, the axial force F_{cv} in the tower from the guy cables is assumed constant. The variation of F_{cv} with v shown in Figure 2.12 supports this assumption. While both cables are taut, the increase in tension in the left hand cable due to deflection of the tower to the right balances the decrease in tension in the right hand cable. As soon as the right hand cable slackens, the increase in tension in the left hand cable is not balanced and the axial force F_{cv} on the tower rises significantly.

The lateral stiffness parameter k_{Bc} for use with tower bending is assumed constant with vertical deflection of the point of attachment of the guy cables to the tower. This variation is shown in Figure 2.13). The scale on the vertical axis of the upper illustration in Figure 2.13 is displaced to show the small reduction of k_{Bc} prior to the cables going slack. If the vertical deflection of the tower exceeds the deflection u_{c0} necessary to make the guys go slack, either during static analysis of gravity and guy loads or in a subsequent static analysis of applied loads, the analysis is repeated with $k_{Bc} = 0$. For modal analysis, the guy cable parameters are either:

1. 0.0; if the cables go slack during any part of the initial static analysis (see Figure 2.10) or

2. constant; the cables are assumed to remain taut during vibrations.

Both static analysis and modal analysis of the structure relies on the assumption of small deflections. The data used here are for the Carter 300 kW machine of the type used at Great Orton Airfield.

After lateral deflection or torsion of the tower under the applied loads, the guy cable strain will increase, increasing the axial load on the tower and the vertical deflection of the tower and decreasing the stiffness equivalent to the cables. This effect is assumed to be insignificant. The variation of the axial force F_{cv} on the tower with torsional deflections θ in Figure 2.14 shows that in fact, the compressive force increases considerably with angular deflections. For large deflection angles (up to $\pm\frac{\pi}{2}$ rad), there are large increases in compressive force on the tower (up to 10× the equilibrium value).

It is also assumed that the effect of the force on the tower normal to its surface (see Figure 2.15) is negligible. This depends on modulus and geometry of the tower material which affect any deformation of the tower cross section. In all Finite Element models in

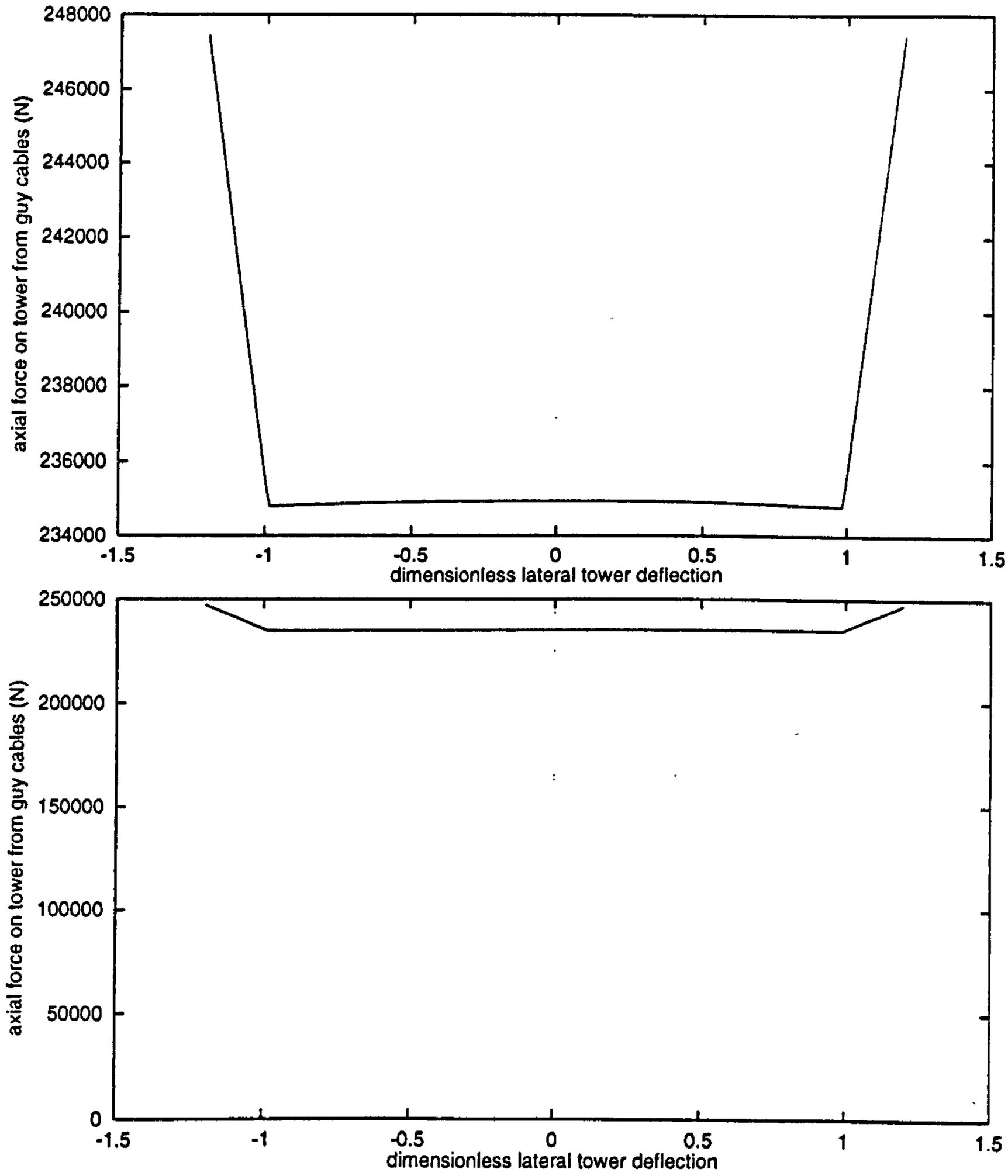

Figure 2.12: The variation of the axial force F_{cv} on the tower from the guy cables with the lateral deflection of the point of attachment of the guy cables to the tower. The initial strain in the guy cables is 0.0005 and the horizontal deflection of the point of attachment of the guy cables to the tower at which one of the cables slackens is 0.0458 m. The data are the same for both top and bottom sets of axes. The range of the vertical scale is smaller on the top set of axes to show the non-linearity of the variation of axial force with horizontal deflection. The horizontal scale is dimensionless with respect to this deflection.

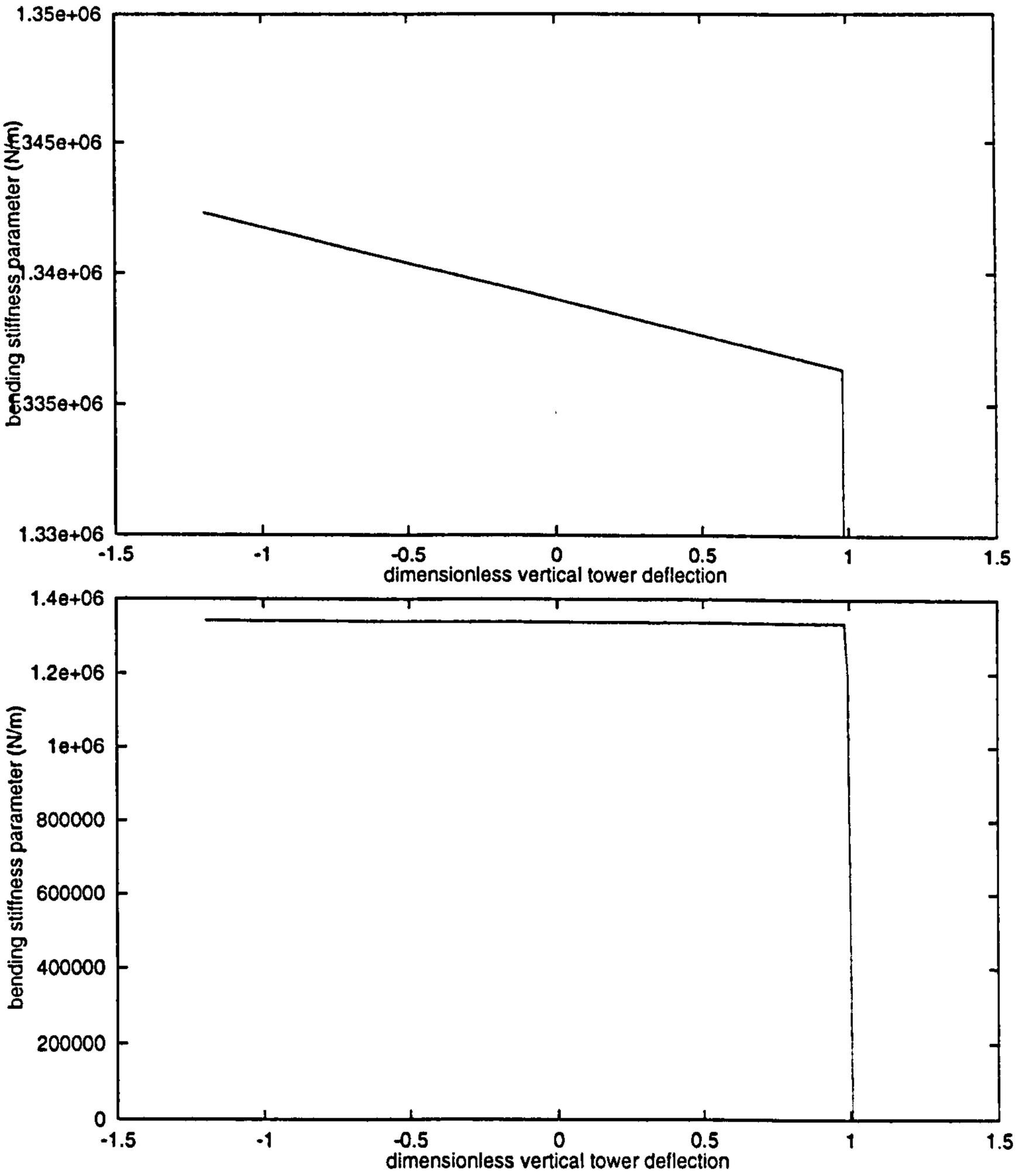

Figure 2.13: The variation of the bending stiffness parameter, k_{Bc} with vertical deflection of the point of attachment of the guy cables to the tower. The initial strain in the guy cables is 0.0005 and the vertical deflection at which the guys slacken is 0.0235 m (values apply to a 300 kW Carter wind turbine of the type at Great Orton Airfield). The range of the vertical scale of the top set of axes is smaller than for the bottom set to show the small variation in bending stiffness of the cables but otherwise the data used are the same for both sets of axes.

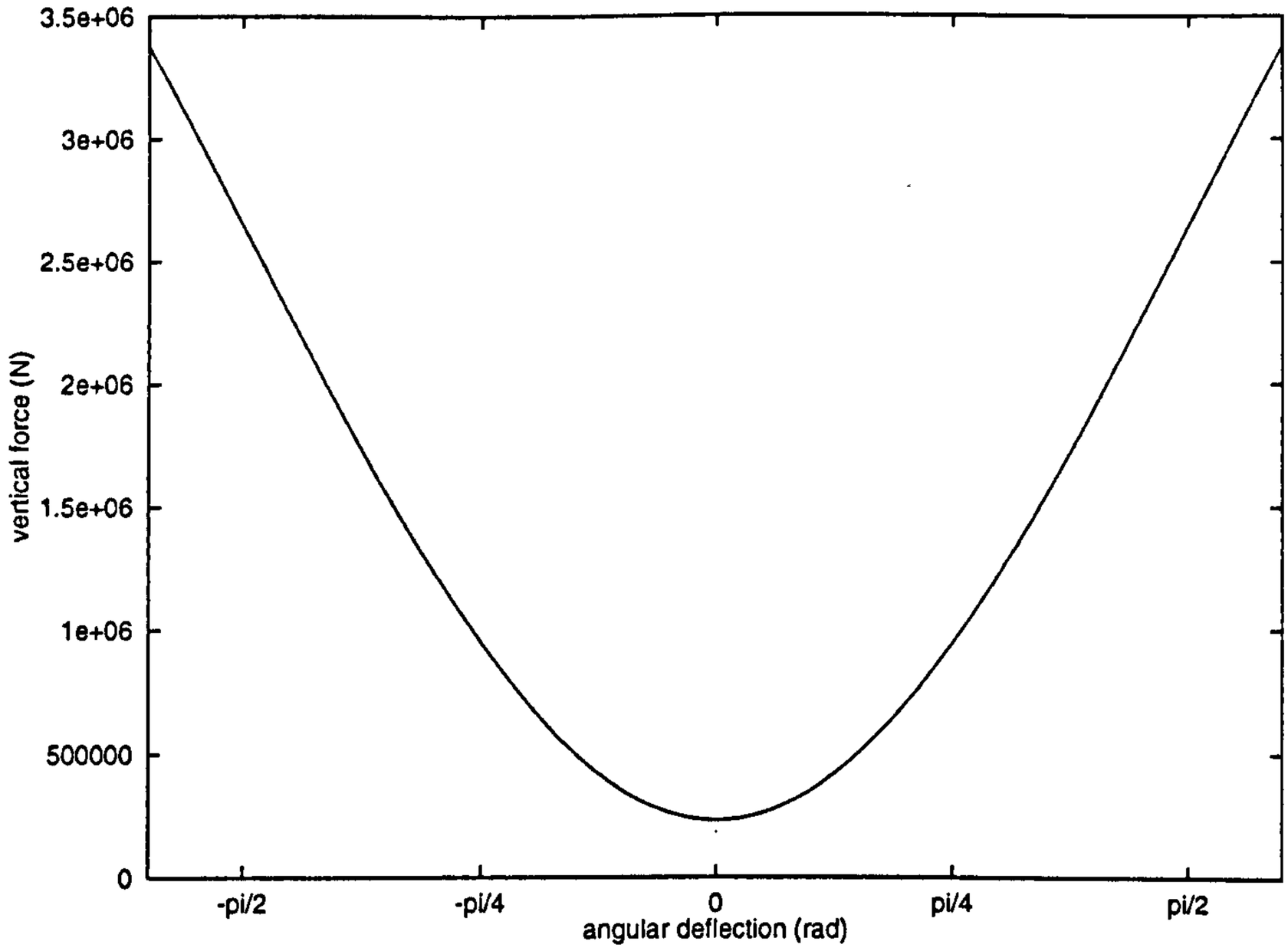

Figure 2.14: The variation of axial force F_{cv} on the tower with angular deflection of the point of attachment of the guys to the tower.

which the hollow tower is represented by three dimensional shell elements, any torsional vibrations of the tower were coupled with a bulging mode. In this combined mode, the angle of twist of the tower and its circumferential distance fluctuate simultaneously. In Figure 2.16, the normal force is plotted on the same axes as the tangential force which gives rise to the restoring torque plotted in Figure B.9.

2.2.3.1 Real Cable Behaviour

The stiffness of the guys will vary with deflection. As the twisted steel cables are stretched, a small torque will result from their tendency to untwist. Static analysis of a structure with non-constant guy stiffness would require an iterative approach which has not yet been implimented. If the cables are sufficiently prestretched and the magnitude of deflections sufficiently small, the variation of the tension about the static equilibrium position will be approximately linear.

2.3 Lateral Deflection

2.3.1 Applied Loads

There are six types of loads applied externally to the mathematical model of the structure which affect lateral deflections and which are illustrated in Figure 2.17:

1. at the tower top (where the nacelle is attached):

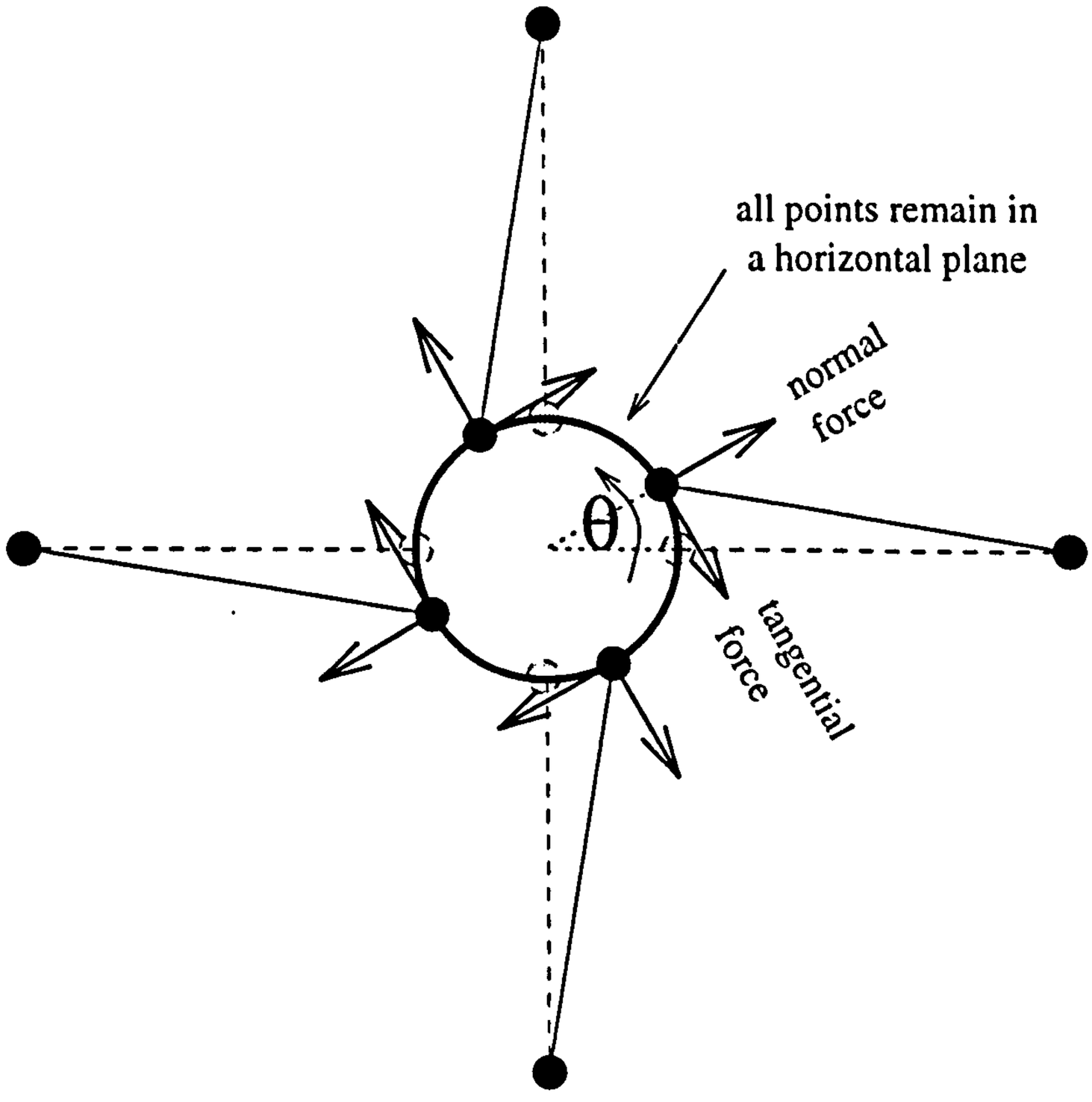

Figure 2.15: The two forces on the tower from each of the four guy cables. The tangential force gives rise to the restoring torque plotted against angular deflection in Figure B.9. The normal forces balance each other but Finite Element analysis shows that such normal forces are responsible for combined torsional and bulging modal vibration of the tower. For simple torsion of the tower, the normal forces due to each of the guy cables are the same and the tangential forces are also the same.

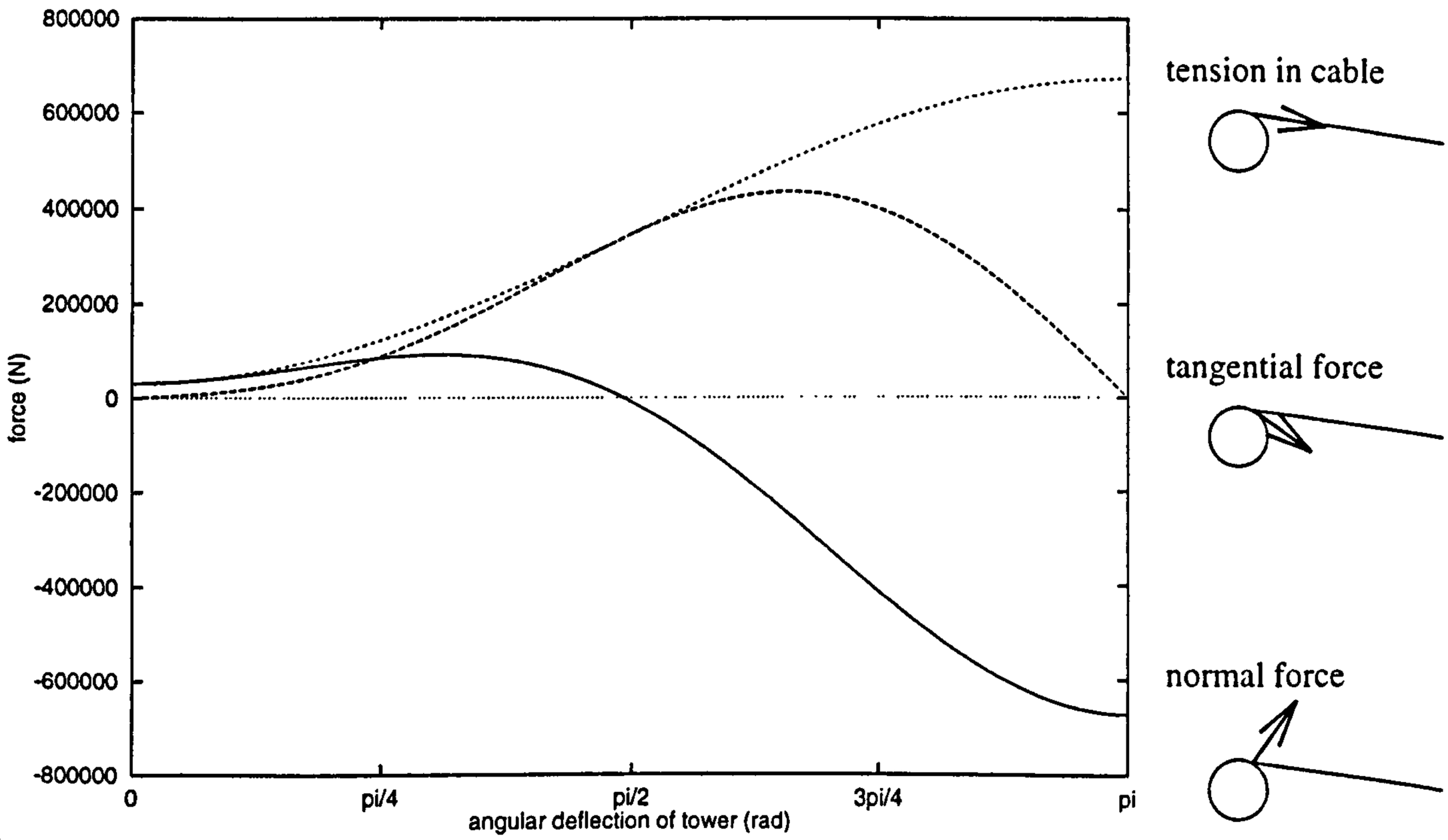

Figure 2.16: The variation with angular deflection of the normal and tangential forces on the tower at the points of attachment of the four guy cables. Only tower torsion is considered so each set of four forces comprises forces of the same magnitude. Forces relating to cable 0 are plotted. The cable tension is equal to the square root of the sum of the squares of the normal and tangential forces.

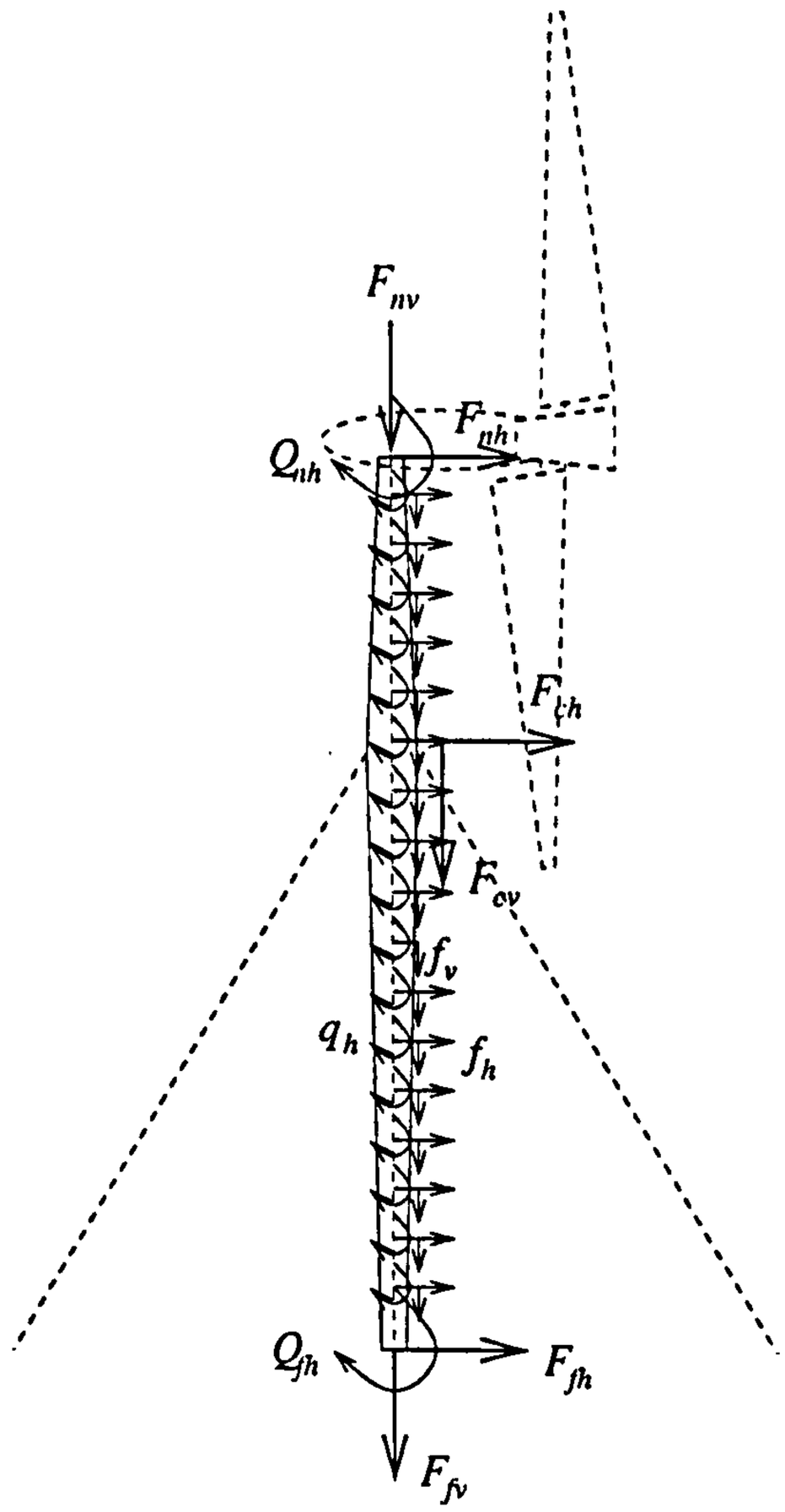

Figure 2.17: The six applied loads which affect lateral deflections of the tower are either distributed over the height of the tower (f_h, f_v and q_h) or concentrated at the nacelle (F_{nh}, F_{nv} and Q_{nh}). The other loads in the figure are reactions, either from the foundation (F_{fv}, F_{fh} and Q_{fh}) or from the guy cables (F_{cv} and F_{ch}).

(a) a concentrated horizontal force (F_{nh} N);

(b) a concentrated vertical force (F_{nv} N);

(c) a concentrated torque about a horizontal axis (Q_{nh} N m);

2. distributed over the height of the tower:

(a) horizontal force densities (f_h N m^{-1});

(b) vertical force densities (f_v N m^{-1});

(c) torque densities about horizontal axes (q_h N m m^{-1}).

In addition, there are 3 loads affecting lateral deflections which arise through deflection of parts of the structure:

1. horizontal force at the base (F_{fh} N);

2. torque at the base about a horizontal axis (Q_{fh} N m);

3. horizontal force at the point of attachment of the guys to the tower (F_{ch} N).

The magnitudes are calculated assuming linear elastic behaviour with no damping and are not known until the deflections have been calculated. This gives rise to unknowns which must be found by solution of an appropriate number of simultaneous equations. These equations arise from other constraints on the system:

1. horizontal forces must be in equilibrium;

2. vertical forces must be in equilibrium;

3. moments about the tower base must be in equilibrium.

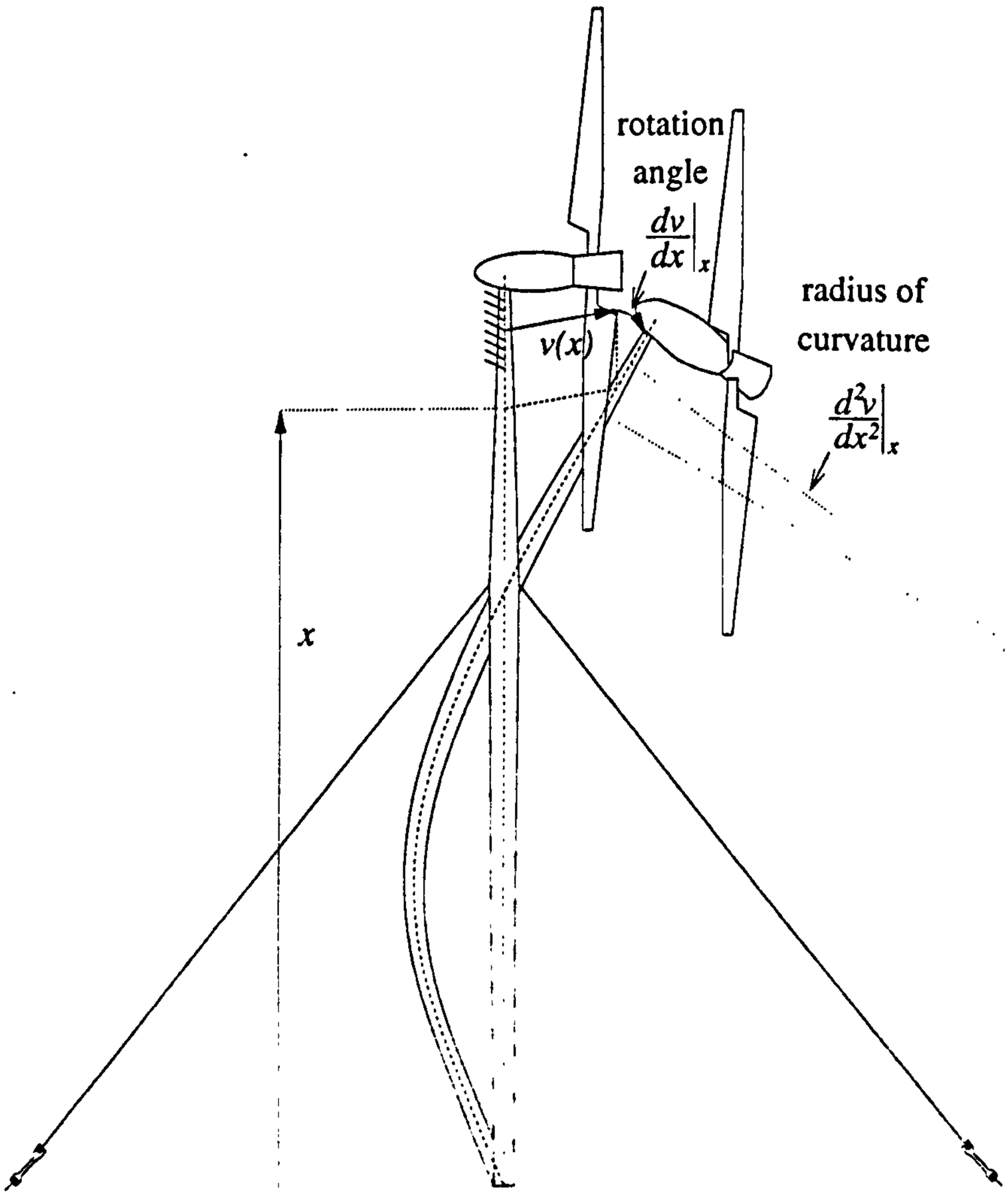

Figure 2.18: The sign conventions for tower bending deflections, rotations and radii of curvature.

The sign conventions for the three classes of deflections are shown in Figure 4.2. For lateral deflections, the sign conventions for the deflection, v, the tower gradient or rotation angle, $\frac{dv}{dx}$ and the radius of curvature, $\frac{d^2v}{dx^2}$ at height, x are illustrated in Figure 2.18.

2.3.2 Smooth Static Deflection Curves

The *general, numerical model* described in this thesis takes applied loads and finds the deflection of the structure. Equation 2.6 is the differential equation which governs lateral deflections.

$$M_t = E_t I_{xt} \frac{d^2v}{dx^2} \tag{2.6}$$

The bending moment, $M_t(x)$ at a height, x up the tower in Equation 2.6 depends on the following two distinct types of applied load.

1. Loads such as horizontal forces and torques about horizontal axes in which the bending moment is independent of the deflection of the tower.

2. Loads such as vertical forces, for which the bending moment is dependent on the product of the force and the deflection at that particular height.

Because of the second category of loads and the four unknown elastic restoring forces, the tower deflections cannot be deduced simply by integrating Equation 2.6 to find v in terms of a set of applied loads.

The approach adopted is to solve a set of simultaneous equations in which both the deflection and the second derivative of the deflection are unknown at each of N_n nodal points. The total number of unknowns is therefore $2N_n$. The relationship between v and $\frac{d^2v}{dx^2}$ is constrained by fitting cubic splines between the nodes. The following conditions are used to generate the necessary $2N_n$ simultaneous equations:

1. 2 linear elastic equations at the base (of the type illustrated by Equations 2.1 to 2.4);

2. N_n equations of elastic bending at each nodal point j (height, x_j up the tower) which use Equation 2.6 to relate the resultant bending moment, $M_t(x_j)$ with radius of curvature of the tower $\left.\frac{d^2v}{dx^2}\right|_{x_j}$ (Figure 2.20 illustrates the loads on the section of tower below the node j);

3. $(N_n - 2)$ equations of gradient continuity between nodal tower sections (see Equation 2.15).

Having found $v(x_j)$ and $\left.\frac{d^2v}{dx^2}\right|_{x_j}$ at all nodes (for $0 < j < N_n$), cubic splines are used to calculate deflections at N_s points between nodes (including the end points of the section which coincide with nodes) to smooth the deflection curve, $v(x)$. By having these extra points between the nodes, loads can be applied at more points up the tower and so can be distributed more evenly. Differentials. $\frac{dv}{dx}$ can also be found with greater accuracy. The total number of points along the length of the tower is $(N_s - 1) \times (N_n - 1) + 1$. An example of

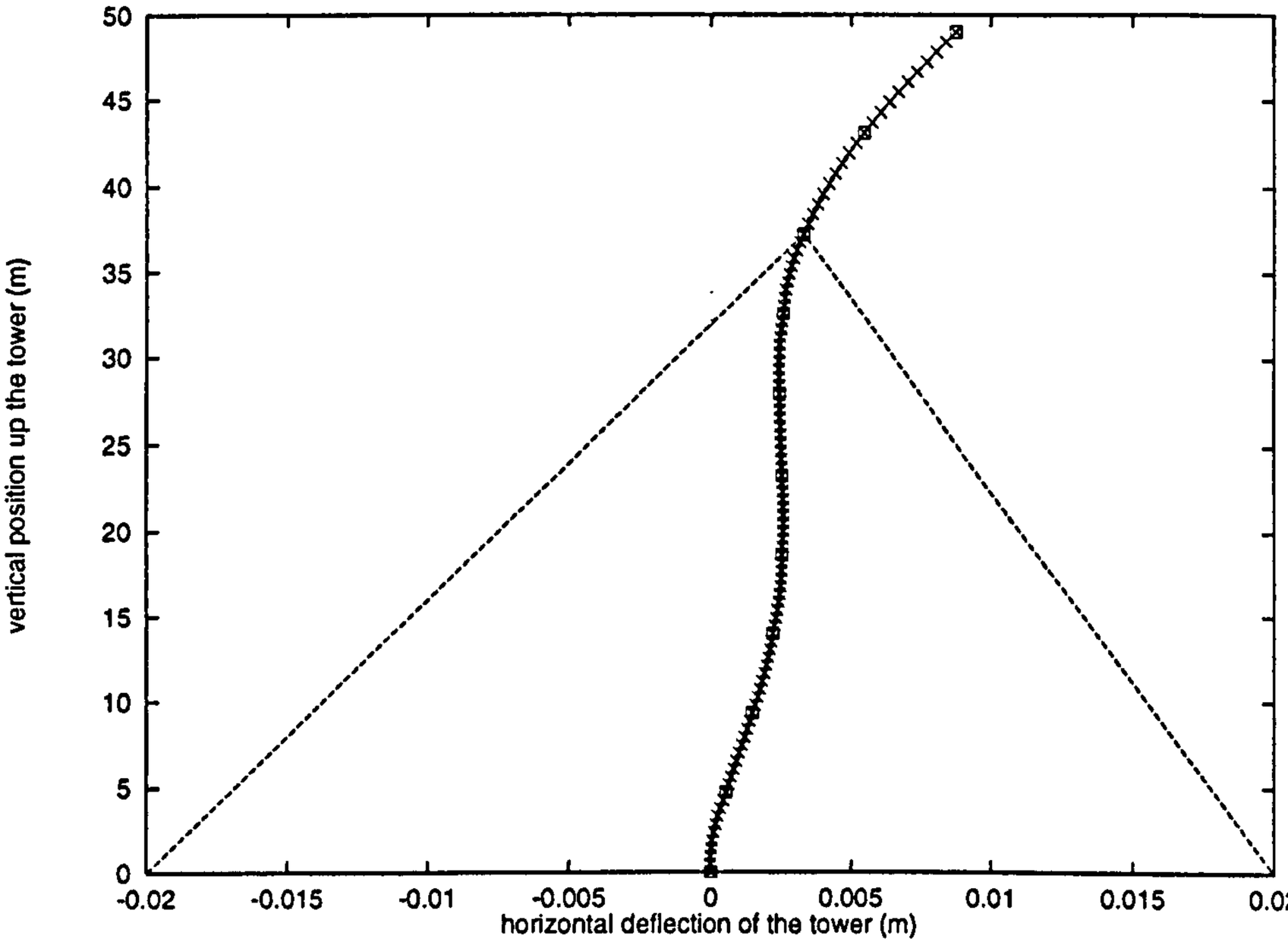

Figure 2.19: Simple lateral deflection of the tower subject to a 1000 N horizontal load at the tower top and 100 N m^{-1} distributed uniformly up the tower. Results are calculated for the Carter 300 kW machine of the type at Great Orton Airfield. The scale for deflections is deliberately different from the scale for the displacement of the guy cable ground anchor points which are displaced 19.6 m horizontally from the tower base. Spline nodes are denoted by boxes and spline interpolation points by crosses. The number of nodal points, N_n includes the nodes at the top and the bottom of the tower. The number of spline interpolation points, N_s includes the two nodes at either end of a spline section. In the case illustrated here, N_n is 11 and N_s is 11. The total number of points along the tower length is therefore 101.

this system is shown in Figure 2.19. There are 11 nodes (N_n) and 11 spline interpolation points on each spline section (N_s) resulting in a total of 101 points.

At the base (node 0 at which $x = x_0$), the reactions, F_{fh}, F_{fv} and Q_{fh} are found by equilibrium. Deflections of the base occur proportional to these reactions (see Section 2.2.2) as defined in Equations 2.7 to 2.9. The two linear elastic conditions at the base which are necessary to find *lateral* tower deflections are defined by Equations 2.7 and 2.9.

$$F_{fh} = -k_{Lf} v(x_0) \tag{2.7}$$

$$F_{fv} = -k_{Cf} u(x_0) \tag{2.8}$$

$$Q_{fh} = -k_{Bf} \left.\frac{dv}{dx}\right|_{x_0} \tag{2.9}$$

At each node, the section of tower below the node is treated as a 'free body'. The bending moment in the tower at the node ($M_t(x_j)$) is found by equilibrium with all applied torques and the moments of all applied forces about the node. It is equal to the flexural rigidity of the tower multiplied by the second derivative of the tower's deflection (see Equation 2.6). This moment equilibrium is illustrated in Figure 2.20. Applied loads are dealt with in more detail in Sections 2.3.3 to 2.3.5.

The standard equation for the cubic spline between two points is given by Equation 2.10 [31]. The deflections (v_j and v_{j+1}) and radii of curvature ($\left.\frac{d^2v}{dx^2}\right|_j$ and $\left.\frac{d^2v}{dx^2}\right|_{j+1}$) are unknown.

$$v = Av_j + Bv_{j+1} + C \left.\frac{d^2v}{dx^2}\right|_j + D \left.\frac{d^2v}{dx^2}\right|_{j+1} \tag{2.10}$$

In Equation 2.10, $v(x)$ is the absolute deflection, A, B, C and D are functions of x, x_j and x_{j+1} only and are given by Equations 2.11, 2.12, 2.13 and 2.14. In each spline section there are N_s spline interpolation points including the end nodes (see Figure 2.19). There are $N_s - 2$ values of x between each pair of nodal heights ($x_j < x < x_{j+1}$).

$$A \equiv \frac{x_{j+1} - x}{x_{j+1} - xj} \tag{2.11}$$

$$B \equiv \frac{x - x_j}{x_{j+1} - xj} \tag{2.12}$$

$$C \equiv \frac{1}{6}\left(A^3 - A\right)(x_{j+1} - x_j)^2 \tag{2.13}$$

$$D \equiv \frac{1}{6}\left(B^3 - B\right)(x_{j+1} - x_j)^2 \tag{2.14}$$

At each node other than those at the ends of the tower, the gradient of spline curves on either side of the node is constrained by Equation 2.15 to be the same. This ensures that although the number of nodes may be relatively small, the deflection curve is smooth.

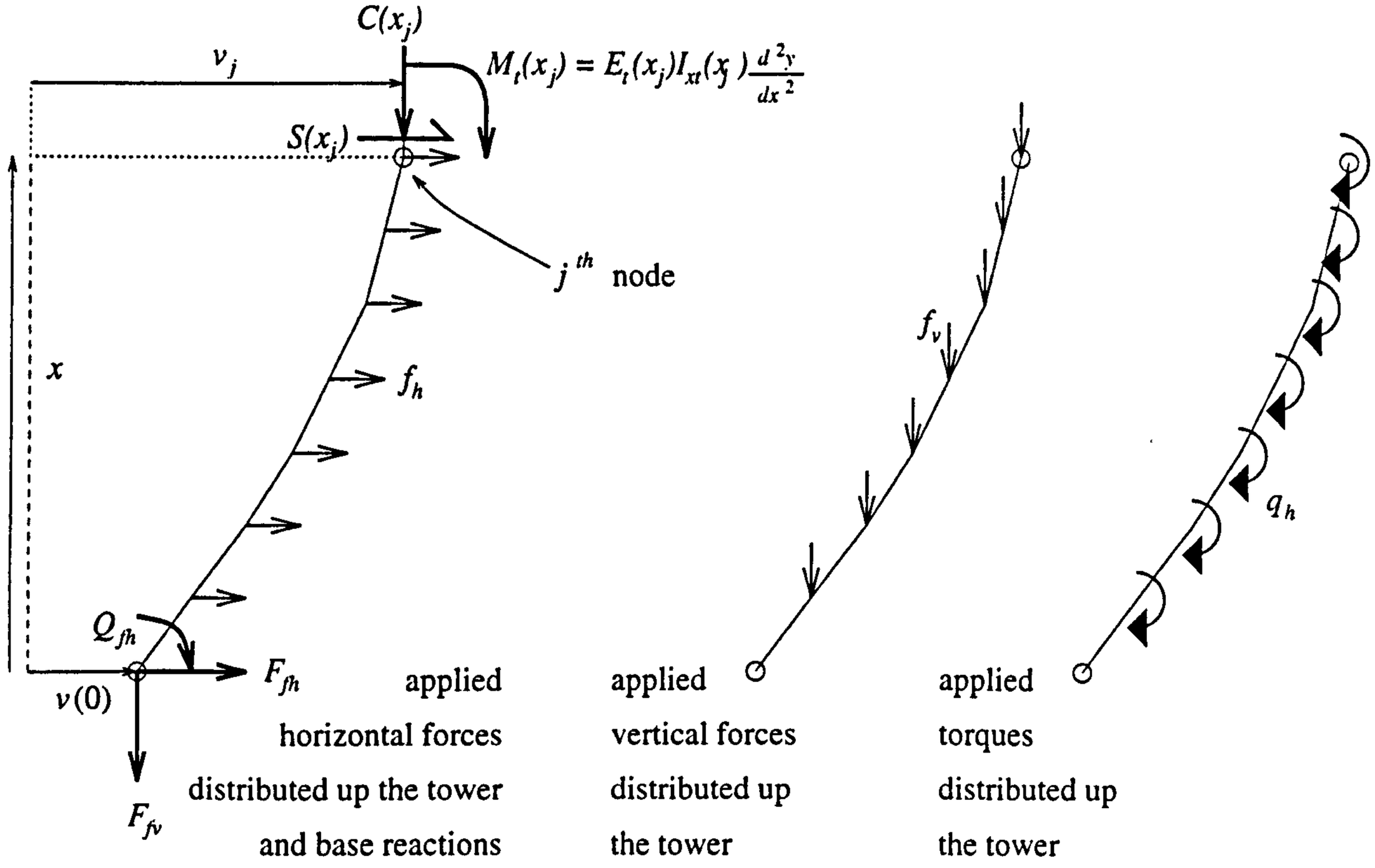

Figure 2.20: Free body diagram of the section of the tower below the node of interest ($0 < x < x_j$). The applied forces and torques are used to calculate ($M_t(x_j)$) at the j^{th} node used in Equation 2.6. Three types of distributed loads are considered by the model. There are also discrete loads applied at the tower top and point of attachment of the guys. The shear force $S(x_j)$ and the axial force of compression $C(x_j)$ in the tower are included in this figure for completeness. They will not be referred to in the text because, by taking moments about the node of interest, it is not necessary to calculate them explicitly.

$$\frac{1}{6}(x_j - x_{j-1})\left.\frac{d^2v}{dx^2}\right|_{j-1} + \frac{1}{3}(x_{j+1} - x_{j-1})\left.\frac{d^2v}{dx^2}\right|_{j} + \frac{1}{6}(x_{j+1} - x_j)\left.\frac{d^2v}{dx^2}\right|_{j+1} = \frac{v_{j+1} - v_j}{x_{j+1} - x_j} - \frac{v_j - v_{j-1}}{x_j - x_{j-1}} \tag{2.15}$$

The three sources of constraint equations described in this section give rise to Equation 2.16. To solve this system of linear equations, 'LU decomposition' [31] is used to invert the matrix M (Equation 2.17). In both Equations 2.16 and 2.17, M is a $2N_n \times 2N_n$ matrix of coefficients and $\mathbf{M}^{-1}$ is its inverse. $\mathbf{C}$ is a column vector of $2N_n$ constants. $\{v_j\}$ is a column vector of N_n unknown nodal deflections. $\left\{\left.\frac{d^2v}{dx^2}\right|_j\right\}$ is a column vector of N_n unknown nodal radii of curvature.

$$\mathbf{M}\left\{\begin{array}{c}\{v_j\}\\ \left\{\left.\frac{d^2v}{dx^2}\right|_j\right\}\end{array}\right\} = \mathbf{C} \tag{2.16}$$

$$\left\{\begin{array}{c}\{v_j\}\\ \left\{\left.\frac{d^2v}{dx^2}\right|_j\right\}\end{array}\right\} = \mathbf{M}^{-1}\mathbf{C} \tag{2.17}$$

The deflection of the tower in response to each of the three classes of applied loads will be described separately in Sections 2.3.3 to 2.3.5. For the general solutions, the bending moments due to all the applied loads are added together at each node. The differential equation (Equation 2.6) is rewritten for the j^{th} node in Equation 2.18.

$$M_t(x_j) = E_t(x_j)I_{xt}(x_j)\left.\frac{d^2v}{dx^2}\right|_{x_j} \tag{2.18}$$

Using Equation 2.18 and the equilibrium of loads on a free body of the kind illustrated in Figure 2.20, the coefficients of v_j and $\left.\frac{d^2v}{dx^2}\right|_j$ can be found for each node j to fill in elements of the matrix M.

2.3.3 Applied Vertical Forces

The reason that the deflection of the tower at each node is unknown is that vertical loads on the tower give rise to a distribution of applied moments about the node of interest when the tower is deflected (see Figure 2.20). Treating nodal deflections as unknowns allows the moments due these applied loads to act on the structure and contribute to its deflection. The dominant source of vertical loading for a guyed tower is the pretension in the cables.

Equation 2.19 gives the bending moment $M_t(x_j)$ at the j^{th} node due only to the vertical component of the foundation reaction F_{fv} and the distributed vertical forces f_v applied to the section of the tower between the base and the j^{th} node.

$$M_t(x_j) = F_{fv}\left(v(x_j) - v(x_0)\right) + \sum_{k=0}^{j-1} \int_{x_k}^{x_{k+1}} (v(x_j) - v(\xi)) f_v(\xi) d\xi \tag{2.19}$$

k is the node number for summations (from 0 to the node below the current node of interest, $j-1$),

x, f_v and v are defined between nodes as well as at each node (x_k, $f_v(x_k)$ and $v(x_k)$),

$M_t(x_j)$ is the bending moment in the tower at the j^{th} node,

$f_v(x)$ is a function giving vertical force densities (N m^{-1}) applied to the tower,

ξ is a dummy variable allowing integration between nodes (in the interval $x_k < \xi < x_{k+1}$) to be distinguished from other heights such as x_k or x_j.

$v(\xi)$ is defined between nodes as in Equation 2.10 replacing j with k for interpolation between nodes k and $k+1$ and replacing x with the dummy variable ξ.

In Equation 2.19, the integral of the moment of the distributed vertical force f_v about the node of interest with respect to ξ has been split up into the sum of integrals performed between consecutive nodes. The distance between every pair of consecutive nodes is the same in the interval $0 < x < \lambda_{ct} H$. The point of attachment of the guys to the tower (height, $\lambda_{ct} H$) is constrained to be a node. Above this point (in the interval $\lambda_{ct} H < x < H$), the distance between consecutive pairs of nodes is also constant but in general different. For this reason, integrals such as those summed in Equation 2.19 can be performed without reference to a particular node. For towers with more than one set of guys, nodal distances are constant between each set of guys. This means that for each section of the tower between sets of guy cables, a new set of arrays representing the spline coefficients A, B, C and D must be generated. A wind turbine tower with three sets of guy cables is illustrated in Chapter 3 in Figure 3.5.

In order to generate the coefficients of v_k and $\frac{d^2v}{dx^2}\Big|_k$ (where k is defined by the limits in Equation 2.19), the unknown nodal deflections and radii of curvature must be factored out of the integrand. This is done by substituting Equation 2.10 for $v(\xi)$ to give Equation 2.20. The spline parameters A, B, C and D are dependent only on x_k. ξ and x_{k+1} (Equations 2.11, 2.12, 2.13 and 2.14) all of which are known before solution of the matrix (Equation 2.17). The spline parameters A, B, C and D are also the same for the same nodal distance. Since the applied loads f_v are known beforehand, the products Af_v, Bf_v, Cf_v and Df_v can also be set up as arrays and integrated before values of $v(x_k)$ and $\frac{d^2v}{dx^2}\Big|_k$ are found.

$$M_t(x_j) = F_{fv}\left(v(x_j) - v(x_0)\right) + \sum_{k=0}^{j-1} \Bigg(v(x_j) \int_{x_k}^{x_{k+1}} f_v(\xi) d\xi - v(x_k) \int_{x_k}^{x_{k+1}} A f_v(\xi) d\xi - v(x_{k+1}) \int_{x_k}^{x_{k+1}} B f_v(\xi) d\xi -$$

$$\left.\frac{d^2v}{dx^2}\right|_{x_k} \int_{x_k}^{x_{k+1}} C f_v(\xi) d\xi - \left.\frac{d^2v}{dx^2}\right|_{x_{k+1}} \int_{x_k}^{x_{k+1}} D f_v(\xi) d\xi \Bigg) \tag{2.20}$$

The foundation reaction is in equilibrium with the vertical components of all loads applied to the tower. The predominant influence on the vertical component of the foundation reaction is the compression in the tower due to the guys. Other axial loads on the tower (f_v N m^{-1}) are due to gravity ($\rho_t A_{xt} g$). Modal analysis of a system in which longitudinal and transverse deflections are coupled has not been attempted but in that case, vertical inertia forces ($M_n u\omega^2$ or $\rho_t A_{xt} u\omega^2$) would also contribute to axial loading on the tower.

An interesting consequence of this proportionality between applied moments and deflection is seen if a hinged tower is subjected to a small horizontal load at the top and its own weight. The deflection found by the technique described above is in the opposite direction to the small applied horizontal load. The tower 'leans into' the applied load so that its weight is in equilibrium with the horizontal load. If the load increases, that deflection increases. The resultant bending moment about the base hinge must be zero. The technique is able to find a deflection such that the moments of the displaced axial loads about the base hinge are in equilibrium with the applied horizontal loads. If a hinged tower is subjected to a series of horizontal loads but no vertical loads (for instance if gravity is zero), no solution can be found because none of the applied loads give rise to moments proportional to deflections. The matrix is singular. It is therefore not possible to consider the unique situation where all applied horizontal loads are in equilibrium and the deflection is indeterminate.

In the case of the static analysis of tower torsion and longitudinal deflection there is no equivalent to this distribution of moments proportional to deflection. The number of unknowns is equal just to the number of elastic elements modelled (for example: guys and base fixing). A model very similar to those used for torsional and longitudinal deflections can be used for lateral deflections if vertical forces are excluded. The static model illustrated by these three cases is described in Appendix A.

The base vertical reaction F_{fv} is independent of any of the unknowns because the axial compression, F_{cv} is assumed to be independent of tower deflection. F_{fv} is found by equilibrium using Equation 2.21.

$$F_{fv} = -F_{cv} - F_{nv} - \int_0^H f_v d\xi \tag{2.21}$$

2.3.4 Applied Horizontal Forces

The contributions from horizontal forces to the bending moment in the tower $M_t(x_j)$ are easier to include than the contributions from vertical forces. The bending moment at each of the nodes is calculated by considering the free body consisting of that portion of the tower below the node of interest (Figure 2.20). Equation 2.22 gives the bending moment as a function of only horizontal forces and force densities.

$$M_t(x_j) = F_{fh}(x_n - x_0) + \sum_{k=0}^{j-1} \int_{x_k}^{x_{k-1}} (x_j - \xi) f_h(\xi) d\xi \tag{2.22}$$

Additionally, above the point of attachment of the guys, there is a restoring force from the displaced guys (Equation 2.23). Since the point of attachment of the guys to the tower is constrained to be a node (Section 2.3.2), $\lambda_{ct}H$ is a nodal height.

$$M_t(x_j) = F_{fh}\,(x_j - x_0) + \sum_{k=0}^{j-1} \int_{x_k}^{x_{k+1}} (x_j - X) f_h(\xi) d\xi + F_{ch}\,(x_n - \lambda_{ct}H)$$

$$M_t(x_j) = F_{fh}\,(x_j - x_0) + \sum_{k=0}^{j-1} \int_{x_k}^{x_{k+1}} (x_j - \xi) f_h(\xi) d\xi - k_{Bc} v(\lambda_{ct}H)\,(x_j - \lambda_{ct}H) \qquad (2.23)$$

Additional forces on the tower not due to the operating wind turbine are from the wind. These are small due to the tower's large aspect ratio (see Glossary).

The base horizontal reaction is calculated by equilibrium of horizontal forces on the tower (Equation 2.24). The most significant is often the horizontal guy reaction, F_{ch} which is dependent on the unknown nodal deflection of the point of attachment of the guys $v(\lambda_{ct}H)$.

$$\begin{aligned} F_{fh} &= -F_{ch} - F_{nh} - \int_0^H f_h d\xi \\ F_{fh} &= k_{Bc} v(\lambda_{ct}H) - F_{nh} - \int_0^H f_h d\xi \end{aligned} \qquad (2.24)$$

2.3.5 Applied Horizontal Torques

The contribution to the bending moment $M_t(x_j)$ from horizontal torques applied to the tower (Equation 2.25) is also easier to include than the influence of vertical forces.

$$M_t(x_j) = -Q_{fh} - \sum_{k=0}^{j-1} \int_{x_k}^{x_{k+1}} q_h(\xi) d\xi \qquad (2.25)$$

The reaction torque (Q_{fh}) at the base, however, is affected by the moments of the displaced vertical forces (Equation 2.26).

$$Q_{fh} = -Q_{nh} - \int_0^H q_h d\xi - F_{nh}H - \int_0^H \xi f_h d\xi + k_{Bc} v(\lambda_{ct}H) - F_{nv} v(H) - \sum_{k=0}^{j-1} \int_{x_k}^{x_{k+1}} (v(\xi) - v(0))\, f_v(\xi) d\xi \qquad (2.26)$$

Again, Equation 2.10 can be used to substitute for $v(\xi)$ so that integrations can be performed before the nodal deflections and second derivatives have been found (Equation 2.27).

$$Q_{fh} = -Q_{nh} - \int_0^H q_h d\xi - F_{nh}H - \int_0^H \xi f_h d\xi + k_{Bc} v(\lambda_{ct} H) - \sum_{k=0}^{N_n-1} \left(v(x_k) \int_{x_k}^{x_{k+1}} A f_v(\xi) d\xi + v(x_{k+1}) \int_{x_k}^{x_{k+1}} B f_v(\xi) d\xi + \left.\frac{d^2v}{dx^2}\right|_{x_k} \int_{x_k}^{x_{k+1}} C f_v(\xi) d\xi + \left.\frac{d^2v}{dx^2}\right|_{x_{k+1}} \int_{x_k}^{x_{k+1}} D f_v(\xi) d\xi - v(0) \int_{x_k}^{x_{k+1}} f_v d\xi \right) \quad (2.27)$$

At the tower top, it is only the applied torque Q_{nh} which contributes to the bending moment $M_t(x_{N_n})$ there.

$$M_t(x_{N_n}) = -Q_{nh} \quad (2.28)$$

2.4 Longitudinal Deflection

The longitudinal deflection of the tower is estimated in a similar way to the lateral deflection. However, as stated above, all loads are independent of deflection apart from:

1. the reaction of the cables and
2. the reaction of the base fixing.

The differential equation (Equation 2.29) which must be integrated numerically is a rearrangement of Hooke's law [32] for the material. Only one constant of integration is involved. It is related to the second of the two unknown loads listed above. By defining a constant guy stiffness and a linear elastic base stiffness, two simultaneous equations can be solved to give the two unknown loads. The whole method is described in Appendix A.1.

$$C_t = E_t A_{xt} \frac{du}{dx} \quad (2.29)$$

Base and cable reactions are calculated by considering equilibrium with all external loads. The tower is split up into *free bodies* of increasing length. For each free body, the internal compressive force in the tower, $C_t(x)$ is calculated by considering its equilibrium with all externally applied forces on the body. Deflections are estimated by successive integration of compressive strains $\frac{du}{dx}$ in the tower.

2.5 Torsional Deflection

The torsional deflection $\theta(x)$ of the tower is estimated in a similar way to longitudinal the deflection. The differential equation is given by Equation 2.30. The method described in Appendix A.2 is summarised for torsional static analysis. Instead of the vertical deflection. u which is the measure of longitudinal deformations, the measure of torsional deformations

is the angle of twist, θ. Loads applied externally give rise to torques in the tower about vertical axes, Q_t the torsional rigidity is $G_t J_{xt}$.

$$Q_t = G_t J_{xt} \frac{d\theta}{dx} \tag{2.30}$$

Chapter 3

Tower Buckling under Axial Loads

3.1 Euler Buckling of a Simple Strut

A straight, slender strut can support axial loads of any magnitude provided it remains straight. If applied axial loads are too large, the strut is in *unstable* equilibrium. That is, if *any* lateral force is applied, the strut buckles. Because of local stress concentrations, local buckling is often possible at lower applied loads than predicted using Euler's technique [32]. The photos of the Aerowat UM70 10 kW wind turbine in Figure 3.1 illustrate a possible consequence of under-designing a wind turbine tower with respect to Buckling.

Buckling is important because:

- buckling is also called 'static instability'. Lateral deflections are no longer proportional to axial or lateral loads and are theoretically without limits;

- although theoretically based on elastic behaviour, buckling is likely to lead to *plastic collapse* and permanent deformation if stress concentrating features give rise to local stresses above the yield stress of the material (the behaviour of the structure after onset of buckling is not dealt with by *Euler's* theory or the analysis described here);

- although theoretically based on elastic behaviour, buckling is likely to lead to *plastic collapse* and permanent deformation if stress concentrating features give rise to local stresses above the yield stress of the material (the behaviour of the structure after onset of buckling is not dealt with by *Euler's* theory or the analysis described here);

- large elastic deflections of, for instance, the tower, may lead to collisions with the rotating blades.

The Euler buckling formula for a slender, *simply supported* strut (Equation 3.5) gives a good indication of the upper limit on the axial stress the wind turbine tower can carry. The hollow tower consists of 5 mm steel plate and the aspect ratio (see Glossary) of the tower is greater than 60 for both 25 kW and 300 kW generators. This suggests that values predicted using Euler's theory may be close to actual buckling loads. However, the details of the structure where the base joins the foundation and the nacelle joins the tower top are

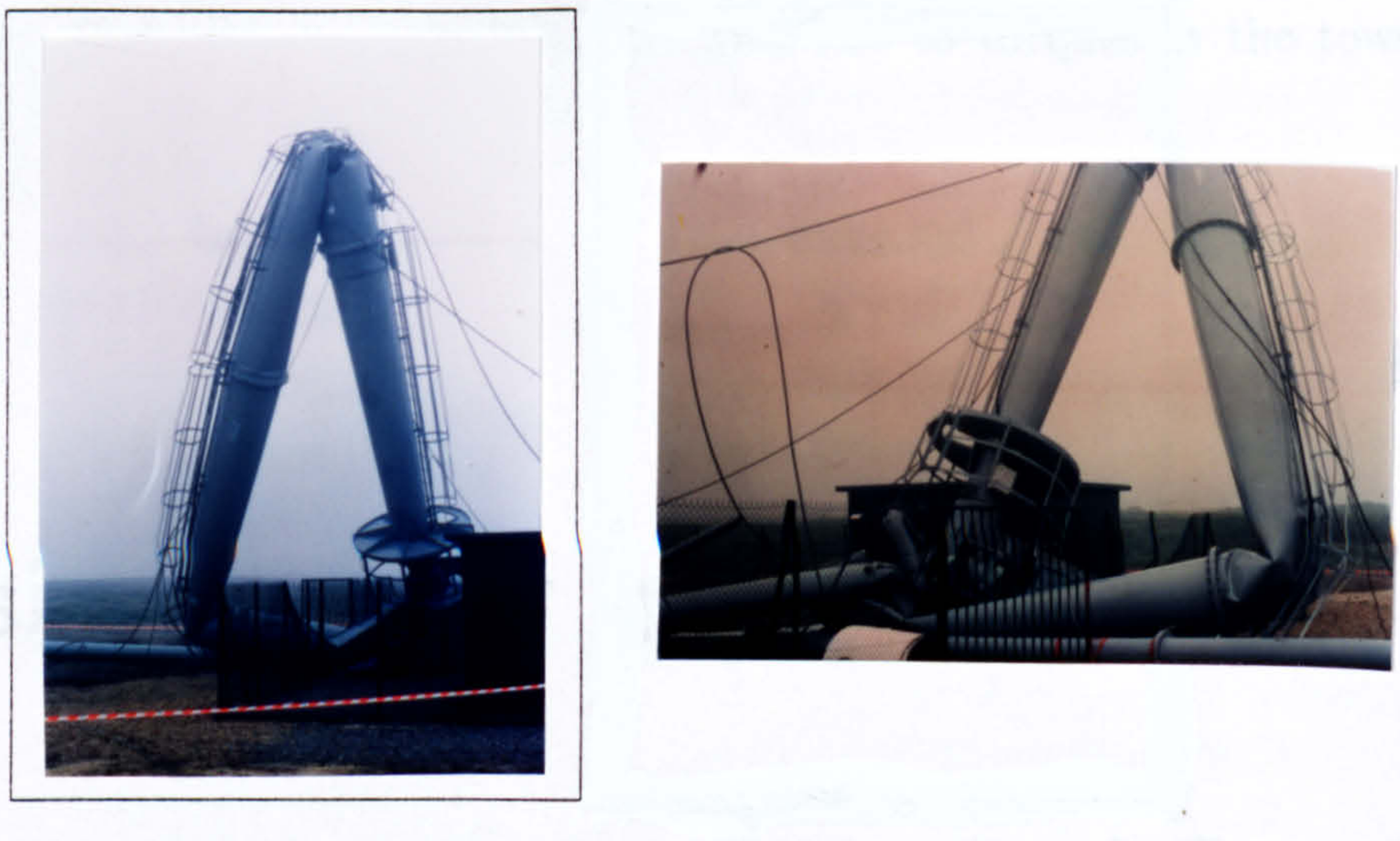

*Figure 3.1: The Aerowatt wind turbine at Oussant which collapsed because of buckling of the tower. (*photo: John Twidell*).*

likely to concentrate any axial stresses carried and could lead to local buckling below the axial load predicted for buckling as a slender strut.

The Euler load is the maximum axial stress the strut can support before buckling. The Euler buckling load arises from consideration of the elastic equation for pure bending of a beam (Figure 3.2, Equation 3.1). Where the bending moment M_t consists of an axial load and a deflection v, Equation 3.1 can be satisfied either for $v = 0$ or for $v = A\cos(\alpha x) + B\sin(\alpha x)$ where $\alpha = \frac{C_t}{E_t I_{xt}}$. A and B are constants which depend on the boundary conditions of the beam.

$$M_t(x) = -C_t v(x) = E_t I_{xt} \frac{d^2 v}{dx^2} \tag{3.1}$$

The ultimate Euler buckling load F_e for a simply supported strut (see Glossary) is given in Equation 3.2. If one end of the strut is built in, the load, F_e is higher (Equation 3.3). If both ends of the strut are built in, F_e is higher still (Equation 3.4).

$$F_e = \frac{\pi^2 E_t I_{xt}}{H^2} \tag{3.2}$$

$$F_e = 2.046 \frac{\pi^2 E_t I_{xt}}{H^2} \tag{3.3}$$

$$F_e = 4 \frac{\pi^2 E_t I_{xt}}{H^2} \tag{3.4}$$

The static equilibrium equation is satisfied for other buckling 'mode shapes' which are integer multiples of the first mode shape (Equation 3.5 gives the Euler buckling load for the i^{th} mode shape of a simply supported strut).

$$F_{ei} = \frac{i^2 \pi^2 E_t I_{xt}}{H^2} \tag{3.5}$$

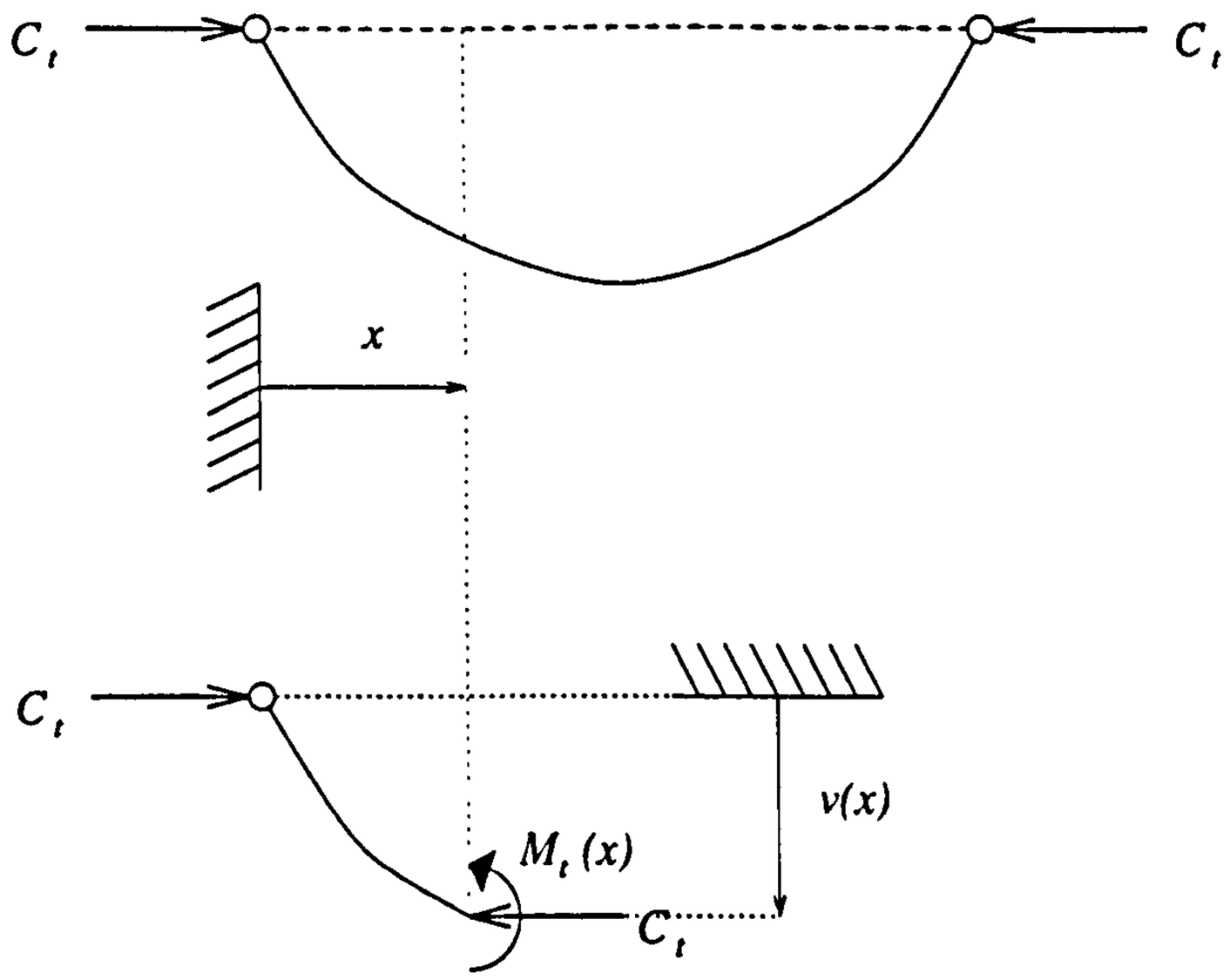

Figure 3.2: The elastic equation for a beam is dependent on the bending moment $M_t(x)$ at a height x. The bending moment can arise from an axial force in the beam C_t if the beam is deflected by $v(x)$.

3.1.1 Effective Tower Length

Equation 3.3 can be rewritten so that instead of multiplying the Euler expression for a simply supported strut by a factor 2.046 (Equation 3.2), the length of the strut is multiplied by a different factor to obtain an effective length, $H_{(\text{eff})}$. The effective length is estimated from knowledge of the construction of the tower. Figure 3.3 below illustrates this point for various physical configurations.

Equation 3.6 is similar to Equation 3.2 except that instead of the physical length H of the tower being used, an effective height, $H_{(\text{eff})}$ is used.

$$F_e = \frac{\pi^2 E_t I_{xt}}{H^2_{(\text{eff})}} \tag{3.6}$$

If the tower buckles elastically, the shape of deformation must be a continuous function. This has implications for towers with other constraints. Towers with rigidly built in bases or with more than one set of guy cables will withstand buckling until higher loads.

3.1.2 Guyed Wind Turbine Towers

The effective length of a wind turbine tower depends on several factors listed below:

- the physical height of the tower which is able to buckle (H if the load is applied at the top of a free-standing tower and $\lambda_{ct}H$ if a guyed tower buckles first under the influence of the axial tension due to the guys):

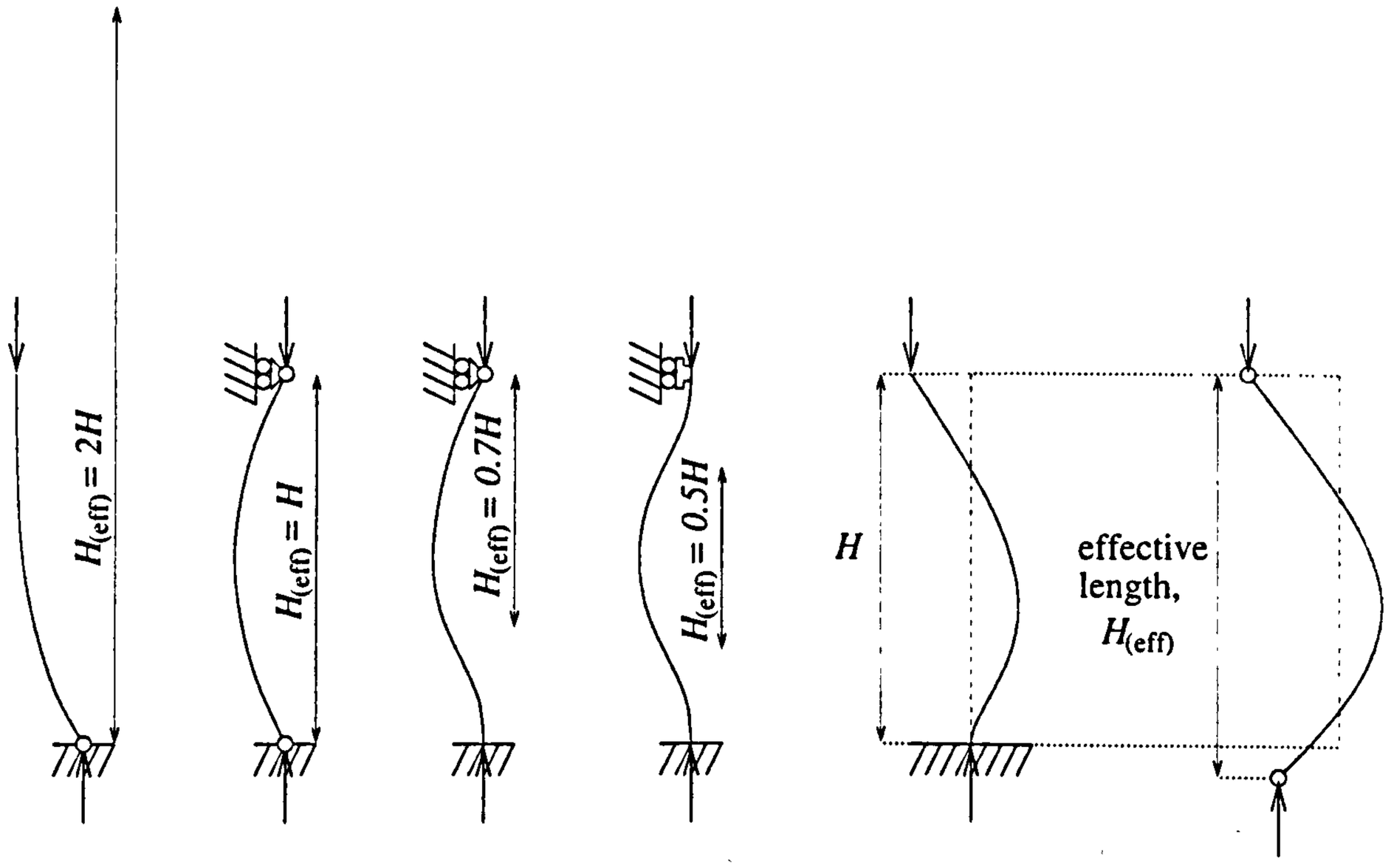

Figure 3.3: The effective lengths, $H_{(eff)}$ of four elementary beam configurations alongside a slender strut that is built in at the base and simply supported *(see the Glossary, for an explanation of beam boundary conditions) part of the way up.*

- the spacing and positions of the points of attachment of the guy cables of which there may be more than one as illustrated in Figure 3.5 (the attachment points of the cables restrict the lateral movement of the tower and so decrease the effective length of the section of the tower which is able to buckle);

- the base stiffness (as discussed in Section 2.2.2, the limits are $k_{Bf} = 0$ implying the tower is *simply supported* and $k_{Bf} = 1 \times 10^{12}$ implying the base is *built in*).

Two buckling scenarios are of interest:

1. buckling because the tension in the guys is too great;

2. buckling in response to vertical loads from the nacelle.

In reality, some combination of effects may lead to the onset of buckling, but it is important to know the theoretical limits the structure can withstand. In the first case, it will be the section of the tower below the cables which buckles. In the second case, it is the whole tower which buckles but the buckling shape is constrained so that the deflection of the tower at the point of attachment of the guy cables is small and the gradient there is continuous.

In both cases, for Euler buckling theory to be applied. the strut must be straight and parallel sided. It must be equivalent to a simply supported strut with some length. $H_{(eff)}$ (used in Equation 3.6). Where a structure deviates from this ideal. Euler buckling is still useful to obtain an initial estimate of the buckling load.

1. If the tower was simply supported at both the base and the point of attachment of the guy cables to the tower, the effective length would be $\lambda_{ct}H$. If the base was built in, the effective length would be $0.7\lambda_{ct}H$ (from Equation 3.3). For values of base fixing rigidity between these extremes ($0 < k_{Bf} < 1\times10^7$ see Figure 5.2), a Weibull function is used to calculate intermediate values of $\lambda_e = \frac{H_{(\text{eff})}}{H}$ (Equation F.1 in Appendix F.1). In Appendix F.1 is an explanation of the method of effective length and a description of the mathematical functions used to approximate different non-ideal boundary conditions.

2. As for the first case, the constraint due to the guy cables is modelled as an ideal pin joint. This time, because the tower is loaded above the constraint, the equivalent Euler strut will be longer than the physical length of the tower (see, Figure 3.4). Because the deflection shape of an ideal Euler strut is symmetrical, the deflection shape of the tower must be also. For a simply supported tower (pin jointed at $x = 0$ and $x = \lambda_{ct}$), the effective length can therefore be calculated using Equation 3.7. If the base is built in, the effective length calculated in Equation 3.7 is multiplied by the factor 0.700 (Equation 3.8). Equation 3.9 is the general formula for the effective length if the base torsional stiffness is intermediate ($0 < k_{Bf} < 1 \times 10^7$ see Figure 5.2). In Equation 3.9, λ_{eb} is a factor relating the effective length for buckling to the total length ($\lambda_{eb} = \frac{H_{(\text{eff})}}{H}$). The factor is calculated using Equation F.3 in Appendix F.1. Satisfactory values of the parameters in Equation F.3 have been found empirically to be, $\lambda_{e(\text{min})} = 0.700$, $\lambda_{e(\text{dif})} = 0.300$, $A = 6.28$ and $B = \frac{1}{9}$.

$$H_{(\text{eff})} = H\left(1 + (1 - \lambda_{ct})\right)$$

$$H_{(\text{eff})} = H\left(2 - \lambda_{ct}\right) \tag{3.7}$$

$$H_{(\text{eff})} = 0.7H\left(2 - \lambda_{ct}\right) \tag{3.8}$$

$$H_{(\text{eff})} = H\left(2 - \lambda_{ct}\right)\lambda_{eb} \tag{3.9}$$

Because the research has focused on the Carter wind turbine designs, only towers with one set of guys are described in the remainder of this chapter. The models have been developed and tested for multi-guyed towers but no experimental measurements have been made with which to validate them. Buckling behaviour is significantly modified by the presence of extra sets of guy cables and so the effect on $H_{(\text{eff})}$ is described in Appendix F. If, for a tower design with just one set of guys, the risk of tower buckling becomes too great, adding extra sets of guy cables at different heights is likely to reduce that risk.

3.2 Non-Euler Buckling

Even the simplest models of guyed wind turbine towers deviate from Euler's model:

- the tower is non-uniform (for instance. the sides aren't parallel):
- the tower is guyed:

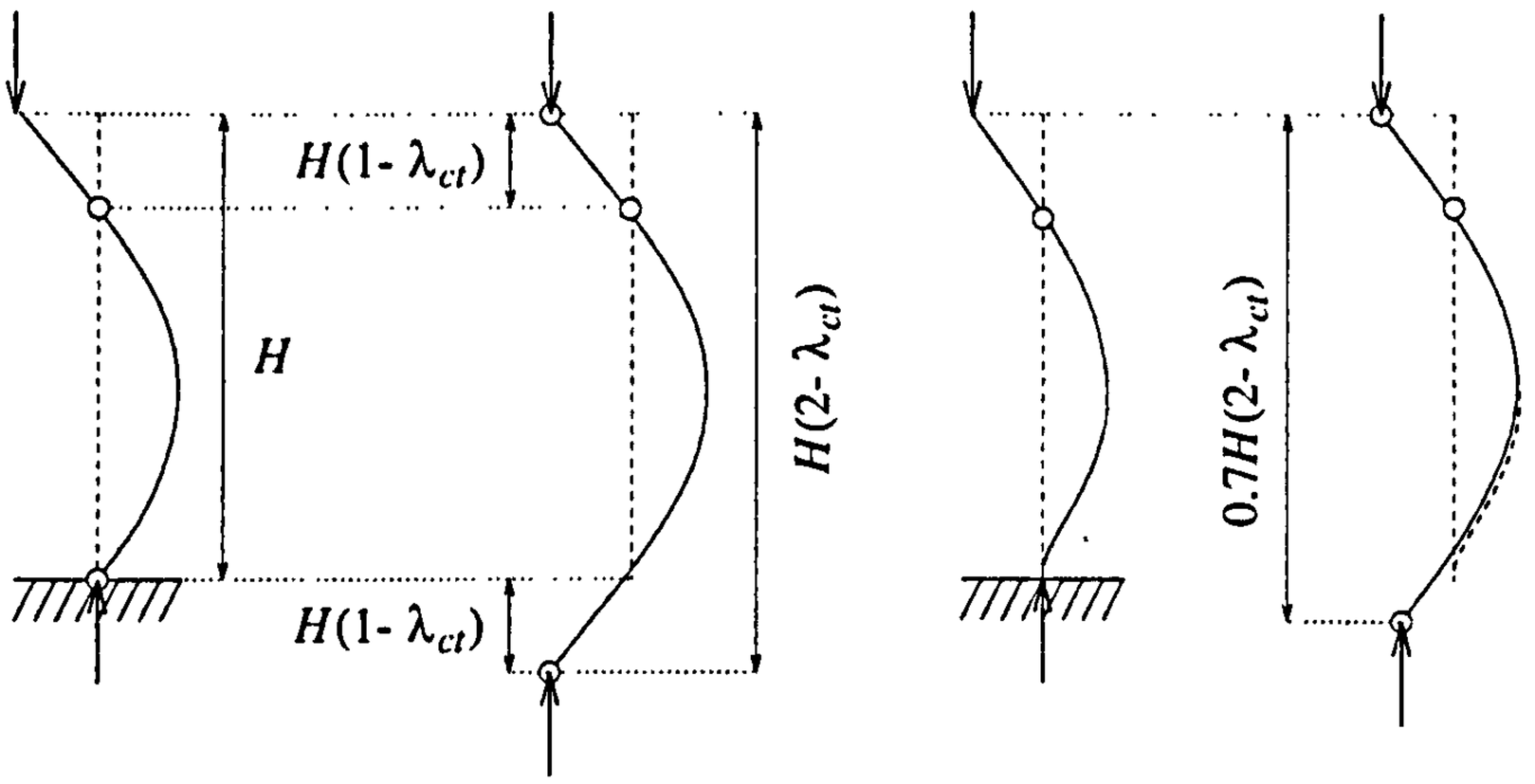

Figure 3.4: The effective lengths of two tower configurations loaded at the top. The case of an Euler strut involves a uniform column, simply supported at both ends. The buckling shape is a half sine wave. For guyed towers, the effective length $H_{(eff)}$ must be chosen so that the buckling shape of the real structure is as near as possible to the ideal buckling shape of an Euler strut.

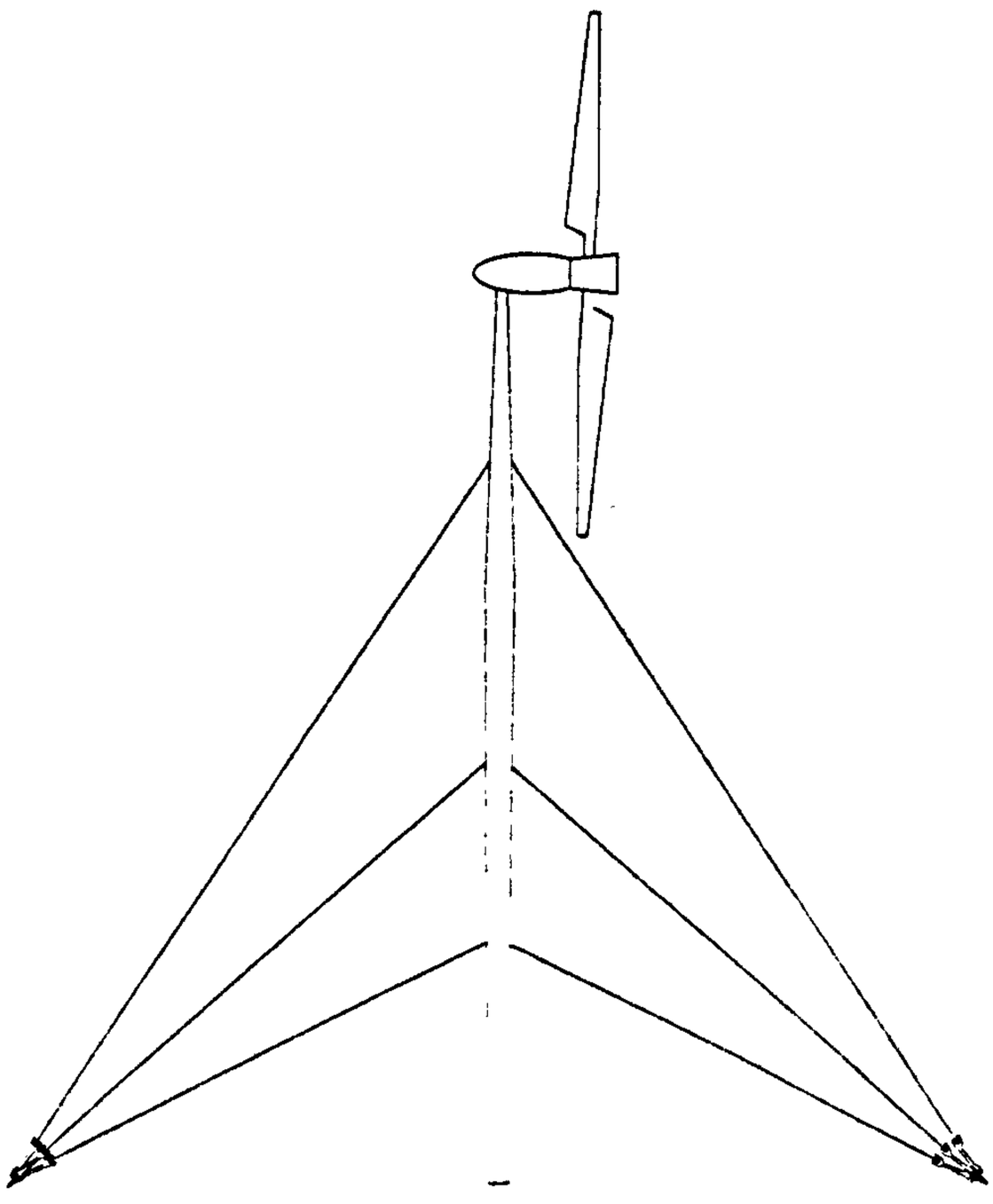

Figure 3.5: A wind turbine with three sets of guy cables.

Table 3.1: Summary of Euler buckling analysis of guyed wind turbine towers with different boundary conditions.

	description	decreasing effective length	
		F_{nv}	F_{cv}
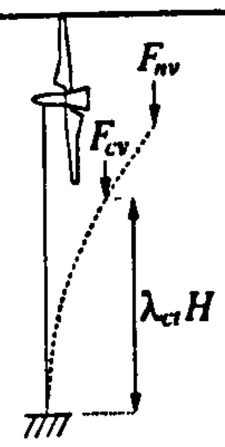	cantilever	$4H$	$4\lambda_{ct}H$
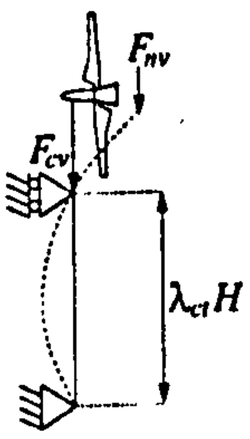	beam simply supported at $x = 0$ and $x = \lambda_{ct}H$	$(2 - \lambda_{ct})H$	$\lambda_{ct}H$
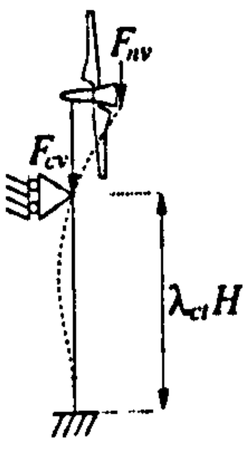	beam built in at $x = 0$ and simply supported at $x = \lambda_{ct}H$	$0.7(2 - \lambda_{ct})H$	$0.7\lambda_{ct}H$

- the base is neither hinged nor built in.

Prior to buckling it is possible to find a deflection shape for which all the loads applied externally are in equilibrium with the internal bending moments $M_t(x) = E_t I_{xt} \left.\frac{d^2v}{dx^2}\right|_x$ in the tower. If a deflection shape is chosen at random for which the resultant moment due to applied loads is greater than $E_t I_{xt} \left.\frac{d^2v}{dx^2}\right|_x$. $E_t I_{xt} \left.\frac{d^2v}{dx^2}\right|_x$ will have to increase. This can only happen if $\left.\frac{d^2v}{dx^2}\right|_x$ increases since $E_t(x)$ and $I_{xt}(x)$ are fixed for any particular structure. As $\left.\frac{d^2v}{dx^2}\right|_x$ increases, $v(x)$ increases. Because the contribution to the bending moment $M_t(x)$ of the axial forces is dependent on the deflection $v(x)$ of the tower, $M_t(x)$ also increases. Prior to buckling, this loop converges on an equilibrium deflection shape. At some critical state of axial loading, this loop becomes unstable, and no equilibrium deflection shape can be found. Above this critical state, stability returns, but deflections are opposite in sign to those for load states below the critical buckling loads. This may just be due to the application of a small lateral load on the tower and so purely the result of the analytical method. The existance of stable tower deflections at load states higher than critical and subsequently higher buckling modes is probably of no practical significance to the designer of wind turbine towers.

The static model of the tower (Section 2.3) includes the effect of these displaced axial loads by direct solution of a system of simultaneous equations rather than the iterative method suggested above. Until the axial load approaches the critical buckling load, deflections will be small and proportional to the applied lateral force. For instance, if a constant lateral force of 1 N is applied at the top of the tower and a vertical force is steadily increased, as some critical load is approached, tower deflections will increase assymptotically. Above that load, the only way that the tower can be in equilibrium is if deflections are negative (Figure 3.7).

An example of non-Euler buckling is given in Figure 3.6 in which the initial estimate of the buckling load F_e is calculated using Equation 3.6. The effective length of the tower is calculated using Equation 3.7. For the static model, the tower is loaded at the top (the tower buckles when $F_{nv} = F_e$). The tower radius and wall thickness vary in the same way as in the tower used for the 300 kW Carter wind turbine of the type used at Great Orton Airfield. The base is built in. A list of other parameters for this wind turbine is given in Appendix H. As well as the geometric factors which make this example deviate from an Euler strut, the tower is also loaded by its own weight under a gravitational acceleration of 9.81 m s^{-1}. This reduces the additional vertical load at the tower top which is necessary to cause buckling.

Euler buckling can also be used to test if vertical forces are treated correctly by the static model. Design parameters must be chosen so as to define a uniform, slender strut. The same ultimate buckling load should be predicted using Euler theory as using the *general static model* (Chapter 2). The comparison is made later in Section 5.1.2.

As well as applying a vertical force to the top of the tower, it is also possible to initiate buckling of the tower by increasing the initial strain in the guys. This increases an axial load on the tower below the point of attachment of the guy cables. This allows the maximum initial guy strain of the guyed wind turbine tower to be estimated.

The variation of the deflection of a point on the tower (for instance, $v(H)$) with ϵ_{ic} is assymptotic, and the variation of the reciprocal of deflection with ϵ_{ic} is approximately linear (particularly close to $\epsilon_{ic(\text{crit})}$). This property is used for the numerical search routine described in the next section.

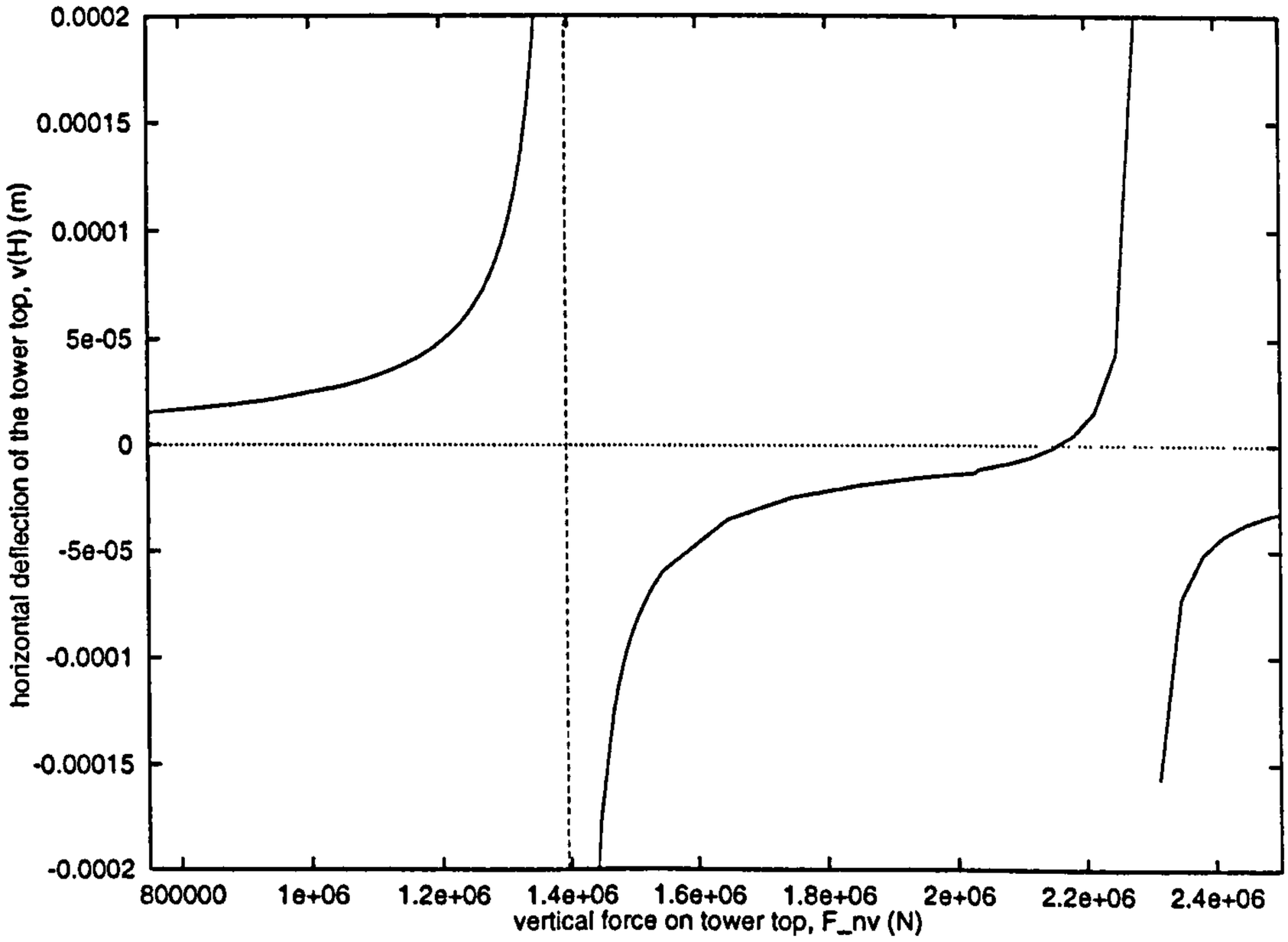

Figure 3.6: The lateral deflection of the top of the tower ($v(H)$) as the vertical load applied there approaches the critical value for buckling of the tower. Tower data are from the Great Orton type design (see Appendix H). The buckling load is 1.395×10^6 N. Euler buckling theory is used to make an initial estimate of the buckling load using Equations 3.6 and 3.7 or 3.8. In this example, the Euler buckling load calculated was 1.336×10^6 *N.*

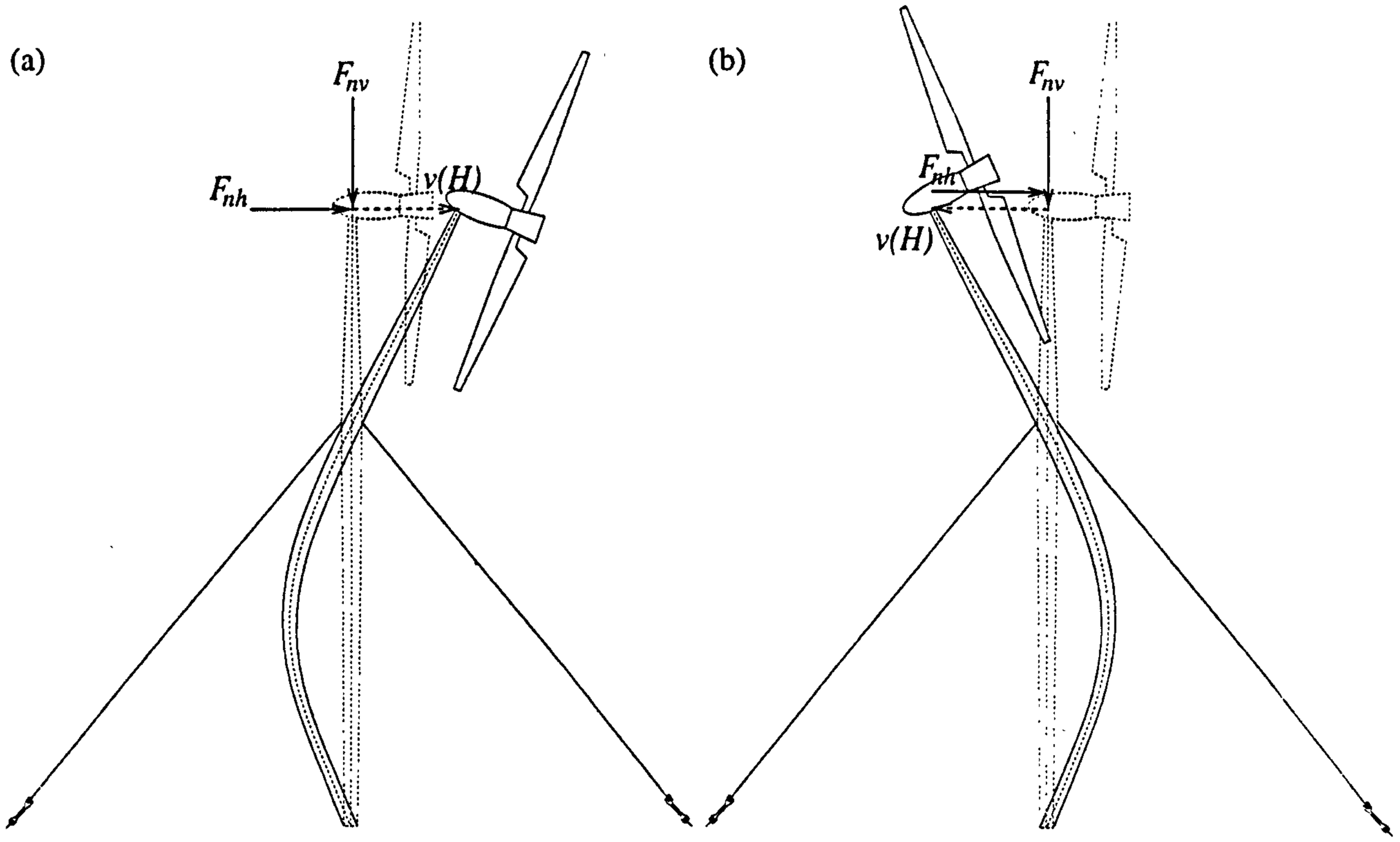

Figure 3.7: Below the critical value of the axial load ($F_{nv} < F_e$), the lateral deflection of the tower top ($v(H)$) is in the same direction as the applied lateral load, F_{nh} (magnitude, 1 N). Above the critical value of the axial load ($F_{nv} > F_e$), the lateral deflection of the tower top ($v(H)$) is in the opposite direction.

3.2.1 Numerical Search Method

In order to find either the critical tower top load or the critical initial strain in the guys, a good initial estimate must be made and a search routine employed. Equations 3.6 and 3.7 or 3.8 are used to make initial estimates.

The function called by the search routine is a modification of the lateral static deflection function (Section 2.3) whose output is the reciprocal of the deflection of the tower at some height $\frac{1}{v(H_v)}$. The height H_v chosen will be the height at which the deflection will be large. At certain heights, the deflection is zero (the buckling mode shape has a node). This may be due to some nearby physical restraint such as the point of attachment of the guys or may be that a buckling mode higher than the fundamental is sought and there are nodes at points other than the physical restraints. Two specific variants of this function have so far been written: one for buckling due to F_{nv} and one for buckling due to ϵ_{ic}. An initial estimate of the buckling mode shape is a sinusoid. The i^{th} Euler buckling mode shapes of simply supported towers loaded at the top (Equation 3.10) or at the point of attachment of the guy cables (Equation 3.11) guyed towers are given.

$$v(x) = \sin\left(i\pi\frac{x}{H}\right) \tag{3.10}$$

$$v(x) = \sin\left(i\pi\frac{x}{\lambda_{ct}H}\right) \tag{3.11}$$

Input to the function are:

1. the current estimate of the critical axial load (either F_{nv} or ϵ_{ic}) and
2. the number of the buckling mode sought.

Within the function, a sinusoidal distribution of very small horizontal force densities, f_h is generated. This distribution (Equation 3.12) is dependent on the number (i) of the buckling mode sought as well as the physical length of the tower able to buckle ($H_{(\text{phys})}$). Along with the current estimate of the critical axial load, this array of distributed horizontal forces is passed to the *general static analysis function* (Section 2.3) and the deflection shape is returned. The reciprocal of the deflection of the tower at the specific height $\frac{1}{v(H_v)}$ is returned to the search routine which attempts to find when this becomes zero.

$$f_h(x) = \sin\left(i\pi\frac{x}{H_{(\text{phys})}}\right) \tag{3.12}$$

The initial estimate is made using Equation 3.6. The effective length is estimated using techniques described in Appendix F.1. The user can specify two offset ratios r_1 and r_2 so that the two initial input values are $r_1\epsilon_{ic}$ and $r_2\epsilon_{ic}$ (or r_1F_{nv} and r_2F_{nv} in the case where it is the critical value of the tower head force. F_{nv} that is sought). This allows some flexibility to ensure that the critical value is within the range defined by the initial estimates.

The variation of tower deflection. $v(H_v)$ with applied axial force (F_{cv} or F_{nv}) is like the curve shown in Figure 3.6. The solution is where the deflection. $v(H_v) \to \infty$. A graph of

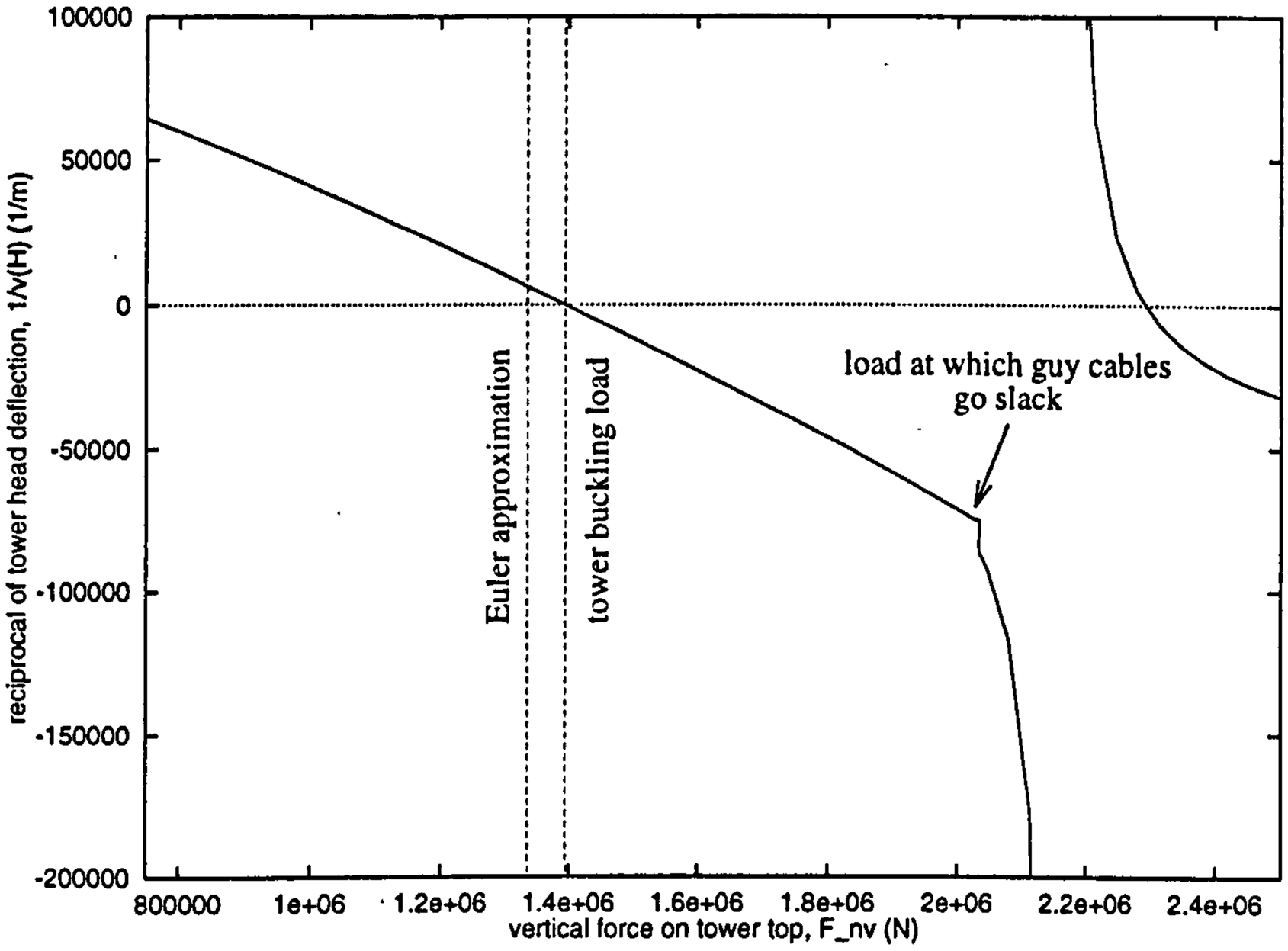

Figure 3.8: A graph of the reciprocal of the deflection of an unguyed tower $\frac{1}{v(H)}$ *against the vertical force* F_{nv} *applied at the top (Figure 3.6). The initial estimate using Euler buckling theory is* 1.336×10^6 *N. The final buckling force predicted is* 1.3950×10^6 *N. A discontinuity is shown on the curve where the guy cables become slack and there is a change i the actual structure being modelled by the analytical method.*

the reciprocal of the deflection, $\frac{1}{v(H_v)}$ against F_{nv} (see Figure 3.8) crosses the horizontal axis at values of F_{nv} which correspond to the modal buckling loads, F_{ei}.

A similar relationship would be seen if $v(H)$ were plotted at various values of ϵ_{ic}. Figure 3.8 has been plotted by changing F_{nv}, finding $v(H)$ and taking the reciprocal, $\frac{1}{v(H)}$. Although values of $v(H)$ can be found using static analysis methods (Chapter 2), the gradient of curves like the one in Figure 3.8 cannot easily be found. Efficient search methods like the Newton/ Raphson method [31] cannot therefore be used. The simplest search method is to take two initial values of F_{nv} calculated from the Euler prediction for a uniform strut (average radius, wall thickness and material properties) and to construct a straight line between the two points. The value of F_{nv} at which this line gives $\frac{1}{v(H)} = 0$ is the next estimate of the buckling load, F_e. This method is fairly slow but will not fail as long as initial estimates are close enough and either side of the point at which $\frac{1}{v(H)} = 0$. The closer the tower is to a uniform, hollow cylinder, the closer the initial estimates to the final solution.

A more elaborate method of finding the Euler load is to find the positions of three points $\left(\left(F_{nv1}, \frac{1}{v(H)}\Big|_1\right), \left(F_{nv2}, \frac{1}{v(H)}\Big|_2\right), \left(F_{nv3}, \frac{1}{v(H)}\Big|_3\right)\right)$ on the curve in Figure 3.8 and construct a parabola between them.

$$\frac{1}{v(H)} = A\,(F_{nv})^2 + B\,(F_{nv}) + C \tag{3.13}$$

In Equation 3.13, the parameters, A, B and C are dependent on the positions of the three points through which the quadratic passes and are found by solving Equation 3.14 using Gaussian elimination.

$$\begin{Bmatrix} A \\ B \\ C \end{Bmatrix} = \begin{bmatrix} F_{nv1}^2 & F_{nv1} & 1 \\ F_{nv2}^2 & F_{nv2} & 1 \\ F_{nv3}^2 & F_{nv3} & 1 \end{bmatrix}^{-1} \begin{Bmatrix} \frac{1}{v(H)}\Big|_1 \\ \frac{1}{v(H)}\Big|_2 \\ \frac{1}{v(H)}\Big|_3 \end{Bmatrix} \tag{3.14}$$

The next estimate of the critical load F_{nv} on the tower is given by solving Equation 3.13 to give Equation 3.15.

$$F_{nv}\Big|_{\frac{1}{v(H)}=0} = \frac{-B \pm \sqrt{(B^2 - 4AC)}}{2A} \tag{3.15}$$

Equation 3.15 is the formula for the value of F_{nv} at which $\frac{1}{v(H)} = 0$. This method often fails because the approximate quadratic curve may not include a value of F_{nv} at which $\frac{1}{v(H)} = 0$. For convergence, the initial estimates must be better for the quadratic method than for the linear method but the quadratic method will require fewer iterations to achieve convergence to the same accuracy.

The method implimented is due to van Wijngaarden, Dekker and Brent [33] and uses the program listing in 'Numerical Recipes in C' [31]. It uses a number of different search techniques (linear and quadratic) to ensure that the solution is found in a short time with a high likelihood of convergence.

Chapter 4

Iterative Modal Analysis

The natural or modal response of a structure is an important way of describing its dynamic characteristics. Although the principle of energy conservation underpins modal analysis, dynamic analysis of non-conservative systems is possible using modal analysis by, for instance, incorporating damping at a later stage. Various methods of finding the modes of free vibration of an idealised, linear structure are available. Rayleigh's method [16] relies on an assumption about the mode shape. Ritz's method [34] allows this shape to optimised. The Improved Rayleigh Method [35] uses static analysis of the structure subject to quasi-static inertia loads to modify the initial assumption about the mode shape. Stodola's method [17] [35] [34] also involves static analysis of the structure. The frequency is estimated from the ratio of two consecutive estimates of the mode shape. This gives rise to an iterative method which is found to converge rapidly [34].

In this thesis a method is described which combines Stodola's approach with Rayleigh's method. Each stage of the iterative process is self-contained with the frequency estimate depending only on the current estimate of the mode shape estimate (Rayleigh's method) and the next mode shape estimate depending only on the previous estimates of the mode shape and frequency. No other examples of the application of this combination of analytical approaches has been found.

Having calculated a sufficient number of structural mode shapes to a required level of accuracy, they can each be weighted by a different factor and combined so as to describe any deformation shape. By considering the natural frequencies of each mode, time histories of structural deformation can also be estimated. This is called linear modal superposition.

The most useful application of linear modal superposition is to calculate the damage due to fatigue of the structure. This has not been reported in this thesis for any of the Carter wind turbines but the techniques are described briefly in the following paragraphs.

The dynamic loading on the wind turbine can be described deterministically and statistically. The frequency of occurrance of a wind of a particular speed at a particular point on the structure (particularly points on the rotor disk) over the life of the wind turbine is known from meteorological measurements or models. The loads due to these wind speeds can be calculated from knowledge of the aerodynamic lift and drag forces generated by different surfaces and the natural modes of the structure. Hence at each chosen point in the structure, the number of cycles of each particular stress amplitude can be added up over the life of the

wind turbine using Miner's rule [25]. Mean stress effects can be included using the *Goodman* formula [25]. The *Rainflow Cycle Counting* method provides a computational means for summarising the damage due to a Power Spectral Density description of the structural loads by calculating *damage equivalent loads* [36] [37].

Garrad and Hassan's paper [38] demonstrates the importance of including atmospheric turbulence in a description of the wind loadings on a wind turbine. This is partly because of the possibility of additive effects of the cyclic and stochastic loads. An overview is given of the strategy of modelling the dynamic response to a realistic model of the temporal and spacial variations of wind loads to predict both extreme loads and fatigue life. In the paper [38], the history of analytical models of wind turbines in response to turbulence is traced back to Rosenbrock's work in 1955 [39].

The methods of fatigue analysis are reviewed with particular reference to data from a Howden HWP330 wind turbine in the paper by Bishop et al [37].

4.1 The Equations of Motion

The most direct way of finding the modal response of structural components is to solve the equations of motion to find the eigenvalues and eigenfunctions. This is only possible for certain, idealised models of the structural components. In this section, eigenanalysis of bars is described.

As already stated, lateral, longitudinal and torsional vibrations of wind turbine towers will be treated separately (see Section 2.1). This is justified for a homogeneous, prismatic bar with a symmetrical cross section. The equations of motion for torsional and longitudinal vibrations are derived in a similar way to give second order partial differential equations (Equations 4.1 and 4.3). For lateral vibrations, a fourth order partical differential equation can be derived from the equations of motion (Equation 4.5 and see also Appendix C). For the complete derivation of any equations in this section (Section 4.1), see Timoshenko's [40] or den Hartog's [34] books. In Equations 4.1, 4.3 and 4.5, the parameters, $C_{\omega iC}$, $C_{\omega iT}$ and $C_{\omega iB}$ are dependent on the particular boundary conditions (the end supports of the beam) and the number i of the mode of interest. These factors also affect the mode shape. Table C.1 in Appendix C lists some values of $C_{\omega iB}$ for different end conditions.

$$\frac{\partial^2 u}{\partial x^2} = \frac{E_t}{\rho_t}\frac{\partial^2 u}{\partial x^2} \tag{4.1}$$

$$\omega_{iC} = C_{\omega iC}\sqrt{\frac{E_t}{\rho_t}} \tag{4.2}$$

$$\frac{\partial^2 \theta}{\partial x^2} = \frac{G_t}{\rho_t}\frac{\partial^2 \theta}{\partial x^2} \tag{4.3}$$

$$\omega_{iT} = C_{\omega iT}\sqrt{\frac{G_t}{\rho_t}} \tag{4.4}$$

$$\rho_t A_{xt}\frac{\partial^2 v}{\partial t^2} = E_t I_{xt}\frac{\partial^4 v}{\partial x^4} \tag{4.5}$$

$$\omega_{iB} = C^2_{\omega iB}\sqrt{\frac{E_t I_{xt}}{\rho_t A_{xt} H^4}} \tag{4.6}$$

The equations of longitudinal, torsional and lateral motion of a wind turbine tower are given by Equations 4.1, 4.3 and 4.5 provided that it is cylindrical with constant material properties and negligible nacelle mass. The base must also be either ideally hinged or rigidly built in. There must either be no guy cables or they must have infinite longitudinal stiffness and zero flexural rigidity. This situation corresponds to an ideal pin joint at the point of attachment of the guy cables to the tower. There must be no damping which would couple the distance and time dependencies of the displacement. The solution ($v(x,t)$) is then a separable function of distance and time ($v(x)\cos(\omega_{nB}t)$).

These conditions are restrictive. Only in certain circumstances will they model a physical system well.

Greater flexibility is offered by the *general numerical method* described in this chapter which relies on Rayleigh's energy method to estimate the frequency of vibrations and Stodola's method to refine successive estimates of the mode shape. The tower may be non-uniform with distributions with height of mass and stiffness described by discrete arrays. Structual elements such as the nacelle and the guy cables may be included in addition to the tower. In Section 4.3.1, *Rayleigh's* method is directly compared with solutions of Equation 4.5. In Section 5.1.3, results from the *general numerical methods* are compared with solutions of Equations 4.1, 4.3 and 4.5 for particular, *ideal* situations.

The most common application of Rayleigh's method is in conjunction with Ritz' method for the optimisation of algebraic representations of the mode shapes (for instance. Rosen 1986 [41], Schmidt 1989 [42] and Wang 1997 [43]). Stodola methods are also in current use (for instance Niblett 1983 [44], Schmidt 1989 [42] and Nakahira et al 1992 [45]). However, none of these publications describes the combination of Rayleigh's and Stodola's methods alone.

4.2 Assumptions for Modal Analysis

During Simple Harmonic Motion, all parts of the structure move in unison and their deflections are sinusoidal with respect to time. The natural mode shapes can be defined in terms of the deformation of all parts of the structure relative to one another.

The method used for this research thesis to estimate the mode shapes and frequencies for Simple Harmonic Motion of the tower is illustrated in Figure 4.1. It is a combination of a quasi-static technique (Stodola's method) and dynamic frequency estimation (Rayleigh's method).

Because vibrations are undamped, neither aerodynamic drag on the rotors. nor surface sliding friction in the structure, nor viscous deformation within materials is modelled. Therefore. all internal and external forces are conservative. Energy changes reversibly from kinetic energy to potential energy and back again during each oscillation of the structure. The maximum kinetic energy of the entire structural system is therefore equal to the maximum potential energy. Rayleigh's method uses an estimate of the mode shape to calculate both

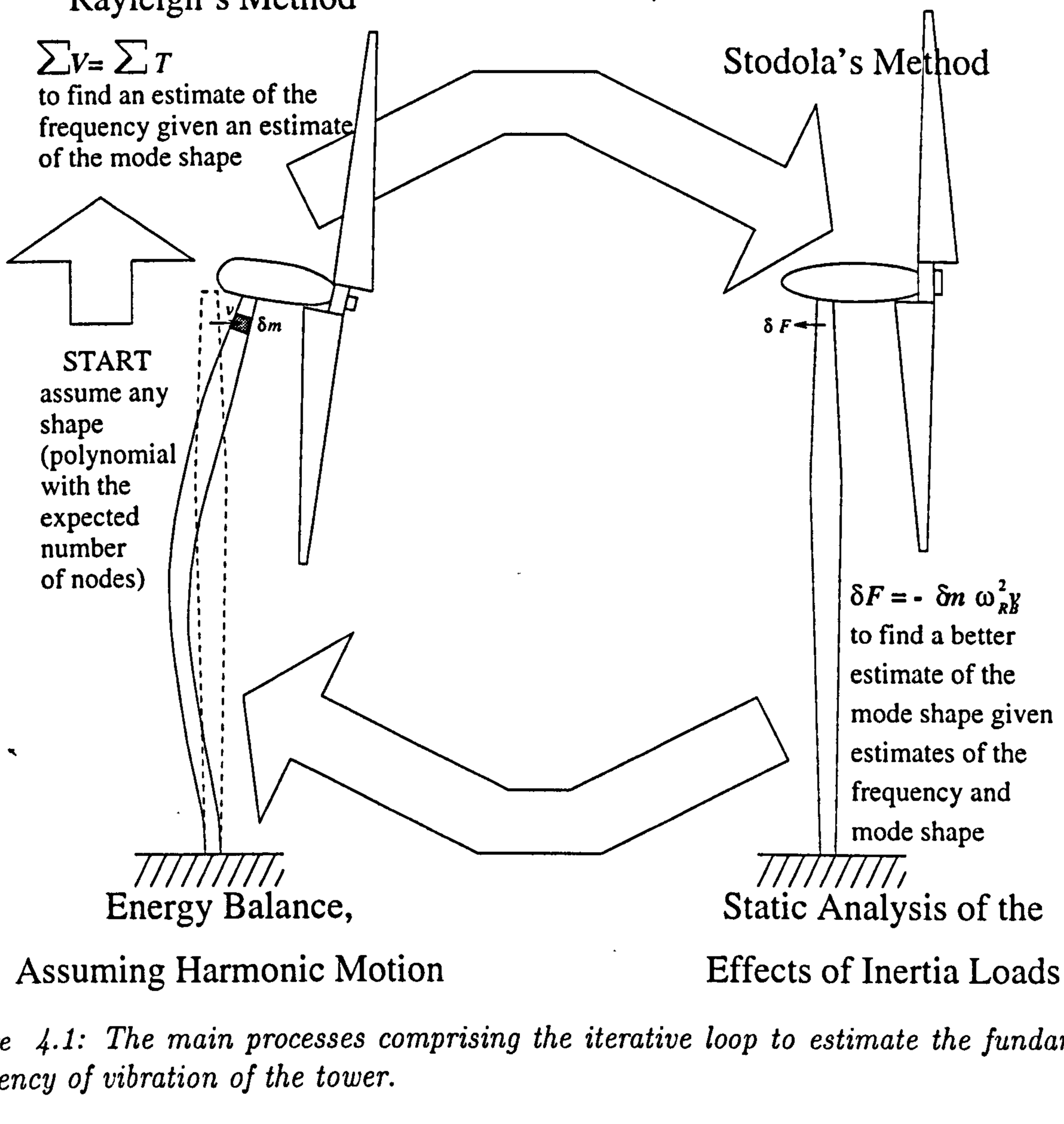

Figure 4.1: The main processes comprising the iterative loop to estimate the fundamental frequency of vibration of the tower.

the maximum kinetic energy and the maximum potential energy and from these, an estimate of the natural frequency, (the *Rayleigh frequency*) can be calculated.

The maximum kinetic energy occurs at the time when the deflections are all zero; the maximum potential energy occurs at the time when all parts of the structure simultaneously reach their maximum deflections.

Because there is no coupling between the variation of the deflection with position in the structure and with time, solutions are separable (see Section 4.1). Since kinetic energy is proportional to the square of the velocity of a particular part of the structure, expressions for the kinetic energy all have the common factor of the square of the *Rayleigh frequency* (see Section 4.3 later). Since all functions of the deflection or its time differentials are directly proportional to the absolute magnitude of deflection, expressions for kinetic energy and potential energy all have the common factor of the magnitude of the deflection and vary linearly with it. The absolute magnitude of deflections will therefore be indeterminate using Rayleigh's method. Only a modal analysis technique that incorporates damping is able to predict absolute deflections.

Given the assumption of linearity, all mode shapes are orthogonal functions. Any complex vibration can therefore be split into a weighted sum of the natural harmonics of the system using a process similar to a reverse Fourier Transformation. It is also possible to split any forcing into a harmonic series so that the response of the system may be found to each of the frequency components of the excitation in turn.

Despite the assumption that different classes of vibrations are not coupled (see Section 2.1), in practice ([16] Ch VII, para 149), the frequencies of longitudinal and torsional vibration are likely to be much higher than bending vibrations. This means that there is a high probability that one of the higher bending harmonics will share the same frequency as the fundamental longitudinal or torsional frequency. In this case, any small inhomogeneity of material properties or deviation of the cross section from circular will provide some coupling force across these classes of vibration and excite the other vibration class. Indeed, when operating, lightweight towers are observed to vibrate in a complex manner involving all classes of vibration (torsional, longitudinal and lateral).

In Stodola's method, it is assumed that the inertia forces on the structure reach equilibrium with the internal elastic stresses in the material. Static analysis of the structure in response to these inertia loads relies on *small deflection theory* (see Section 2.1). It is normally assumed that an infinite period of time is available in which the system can reach equilibrium. In reality, the system is in continuous motion at high speed. However, the assumption is justified [17] if the amplitude of the vibrations (and therefore the loading changes between each iteration step) are small. The values of Young's modulus are those measured in static experiments and no strain-rate stiffening is considered.

In order to use small deflection theory to calculate deflections in response to inertia loads. (Section 4.4), movements of points on the structure must be small. Since absolute deflections are indeterminate from modal analysis. this additional constraint is incorporated by normalising the modal deflection shape so that the maximum structural deflection is unity and dividing by a large number. This is particularly important for modal anlalysis of prestressed structures where large structural deflections may involve discontinuous load responses.

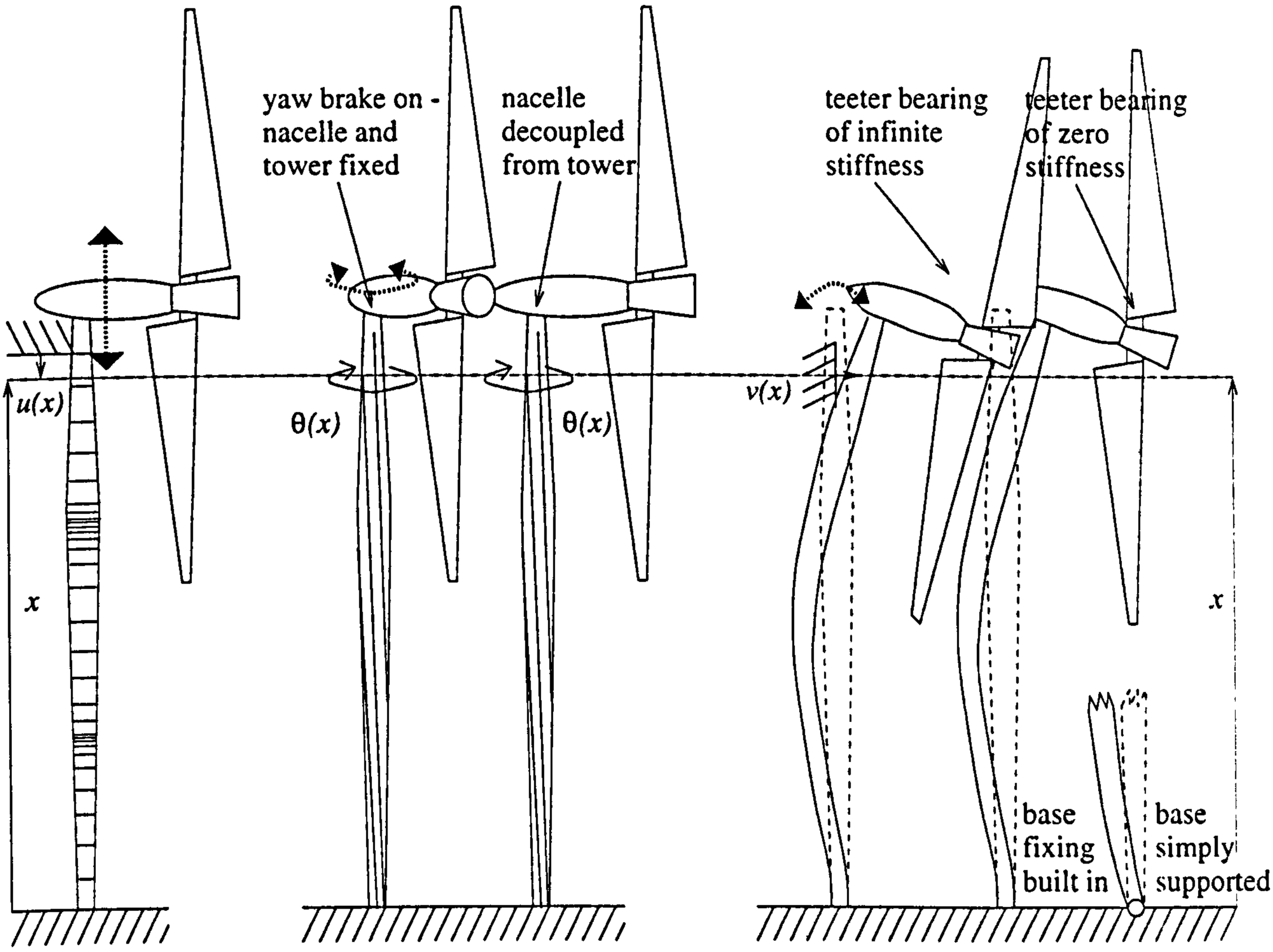

Figure 4.2: The three classes of vibration. For this analysis they are assumed to be decoupled.

4.2.1 Coupling Between Components

For Carter wind turbines, certain components are assumed to be mechanically uncoupled. The two bladed rotor is connected to the low speed shaft via a teeter bearing which is assumed to transfer no torque. Figure 4.2 shows the effect on the motion of tower and nacelle of including a teeter bearing. This reduces bending moments in the low speed shaft. Such isolation of the rotor prevents, for instance, gyroscopic torques being passed from the rotor to the low speed shaft in situations such as the two illustrated in Figure 4.3:

1. tilting of the nacelle with the spinning rotor horizontal,
2. yawing of the nacelle yaws with the spinning rotor vertical

In neither case are the gyroscopic torques generated passed to the nacelle unless the rotor hits its teeter stops. The rotor can be treated as a lumped mass in these cases. The rate and duration of rotor teeter is limited by aerodynamic damping and viscous damping in the teeter bearing.

In situations in which the rotor is perpendicular to the orientations illustrated in Figure 4.3, gyroscopic torques are passed to the low speed shaft because the blades are rotationally rigid along their axes. Because the moments of inertia of the blades are smaller about these axes than about the axis of rotation, the torques are correspondingly smaller. However, if yaw or tilt rates are high, these gyroscopic torques may be significant. This suggests the possibility of coupling between blade torsional and tower lateral modes which have not been analysed for this thesis.

The low speed shaft is fixed directly to the drivetrain so that the roll moment of inertia of the nacelle includes the moment of inertia of the rotor about its axis of rotation (Figure 4.5 in section 4.2.2 shows the model representation of these moments of inertia).

Likewise, it is assumed there is no coupling in yaw between the nacelle and the tower in normal operating conditions. The Carter 300 kW wind turbine operates down-wind with free yaw. The yaw motor is only used to orientate the nacelle in low winds or to untwist the power cables which pass from the generator down the tower. Therefore, the practical coupling between the nacelle and tower is likely to be small if any. However, by including a torsional spring with stiffness parameter, k_{yn} between the nacelle and tower, the model is able to simulate a variety of possible situations.

Two extreme situations can be modelled by setting k_{yn} to two extreme values:

1. Because the mass of the nacelle is usually large, when it is coupled rigidly to the tower ($k_{yn} > 1 \times 10^7$), it has a significant effect on the natural frequency of the structure (for example, using the description of the Carter 300 kW wind turbine at Great Orton Airfield. the fundamental torsional frequency is 2.30 Hz);

2. When the nacelle and tower are completely decoupled ($k_{yn} = 0$), the natural frequency of the structure is the same as that of the tower alone which is usually higher than with the nacelle attached (using the same example as quoted above. the fundamental torsional frequency is 13.7 Hz).

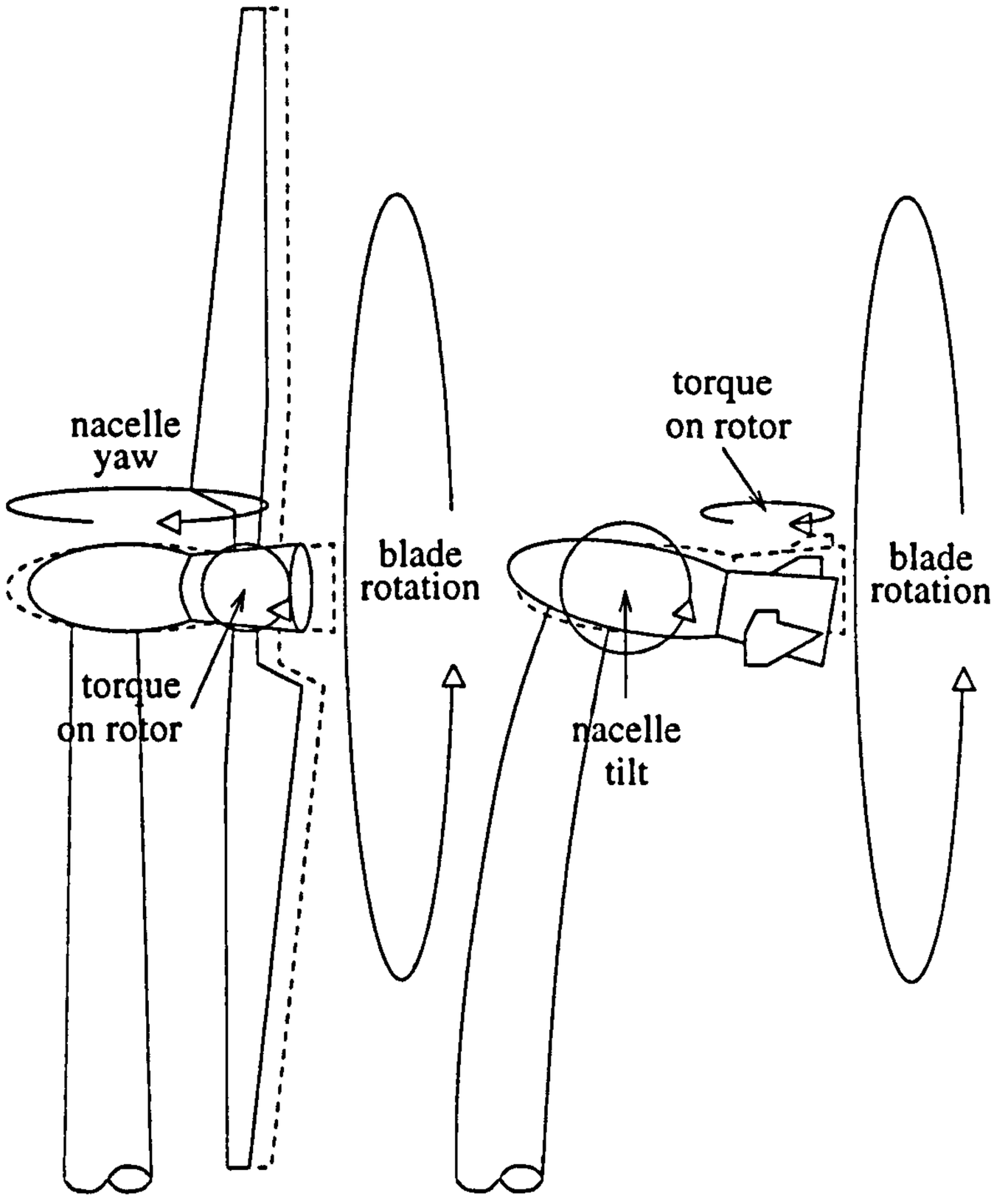

Figure 4.3: Two situations in which the low speed shaft is isolated from potential gyroscopic torques which arise because of the rotation of the blades.

As was stated in Section 2.2.2, two extreme settings for various parameters give the limits of a *range* of frequencies within which the natural frequency of a practical tower will fall. It is possible to employ this approach of modelling extremes for any of the other coupling situations described above. The Rayleigh method allows the addition to the model of new stiffness elements representing coupling between any two parts of the system. The stiffnesses must be linear (restoring force or torque must be proportional to deflection or angle of twist). However, it is not possible to include damping into these elements.

4.2.2 Parametric Models of the Nacelle

The nacelle houses the transmission and generator. In free-standing towers, there is usually a ladder to reach the nacelle. The diameter of the tower necessary for this may increase the tower's stiffness. The nacelle is large and strong enough for access, powertrain components are mounted on a bedplate and there is a fibreglass enclosure for protection and aesthetic reasons. For maintenance or replacement of large components, cranes are used. Lightweight towers, however, may be tilted down. This saves the expense of providing safe access to the nacelle. Figure 4.4 shows the tower of a Carter 300 kW wind turbine tilted down. This is a close-up picture of the tilted down tower shown in Figure 2.3.

One reason that the nacelle of the Carter wind turbines is smaller than wind turbines in which drivetrain components are mounted on a bedplate is that in the Carter design, the loads are carried by the drivetrain housing. The difference is similar to the difference between car and tractor designs. All components of a tractor are supported on the housing of the engine and transmission. In a car, engine and transmission are attached separately to the car body. Paul Gipe [46] suggests that this *integrated drivetrain* is illustrative of the difference in design philosophy between American and European wind turbine manufacturers. The latter, he argues are more conservative.

The tower mass is spread out over its height but in comparison the mass of the nacelle is lumped. The nacelle has therefore been modelled as a lumped mass. Nacelle moments of inertia are defined about yaw, roll and two tilt axes centred on the top of the tower. Included in these moments of inertia are those of the rotor.

'Aeroelastic' analysis is important and has already attracted some research (for example Bisplinghoff and Ashley's book [47] or Kiessling's derivation of the equations of motion using symbolic processing [48]). It includes the aerodynamic lift and drag forces in the elastic analysis of rotor deformations to predict the complicated dynamic response of the rotor when power is being generated. The powertrain is affected by this interaction because of the torque passed to it along the low speed shaft from the rotor. The tower provides certain reaction forces and torques through the generator and gearbox. The whole system therefore responds mechanically and electrically to the aerodynamic loads applied. In this thesis. the rotor is treated as a lumped mass (see Figure 4.5) and part of the nacelle. These complex interactions are therefore not modelled.

Figure 4.4: Access to the powertrain and other components housed in the nacelle is via a hatch in the GFRP pod.

4.3 The Rayleigh Method of Calculating Frequencies

Rayleigh's technique is to assume that, at resonance, the maximum potential energy of the whole system at time t is equal to its maximum kinetic energy at time $t + \frac{\pi}{2\omega}$ (where ω is the natural frequency of the mode of interest). This relies on the assumption that there are no dissipative effects like friction or any discontinuities. Without damping, energy is conserved and sinusoidal motion continues without attenuation.

The model of the physical structural support system is composed of several elements each of which has associated with it a mathematical term for energy (either kinetic, T or potential, V). These terms fit into the Rayleigh equation 4.8. The equations is a rearrangement of Equation 4.7. Because all terms for the kinetic energy of various parts of the structure have ω_{R1B} as a common factor, Equation 4.8 allows this angular frequency to be calculated. The expressions $\sum V$ and $\sum \frac{T}{\omega_{R1B}^2}$ are functions of the geometric and material properties of the structure and its modal deflection. Equations 4.12 and 4.13 give examples of these energy terms for the tower, a complete list is given in Appendix D).

$$\sum V = \sum T \tag{4.7}$$

$$\omega_{R1B} = \sqrt{\frac{\sum V}{\sum T/\omega_{R1B}^2}} \tag{4.8}$$

To explain the Rayleigh method more simply than if all model elements were described simultaneously, bending vibrations of the tower will be considered as an example. Kinetic energy is a function of the mass and the deflection of the structure and strain potential

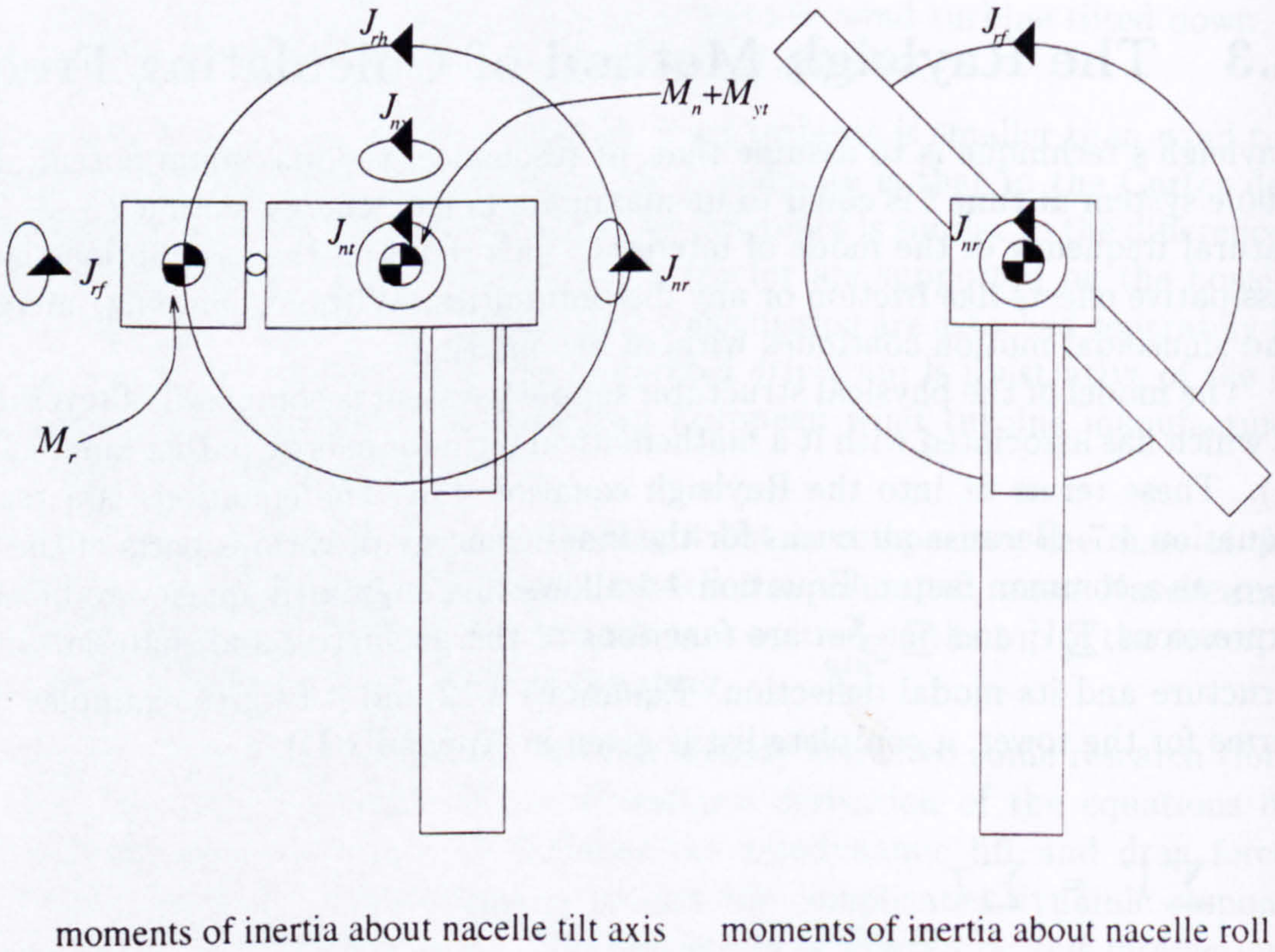

Figure 4.5: A photo of the nacelle and rotor of a 300 kW Carter wind turbine alongside schematic diagrams showing how nacelle masses and moments of inertia (about the axis of tilt in this case) are modelled.

energy is a function of its stiffness and curvature. The tower has both mass and stiffness (represented by its density, ρ_t and flexural rigidity, $E_t I_{xt}$) and so contributes to both left and right hand sides of the energy balance (Equation 4.7). In contrast, the nacelle has only mass and so contributes only to the right hand side. The guy cables have only stiffness and so contribute only to the left hand side.

The strain potential energy will be greatest when the system is in a state of maximum strain (or deflection). Gravitational potential energy is disregarded because only small, lateral, modal vibrations are considered and the vertical components of these movements of the tower are smaller still. Because of the continuous, periodic, reversible transfer of energy between potential and kinetic forms, the kinetic energy will be greatest as the system passes through its position of zero strain.

For simple harmonic motion, there is no damping and the motion is sinusoidal with respect to time. The deformation shape of the tower at any time is equal to the product of the *mode shape*, $v(x)$ and a time varying sinusoid, $\sin(\omega_{1B}t)$ where ω_{1B} is the fundamental angular frequency of bending vibrations (units: rad s^{-1}). The assumptions of simple harmonic motion, the conservation of energy and restoring loads being proportional to displacements are equivalent to the mathematical assumption that the partial differential equation (Equation 4.5) has separable solutions ($v(x,t) = v(x)\sin(\omega_{1B}t)$). The *mode shape* is a function only of tower height. The velocity (Equation 4.10) and the acceleration (Equation 4.11) of any point on the tower can be calculated by differentiating the displacement with respect to time:

$$\text{displacement} = v = v(x)\sin(\omega_{1B}t) \tag{4.9}$$

$$\text{velocity} = \dot{v} = -\omega_{1B}v(x)\cos(\omega_{1B}t) \tag{4.10}$$

$$\text{acceleration} = \ddot{v} = -\omega_{1B}^2 v(x)\sin(\omega_{1B}t) \tag{4.11}$$

From the mode shape, ($v(x)$), energy terms in Equation 4.8 can be calculated. The parameters used in these expressions to simulate the real structure are illustrated later in Appendix H, Figure H.1. As examples, expressions for the kinetic energy and strain potential energy of the tower are given in Equations 4.12 and 4.13. These equations apply to beams for which materials and geometric properties may vary with height and derivations are given in, for instance [16] and [35]. The summations in Equations 4.7 and 4.8 become integrals over the length of the tower. In this case the integrals must be evaluated at discrete points as for static analysis (see Section 2.3.2).

$$V_{Bt} = \int_0^H \frac{1}{2} E_t I_{xt} \left(\frac{d^2 v}{dx^2}\right)^2 dx \tag{4.12}$$

$$\frac{T_{Bt}}{\omega_{R1B}} = \int_0^H \frac{1}{2}\rho_t A_{xt}\left(\frac{\partial v}{\partial t}\right)^2 dx + \int_0^H \frac{1}{2}\rho_t I_{xt}\left(\frac{\partial}{\partial t}\frac{\partial v}{\partial x}\right)^2 dx$$

$$T_{Bt} = \omega_{1B}^2\left(\int_0^H \frac{1}{2}\rho_t A_{xt}\left(v\left(x\right)\right)^2 dx + \int_0^H \frac{1}{2}\rho_t I_{xt}\left(\frac{dv}{dx}\bigg|_x\right)^2 dx\right) \tag{4.13}$$

The common factor, ω_{1B}^2, in Equation 4.13 appears in all expressions for the kinetic energy of the vibrating structure.

In this thesis, f_{R1B} is called the *Rayleigh frequency* and is an estimate of the true, modal frequency of the structure. The accuracy of this approximation depends on the accuracy of the choice of modal deflection shape, $v(x)$. Improving the accuracy of this mode shape estimate is the subject of Section 4.4. Rayleigh's theory [16] is that of all mode shapes chosen, the one with the lowest *Rayleigh frequency* is the true mode shape for that model of the structure. This is because inaccuracies in any one mode shape estimate make it more conservative and increase the stiffness and hence the *Rayleigh frequency* f_{R1B}. Therefore f_{R1B} will always be an overestimate of f_{1B}.

$$f_{R1B} = \frac{\omega_{R1B}}{2\pi} = \frac{1}{2\pi}\sqrt{\frac{\int_0^H \frac{1}{2}E_t I_{xt}\left(v''(x)\right)^2 dx}{\int_0^H \frac{1}{2}\rho_t A_{xt}\left(v(x)\right)^2 dx + \int_0^H \frac{1}{2}\rho_t I_{xt}\left(\frac{dv}{dx}\right)^2 dx}} \tag{4.14}$$

The amplitude of the mode shape is indeterminate as stated in Section 4.2. If the amplitude of the mode shape function, $v(x)$ is increased by multiplying by any factor v_a, the right hand sides of both Equations 4.12 and 4.13 are multiplied by v_a. This applies for all expressions for kinetic or potential energy (Appendix D). In Equation 4.14, v_a will always cancel out and will not affect the value of f_{R1B}. This is intuitive since for systems with no damping the magnitude of vibrations at resonance is undefined or infinite.

In Equation 4.13, the second part of the expression for the kinetic energy, $\frac{1}{2}\rho_t I_{xt} v'(x)^2 \delta x$ occurs due to the rotation of elements δx of the tower (Figure 2.18). It contains a term $\frac{\partial}{\partial t}\frac{\partial v}{\partial x}$ representing the angular speed. This is described by Rayleigh as the rotational kinetic energy of a beam. This should not be confused with the actual rotational kinetic energy of the moving parts of the wind turbine such as the blades and powertrain. The 'rotational kinetic energy' of the tower is used for the analysis of beam vibrations only. Another term could be included [40] to model the shear deformation of the tower but because the tower is tall and slender, the effect of shear deformations is negligible.

4.3.1 Rayleigh Method for Simply Supported Beam

Equations 4.5 and 4.6 model the tower alone. They model the real structure closely, only if the tower mass predominates and the structure is not guyed. The value of the constant $C_{\omega iB}$ is dependent on the end fixing conditions of the tower.

It is possible to find the solution of Equation 4.5 in some idealised situations. For example, if the beam is simply supported, the eigenfunctions of Equation 4.5 can be shown to be multiples of a half sine wave (Equation 4.15) and $C_{\omega iB}$ is $i^2\pi^2$ (see Appendix C, Table C.1).

$$\begin{aligned} v(x) &= v_a \sin\left(i\pi\frac{x}{H}\right) \\ C_{\omega iB} &= i^2\pi^2 \end{aligned} \tag{4.15}$$

Using Equations 4.12 and 4.13 for the potential energy and the kinetic energy of the tower but neglecting the kinetic energy due to rotary inertia of the tower ($\frac{\partial}{\partial t}\frac{\partial v}{\partial x} \approx 0$), Equation 4.16 can be derived. The tower material properties must be constant along its height.

$$\omega_{R1B} = \sqrt{\frac{E_t I_{xt} \int_0^H \frac{1}{2} \left(v''(x)\right)^2 dx}{\rho_t A_{xt} \int_0^H \frac{1}{2} \left(v(x)\right)^2 dx}} \tag{4.16}$$

Using a dimensionless measure of vertical distance up the tower ($X = \frac{x}{H}$), Equation 4.16 can be rewritten as Equation 4.17.

$$\omega_{R1B} = \sqrt{\frac{E_t I_{xt} \int_0^H \frac{1}{2} \left(v''(X)\right)^2 dX}{\rho_t A_{xt} H^4 \int_0^H \frac{1}{2} \left(v(X)\right)^2 dX}} \tag{4.17}$$

Using Equation 4.6, Equation 4.17 can be rewritten to calculate the coefficient, $C_{\omega iB}$ (Equation 4.18).

$$C_{\omega iB} = \sqrt{\frac{\int_0^H \frac{1}{2}(v''(x))^2 dx}{\int_0^H \frac{1}{2}(v(x))^2 dx}} \tag{4.18}$$

Because the mode shape is already known to be a half sinusoid (Equation 4.15), this shape can be substituted into Equation 4.18 which gives $C_{\omega iB} = i^2\pi^2$. Rayleigh's method of calculating the frequency from an estimate of the mode shape (Equation 4.15) therefore gives the same value of $C_{\omega iB}$ as the solution of Equation 4.5 given in Appendix C.

The frequency of vibrations is given in Herz by Equation 4.19 and the complete solution to the fourth order partial differential equation (Equation 4.5) is given by Equation 4.20.

$$f_{R1B} = f_{1B} = \frac{i^2\pi}{2}\sqrt{\frac{E_t I_{xt}}{\rho_t A_{xt} H^4}} \tag{4.19}$$

$$v = v_a \sin(i\pi\frac{x}{H}) \sin\left(\sqrt{\frac{E_t I_{xt}}{\rho_t A_{xt} H^4}} i^2\pi^2 t\right) \tag{4.20}$$

4.4 Quasi-Static Analysis of Inertia Loads - the Stodola Method

To estimate the mode shape for a particular natural frequency, the Stodola technique is used to close each iterative loop (Figure 4.1). Initially, a smooth curve is generated with a number of nodes appropriate to the number of the harmonic sought. A sinusoidal or polynomial expression is used depending on the class of vibrations. From this the Rayleigh frequency is calculated. Stodola's method is to calculate inertia loads using the previous approximations of the mode shape and the natural frequency. These loads are used in static analysis of the structure to obtain a deflection shape which is the next approximation of the natural mode shape.

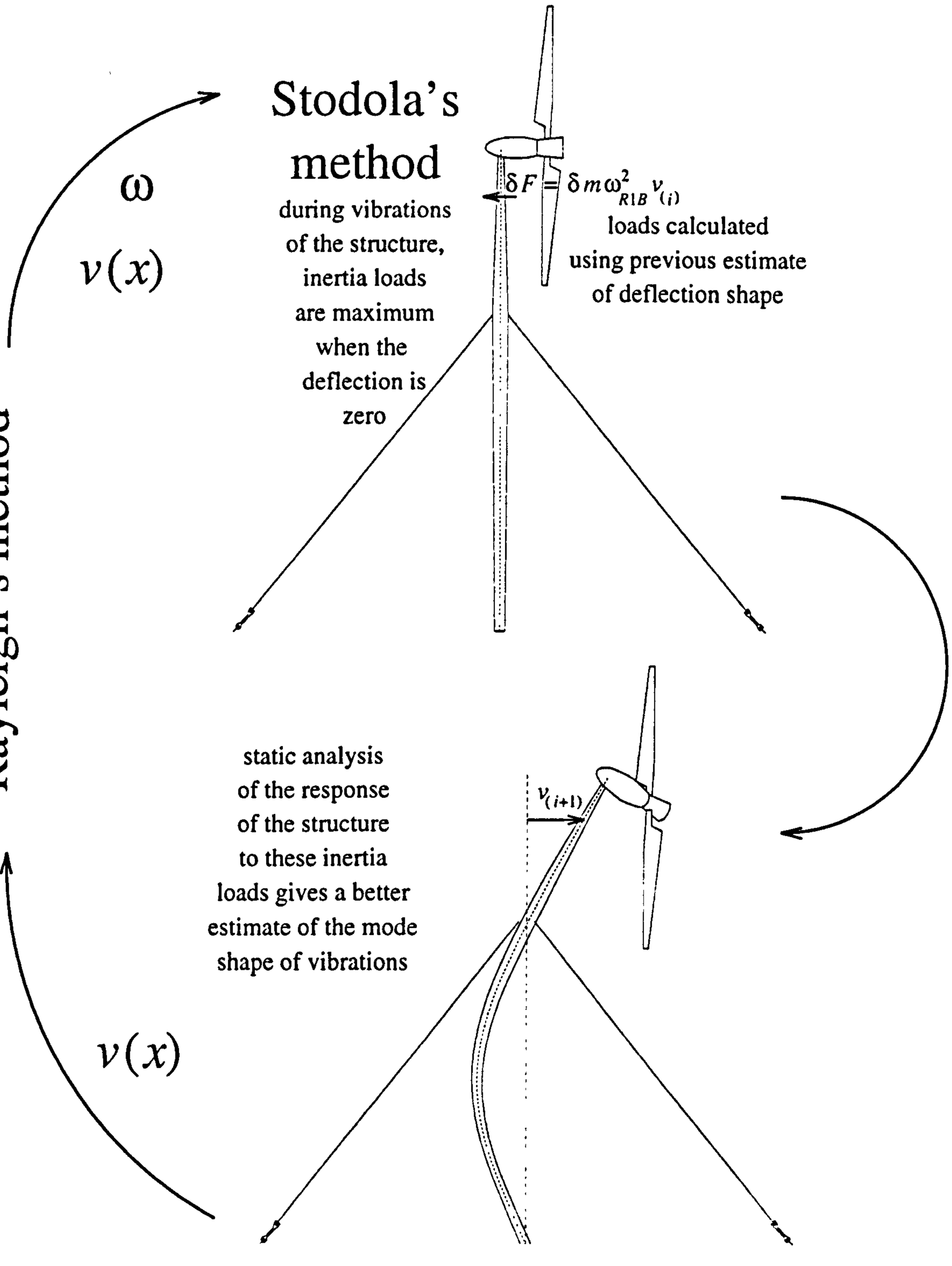

Figure 4.6: Stodola's method for calculating the fundamental frequency of bending vibrations of a wind turbine tower. Inertia loads are calculated given estimates of the natural frequency, ω_{1B} and the mode shape, $v(x)$. A quasi-static analysis of the structural response to these loads gives a better estimate of the mode shape, $v(x)$. Section 4.6 describes a method to calculate frequencies of harmonics higher than the fundamental.

Because the deflection is sinusoidally dependent on time, the velocity and acceleration are also sinusoidally time-dependent (see Equations 4.10 and 4.11). Newton's second law that force is equal to the product of mass and acceleration can be rearranged so that all terms are on the left hand side and the right hand side is 0.0. The products of mass and acceleration which now appear as negative terms on the left hand side are often called *d'Alembert* inertia loads. This is described in Meriam and Kraige [32] for example.

To illustrate the combined Rayleigh/ Stodola method, the lateral vibrations of a uniform, simply-supported tower are considered. This is the same example as was used to illustrate Rayleigh's method in Section 4.3.1. As an initial estimate, the mode shape is represented by a quadratic function (Equation 4.21).

$$v_{(1)1B} = v_a \left(x^2 - Hx\right) \tag{4.21}$$

Using Rayleigh's method and omitting the rotational kinetic energy term, the estimate of the frequency is given in Equation 4.22.

$$\omega_{R1B} = \sqrt{120}\sqrt{\frac{E_t I_{xt}}{\rho_t A_{xt} H^4}} \tag{4.22}$$

$$C_{\omega 1B} \approx 10.95 \tag{4.23}$$

The distributed *d'Alembert* load on the tower, f_h N m^{-1} is given in Equation 4.25. The reactions at the supports can be found by symmetry to be equal to F_{fh}, which is given in Equation 4.26are used as an example of this method. Static analysis of the tower subject to these loads gives the deflection $v_{(2)1B}$ in Equation 4.27.

$$f_h = -\omega_{R1B}^2 v_{(1)1B} \rho_t A_{xt} \tag{4.24}$$

$$f_h = -\frac{120 E_t I_{xt}}{H^4} v_a \left(x^2 - Hx\right) \tag{4.25}$$

$$F_{fh} = -10\frac{E_t I_{xt}}{H} v_a \tag{4.26}$$

$$v_{(2)1B} = v_a \left(Hx - \frac{5x^3}{3H} + \frac{x^5}{H^3} - \frac{x^6}{3H^4}\right) \tag{4.27}$$

In Equations 4.21, 4.26 and 4.27, $v_{(1)1B}$ is the first estimate of the fundamental frequency of bending vibrations of the tower and $v_{(2)1B}$ is the second estimate. Figure 4.7 compares the errors in the two estimates given in Equations 4.21 and 4.27.

Sections 4.4.1 to 4.4.4 give the origins of all the loads used in static analysis of bending of the structure (Section 2.3).

For simple harmonic motion, the maximum value of any type of inertia load on the structure will be proportional to the magnitude of the deformation and the square of the natural frequency (this follows from Equation 4.11 for the acceleration of any point on the structure).

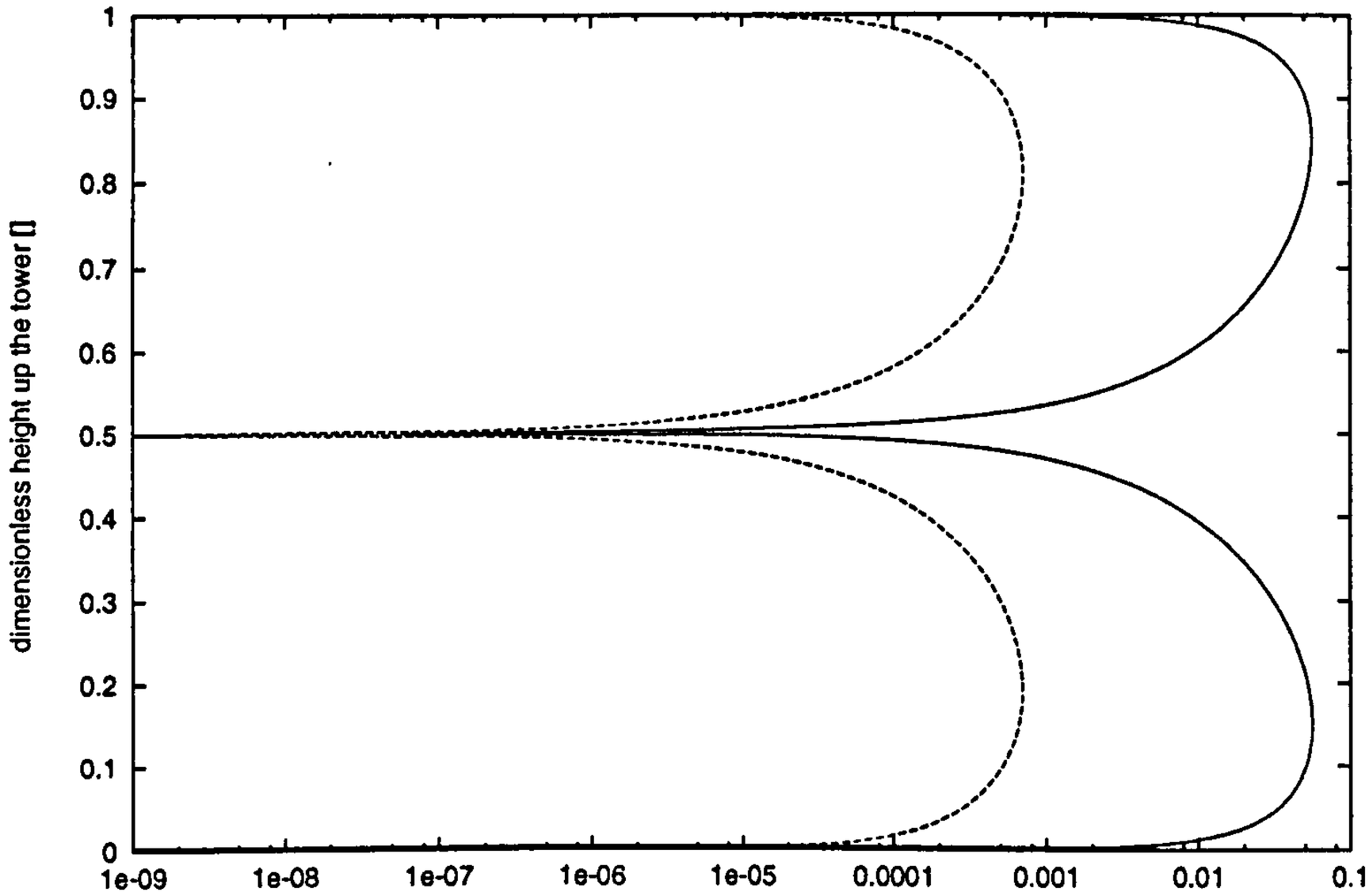

Figure 4.7: Comparison between the errors in two estimates of the mode shape of a uniform, simply supported tower. The vertical ordinate is scaled with respect to the tower height. The solid line shows the difference between Equation 4.21 and the sinusoidal mode shape 4.15. The dotted line shows the difference between Equation 4.27 and the sinusoidal mode shape.

Prior to convergence, inertia loads are not proportional to deflection. However, the loads on the structure are calculated in the same way. As the mode shape estimate approaches the true mode shape, deviations from simple harmonic motion become smaller.

It is found that if these two steps are repeated a small number of times, the frequencies calculated using the Rayleigh equation converge to the natural frequency of the structure.

Sections 4.4.1 to 4.4.4 illustrate the inertia (*d'Alembert*) loads on the structure used in Stodola's method for bending vibrations. A complete list of *d'Alembert* loads is given in Appendix E.

4.4.1 Concentrated Tower Head Force, F_{nh}

Figure 4.8 illustrates the two types of forces due to vibration of the structure. In the Figure are shown the point load, F_{nh}, at the tower top due to the nacelle inertia and the distributed horizontal loads, f_h due to the tower inertia (described in Section 4.4.2).

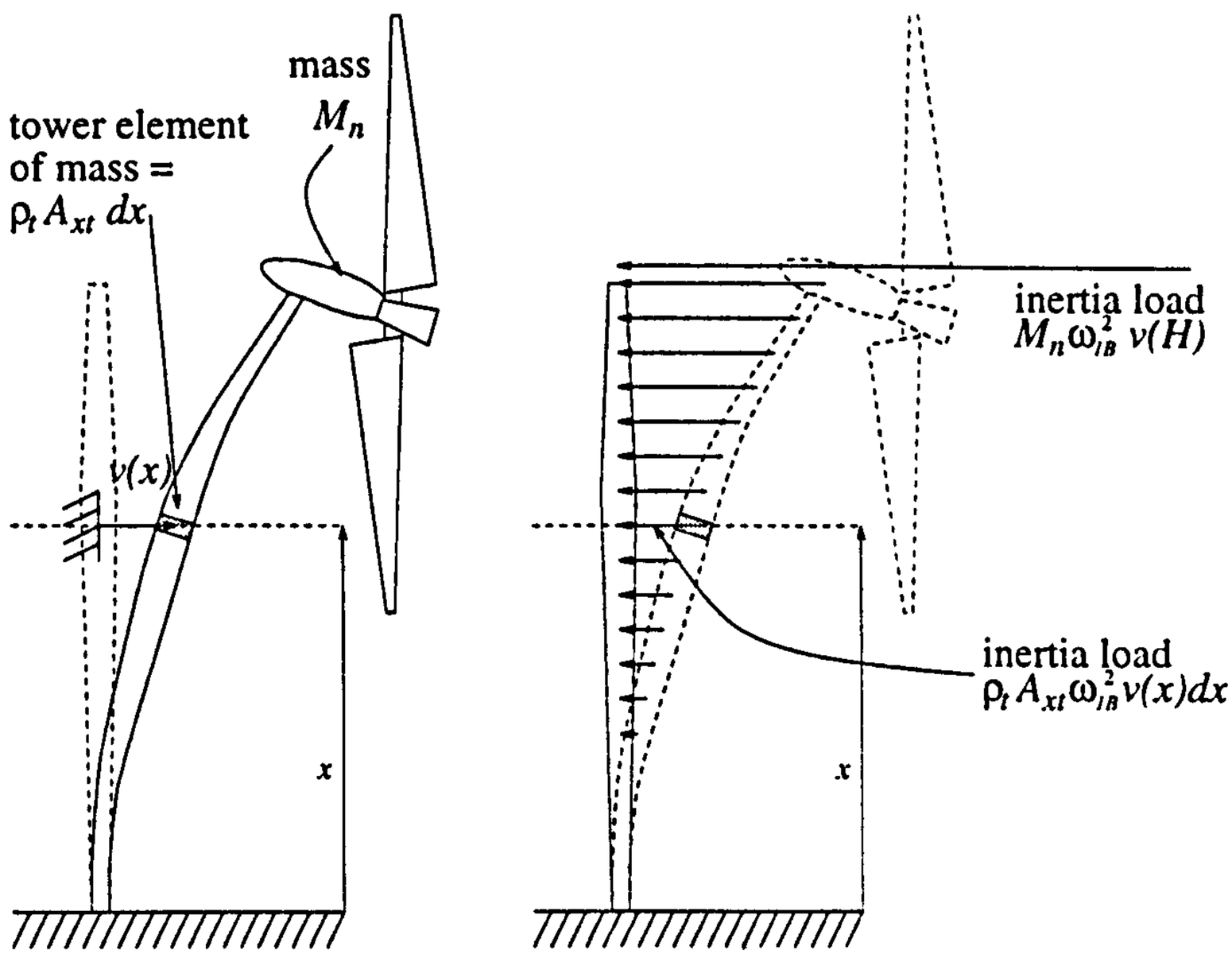

Figure 4.8: The dynamic loads on the tower due just to the inertia of the tower itself.

For simple harmonic motion (from Equation 4.11) at the fundamental frequency of bending vibrations, ω_{1B}, the force at the tower top due to the acceleration of the nacelle is given by Equation 4.28.

$$F_{nh}(t) = -M_n \omega_{1B}^2 v(H) \sin(\omega_{1B} t) \tag{4.28}$$

The maximum value of F_{nh} during one oscillation is given by Equation 4.29. It is an estimate of the inertia load given by F_{nh} in Equation 4.29 based on estimates of the natural frequency, ω_{R1B} and the deflection, $v_{(n)1B}(H)$ that is applied to the structure in *Stodola's* method.

$$F_{nh} = -M_n \omega_{1B}^2 v(H) \tag{4.29}$$

4.4.2 Distributed Force Density, f_h

In the same way as for the inertia load due to the nacelle, Equation 4.31 is the expression for the maximum lateral forces distributed up the tower (units: N m^{-1}).

$$f_h(x,t) = -\rho_t A_{xt} \omega_{1B}^2 v(x) \sin(\omega_{1B} t) \tag{4.30}$$

$$f_h = -\rho_t A_{xt} \omega_{1B}^2 v(x) \tag{4.31}$$

4.4.3 Concentrated Tower Head Torque, Q_{nh}

If the top of the tower rotates ($\frac{dv}{dx}\Big|_H \neq 0$), and the nacelle moment of inertia is not inconsiderable (J_{tn} or $J_{rn} \neq 0$), there will be an inertia torque there. Like the lateral deflection $v(x)$. the rotation of the tower top also varies sinusoidally, since the solutions of Equation 4.5 are separable for simple harmonic motion (Equation 4.32).

$$\text{tower top rotation} = \frac{\partial v}{\partial x}\Big|_{x,t} = \frac{dv}{dx}\Big|_x \sin(\omega_{1B} t) \tag{4.32}$$

$\frac{\partial v}{\partial x}\Big|_{x,t}$ is the rotation as a function of both tower height, x and time, t; $\frac{dv}{dx}\Big|_x$ is the magnitude of sinusoidal time variations of the rotation.

$$Q_{nh}(t) = -J_{tn} \frac{dv}{dx}\Big|_H \omega_{1B}^2 \sin(\omega_{1B} t)$$

$$Q_{nh} = -J_{rn} \omega_{1B}^2 \frac{dv}{dx}\Big|_H \tag{4.33}$$

The maximum torque about a horizontal axis which is applied at the tower top due to rotation of the nacelle is given by Equation 4.33.

4.4.4 Distributed Torque Density, q_h

Torques distributed with tower height are due to tower rotations (the first derivative of the deflection, $\frac{dv}{dx}\Big|_x$). The moment of inertia of the tower per unit length is $\rho_t I_{xt}$. The inertia load on a tower element δx is therefore $\rho_t I_{xt} \omega^2 \frac{dv}{dx} \delta x$. The distribution of these loads is continuous like the lateral loads illustrated in Figure 4.8. The units of the function are N m m^{-1}.

$$q_h = -\rho_t I_{xt} \omega_{1B}^2 \frac{dv}{dx}\Big|_x \tag{4.34}$$

If the torque density is distributed uniformly up a uniform tower, the effect is the same as applying a concentrated force. F_{nh} at the top of the tower of the same magnitude. q_h. In all equations, F_{nh} and q_h appear in the same position. This can be seen in the equations listed in Section 5.1.1.1.

4.5 Modal Analysis using Energy Techniques

I have not found references to an application of the combination of the methods of Rayleigh and Stodola described here. The technique is similar to the *improved Rayleigh method* described by Clough and Penzien [35] and the pure Stodola technique [17].

1. **The Rayleigh/ Stodola Method** involves calculating the *Rayleigh frequency* from an initial estimate of the mode shape and using both the mode shape and frequency estimates to improve the mode shape estimate by static analysis of the structure.

2. **The Improved Rayleigh Method** uses static analysis of the structure to make a new estimate of the mode shape. A better estimate of the natural frequency is then made using the work done on the structure by the inertia loads (Sections 4.4.1 to 4.4.4) rather than the strain potential energy stored in the structure (Equation 4.8). This technique has the advantage that the second derivative of tower deflections do not have to be calculated to obtain this second estimate of the frequency.

3. **Stodola's Method** is to calculate the ratio of the inertia loads to the square of the natural frequency and hence the ratio, $\bar{v}_{(n)}$ of the n^{th} estimate of the tower deflection to the square of the natural frequency. The natural frequency is never explicitely calculated at each step in the iterative process. It is inferred by noting that values of the ratio of $v_{(n)}$ to $\bar{v}_{(n+1)}$ will be different at different heights, x up the tower. An estimate of the frequency is made by taking an average of this ratio using integration and then taking the square root.

No objective comparison of these techniques is given here in terms of speed of convergence, accuracy or computational efficiency.

4.6 Calculating Higher Modes of Vibration

If the integration over some interval of the product of two functions is zero, they are said to be *orthogonal* in that interval. Because each mode shape is *orthogonal* to all others [34], if the first i modes of vibration have been estimated accurately, the $(i+1)^{\text{th}}$ can also be estimated.

Den Hartog [34] uses Maxwell's reciprocity theorem to show that, for normal modes of vibration of linear elastic systems, the relation given by Equation 4.35 holds. This is similar to saying that the two functions, $v_{jB}(x)$ and $v_{kB}(x)$, are orthogonal except that in Equation 4.35, the product of $v_{jB}(x)$ and $v_{kB}(x)$ is also multiplied by the mass distribution. $\mu(x)$.

$$\int_0^H \mu(x) v_{jB}(x) v_{kB}(x) dx = 0. \text{ where } (j \neq k) \tag{4.35}$$

Section 4.6 paraphrases the theory described in [34] using the example of iterations towards an estimate of the third lateral mode of vibration.

Equation 4.36 is specific to lateral vibrations of the tower but similar relations hold true for all classes of vibration. The function $\mu(x)$ is the mass distribution function and defines the variation of mass with height. Discrete masses such as the nacelle are included in $\mu(x)$.

$$\int_0^H \rho_t A_{xt}(x) v_{jB}(x) v_{kB}(x) dx + M_n v_{jB}(H) v_{kB}(H) = 0, \text{ where } (j \neq k) \tag{4.36}$$

Until sufficiently accurate convergence towards the true, k^{th} mode shape ($v_{kB}(x)$), any particular estimate ($v_{(i)kB}(x)$) after i iterations (Figure 4.6) can be expressed as the sum of the true, k^{th} mode shape and other *impurities*. Using notation adopted for Section 4.6 only, Equation 4.37 gives the i^{th} estimate of the k^{th} mode shape of bending vibrations of the tower, $v_{(i)kB}(x)$. The *impurities* can be expressed as a weighted sum of the lower harmonics: $v_{1B}(x)$ to $v_{(k-1)B}(x)$ all of which have already been calculated to the required accuracy (Equation 4.38). The coefficients are $C_j \in \Re$ where $j = 1 \rightarrow (k-1)$.

$$v_{(i)kB}(x) = v_{kB}(x) + \text{some impurity function of } x \tag{4.37}$$

$$v_{(i)kB}(x) = v_{kB}(x) + \sum_{j=1}^{k-1} C_j v_{jB}(x) \tag{4.38}$$

For the case of the calculation of the 3^{rd} mode shape, Equation 4.39 gives the current (i^{th}) estimate as the sum of the next ($(i+1)^{\text{th}}$) estimate and the first two mode shapes already calculated to sufficient accuracy. The $(i+1)^{\text{th}}$ estimate is slightly closer to $v_{3B}(x)$ than the i^{th} estimate.

$$v_{(i)3B}(x) = v_{(i+1)3B}(x) + C_1 v_{1B}(x) + C_2 v_{2B}(x) \tag{4.39}$$

Equation 4.39 is multiplied by the first mode shape which is accurately known and the mass function, $\mu(x)$ for the tower. Each term is integrated over the height of the tower (Equation 4.40).

$$\int_0^H \mu(x) v_{(i)3B}(x) v_{1B}(x) dx = \int_0^H \mu(x) v_{(i+1)3B}(x) v_{1B}(x) dx + C_1 \int_0^H \mu(x) v_{1B}(x) v_{1B}(x) dx + C_2 \int_0^H \mu(x) v_{2B}(x) v_{1B}(x) dx \tag{4.40}$$

Equation 4.35 states that the integrals over the tower height of the product of different mode shapes are zero. Because $v_{(i+1)3B}(x)$ is a better estimate of $v_{3B}(x)$ than $v_{i3B}(x)$. $\int_0^H v_{(i+1)3B}(x) v_{1B}(x) dx \ll \int_0^H v_{(i)3B}(x) v_{1B}(x) dx$. Equation 4.40 can be rearranged to find the unknown constant, C_1 (Equation 4.41).

$$C_1 = \frac{\int_0^H \mu(x) v_{(i)3B}(x) v_{1B}(x) dx}{\int_0^H \mu(x) v_{1B}(x) v_{1B}(x) dx} \tag{4.41}$$

Similarly, if all the terms in Equation 4.39 are multiplied by the product of the mass function and the accurate estimate of the second mode shape ($\mu(x)v_{2B}(x)$), the constant C_2 can be found (Equation 4.42).

$$C_2 = \frac{\int_0^H \mu(x)v_{(i)3B}(x)v_{2B}(x)dx}{\int_0^H \mu(x)v_{2B}(x)v_{2B}(x)dx} \tag{4.42}$$

Equation 4.39 is rearranged to give Equation 4.43 so that a better estimate of the 3rd mode shape can be made.

$$v_{(i+1)3B}(x) = v_{(i)3B}(x) - C_1 v_{1B}(x) - C_2 v_{2B}(x) \tag{4.43}$$

Generalising Equations 4.41 to 4.43 to describe iterations towards an accurate estimate of the k^{th} mode shape Equation 4.44 is obtained.

$$\{v_{(i+1)kB}\} = \{v_{(i)kB}\} - \{C\}^{\mathrm{T}}\mathbf{V} \tag{4.44}$$

In Equation 4.44, $\{v_{(i)kB}\}$ is an array of values of $v_{(i)kB}(x)$ at the x value of each point up the tower.

$$\text{where } \{C\} = \begin{bmatrix} C_1 \\ C_2 \\ \cdots \\ C_{k-1} \end{bmatrix} \text{ and } \mathbf{V} = \begin{bmatrix} \{v_{1B}\} \\ \{v_{2B}\} \\ \cdots \\ \{v_{(k-1)B}\} \end{bmatrix}$$

$$C_j = \frac{\int_0^H \mu(x)v_{(i)kB}(x)v_{jB}(x)dx}{\int_0^H \mu(x)v_{jB}(x)v_{jB}(x)dx} \text{for } j = 1 \rightarrow (k-1) \tag{4.45}$$

As a consequence of Rayleigh's theory [16], the Rayleigh/ Stodola method will always converge on the natural mode of the lowest frequency. If, however, after each iteration towards the k^{th} natural frequency, the mode shape is *purified* of all components of known lower mode shapes (Equations 4.44 and 4.45), then the Rayleigh/ Stodola method can be forced to converge on the k^{th} mode shape.

To validate these techniques, their results have been compared to those obtained by direct solution of the equation of motion (Equation 4.5) as described later in Section 5.1.3.1.

4.7 Prestressed Structures

In the analysis of wind turbine vibrations, three situations are likely to be encountered in which the structure is prestressed:

1. Longitudinal vibrations of the tower which is prestressed both by its own weight (gravity) and by the axial component of the pretension in the guy cables.

2. Lateral vibrations of the tower during operation. A horizontal force on the powertrain from the rotor prestresses the structure with respect to lateral deflections. The horizontal force must be treated as constant.

3. Vibrations of a rotor blade which experiences axial forces due to centrifugal acceleration and lateral forces due to the oncoming wind.

4.7.1 Introduction to Prestressed Systems

It is not intuitive as to whether or not the Rayleigh/ Stodola method can be applied to prestressed structures and if so, what form the energy terms should take. The following introductory section uses three simple illustrations to support the implimentation of the Rayleigh/ Stodola method for prestressed structures (Figure 4.9).

1. A second order spring/ mass system without gravity (not prestressed).

2. A second order spring/ mass system prestressed by gravity.

3. A second order spring/ mass system prestressed by opposing springs of different stiffness and natural length parameters.

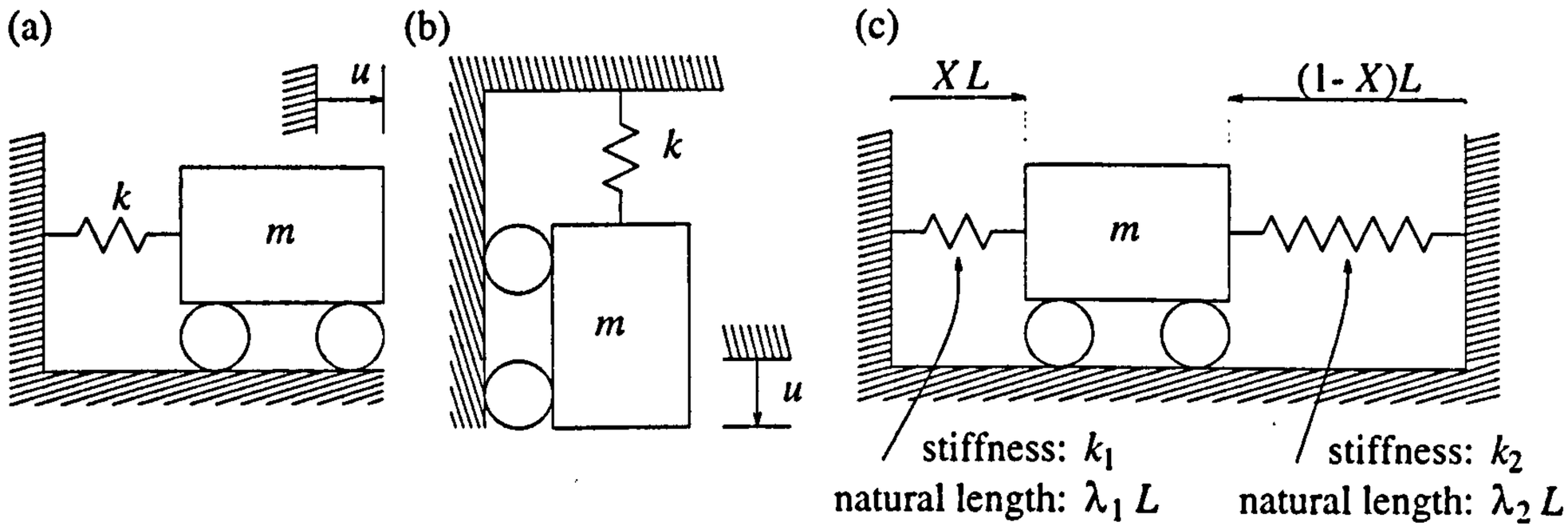

Figure 4.9: Spring/ mass systems compared in Section 4.7. (a) A system without gravity (g = 0). (b) A system with gravity. (c) A prestressed system with opposing springs of different stiffness and natural length parameters.

4.7.1.1 Simple Spring/ Mass System

Figure 4.9 shows three second order linear systems. The equation of motion of the first (Figure 4.9 (a)) is Equation 4.46 whose solution is Equation 4.47. The values of the constants v_a and t_0 depend on the initial conditions.

$$\frac{d^2v}{dt^2} = -\frac{k}{m}v \tag{4.46}$$

$$v = v_a \cos\left(\omega_0 \left(t - t_0\right)\right) \tag{4.47}$$

$$\text{where: } \omega_0 = \sqrt{\frac{k}{m}} \tag{4.48}$$

Rayleigh's method (Section 4.3) is to equate the maximum kinetic energy during a cycle with the maximum potential energy. To calculate the kinetic energy, the velocity $\dot{v}$ must be known. $\dot{v}$ can be found by assuming sinusoidal motion and differentating a general equation

for the deflection ($v = v_a \cos(\omega_0(t - t_0))$). The kinetic energy of the system is given by Equation 4.49. Potential energy arises in the system due to stretching of the spring. This strain potential energy is given by Equation 4.50. The natural frequency of the system is given by equating Equations 4.49 and 4.50 and making ω_0 the subject (Equation 4.51). The result is the same as in Equation 4.48.

$$T = \frac{1}{2} m v_a^2 \omega_0^2 \tag{4.49}$$

$$V_s = \frac{1}{2} k v_a^2 \tag{4.50}$$

$$\omega_0 = \sqrt{\frac{k}{m}} \tag{4.51}$$

4.7.1.2 Vertical Mass/ Spring System

If the same spring/ mass system is vertical, the weight of the mass must be included and the equation of motion is Equation 4.52. Deflections v are measured from the position of the end of the unstretched spring. The solution (Equation 4.54) includes the steady state deflection $v_0 = \frac{mg}{k}$ at which the two forces on the mass (mg and kv) are in equilibrium. Having calculated this deflection at static equilibrium, Equation 4.52 can be rearranged to give Equation 4.53 in which $\frac{v_0 k}{m}$ is substituted for g. The constants v_a and t_0 depend on the initial conditions. Figure 4.10 shows the variation of deflection v with time. If the spring stiffness is the same in compression as in tension or the amplitude of vibrations is less than the equilibrium deflection ($v_0 = \frac{mg}{k}$), then the spring never goes slack. The static force/ deflection curve for the spring is linear for all deflections. The shape of oscillations is sinusoidal. For larger amplitude vibrations, if the spring goes slack, for a certain portion of the vibration period, the only restoring force on the mass is its own weight and the shape of vibrations is parabolic. During the rest of the period, the shape is sinusoidal. This is also plotted in Figure 4.10.

$$\frac{d^2v}{dt^2} = -\frac{k}{m} v + g \tag{4.52}$$

$$\frac{d^2v}{dt^2} = -\frac{k}{m}(v + v_0) \tag{4.53}$$

$$v = \frac{mg}{k} + v_a \cos\left(\sqrt{\frac{k}{m}}(t - t_0)\right) \tag{4.54}$$

Rayleigh's method can be applied to this system which is prestressed by its own weight. The initial potential energy of the system is not zero because the spring is stretched. The deflection at which gravitational potential energy is zero is arbitrary and so is taken as the same as the deflection for which elastic strain potential energy is zero. This is the reference deflection used in Figure 4.10 at which the spring is not stretched. In Equation 4.55. V_{g0} is the gravitational potential energy and in Equation 4.56, V_{s0} is the strain potential energy.

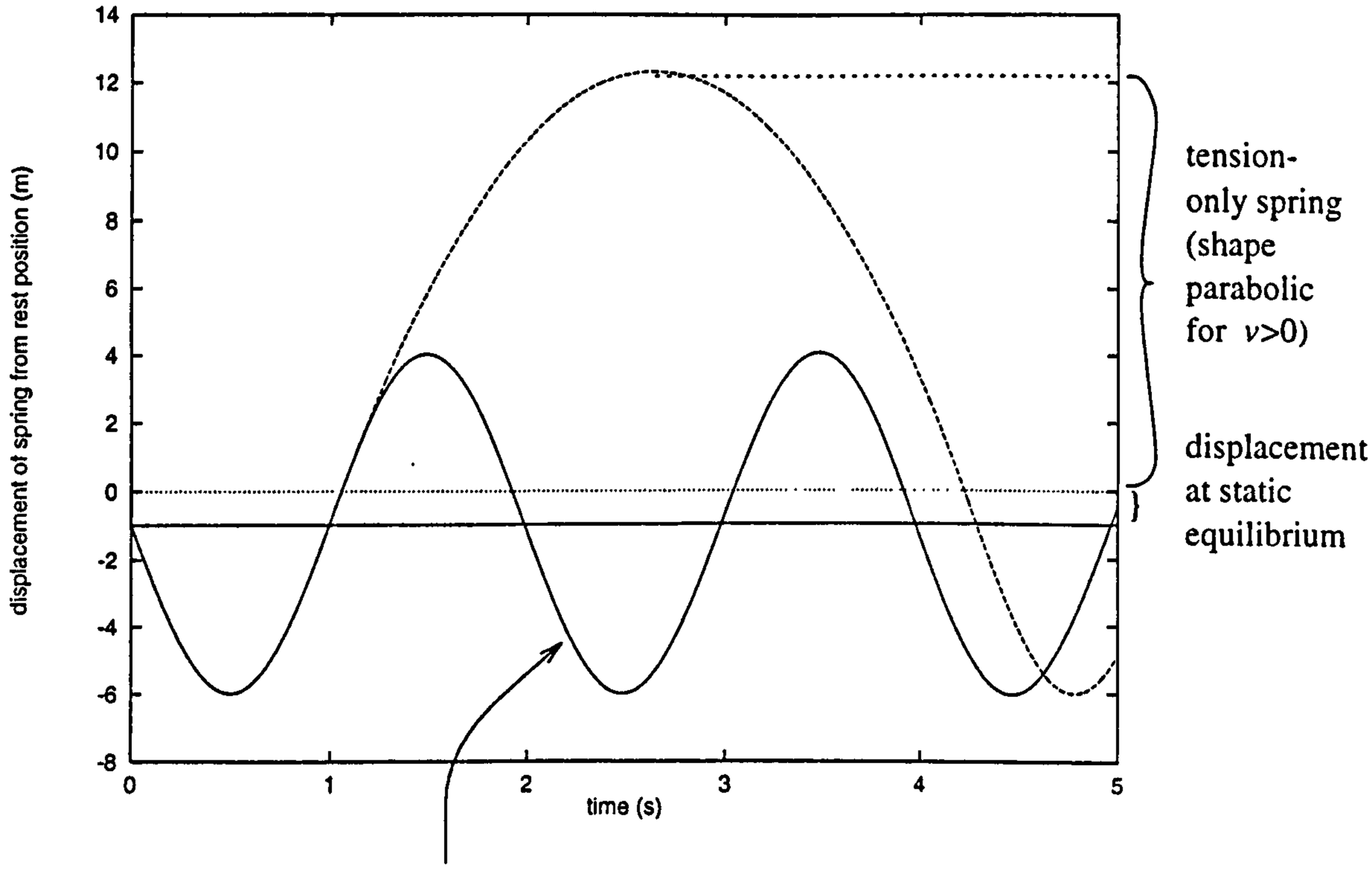

Figure 4.10: Comparison between the steady vibration of two different vertical spring/ mass systems. In one, the spring can take compressive loads, in the other it cannot. In both cases, the time offset t_0 is 0.497 s and the amplitude, v_a of vibrations is initially set to 5 m.

$$V_{g0} = -mgv_0 = -\frac{m^2g^2}{k} \tag{4.55}$$

$$V_{s0} = \frac{1}{2}kv_0^2 = \frac{1}{2}\frac{m^2g^2}{k} \tag{4.56}$$

During vibrations, the maximum potential energy is given by V in Equation 4.57 and the maximum kinetic energy is given by T in Equation 4.58. From these expressions, the natural angular frequency of vibrations $\omega_0 = \sqrt{\frac{k}{m}}$ (Equation 4.59).

$$\begin{aligned} V &= \frac{1}{2}k\left(v_a + \frac{mg}{k}\right)^2 - V_{s0} - mg\left(v_a + \frac{mg}{k}\right) - V_{g0} \\ \Rightarrow V &= \frac{1}{2}k\left(v_a + \frac{mg}{k}\right)^2 - \frac{1}{2}\frac{m^2g^2}{k} - mg\left(v_a + \frac{mg}{k}\right) + \frac{m^2g^2}{k} \\ \Rightarrow V &= \frac{1}{2}kv_a^2 \end{aligned} \tag{4.57}$$

$$T = \frac{1}{2}mv_a^2\omega_0^2 \tag{4.58}$$

$$\omega_0 = \sqrt{\frac{k}{m}} \tag{4.59}$$

Rayleigh's equation cannot be used to model a situation in which the spring goes slack (see Figure 4.10). For this reason, the amplitude of vibrations v_a must be kept small as stated at the end of Section 4.2.

4.7.1.3 System of Mass and Opposing Springs

Initial stress arises from elastic as well as gravitational forces on the mass. Figure 4.9 (c) shows a system in which the two opposing springs are initially prestressed. The combined, stretched lengths (XL and $(1-X)L$) of the two springs is L and the natural lengths are $\lambda_1 L$ and $\lambda_2 L$. The stiffnesses of the springs are k_1 and k_2. The mass is in static equilibrium when the dimensionless deflection, X_0 is given by Equation 4.60.

$$X_0 = \frac{k_1\lambda_1 + k_2(1-\lambda_2)}{k_1 + k_2} \tag{4.60}$$

If all deflections, X are dimensionless and scaled by the combined stretched spring length. L, the equation of motion of the system is given by Equation 4.61. Equation 4.60 can be substituted and Equation 4.61 rearranged to give Equation 4.62 which is of the same form as Equation 4.53 above.

$$\frac{d^2X}{dt^2} = -\frac{k_1 + k_2}{m}X + \frac{k_1\lambda_1 + k_2(1-\lambda_2)}{m} \tag{4.61}$$

$$\frac{d^2X}{dt^2} = -\frac{k_1 + k_2}{m}(X + X_0) \tag{4.62}$$

The solution (Equation 4.63) is of the same form as Equation 4.54, where the constants X_a and t_0 depend on the initial conditions.

$$X = X_0 + X_a \cos\left(\sqrt{\frac{k_1 + k_2}{m}}(t - t_0)\right) \tag{4.63}$$

By subtracting the strain potential energy of the system at static equilibrium from the strain potential energy of the system at maximum deflection (amplitude X_a) during vibrations, an expression for the maximum net potential energy of the system can be obtained (given by Equation 4.64). An expression (Equation 4.65) for the maximum kinetic energy of the system during vibrations is obtained assuming an amplitude X_a and an angular frequency ω_0. Using Rayleigh's method, these give the same predictions of the natural frequency as solution of the equation of motion (Equation 4.62).

$$V = \frac{1}{2}(k_1 + k_2)X_a^2 \tag{4.64}$$

$$T = \frac{1}{2}mX_a^2\omega_0^2 \tag{4.65}$$

4.7.1.4 Conclusions about General Prestressed Systems

This analysis suggests that the modal analysis of prestressed structures of the kind encountered in the analysis of wind turbines is possible provided that care is taken in formulating the expressions for the total maximum potential energy and kinetic energy of the system with reference to the initial equilibrium values. Specifically it is vital that:

1. gravitational potential energy is always calculated with reference to the same vertical point,

2. the potential energy of the system at equilibrium is calculated and subtracted from subsequent formulations of the potential energy during vibrations and

3. kinetic energy is calculated using the amplitude v_a of vibrations rather than the absolute deflection, v.

The Rayleigh/ Stodola analysis in Section 4.7 relies on the system being conservative. There are no damping forces in any of the systems described. There are also no discontinuities. Either of these factors would result in vibrations which were not sinusoidal with respect to time like the case of the tension-only spring illustrated in Figure 4.10. This would negate the assumptions underlying Rayleigh's and Stodola's methods. In the case of longitudinal vibrations of wind turbine towers. the amplitude of vibrations must be small enough that the cables are always taut.

4.7.2 Longitudinal Vibrations

As has been stated in Section 2.4, the tower is prestressed by the initial tension in the guys and by its own weight in normal gravity. The simple examples in the previous section suggest that Rayleigh/ Stodola analysis of such a system should be possible.

To illustrate the behaviour of the various components of the wind turbine, a vertical force of varying magnitude was applied at the tower top and the variations of potential energy stored are plotted in Figure 4.11. This does not illustrate the actual potential energy variations during longitudinal vibrations of the tower since, in general, all parts of the tower are vibrating and so the potential energy stored in the tower depends on the longitudinal deflections of all $(N_n-1)(N_s-1)+1$ points. Figure 4.11 would indicate the potential energy variations in a light tower with a heavy nacelle.

Some observations can be made about the variations of potential energy with deflections of the top of the tower.

- The minimum strain potential energy stored in the tower coincides with zero deflection of the tower top since this represents a state of zero strain.

- The variation of the strain potential energy due to movements of the base with tower top deflection is very small because the base stiffness is large (1×10^{12} N m rad^{-1} in this case; see Section 2.2.2). It is the shape of this variation and the fact that the potential energy is zero for some small negative deflection of the tower top which is of interest.

- The point of zero gravitational potential energy is arbitrary since the earth is large relative to any deflections, the gravitational acceleration is assumed constant and the variation of potential energy with deflection is linear.

- By comparing the reflection of the variation of the total potential energy with deflection about the equilibrium deflection, it can be confirmed that the variation is symmetrical. For small deflections, a parabola can be fitted accurately to the data. Motion will therefore be sinusoidal. For larger states of pre-compression, the total potential energy curve moves further from the origin (as illustrated in Figure 4.12).

- In order to generate Figure 4.11, the equivalent vertical stiffness of the guys and the axial compression in the lower portion of the tower were calculated for each successive load step to calculate the true strain potential energy stored. For modal analysis, deflections are assumed to be small. The stiffness parameter relating to the guy cables is therefore almost constant. It is calculated just once before modal analysis.

If the pretension in the guy cables ϵ_{ic} is increased, the potential energy stored in the structure increases as shown in Figure 4.12. The shapes of the variations of potential energy with movement of the top of the tower remain approximately the same.

4.7.2.1 Modal Analysis

The vibration mode shape. $u_m(x)$ of a prestressed structure is the variation with height of the deflection from the equilibrium deflection ($u_m(x) = u(x) - u_0(x)$). The equilibrium

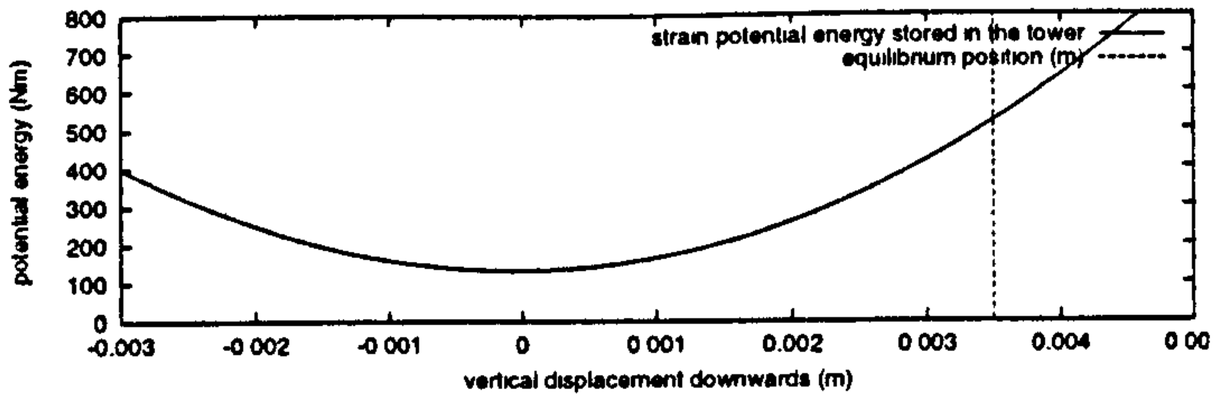

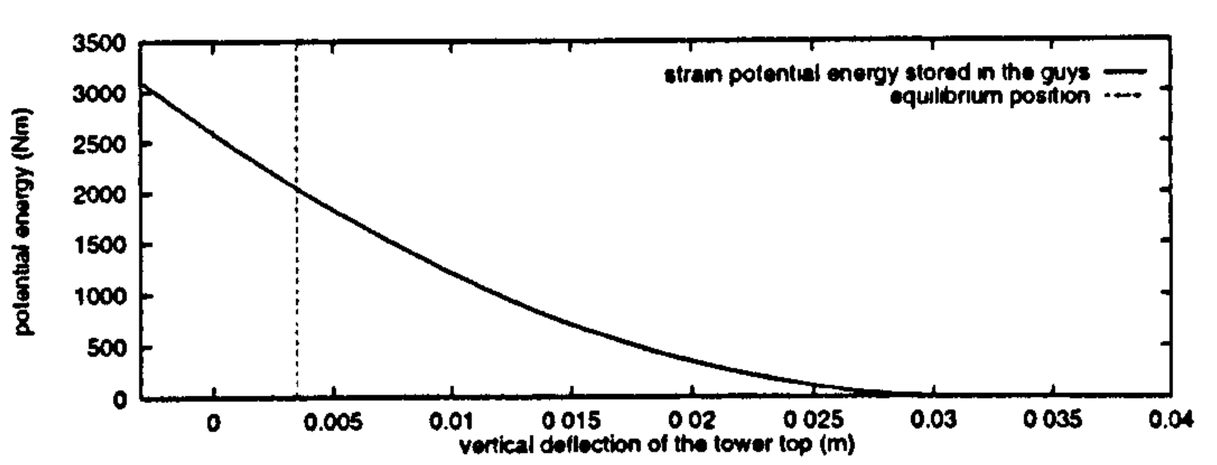

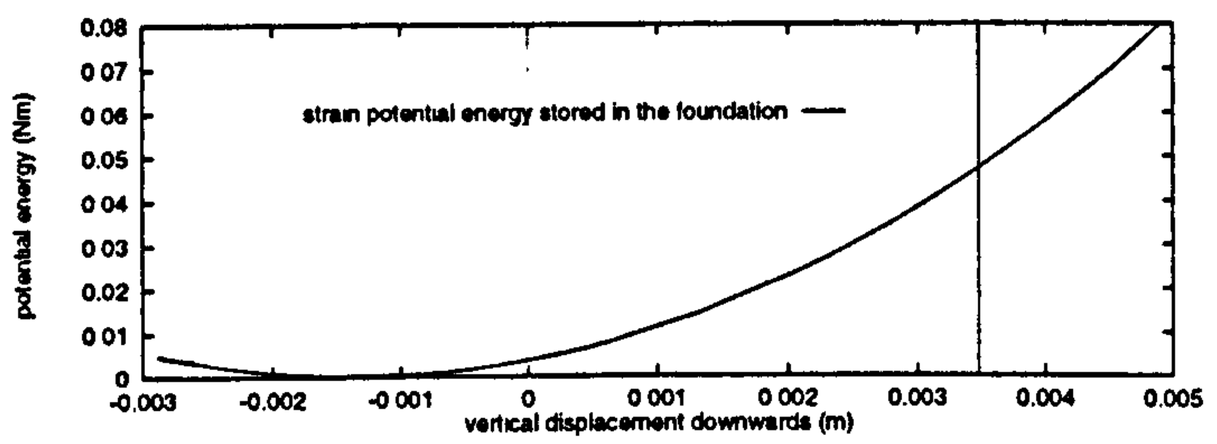

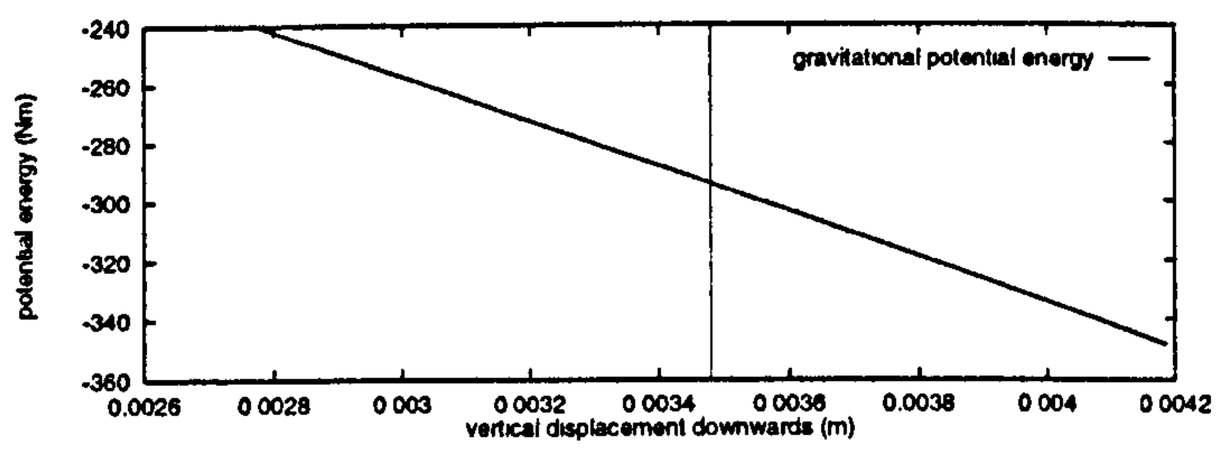

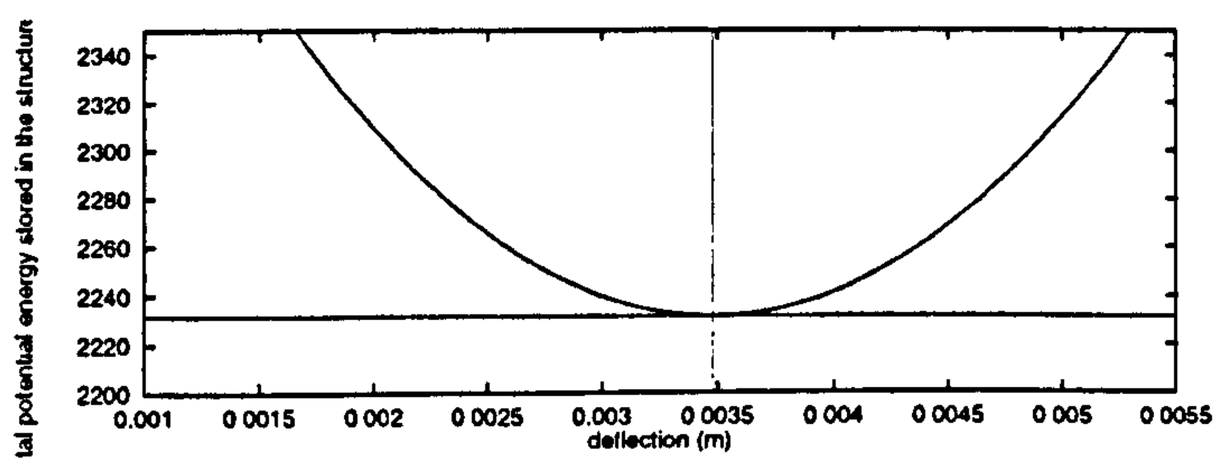

Figure 4.11: Potential energy stored in the structure at different deflections of the tower top. Deflections are measured from the undisturbed position of the tower. The initial strain in the guys at assembly is 0.0005. The rest of the tower design data are for the Carter 300 kW machine (Great Orton Airfield type). The only load on the tower apart from its own weight and the reaction from the guy cables is at the top (F_{nv}). In all illustrations, a vertical line indicates the position of the top of the tower at static equilibrium (0.0035 m). For these illustrations, design data was used from the Carter 300 kW wind turbine tower of the type found at Great Orton Airfield.

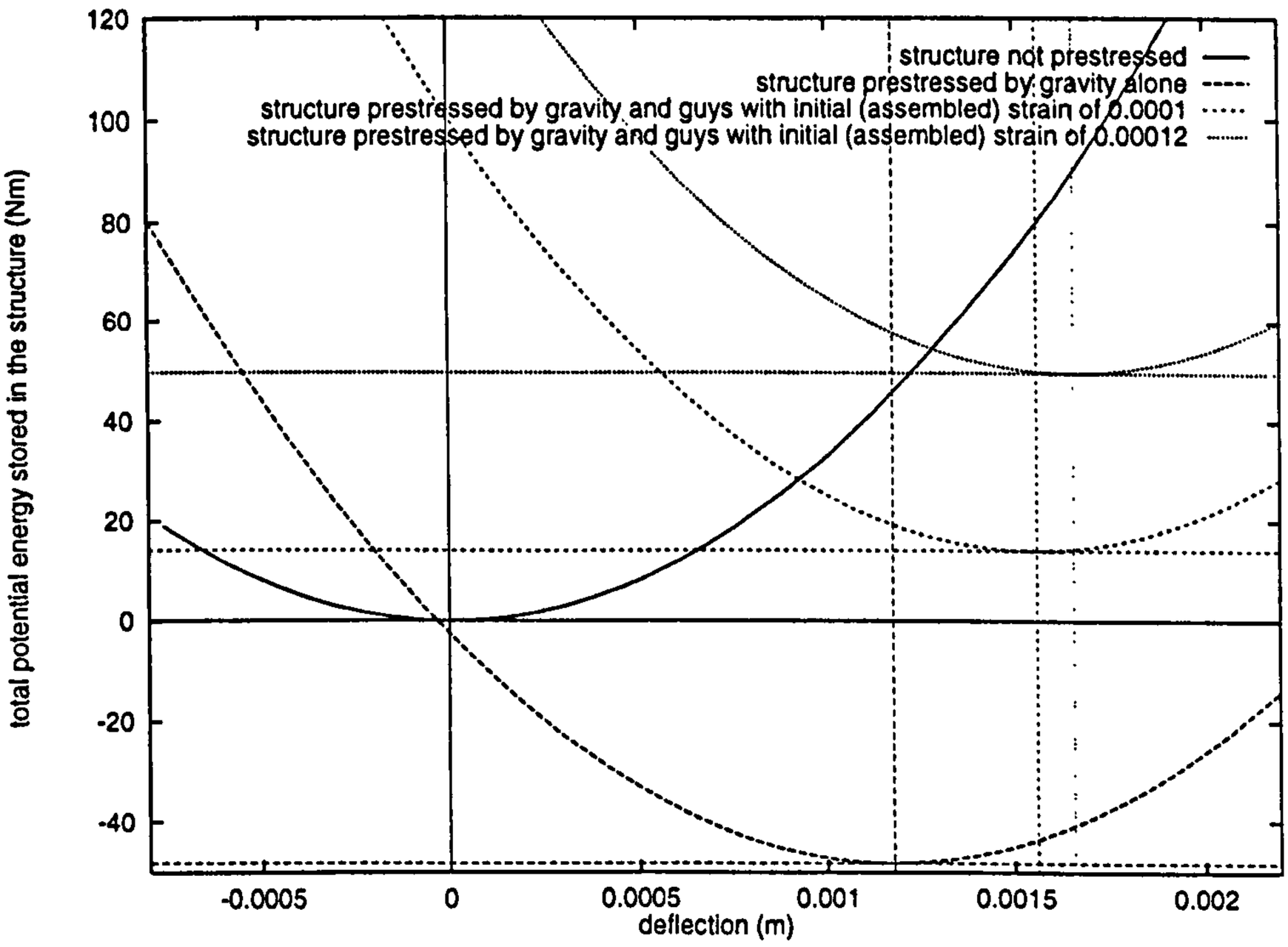

Figure 4.12: The shift in the total potential energy curve at greater precompression of the tower by the guys. The curve nearest the origin represents an unstressed structure. Subsequent curves represent an unguyed structure prestressed by gravity and structures prestressed by initial guy strains (ϵ_{ic}) of 0.0001 and 0.00012.

deflection ($u_0(x)$) must first be calculated by static analysis of the structure under gravity and the pretension in the guys. In order to apply Rayleigh's method to the structure, the total equilibrium potential energy, V_{C0} is also initially calculated.

For subsequent modal analysis, an initial estimate of the mode shape is made ($u_m(x)$). Rayleigh's method is applied as described above (Section 4.3), the potential energy of the deformed structure is calculated using the extreme deflection, $u(x)$. The potential energy at equilibrium is subtracted. It is the residual potential energy which is converted to kinetic energy each cycle. The kinetic energy is calculated based on the actual harmonic movement of the structure ($u_m(x)$). The formulae for strain potential energy, gravitational potential energy and kinetic energy are listed as Equations 4.66 to 4.71. Rayleigh's Equation (Equation 4.8) is rewritten for prestressed compressive vibrations as Equation 4.72.

$$V_{Ct} = \int_0^H \frac{1}{2} E_t A_{xt} \left(\frac{du}{dx}\right)^2 - \rho_t A_{xt} g u(x) dx \tag{4.66}$$

$$V_{Cc} = \frac{1}{2} k_{Cc} \left(u_{c0} - u\left(\lambda_{ct} H\right)\right)^2 \tag{4.67}$$

$$V_{Cn} = -M_n g u(H) \tag{4.68}$$

$$V_{Cf} = \frac{1}{2} k_{Cf} u(0)^2 \tag{4.69}$$

$$T_{Ct} = \omega_{RiC}^2 \left(\int_0^H \frac{1}{2} \rho_t A_{xt} \left(u(x) - u_0(x)\right)^2 dx\right) \tag{4.70}$$

$$T_{Cn} = \omega_{RiC}^2 \left(\frac{1}{2} M_n \left(u(H) - u_0(x)\right)^2\right) \tag{4.71}$$

$$\omega_{RiC}^2 = \frac{V_{Ct} + V_{Cc} + V_{Cn} + V_{Cf} - V_{C0}}{\left(T_{Ct} + T_{Cn}\right) / \omega_{RiC}^2} \tag{4.72}$$

where:

$u(x)$	the total vertical deflection of the tower
$u(H)$	the total vertical deflection of the top of the tower
$u(\lambda_{ct} H)$	the total vertical deflection of the point of attachment of the guys
$u_0(x)$	the equilibrium vertical deflection of the tower
$u_0(H)$	the equilibrium deflection of the top of the tower
u_{c0}	the vertical equivalent extension of the cables from their natural length at which the cables will go slack
ω_{iC}	the required i^{th} longitudinal natural frequency

Additionally, inertia loads are calculated using the modal deflections rather than the absolute deflections (Equations 4.73 and 4.74).

$$F_{nv} = M_n \left(g - \left(u(H) - u_0(H)\right) \omega_{iC}^2\right) \tag{4.73}$$

$$f_v = \rho_t A_{xt} \left(g - \left(u(x) - u_0(x)\right) \omega_{iC}^2\right) \tag{4.74}$$

In the software, the input to the function representing Rayleigh's method is the absolute deflection ($u(x)$) rather than the modal deflection ($u_m(x)$). Although the total potential energy of the structure is a minimum at equilibrium, the various constituent structural elements are in states of minimum potential energy at different deflections (see Figure 4.11).

Since the total potential energy variation with deflection of the tower top (Figure 4.11) is approximately parabolic, it might be tempting to approximate the curve by a quadratic and use that to calculate potential energy values. That would be the same as calculating an equivalent stiffness for the whole structure. The potential energy stored in the structure is not dependent just on the deflection of the tower top Figure 4.11, but on the deflections of the $(N_n - 1)(N_s - 1) + 1$ points over the height of the tower as well.

In practice, the method described in Section 4.7.2 often does not converge quickly. It is not clear why this is. Because the model consists of a continuous element (the tower) as well as discrete elements (the nacelle and the guys), Rayleigh energy terms include integrals of strain. The inertia force array can only be exact if vibrations are sinusoidal with respect to time (see Section 4.4) and the current shape is the true mode shape of vibrations. This is not the case prior to convergence. The result is that in certain circumstances, iterations settle down to two distinct but similar mode shapes having two closely-separated but distinct frequencies.

For purposes of validation (Section 5.1.1.2), it has been found that if convergence towards this situation of two stable solutions has reached the accuracy required for true convergence, the average of the two frequencies is equal to the validation frequency. In practice, this means that instead of comparing the difference between successive pairs of frequency estimates with the accuracy required for convergence, the difference between pairs of frequency estimates separated by one iteration is compared with the accuracy requirement. So, in the example illustrated in Figure 4.13, convergence was deemed to have occurred when the difference between the 13^{th} and the 15^{th} iterations (or the difference between the 12^{th} and the 14^{th} iterations) fell to less than 1×10^{-12} rad s^{-1}. The example illustrated in Figures 4.13 and 4.14 was obtained using design data for the tower used in the Carter 300 kW wind turbine of the type used at Great Orton Airfield. The average frequency at convergence was 16.16 Hz.

Another way to improve convergence and reduce the effects described in the previous two paragraphs is to change the prescribed modal amplitude. As stated elsewhere in this chapter, vibration amplitudes must be small. This is achieved by dividing the array of modal deflections by a constant value each iteration step. It has been found that if this constant is too large or two small, bistable convergence occurs as described above.

Figure 4.14 shows that the % errors between mode shape estimates are not more than 0.2% at any position over the height of the tower. The % error in the frequency estimates is 0.10%. These are acceptable particularly since the model can be validated for simple cases (Section 5.1.1.2).

4.7.3 Bending Vibrations

The same approach can be taken for the analysis of bending vibrations of a prestressed structure as for longitudinal vibrations. Analysis of any guyed tower includes prestresses.

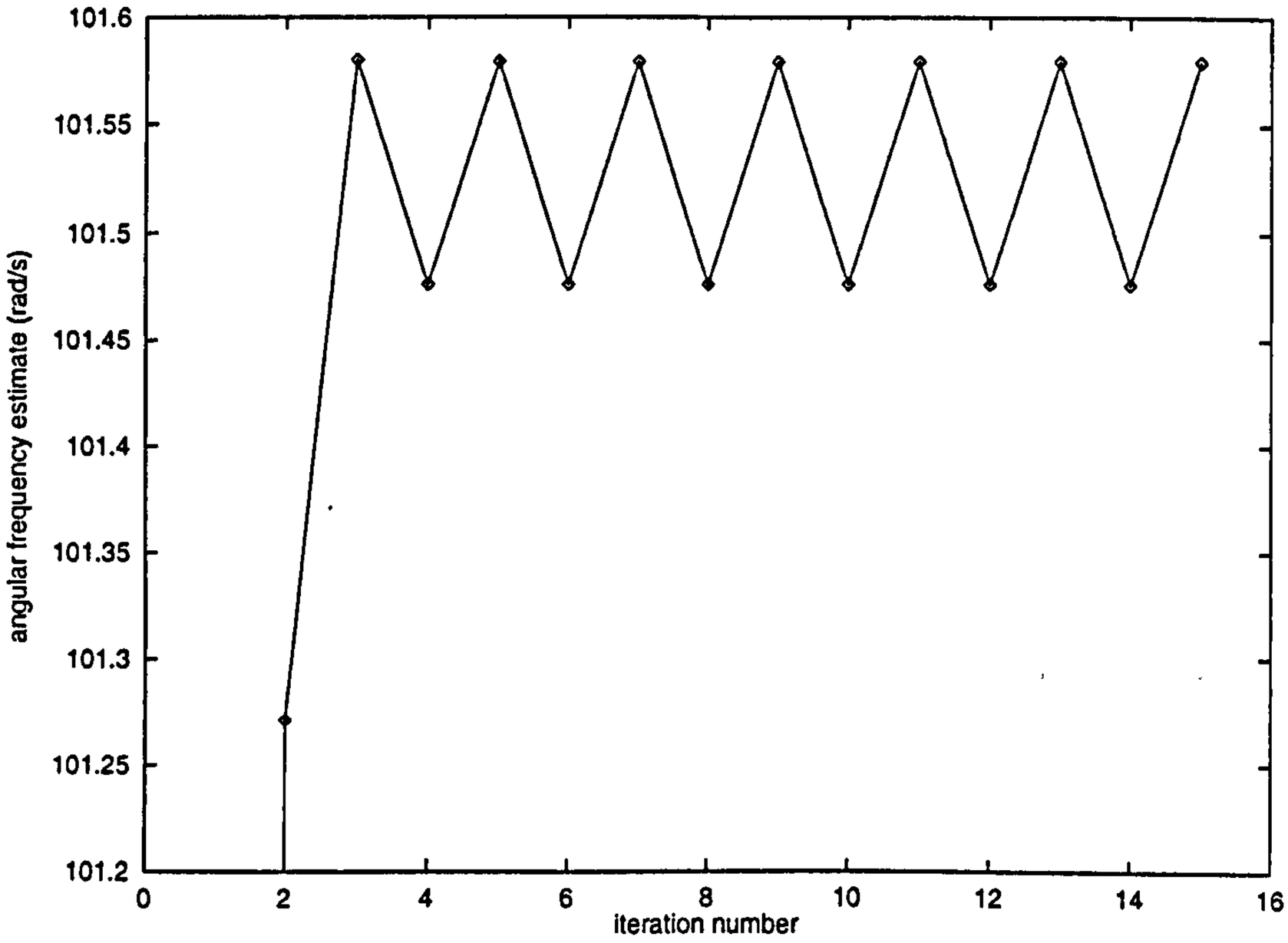

Figure 4.13: Successive estimates of the fundamental angular frequency of longitudinal vibrations of a wind turbine tower. Design data were from the Carter 300 kW machine of the type used at Great Orton Airfield. Being an arbitrary estimate, the first estimate is not within the range of values plotted . At convergence, estimates were 16.15 Hz and 16.17 Hz, representing a spread of 0.10%.

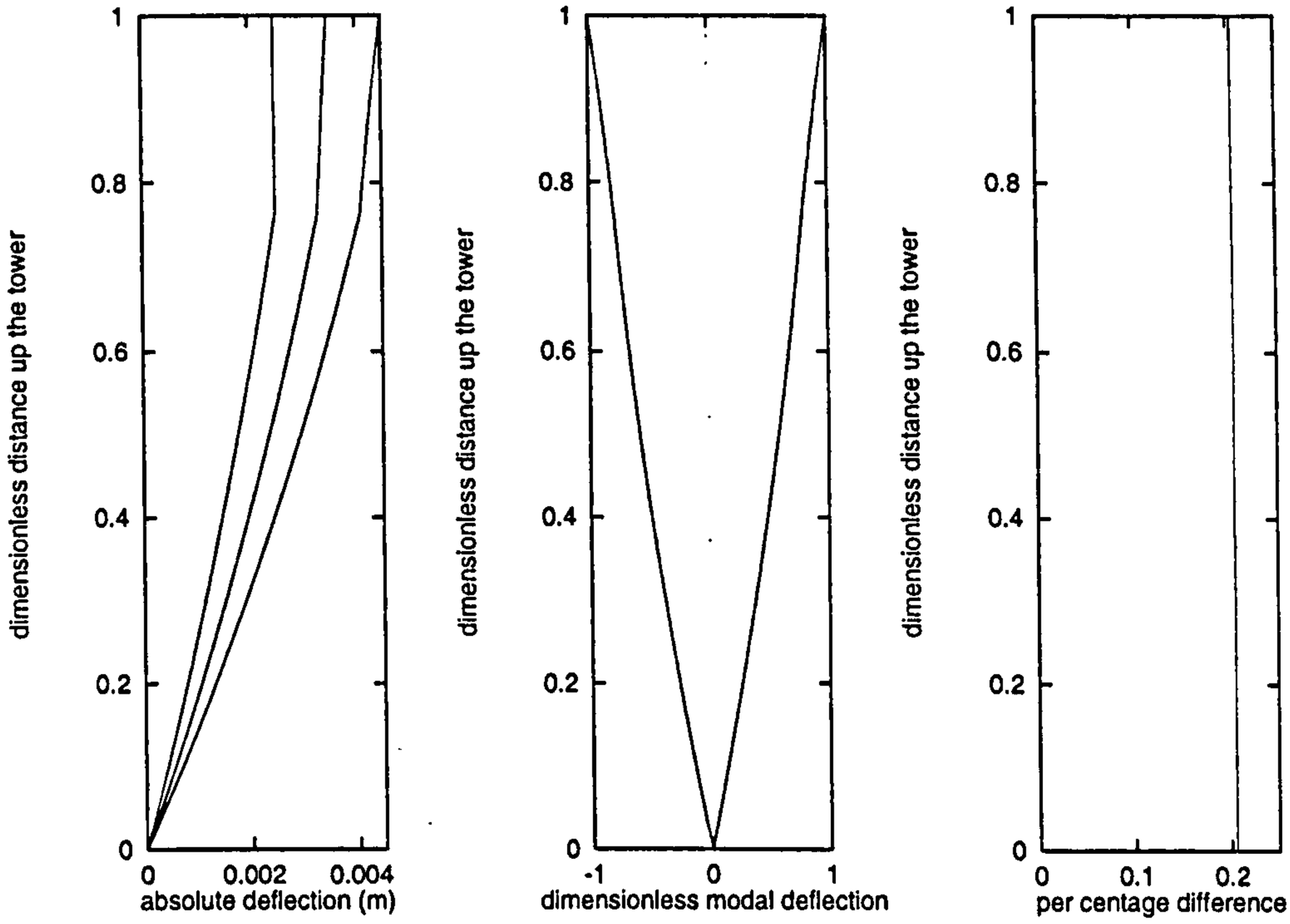

Figure 4.14: Three illustrations of the mode shape estimates at convergence for the tower used for the Carter 300 kW wind turbine of the type used at Great Orton Airfield (Figure 4.13 shows the convergence of frequency estimates). On the left are shown the absolute deflections of the tower. The left hand curve is the upper limit of deflections ($u(x)$), the central curve is the equilibrium deflection ($u_0(x)$) and the right hand curve is the lower limit of deflections ($u(x)$). Positive values indicate deflections vertically downwards. On the central set of axes are shown the modal deflections calculated by taking the differences between the absolute values of the extreme deflections and the equilibrium deflection ($u_m(x)$ as described in Section 4.7.2) and normalising with respect to the maximum deflection. On the right hand set of axes are shown the per centage differences between the positive and negative extreme modal deflection shapes.

The guy cables exert an axial force in the lower part of the tower. In this analysis, this is treated as constant (see Section 2.2.3). As the tower vibrates, work is done against this axial force, F_{cv}. The simplified geometry for calculating the work done is shown in Figure 4.15. The work done is given by Equation 4.75 and is negative for positive displacements (such displacements involve vertical movement in the same direction as the axial force).

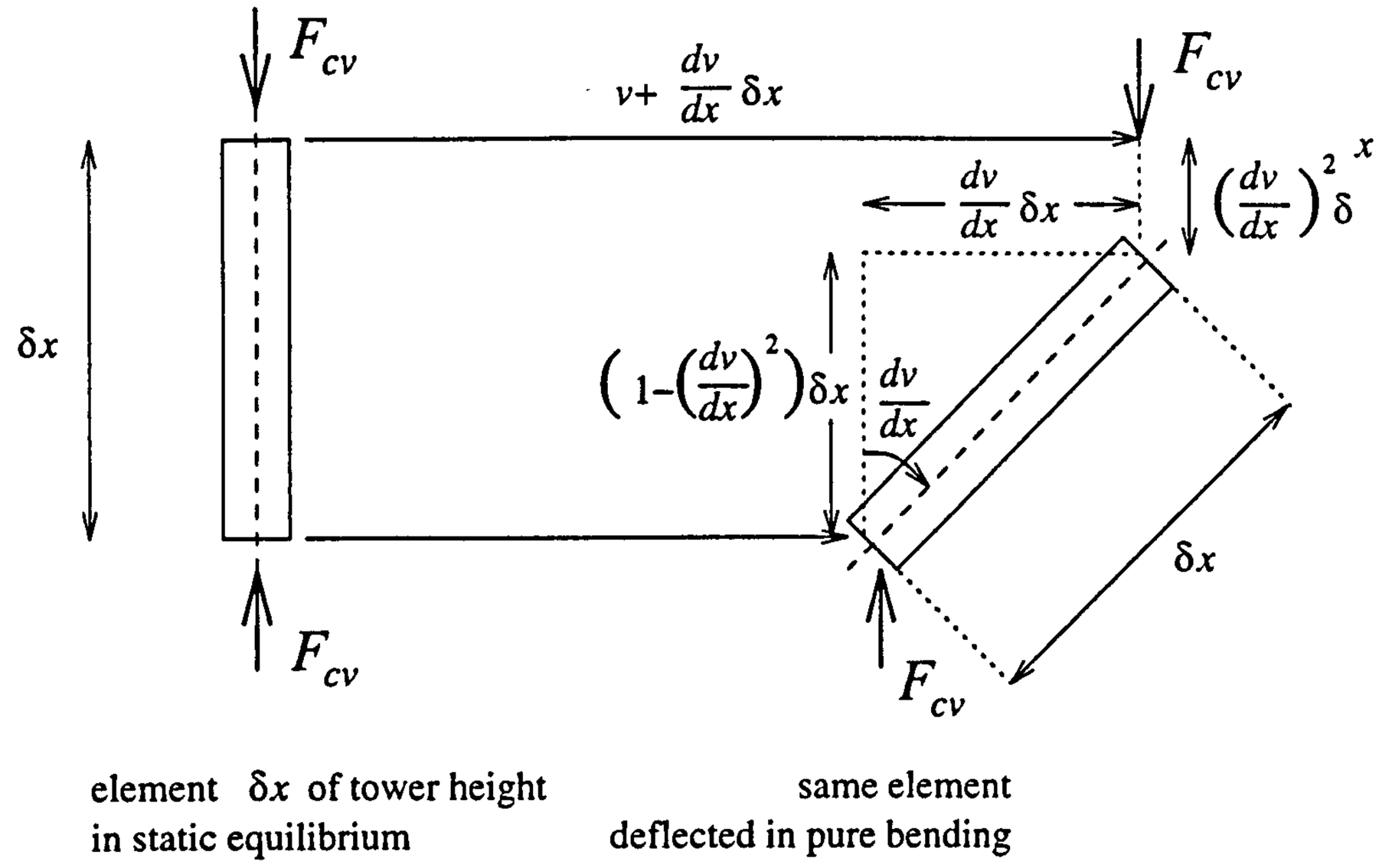

Figure 4.15: The simplified geometry of tower deflections during bending vibrations used to calculate the work done against the axial compression F_{cv} in the lower part of the tower. From this geometry, Equation 4.75 is derived.

$$\text{work done against } F_{cv} = -\int_0^{\lambda_{ct} H} \frac{1}{2} F_{cv} \left(\frac{dv}{dx}\right)^2 dx \tag{4.75}$$

The potential energy at the time of maximum deflection of the tower for use in Rayleigh's Equation (Equation 4.8) is given by the total of Equations 4.12 and 4.15. This total, Equation D.2 is listed in Appendix D. The effect of increasing F_{cv} is to decrease the lateral frequencies of vibration. If F_{cv} is increased too much, the fundamental lateral frequency falls to zero and the tower buckles. This is described in more detail in Section 8.1.

The modified Rayleigh/ Stodola method used to calculate the modes of prestressed structures is summarised by the following 9 steps. The approach is based on the strategy illustrated in Figure 4.6 but inertia loads and kinetic energy are calculated using the modal or relative deflection of the tower and potential energy is calculated using the absolute deflection.

1. The static equilibrium deflection of the tower subject to all the prestress loads is derived and the total potential energy stored in the structure calculated.

2. An estimate of the mode shape is made.

3. This is added to the static deflection at equilibrium to give a new state of strain from which the potential energy of the structure is again calculated.

4. Added to the potential energy is the work done against the applied static pre-loads. For this the modal deflections are used. Modal deflections are found by subtracting the initial equilibrium deflections from the absolute maximum deflections.

5. The total potential energy at static equilibrium is then subtracted.

6. The kinetic energy is calculated using the modal deflections.

7. Equation 4.8 is used to calculate the Rayleigh frequency.

8. Inertia forces are calculated using Equations 4.29, 4.31, 4.33 and 4.34 again using the modal deflections.

9. The static model of the structure is used to make a new, better estimate of the mode shape.

Steps 3–9 are followed until convergence occurs. For the analysis of pre-loaded structures, extra expressions for the work done by the tower against all the applied loads are necessary (Equations 4.76 to 4.79). The subscript 0 denotes initial, static equilibrium conditions (examples are the pre-load distributed torques, q_{h0} or the initial deflection, v_0).

$$W_{tr} = \int_0^x q_{h0} \left(\left.\frac{dv}{dx}\right|_{0X} - \left.\frac{dv}{dx}\right|_X \right) dX \tag{4.76}$$

$$W_{tl} = \int_0^x f_{h0} \left(v_0 - v\right) dX \tag{4.77}$$

$$W_{nr} = Q_{nh0} \left(\left.\frac{dv}{dx}\right|_{0H} - \left.\frac{dv}{dx}\right|_H \right) \tag{4.78}$$

$$W_{nl} = F_{nh0} \left(v_0(H) - v(H)\right) \tag{4.79}$$

Increasing horizontal forces and torques applied to the tower has no effect on the lateral vibration frequencies (Figure 4.16) but affects the mode shapes (Figure 4.17).

An example of the mode shape of bending vibrations of a pre-loaded structure, is given in Figure 4.17.

At loads between 35 000 N and 40 000 N, the right hand guy cable goes slack and the axial load carried by the tower increases considerably (see Figure 2.12 for the effect on the axial load of horizontal tower deflections). As F_{nh} is increased still further, the frequency of bending vibrations falls because of this increased compression in the tower. At the same time, the lateral stiffness parameter, k_{Bc} changes but the effect on the lateral frequency is much less. The absolute frequencies plotted in Figure 4.16 for values of F_{nh} greater than 40 000 N are inaccurate because the guy cable parameters (F_{cv} and k_{Bc}) are no longer constant with tower deflections. The vibrating tower will no longer be undergoing simple harmonic motion.

In order to estimate the frequency of *small vibrations* of the structure. the mode shape is normalised during each iteration by dividing all deflections by the largest absolute deflection

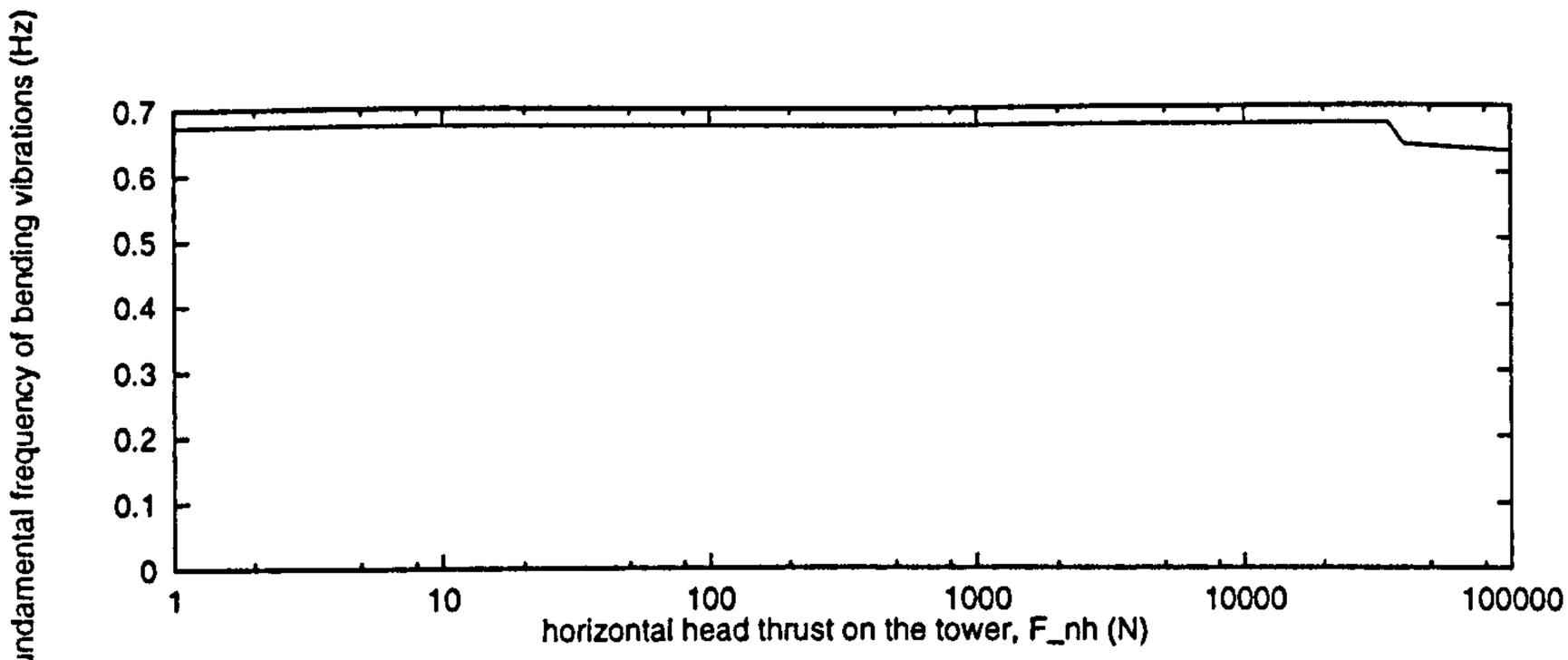

Figure 4.16: The variation of fundamental bending frequency with applied horizontal force, F_{nh}.

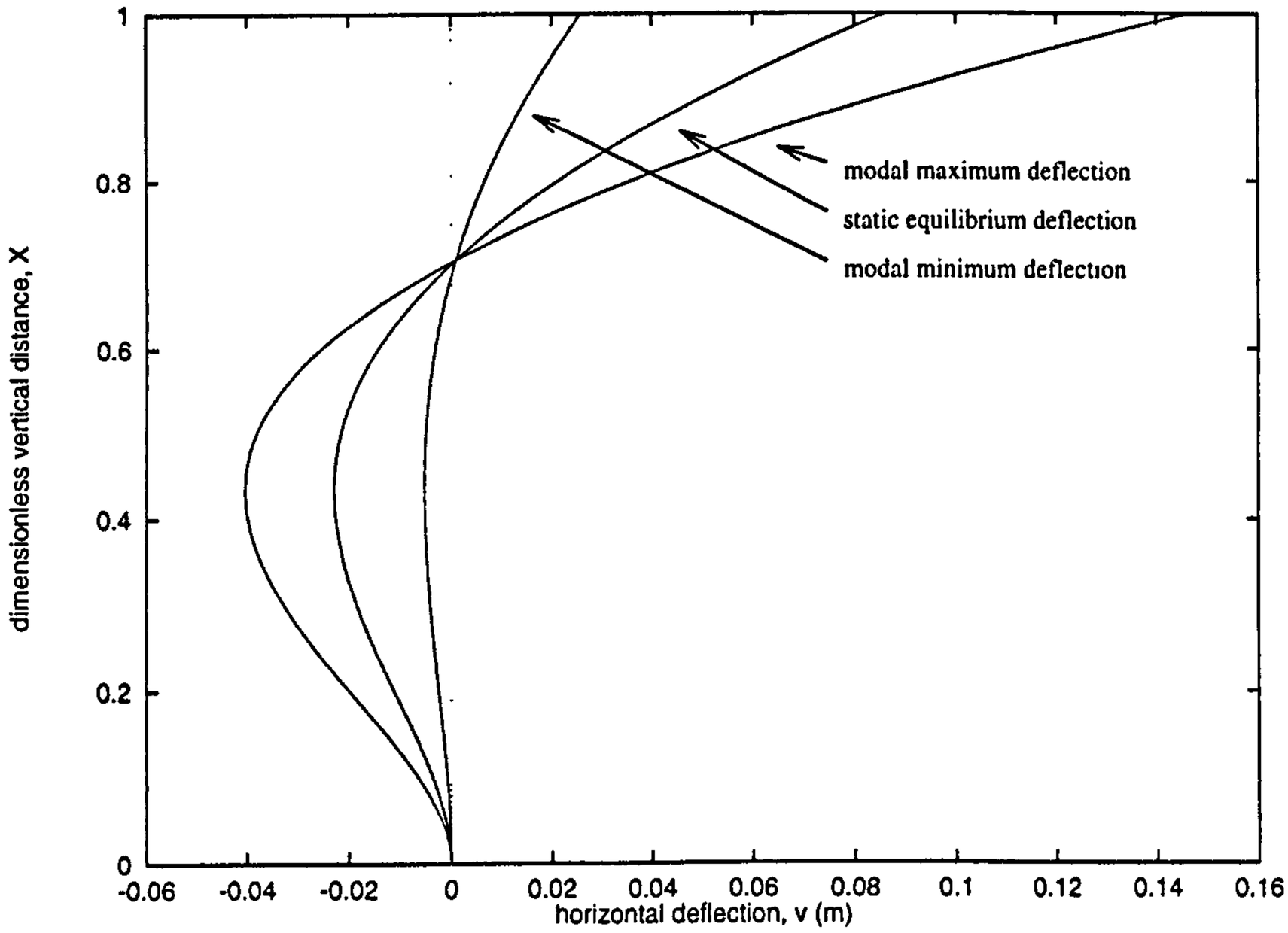

Figure 4.17: The mode shape of bending vibrations of a wind turbine tower of the type used for the Carter 300 kW wind turbines at Great Orton Airfield. The initial load condition is $F_{nh} = 10.8$ kN. The base torsional stiffness, k_{Bf} is 1×10^{12} N m rad^{-1}. The bending mode shape is scaled so that, at the height of the maximum modal deflection, the modal deflection is 70% of the static deflection. The frequency calculated was 0.763 Hz.

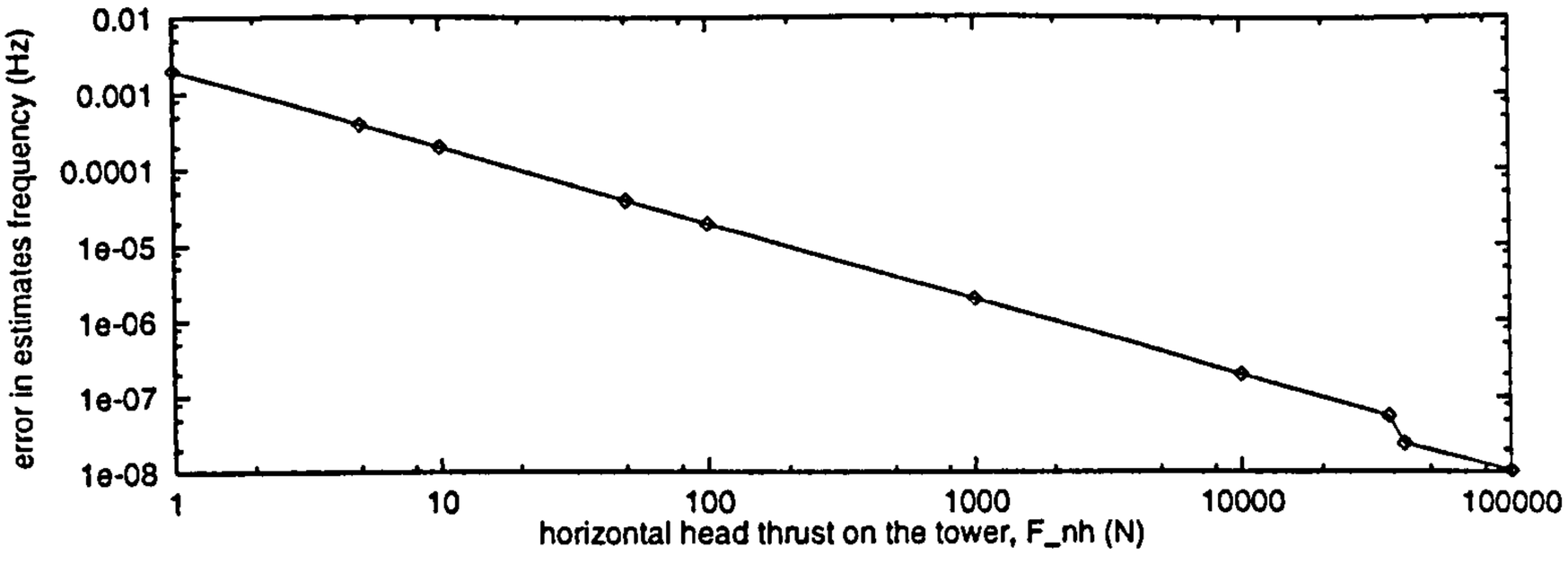

Figure 4.18: The variation of error (the difference between consecutive estimates of the fundamental bending frequency) with applied horizontal force, F_{nh}. The convergence criterion is that the difference between alternate estimates of the fundamental bending frequency is less than $\pm 1 \times 10^{-10}$.

and then dividing by 1×10^6. This ensures that, for example, there are no discontinuous changes of stiffness of the guy cables. If this factor is not large enough, the differences between consecutive estimates of the frequency (plotted in Figure 4.18) become large and the frequencies predicted become inaccurate.

When the tower is not subject to any pre-stresses apart from the axial load, F_{cv} due to the guy cables, convergence is smooth and the difference between consecutive frequency estimates quickly falls to zero. As the pre-stress load on the tower, F_{nh} increases, the difference between consecutive frequency estimates at convergence falls.

The equivalent stiffness parameters of the guy cables (k_{Bc}, k_{Cc}, k_{Tc} and F_{cv}) vary non-linearly with deflection. However, if the initial strain in the guy cables is small and the deflections are small, the only non-linear characteristics are discontinuities when one or other of the cables goes slack. Otherwise, stiffness parameters are nearly constant as illustrated by the variation of k_{Bc} plotted in Figure 4.19.

The stiffness parameters are calculated:-

1. using the method which simulates assembly of the guy cables (Section 2.2.3, Figure 2.10) followed by

2. static analysis of the tower under the prescribed loads followed by

3. a final calculation of the stiffness parameters using a modified routine which includes as input the horizontal, vertical and angular deflection of the point of attachment of the guy cables to the tower.

As stated above, the variations of the guy cable stiffness parameters are piecewise linear. Because this method uses an estimate of the lateral stiffness of the guy cables to calculate deflections of the structure from equilibrium and because there is a discontinuity in the variation of this stiffness parameter with deflection, it is not possible to use a constant value for k_{Bc} to calculate large lateral deflections of the structure. To calculate lateral deflections of the tower greater than $\lambda_{cv0}H$ (where λ_{cv0} is defined in Equation B.21 in Appendix B.2). a different static structural analysis technique must be developed. Techniques for the calculation of non-linear static deflections are proposed in Section 9.1.3.

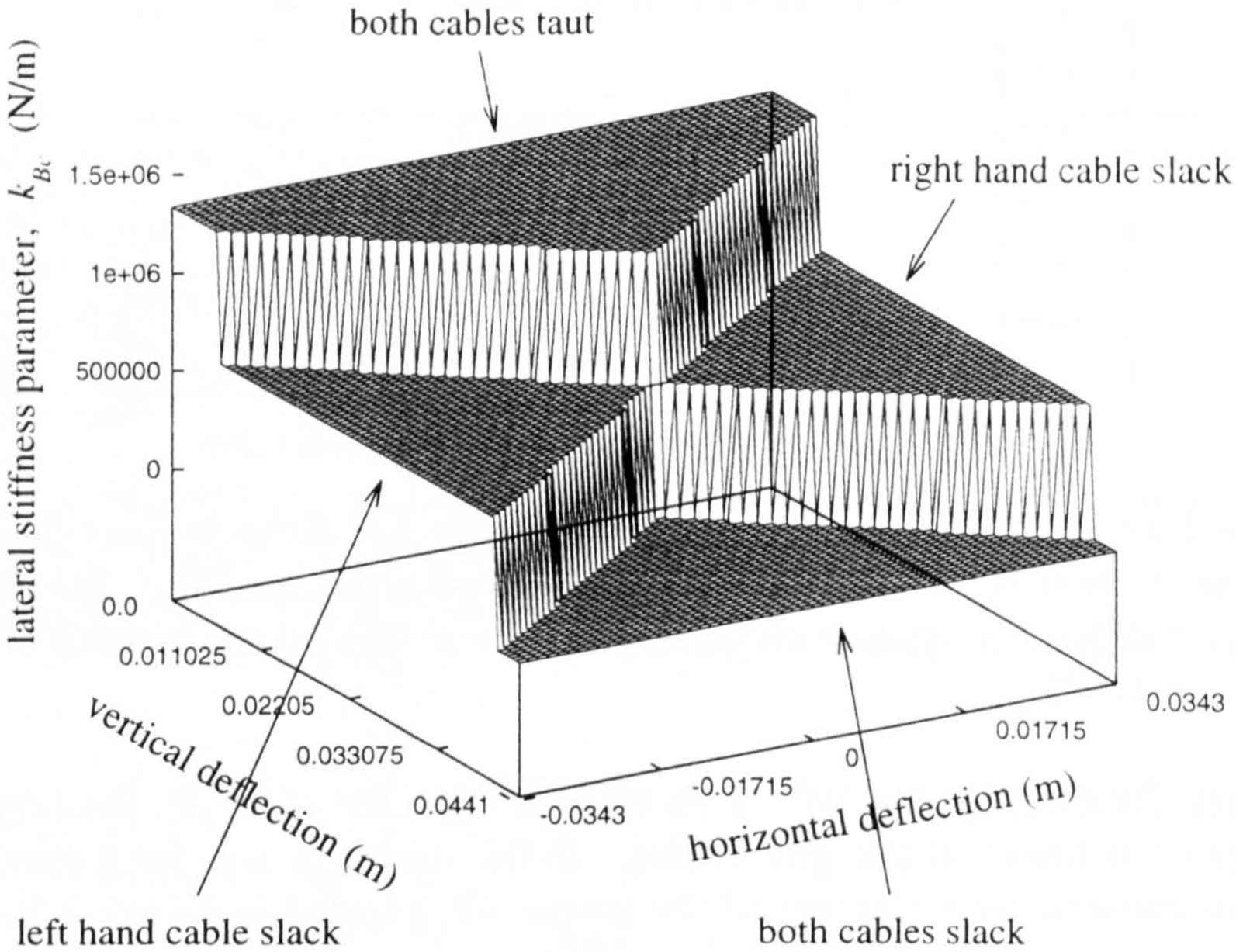

Figure 4.19: The variation of the lateral stiffness parameter of the guy cables, k_{Bc} with horizontal and vertical deflection of the point of attachment of the guy cables to the tower. The initial strain in the guy cables is 0.0005.

For modal analysis as well as static analysis, it is assumed that stiffness parameters are constant and that tower deflections do not cause the stiffness parameters to jump to grossly different values, crossing to different planes in Figure 4.19. In a non-linear, time-stepping approach, it is necessary to use very small time-steps in order that the conversion of kinetic energy to potential energy is calculated with the correct value of stiffness parameter for the particular, momentary deflection of the structure. The dangers, even for analysis of a linear system, of using time-steps that are too big are illustrated in Section 9.1.4, Figure 9.3.

If the initial strain in the guy cables is large (10% in Figure 4.20), there are not regions within which k_{Bc} is approximately constant and the variation of k_{Bc} with horizontal and vertical deflections is highly non-linear.

4.7.4 Bending Vibrations of Wind Turbine Blades

Having shown that the Rayleigh/ Stodola model of tower vibrations is applicable for pre-stressed structures, vibration of the rotor blades is considered. Blade vibrations are more complicated than tower vibrations for three main reasons:

1. The blades are subject to centrifugal forces which arise because of their rotational speed.

2. The blades are highly assymmetrical and so the possibility of *flutter* modes arises (see Section 2.2.1). Figure 4.21 shows the variation of chord length and twist of a blade

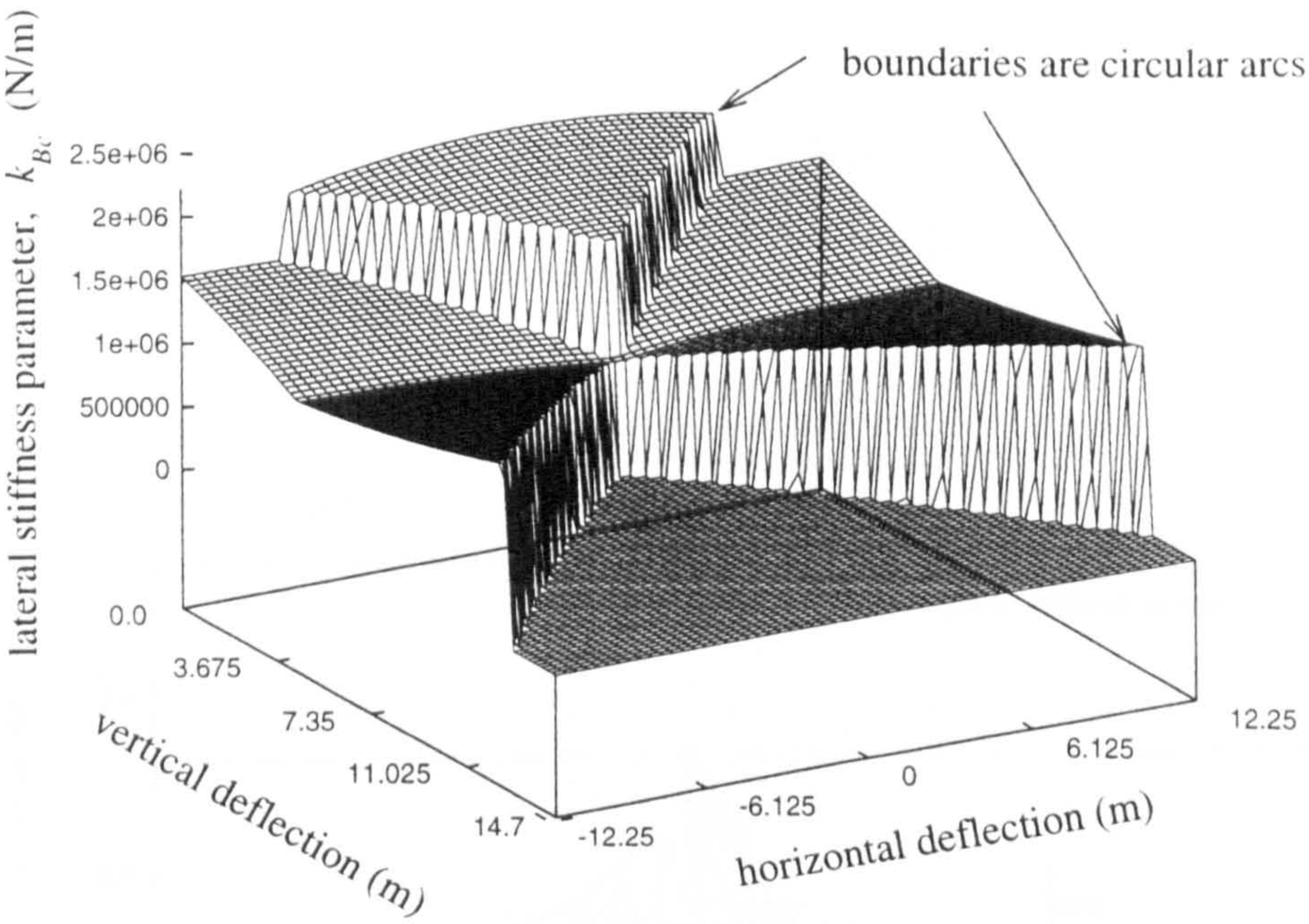

Figure 4.20: The variation of the lateral stiffness parameter of the guy cables, k_{Bc} with horizontal and vertical deflection of the point of attachment of the guy cables to the tower. The initial strain in the guy cables is 0.1.

from the Carter 300 kW wind turbine.

3. The blades are subject to aerodynamic forces as they rotate and vibrate in a turbulent wind field which excite or damp the vibrations.

Only the first of these factors is included in the analysis of blade vibrations in this thesis. During constant power generation, the blade rotation generates constant, axial, centrifugal forces on the blades. The fundamental lateral frequency of vibration is increased by increasing the speed of rotation. It is important to know the relationship between natural rotor modes and the speed of rotation particularly if the wind turbine is designed to operate at variable speed.

The modal response of a rotor blade not subject to aerodynamic loads or the effects of its own assymmetry is still useful as a first approximation to assess the natural, dynamic behaviour of the blade. Figure 4.22 shows the variation with rotor frequency of the fundamental edgewise and flatwise lateral vibration modes of a single rotor. The hub is assumed to be longitudinally rigid and rigid in torsion about all axes.

The monitoring program completed by Garrad Hassan [22] revealed that with the rotor parked and therefore rotationally fixed, the frequencies of flatwise and edgewise lateral vibrations were 0.50 Hz and 2.64 Hz. Using the same mass and stiffness data, the model described in Chapters 2 and 4 predicted flatwise vibrations at 0.53 Hz and edgewise vibrations at 3.1 Hz.

This variation with rotational frequency of the natural frequency of vibration of the blades can be plotted on an interference diagram as shown in Figure 4.23. The P and

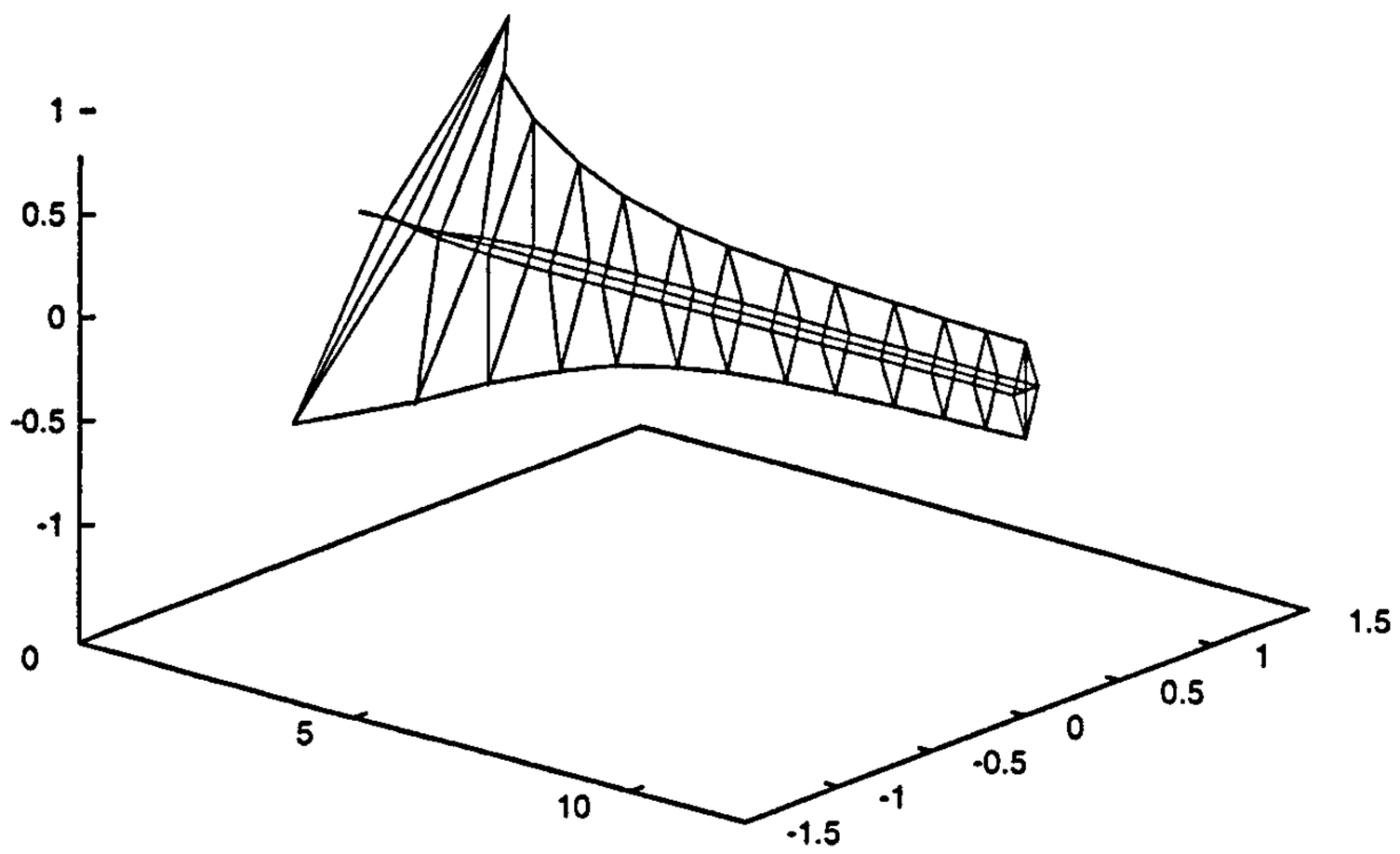

Figure 4.21: The geometry of a single rotor blade from the Carter 300 kW wind turbine. The chord and thickness axes of the blade tip are aligned with the vertical and horizontal axes of the figure. The data for this figure were obtained from a survey of the Carter 300 kW wind turbine by Garrad Hassan and Partners Ltd. [22].

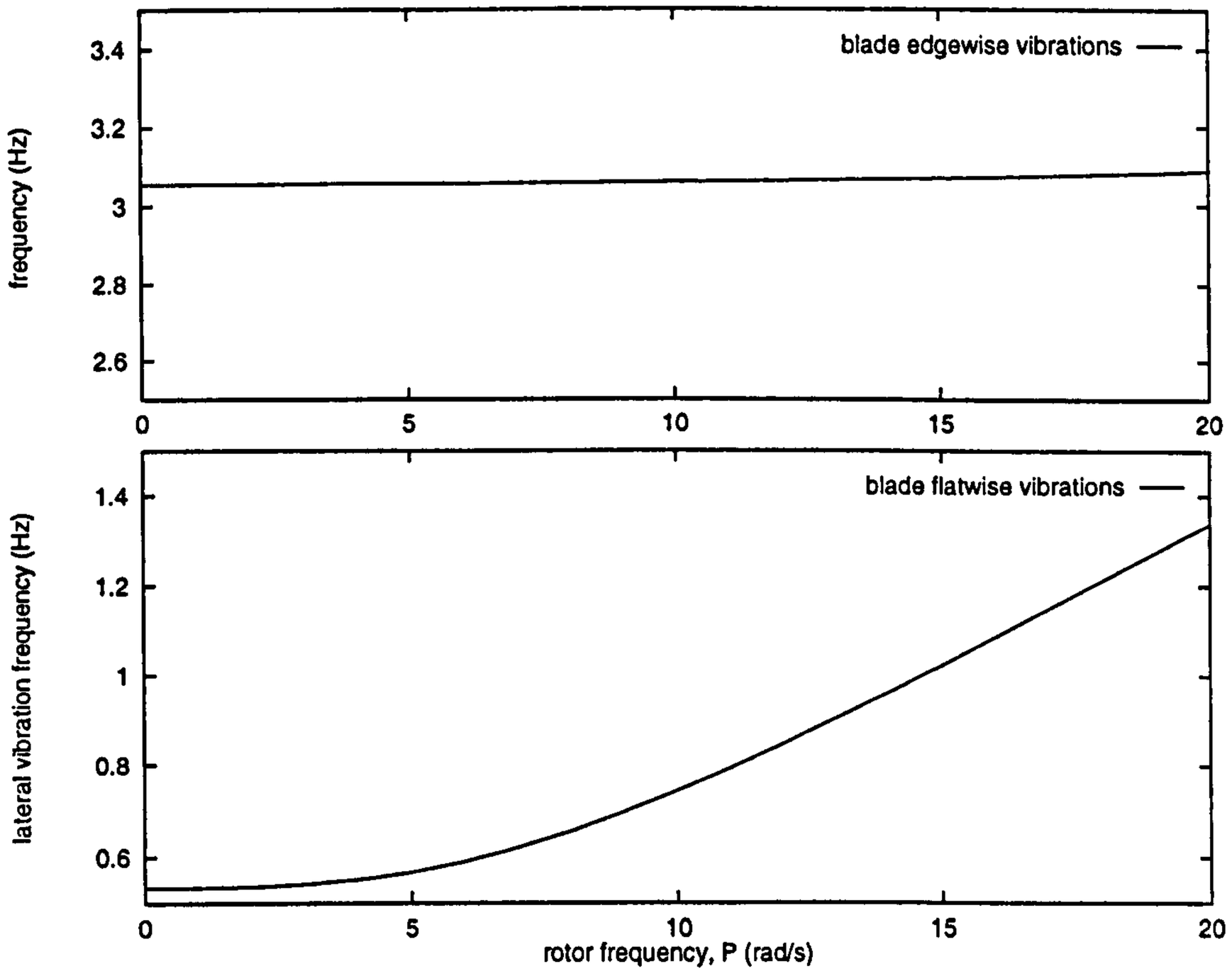

Figure 4.22: The fundamental frequencies of vibration of a single, rigidly fixed rotor blade from the Carter 300 kW wind turbine. The mass and stiffness data were taken from the survey of the wind turbine performed by Garrad Hassan and Partners Ltd. [22].

$2P$ lines represent the forcing and where they cross one of the natural modes of vibration, resonance is expected to occur. At the operating point (1,1), no resonance occurs with P but resonance of the tower first harmonic may occur with $2P$. However, given that k_{Bf} is likely to be near 0, this frequency is likely to be in the lower part of the range. The Carter 300 kW was designed to operate at fixed speed but if the design were to be changed and higher speeds of operation used, the blade fundamental flatwise mode may be excited by the rotational frequency, P.

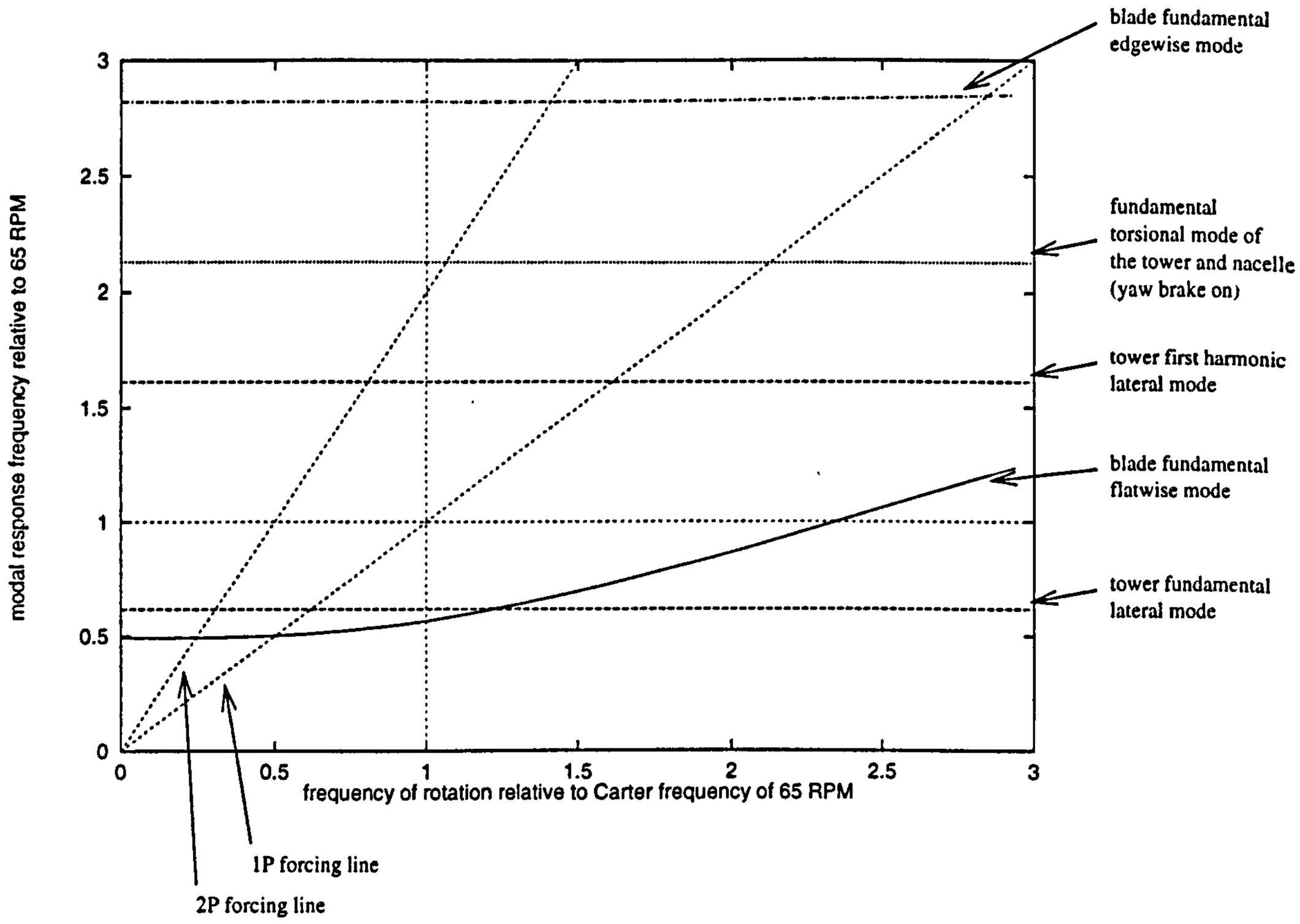

Figure 4.23: An interference diagram for the lowest frequencies of vibration of the tower and blades. Frequency axes used in Figure 4.22 are converted into relative units by dividing by the rotational speed (P) of the Carter 300 kW wind turbine which is 65 RPM (or 1.08 Hz, or 6.807 rad s^{-1}). Since the base of the Carter 300 kW is supposed to be an ideal hinge, k_{Bf} is set to 0 N m rad^{-1}. The lowest possible tower first torsional frequency is plotted. This corresponds to a rigid yaw bearing ($k_{yn} = \infty$).

Chapter 5

Validating the Models

Comparisons are made between the modelling techniques used for this thesis and other established techniques. Comparisons are made for:

- static analysis;
- non-linear buckling;
- modal analysis.

Two approaches are taken:

1. The model parameters are used to limit the complexity of the problem. In this case: uniform tower, no guys. Direct mathematical solutions are possible. Comparisons are made between:
   (a) results from direct mathematical solutions;
   (b) results obtained by using appropriate elements of the *general, numerical model* described in this thesis;
   (c) Finite Element analysis using a recognised commercial package.
2. The full complexity of the *general, numerical model* described here is tested by comparing results for different commercial tower designs in three ways:
   (a) Finite Element analysis using a recognised commercial package;
   (b) appropriate elements of the *general, numerical model* described in this thesis;
   (c) measurements from towers on operating wind turbines.

Validation of the *general, numerical model* is possible given a set of design parameters (Appendix H) by comparing two particular approaches. Design parameters are set in order that the two approaches are dealing with situations that are as similar as possible. The specific conditions under which any validation applies are described in the appropriate section of Chapter 5.

Comprehensive models include linear guy elements, towers of variable cross section and nacelles with lumped masses. *General. numerical models* are as described in Chapters 2. 3

and 4. Models generated for Finite Element analysis will be described in the appropriate section of Chapter 5). Results are compared using design parameters for three different commercial towers. Some of the model parameters are listed in Table 5.1. Complete parameter sets are given in Appendix H.

Table 5.1: Summary comparison of various wind turbine structural designs.

tower design	rated power (kW)	height, H (m)	average outside tower radius (m)	λ_{ct}	total nacelle mass (kg)
Carter wind turbine at Great Orton Airfield	300	49	0.383	0.74	4600
Carter wind turbine at Faccombe Estate	300	38.8	0.396	0.70	4600
Carter wind turbine at West Beacon Farm	25	23.3	0.159	0.66	380

5.1 Simplified Models of the Structure

With simple model configurations, direct solutions are possible to obtain:

- deflections at static equilibrium
- ultimate buckling loads
- modal frequencies and deflection shapes

In Subsections 5.1.1, 5.1.2 and 5.1.3, these direct results are compared with results from the general, numerical model described in this thesis.

5.1.1 Static Deflections

For static analysis, combinations of both uniformly distributed and concentrated loads were used in the modelling. In this section, uniformly distributed loads are denoted by a lower case f and q and concentrated loads by upper case F and Q. Elsewhere, lower case notation means a distributed load although not necessarily uniform. The three classes of deflection and the loads associated are illustrated in Figure 5.1.

For static analysis, the simple model consists of a straight, cylindrical tower, constant wall thickness and material properties. The base is either freely hinged (the tower is *simply supported*) or rigidly *built in*. The parameter k_{Bf} used in the *general, numerical model* controls the torsional stiffness of the base for lateral bending of the tower. If it is zero, the base is an ideal hinge. If it is large, the base is built in. The changeover occurs sharply

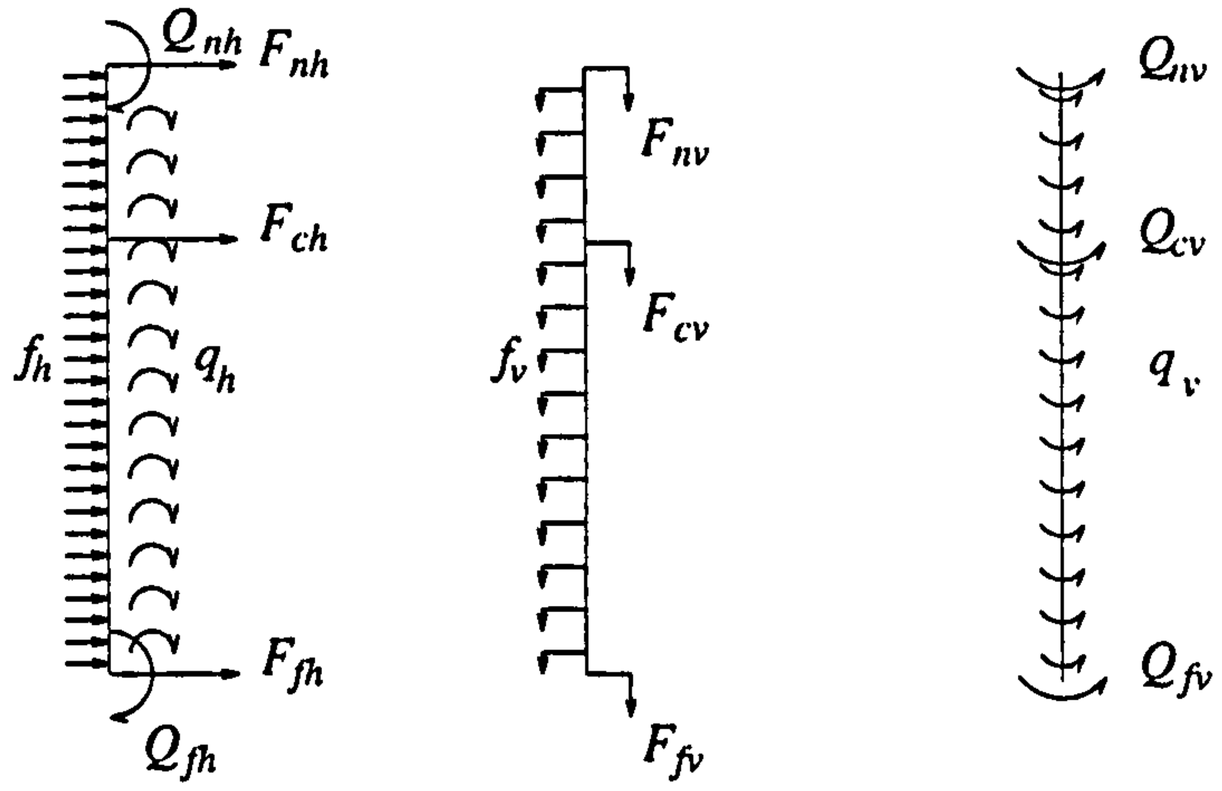

lateral loadings longitudinal loadings torsional loadings

Figure 5.1: Equilibrium between applied loads and reactions for the three classes of deformations.

between 1×10^6 and 1×10^8 N m rad^{-1} for the case of static bending. This is illustrated in Figure 5.2. Throughout this thesis, the base is modelled as built in by setting k_{Bf} to 1×10^{12} N m rad^{-1} and simply supported by setting k_{Bf} to 0.0.

5.1.1.1 Lateral Deflections

The simplest model of the tower is a vertical cantilever beam with no guys. With a nacelle thrust, F_{nh}, a nacelle couple, Q_{nh}, a load, f_h distributed uniformly up the tower and a uniform torque distribution, q_h, the lateral deflection of the tower can be derived exactly using *small deflection theory* for pure bending (see Equation 5.3). The base is built in ($k_{Lf} = k_{Bf} = \infty$). The flexural rigidity, $E_t I_{xt}$ of the tower is constant with height. The guys are ignored (ρ_c = 0.0 kg m^{-3}). The base reactions (Equations 5.1 and 5.2) are found by equilibrium. For positive values of any of the load parameters, the deflection increases monotonically with height. Rather than reproduce illustrations of this variation for every load case. deflections at the tower top ($v(H)$) calculated using each method are shown in Table 5.2.

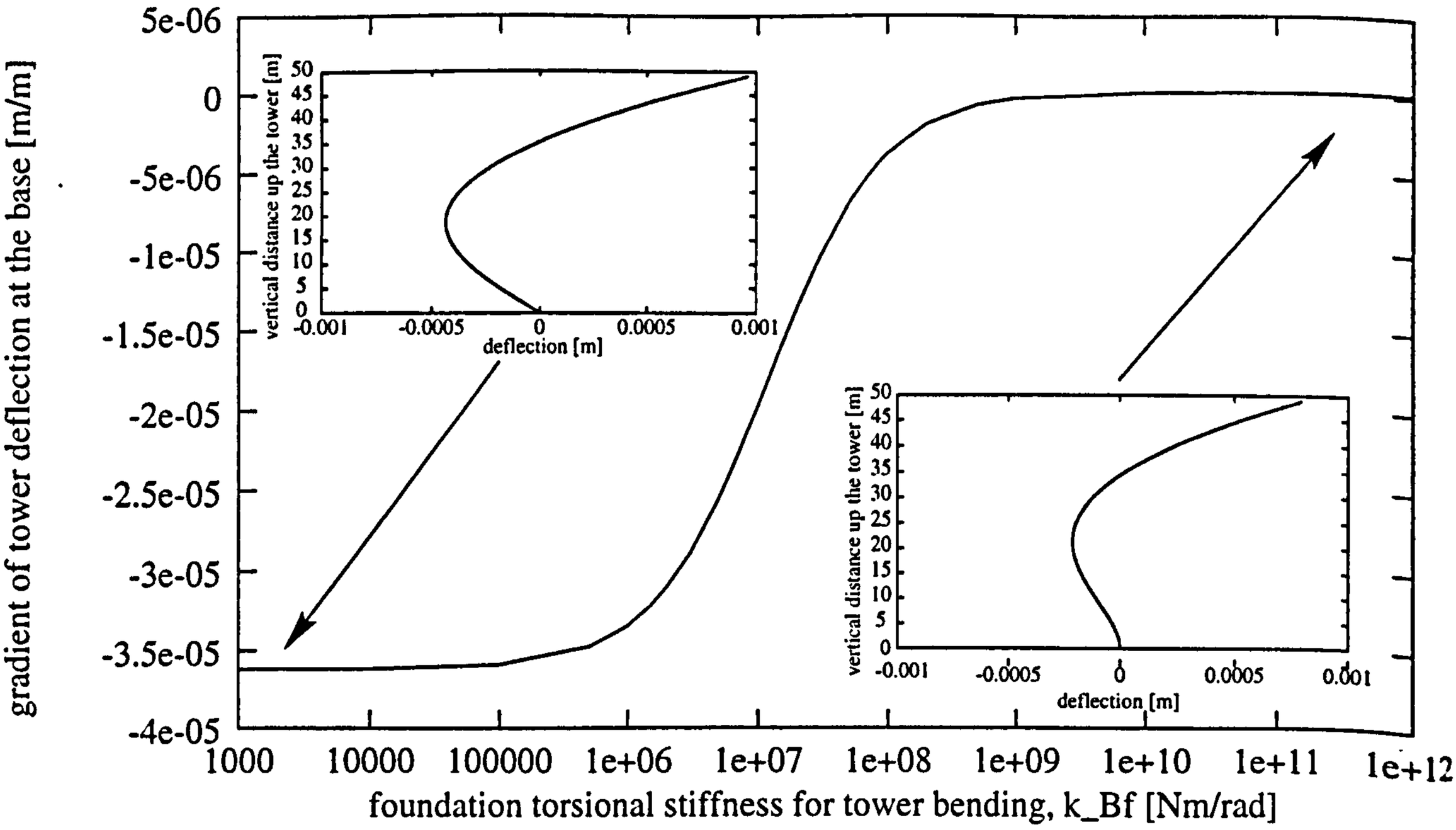

Figure 5.2: Comparison of different values of base bending stiffness (parameter: k_{Bf}). The gradient of the deflection at the base is plotted against the base stiffness (log scale used). All points represent lateral deflection of the tower in response to a 100 N load applied at the top.

Table 5.2: Comparison between the deflection of the tower head calculated with Equation 5.3 and calculated using the structural spline *model. Models are cylindrical with parallel sides. There are no guy cables.*

applied load	results from Equation 5.3 (m)	results from *structural spline* model (m)	number of significant figures of similarity
$F_{nh} = 1$ N	1.66×10^{-4}	1.66×10^{-4}	5
$Q_{nh} = 1$ N m	5.09×10^{-6}	5.09×10^{-6}	4
$f_h = 1$ N m^{-1}	3.05×10^{-3}	3.05×10^{-3}	4
$q_h = 1$ N m m^{-1}	1.66×10^{-4}	1.66×10^{-4}	5

$$F_{fh} = -(F_{nh} + f_h H) \tag{5.1}$$

$$Q_b = -(F_{nh} H + \frac{1}{2} f_h H^2 + q_h H + Q_n) \tag{5.2}$$

$$v = \frac{H^3}{E_t I_{xt}} \left(-\frac{1}{6} (F_{nh} + q_h) \left(3X^2 - X^3\right) + \frac{1}{24} f_h H X^2 \left(X^2 - 4X + 6\right) + \frac{1}{2} Q_{nh} X^2 \right) \tag{5.3}$$

A slightly more complicated model of the tower includes the guys but models them as linear springs exerting a horizontal force proportional to their horizontal deflection. The base may now be either built in or hinged. The deflection is given by Equation 5.4 if the base is built in and Equation 5.6 if the base is hinged. No axial or vertical forces are considered. The axial compression in the tower due to the guys is set artificially to zero after calculating the equivalent lateral stiffness parameters for the guys. The geometric and material properties of the tower are uniform.

$$v = \begin{cases} \text{if the base fixing is built in:} \\ \frac{H^3}{E_t I_{xt}} \left(\begin{array}{l} (F_{nh} + q_h) \left(\frac{1}{2}X^2 - \frac{1}{6}X^3\right) + \\ \left(\frac{1}{4}X^2 - \frac{1}{6}X^3 + \frac{1}{24}X^4\right) f_h H + \\ \frac{1}{2}\frac{Q_{nh}}{H}X^2 + F_{ch}\left(\frac{1}{2}\lambda_{ct}X^2 - \frac{1}{6}X^3\right) \end{array} \right) \\ \text{in the range } (0 < x < \lambda_{ct} H) \\ \frac{H^3}{E_t I_{xt}} \left(\begin{array}{l} (F_{nh} + q_h) \left(\frac{1}{2}X^2 - \frac{1}{6}X^3\right) + \\ \left(\frac{1}{4}X^2 - \frac{1}{6}X^3 + \frac{1}{24}X^4\right) f_h H + \\ \frac{1}{2}\frac{Q_{nh}}{H}X^2 + F_{ch}\left(\frac{1}{2}\lambda_{ct}X^2 - \frac{1}{6}X^3\right) + F_{ch}\left(X - \lambda_{ct}\right)^3 \end{array} \right) \\ \text{in the range } (\lambda_{ct} H < x < H) \end{cases} \tag{5.4}$$

where:

$$F_{ch} = -\frac{\left(\begin{array}{l} \frac{1}{2} Q_{nh} \lambda_{ct}^2 H^2 + F_{nh} \lambda_{ct}^2 H^3 \left(\frac{1}{2} - \frac{1}{6}\lambda_{ct}\right) + \\ f_h \lambda_{ct}^2 H^4 \left(\frac{1}{4} - \frac{1}{6}\lambda_{ct} + \frac{1}{24}\lambda_{ct}^2\right) + \\ q_h \lambda_{ct}^2 H^3 \left(\frac{1}{2} - \frac{1}{6}\lambda_{ct}\right) \end{array} \right)}{\frac{E_t I_{xt}}{k_{Bc}} + \frac{1}{3}\lambda_{ct}^3 H^3} \tag{5.5}$$

$$v = \begin{cases} \text{if the base fixing is hinged:} \\ \frac{H^3}{E_t I_{xt}} \left(\begin{array}{l} -\frac{1}{6} (F_{nh} + F_{ch} + q_h) X^3 + \\ \frac{1}{24} f_h H X^3 (X - 4) + C_I X \end{array} \right) \\ \text{in the range } (0 < x < \lambda_{ct} H) \\ \frac{H^3}{E_t I_{xt}} \left(\begin{array}{l} -\frac{1}{6} (F_{nh} + F_{ch} + q_h) X^3 + \\ \frac{1}{24} f_h H X^3 (X - 4) + C_I X \frac{1}{6} F_{ch} (X - \lambda_{ct})^3 \end{array} \right) \\ \text{in the range } (\lambda_{ct} H < x < H) \end{cases} \tag{5.6}$$

where:

$$F_{ch} = -\frac{1}{\lambda_{ct}}\left(F_{nh} + \frac{Q_{nh}}{H} + \frac{1}{2}f_h H + q_h\right) \tag{5.7}$$

and:

$$C_I = \frac{1}{\lambda_{ct}}\left(\begin{array}{l}\left(\frac{1}{6}\lambda_{ct}^3 - \frac{E_t I_{xt}}{k_{Bc} H^3}\right) F_{ch} + \frac{1}{6}\left(F_{nh} + q_h\right)\lambda_{ct}^3 + \\ \frac{1}{24} f_h H \lambda_{ct}^3 (4 - \lambda_{ct})\end{array}\right) \tag{5.8}$$

Comparisons have been made for a set of applied loads each of which results in a deflection of a similar magnitude. The results are illustrated in Figure 5.3 for built in base fixing and Figure 5.4 for hinged base. The tower design is based on the tower used for the Carter 300 kW (Great Orton Airfield type) but with parallel sides (cylindrical).

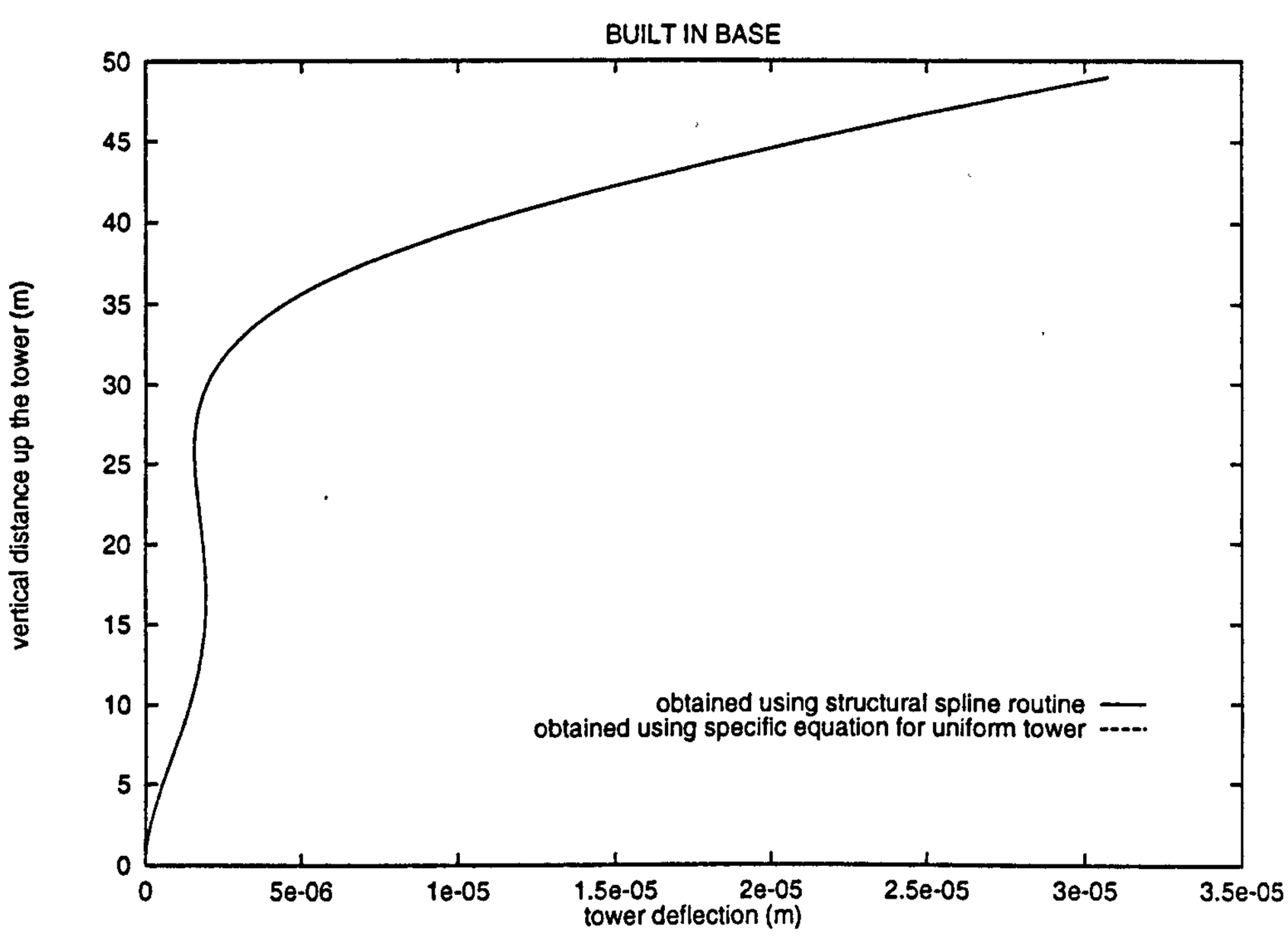

Figure 5.3: Comparison between deflection shapes of a guyed, uniform tower with built in base and applied loads: $F_{nh} = 1$ N, $f_h = 0.2$ N m^{-1}, $Q_{nh} = 10$ N m and $q_h = 1$ N m m^{-1}.

5.1.1.2 Longitudinal Deflections

E The longitudinal deflections of a uniform tower can by calculated by direct solution of the equations of static equilibrium. Downwards deflections are treated as positive. The deflection at which the guy cables go slack is given by $\lambda_{cu0}H$ in Equation 5.9.

$$\lambda_{cu0} = \lambda_{ct} - \sqrt{\lambda_{cn}^2 - \left(\lambda_{cg} - \lambda_{ro2}\right)^2} \tag{5.9}$$

So long as deflections are less than $\lambda_{cu0}H$, the vertical force on the structure from the guy cables is given by F_{cv} in Equation 5.10.

$$F_{cv} = \frac{k_{Cc}}{E_t A_{xt}}\left(\frac{E_t A_{xt}\lambda_{cu0}H - F_{nv}\lambda_{ct}H - f_v H^2 \lambda_{ct}(1 - \frac{1}{2}\lambda_{ct})}{1 + \frac{k_{Cc}}{E_t A_{xt}}\lambda_{ct}H}\right) \tag{5.10}$$

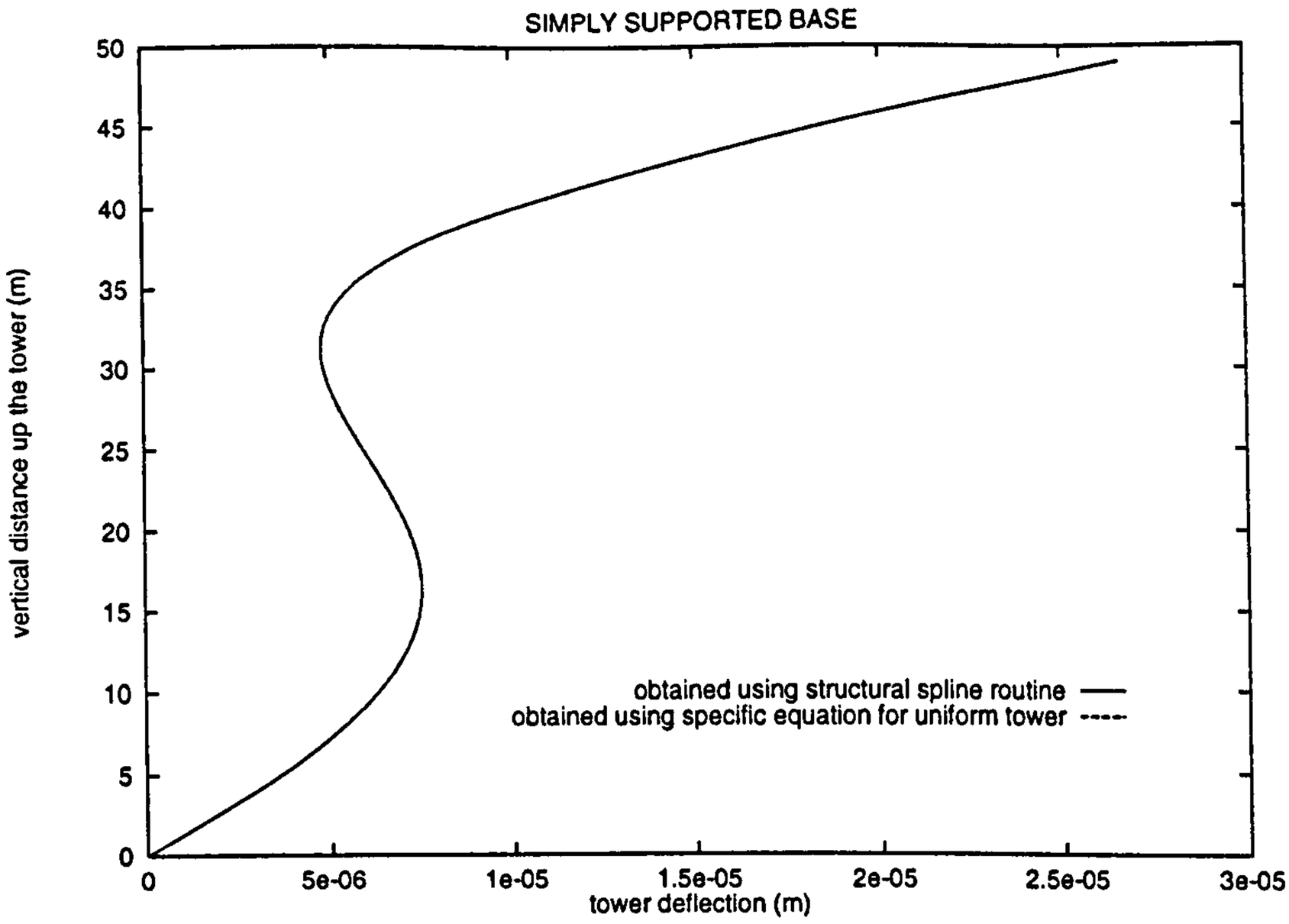

Figure 5.4: Comparison between deflection shapes of a guyed uniform tower with hinged base and applied loads: $F_{nh} = 1\ N$, $f_h = 0.2\ N\ m^{-1}$, $Q_{nh} = 10\ N\ m$ *and* $q_h = 1\ N\ m\ m^{-1}$.

The compressive force in the tower, C_t is given by Equation 5.11 for the two sections of the tower (above and below the point of attachment of the guys to the tower).

$$C_t = \begin{cases} F_{nv} + F_{cv} + f_v\,(H - x) & (0 < x < \lambda_{ct} H) \\ F_{nv} + f_v\,(H - x) & (\lambda_{ct} H < x < H) \end{cases} \tag{5.11}$$

The solution of the differential equation for longitudinal deflections of a uniform tower (Equation 2.29) is given by Equation 5.12.

$$u = \begin{cases} \frac{1}{E_t A_{xt}} \left((F_{nv} + F_{cv} + f_v H)\, x - \frac{1}{2} f_v x^2 \right) & (0 < x < \lambda_{ct} H) \\ \frac{1}{E_t A_{xt}} \left((F_{nv} + f_v H)\, x - \frac{1}{2} f_v x^2 + F_{cv} \lambda_{ct} H \right) & (\lambda_{ct} H < x < H) \end{cases} \tag{5.12}$$

Comparisons can be made between deflections predicted using the *general numerical model* and those from the model described above of a uniform tower (see Figure 5.6). In this section, the distribution of shear stress in the tower has also been compared (see Figure 5.5). Data for Figures were calculated using a tower design similar to that used for the Carter 300 kW machine (Great Orton Airfield type) but with parallel sides (cylindrical).

On Figure 5.5, the discontinuity at $x = \lambda_{ct} H$ is due to the additional compressive force on the lower portion of the tower ($0 < x < \lambda_{ct} H$) because of the initial strain, ϵ_{ic} in the guys. The vertical deflection of the lower portion of the tower in Figure 5.6 is correspondingly greater than the vertical deflection of the upper portion of the tower relative to the lower portion.

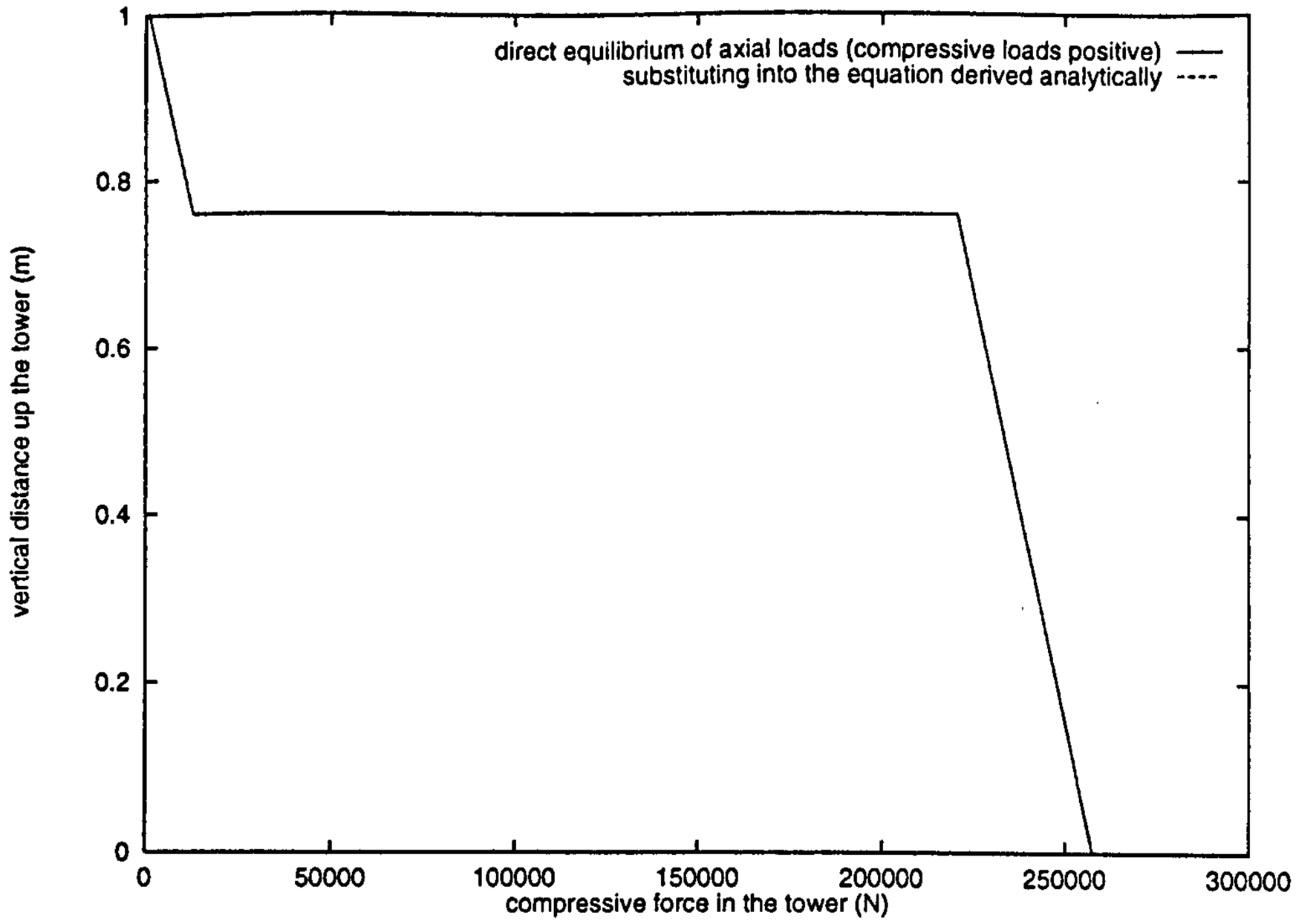

Figure 5.5: Comparison of the shear stress distribution estimated using the general, numerical *routine and that obtained from Equation 5.11 for a simple model of a guyed tower. Gravity forces are neglected and the tower is subject just to two types of load, F_{nv} is 1000 N and f_v is 1000 N m^{-1}, distributed uniformly.*

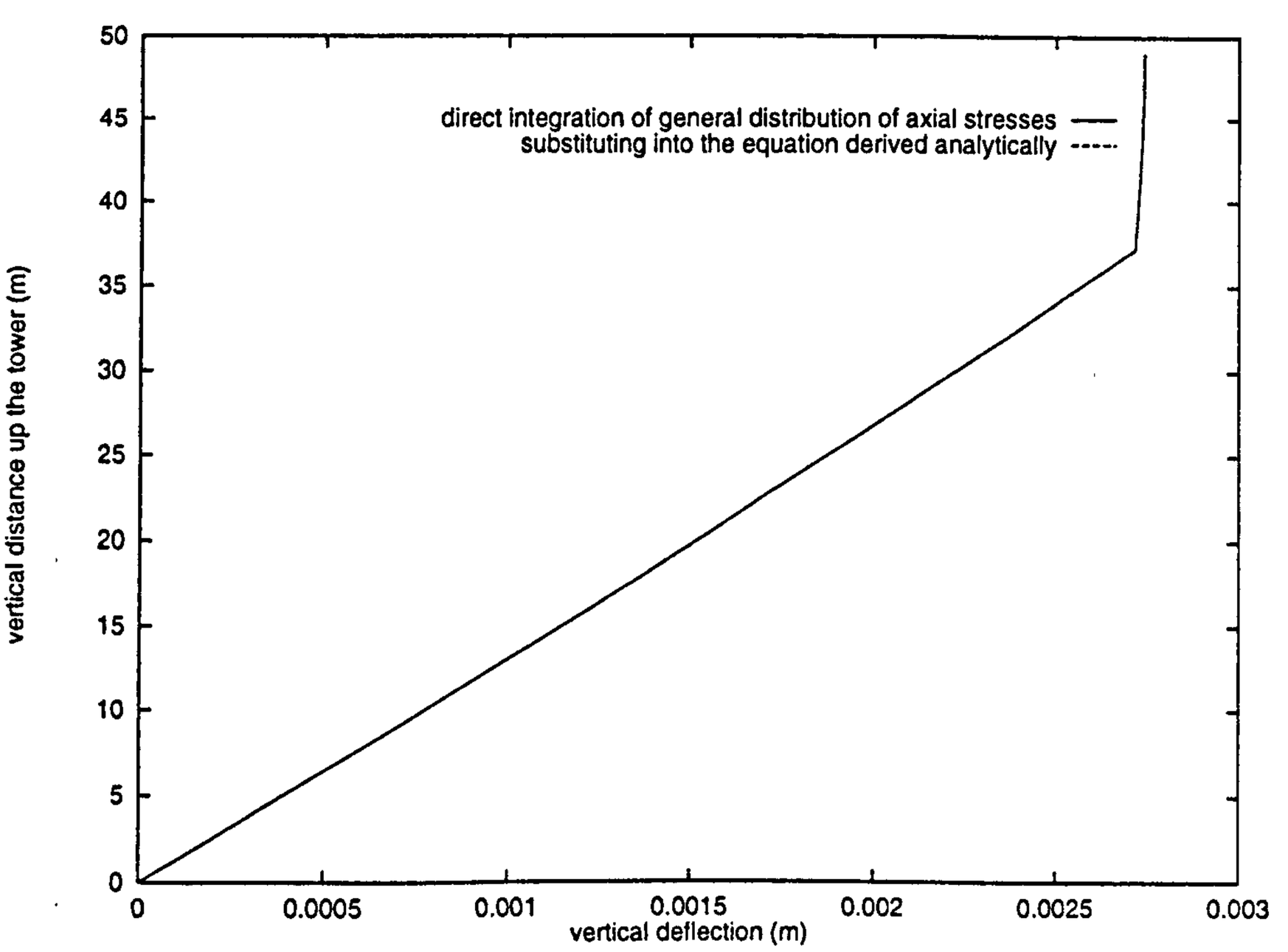

Figure 5.6: Comparison of the distribution of vertical deflections with height estimated using the general, numerical *routine and that obtained by applying Equation 5.12. The same loads are applied as for Figure 5.5 above.*

5.1.1.3 Torsional Deflections

The torsion of the tower in response to a tower head torque Q_{nv} and a distributed torque q_v is given in Equation 5.15 below. The distribution of torques is given in Equation 5.14.

The torque distribution with height is given for a typical load case in Figure 5.7. The discontinuity at $x = \lambda_{ct}H$ is due to the restoring torque from the guys which is in the opposite direction to the deflection of the point of attachment of the guys ($\theta(\lambda_{ct}H)$). For this load case, the discontinuity is relatively small, so the deflection shape appears smooth (Figure 5.8). The deflection, θ_n of the nacelle (Appendix A.2, Equation A.17) is responsible for the deflection spike at the top of the curve in Figure 5.8.

$$Q_c = -\frac{k_{Tc}}{G_t J_{xt}} \left(\frac{Q_{nv}\lambda_{ct}H + q_v H^2 \lambda_{ct}\left(1 - \frac{1}{2}\lambda_{ct}\right)}{1 + \frac{k_{Tc}}{G_t J_{xt}}\lambda_{ct}H} \right) \tag{5.13}$$

$$Q_t = \begin{cases} Q_{nv} + Q_{cv} + q_v\left(H - x\right) & \left(0 < x < \lambda_{ct}H\right) \\ Q_{nv} + q_v\left(H - x\right) & \left(\lambda_{ct}H < x < H\right) \end{cases} \tag{5.14}$$

$$\theta = \begin{cases} \frac{1}{G_t J_{xt}}\left(\left(Q_{nv} + Q_c + q_v H\right)x - \frac{1}{2}q_v x^2\right) & \left(0 < x < \lambda_{ct}H\right) \\ \frac{1}{G_t J_{xt}}\left(\left(Q_{nv} + q_v H\right)x - \frac{1}{2}q_v x^2 + Q_c \lambda_{ct} H\right) & \left(\lambda_{ct}H < x < H\right) \end{cases} \tag{5.15}$$

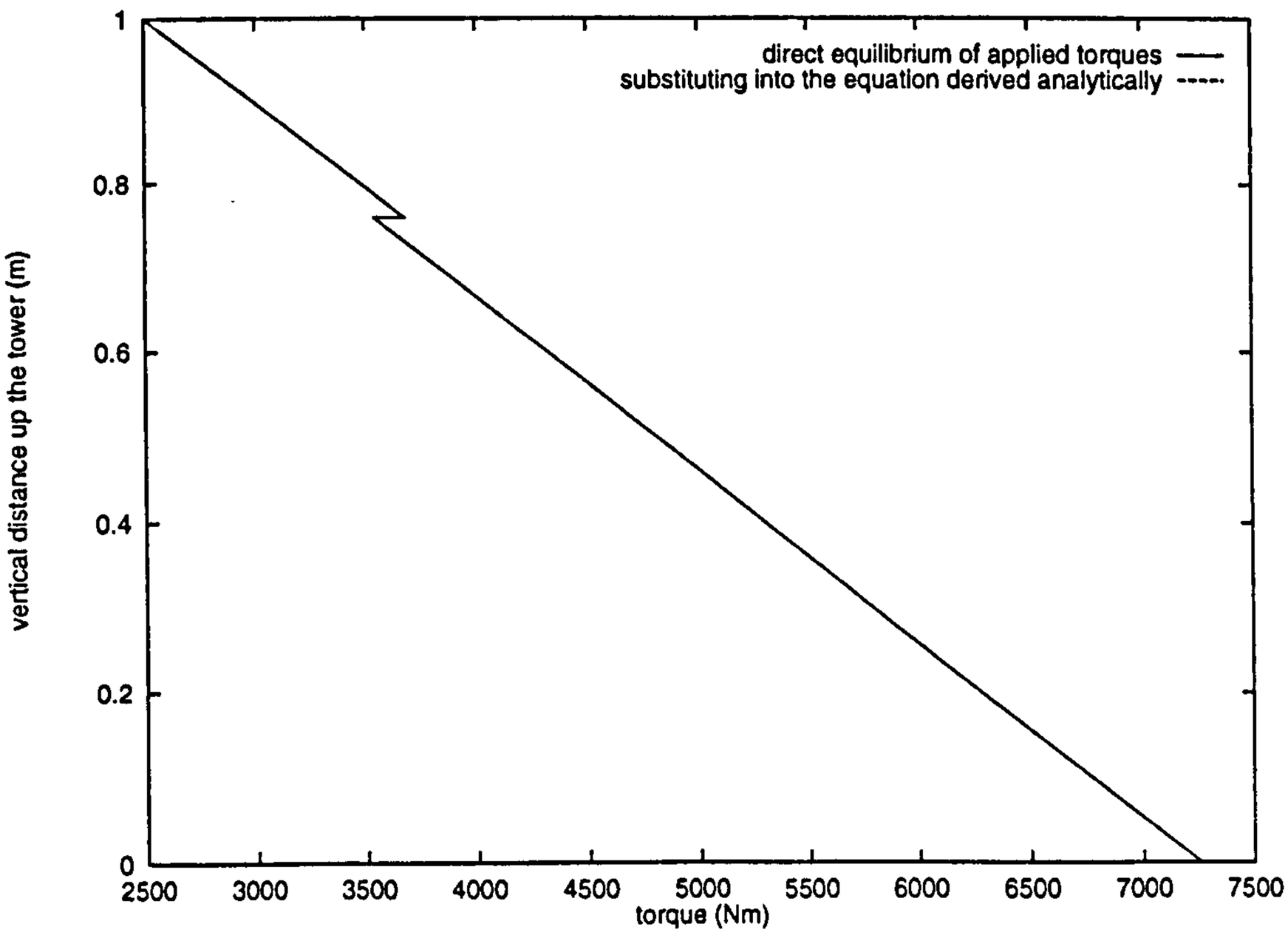

Figure 5.7: Comparison of the torque distribution estimated using the general, numerical *routine and that obtained from Equation 5.14 for a simple model of a guyed tower. The tower is subject just to two types of load, Q_{nv} is 2500 N m and q_v is uniformly distributed and is 100 N m m^{-1}.*

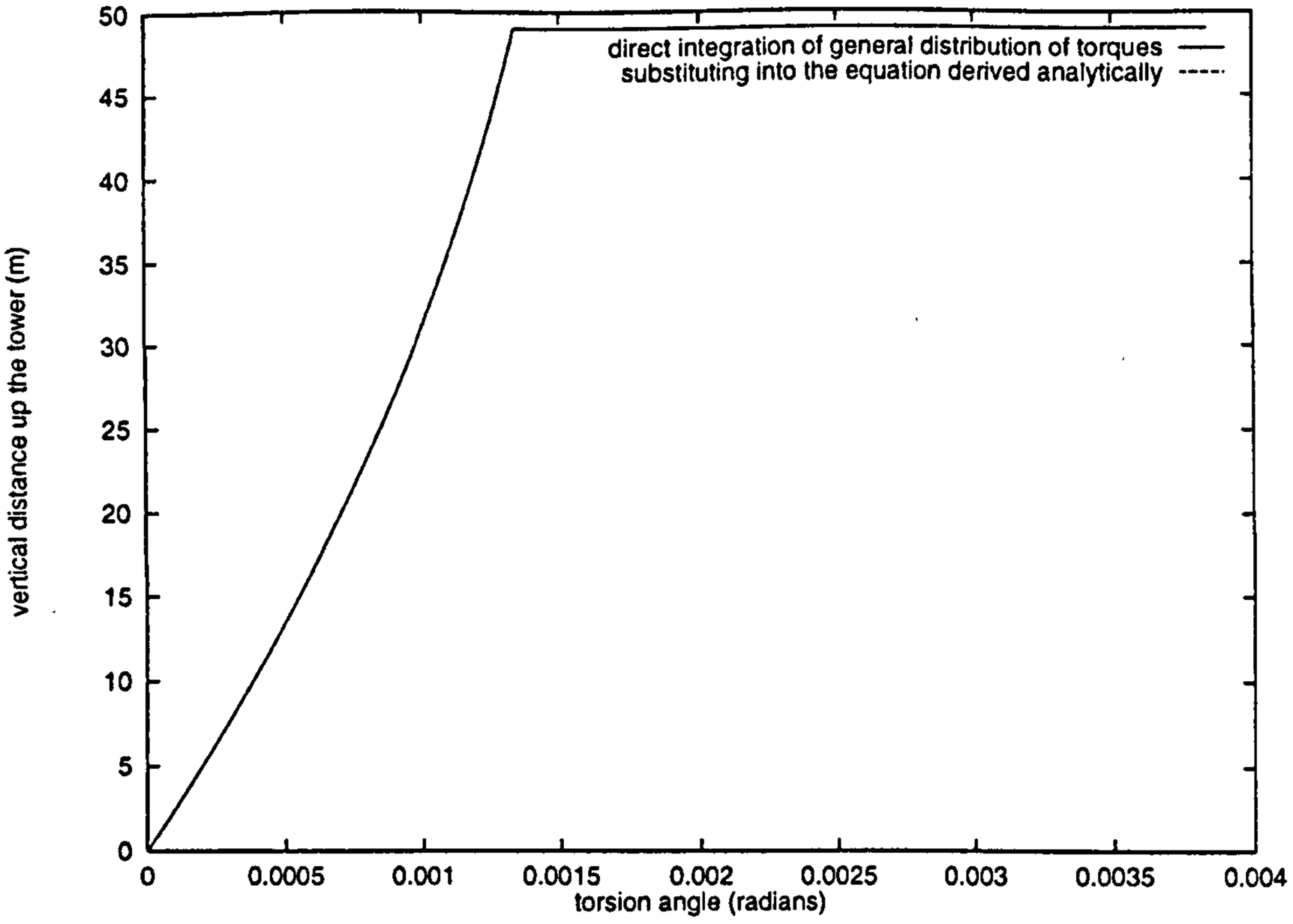

Figure 5.8: Comparison of the distribution of torsion angle with height estimated using the general, numerical *routine and that obtained by applying Equation 5.15. The same loads are applied as for Figure 5.7.*

5.1.2 Tower Buckling

The complete static analysis method includes the effects of applied vertical forces. As already described, buckling occurs when the combination of vertical loads applied exceeds a certain threshold (Section 3.2). To test that vertical loads are treated correctly in the *structural spline method*, comparisons are made between the buckling loads predicted using this method and the values predicted using Euler's formula (Equation 3.5 or 3.6). For a cantilever (one end *built in*, the other *free*), the Euler buckling load, F_{ei} and the shape of the i^{th} mode are given by Equations 5.16 and 5.17, where X is the vertical ordinate in dimensionless units. The mode shape $v(X)$ is also dimensionless since when the tower buckles deflections are infinite.

Data for the model are based on one of the real wind turbine tower designs, but the average tower diameter and wall thickness values are used throughout.

$$F_{ei} = \frac{i^2 \pi^2 E_t I_{xt}}{(2H)^2} \tag{5.16}$$

$$v = \sin\left(N_e \frac{\pi}{2} X\right) \tag{5.17}$$

Using an organised search (Section 3.2.1), deflection shapes are indeed almost indistinguishable from the pure sinusoidal functions predicted using Euler buckling theory. In terms

of ultimate buckling loads, Table 5.3 compares the Euler results obtained using Equation 5.16 with the estimates from the static tower model.

Table 5.3: The ultimate buckling load on the tower. Comparison of Euler solutions (Equation 5.16) with estimates obtained from the structural spline method. *The comparisons are for a 50 m, hollow, uniform tower with no guys and an ideal hinged at the base. Outside radius is 0.5 m and wall thickness is 3 mm. The buckling force is applied vertically at the tower top. A lateral force of 0.1 N m^{-1} is distributed uniformly between $\frac{H}{8}$ and $\frac{3H}{8}$. Convergence to a value of $F_{nv} \pm 1 \times 10^{-6}$ is deemed to have occured when $\frac{1}{v\left(\frac{H}{8}\right)}$ falls below 1×10^{-9}.*

mode number	Euler results (N)	estimate from static model (N)	number of significant figures of similarity
1	0.968×10^6	0.968×10^6	3
2	3.87×10^6	3.87×10^6	3
3	8.71×10^6	8.75×10^6	3
4	15.5×10^6	15.6×10^6	2
5	24.2×10^6	24.5×10^6	2

Data from commercial tower designs was used as the basis for the set of parameters used for comparisons between two methods of calculating the maximum initial guy tension before buckling. In each case, the tower defined comprised a uniform cylinder with outside radius (r_o) and wall thickness (t_t) set to the average values for the commercial designs. The Young's modulus of the guy cables is set high to prevent lateral movement of the point of attachment to the tower. Number of nodal points $N_n = 91$, number of spline interpolation points $N_s = 51$. $H_{(\text{ef})}$ is calculated using Equation 5.18. λ_e is calculated using the general approximating function given in Appendix F.1.2 (Equation F.3) with $\lambda_{e(min)} = 0.7$, $\lambda_{e(dif)} = 0.3$, $A = 6.28$ and $B = \frac{1}{9}$. F_{ei} is calculated using Equation 5.19 which is the general form of Equation 5.16 expressed using the effective length rather than the physical length.

$$H_{(\text{ef})} = \lambda_{ct} H \lambda_e \tag{5.18}$$

$$F_{ei} = \frac{i^2 \pi^2 E_t I_{xt}}{H^2_{(\text{ef})}} \tag{5.19}$$

Equation 5.20 is obtained by resolving vertically the forces in the four guy cables and rearranging the equation to make ϵ_{ic} the subject. Having worked out the vertical force on the tower necessary for buckling, the initial strain in the guy cables that corresponds to that force can be worked out using Equation 5.20.

$$\epsilon_{ic} = F_{ei} \frac{\rho_c}{(4 E_c m_c \sin(\frac{\lambda_{ct}}{(\lambda_{cg} - \lambda_{roi})}))} \tag{5.20}$$

Table 5.4: Comparison of Euler first buckling mode solutions (Equations 5.18 to 5.20) with estimates obtained from the structural spline method. *The basis for the tower design is listed. The design parameter which defines the initial strain in the guys (ϵ_{ic}) is increased until buckling occurs. ϵ_{ic} is the strain in the cables at assembly (see Section 2.2.3.1).*

design data basis	base fixing stiffness, k_{Bf}	euler solution (N) using Equations 5.18 to 5.20		estimate from static model	
		axial load on tower, F_{cv} (N)	initial strain, ϵ_{ic}	axial load on tower, F_{cv} (N)	initial strain, ϵ_{ic}
Great Orton design	0.0	1.68×10^{6}	4.08×10^{-3}	1.68×10^{6}	4.10×10^{-3}
Great Orton design	1.0×10^{12}	3.43×10^{6}	7.81×10^{-3}	3.42×10^{6}	7.83×10^{-3}
Faccombe design	0.0	3.63×10^{6}	8.50×10^{-3}	3.64×10^{6}	8.56×10^{-3}
Faccombe design	1.0×10^{12}	7.41×10^{6}	17.3×10^{-3}	7.38×10^{6}	17.4×10^{-3}
West Beacon Farm design	0.0	0.485×10^{6}	7.32×10^{-3}	0.486×10^{6}	7.37×10^{-3}
West Beacon Farm design	1.0×10^{12}	0.991×10^{6}	14.9×10^{-3}	0.986×10^{6}	15.0×10^{-3}

Predictions about buckling due to a vertical force, F_{nv} at the tower top can also be compared. Table 5.5 shows comparisons of predictions of the critical load ($F_{nv} = F_{ei}$) using Euler's formula (Equation 5.19) and the *general numerical model* described in Chapters 2 and 3. In Equation 5.19, the critical load ($F_{nv} = F_{ei}$) is calculated using an effective length calculated using Equation 3.9. Equation F.3 in Appendix F is used to calculate λ_{ea} with $\lambda_{e(min)} = 0.700$, $\lambda_{e(dif)} = 0.300$, $A = 6.28$ and $B = \frac{1}{9}$.

Table 5.5: Comparison of Euler solutions for the first buckling mode with estimates obtained from the static analysis software. The basis for the tower design is listed. The guys are attached at the top of the tower and the spacing of the guy foundations is 4 times the tower height.

design data basis	base stiffness, k_{Bf}	euler solution, F_{nv} (N)	estimate from static model, F_{nv} (N)
Great Orton design	0.0	1.01×10^{6}	1.00×10^{6}
Great Orton design	1.0×10^{12}	2.06×10^{6}	2.05×10^{6}
Faccombe design	0.0	1.94×10^{6}	1.93×10^{6}
Faccombe design	1.0×10^{12}	3.95×10^{6}	3.93×10^{6}
West Beacon Farm design	0.0	0.152×10^{6}	0.150×10^{6}
West Beacon Farm design	1.0×10^{12}	0.310×10^{6}	0.308×10^{6}

5.1.2.1 The Effect of the Model Parameters, N_n and N_s

Because axial forces in the tower only have an effect on the deflection at the nodal points in the model (see Section 2.3.2), the accuracy is dependent on the number of nodes (N_n) included. If the axial load on the tower is expected to have a substantial effect on the deflection, the number of nodes must be increased. This can be seen clearly in Figure 5.9 where increasing the number of nodes causes steady convergence. Increasing the number of spline interpolation points N_s has no effect.

If the number of nodes, N_n is increased but N_s is held constant, the size of available computer memory is the limiting factor because of the need to invert a $2N_n \times 2N_n$ matrix (Section 2.3.2).

If the number of nodes N_n is held constant and well within the memory capacity for the computer, but the number of spline points N_s is increased, the time taken to calculate $\epsilon_{ic(\mathrm{crit})}$ increases. This is because many quantities that change with tower height (such as cross sectional area or compressive force) are stored in arrays of length $(N_n-1)\times(N_s-1)+1$. As the length of these arrays increases, the time taken to evaluate or integrate these arrays also increases.

Supposing that by holding N_s at 11, it has been found that for a certain computer. N_n cannot be increased above 71 without memory problems (due to inverting a (142 × 142) matrix). arrays are then of length 701. The number of array integrations depends on the

required accuracy and the routines it is necessary to use for a particular problem. The number of such arrays it is necessary to store at any one time is of the order of 10. So storing these arrays increases the total memory usage from 20,000 for the (142×142) matrix alone to 27,000. If alternatively, the number of nodes N_n is held constant at 31, the size of the matrix is (62×62) requiring 3800 numbers to be stored. Assuming the same memory limitations, N_s can be increased to 76. The time taken to find a solution depends more heavily on the length of the arrays (2251 as opposed to 701 in the example above) which have to be integrated numerically at various points and so becomes the limiting factor on the overall number of points $(N_n - 1)(N_s - 1) + 1$ well before N_s has been increased to 76.

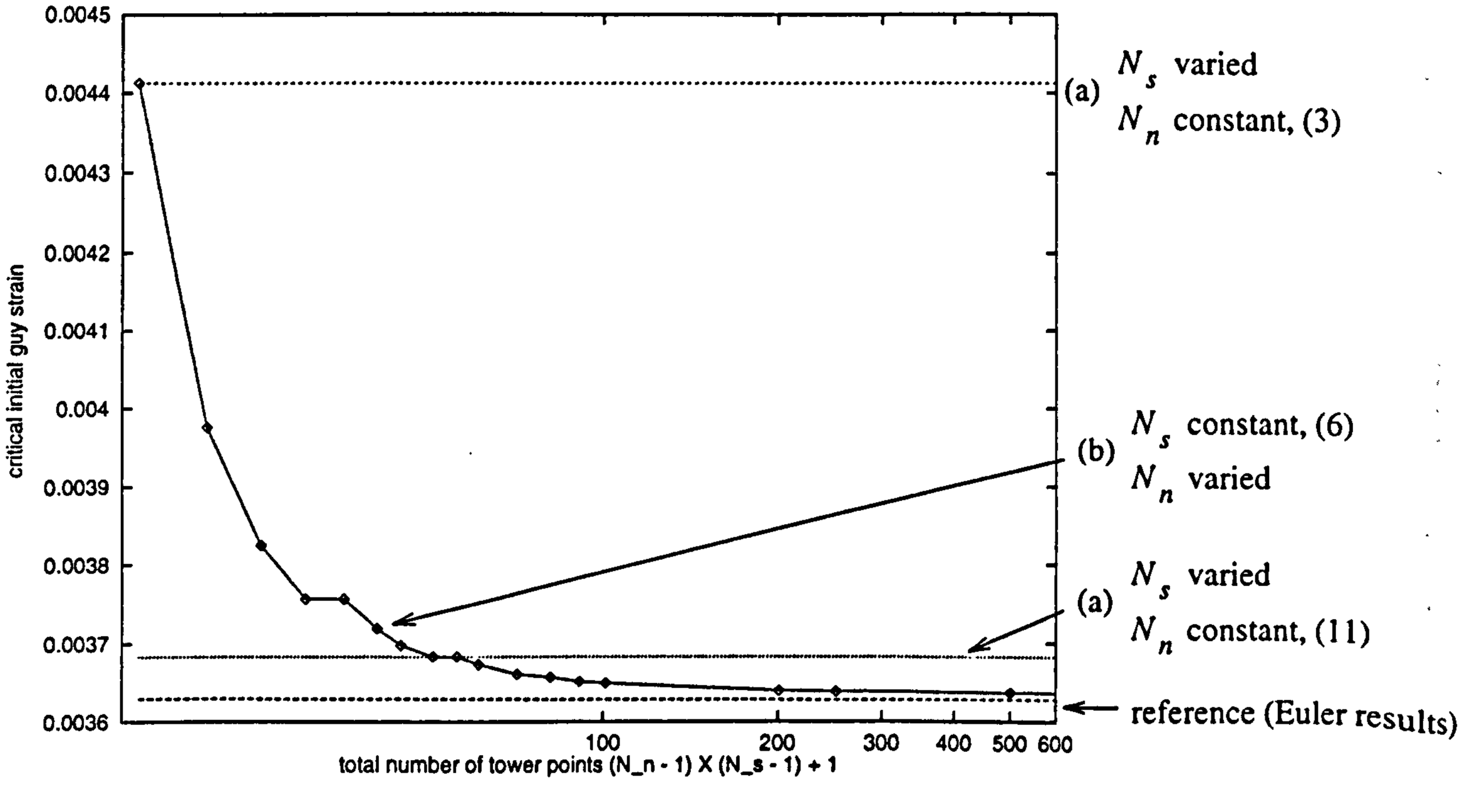

Figure 5.9: The convergence of approximations of the critical initial guy strain, $\epsilon_{ic(crit)}$ with increasing number of tower points. Either, (a) the number of spline interpolation points, N_s is increased or (b) the number of nodal points, N_n is increased. The base bending stiffness parameter, $k_{Bf} = 0.0\ N\ m\ rad^{-1}$. The convergence with increasing number of nodal points is clearly visible in curve (b). Steps in the graph occasionally occur because the number of nodal points increases but the number of nodal points in the range $(0 < X < \lambda_{ct})$ remains unchanged.

5.1.3 Modal Analysis

For a simple model of the structure, equations of motion may be derived and solved directly to find eigenvalues and eigenfunctions. Two approaches have been considered here to compare results with those obtained from the Rayleigh/ Stodola approach.

1. The structure consists of a slender, elastic, massless tower with a lumped nacelle on the top. The whole structure is modelled as a second order system with one eigenvalue

(one of the left hand illustrations in Figure 5.10).

2. The structure consists of a massive tower with a nacelle of negligible mass. The whole structure is modelled as a uniform, continuous beam (see Section 4.1) with a family of eigenfunctions (one of the right hand illustrations in Figure 5.10).

The following section of this chapter describes how these 2 simplified schemes may be implemented for longitudinal, torsional and bending vibrations and compared with results calculated using Rayleigh/ Stodola method.

5.1.3.1 Bending Vibrations

Figure 5.11 (a) shows how a simple model is used for validation purposes: the nacelle is a lumped mass and the tower is a massless spring. The moment of inertia of the nacelle is not considered. From Equations 5.4 and 5.6, the deflection, $v(H)$ of the top of the tower can be found when a force F is applied at the top (see Figure 5.12). The stiffness parameters are $\frac{dF}{dv}\Big|_{v(H)=0}$ and are given in Equations 5.21 and 5.22.

In the Rayleigh/ Stodola method, the same parameter settings are made as for static analysis of a uniform beam (see Section 5.1.1.1 above). In addition, the nacelle moment of inertia (J_{tn} or J_{rn}) and the tower density are set to zero.

If the base is built, in the equivalent stiffness of the guy cables for use in calculating bending vibration modes is given by Equation 5.21.

$$k_{(\mathrm{eq})B} = \frac{E_t I_{xt}}{H^3}\left(\frac{\left(\frac{E_t I_{xt}}{k_{Bc}H^3}+\frac{1}{3}\lambda_{ct}^3\right)}{\frac{1}{3}\left(\frac{E_t I_{xt}}{k_{Bc}H^3}+\frac{1}{3}\lambda_{ct}^3\right)+\left(\frac{1}{6}-\frac{1}{2}\lambda_{ct}-\frac{1}{6}\left(1-\lambda_{ct}\right)^3\right)\left(\frac{1}{2}\lambda_{ct}^2-\frac{1}{6}\lambda_{ct}^3\right)}\right) \tag{5.21}$$

If the base is hinged, the equivalent stiffness of the guy cables for use in calculating bending vibration modes is given by Equation 5.22.

$$k_{(\mathrm{eq})B} = \frac{E_t I_{xt}}{H^3}\left(\frac{\lambda_{ct}^2}{-\frac{1}{6}\lambda_{ct}^2+\left(\frac{1}{6}-\frac{1}{6}\left(1-\lambda_{ct}\right)^3\right)\lambda_{ct}+\frac{E_t I_{xt}}{k_{Bc}H^3}+\frac{1}{6}\left(\lambda_{ct}-1\right)\lambda_{ct}^3}\right) \tag{5.22}$$

In both cases, the formula for the modal frequency of a simple spring/ mass system is Equation 5.23.

$$f_{1B} = \frac{1}{2\pi}\sqrt{\frac{k_{(\mathrm{eq})B}}{M_n}} \tag{5.23}$$

For wind turbines, because the tower is slender and therefore less stiff in bending than in torsion or compression, the distribution of the tower mass has a larger effect on the mode

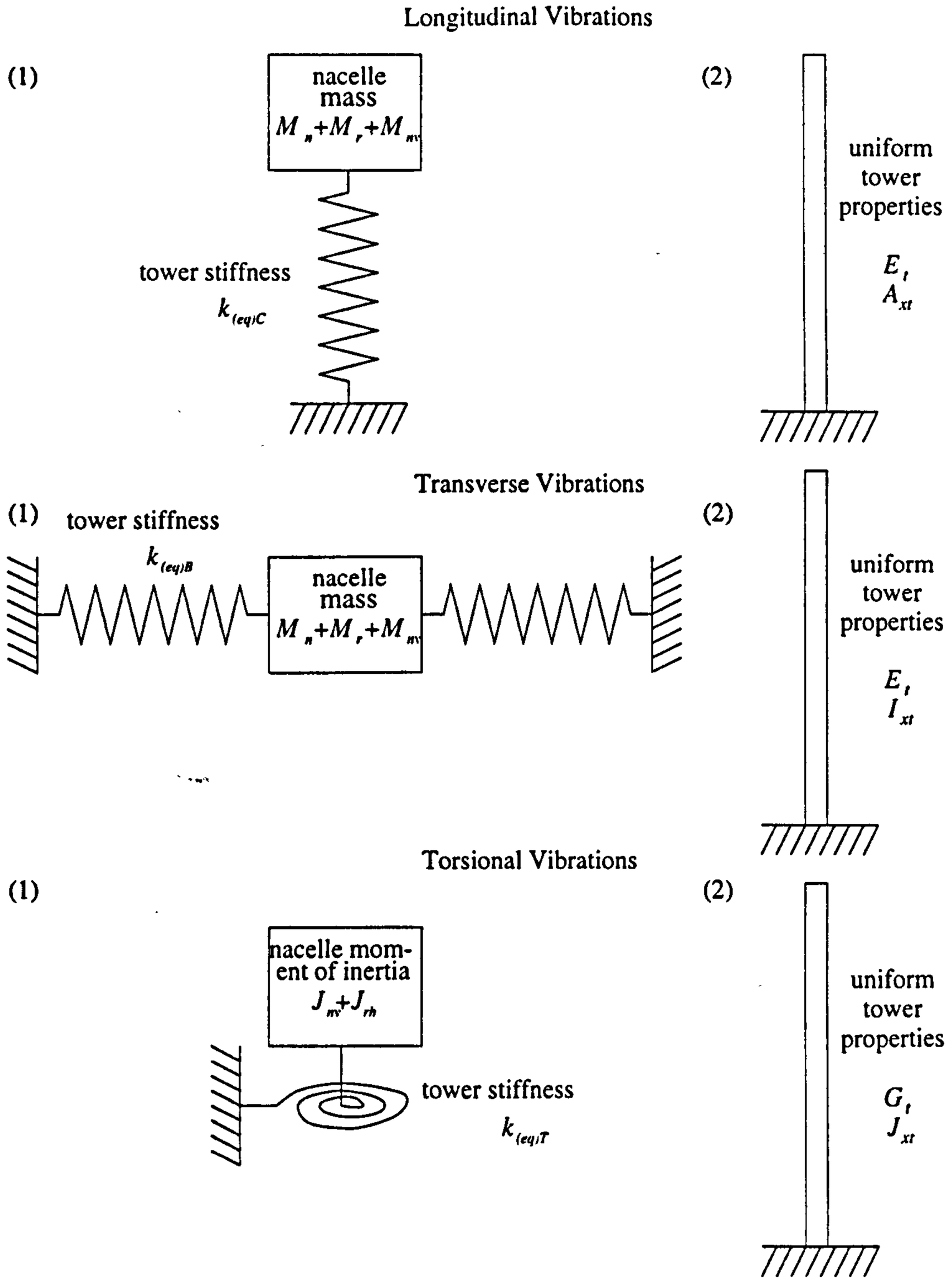

Figure 5.10: For each of the three classes of vibrations, two approaches are shown for the validation of the general, numerical model *with direct solution of the equations of motion. (1) The nacelle mass is finite, the tower mass is zero but the stiffness is finite. (2) The tower mass and stiffness are finite but the nacelle mass is zero.*

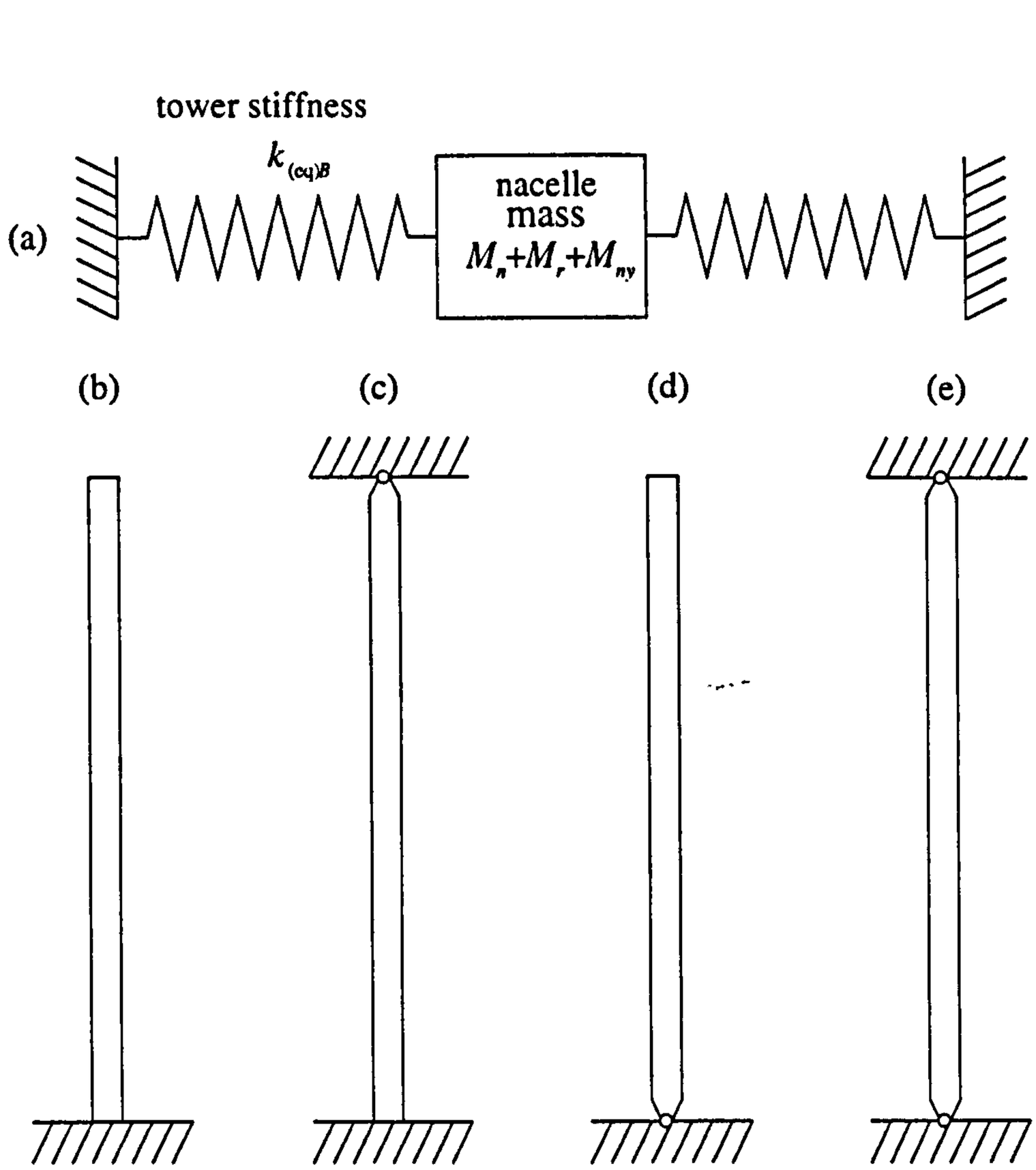

Figure 5.11: Models of bending vibrations of the tower used to allow equations of motion to be solved directly.

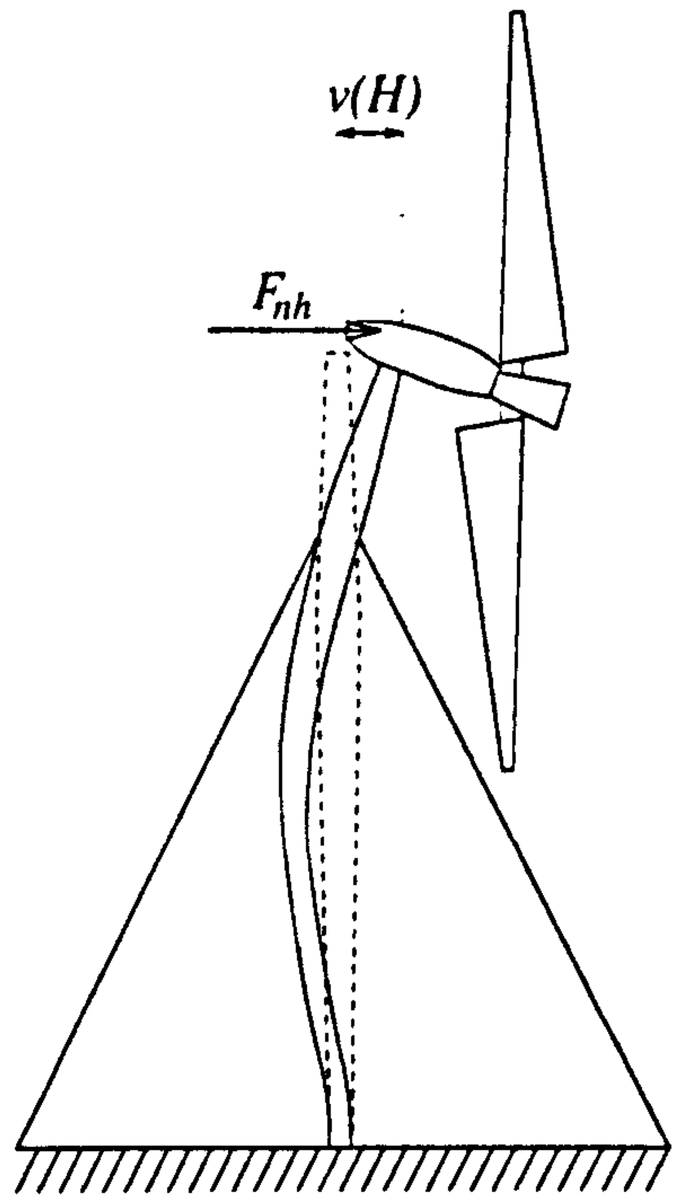

Figure 5.12: The tower deflects an amount $v(H)$ when subject to a force F_{nh} at the top. The stiffness is $\frac{dF_{nh}}{dv}\Big|_{x=H,v(H)=0}$.

shapes of bending vibrations than on torsional or compressive vibrations. For example, the tower of the Carter machine tapers both above and below the point of attachment of the guys. The frequencies of bending vibrations of a uniform tower are 0.697→0.750 Hz ($k_{Bf} = 0.0 \rightarrow 1.0 \times 10^{12}$ N m rad^{-1}). The frequencies of bending vibrations of a double-tapered tower of the same average outside diameter are 0.782→0.837 Hz. The stiffness of two towers of the same overall mass can be quite different. The stiffnesses of towers of the same mass but different geometries are compared in Section 8.3.

The results in Table 5.6 compare the Rayleigh/ Stodola model with frequencies calculated using Equations 5.21, 5.22 and 5.23. The three different designs of Carter wind turbines are used as bases for the comparison. Parameters for each type are listed in Appendix H. Only the changes described above have been made to the parameter set (in order to make the tower uniform and minimise the axial tension in the tower due to the guys).

The number of points on the tower at which quantities are evaluated is again important (see Section 5.1.2 above). This is particularly the case for differentials. If the base of the tower is built in, the angle made by the tower to the vertical there is zero. For small deflections, this angle is equal to the gradient of the deflection curve there ($\frac{dv}{dx}\Big|_{x=0}$). The base bending stiffness, k_{Bf} is very high ($> 1 \times 10^9$, see Section 5.1.1 Figure 5.2). If the gradient is not zero, the torsional strain energy stored is very high ($= \frac{1}{2} k_{Bf} \left(\frac{dv}{dx}\Big|_{x=0}\right)^2$ Equation D.6). This will unbalance the Rayleigh formula (Appendix D.1. Equation D.1) making the Rayleigh frequency calculated too large. The larger the number of points on the tower, the more accurate the estimate of the gradient. However, the relationship between the number of points and the accuracy of the frequency approximation is not straightforward as is shown

Table 5.6: Testing the Rayleigh/ Stodola method against a lumped mass second order system (Equation 5.23). Comparison between results assuming a uniform massless tower and results from the Rayleigh/ Stodola method. Wind turbine designs are summarised in Table 5.1. The full list of parameters given in Appendix H is modified so as to define a uniform, cylindrical tower with no guys or nacelle.

tower design	base bending stiffness	frequency by substitution into Equation 5.23 (Hz)	frequency from Rayleigh/ Stodola routine (Hz)	number of significant figures of similarity
Great Orton type	0.0	0.697	0.697	6
Great Orton type	1×10^{12}	0.750	0.750	6
Faccombe type	0.0	0.817	0.817	6
Faccombe type	1×10^{12}	0.861	0.861	5
West Beacon Farm type	0.0	1.13	1.13	7
West Beacon Farm type	1×10^{12}	1.19	1.19	7

in Section 5.1.3.2.

The second test for the *general, numerical model* is to calculate frequencies of a continuous element with both mass and stiffness constant with height as in Figure 5.11 (b), (c), (d) and (e) above. Solutions of the biharmonic equation are derived in Appendix C. In order for such solutions to represent accurate models of a real structure, nacelle and guys must be excluded. The base is either hinged or built in (set in the code using parameter: k_{Bf}) and the top is either free or hinged. Comparisons between results are listed in Table 5.7.

Situations in which the top of the tower is hinged (Figure 5.11 (c) and (e)) are simulated in the *general, numerical model* by defining guys attached to the top of the tower ($\lambda_{ct} = 1.0$). Having calculated the equivalent stiffness of the guys, k_{Bc}, the axial load on the tower due to the guys, F_{cv} is artificially set to zero. It is possible to derive the biharmonic inclusive of axial loads in the beam [40] but this has not been used in this thesis as a further test with which to validate the general numerical model of lateral vibrations. The details of the numerical solution of the biharmonic equation are given in Appendix C.

Table 5.7: Lateral vibrations of a cantilever. Comparison between results from the Rayleigh/ Stodola method and direct solution of Equation 4.5 for various sets of boundary conditions. Mode shapes and values of $C_{\omega iB}$ for Equation 4.6 are listed in Appendix C. The guy attachment point is set to the top of the tower, the cable anchor points are 4 tower heights away, average tower diameter and wall thickness parameters are calculated and then used. Otherwise, the tower design parameters are based on the Carter 300 kW machines at Great Orton Airfield.

boundary conditions		frequency comparisons			
base	tower top	mode number	frequency by direct solution Equation 4.5 (Hz)	frequency from Rayleigh/ Stodola method (Hz)	number of significant figures of similarity
built in	free	1	0.325	0.325	4
built in	free	2	2.03	2.03	3
built in	hinged	1	1.42	1.42	3
built in	hinged	2	4.61	4.61	3
hinged	free	1	0.0	0.0	
hinged	free	2	1.44	1.44	3
hinged	free	3	4.67	4.67	3
hinged	hinged	1	0.911	0.911	3
hinged	hinged	2	3.65	3.65	3

5.1.3.2 Convergence of Frequency Approximations

The number of points on the tower at which quantities are evaluated affects the accuracy of the approximate frequency calculated. To illustrate this. one of the situations described

in Section 5.1.3.1 is used. The tower is uniform and massless, the base is built in ($k_{Bf} = 1 \times 10^{12}$). The analytical solution (Equation 5.23) gives the answer 0.750 Hz for a tower with other parameters (Appendix H) taken from the Carter 300 kW tower design (Great Orton Airfield type).

Unlike for tower buckling (Figure 5.9), there is not a straightforward relationship between the number of nodal points and the accuracy of the approximation.

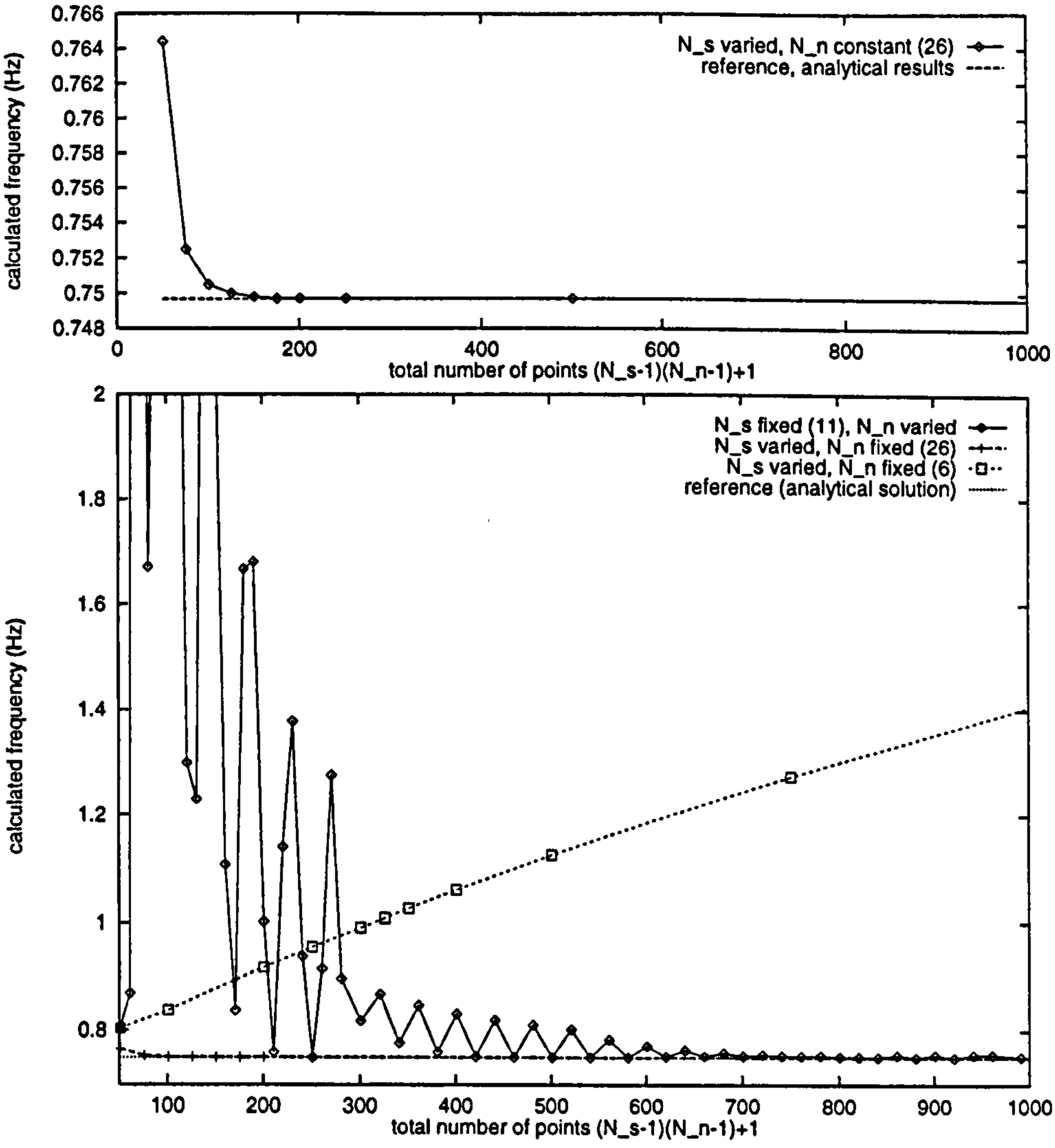

Figure 5.13: The top illustration shows the convergence with increasing number of spline interpolation points of a tower with 26 nodes. The bottom illustration shows the same convergence of a 26 node tower but approximations for a 6 node tower diverge. If the number of nodes is increased, it is not necessarily the case that results will converge with increasing numbers of spline interpolation points. If the number of nodes is increased, keeping the number of spline points constant ($N_s = 11$) the convergence is erratic.

Figure 5.13 shows three cases. In two cases. the number of nodes is kept constant. For 26 nodes, the approximations converge quickly to 0.750 Hz. For 6 nodes. the approximations diverge from the analytical result of 0.750 Hz with increasing number of spline interpolation

points N_s. Tests carried out for other numbers of nodes show that divergence is common. In fact, frequencies diverge for towers with as many as 30 nodes. The first curve on the second set of axes shows that, for some numbers of nodes N_n, divergence occurs but for others, approximations converge (the number of spline points is constant $N_s = 11$). This curve shows the convergence towards 0.750 Hz of tower with increasing numbers of nodes. The convergence is erratic rather than smooth and continuous. This is because for some numbers of nodes, convergence is more rapid than for others. For some numbers, N_n, divergence occurs. Thus it is again N_n rather than N_s which seems to be more important in ensuring convergence towards a true value.

The Carter 300 kW tower (Great Orton Airfield type) has a value of the parameter λ_{ct} of 0.76. Since the point of attachment of the guys to the tower is forced to be a node, this means that for a 26 node tower, the number of nodes below that point is 20 and the number above is 7. The spacing of nodes is the same for the entire tower. This may be why convergence is so rapid for 26 node towers. If the number of nodes was 27, then there would be 21 below the guy cable attachment point and 7 above. The spacing between nodes would be different for the lower section of the tower (see Figure 5.14).

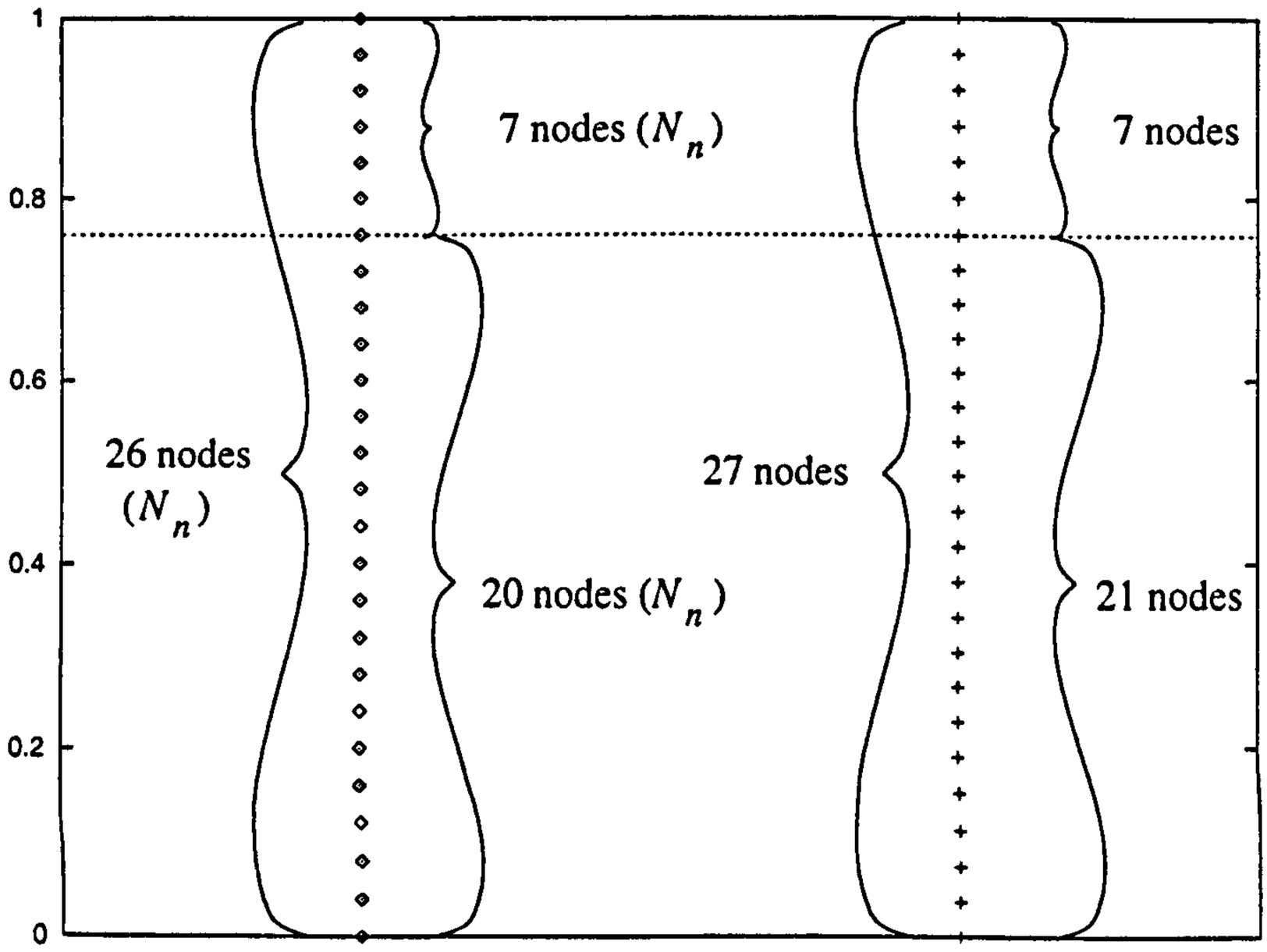

Figure 5.14: For a tower of the type used for the 300 kW wind turbines at Great Orton Airfield, the nodes are equally spaced if the total number of nodes is 26. If the number of nodes is 27, the nodes are slightly more closely spaced in the region $0 < X < \lambda_{ct}$. For the Great Orton wind turbines, λ_{ct} is 0.76.

A more general trend can be seen from the data series generated with N_s constant ($N_s = 11$) from which the first of the curves in Figure 5.13 was drawn. Where $(N_n - 1)$ is any multiple of 25, the accuracy is significantly better than other N_n values. It is possible that for fastest convergence, $(N_n - 1)\lambda_{ct}$ must be an integer. The result of this is that the spacing

between nodes is the same above and below the point of attachment of the guy cables to the tower. The three designs of commercial wind turbines studied are compared in Table 5.8. Results in the fifth column were obtained with models in which the nodal spacing was not constant. Results in the final column were obtained from models in which N_s and N_n were set to the values listed in the sixth and seventh columns and the spacing between nodes is the same all the way up the tower. In both cases, the criteria for convergence were the same; the difference between successive frequency estimates had to be less than 1×10^{-12}. Greatest accuracy seems to be achieved when the spacing between nodes is constant throughout the tower.

Table 5.8: Frequencies of lumped mass/ light spring systems. In each case, the basis for the design is one of the commercial machines. In addition, the tower is made to be uniform and massless. The point of attachment of the guys to the tower is $\lambda_{ct}H$. In all cases, where the nodal spacing above and below the point of attachment is the same, the frequencies are closer to the reference values.

tower design	λ_{ct}	base bending stiffness	reference frequency (Hz) Equation 5.23	$N_s = 51$ and $N_n = 91$ (frequency Hz)	N_s	N_n	N_s and N_n set as in previous columns (frequency Hz)
Great Orton type	0.760	0.0	0.697	0.705	41	101	0.697
Great Orton type	0.760	1×10^{12}	0.750	0.764	41	101	0.750
Faccombe type	0.696	0.0	0.817	0.823	21	126	0.817
Faccombe type	0.696	1×10^{12}	0.861	0.870	21	126	0.861
West Beacon Farm type	0.690	0.0	1.13	1.14	41	101	1.13
West Beacon Farm type	0.690	1×10^{12}	1.19	1.24	41	101	1.19

The second test of the *general, numerical model* for a continuous. massive beam is not affected by the number of nodes except that the accuracy of the approximate frequency calculated is increased by increasing either the number of nodes or the number of spline interpolation points.

5.1.3.3 Longitudinal Vibrations

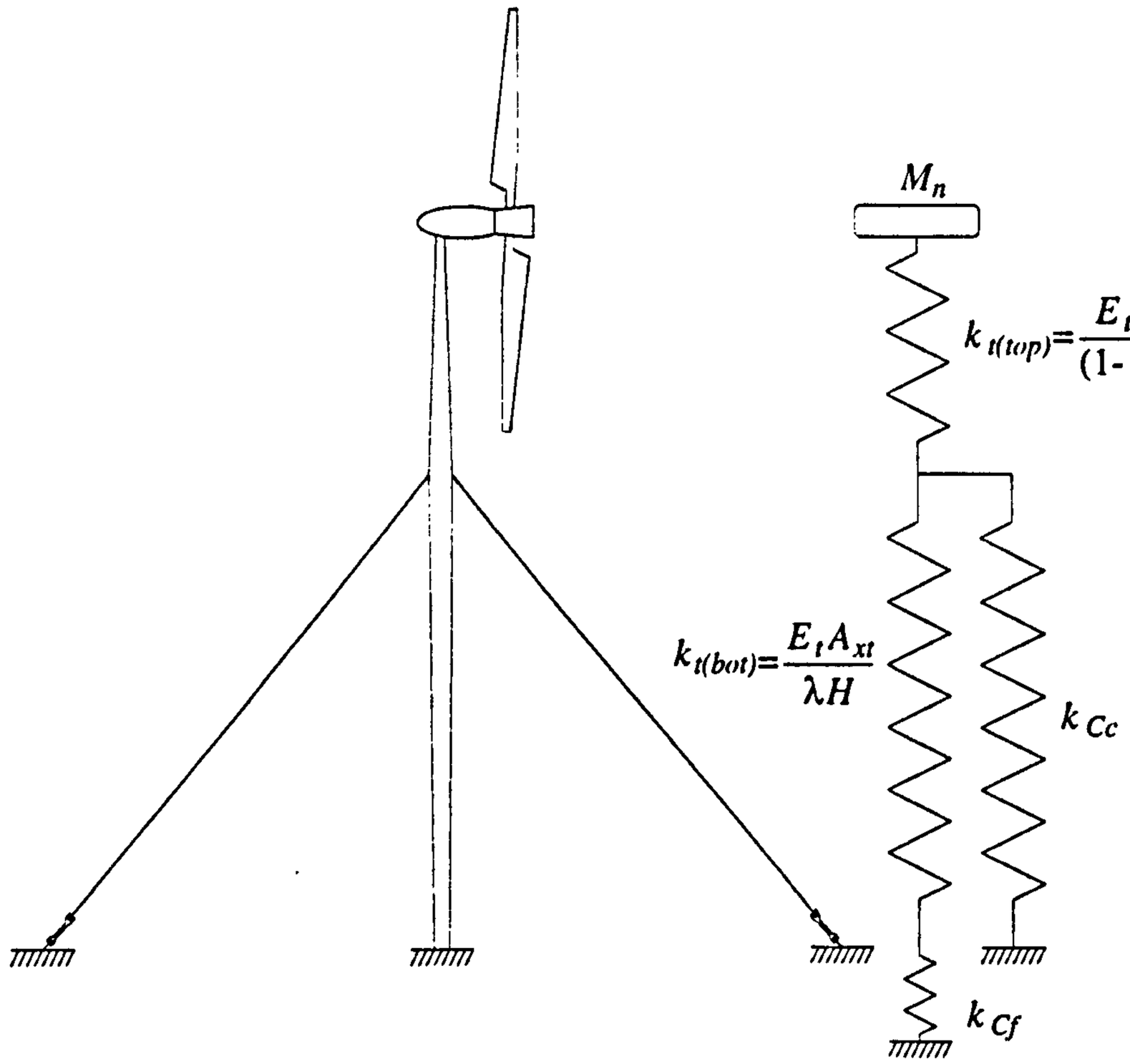

Figure 5.15: Simplified model of the tower for the purposes of longitudinal vibrations. The nacelle is a lumped mass and the tower, guys and base fixing are four massless, linear springs.

The equivalent lumped mass/ spring model of longitudinal vibrations of the wind turbine is shown in Figure 5.15. In order to compare results from the Rayleigh/ Stodola model of longitudinal vibrations, the tower outside diameter is set to the average value for the Carter machine. The tower density is set to zero. Otherwise, model parameters are used from the Carter 300 kW machine of the type installed at Great Orton Airfield.

$$f_{(\mathrm{dir})1C} = \frac{1}{2\pi}\sqrt{\frac{k_{(\mathrm{eq})C}}{M_n}} \tag{5.24}$$

Equation 5.25 shows how the springs illustrated in Figure 5.15 are combined to give one equivalent stiffness parameter, $k_{(\mathrm{eq})C}$. The tower top and bottom sections have the same stiffness per unit length but are illustrated separately because of the different relationships each has to the guy stiffness, k_{Cc}. The stiffness of the combined tower and guys (Equation 5.26) can be calculated assuming that the stiffness of the guys is constant for small vertical deflections (Appendix B). This formula has been derived $\frac{dF_{nv}}{du}\Big|_{x=H.u(H)=0}$ by integrating the strain

distribution up the tower (Equation 5.12).

$$k_{(\mathrm{eq})C} = \left(\frac{1}{\left(k_{Cc} + \frac{1}{1/k_{Cf} + \lambda_{ct} H / E_t A_{xt}} \right)} + \frac{(1 - \lambda_{ct})\, H}{E_t A_{xt}} \right)^{-1} \tag{5.25}$$

Equation 5.25 can be simplified to give Equation 5.26.

$$k_{(\mathrm{eq})C} = \frac{E_t A_{xt} \left(k_{Cf} E_t A_{xt} + k_{Cc} \left(E_t A_{xt} + k_{Cf} \lambda_{ct} H \right) \right)}{E_t^2 A_{xt}^2 + E_t A_{xt} H k_{Cf} + H k_{Cc} (1 - \lambda_{ct}) \left(E_t A_{xt} + k_{Cf} \lambda_{ct} H \right)} \tag{5.26}$$

The resulting fundamental frequencies calculated are compared in Table 5.9.

Table 5.9: Comparison between longitudinal vibrations of a simple lumped mass model and general iterative model (Rayleigh/ Stodola method) with simplified parameter set (uniform, cylindrical tower, $\rho_t = 0$).

	general Rayleigh/ Stodola technique (Hz)	analytical technique - Equation 5.26 (Hz)	significant figures of accuracy
guys attached ($\epsilon_{ic} = 0.0005$)	19.593	19.593	7
no guys attached	18.821	18.821	12 (limited only by the convergence tolerance parameter)

The second approach to validate the *general, numerical model* is with a model of a continuous beam illustrated in Figure 5.10 (2). Vibrations of the beam are described by Equation 4.1 which may be solved directly to give Equation 5.27 for the frequency of the i^{th} mode. The mass of the nacelle is set to zero instead of setting the tower density to zero. In addition to the similarity between calculated frequencies shown in Table 5.10, the estimated mode shapes are almost identical to the sinusoidal shapes which are predicted for the continuous beam. The agreement is less good if gravity is included.

$$f_{(\mathrm{dir})iC} = \frac{2i - 1}{4H} \sqrt{\frac{E_t}{\rho_t}} \tag{5.27}$$

5.1.3.4 Torsional Vibrations

Similar to longitudinal vibrations (Figure 5.10), the two simplifications of torsional vibrations are either a lumped mass on a spring (similar to Figure 5.15 but with torsion springs instead of linear springs) or a continuous torsion bar.

Table 5.10: Comparison between longitudinal vibrations of a simple continuous beam model and general iterative model (Rayleigh/ Stodola method) with simplified parameter set (uniform, cylindrical tower, $\lambda_{cg} = 4.0$, $M_n = 0$).

	general Rayleigh/ Stodola technique (Hz)	analytical technique - Equation 5.26 (Hz)	number of significant figures of similarity
—zero gravity:—			
fundamental mode	26.47	26.47	4
first harmonic	79.41	79.42	3
second harmonic	132.4	132.4	4
—gravity (9.81 m s^{-2}):—			
fundamental mode	26.47	26.47	3
first harmonic	79.41	79.42	4
second harmonic	132.4	132.4	4

In the first case, Equation 5.28 is equivalent to Equation 5.24 for longitudinal vibrations. Instead of linear springs, the tower is modelled by a network of torsion springs. The only difference is that the yaw connection of the nacelle to the tower is modelled by a fifth spring k_{Yn}. The combined spring constant is given by Equations 5.29 and 5.30. The comparison between the general Rayleigh/ Stodola method and results obtained using Equation 5.28 is made in Table 5.11.

$$f_{(\text{dir})1T} = \frac{1}{2\pi}\sqrt{\frac{k_{(\text{eq})T}}{J_{yn}}} \tag{5.28}$$

$$k_{(\text{eq})T} = \left(\frac{1}{\left(k_{Tc} + \frac{1}{1/k_{Tf}+\lambda_{ct}H/G_tJ_{xt}}\right)} + \frac{(1-\lambda_{ct})\,H}{G_tJ_{xt}} + \frac{1}{k_{Yn}}\right)^{-1} \tag{5.29}$$

$$k_{(\text{eq})T} = \frac{G_tJ_{xt}k_{Yn}\left(G_tJ_{xt}\left(k_{Tf}+k_{Tc}\right)+k_{Tf}k_{Tc}\lambda_{ct}H\right)}{\left(\begin{array}{c} k_{Yn}(G_t^2J_{xt}^2+G_tJ_{xt}H\left(k_{Tf}+k_{Tc}\left(1-\lambda_{ct}\right)\right)+k_{Tf}k_{Tc}\lambda_{ct}H^2\times \\ \left(1-\lambda_{ct}\right))+G_tJ_{xt}\left(G_tJ_{xt}\left(k_{Tf}+k_{Tc}\right)+k_{Tf}k_{Tc}\lambda_{ct}H\right) \end{array}\right)} \tag{5.30}$$

To calculate torsional harmonics of a uniform, hollow, cylindrical tower, Equation 4.3 can be solved to give Equation 5.31.

$$f_{(\text{dir})iT} = \frac{2i-1}{4H}\sqrt{\frac{G_t}{\rho_t}} \tag{5.31}$$

In Table 5.12, Equation 5.31 was used to calculate torsional harmonics of a uniform cylindrical tower.

Table 5.11: Comparison between predictions of the fundamental torsional natural frequency of the structure using (1) Equation 5.28 for the vibrations of a second order spring/ moment of inertia system and (2) the Rayleigh/ Stodola iterative technique. The nacelle is rigidly attached to the top of the tower ($k_{Yn} = 1 \times 10^{22}$).

brief description of the machine	frequency predicted using Equation 5.28 (Hz)	frequency estimated using the Rayleigh/ Stodola technique (Hz)	significant figures of accuracy
Carter 300 kW at Great Orton Airfield	2.45	2.45	9
Carter 300 kW at Faccombe Estate	2.93	2.93	8
Carter 25 kW at West Beacon Farm	3.48	3.48	10

Table 5.12: Comparison between predictions of the fundamental torsional natural frequency of the structure calculated using (1) Equation 5.31 for the vibration of a continuous bar and (2) the Rayleigh/ Stodola iterative technique. The nacelle is rigidly attached to the top of the tower ($k_{Yn} = 1 \times 10^{22}$).

brief description of the machine	frequency predicted using Equation 5.28 (Hz)	frequency estimated using the Rayleigh/ Stodola technique (Hz)	significant figures of accuracy
Carter 300 kW at Great Orton Airfield (fundamental)	16.24	16.24	5
Carter 300 kW at Great Orton Airfield (first harmonic)	48.78	48.78	2
Carter 300 kW at Great Orton Airfield (second harmonic)	81.18	81.50	1

Figure 5.16 shows the good match between the shape of the first torsional vibration mode of a uniform, hollow, cylindrical tower and the estimate using the Rayleigh/ Stodola method. Also shown is the effect on both frequency and mode shape of increasing the initial tension in the guys.

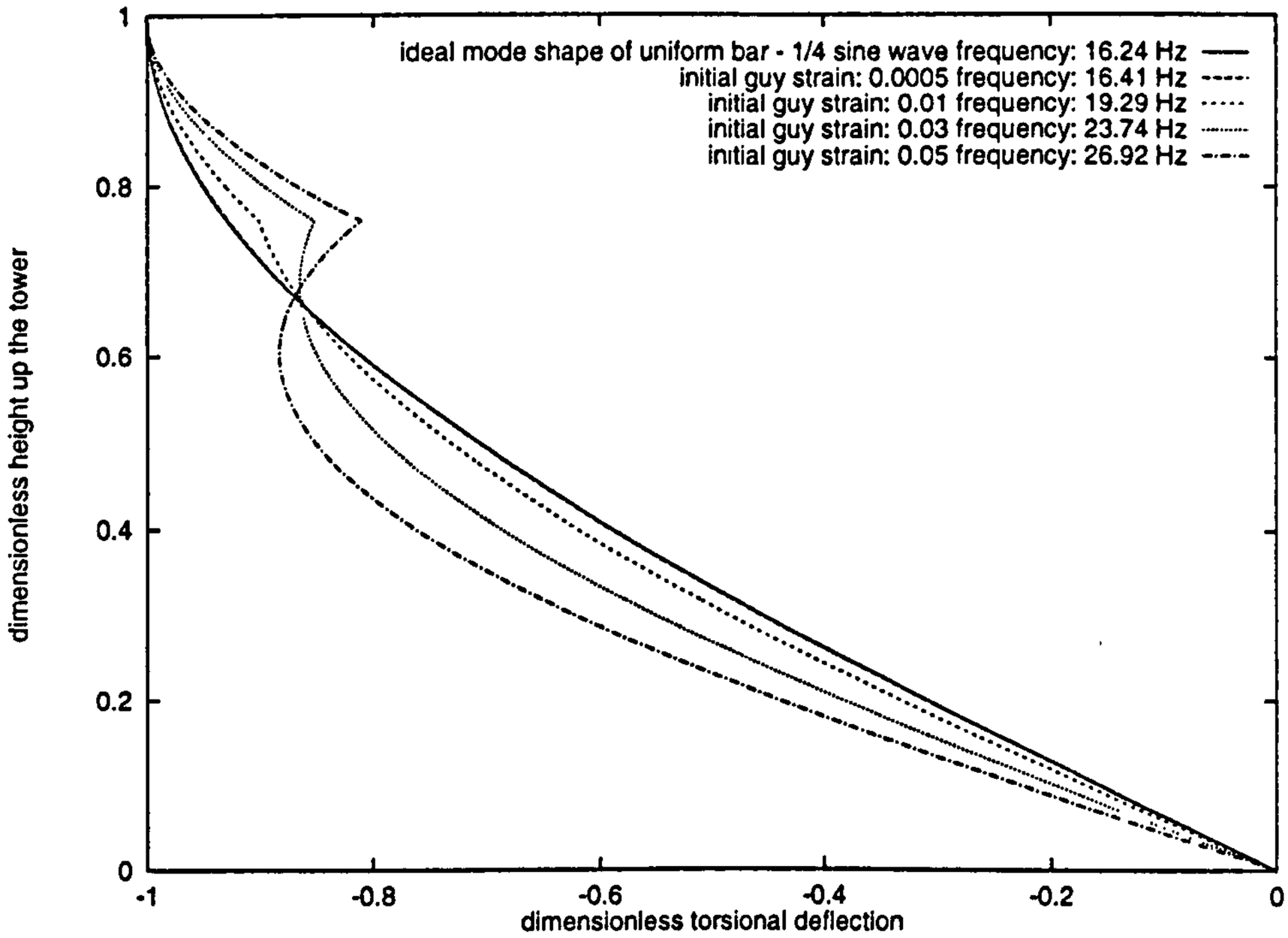

Figure 5.16: The effect of increasing the initial tension in the guys on the shape of the first mode of torsional vibration of a uniform, cylindrical, hollow tower. The frequency increases and the shape is progressively distorted.

5.2 Complete Models of Commercial Wind Turbines

The complete model of the Carter wind turbine is the model which includes the machine's guy cables and nacelle as well as material and geometric variations with height. A recognised method for analysing such complex structures is Finite Element Analysis (F.E.A.). To use commercial F.E.A. software such as ANSYS 5.0 [49], a model must be described including the geometry and material properties of the real machine. Once described, the geometry can be viewed on the screen. The analysis must then be described. For a static analysis this comprises load magnitudes, directions and points of application. Buckling analysis is only possible by repeated static analysis with increasing axial loads until a point of instability is reached. For modal analysis, the number of modes must be specified. Other considerations are often applicable such as stress stiffening effects (stiffening due to applied loads), large deflections, acceleration fields (such as gravity) and prestress effects. The results can be viewed in pictorial or tabular forms.

Some analysis of wind turbine structures using F.E.A. is documented. In 1977, L. S. Timothy [50] subdivided vertical sections of a lattice tower to model each as a single beam

element. Each beam had a different cross sectional area in order that the stiffness was the same as the equivalent lattice section on the real structure. In ANSYS, the second moment of area of a certain beam element can be specified at each end of the beam independently of the area and the thickness of the beam. In 1984, D. W. Lobitz [51] used a NASTRAN [52] finite element model to predict modal behaviour and blade bending moment time histories for a beam-element model of the whole structure. The tower only consisted of 2 elements. This was the inspiration for the development of the complete wind turbine model developed at Garrad Hassan and Partners Ltd. and described during the final phase in 1990 by Patel and Garrad [53]. In 1993, N. El Chazly [54] described her use of F.E.A. to choose between three different designs of stiff tubular towers: cylindrical, conical and stepped. Her model consisted of triangular shell elements.

The advantage of F.E.A. is that if appropriate element types and sizes are chosen and the boundary conditions are specified, a comprehensive picture of the dynamic and static behaviour of the complete structure can be built up. Coupling between classes of vibrations may be considered. Shear deformations may be considered. The decreased stiffness of the tower due to axial compression in the section below the guys is also included. Having built up the model, many different analyses are possible:

- static analysis;
- buckling (*Euler* and non-*Euler*) analysis;
- modal analysis;
- non-linear transient analysis;

Existing software is widely available. The package used for comparisons detailed in this thesis is ANSYS 5.0 [49]. Results are obtained for comparison with the structural analysis techniques proposed earlier. Elements of the Finite Element and Rayleigh/ Stodola models must be equivalent. Comparisons between the modelling elements and techniques used in the two approaches are given in this Chapter. Models of the tower that have been compared include:

- many cylindrical beam elements of different cross sections with abrupt changes of cross section;
- 2 tapered beam elements with continuous changes of cross section:
- many tapered beam elements with continuous changes of cross section;
- many shell elements modelling 12-sided (and 8-sided) prismatic steel tower.

Results obtained from each of the approaches were compared and the only ones which were consistantly alike were from the third and fourth.

Results were not available from some of the models because of unexplained numerical breakdowns. No detail is given here except to describe the occasions when such breakdowns occurred. Unexpected results included bulging distortion of hollow towers and uneven guy cable deflection shapes. The uneven shape was jagged rather than smooth with an erratic

structure. It was also not possible to converge to a modal solution if the guy cables were prestressed too much or too little (allowed to go slack). This could often be eliminated by instructing the software to include stress stiffening effects.

The model chosen for comparison here comprises a series of tapered beams using many elements for each guy cable so that interactions between tower and guys may be observed.

At first, static analysis of the tower was carried out to calculate pre-stresses due to gravity and the tension in the guy cables. The results of this analysis are used to modify the subsequent modal analysis. The effect of guy pre-tension on natural frequencies of vibration could then be deduced and is described in more detail in Chapter 8, Section 8.1.

The boundary conditions were simplified by considering just the two extreme cases: freely hinged and completely 'built in' base. Both cases were included in the same model by constraining the base like an ideal hinge which is free in only one plane.

The rotor and nacelle were lumped together and described by a single element having mass and moments of inertia about three axes. This is the same as for the Rayleigh/ Stodola model.

Comparisons between direct mathematical solutions and the Rayleigh/ Stodola model have already been made in Section 5.1.1. These comparisons are augmented here in order to include comparisons with Finite Element models.

5.2.1 Static Deflections

5.2.1.1 Lateral Deflections

The results obtained from the *structural spline* model proposed here can be compared directly with results from an equivalent Finite Element model. Beam elements are used for the tower and link elements for the guys. Link elements may go slack if the tension falls to zero. This property is not used for modal analysis but is for static and non-linear transient analyses. The following properties are identical for the two approaches (Finite Element Analysis and Rayleigh/ Stodola method:

- nacelle mass and moments of inertia;
- tower cross sectional area, radii and second moments of area at nodes;
- position of guy anchors, nacelle and guy cable attachment points;
- strain in the guys at assembly.

In the finite element model. only two different base conditions are defined: rigidly built in and freely hinged. In the *structural spline* model, the base stiffnesses are prescribed by the designer. In both cases. the only coupling between lateral deflection of the tower and vertical deflection is that the strain in the guys (and therefore k_{Cc}, k_{Bc}, F_{cv} etc.) will be changed by vertical deflections of the point of attachment of the guy cables to the tower.

First, comparisons are made for structures from which the guy cables have been excluded. Otherwise. the structures are the same as the three commercial machines considered (Appendix H). Because there is no constraint part-way up the tower due to cables. the shapes

of deflection curves are similar for any of the load types (load types listed in Figure 5.1. So, the comparison given in Table 5.13 and Table 5.14 is between tower head deflections.

Table 5.13: Comparison of head deflections of a tower subject to various loads predicted by a Finite Element model (generated using ANSYS 5.0) and by the structural spline model.

load type (Figure 5.1)	load	deflection (m)	
		Finite Element Analysis	*structural spline* method
F_{nh}	1000 N	0.212	0.212
f_h	100 N m	0.00591	0.00592
Q_{nh}	10 N m^{-1}	0.0422	0.0417
q_h	10 N m m^{-1}	0.00214	0.00212

It is not known why, when deflections are very small, the relative differences between results from the Finite Element model and from the *structural spline model* increase significantly.

If the guys are included in the model, the results in Figure 5.17 and Figure 5.18 are obtained. In all cases the Finite Element model of the tower consists of 100 beam elements; the *structural spline* model consists of 30 spline sections each comprising 51 points.

5.2.1.2 Longitudinal Deflections

The following results (Table 5.15) were obtained for the complete model of the wind turbine tower design used on 300 kW Carter machines at Great Orton Airfield.

5.2.2 Buckling

The predominant axial loads come from the weight of the nacelle and the vertical component of the pre-tension in the guy cables. An important use of buckling predictions is to find out the safe limit for the initial tension in the guys. On a structure with one set of cables. the longer section of the tower is between the base and the point of attachment of the guys. The axial tension due to the guys makes probably the largest contribution to the axial force in the tower. For both these reasone, the lower section is of more interest ($0 < \lambda < \lambda_{ct}$).

Table 5.16 shows results for different tower design configurations of buckling induced by critical guy cable initial strain.

By making assumptions about the tower restraints, approximate buckling predictions using Euler's theory can be made. Using the incremental static analysis method. it is also possible to predict any number of buckling modes. This is possible using *structural spline* method. but the Finite Element analysis package only finds the first buckling mode. Illustrations of the first three buckling modes predicted by non-linear analysis using *structural spline* software are given in Figure 5.19.

Table 5.14: Comparison of head deflections of a tower subject to various loads (gravity forces on the tower and nacelle masses are included) predicted by a Finite Element model (generated using ANSYS 5.0) and by the structural spline model.

load type (Figure 5.1)	load	deflection (m)	
		Finite Element Analysis	*structural spline* method
F_{nh}	1000 N	0.318	0.319
F_{nh}	5000 N	1.59	1.60
F_{nh}	8000 N	2.55	2.55
Q_{nh}	100 N m	5.91×10^{-4}	8.89×10^{-4}
Q_{nh}	5000 N m	0.0296	0.0445
Q_{nh}	8000 N m	0.0473	0.0712
f_h	10 N m^{-1}	0.0422	0.0628
f_h	1000 N m^{-1}	6.33	6.28
f_h	5000 N m^{-1}	31.6	31.4
f_h	10N m m^{-1}	0.00214	0.00319
f_h	1000N m m^{-1}	0.320	0.319
f_h	5000N m m^{-1}	1.60	1.60
f_v and F_{nv}	self weight	0.00118	0.00118

Table 5.15: Comparison of vertical head deflections of a tower subject to various loads (gravity forces on the tower and nacelle masses are excluded) predicted by a Finite Element model (generated using ANSYS 5.0) and by the structural spline model.

load	guys included	point of application	deflection (m) from Finite Element Analysis	deflection (m) from *general, numerical method*
10000 N m	no	tower head	0.000152	0.000152
10000 N m	yes	tower head	0.00253	0.00254
1000 N m^{-1}	no	distributed up the tower	0.000384	0.000381
1000 N m^{-1}	yes	distributed up the tower	0.00204	0.00274

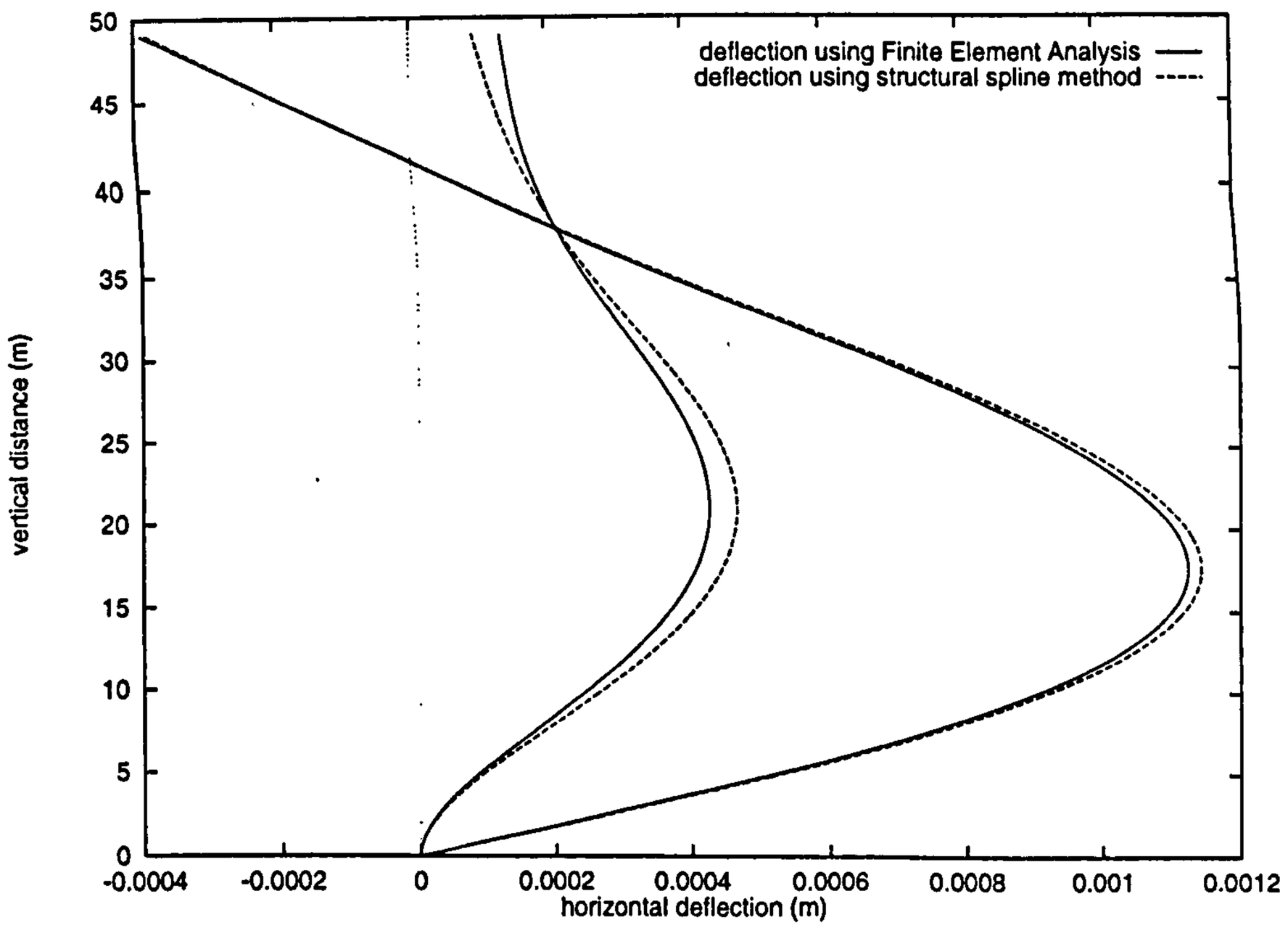

Figure 5.17: Comparison between lateral deflection shapes output from Finite Element Analysis (ANSYS) package and the structural spline *method. 10 N m^{-1} force distributed uniformly over the entire height of the tower. Both extremes of tower base fixing are illustrated: freely hinged and rigidly build in.*

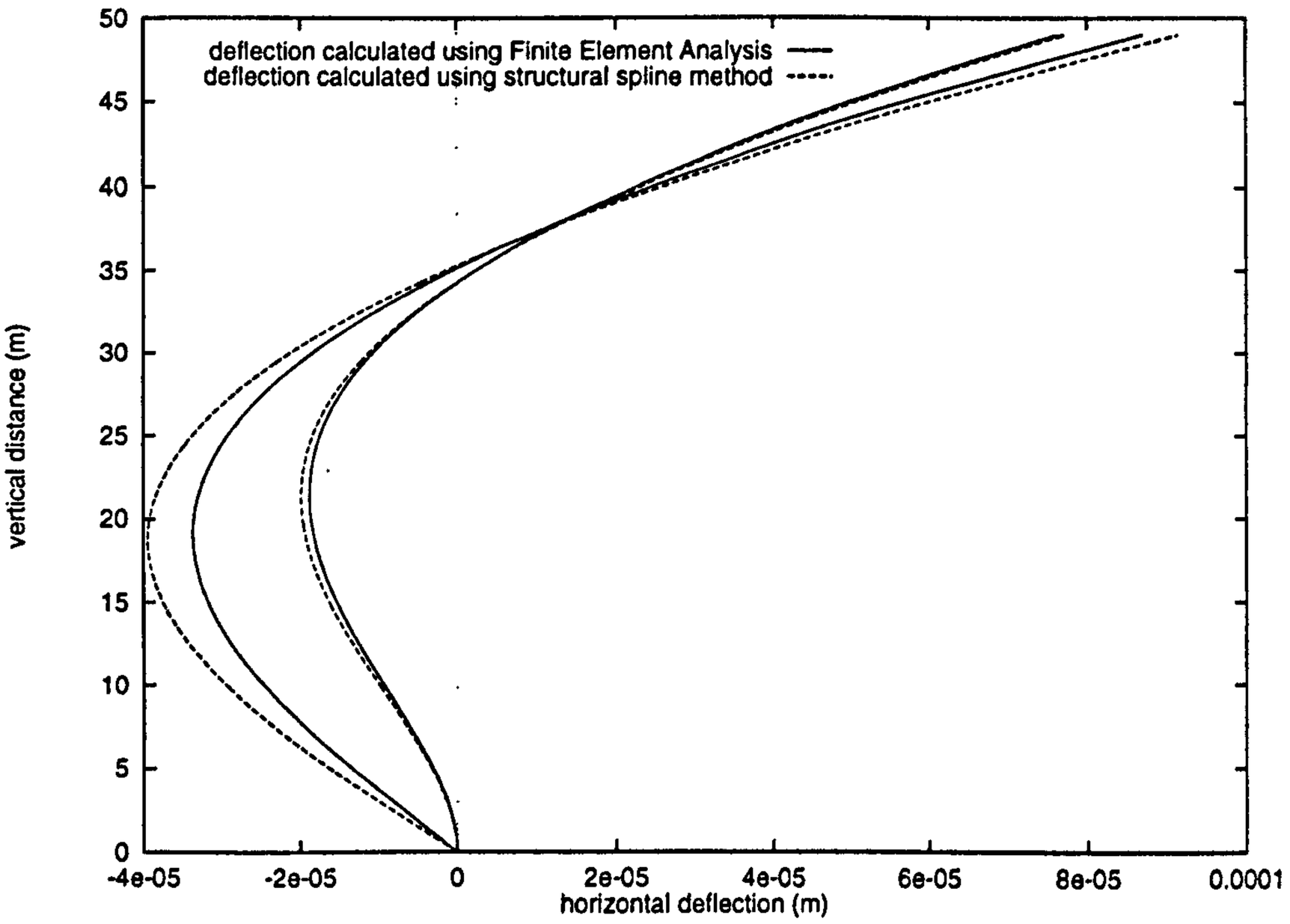

Figure 5.18: Comparison between lateral deflection shapes output from Finite Element Analysis (ANSYS) package and the structural spline *method. 10 N m* m^{-1} *torque distributed uniformly over the entire height of the tower. Both extremes of tower base fixing are illustrated: freely hinged and rigidly build in.*

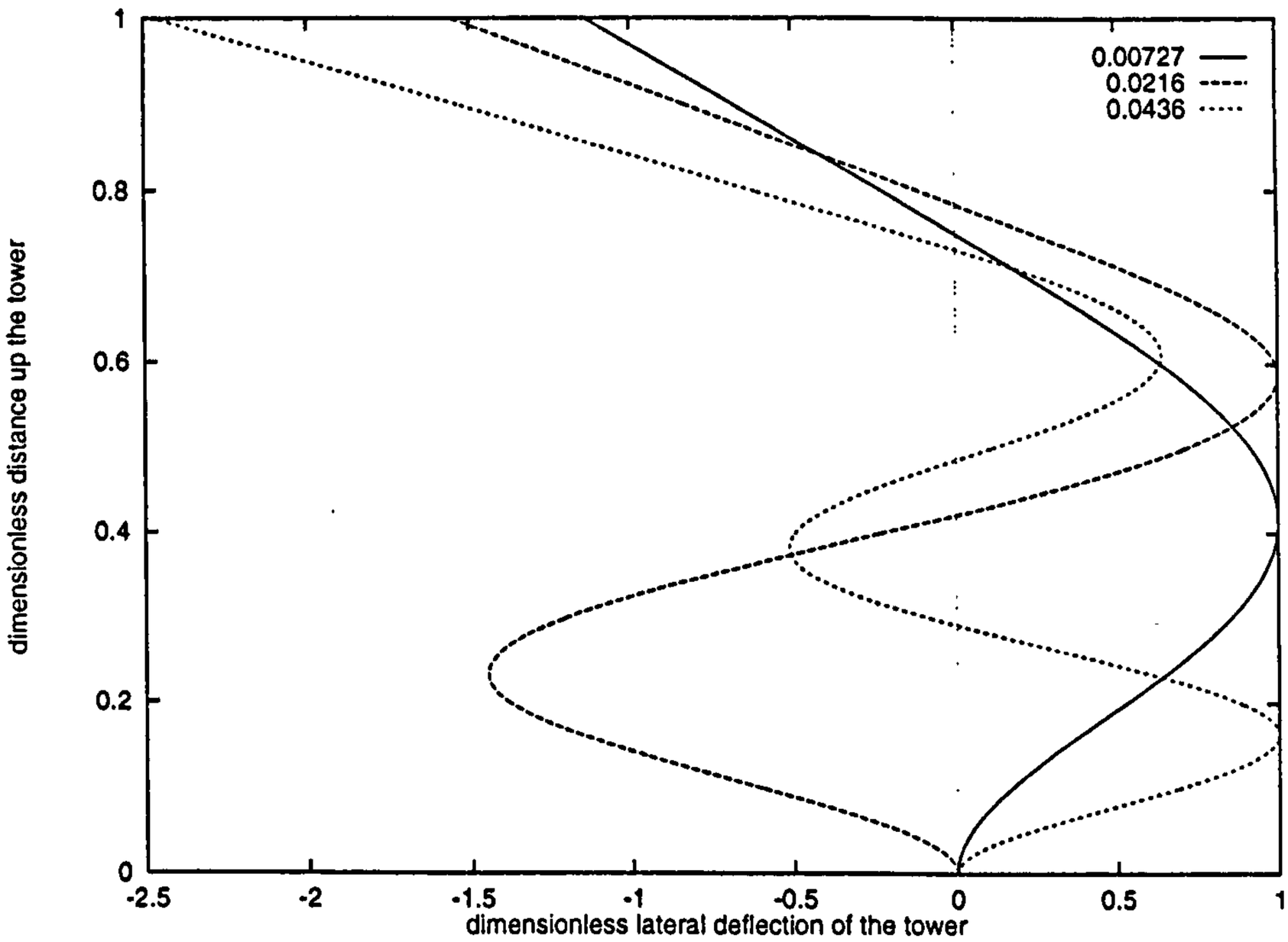

Figure 5.19: The first three buckling modes calculated by static analysis of tower structures subject to increasing guy tension ($\epsilon_{ic(crit)}$ is given in the legend of the figure). The tower design chosen for this example is the structure used on the Carter 300 kW machines at Great Orton Airfield, the base is treated as built in ($k_{Bf} = 1 \times 10^{12}$). The critical guy tension for the first buckling mode is also included in Table 5.16.

Table 5.16: Values of initial guy strain critical for buckling of the tower, tabulated against the three design configurations studied.

tower design	base	direct Euler buckling load	results from Finite Element software	results from *structural spline* software	
		initial guy strain for buckling	initial guy strain for buckling	initial guy strain for buckling	axial tension due to guys (N)
Great Orton type	built in	0.00723	0.00778	0.00727	3.38×10^6
Great Orton type	hinged	0.00358	0.00371	0.00360	1.66×10^6
Faccombe type	built in	0.0148	0.0202	0.0187	7.94×10^6
Faccombe type	hinged	0.00725	0.00983	0.00917	3.92×10^6
West Beacon Farm type	built in	0.0139	0.0106	0.0101	0.669×10^6
West Beacon Farm type	hinged	0.00725	0.00510	0.00496	0.329×10^6

The accuracy of the direct Euler buckling technique is strongly dependent on the accuracy of the estimated effective lengths. The iterative solutions may take longer but are much more accurate provided good initial estimates of the buckling load are made. Therefore, the Euler method is only used as a rough estimate in order to choose the initial values used to start the search method.

5.2.3 Modal Analysis

5.2.3.1 Checking the Validity of Finite Element Models

Comparison between different models generated for Finite Element Analysis shows the effect of different numbers and types of elements. As for the Rayleigh/ Stodola method, the results of F.E.A. can be checked against the simplest model cases. Comparisons between modal frequency estimates by three approaches for a free-standing cantilever are given in Table 5.17.

Table 5.17: Lateral natural frequencies estimated for a uniform cantilever beam based on the Carter 300 kW tower (Great Orton Airfield type) with constant diameter and wall thickness and without guy cables. Three approaches were used to obtain the estimates in Hz.

brief description of the model used	funda-mental lateral mode	1st harm-onic	2nd harm-onic	3rd harm-onic
direct, analytical solution of the equations of motion (biharmonic)	0.325	2.03	5.70	11.2
iterative solution to the same model geometry	0.325	2.03	5.69	11.1
Finite Element Model using beam elements	0.310	2.03	5.70	11.2

Figures 5.20, 5.21 and 5.22 compare estimates of the first four natural frequencies of the towers used on wind turbines at Great Orton Airfield, West Beacon Farm and Faccombe Estate.

The best agreement between the Finite Element method and the Rayleigh/ Stodola method is for calculation of the fundamental frequency of vibration. The difference between results increases for higher and higher harmonics. The accuracy of higher harmonics depends on the accuracy of all converged lower frequencies (Section 4.6). This suggests that the Rayleigh/ Stodola method depends more strongly on the accuracy of lower mode estimates than do the methods used in the Finite Element package.

Comparisons between the longitudinal and torsional vibration frequencies calculated using various finite element models can be made with Tables 5.18 and 5.19. Predictions of the frequencies of these modes of vibration were found to be relatively independent of the type of model used.

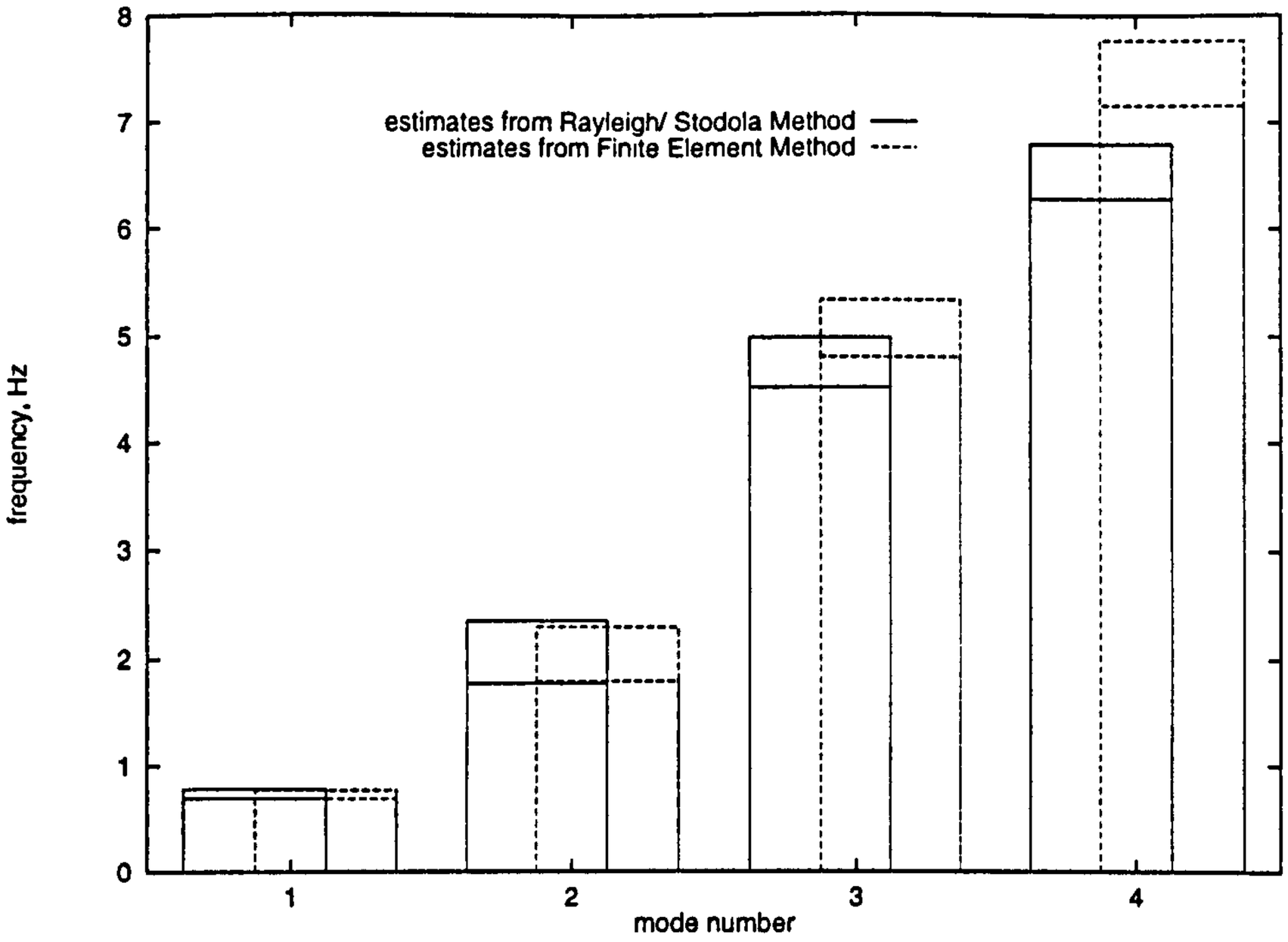

Figure 5.20: Comparison between modal frequencies of the Carter 300 kW machine of the type at Great Orton Airfield estimated using the Rayleigh/ Stodola method and using the Finite Element method. The two values plotted on each bar represent the two extreme base boundary conditions: hinged and built in.

Table 5.18: Comparison of estimated longitudinal resonant frequencies of the Carter 300 kW tower design (Great Orton Airfield type).

brief description of the model used	fundamental longitudinal mode
guys: 43 elements; tower: 39 elements (tapered beams)	16.477
guys: 43 elements; tower: 39 elements (tapered beams)	16.156
guys: 1 element; tower: 1500 elements (shells)	15.256

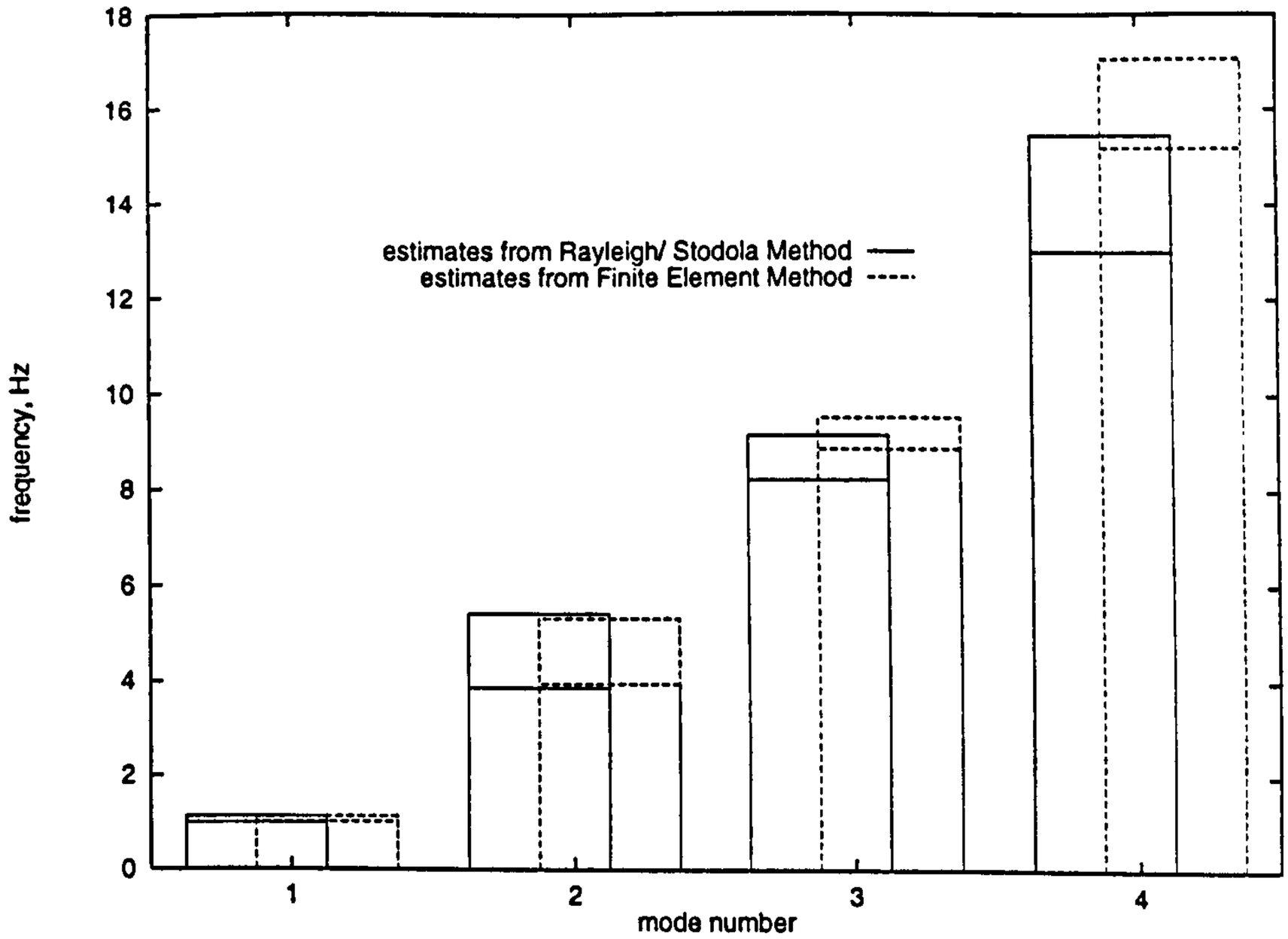

Figure 5.21: Comparison between modal frequencies of the Carter 25 kW machine of the type at West Beacon Farm estimated using the Rayleigh/ Stodola method and using the Finite Element method. The two values plotted on each bar represent the two extreme base boundary conditions: hinged and built in.

Table 5.19: Comparison of estimated torsional resonant frequencies of the Carter 300 kW tower design (Great Orton Airfield type).

brief description of the model used	fundamental torsional mode	1st harmonic
iterative method with nacelle rigidly fixed to tower top (moment of inertia: 55350 kg m^2)	1.25	25.7
guys: 0 elements; tower: 1200 elements (shells)	1.95	25.1
guys: 100 elements; tower: 1200 elements (shells)	1.96	.

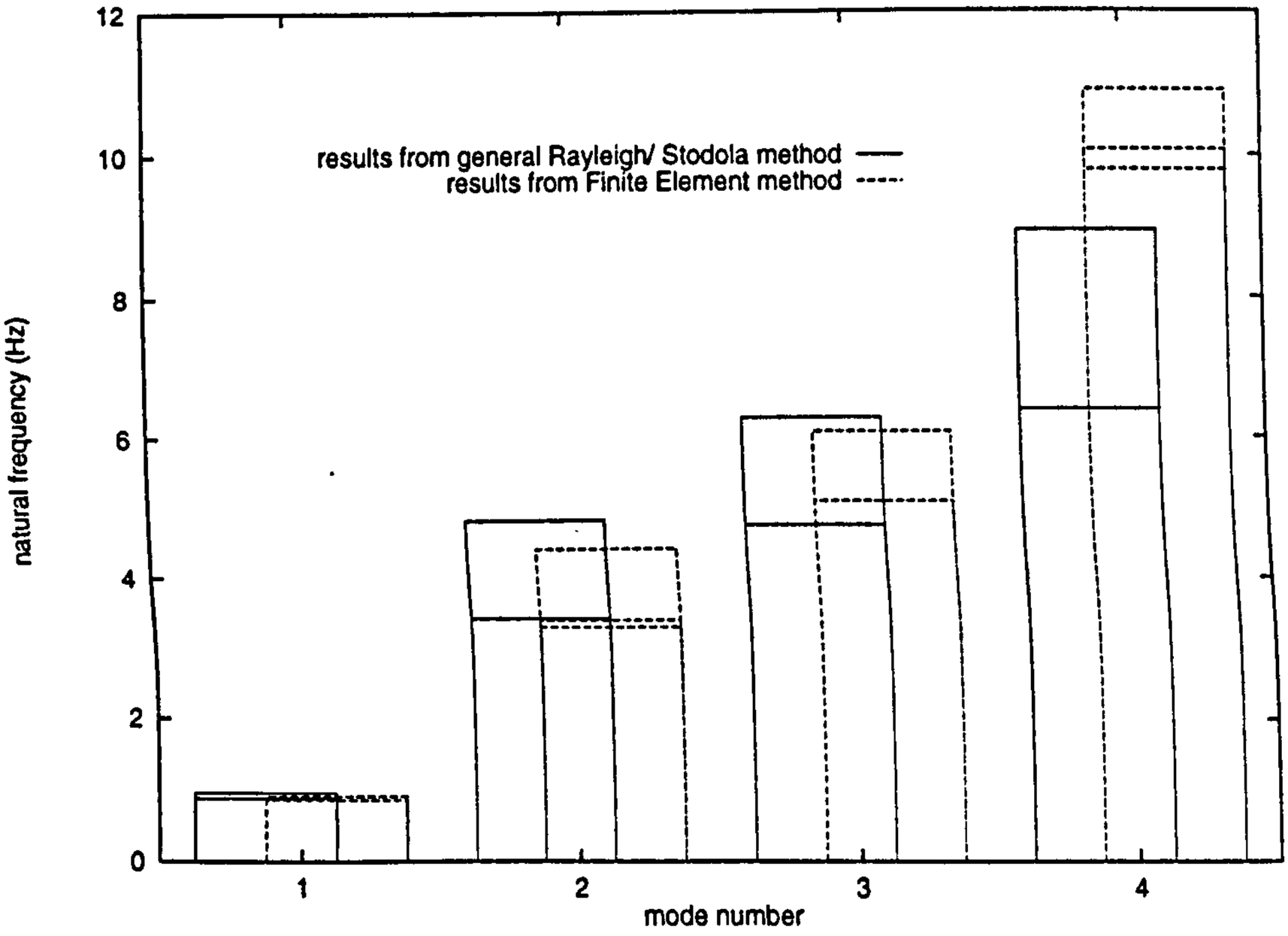

Figure 5.22: Comparison between modal frequencies of the Carter 300 kW machine of the type at Faccombe Estate estimated using the Rayleigh/ Stodola method and using the Finite Element method. The two values plotted on each bar represent the two extreme base boundary conditions: hinged and built in.

There is also some unexpected coupling between the torsional mode of the tower and a mode involving some bulging of the tower regardless of whether or not guys are included in the model. This would only have been predicted by modelling the tower as a hollow cylinder with hoop stiffness (not included in the Rayleigh/ Stodola model).

Chapter 6

Measurements of Tower Vibrations

6.1 Objectives

In order to validate the software developed for rapid assessment of the dynamic response of a new wind turbine design, its predictions must be shown to match experimental observations. Most importantly, the frequencies of vibration of the tower must be the same as those predicted analytically.

Two methods have been used to measure the tower vibration frequencies:

1. A video camera has been used to record vibrations of the tower in its fundamental mode. Measurements of deflections have been taken from the screen.

2. Spot readings of strain or acceleration at a point on the tower have been recorded as a time series. From these time series, frequency spectra have been generated and modal frequencies of the structure inferred.

The modal frequencies measured must be matched to mode shape classes. Ideally, the precise mode shape should be measured by attaching accelerometers or strain gauges to the tower at many points. However, in order to validate the software developed, it is adequate to distinguish between:

- lateral vibrations in a particular plane,
- longitudinal vibrations and
- torsional vibrations.

Video measurements although less accurate are more transparent. It is easy to see what mode is being excited. Techniques for measurement and analysis of data using low-frequency accelerometers are more complex than for video recordings but allow more precise measurements of accelerations and hence frequencies. However, accelerometers are also expensive. The externally excited models used for this work and described in Appendix G were around £600 each. If the mode shapes are to be measured, it is probably more appropriate to attach many strain gauges to the structure.

In Appendix G, descriptions are given of the protection of the accelerometers against mechanical or electrical damage, programming of the data logger, storage of data and procedures for the calibration and estimation of the errors inherent in the whole data collection system.

In Chapter 6, predictions of mode shapes and frequencies obtained using the models discribed in Chapters 2 and 4 are compared with results from both the measurement techniques discribed above and also with results from a survey of the Carter 300 kW wind turbine by Garrad Hassan and Partners Ltd. [22]. Table 6.2 compares results from video measurements with theory. Tables 6.3.5 and 6.3.5 compare predicted results with those from spectral analysis of the accelerometer measurements. Table 6.6 gives the results of spectral analysis of the strain gauge data published by Garrad Hassan and Partners Ltd.

6.2 Video Measurements

It had been noticed that movements of the tower were visible from the ground particularly during an emergency shutdown of the generator. For the Carter design this is a step change in powertrain thrust. The blades pitch up into stall. The aerodynamic lift generated over the surface of each blade drops quickly to zero and with it the torque exerted on the hub. The time taken for the rotational speed to fall to zero is several seconds. While the blades are generating lift, the tower is initially deflected by a few cm. When the step change in powertrain thrust occurs, the natural modes of the tower are excited, especially the fundamental which involves most movement of the tower top. This is a *fail safe* feature of the design, ensuring that if the turbine experiences either excessive windspeeds or disconnection from the grid, it will respond in a way that brings the rotor to rest. The blades are then reset automatically so that, if the wind speed falls or the grid connection is regained, the wind turbine can recommence generating electricity.

Initial deflections and subsequent vibrations of operating machines were recorded on video tape. Measurements were later taken from the television screen. Just before the shutdown sequence started, a line was drawn on a piece of acetate film secured to the screen. The line corresponded to the steady position of the wind turbine tower while generating constant electrical power. As the tower subsequently vibrated, measurements of its position were taken from the screen on every frame (every 1/25 s). Figure 6.1 shows how the camera was pointed at 6 stations up the tower consecutively to record movements during 6 separate shut-down operations. The camera was rotated by 90° so that as much as possible of the tower would fit into each picture.

The equipment used in the recording and measurement of tower vibrations is listed below:-

- Panasonic F15 camera
- Panasonic 7450 recorder box
- Manfrotto tripod 144 legs/ 128 head
- Panasonic AG-7510 video player
- Panasonic AG-7500 video recorder

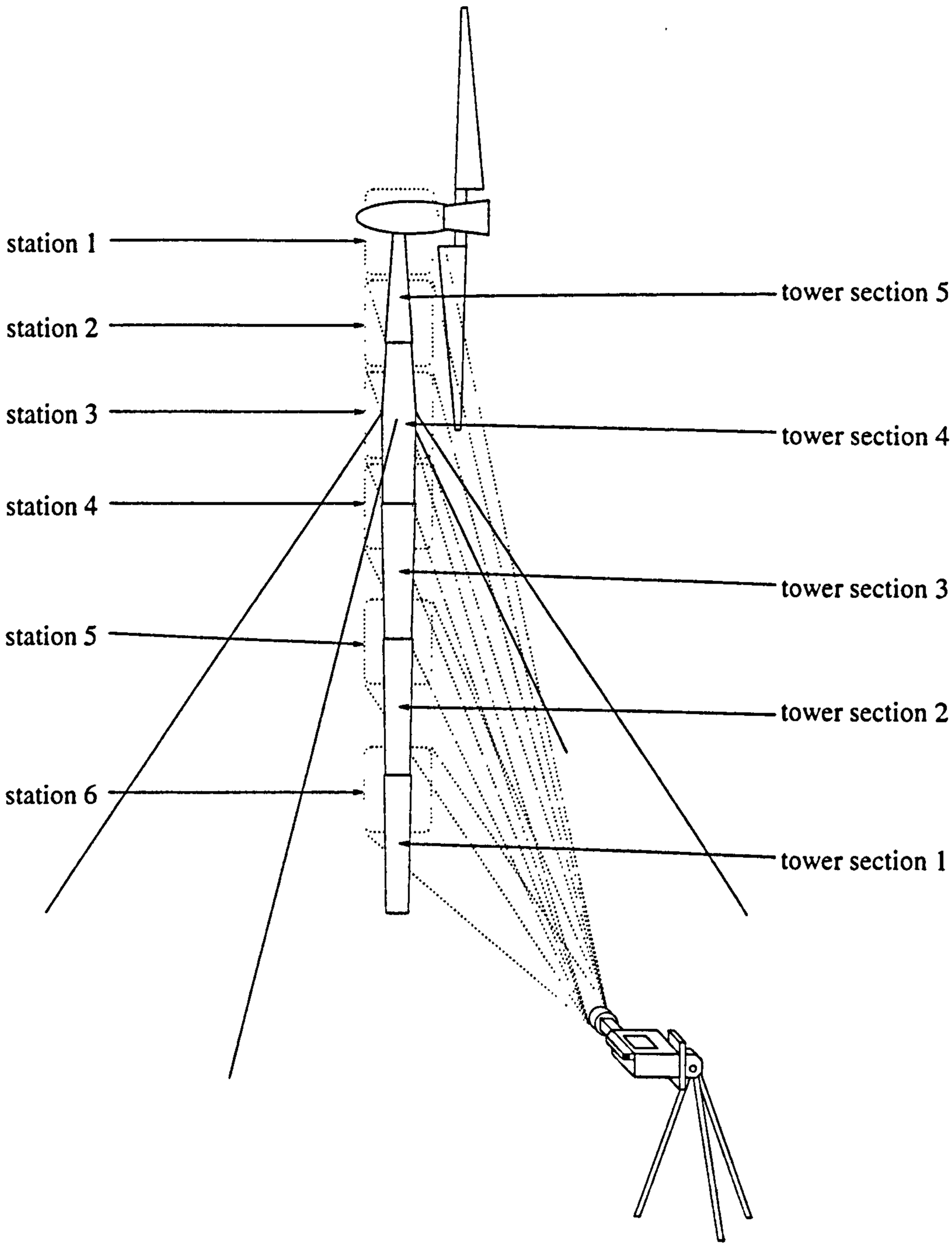

Figure 6.1: The video camera secured at a 90° angle on a tripod, pointing at the six different stations up the tower.

- Panasonic A-750 edit controller
- Panasonic MX12 vision/ sound mixer

6.2.1 Sources of Error

For the method described above, five sources of inaccuracy have been identified and are listed below. Estimates of errors in the measurements total ±0.016 m.

camera shake Gusts of wind, blowing past the camera caused the tripod to rock. These events were not common and could later be neglected in terms of data collection because of the obvious difference on the picture between camera shake and tower movement and because of the accompanying audible noise due to the gust.

sweep variability Unlike conventional film, there is not a rectangular area on a video tape on which each discrete image is stored. Every 1/25 s, the next frame is sent by the video player to the screen by scanning one line at a time from the top to the bottom. On many editting suites, a 'noise bar' passes down the screen as the frame changes. Just before and just after the frame changes, it's position on the screen may fluctuate a little. For greatest consistency, measurements must be made at the same time relative to the time when the frame changes (±0.008 m).

frame flicker Even with the 'noise bar' off-screen and the picture frozen electronically, some flicker is experienced (±0.004 m).

paralax The thickness of the glass from which the electron tube is made gives rise to paralax between the stationary reference mark on the surface of the screen and the projected image (±0.004 m).

timebase variation By repeating a series of measurements, an estimate of overall errors can be made. Although absolute displacement recorded tended to be very similar, some variation (±0.2 s) of times was noticed (this is not an error applicable to frequency or deflection measurements).

6.2.2 Analysis of the Results

Table 6.1: Fundamental tower frequency as measured at six different stations up the tower during six different shutdown sequences.

station	1	2	3	4	5	6	average
period (s)	1.38	1.41	1.47	–	1.43	1.47	1.43
frequency (Hz)	0.725	0.709	0.680	–	0.699	0.680	0.699

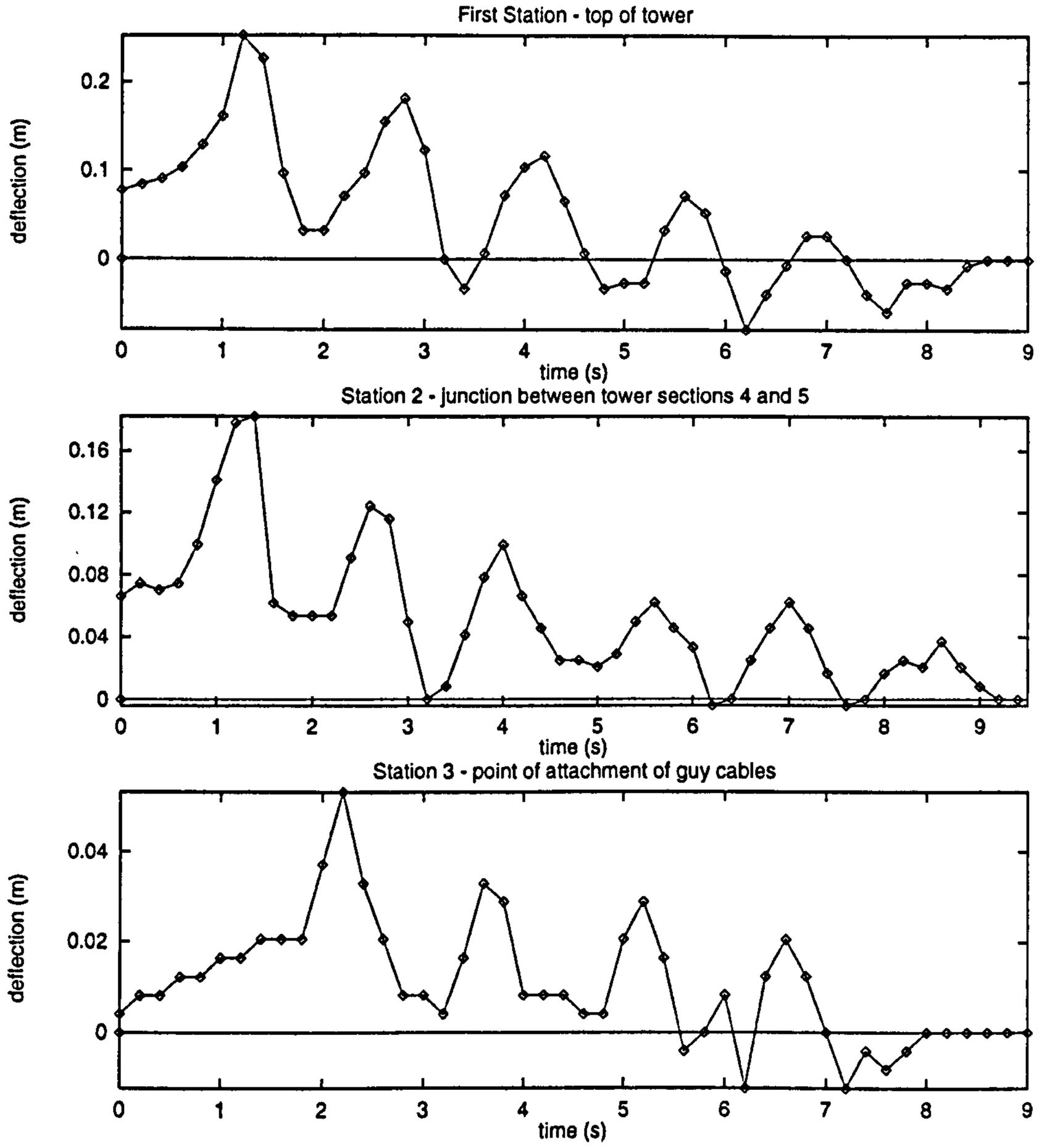

Figure 6.2: The deflections of the top three tower stations as functions of time after consecutive emergency shutdown sequences. In each case, the wind turbine was initially generating 100 kW. Measurements were taken from video recordings which were made on 14th September 1994 at machine 9 of the array of 10 wind turbines at Great Orton Airfield.

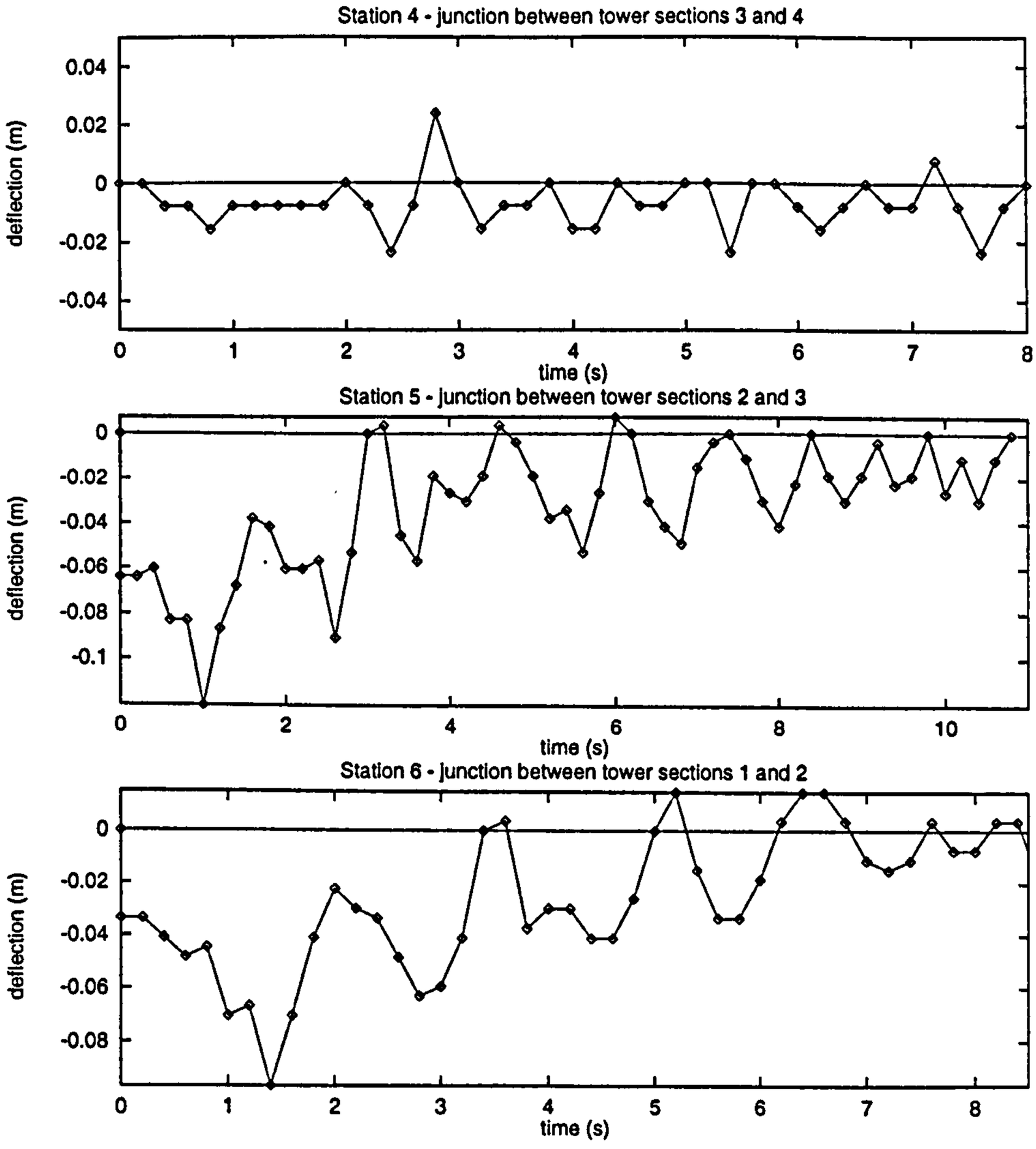

Figure 6.3: The deflection of the bottom three tower stations as functions of time after three consecutive emergency shutdown sequences. In each case, the wind turbine was initially generating 100 kW.

Figures 6.2 and 6.3 show the variation of tower position with time. Positions are measured relative to the final resting position of that tower station. From each time series, the frequency of oscillations is calculated (Table 6.1).

In Table 6.1, no frequency has been calculated for the data from Station 4 as movements were too small to be accurate. The guys are attached to the tower at Station 3 but a vibration node is forced nearer to Station 4.

In each case, it is interesting that the tower initially moves further from its final resting position. The thrust on the tower top is initially fairly constant as the wind speed was constant and the power generated was 100 kW. From the video recordings it appears that when the wind turbine is disconnected from the grid, the thrust increases considerably and then falls to zero over several seconds. This may be because, when the wind turbine is disconnected from the grid, there is no electrical load from the grid preventing the speed of rotation of the blades from increasing. The the horizontal thrust, F_{nh} on the tower top increases with the increase in speed. It is this step change in thrust at the tower top which excites the fundamental bending mode of the tower.

The Carter wind turbine includes a fail safe mechanism which shuts the machine down if the wind speed is too great or if the generator is disconnected from the grid. In both cases, the speed of rotation of the blades increases. The off-centre masses attached to the blades exert a moment about the blade root trying to pitch each of the blades about an axis along its length. The off-centre masses can be seen in Figure 2.3 and in close-up in Figure 4.4. This moment arises due to centrifugal forces on the masses and so increases with speed of rotation. This moment is resisted by the spar which extends outwards from the hub inside a portion of each hollow blade. It is also normally resisted by a solenoid. The current to this solenoid drops to zero as the wind turbine is disconnected from the grid. Above a certain speed, the centrifugal forces on the masses override this solenoid and the torsion spar and the blades pitch and cease generating power. The speed of rotation now falls rapidly.

Using the design parameters listed in Appendix H, the fundamental mode of bending vibrations was calculated by the Rayleigh/ Stodola method. The measured and calculated frequencies are compared in Table 6.2.

Table 6.2: Comparison between frequency measured as described in Section 6.2 (Table 6.1) and calculated by Rayleigh/ Stodola modal analysis of the machine described by parameters listed in Appendix H. The lateral tower modes were calculated with an initial strain, ϵ_{ic} of 0.0005.

measured (Hz)	calculated	
	base bending stiffness parameter, k_{Bf} (N m rad^{-1})	frequency (Hz)
0.699	0.0	0.670
	1×10^{12}	0.762

Because the 6 sets of data were collected during 6 separate shutdown sequences. it would be confusing if they were plotted on one time axis. However. given the step input is the

same in each case, the fundamental bending mode shape can be estimated by measuring the amplitude of the first oscillation at each tower station and plotting each point with respect to the height of each tower station. The curve which results can be smoothed using cubic splines (Figure 6.4). The shapes of calculated and measured fundamental modes are similar. The conditions at the beginning of each sequence are the same: the turbine was generating 100 kW constant power. As already stated, it is inaccurate to plot dislacement measurements from different shutdown experiments on the same axis. The fundamental mode shape could be measured with greater accuracy by recording simultaneously the tower movement at a greater number of tower stations.

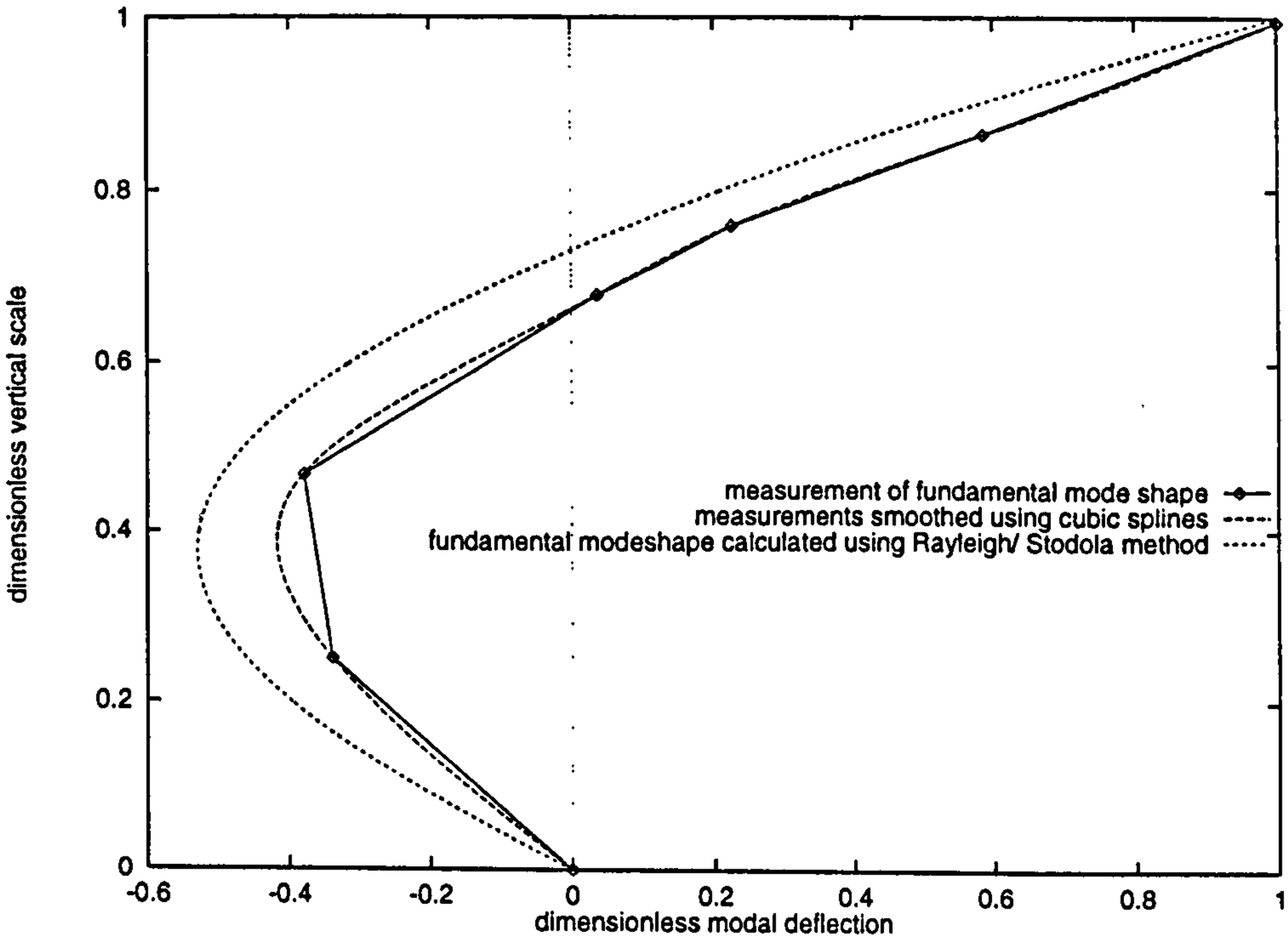

Figure 6.4: Approximate measurement of the shape of the fundamental mode of bending vibrations of the tower of wind turbine number 9 of the array of 10 at Great Orton Airfield in Cumbria. Measurements were taken from video recordings made on 14th September 1994.

The variations of displacement with time are not clean. There are harmonics due either to measurement errors or genuine tower harmonics. Variations in measurements of frequencies from the data are not included in the estimates of error given above but can be gauged from the standard deviation of values quoted in Table 6.1 which is 0.02 Hz. Using estimates of the errors in measured values to estimate the errors in frequencies on an estimate of the power spectrum is discussed in Section 6.3.4.

Significant improvements could be acheived by using high-speed photography and directing a laser spot onto the tower at each station as a fixed reference point. The camera could also have been more securely positioned. Taking six simultaneous pieces of video film at the stations would give information about the relative phase of each station and allow checking of the frequencies.

This video technique is not suitable for measurement of longitudinal or torsional vibra-

tions.

Using a high-speed camera with a photographic compact disk would allow pictures to be transferred directly to a computer. Electronic measurements between the fixed reference point (the laser spot, for example) and a point on the moving tower could be subsequently automated. The data could be processed in real time to record the position of the tower at each station at successive times. The accuracy would then be limited by the picture timing accuracy of the camera and the resolution of the two points on each picture.

Using electronic theodolytes making simultaneous recordings of tower position automatically at pre-determined times would be the most accurate remote sensing method. This is the method chosen by Taywood Engineering [55] to test the blades of the prototype Wind Energy Group MS4-600 wind turbine. They have built a rigid test frame onto which both the theodolytes and the specimen are attached so that no rigid attachment to the floor is necesary. This procedure would be equally applicable for the testing of soft towers.

6.2.3 Static Tower Deflection

All the experiments started with the wind turbine generating at constant output of 100 kW. The predominant force on the tower is due to the thrust from the powertrain. At constant output power, this force is constant. It is equivalent to the horizontal nacelle force, F_{nh} in Figure 2.17. The power curve for the Carter 300 kW wind turbine is shown in Figure 6.5. The electrical power generated is 100 kW when the wind speed is 9.25 m s^{-1} at hub height.

The power generated, P_t by the wind turbine is given by Equation 6.1 from the book by Twidell and Weir [56]. If the density of air is taken as 1.3 kg m^{-3} [57] and the swept area of the rotor is 444 m^2, the Power Coefficient, C_P can be calculated by rearranging Equation 6.1 (C_P is 0.438).

$$P_T = C_P A \frac{\rho u_o^3}{2} \tag{6.1}$$

If the thrust on the rotor is approximately proportional to the electrical power generated, the force coefficient in Equation 6.2 can also be taken to be 0.438. The horizontal thrust on the tower top, F_{ch} is calculated to be 10.8 kN. If this is the only significant force on the tower, the lateral deflection shown in Figure 6.6 (b) is predicted using the *general numerical model* described in Chapter 2.

$$F_A = C_F A \frac{\rho u_0^2}{2} \tag{6.2}$$

The predictions and measurements of tower deflections are similar. Measurements were made on 6 separate occasions and so although the electrical power generated was 100 kW in each case, they do not represent the simultaneous positions of the stations. Just as stated in Section 6.2.2, measuring the deflections of many more stations on the tower simultaneously would provide more comprehensive validation of the *general numerical model* of static deflections.

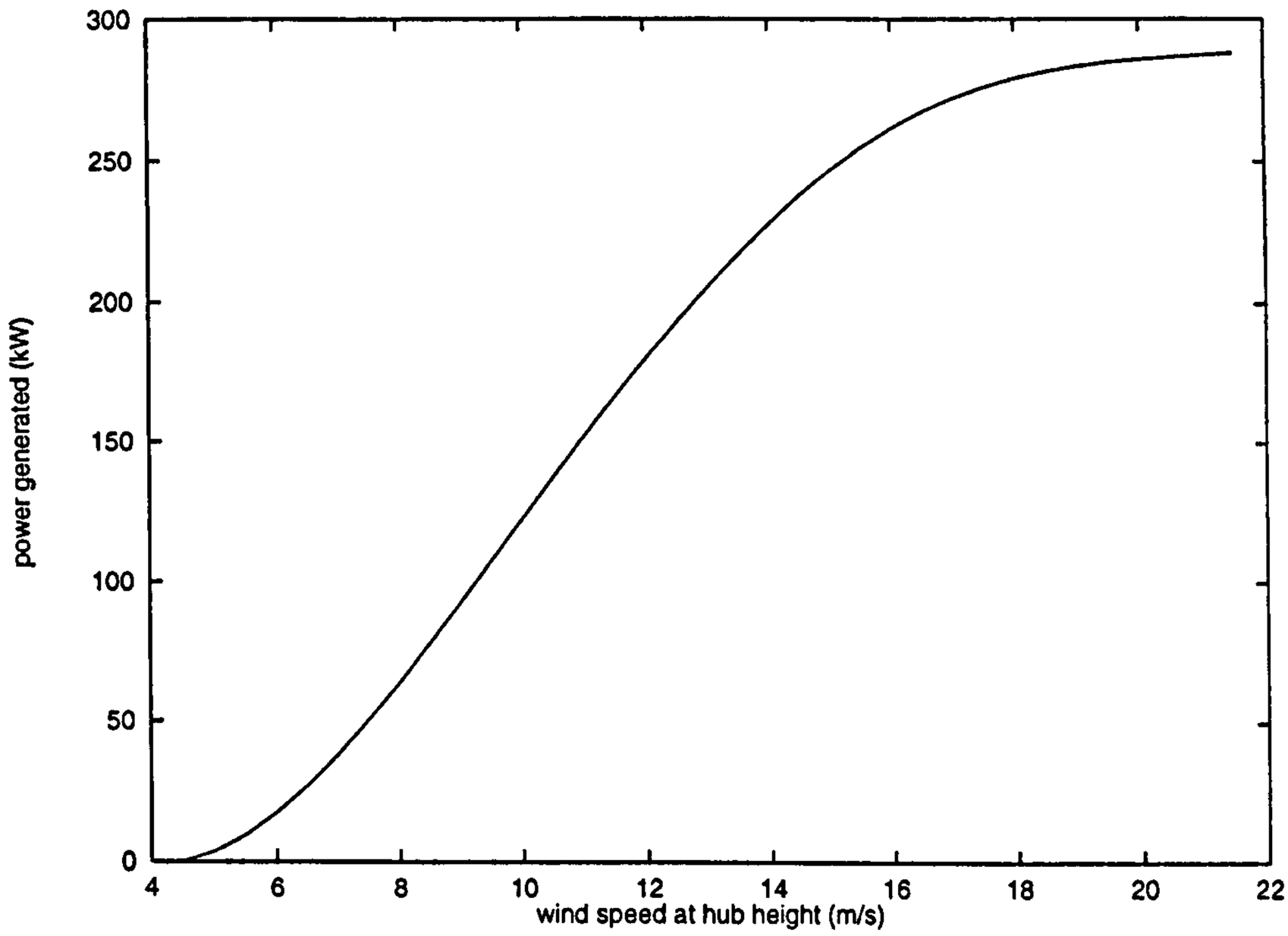

Figure 6.5: The power curve for the Carter 300 kW wind turbine of the type at Great Orton Airfield. The electrical power generated is plotted against the wind speed at hub height in an undisturbed airstream. The data were independently verified by Garrad Hassan and Partners Ltd. in accordance with ECN-217. The pitch setting was 1.25°.

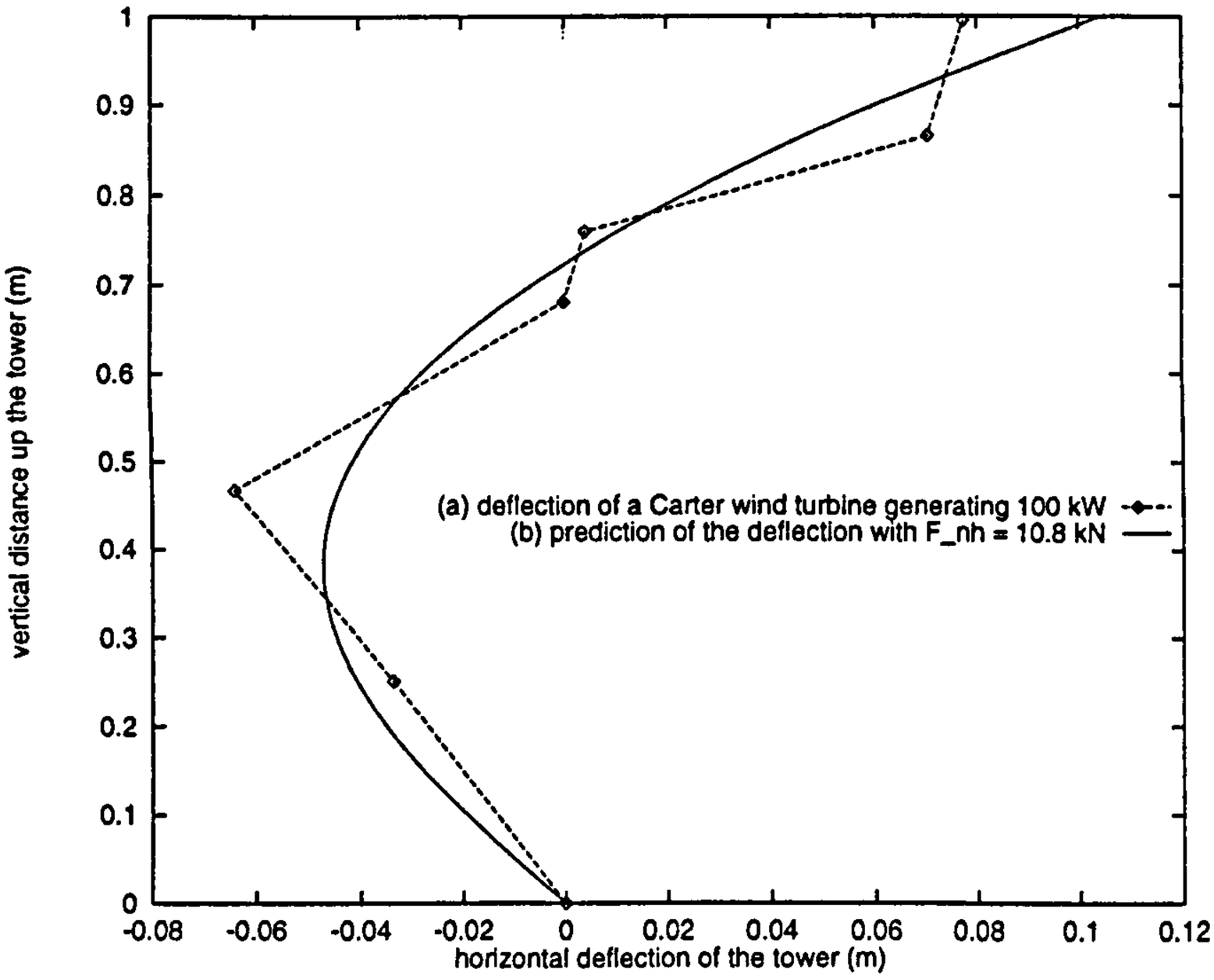

Figure 6.6: (a) deflection of the tower of a Carter 300 kW wind turbine (number 9 of the array of 10 at Great Orton Airfield) when generating constant electrical power of 100 kW. (b) prediction of the deflection of the same wind turbine design using the general numerical model *described in Chapter 2. The base of the tower is hinged ($k_{Bf} = 0$ N m rad^{-1}).*

6.3 Acceleration Measurements

6.3.1 Practical Considerations

Time series are obtained by measuring accelerations at regular intervals of time. Accelerometers have been attached to the tower between the ground and the point of attachment of the guys (the accelerometers and their calibration are described in Appendix G.2). Measurements were taken during normal operation. It was hoped that all natural modes of vibration were excited. Vibration classes are distinguished by combining time series from two accelerometers (see Appendix G, Section G.1).

6.3.1.1 Distinguishing Modes

It is important that it is possible to distinguish between lateral, torsional and longitudinal modes and between various modal harmonics from the data collected. It is expected that modal harmonics are far enough apart to be distinguished on the frequency spectrum of the data. Longitudinal modes are excited at far higher frequencies than either lateral or torsional modes and so are also distinct. However, frequencies of torsional modes are similar to those of lateral modes. For this research, only torsional and lateral frequencies are distinguished experimentally. The method is described in Appendix G, Section G.1.

6.3.1.2 Data Processing

The data are processed after collection on a computer separate from the data logging hardware.

Time series data are converted into a frequency spectrum using a Discrete Fourier Transform as described in a text book on communications [58]. The Fast Fourier Transform algorithm is available on the MATLAB platform [59]. Equation 6.3 shows the equivalence of time and frequency representations of the data.

For example, the time series is stored as an array, x, of N acceleration measurements at regular intervals of time between 0 and T seconds. X is then a series of spectral magnitudes at integer multiples of $\frac{1}{T}$. In order to make most efficient use of the FFT algorithm, the length of the array, x must be an integer power of 2. This can be acheived by increasing the time series to length, T_F. The extra $N_F - N$ elements which make up the input to the FFT algorithm are set to zero in the MATLAB FFT function. Alternatively, a slower Discrete Fourier Transform algorithm can be used. The resolution of the frequency spectrum will be $\frac{1}{T_F}$.

$$x(j) = \frac{1}{N_F} \sum_{k=1}^{N_F} X(k) \omega_{N_F}^{-(j-1)(k-1)} \tag{6.3}$$

where:-

$$\omega_{N_F} = e^{-\frac{2\pi i}{N_F}}$$

$$N_F = \frac{T_F}{T} \times N$$

x	Time series data array.
X	Frequency spectrum array. Acceleration as a function of frequency.
j	Index into the time series of data.
k	Index into the frequency spectrum array.
N	Number of elements in the time series array.
N_F	Number of elements in the frequency array (N_F is corrected to ensure that it is an integer power of 2).
i	Square root of -1.
T	Time series data measured over time T s.
T_F	Length of time window (usually longer than T) of data input to the FFT algorithm.

The frequency spectrum X is an array of complex numbers. Multiplying each by its complex conjugate X^* gives an array of real numbers which is a measure of the power in the signal. The maximum frequency corresponding to $X(N_F)$ is the sampling frequency, f_s. A frequency scale is then generated using $\frac{1}{T_F}$ as the basic unit of resolution and containing the same number of elements as in X (see Equation 6.4). A short data processing program has been written on the MATLAB [59] platform to obtain a graphical plot of the power spectrum in this way.

$$f(k) = f_s[0, \frac{1}{N_F}, \frac{2}{N_F}, \frac{3}{N_F}, \ldots, 1] \tag{6.4}$$

6.3.1.3 Avoiding Aliasing of Data

The Nyquist sampling criterion [58] is that, to avoid aliasing, the highest frequency expected in the data should be less than half the sampling frequency. This is because the spectrum described above is symmetrical about $\frac{1}{2}f_s$ (see Figure 6.7). For this reason, only half the spectral array output from the Fast Fourier Transform algorithm is plotted in any graphical results reproduced here. In fact, the shape of the frequency spectrum is cyclic and consists of identical lobes each of which is symmetrical about integral multiples of period f_s on the frequency axis (see Figure 6.7).

Aliasing occurs when the measurements vary at any frequency higher than $\frac{1}{2}f_s$ (see Figure 6.8 (a)). Aliasing is represented on the frequency axis as overlap between consecutive lobes of the frequency spectrum (see Figure 6.8 (b)). Because the frequency spectrum is symmetrical about $\frac{1}{2}f_s$, this erroneous frequency $(f_s - f_{(\text{real})})$ is a peak at the lower end of the second lobe. The same peak $(f_{(\text{real})})$ occurs at the upper end of the first lobe but is normally not plotted because the frequency scale is defined only between 0 Hz and $\frac{1}{2}f_s$ Hz and $f_{(\text{real})} > f_s$. In Figures 6.9 and 6.10, the same synthesised wave is sampled at two different frequencies. One frequency (10 Hz) gives rise to an aliased Power Spectral Density function, the other (14 Hz) is just high enough to avoid aliasing.

Aliasing may be overcome either by:-

1. sampling at such a high rate that variations at frequencies above the sample rate contain very low power relative to the frequencies of interest and the background noise;

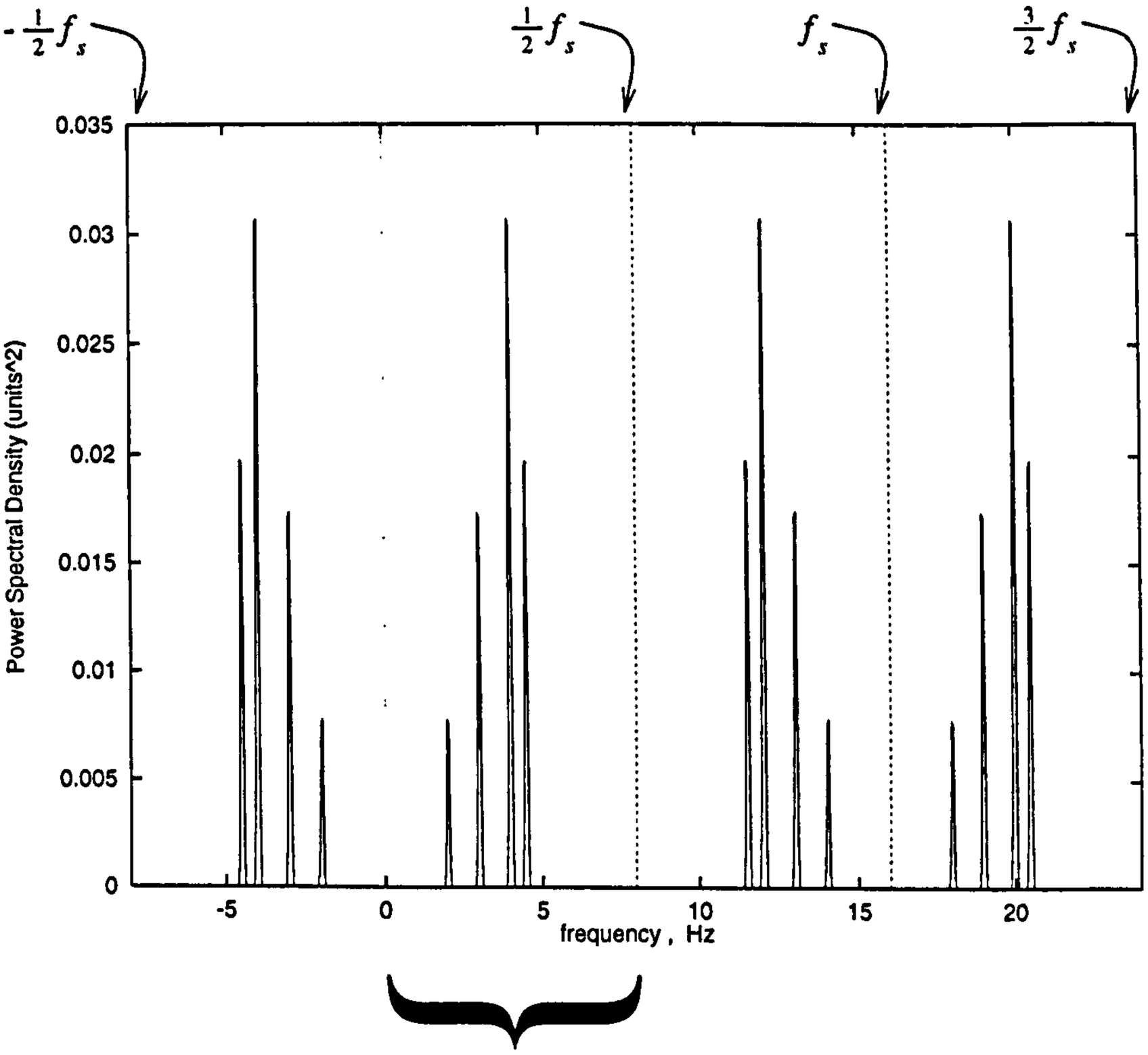

Figure 6.7: The fast fourier transform of a 16 s sample of a synthesised waveform. The waveform has 4 components (2 Hz, 3 Hz, 4 Hz and 4.5 Hz). Sampling was at 16 Hz (giving a data series of 256 points). The data processing technique used is described in Section 6.3.1.3. The Nyquist sampling criterion is satisfied because $f_{(\max)} < \frac{1}{2}f_s$ (4.5 Hz < 8 Hz).

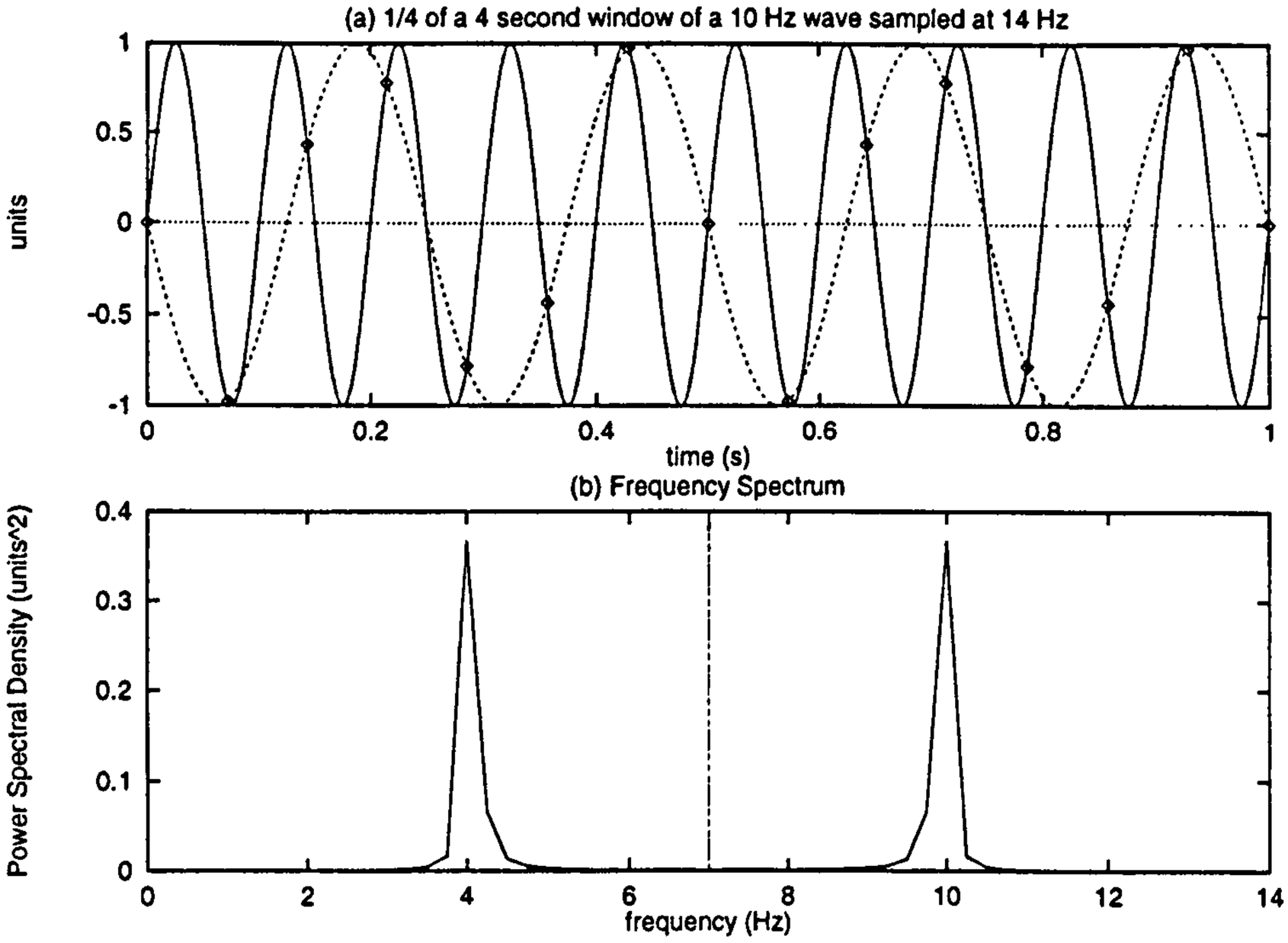

Figure 6.8: An example of aliasing: *(a) a wave constructed numerically with a frequency of* $f_{real} = 10$ *Hz. It is sampled at a frequency of* $f_s = 14$ *Hz as shown by the positions of the point markers on the graph. It is possible to join up the markers with a sinusoid of frequency 4 Hz which is lower than* f_{real}*. It is* $f_s - f_{(\text{real})}$ *(14 Hz - 10 Hz). Only 1 second of the 4 second window actually analysed is displayed here. (b) the frequency spectrum of the constructed wave illustrated in (a) showing aliasing whereby Fourier analysis of a 10 Hz wave gives rise to peaks at both 4 Hz* ($f_s - f_{(\text{real})}$) *and 10 Hz* ($f_{(\text{real})}$).

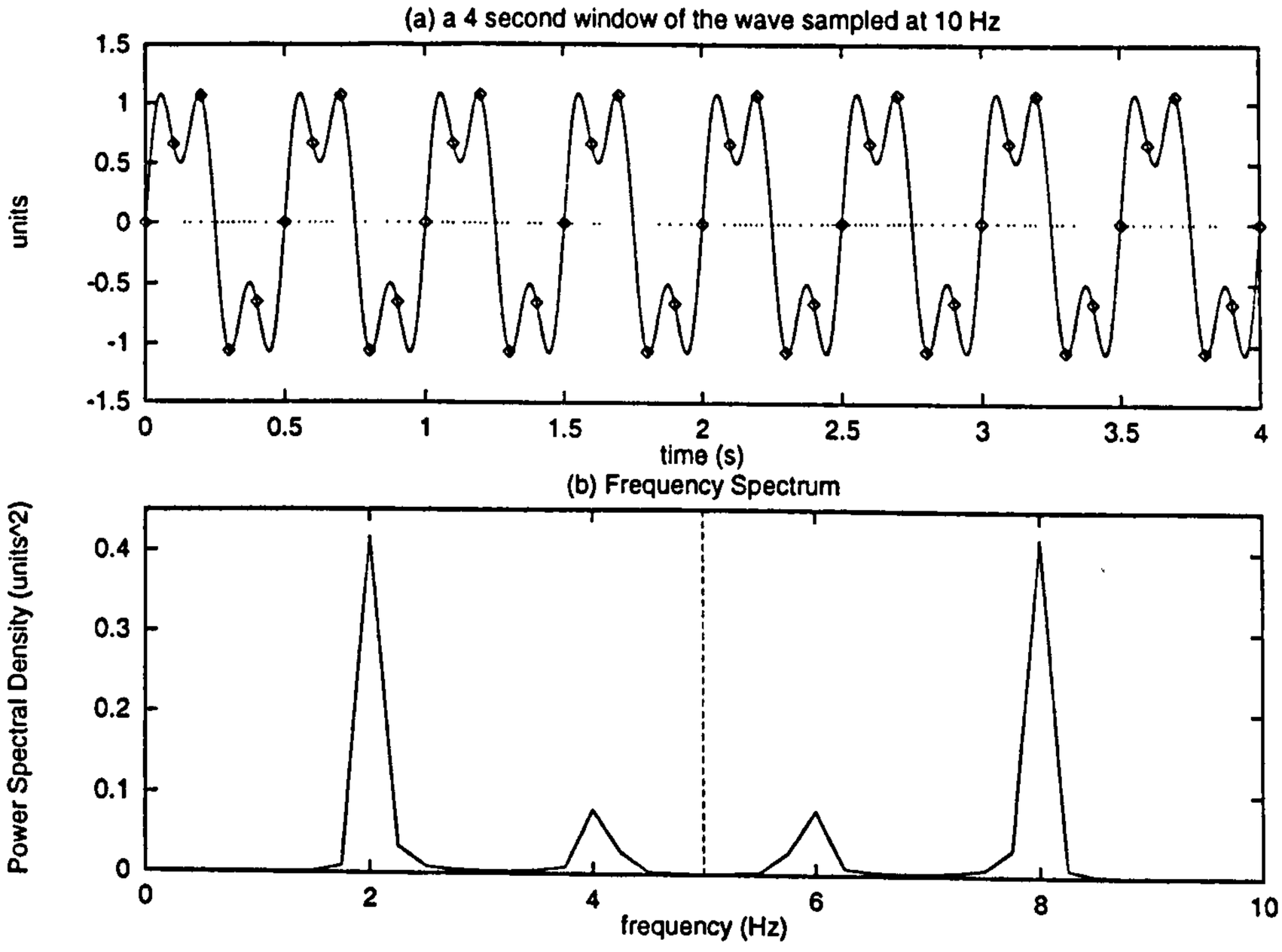

Figure 6.9: Aliasing: *(a) a combination of 2 Hz and 6 Hz waves sampled at 10 Hz. (b) the resulting spectrum. Aliasing occurs and there are peaks at both 4 Hz and 6 Hz.*

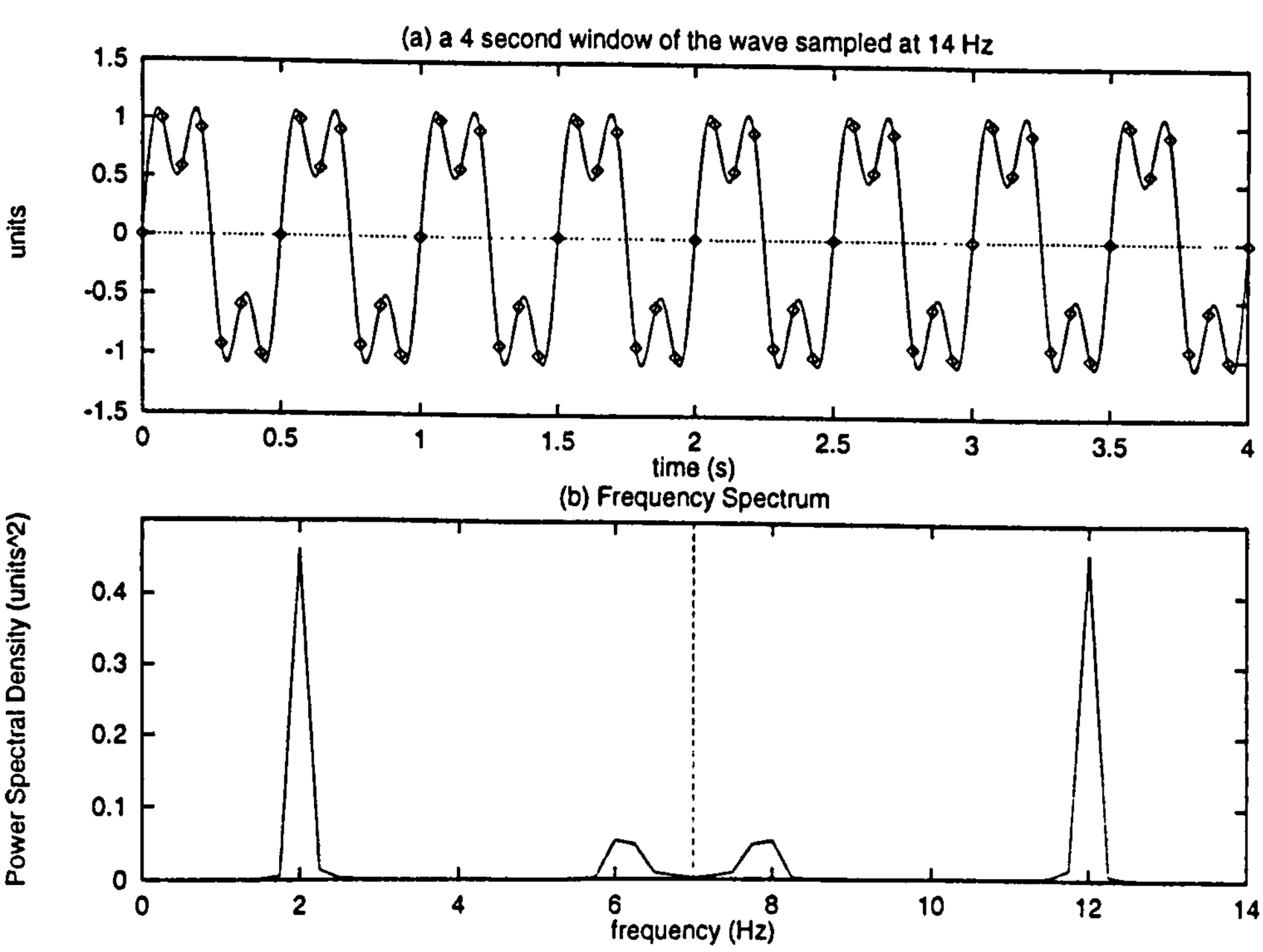

Figure 6.10: (a) the same signal as in Figure6.9 (a) sampled at 14 Hz. (b) the resulting spectrum shows that the signal has been accurately sampled. Because the highest frequency present in the signal is less than half the sampling frequency.

2. connecting a low pass filter in series with the signal cable between the accelerometer and the data logger and sampling at about 40% higher than the low pass cut-off frequency.

Initially, the tower vibration data have been sampled at 275 Hz. This yields far more data than are needed for validation of the predictions of tower modal frequencies which are accurate for the first few harmonics only (between 0 and 10 Hz).

The data sampling rate can be reduced with confidence if a low-pass filter is present because the frequency characteristic of the filter is known beforehand (see Appendix G, Section G.4.3).

6.3.1.4 Time Sample Window

Data are collected within a 'time window' bounded by times, T_1 and T_2 s. The simplest window is square corresponding to instantaneous switching on of the data collection equipment at T_1 and instantaneous switching off at T_2. It is not possible to set these times so that there is, between times T_1 and T_2 s, a fixed number of periods of each of the periodic components. Figure 6.11 shows some data from an operating wind turbine. The number of different frequencies and the number of different phase relationships between them are large. There will be some truncation of periodic signals.

Figure 6.12 (a) shows the portion of a synthesised signal which lies between times T_1 and T_2. The fourier transform of the data within this small period of time is the same as the fourier transform of the cyclical signal shown in Figure 6.12 (b). The actual signal from which the data was taken is shown in Figure 6.12 (c). The distortion of the original signal can be seen by comparing Figure 6.12 (b) and (c) which are plotted on the same axes in Figure 6.12 (d). This distortion results in significant extra Power Spectral Density peaks at high frequencies. The distortion only occurs when there are not a whole number of wavelengths within the interval $[T_1, T_2]$.

An alternative explanation for the distortion of the signal if sampled with a square window is given in "Numerical Recipes in C" [31] by looking at the signal in the frequency domain. A window is a function by which the signal being measured is multiplied. A unit square window is illustrated in Figure 6.13 (a). This is analogous to switching on the measuring equipment at time $t = T_1$ with unity amplification and switching it off at time $t = T_2$. The window function is a signal with its own power spectral density function Figure 6.13 (b). If two signals are multiplied together in the time domain, it is equivalent to the convolution of the frequency response functions.

The problem with sampling the signal over a finite time window may be overcome by attenuating the signal towards the edge of the time window. This is equivalent in the frequency domain to reducing the power in the side lobes (Figure 6.13 (b)). Once collected, the data are multiplied by a weighting function whose value is unity in the centre of the time window and falls towards zero at either edge. The cosine weighting function, $h(t)$, described in Equation 6.5 is called the generalised Hamming window after Richard W. Hamming who also optimised α (Equation 6.6). Of all raised cosine windows Equation 6.6 has the smallest maximum side lobe level (side lobes of a square window are visible in Figure 6.13 (b). further descriptions are given in [60] p.99).

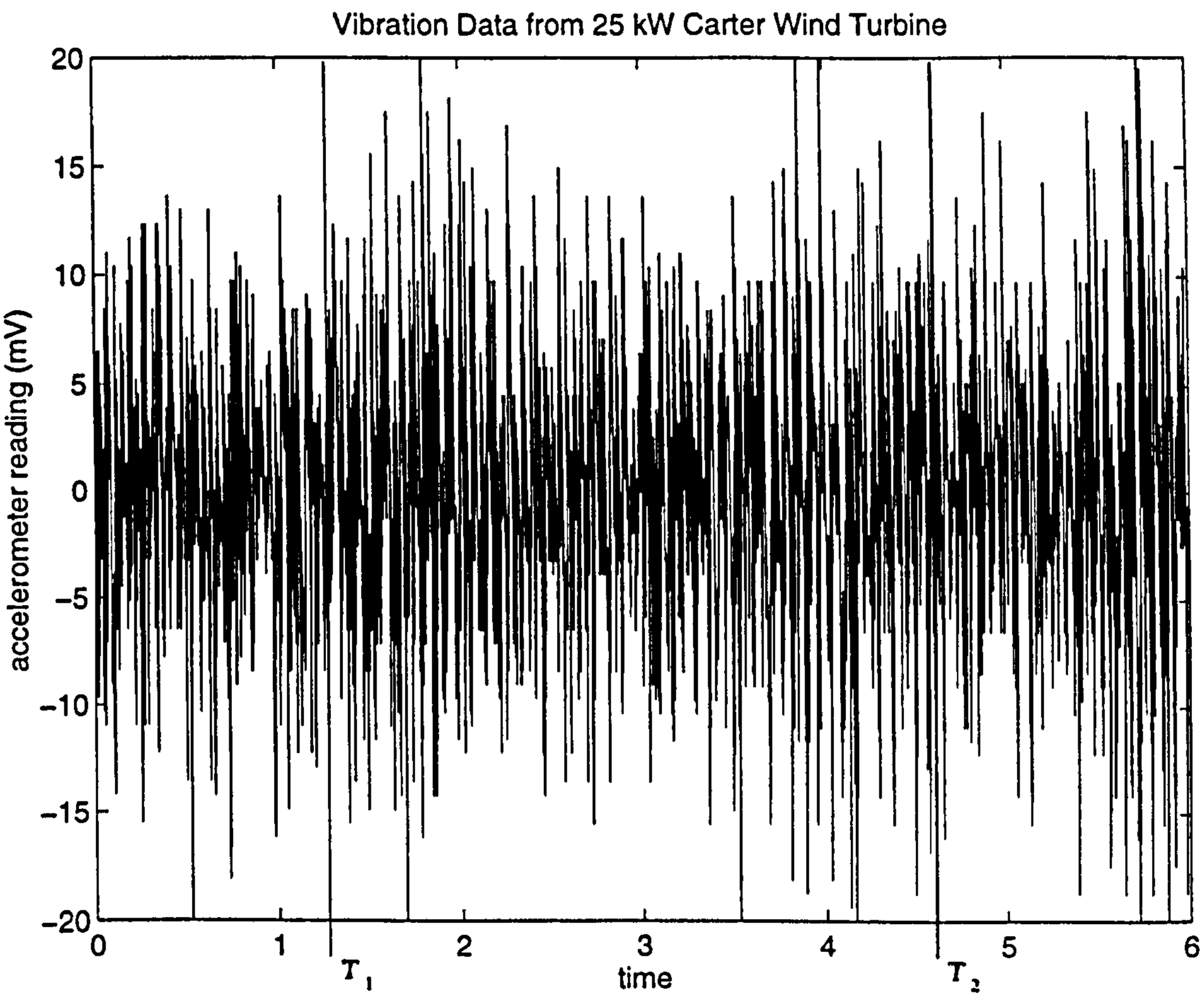

Figure 6.11: The acceleration data recorded at West Beacon Farm on 29/04/96 on a 25 kW Carter wind turbine. If the power density spectrum is to be estimated accurately using a square window, there must be a whole number of periods of all the frequencies of interest between T_1 and T_2.

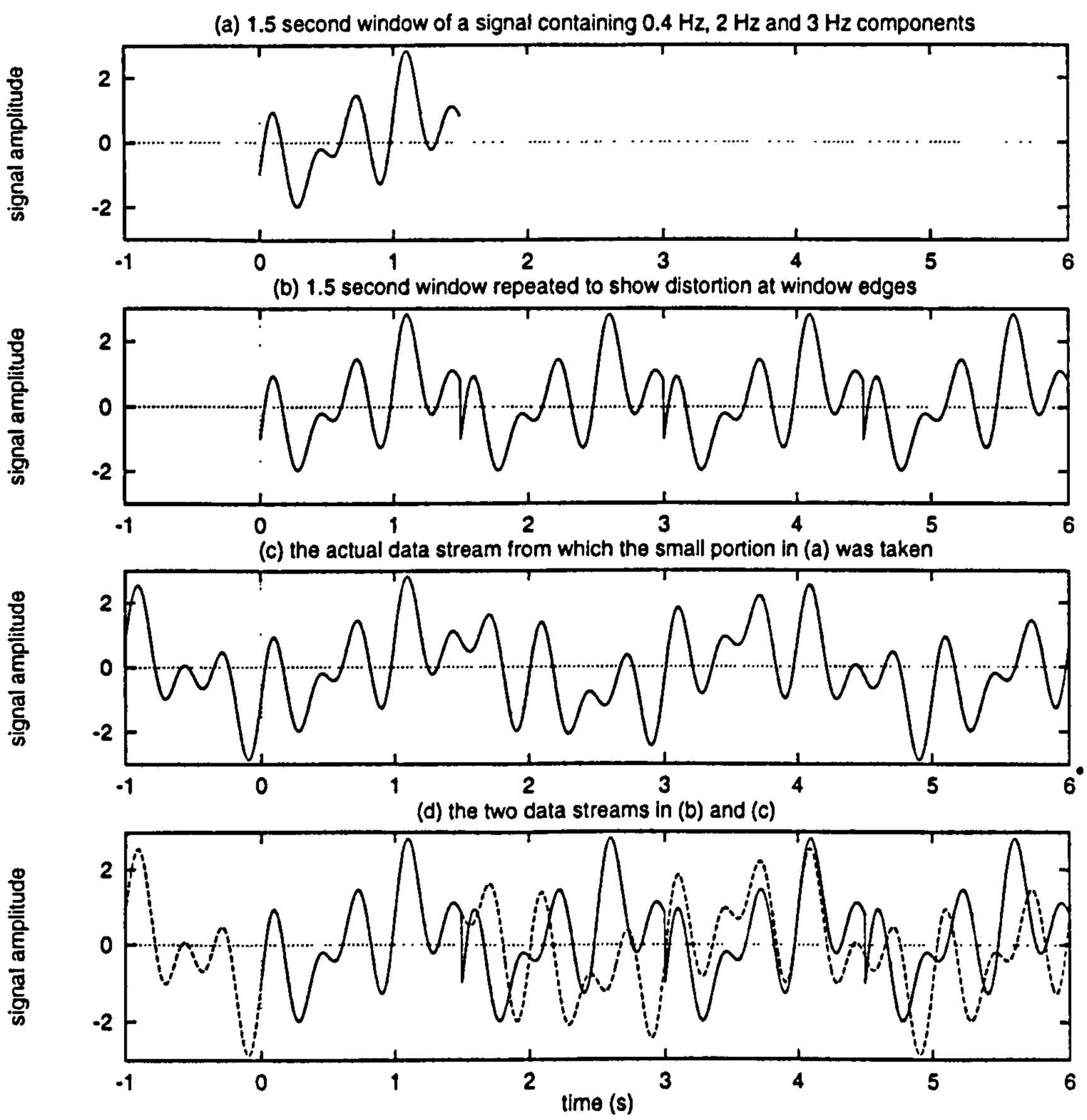

Figure 6.12: (a) A time window of the periodic signal constructed from variations of frequencies 0.4 Hz, 2 Hz and 3 Hz. (b) The data in (a) could have come from either of the signals shown in (b) or (c). However, (b) and (c) are clearly different. (c) is the genuine periodic signal. The distortion of signal (c) resulting from sampling between T_1 and T_2 is clearly visible in (d) which shows signals (b) and (c) on the same axes.

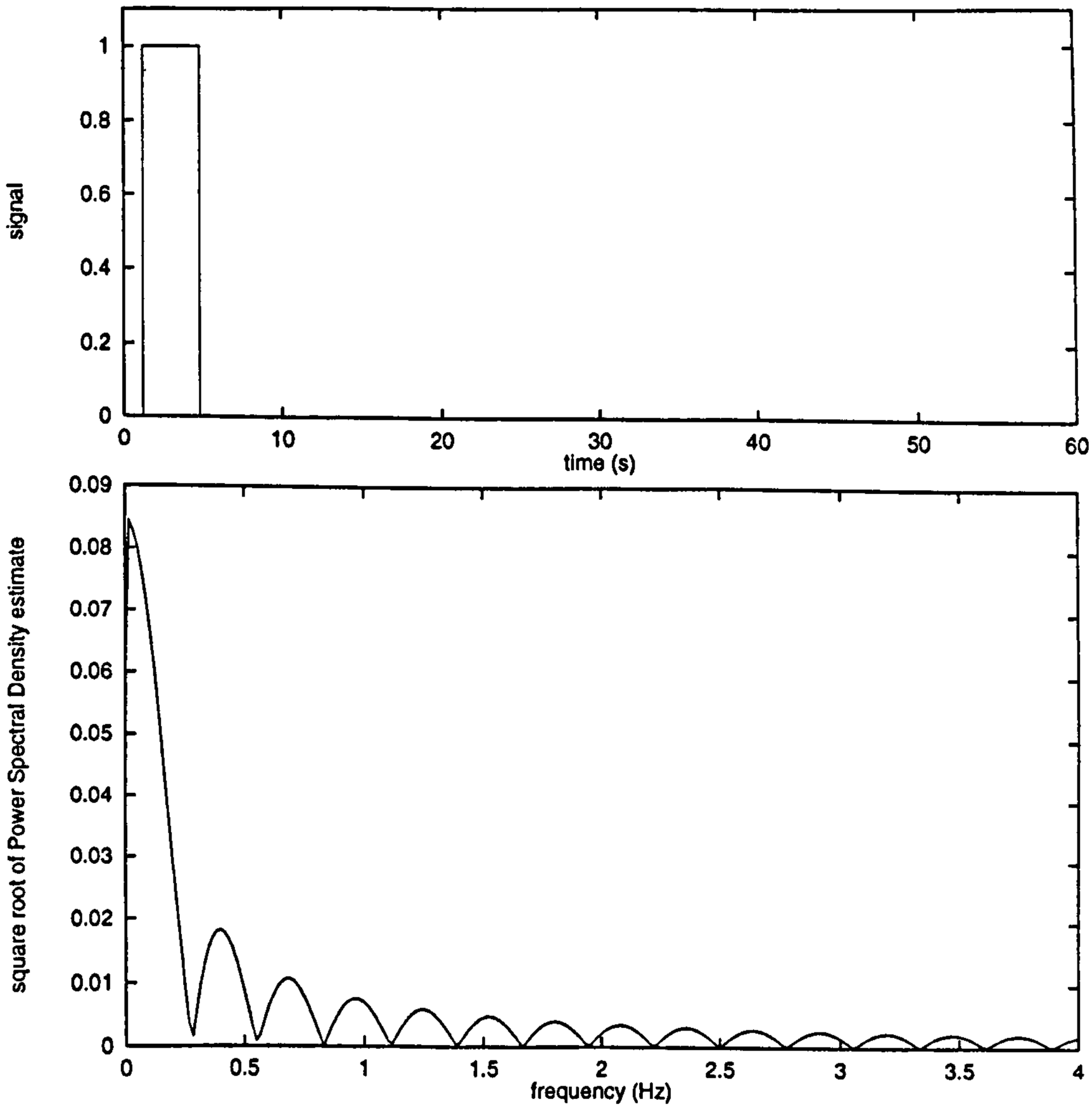

Figure 6.13: (a) a time window with unity amplification. The horizontal axes represents 1000 samples per second. (b) the first 4 Hz range of the estimate of the Power Spectral Density function of the square time window shown in (a). The horizontal range extends to 500 Hz and the resolution is 0.0167 Hz.

$$h(t) = \alpha - (1-\alpha)\cos\left(\frac{2\pi t}{T_2 - T_1}\right) \tag{6.5}$$

$$h(t) = 0.54 - 0.46\cos\left(\frac{2\pi t}{T_2 - T_1}\right) \tag{6.6}$$

In order not to attenuate the data at the beginning and end of the series too much, the data stream is split into several overlapping windows each of which is multiplied by the Hamming function. The spectra are later added. This decreases the resolution of the spectrum but also decreases the variance of estimates of the Power Spectral Density of the signal. It can be shown [31] that the optimum overlap is $\frac{1}{2}$ the window length. If there are K overlapping windows the resolution is reduced from $\frac{1}{T_F}$ to $\frac{K}{T_F}$. It can be shown [31] that the variance of the estimate is reduced by a factor $\frac{9K}{11}$. A paper by P. D. Welch in *Modern Spectral Analysis* [61] has been cited by Press *et al* [31] as a good source of the equations and analysis for comparing various windowing strategies.

Figure 6.14 shows the difference between:

1. sampling a signal with a square window whose length is an integer multiple of the highest frequency in the signal;

2. sampling the signal so that the period is truncated and

3. sampling a truncated signal with an optimised 'Hamming window'.

When the window length is 19.8 s rather than 20 s, extra, low-power frequencies appear in the spectrum. If the ratio of the length of the sample window to the period of the signal is irrational, an infinite number of extra frequencies are required in the spectrum to build up the signal being analysed. The main frequency components are present but they are 'spread' out and less distinct. Using the Hamming window clearly improves the definition of the frequency spectrum.

6.3.2 Measurements from Operating Wind Turbines

6.3.2.1 Vibrations of the 25 kW Machine

Measurements of vibrations of the 25 kW Carter wind turbine at West Beacon Farm have been obtained at low wind speeds. Below cut-in windspeed. the machine free-wheels. The generator is disconnected from the grid and the speed of the rotor is unconstrained. The advantage is that as the rotor speed changes, the tower modes, which are lower than the normal operating frequency, are excited.

Two accelerometer housings were strapped to the tower at a height of approximately 2 m above ground level (see Figure 6.15). The fundamental lateral tower vibration frequency was occasionally observed to be excited by the conditions.

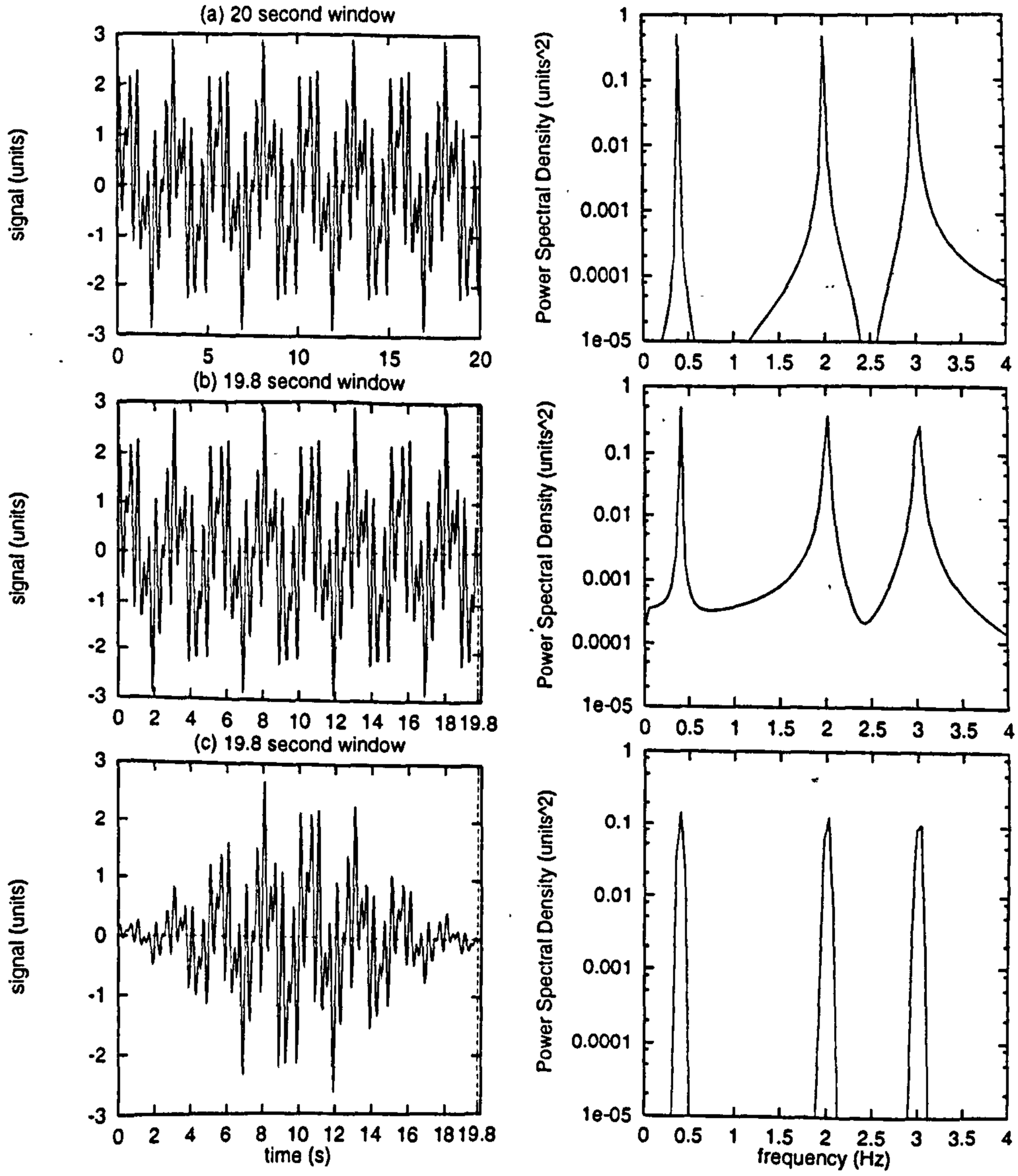

Figure 6.14: Three different time windows. The signal is the same in each case and includes three periodic components at 0.4 Hz, 2 Hz and 3 Hz. The sampling frequency is in all cases 20 Hz. (a) the first time window contains a whole number of periods. Because they have been reduced to 99%, (b) the second and (c) third windows truncate the signal. (c) the third is the same as the second but uses a 'Hamming window' (Equation 6.6).

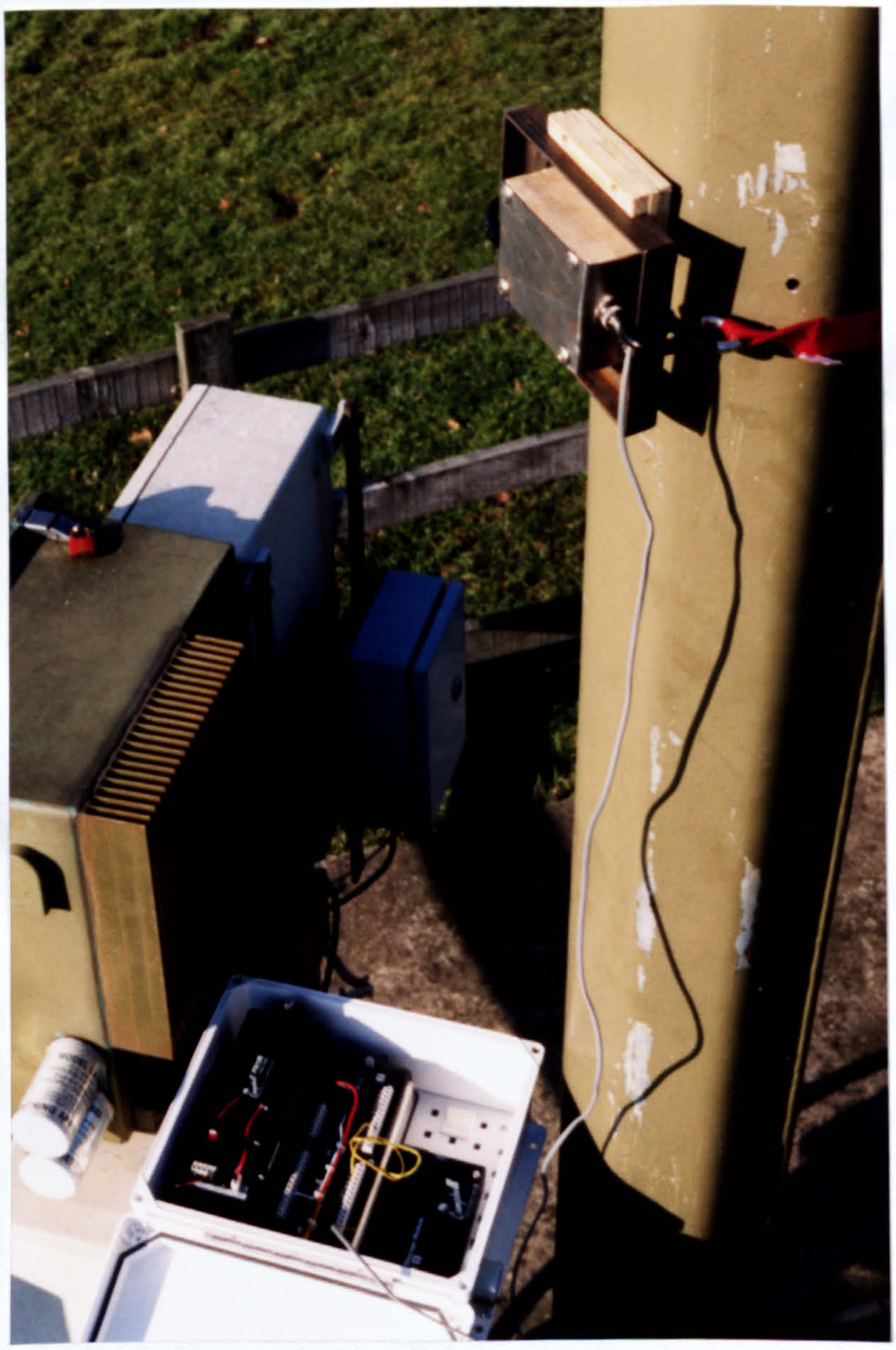

Figure 6.15: The data collection system consisting of the accelerometer housing strapped to the wind turbine tower and connected to the CR10 logger by a screened, four-stranded cable.

Figure 6.16: Noting the direction of the prevailing wind relative to the orientation of the accelerometer on the side of the tower and the orientation of the tower base hinge.

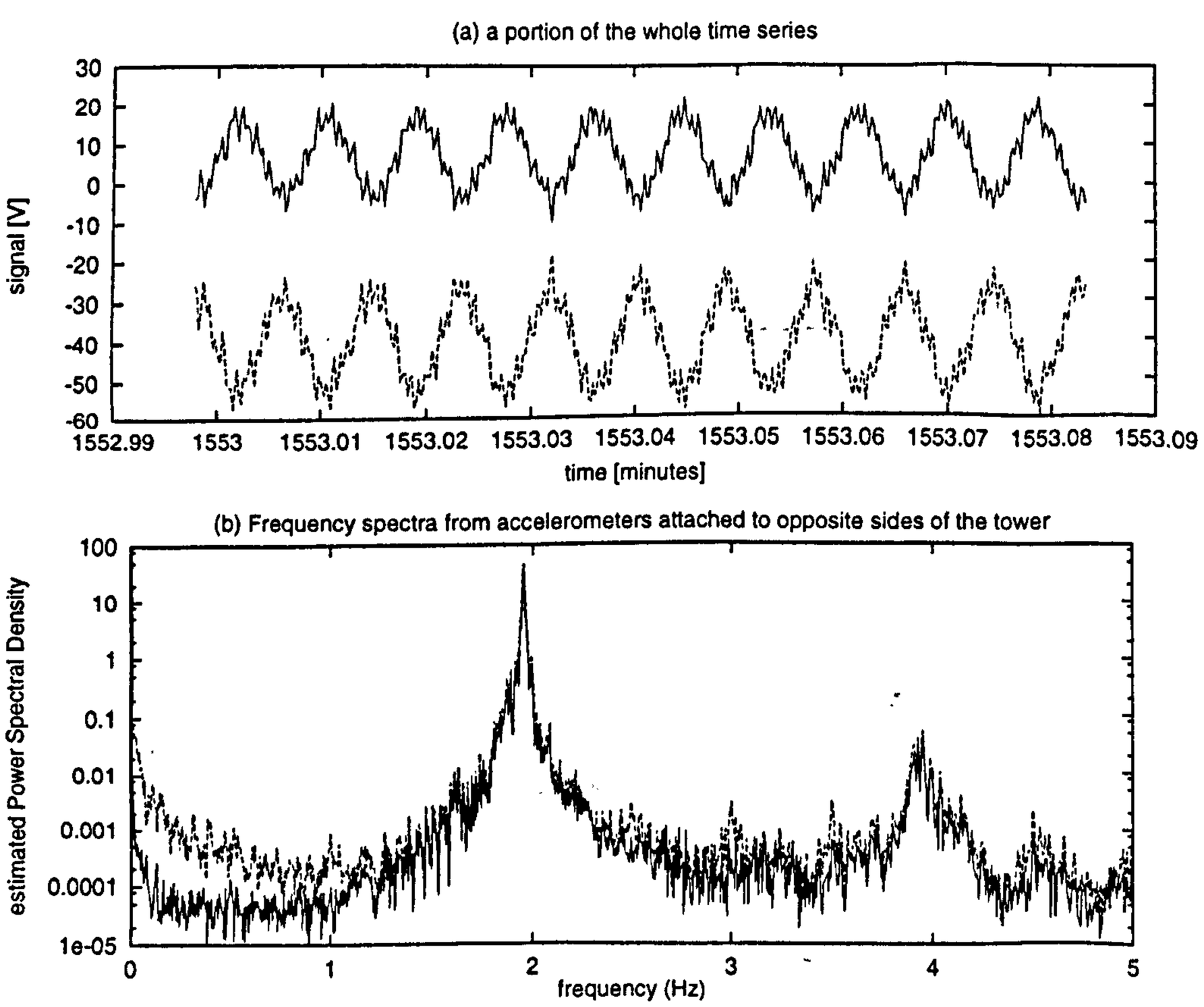

Figure 6.17: Examples of data recorded at West Beacon Farm between 1346 and 1356 on 27th June 1996: (a) sections of the time series from both channels (the higher readings are from channel 1 which is from accelerometer S/N 381697 strapped to the upwind side of the tower nearest the gin pole, the lower readings are from channel 2 which is from accelerometer S/N 559949 on the opposite side of the tower). (b) the power spectra from both accelerometers. During the measurements, the windspeed was variable. At times, the wind turbine was free-wheeling, disconnected from the grid. The wind direction is in the tilt plane of the base hinge. Sampling frequency was 80 Hz.

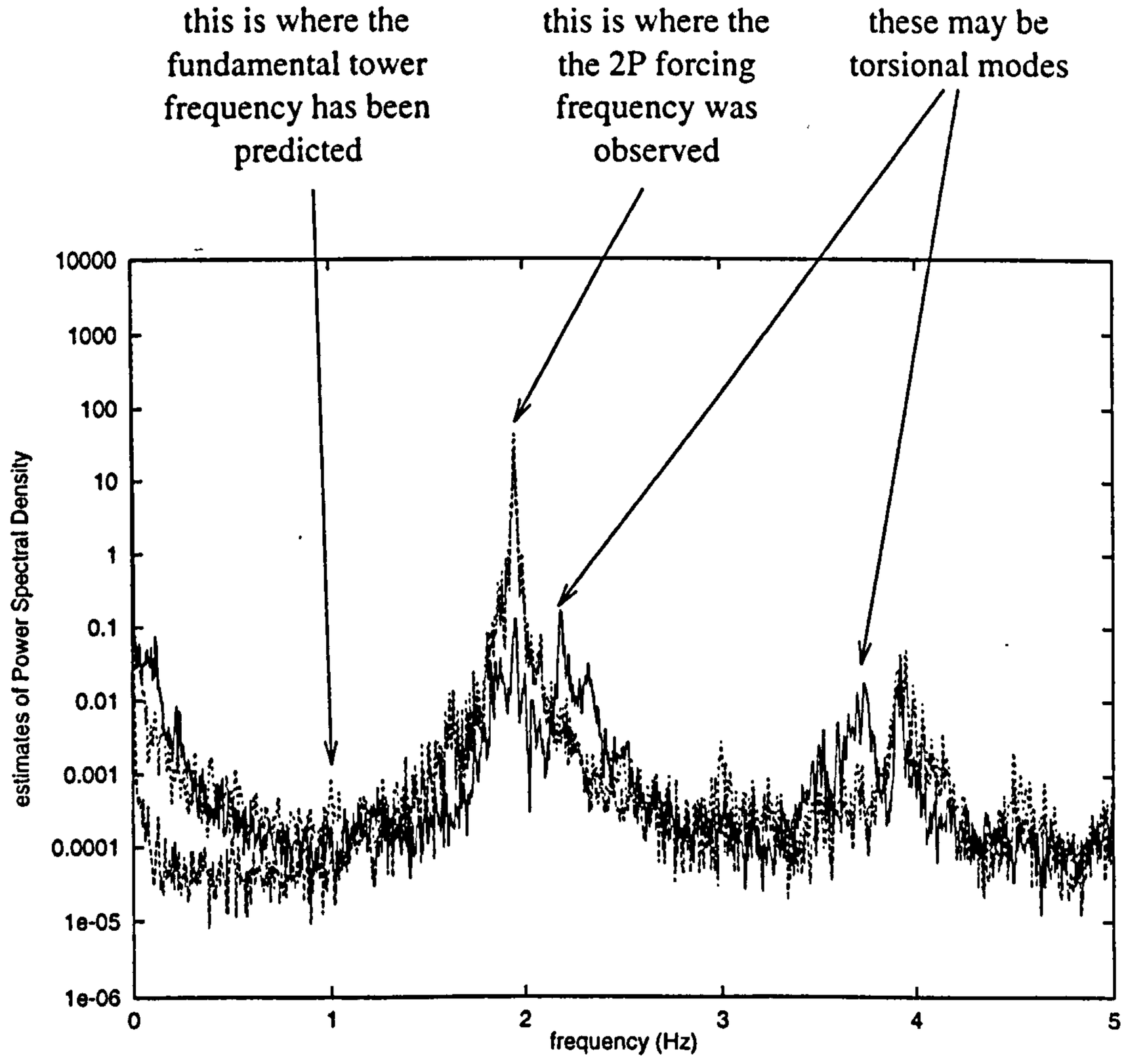

Figure 6.18: Power Spectral Density function estimated from data collected at West Beacon Farm between 1307 and 1317 on 27^{h} June 1996. The accelerometers are strapped to the tower so as to measure torsional vibrations (Section G.1). The dotted lines show the spectra illustrated in Figure 6.17 for comparison. Sampling frequency was 50 Hz.

6.3.3 Results from Acceleration Measurements

Having generated from each data series an estimate of the power spectral density function, the spectrum is examined to find the most prominent peaks.

Data quoted in this section has been analysed using the signal processing routines described in Sections 6.3.1.3 and 6.3.1.4. Unless otherwise stated, 5 overlapping, Hamming windows were used.

Table 6.3: The most prominent peaks on estimates of the power density spectra made on series of data from each of the three machines. Most data series were 10 minutes and 19 overlapping Hamming windows were then used. Most sampling frequencies were 64 Hz. For each machine is listed the number of occurrances of the particular peak as a fraction of the total number of data series examined.

West Beacon farm		Great Orton airfield		Faccombe estate	
frequency (Hz)	number of observations/ total number of experiments	frequency (Hz)	number of observations/ total number of experiments	frequency (Hz)	number of observations/ total number of experiments
1.15	2/16	1.05	4/5	2.12	6/6
1.26	1/16	1.42	2/5	3.09	2/6
1.95	13/16	4.23	5/5	4.24	3/6
2.50	2/16			5.67	3/6
3.00	2/16			6.35	6/6
3.50	2/16				
3.91	11/16				

For the 25 kW Carter wind turbine at West Beacon Farm, the predominant peak on the estimate of the Power Spectral Density function is at 1.95 Hz. This is the frequency of the blades when the generator is connected to the grid ($2P$). Although the tower was seen to vibrate strongly at a frequency close to the predicted fundamental lateral vibration frequency (0.980 Hz), this vibration only lasted a fraction of a second because the frequency of rotation ($2P$) was only 0.980 Hz as the machine free-wheeled prior to synchronisation with the grid. On the occasions when the machines at Great Orton Airfield and Faccombe Estate were analysed, wind speeds were strong and there were no times during which the rotor was seen free-wheeling.

It has not been possible to distinguish the first torsional mode from the first bending mode. This may be because the coupling between the tower and nacelle was relatively flexible and so, the first torsional mode of the tower may be high. It was also difficult to calibrate the accelerometers accurately enough so as to measure absolute accelerations (see Appendix G).

6.3.4 Estimation of Errors

Errors in the quantities measured can be estimated. If the values of the quantity measured are independent and normally distributed, then it can be shown [62] that the estimates of power spectral density have chi-squared distributions.

The estimates of the power spectral density of the signal are obtained at discrete frequencies whose values are determined by the window length, T_F and the sampling frequency. A peak on the power spectral density estimate will be selected as a natural mode of the structure if the following three factors are true:

1. it is sharp,
2. its height is significantly greater than the heights of nearby points on the spectrum and
3. it is observed in the same position on other spectra obtained from the same structure on different occasions.

It would be possible to calculate the probability that the power spectral density at a particular frequency f will be lower than one of its nearest neighbours $f + \frac{1}{T_F}$ or $f - \frac{1}{T_F}$. Given a consistent strategy for selecting a peak, the probability that the peak will be wrongly selected can be calculated. Repeating this calculation for all frequencies on the spectrum would reveal the probability that a peak would be wrongly selected at any distance from the true peak. This would give the probability distribution of values of the natural frequency of interest. From this the standard deviation of frequency estimates can be calculated for each estimate on the spectrum. This has not been reported in this thesis.

However, an estimate of the errors involved in the entire data collection process is the signal to noise ratio. Figure 6.19 shows the same spectra illustrated in Figure 6.17 along with a spectrum obtained from data from one of the accelerometers which had been switched off.

Readings from both accelerometers are not within the noise band at zero frequency. This may be due to any of the following three reasons.

- There is a real d.c. offset as would be expected from one of these accelerometers if it were not accurately aligned perpendicular to the gravitational field. See Appendix G, Section G.2.
- There are systematic errors due to d.c. induced in the electronic circuit.
- Inevitably some vibrations of the tower occur at frequencies too low for a whole period to fit within the sampling window. Truncation of the signal introduces high frequencies which may be aliased to the low end of the Power Spectral Density function. Truncation can be minimised by taking long windows of data (10 minutes in this case) and by using non-square windows. See Section 6.3.1.4.

Backgound noise has only been plotted in Figure 6.19 for Channel 1. However. the background noise can be estimated by measuring the power in the spectrum between distinct

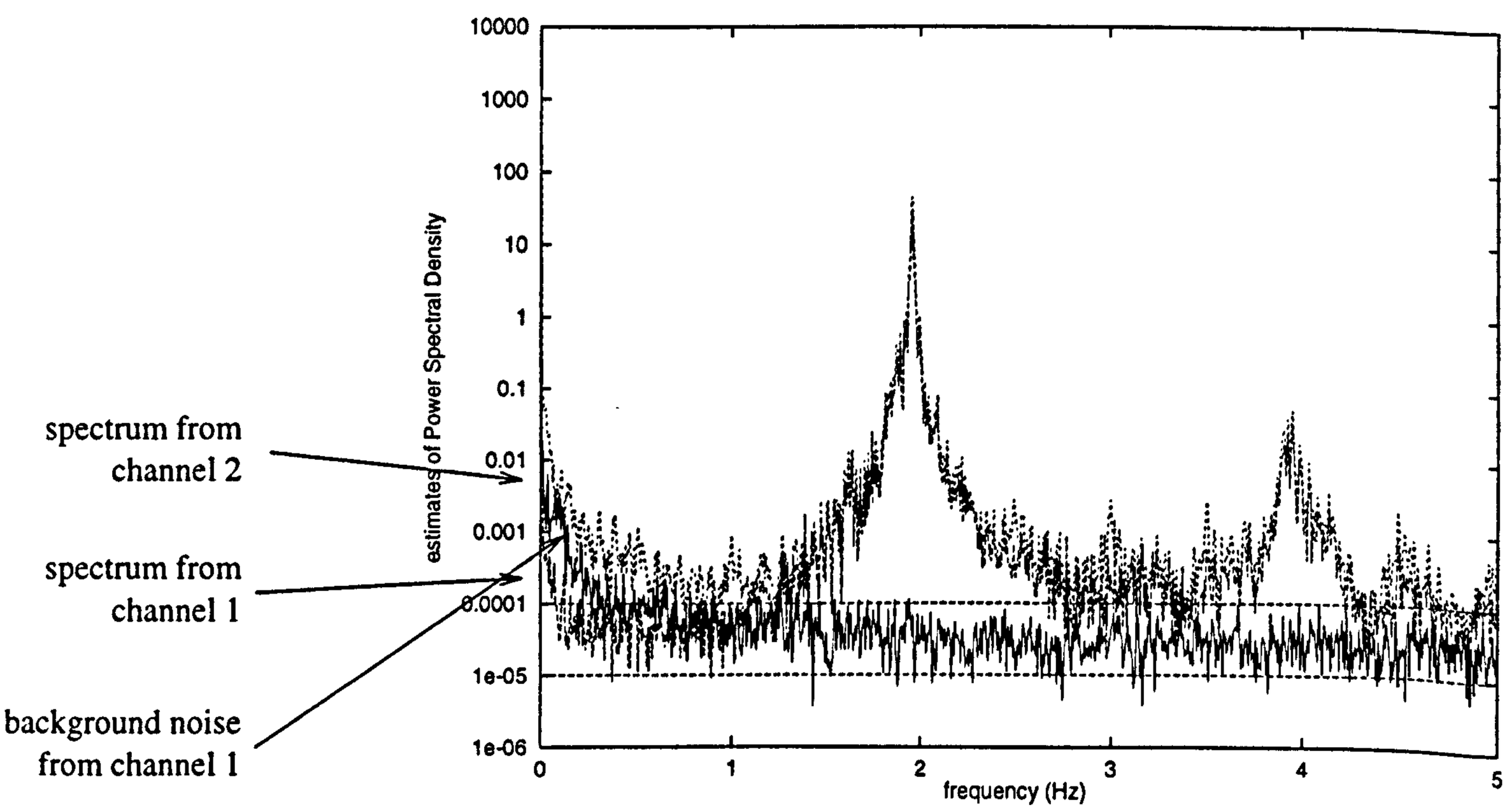

Figure 6.19: The background noise passed from an idle accelerometer through the cabling and data collection system to Channel 1 as compared with the estimates of Power Spectral Density illustrated in Figure 6.17 (b). The background noise was collected on 27th June 1996 between 1517 and 1527.

peaks. By comparing the two time series in Figure 6.17 (a), it can be seen that the background noise at zero frequency is greater from Accelerometer 2 than from Accelerometer 1. This is also evident from Figure 6.19 where there is higher power at low frequencies for Channel 2 than for Channel 1. This is likely to be due to differences in alignment or sensitivity between the two accelerometers. At higher frequencies, the background noise is similar for both channels at between 1×10^{-5} and 1×10^{-4}. The signal to noise ratio for all spectral peaks listed in Table 6.3 is at least 10. For the peak at 1.95 Hz, the error in amplitude is $\pm0.0001\%$. The error is therefore $\pm10\%$ or better.

6.3.5 Comparison of Frequency Measurements with Predictions

Table 6.4: Predictions of the lowest frequencies of tower vibration made using the models described in Chapters 2 and 4.

mode predicted	West Beacon Farm	Great Orton Airfield	Faccombe Estate
fundamental bending mode (lower limit: $k_{Bf} = 0$ N m rad^{-1})	0.980	0.670	0.850
fundamental bending mode (upper limit: $k_{Bf} = 1\times10^{12}$ N m rad^{-1})	1.097	0.762	0.917
first harmonic of bending vibrations (lower limit: $k_{Bf} = 0$ N m rad^{-1})	3.820	1.749	3.328
first harmonic of bending vibrations (upper limit: $k_{Bf} = 1\times10^{12}$ N m rad^{-1})	5.004	2.334	4.481
fundamental torsional mode (lower limit: $k_{Yn} = 1\times10^{20}$ N m rad^{-1})	3.125	2.303	2.777
fundamental torsional mode (upper limit: $k_{Yn} = 0$ N m rad^{-1})	22.497	13.722	19.724

The measurements did not show a large response at the fundamental bending frequency for any of the three commercial machines. This may have been because the forcing frequency

Table 6.5: Predominant two frequencies measured using accelerometers attached to the lower end of the tower (Hz).

West Beacon Farm	Great Orton Airfield	Faccombe Estate
1.15	1.05	2.12
1.95	4.23	4.24

was predominantly much higher. In fact, it is desirable that normal operating conditions provide very little excitation of the fundamental tower mode. In the case of the Carter 25 kW wind turbine at West Beacon Farm there were significant periods during which the fundamental bending mode could be seen to be excited. It may be that the position of the accelerometers was not optimal to measure the tower movements sought.

6.3.6 Future Acceleration Measurements

Several practical measures can be taken to improve the quality of the data series from future activities. Many of these points did not prove possible because they would have involved disrupting the generation of electricity by the commercial machine (tilting the tower down to attach accelerometers or exciting particular modes).

As mentioned in Section 6.3.5, the modes predicted were not measured sufficiently strongly. This could have been overcome in two ways: firstly, through better excitation of natural modes of vibration. This is normally achieved by subjecting the system to an impulse or to white noise either of which consist of many frequencies of equal amplitude. The response of the system at any one frequency can then be compared with the response at any other frequency.

Secondly, even though the excitation of the system was less than ideal, the analysis of the results could be improved. Using wavelet transforms rather than Fast Fourier Transforms, snapshots of the power spectral density of the system response could be recorded at different times. If the fundamental tower frequency was observed to be excited only for a fraction of a second, the power spectral density function of the system response at that moment on the time axis would reveal what frequency that movement corresponded to.

Another improvement to the analysis of the existing data would be to automate the recognition of spectral peaks to improve accuracy. For this analysis, the frequencies of spectral peaks were estimated by hand from graphs of power spectral density.

A list of specific improvements to the experimental method is given below:-

systematic positioning of accelerometers The accelerometers were placed on the tower by hand and so the positions were limited by the author's height. If the wind turbine had been stopped and the tower lowered to the ground, the accelerometers could have been attached higher up the tower.

measure events As with the video measurements, specific events known to excite certain vibration modes could form the basis for measurements. Machine shutdown is one such event. Others would be more specifically controlled such as exciting the tower at a known frequency by moving or changing the tension in one of the cables. These experiments could be carried out under otherwise similar conditions.

measure rotor speed The speed of rotation of the wind turbine's rotor could be logged simultaneously with the accelerometer outputs. The measurements of tower frequency could then be matched to measurements of excitation frequency from the rotor. The clarity of comparions between excitation and response frequencies could be improved by using Wavelet transforms as mentioned above.

restrict the real system In order to model the real system, it can be restricted or simplified during test work. Examples of this strategy are engaging the rotor or yaw brake and replacing the rotor and nacelle with something with the same total mass but concentrated at the tower top (negligible moment of inertia).

measure mode shapes By attaching many accelerometers to the tower at different heights. the accelerations of points on the tower can be recorded simultaneously. From this information the mode shape can be measured as well as the modal frequency using the imaginary part of the Fourier transforms of the signals as illustrated later in Figure 6.21 and described in Chapman and Turnbull's paper [63].

filter data The filters used required 240 V mains electricity which was not available at the bases of Great Orton and Faccombe towers. Portable, battery-powered filters could be incorporated into the accelerometer housings to prevent aliasing of data. For this, two 12 V, rechargeable batteries would need to be carried in addition to the one already used to power the Campbell logger. Existing logging equipment only requires one.

In order to subtract acceleration readings, the absolute values recorded by each instrument had to be calculated. The calibration planes for each accelerometer were estimated (see Appendix G) and the voltage of the 9 V battery was recorded at the beginning and end of each data collection run. The fall in battery voltage during each run was probably not linear. In a future experiment it could be recorded by the data logger at the same time as the acceleration measurements.

Even the data series obtained from two such different accelerometers can be normalised assuming that the acceleration of the two instruments was the same during excitation of the fundamental lateral tower vibration mode. From specific periods of the time series normalising factors could be calculated to enable the data to be subtracted and the power spectrum of tower torsional vibrations to be estimated.

The intention in the original plan for the AMSET Centre was to establish a test site for a Carter 300 kW wind turbine. With an experimental machine, a schedule of experimental work would have been devised. Initially, the machine would be monitored under controlled circumstances in order to test simple analysis techniques. Later, its behaviour under normal operating conditions would be studied and finally, analysis techniques might have to be developed to explain unusual responses.

6.4 Monitoring Program on 300 kW Wind Turbine

Between 1993 and 1996, a formal monitoring program was being conducted by Garrad Hassan and Partners Ltd. on behalf of the Energy Technology Support Unit [22]. The intention was for a complete operational survey of the machine's static and dynamic behaviour. A second purpose was to validate Garrad Hassan's commercial software: `Bladed for Windows` for a soft structure.

The rotor was monitored with 4 strain gauges on one blade and 2 on the other. The tower was monitored in each of two orthogonal planes with 3 strain gauges along its length (at heights of 18 m, 36 m and 47 m) and one strain gauge on each of the guy turnbuckles

(see Figure 6.20). No explicit excitation of tower frequencies was attempted. Measurements were made:-

1. during normal operation and

2. with the rotor parked and wind blowing past the rotors and tower.

Unfortunately, the time series data have not been available. Given simultaneous time series from all the strain gauges, the mode shape could be estimated for any single frequency. The Fourier transform would be taken of each time series. At each resonant frequency, the imaginary part of the transform would be plotted against the distance up the tower of the strain gauge. The procedure is discussed by Turnbull and Chapman [63]. By fitting a curve through the points, the mode shape at that frequency could be estimated.

This is illustrated in Figure 6.21 for a mathematical function of both time and distance given in Equation 6.7. v_a is an arbitrary wave amplitude and ω is an arbitrary wave angular frequency.

$$v = v_a \sin\left(\pi \frac{X}{\lambda_{ct}}\right) \cos(\omega t) \tag{6.7}$$

With only three strain gauges, the estimate would not be precise. It would, at least, be possible to distinguish first, second and third bending modes. The frequency of the first torsional mode could also be identified.

The procedure relies on all strain gauges giving the same output for a given strain. This is unlikely. They could, however, be calibrated with respect to a reference strain or reference state of strain for the structure. By dividing every output by the particular value of this reference strain for the particular strain gauge, comparisons could be made.

Frequency spectra have been obtained for many data streams. For each spectral peak, the mode of vibration to which it corresponds has been inferred from position of the measurement device. The results are summarised in Table 6.6.

The 0.74–0.76 Hz mode is probably the first bending mode of the tower since it is spectra from the tower bending moment signals which show the largest relative peaks at those frequencies. This is similar to the frequencies predicted theoretically for the extreme boundary base conditions (hinged and built in) by Finite Element analysis and the Rayleigh/ Stodola method (see Figure 5.20: 0.690 Hz–0.776 Hz). In fact, the comparison suggests that the base is nearer built in. There was no explanation for or detailed description of the complex mode whose frequency lies in the range [4.12, 4.18].

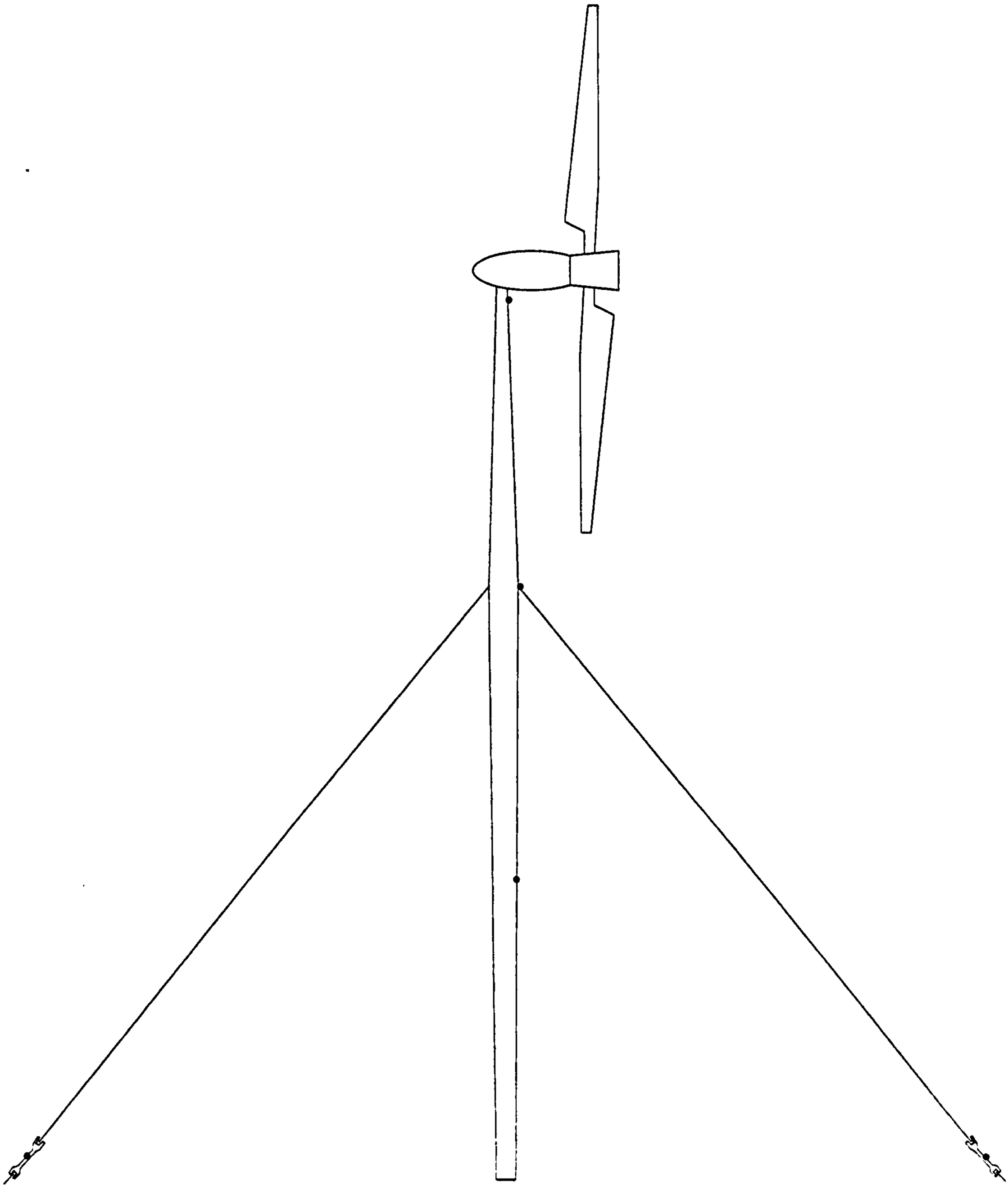

Figure 6.20: The positions of the strain gauges measuring tower bending moments and guy tension in one plane for the survey of the Carter 300 kW wind turbine by Garrad Hassan and Partners Ltd. There are the same number of strain gauges measuring tower bending moments and guy tension in the orthogonal plane (not shown here).

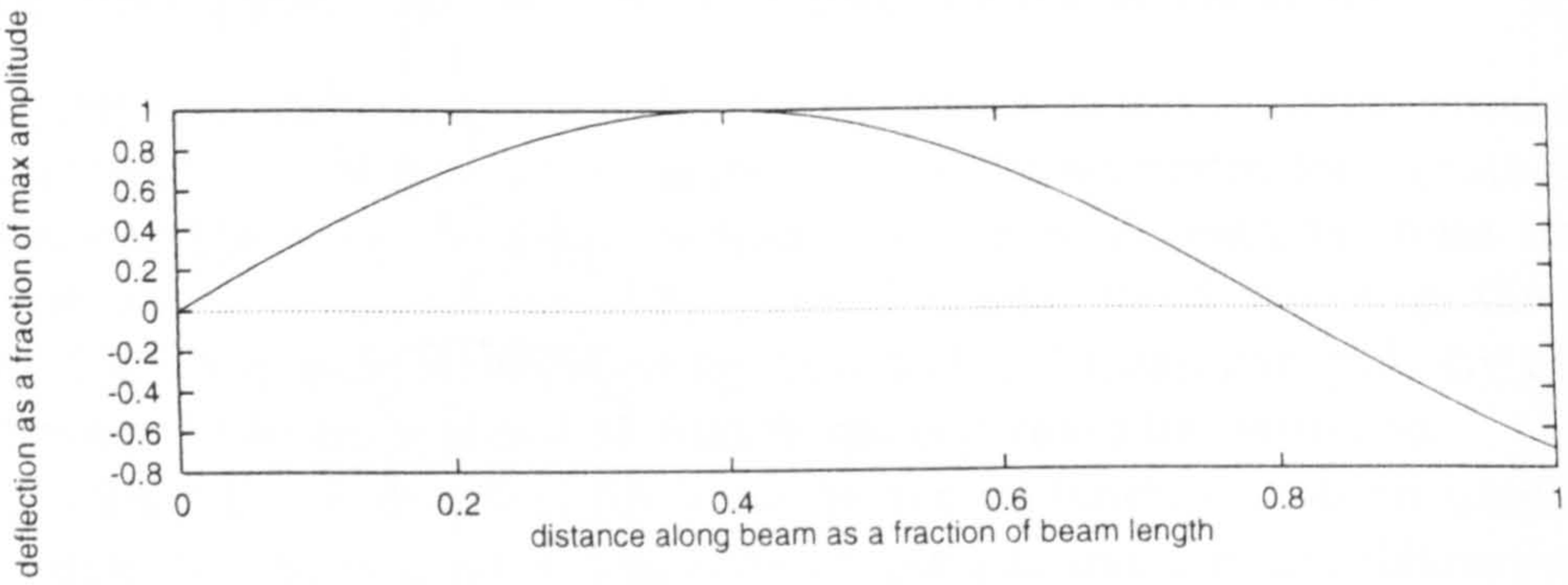

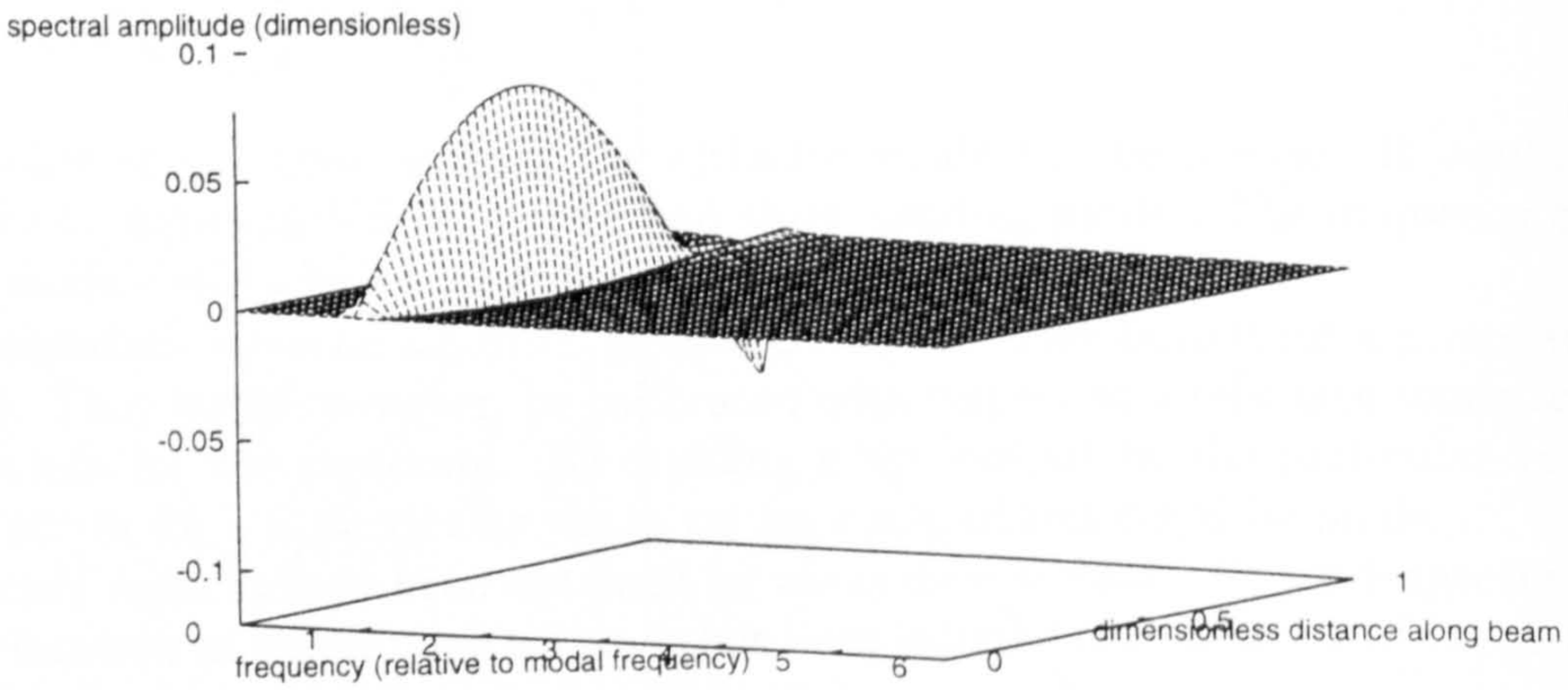

Figure 6.21: The deflection shape of a beam simply supported at one end and part way along. The deflection is at a snapshot in time. The motion with respect to time of each of 50 stations along the beam has also be calculated. Using Fourier transforms of these time series, the variation of spectral power with position can be estimated. The second plot is of the imaginary component of these Fourier transforms. The mode shape is clearly proportional to the variation of amplitude with distance along the beam at the resonant frequency.

Table 6.6: Table of tower frequencies measured and identified visually by Garrad Hassan and Partners Ltd. Variations are due most often to the different wind speed values at which spectra were calculated.

frequency (Hz)	description of mode by signal involved
0.74–0.76	tower movement
1.31	tower side-to-side (vertical rotor position)
1.39–1.46	tower fore-aft
2.64	assymmetrical flatwise rotor movement, teeter movement and tower movement (rotor parked vertically and nacelle between two sets of guys)
3.34	symmetrical edgewise rotor movement and tower movement
3.91	edgewise rotor movement, fore-aft nacelle movement, tower movement in 'y' direction (rotor parked horizontal)
4.12–4.18	asymmetrical edgewise rotor movement, lowspeed shaft torsion, nacelle side-to-side movement, nacelle fore-aft movement, nacelle yaw and tower roll-nodding
5.12–5.18	tower movement

Chapter 7

Comparing Tower Models of Different Complexity

7.1 Simple Models of Tower Designs

Because towers are slender and changes of cross section and materials with height are only slight, the models needed for structural analysis are often not complex. The simpler and more direct the models are, the quicker the results are obtained and the easier it is to see the relationship between the model parameters and the design outcomes (such as ultimate buckling load, maximum stress or vibration frequencies). Designers are thus enabled to appreciate general trends.

In some situations models which are even simpler than the *general numerical methods* described in Chapters 2, 3 and 4 are adequate to simulate real designs. Throughout this section comparisons will be made between results from the general methods proposed here and simpler models. Because the designs considered are hypothetical, no comparisons can be made with structures actually built.

The simplest models have already been described and are those used for validation purposes in Chapter 5.

7.1.1 Longitudinal Vibrations

For a real tower such as that used for the Carter 300 kW wind turbine (of the type used at Great Orton Airfield), $E_t A_{xt}$ is not constant over the height of the tower. However, the simple models represented by Equations 5.24 to 5.26 for a lumped mass on a light spring and by Equation 5.27 for vibrations of a heavy bar with zero nacelle mass are appropriate for certain combinations of design parameters. Results predicted by the simple models (Section 5.1.3.3) can be compared with the *general, numerical model* described in Section 4.7.2 (and based on the Rayleigh/ Stodola method).

Figure 7.1 compares the fundamental longitudinal frequencies predicted using three models. For the case of the tower design used for the Carter 300 kW wind turbine (Great Orton Airfield type). if the nacelle mass is less than 390 kg. the difference between the continous bar model and the Rayleigh/ Stodola model is less than 5%. Similarly. if the mass is greater than

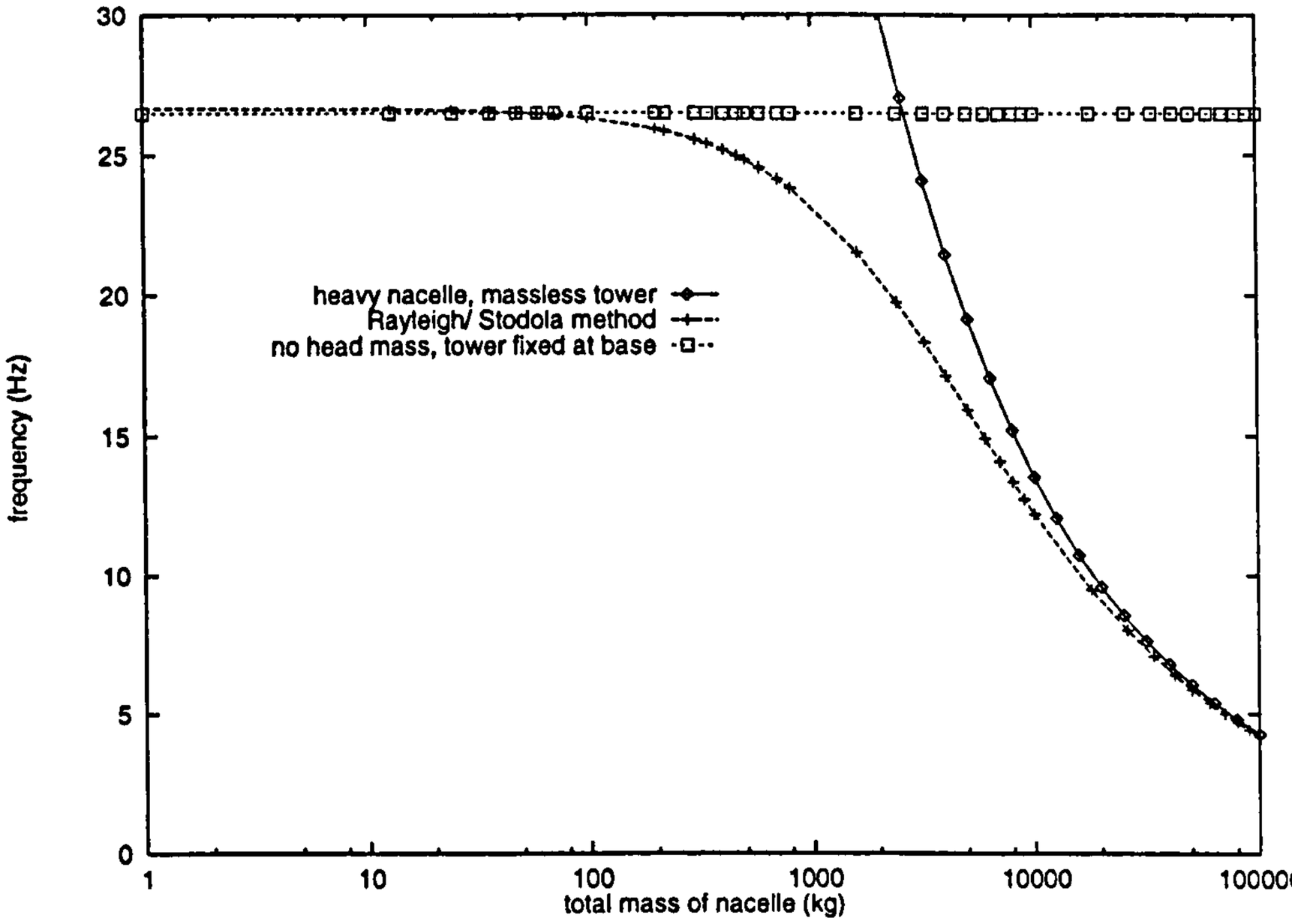

Figure 7.1: Comparison between fundamental longitudinal frequencies of three models of a wind turbine tower obtained by varying the total mass, M_n of the nacelle. The model which is analysed using the Rayleigh/ Stodola method is the only one to include the guy cables. In this model, as in the other two, the tower is uniform. Values predicted using this method can be seen to be similar to frequencies of vibration of a bar when the nacelle is small and to be similar to values predicted using a lumped mass/ light spring model when the nacelle is large. The density of the tower is 7800 kg m^{-1} in all cases.

24000 kg, the difference between the lumped mass/ light spring model and the Rayleigh/ Stodola model is less than 5%. For the Carter 300 kW machine the nacelle mass is 4780 kg and so the difference between the Rayleigh/ Stodola and the lumped mass/ light spring models is 22%. Despite its complexity, the general numerical model is therefore justified for analysis of this design.

For structures in which the nacelle mass is very small, the Rayleigh/ Stodola method predicts values of the fundamental longitudinal frequency higher than the continuous bar model. This is because the extra stiffness in the system due to the guy cables is included in the Rayleigh/ Stodola model but not in the continuous bar model.

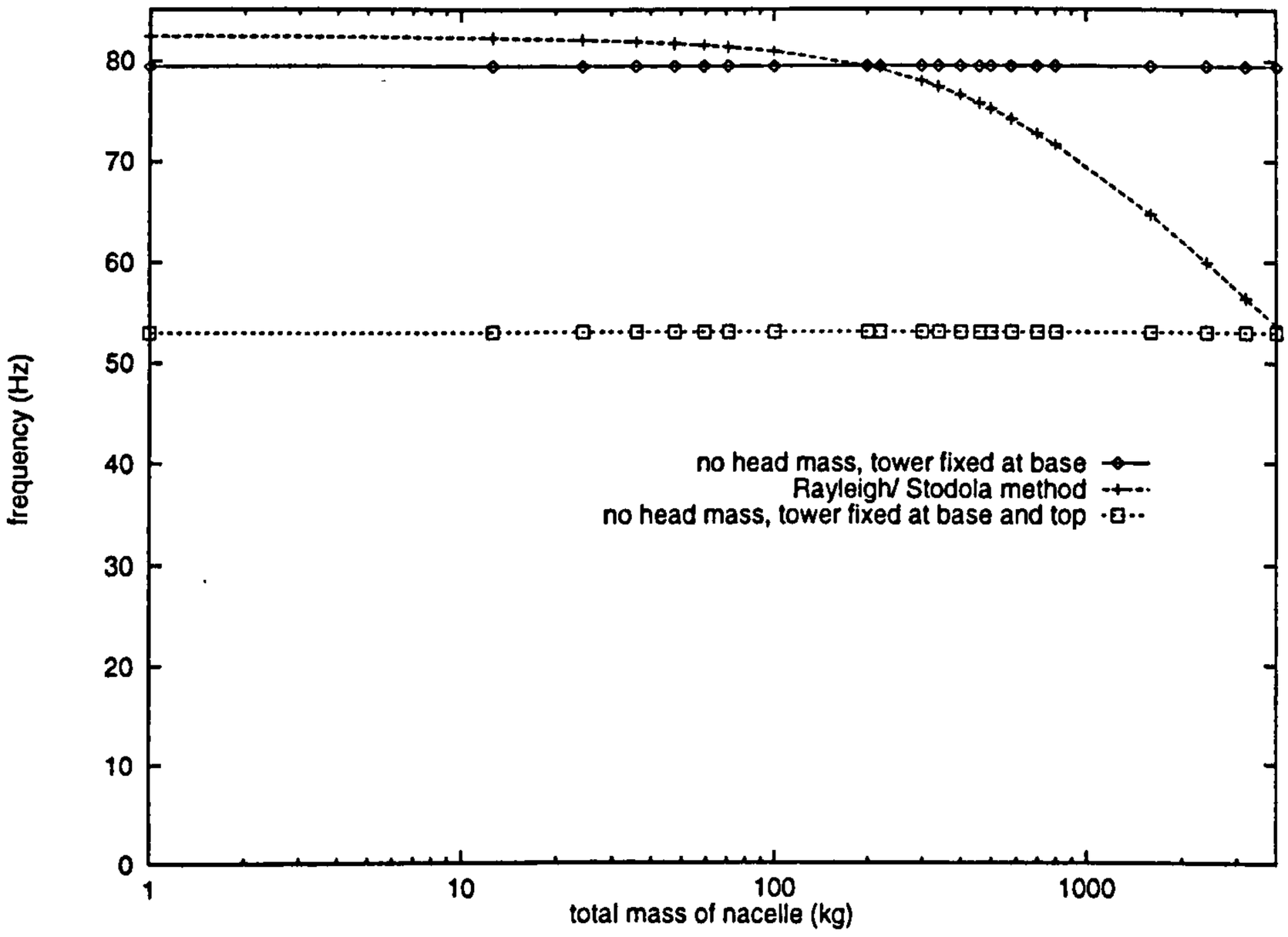

Figure 7.2: Comparison between longitudinal first harmonic frequencies of three models of a wind turbine tower obtained by varying the total mass, M_n of the nacelle. The model which is analysed using the Rayleigh/ Stodola method is the only one to include the guy cables. In this model, as in the other two, the tower is uniform. Values predicted using this method can be seen to be similar to frequencies of vibration of a bar fixed at the bottom when the nacelle is small and to be similar to frequencies of vibration of a bar fixed at the bottom and the top when the nacelle is large. The density of the tower is 7800 kg m^{-1} in all cases.

Figure 7.2 shows predictions of the first harmonic longitudinal frequency of three different models.

1. Vibration of a uniform bar fixed at the bottom and free at the top.

2. Vibration of the guyed tower structure used for the Carter 300 kW wind turbine (Great Orton Airfield type) predicted using the Rayleigh/ Stodola method.

3. Vibration of a uniform bar fixed at both ends.

The model based on Rayleigh's and Stodola's techniques is the most general. The transition of the values predicted using this method can be seen between those similar to the first model listed above towards the third model. It is interesting that for structures with massive nacelles, the results from the Rayleigh/ Stodola method and frequencies of a bar fixed at both ends are similar. This implies that the first harmonic mode shape of the guyed wind turbine tower has a node near the top of the tower. This may be because, as the nacelle mass increases, the contribution from the nacelle to the maximum kinetic energy of the system increases (Equations 4.70 and 4.71). The fundamental mode shape will have a large deflection of the tower top with a steep gradient near the top. When used in Equation 4.43 to find the first harmonic mode shape, this fundamental shape gives rise to a first harmonic mode shape with a small deflection of the top relative to the rest of the tower. This method is used by Niblett [44] to model an *encastré–encastré* beam using a *free–free* beam with end masses and moments of inertia.

7.1.2 Torsional Vibrations

The same transition between predicted values of natural frequency can be observed for torsional vibrations of the tower as described in Section 7.1.1 for longitudinal vibrations. For this section, the Rayleigh/ Stodola model has been used to analyse a tower whose outside radius is not independent of height. This double-tapered tower is the same as for the Carter 300 kW wind turbine of the type used at Great Orton Airfield.

As long as the moment of inertia, J_{nv} is small, a model of the structure consisting of a heavy bar with no nacelle predicts frequencies which are similar to those predicted using the more general Rayleigh/ Stodola method. If J_{nv} is very large, results from the Rayleigh/ Stodola method are similar to results from a model consisting of a mass with moment of inertia J_{nv} on a light, torsional spring. The torsional spring stiffness parameter iscalculated using Equation 5.26.

Figure 7.3 shows the transition of the most accurate frequency calculations between the results of the two simplest models. Unlike Figure 7.1 for longitudinal vibrations, the Rayleigh/ Stodola frequencies are initially lower than those for the continuous torsion bar by 18% of the Rayleigh/ Stodola values. This is because it is the average polar second moment of inertia of the tower $\bar{J}_{xt}$ that is used in calculating the frequencies of a continuous bar (Equation 7.1). The actual variation for the double-tapered tower that is used for the Carter 300 kW wind turbine gives rise to a significant decrease in overall stiffness. Using the Rayleigh/ Stodola technique the fundamental mode shapes of two towers has been calculated and can be compared in Figure 7.4. One tower is cylindrical with parallel sides, the other has double-tapered sides like the towers used for Carter 300 kW wind turbines.

$$\bar{J}_{xt} = \left(\frac{1}{(N_s-1)(N_n-1)+1}\right)\frac{\pi}{2}\sum_{i=0}^{(N_s-1)(N_n-1)}\left(r_o^4-(r_o-t_t)^4\right) \qquad (7.1)$$

In Figure 7.4, the mode shape of a parallel-sided, cylindrical tower is a quarter sinusoid. The mode shape of a double-tapered tower of the same geometry as the tower used for the Carter 300 kW wind turbine has a significantly higher gradient near the tower base because the torsional stiffness of the tower is significantly lower there. This relationship between

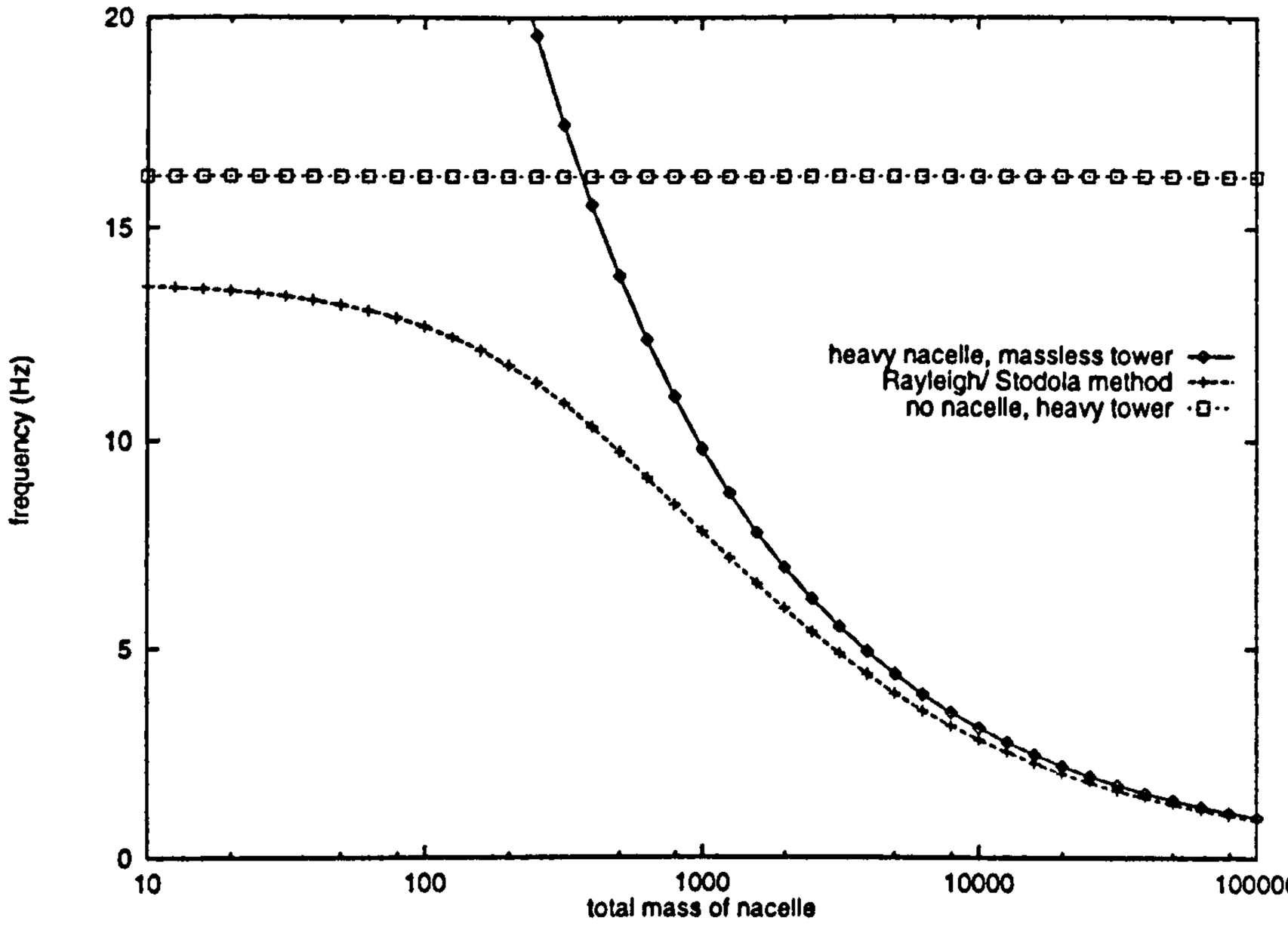

Figure 7.3: Comparison between fundamental torsional frequencies of three models of a wind turbine tower obtained by varying the moment of inertia, J_{nv} of the nacelle. The model which is analysed using the Rayleigh/ Stodola *method is the only one to include the guy cables and the only one in which the tower is double-tapered. Values predicted using this method can be seen to be similar to frequencies of vibration of a bar when the nacelle is small and to be similar to values predicted using a lumped mass/ light spring model when the nacelle is massive. The density of the tower is 7800 kg m^{-1} in all cases.*

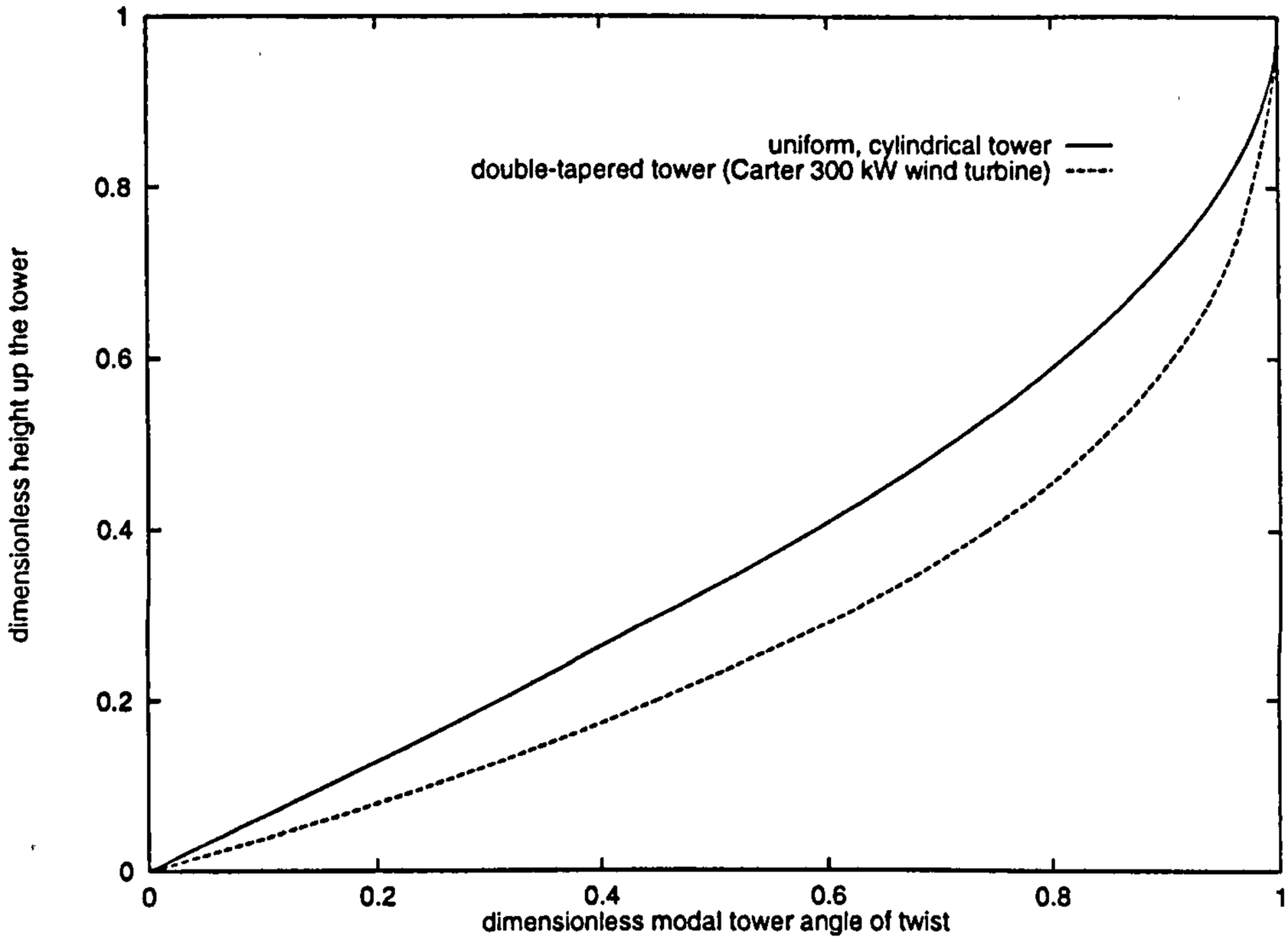

Figure 7.4: Comparison between fundamental torsional modes of two systems. In one the outside radius of the tower is invariant with height and the tower is a parallel-sided cylinder. By direct solution of the wave equation for torsional vibrations, the fundamental frequency is 16.24 Hz. In the other, the tower outside radius varies in the same way as the tower of the Carter 300 kW wind turbine. The fundamental frequency calculated using the Rayleigh/ Stodola method is 13.72 Hz. All other design parameters are as for the Carter 300 kW wind turbine.

the torsional rigidity, $G_t J_{xt}$ and the gradient of the mode shape arises from the differential equation of static deflection in response to a torque, Q_t in the tower at a height x given in Equation 2.30. Near the top of the tower, although the torsional stiffness is again lower than the average for the tower, the mass per unit length is also lower than the average. During vibration of the structure, the decreased mass relative to a parallel-sided tower decreases the inertia torque in that region of the tower (Equation 2.30). This gives rise to a mode shape with a less steep gradient near the top of the tower.

7.1.3 Bending Vibrations

Certain structures can be modelled well by the two simplifications described in Chapter 5. In this section, the density of the tower and the mass of the nacelle are varied and the two models compared with the *general, numerical model* described in Chapter 4.

1. For the first model, it is assumed that the tower mass is small in comparison with the nacelle mass. The tower is treated like a linear elastic spring. The spring constant is estimated by calculating the deflection for a unit force applied at one end ($k_{(\mathrm{eq})B} = \frac{dF_{nh}}{dv(H)}\Big|_{v(H)=0}$). Formulae for this spring constant are given in

   (a) Equation 7.2 (built in base, free tower),

   (b) Equation 7.3 (built in base, guyed tower),

   (c) Equation 7.4 (hinged base, free tower).

   (d) and Equation 7.5 (hinged base, guyed tower).

2. The second is the Rayleigh/ Stodola method described in Chapter 4.

3. The third assumes small head mass and involves the solution of the biharmonic equation 4.1 for bending vibrations of a slender, cantilevered beam (Figure 5.11(b)).

$$k_{(\mathrm{eq})B} = \frac{E_t I_{xt}}{\frac{1}{3}H^3} \tag{7.2}$$

$$k_{(\mathrm{eq})B} = \frac{E_t I_{xt}}{H^3}\left(\frac{\left(\frac{E_t I_{xt}}{k_{Bc}H^3}+\frac{1}{3}\lambda_{ct}^3\right)}{\frac{1}{3}\left(\frac{E_t I_{xt}}{k_{Bc}H^3}+\frac{1}{3}\lambda_{ct}^3\right)+\left(\frac{1}{6}-\frac{1}{2}\lambda_{ct}-\frac{1}{6}\left(1-\lambda_{ct}\right)^3\right)\left(\frac{1}{2}\lambda_{ct}^2-\frac{1}{6}\lambda_{ct}^3\right)}\right) \tag{7.3}$$

$$k_{(\mathrm{eq})B} = 0 \tag{7.4}$$

$$k_{(\mathrm{eq})B} = \frac{E_t I_{xt}}{H^3}\left(\frac{\lambda_{ct}^2}{-\frac{1}{6}\lambda_{ct}^2+\left(\frac{1}{6}-\frac{1}{6}\left(1-\lambda_{ct}\right)^3\right)\lambda_{ct}+\frac{E_t I_{xt}}{k_{Bc}H^3}+\frac{1}{6}\left(\lambda_{ct}-1\right)\lambda_{ct}^3}\right) \tag{7.5}$$

A tower which is built in at the base but has no guys is a free-standing structure, similar to many used by commercial machines. This is illustrated schematically in Figure 5.11 (b). Using data for the Carter 300 kW wind turbine tower design but varying only the tower head mass, the comparisons in Figure 7.5 have been obtained. The three different analytical approaches outlined above have been used.

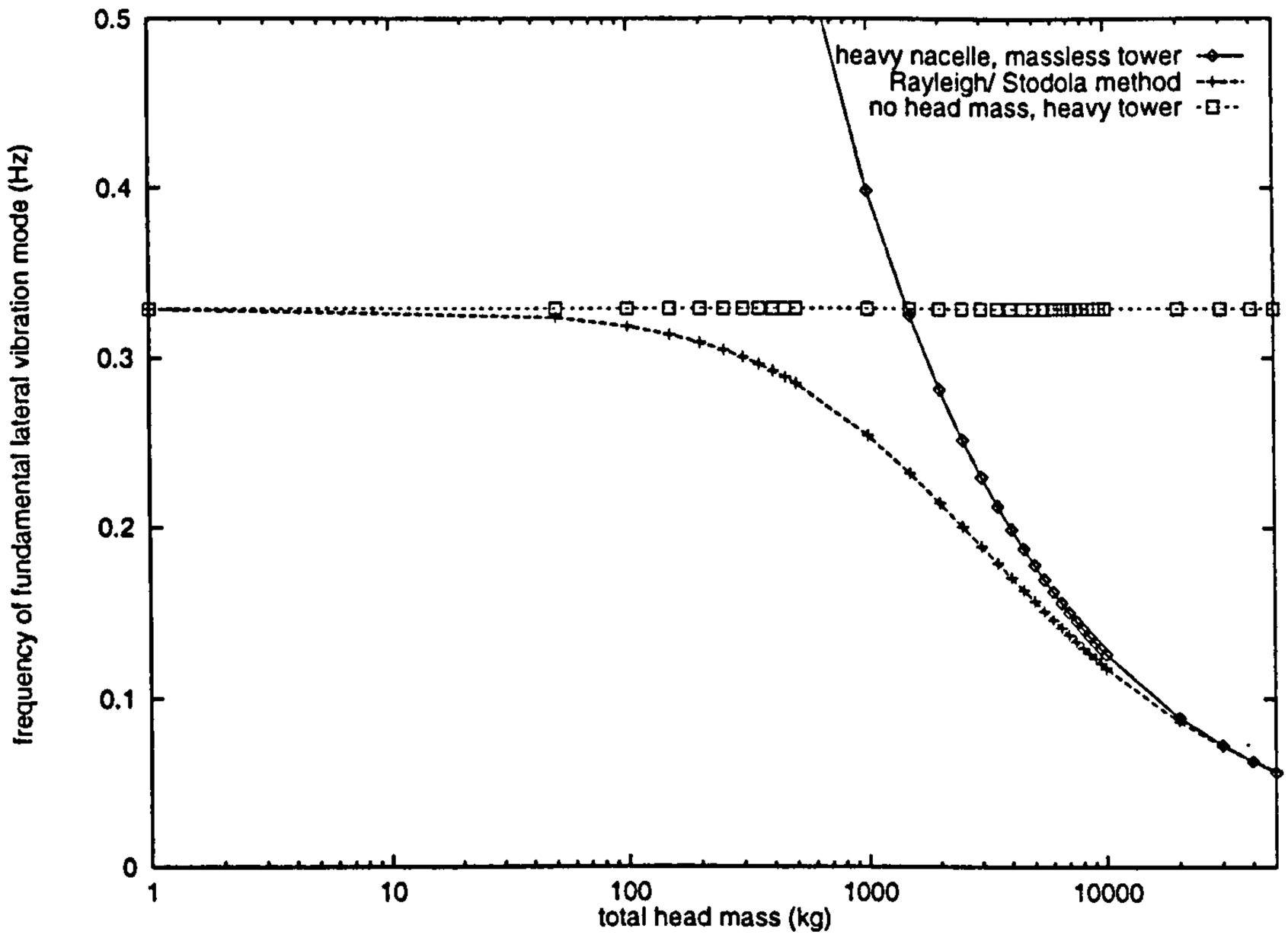

Figure 7.5: Comparison between estimates from three models: two involving direct mathematical solution of the equations of motion and one using the Rayleigh/ Stodola iterative process. The nacelle mass is varied and estimates made of the fundamental frequency of bending vibrations using each of three models. The tower is based on the Carter 300 kW design but is unguyed, free-standing and cylindrical (uniform cross-section). The nacelle moments of inertia are zero ($J_{nr} = J_{nt} = 0$). The boundary conditions used for both models are: free top and built in base. A logarithmic scale is used for the horizontal axis.

Figure 7.5 shows the transition of the behaviour of the Rayleigh/ Stodola method for free-standing tower designs. For low head mass, there is good agreement between the solution of the biharmonic equation for a continuous beam and the Rayleigh/ Stodola approach but at high values of the nacelle mass, the tower natural frequency has fallen well below that predicted by analysis of a beam alone. At large values of the head mass, the lumped mass model yields results very close to those from the Rayleigh/ Stodola method. It is therefore often adequate to use one of the methods which is simpler and quicker than the Rayleigh/ Stodola method.

It is also possible to see this transition by varying the density of the tower (Figure 7.6) but keeping the nacelle mass constant at 4780 kg. In this case, at low values, the Rayleigh/ Stodola model produces results which agree well with results from the lumped mass model. As the tower density increases, the results become closer and closer to those from the con-

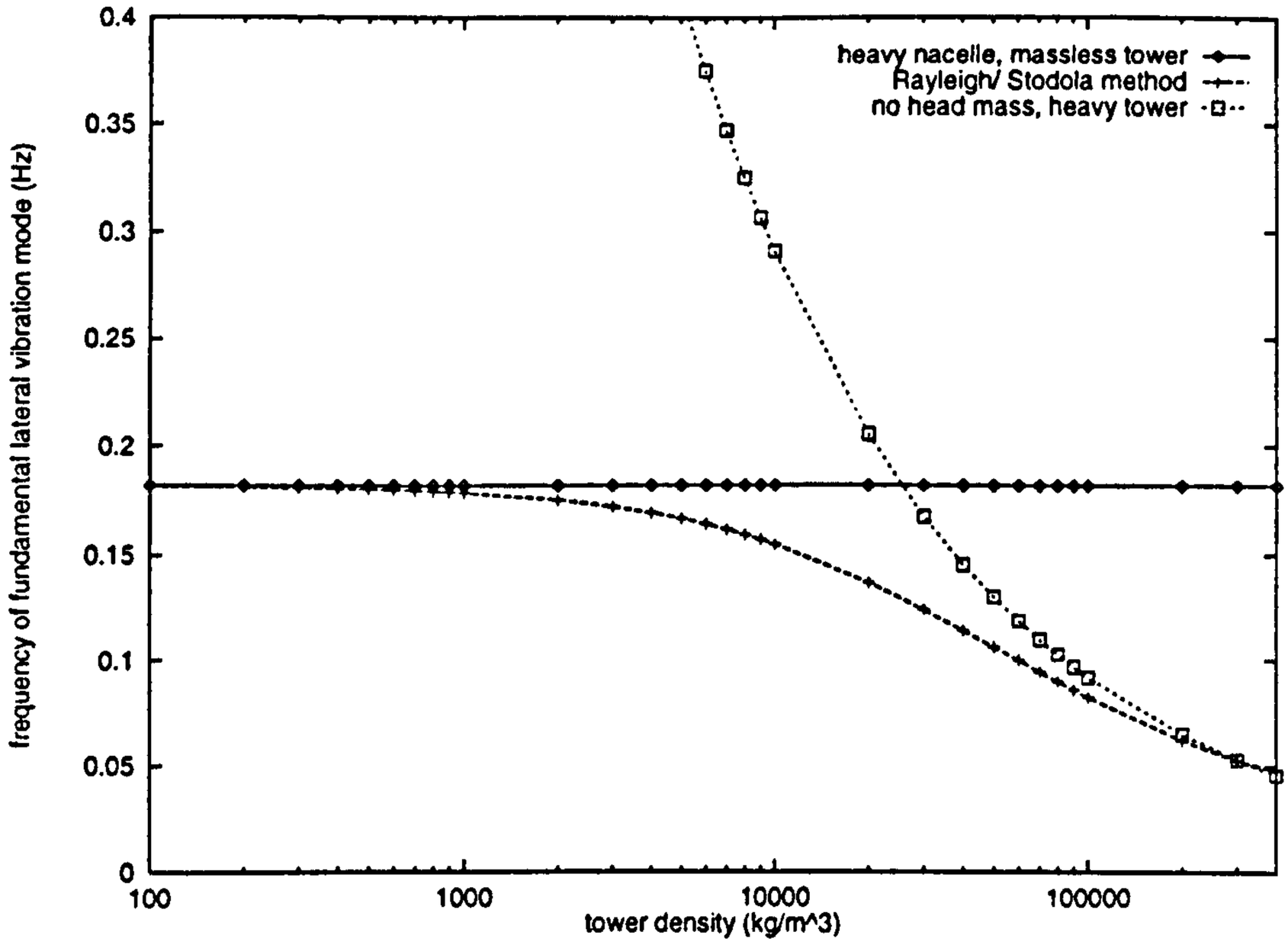

Figure 7.6: Comparison between estimates from two models using direct mathematical solution of the equations of motion and one using the Rayleigh/ Stodola iterative process. The tower density is varied and estimates made of the fundamental bending frequency using three models. The tower is based on the Carter 300 kW design but is unguyed, free-standing and cylindrical (uniform cross-section). The nacelle moments of inertia are zero ($J_{nr} = J_{nt} = 0$). The boundary conditions used for both models are: free top and built in base. A logarithmic scale is used for the horizontal axis.

tinuous beam model.

The third example illustrated in Figure 7.7 includes the guys and assumes that the effect is to 'pin' the tower at the point of attachment. This is similar to the illustration in Figure 5.11 (e) but the tower is simply supported at the base and at the point $x = \lambda_{ct}H$ instead of at top and bottom. The biharmonic solution is therefore for a shorter beam (of length $\lambda_{ct}H$). The equivalent stiffness $k_{(eq)B}$ of the tower for the lumped mass solution is calculated using Equations 7.4 and 7.5 (beam simply supported at $x = 0$ and $x = \lambda_{ct}H$).

The effect of gravity on the vibrations can be seen since, in Figure 7.7. curves are plotted including and excluding gravity loads. Above a head mass of 50,000 kg, values of fundamental frequency calculated using the Rayleigh/ Stodola model start to increase. For all other experiments with bending vibrations (Figures 7.5, 7.6 and 7.8) gravity loads are included and a similar frequency rise occurs only at values of head mass or tower density higher than the maximum of the horizontal scale. It is not clear why the frequency should rise in this way. As the weight of the system increases, it increases the axial compression in the tower which should cause the frequency to decrease. However, the deformation of the tower also increases at high structural weights causing the point of attachment of the guy cables to the tower to move downwards. This shortens the guy cables decreasing the initial tension ϵ_{ic}. This decreases the axial compression in the tower tending to increase the frequency of vibrations. This may be the process which predominates giving rise to the frequency increase in Figure 7.7. In Figure 7.7, the frequency tends towards the value predicted using the continuous beam model. At very high weights, the cables may become slack.

The fourth example illustrated in Figure 7.8 is of a tower design with guy cables and a built in base. This is similar to the illustration in Figure 5.11 (c).

Because the axial loads on the tower due to the guys and the weight of the tower and nacelle lower the fundamental frequency and are neglected by the continuous beam method, results from the latter are scarcely close to the tower natural frequency predicted using the Rayleigh/ Stodola method even if the tower is very massive relative to the nacelle. The relationship between the results obtained from the three models and the density of the tower would be similar for a guyed tower to the illustration in Figure 7.6 for a free-standing tower except that the agreement between the Rayleigh/ Stodola method and the continuous beam method would be less good. This would be made worse by the fact that the axial load caused by the tower's own weight would increase considerably at high tower densities.

Other interesting experiments might include changing the diameter of the guy cables and noting the transition between models of free-standing towers and models of simply supported towers. Also, standard models of continuous conical towers could be used to note the effect of increasing the base diameter of a conical tower.

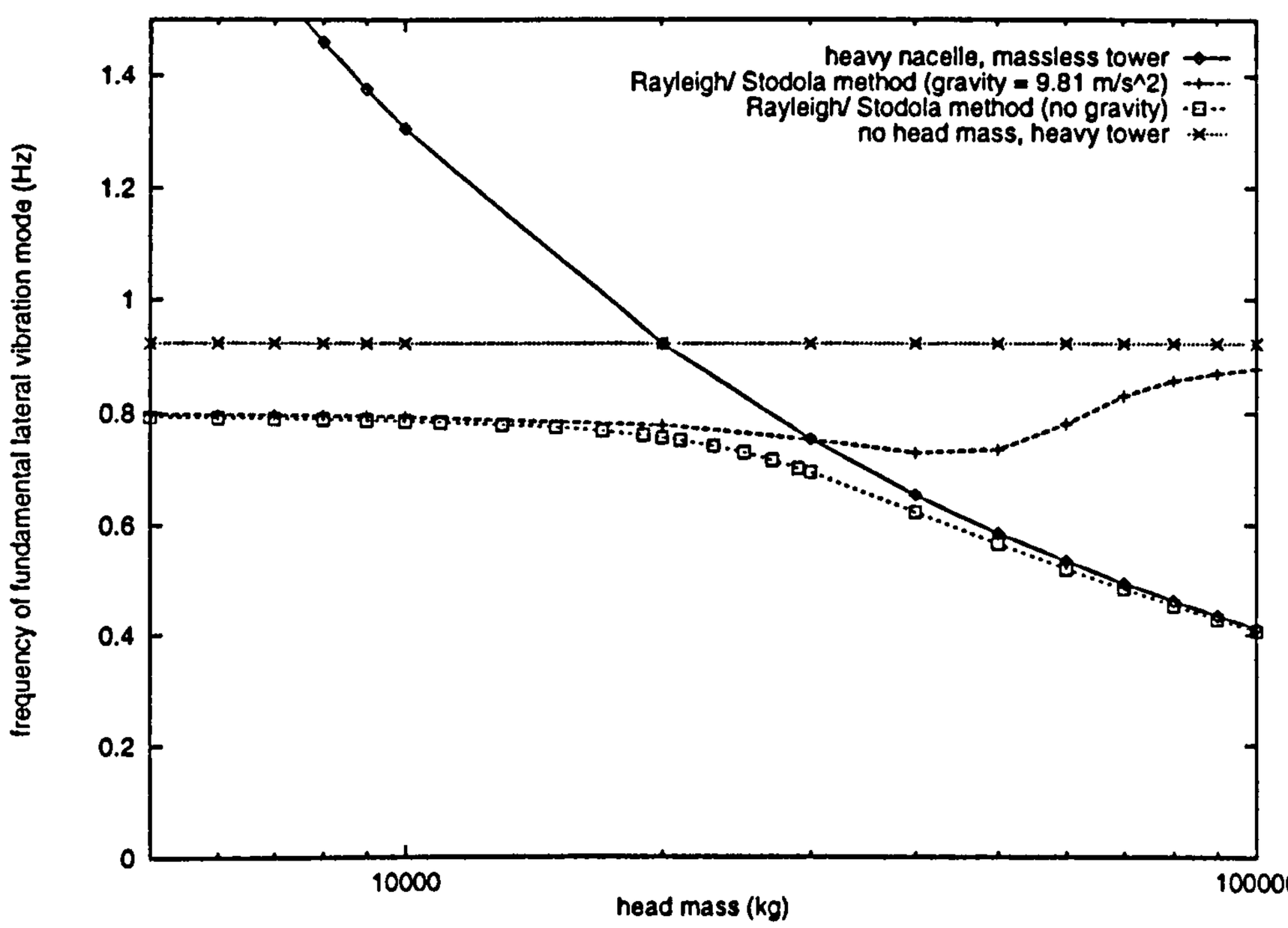

Figure 7.7: Comparison between fundamental frequencies of bending vibrations calculated by two direct mathematical solutions of the equations of motion and by the Rayleigh/ Stodola iterative process. The tower is based on the Carter 300 kW design except being cylindrical (uniform cross-section). The nacelle moments of inertia are zero ($J_{nr} = J_{nt} = 0$). The base fixing is hinged ($k_{Bf} = 0$) and guys at $\lambda_{ct}H$ are of mass 4.9 kg m^{-1} with initial strain 0.0005.

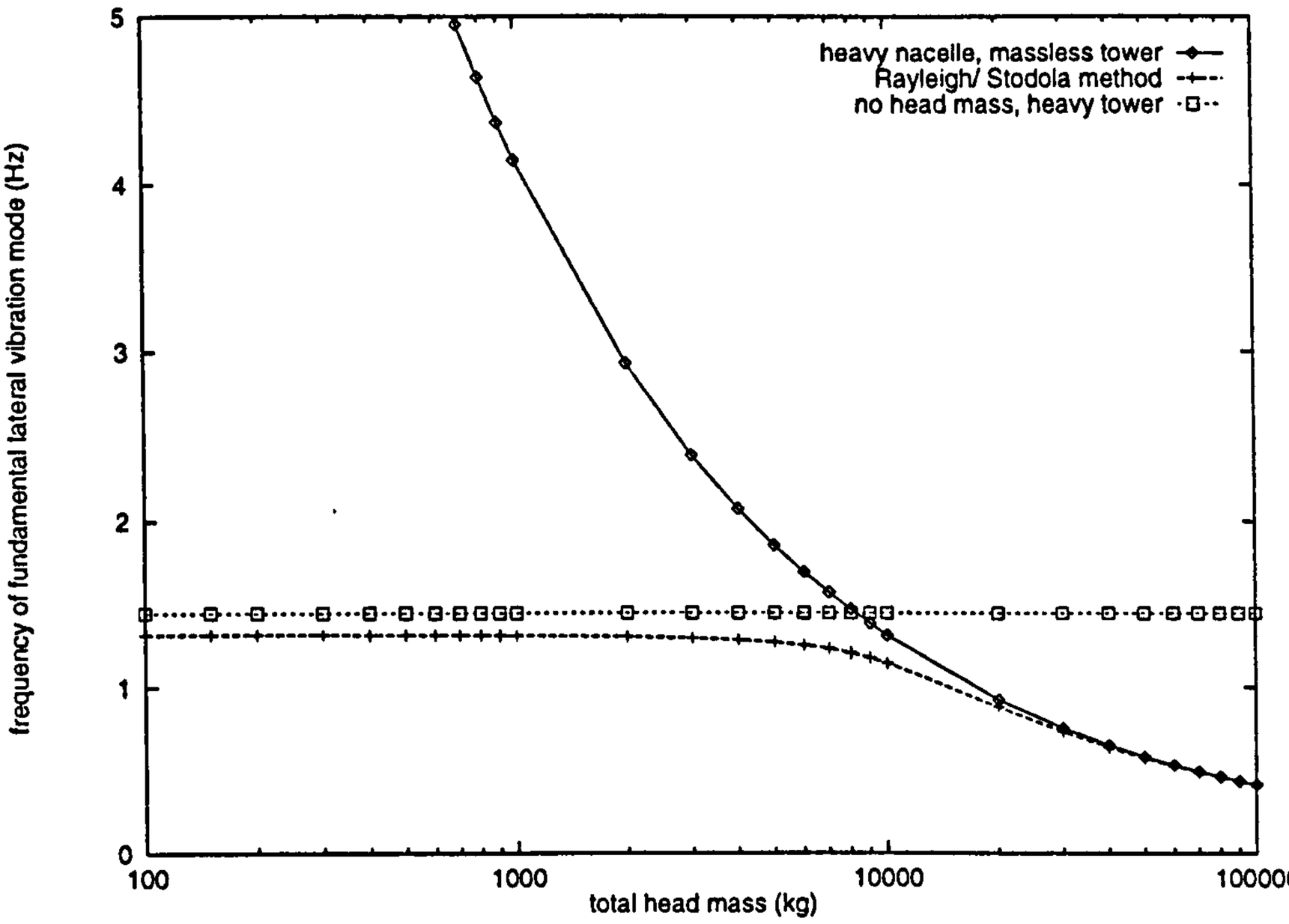

Figure 7.8: Comparison between fundamental frequencies of bending vibrations calculated by two direct mathematical solutions of the equations of motion and by the Rayleigh/ Stodola iterative process. The tower is based on the Carter 300 kW design except being cylindrical (uniform cross-section). The nacelle moments of inertia are zero ($J_{nr} = J_{nt} = 0$). The base fixing is built in ($k_{Bf} = 1 \times 10^{12}$) and guys at $\lambda_{ct}H$ are of mass 4.9 kg m^{-1} with initial strain 0.0005.

Chapter 8

Optimising Tower Designs

8.1 Guyed Support Structures for Wind Turbines

An important feature of the Carter wind turbine design is the guyed tower. In 1981, Carne [64] asserted that design of a guyed structure was driven either by the need:

1. for strength in high winds

2. for structural stiffness.

In either case the design objectives (maximum stress or minimum frequency of vibration) could be met by a structure of lower overall mass if guy cables were added. The unavoidable penalty identified was the axial compression in the tower. This axial load lowers the frequency of lateral vibration of the tower. There is also the danger of tower buckling if the guy tensions are too high.

Sag and vibrations of the cables are also important. Sag is not dealt with in this thesis but has been calculated using the method of Peyrot and Goulois [29]. In the case of the Carter wind turbine, the tension of the cables is increased until the sag is equal to one cable diameter. Occasional checks ensure that the cable has not relaxed with time. The focus of Carne's work [64] was the improvement of Darieus vertical axis machines. For such machines, (see for example Twidell and Weir [56]) cable sag may cause interference between cables and the moving blades. Cable vibrations are dealt with in detail by N. Ben Kahla [30]. A simple model of taut cables enables a designer to avoid the potential for coupling between cables and tower by ensuring that the natural frequencies are not close. An effective concept for cable damping has been tested by Carne [64].

Because results can be obtained fairly rapidly and design changes can be compared for many similar designs, the models described in Chapters 2 and 4 are suitable for optimisation of the mass of the structure. This application is demonstrated in Section 8.3. It has been found that although a free-standing conical tower is significantly stiffer and stronger than a tower of constant radius, when guyed it is the cylidrical tower which performs better. The double-tapered concept adopted for the Carter 300 kW wind turbines has been shown to perform the best of the guyed towers compared. For free-standing towers however, it has been possible to optimise the tower radius so that the maximum tensile stress over the

cross section is the same at all heights up the tower. The principle of this optimisation is applicable to guyed towers but it has not been attempted here due to the extra complexity of the search algorithms required.

8.2 Effect of Increasing Guy Cable Tension

The effect of increasing the value of the parameter, ϵ_{ic} which sets the guy cable initial tension (before assembly) is to reduce the frequencies of vibration of the whole structure. The fundamental lateral frequency falls to zero at the value of ϵ_{ic} at which the tower buckles (see Table 5.16). The same effect is observed using both the *general numerical model* using the Rayleigh/ Stodola method and a Finite Element model. The variation of fundamental frequency and first harmonic are shown in Figures 8.1 and 8.2. Increasing ϵ_{ic} will increase the value of the lateral stiffness of the guy cables k_{Bc} which will increase the maximum potential energy stored in the guy cables during vibrations of the tower (Equation D.4 in Appendix D). However, the value of the vertical (axial) force on the tower, F_{cv} will also increase. This will increase the potential energy stored in the tower at static equilibrium and therefore decrease the maximum potential energy stored in the tower during vibrations given by Equation D.2 in Appendix D. A decrease in maximum potential energy will result in a reduction in the Rayleigh frequency (Equation 4.8).

Predictions of the first harmonic frequency of bending vibrations obtained using the models described in Chapters 2 and 4 diverge from predictions obtained using finite element analysis (Figures 8.1 and 8.2). However, once the fundamental freqency of vibration has fallen to zero, the tower has buckled in its first mode. Calculating the frequency of lateral vibration of the structure therefore has doubtful practical value. Since to calculate a mode shape using either the Rayleigh/ Stodola or Finite Element methods relies on having already made accurate estimates of lower harmonic mode shapes (see Section 4.6), it is not clear what the effect of a zero fundamental lateral frequency has on estimates of the first harmonic. The divergence of the first harmonic lines calculated using Rayleigh/ Stodola and Finite Element methods in Figures 8.1 and 8.2 is therefore not particularly significant.

Results from Finite Element analysis show that there is some interaction between the guys and the tower but only when frequencies of lateral vibration are similar for both elements. It was expected that the first lateral mode of the guy cables might coincide with a tower lateral mode at twice the frequency since there is a force on the tower from the guy cable twice during each cable period (see Figure 8.3). This was not shown by Finite Element analysis.

The guy modes can be predicted using Equations 8.1 and 8.4. The results are the same as those obtained by using the Finite Element model. The variation of frequency of the fundamental and first harmonic modes of guy cable vibrations are shown in Figure 8.4 on the same axes as the variation of tower vibration frequencies obtained by Finite Element analysis and already plotted in Figures 8.1 and 8.2.

$$f_c = \frac{i+1}{2\lambda_{c0}H}\sqrt{\frac{E_c\epsilon_c}{\rho_c}} \tag{8.1}$$

where:-

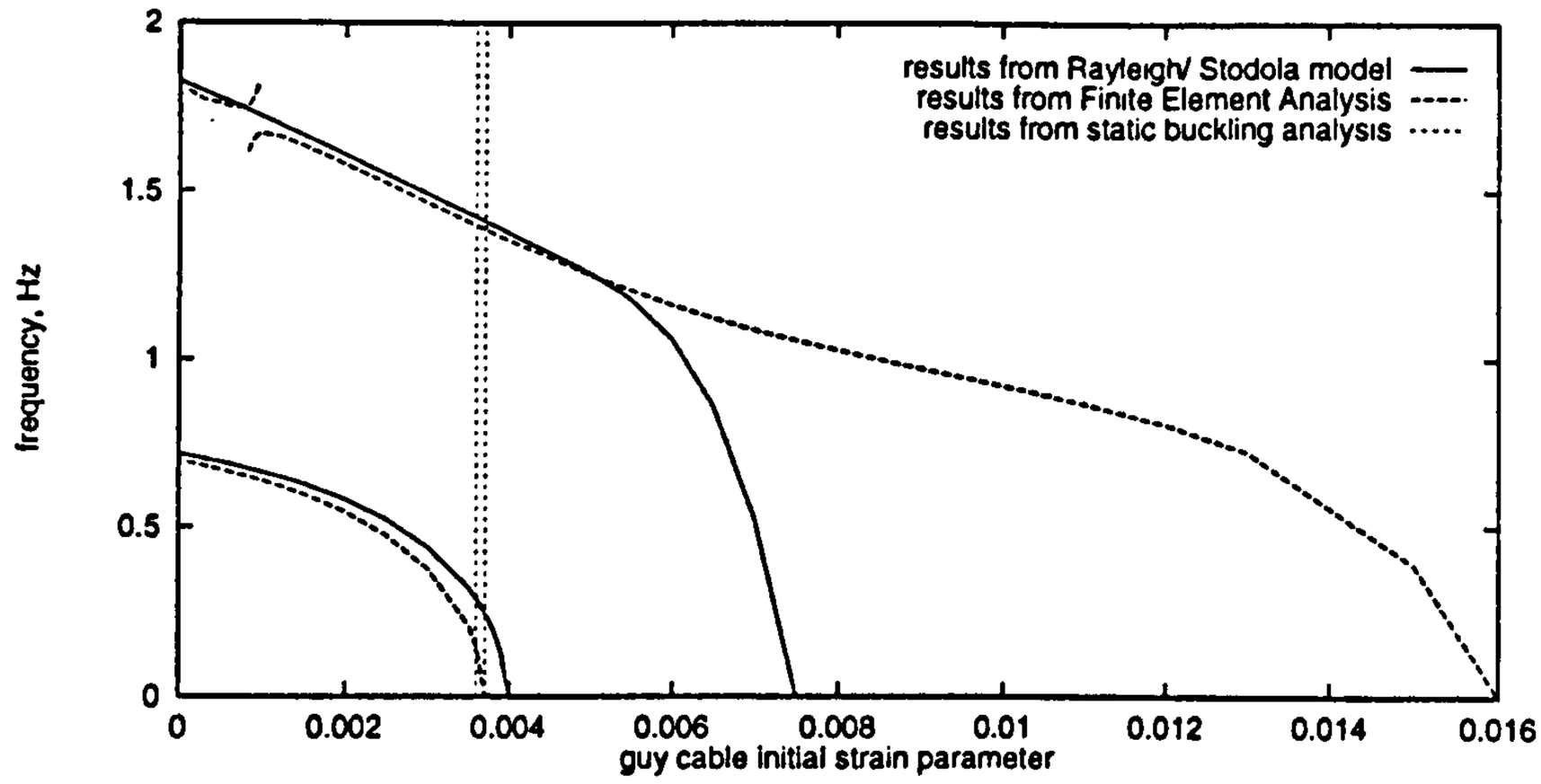

Figure 8.1: The variation of the fundamental and first harmonic frequencies of bending vibrations of a guyed tower of the kind used at Great Orton Airfield with the value of the initial strain parameter, ϵ_{ic}. The base of the tower is hinged.

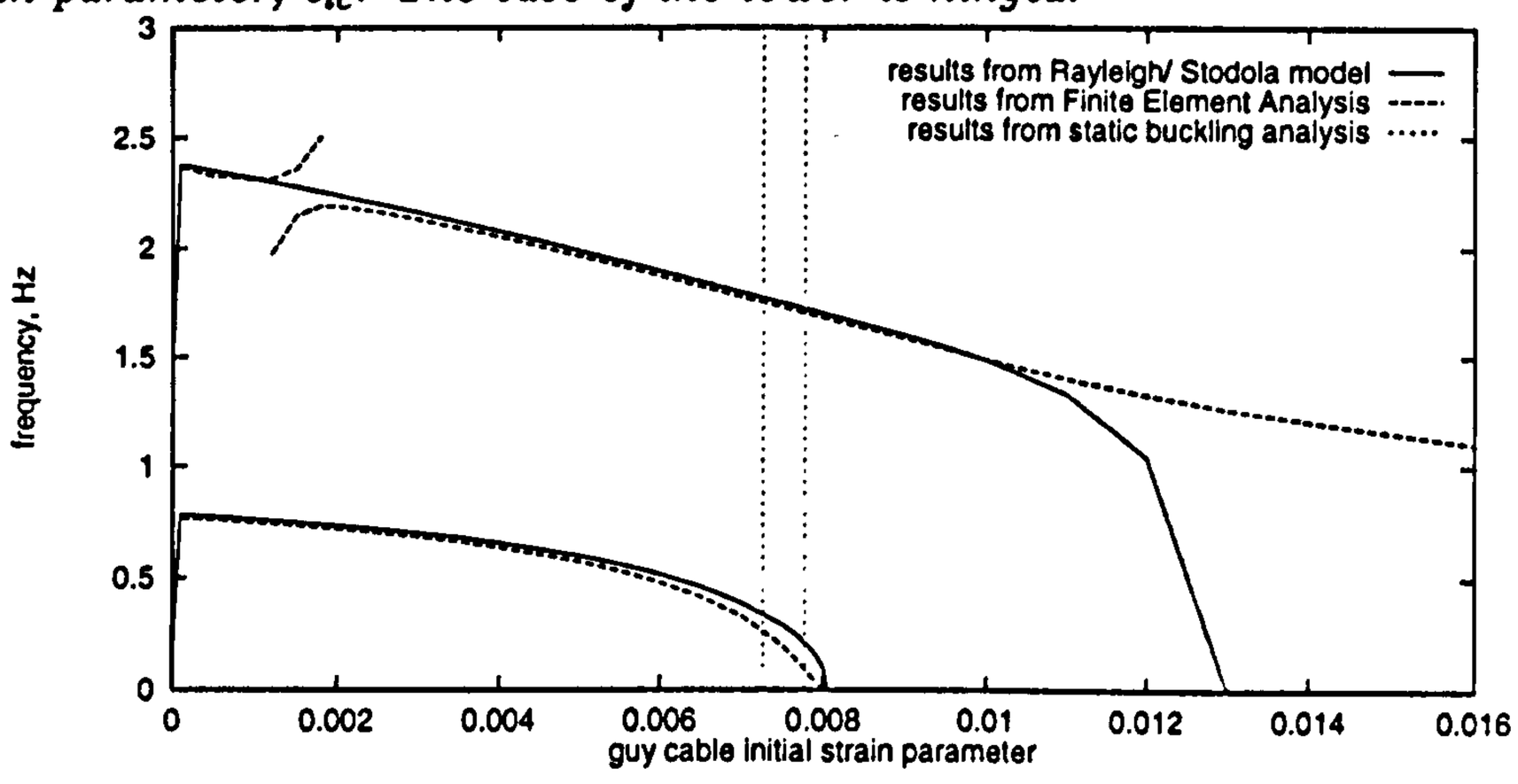

Figure 8.2: The base of the tower is built in.

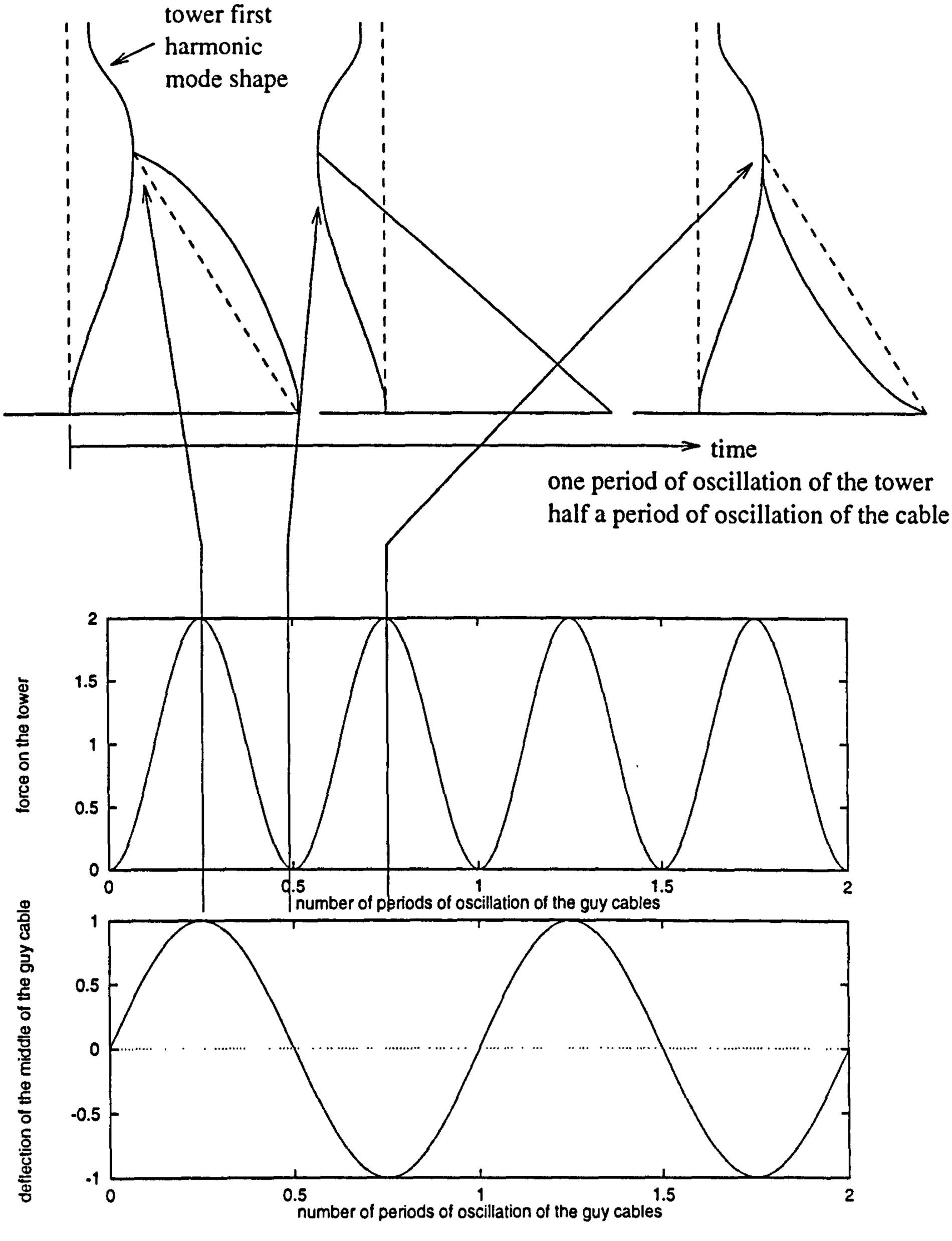

Figure 8.3: Twice during each period of oscillation of a guy cable there is a force exerted on the tower.

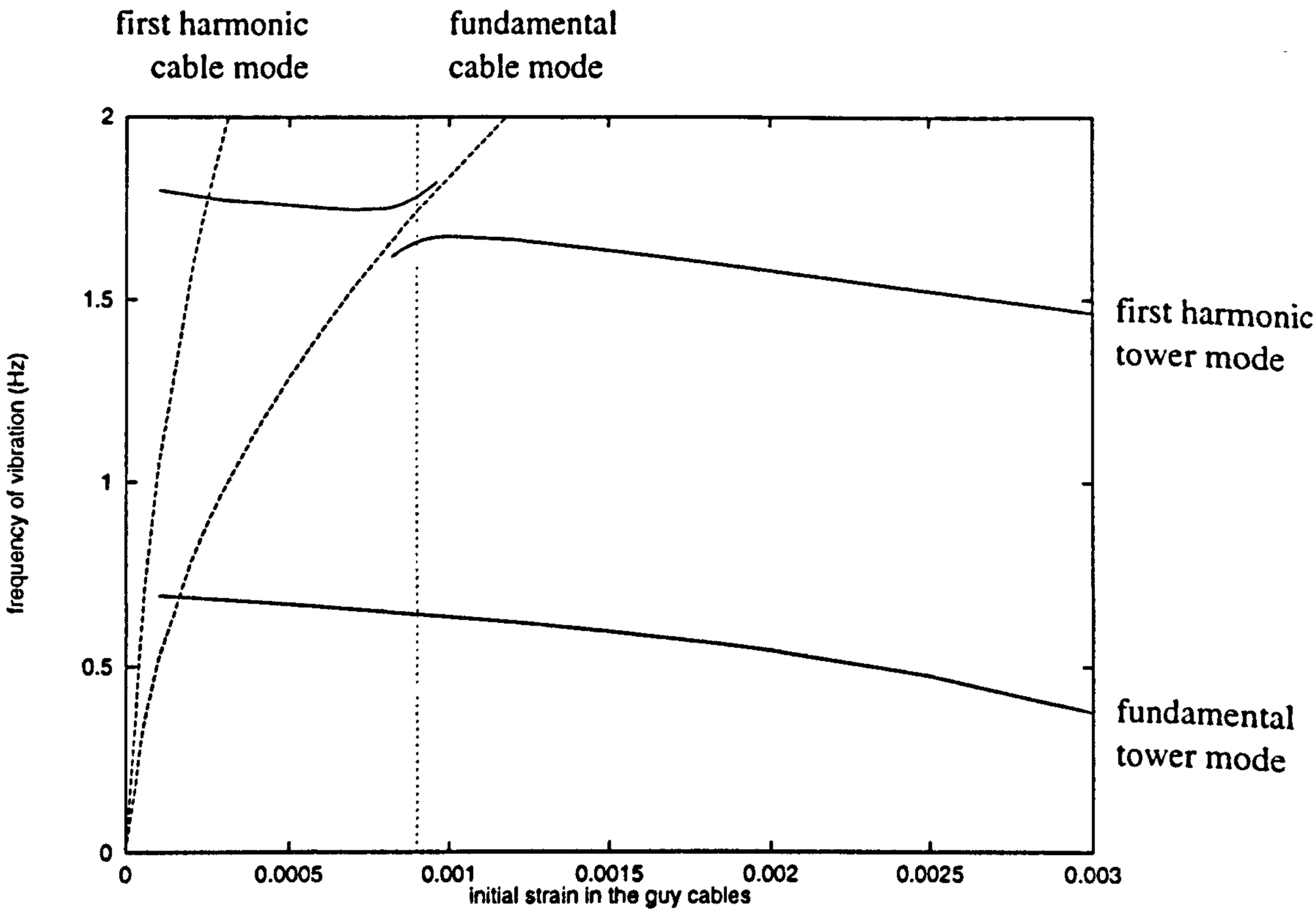

Figure 8.4: The variation of frequencies of vibration of tower and guy cables with different values of the parameter which sets the initial strain in the cables ϵ_{ic}. The base of the tower is hinged. The initial strain at which the mode shapes in Figure 8.5 calculated is shown as a vertical dotted line ($\epsilon_{ic} = 0.0009$).

$$\epsilon_c = \frac{\lambda_{c0} - \lambda_{cn}}{\lambda_{cn}} \tag{8.2}$$

and $\lambda_{c0}H$ is the length (m) of the cable after assembly:-

$$\lambda_{c0} = \sqrt{\left(\lambda_{ct} - \frac{u(\lambda_{ct}H)}{H}\right)^2 + (\lambda_{cg} - \lambda_{tr})^2} \tag{8.3}$$

and $u(\lambda_{ct}H)$ is the vertical displacement (m) of the point of attachment of the guy cables to the tower after assembly.

$$v_c = \sin(X(i+1)\pi) \tag{8.4}$$

where v_c is the deflection of a point on a guy cable from the undeflected position and X is dimensionless distance along the cable.

When the frequencies of lateral vibration of the tower and the guy cables coincide, a joint mode has been predicted. Figure 8.4 shows that if the initial strain in the guy cables is slightly lower or higher than the value at which these modes coincide, the modes involving both tower and guys are split and are predicted to vibrate at frequencies both higher and lower than the predicted guy mode. This is illustrated in Figure 8.5 where nine modes are depicted in increasing order of frequency. 7 of the modes involve vibration of the guy cables only (at almost identical frequencies). The first and ninth show combined modes involving vibration of the tower and the guy cables neither of which vibrates at the same frequency as predicted for the guy cables alone using Equation 8.1.

8.2.1 Improved Models of the Guy Cables

In Section 8.1, the dynamics of the combined system of tower and guy cables were assessed using Finite Element analysis. There was found to be little interaction between the two structural elements. It was expected that any such interactions would show up with Finite Element analysis because the tower and guy cables were constructed from many elements with both mass and stiffness. This is not the case for the Rayleigh/ Stodola method described in Sections 2 and 4. The mass of the guy cables is not included and so no combined modes of vibration of the tower and guy cables would be predicted. If the distributed mass of each guy cable were lumped and included in the overall mass of the structure as has been suggested by Goodall and Austin [65], this short-coming could be partially overcome.

8.3 Optimising Tower Mass

The importance and difficulties of optimising wind turbine towers are stressed in the recent paper by Andreas Reuter and Alexander Bormann [5]. Often, it is not possible to design a tower which meets all the design criteria. A heuristic approach to the optimisation of guyed towers which carry microwave antennae is proposed by Bell [66]. This Section of the thesis describes uses of the software described in Chapters 2, 3 and 4 for tower mass optimisation. The automatic optimisation described is limited to stress-limited mass minimisation. This is just one part of the design process described by Bell [66] which must also include selection of the number of cables, their heights, material and geometric properties. Alexander Bormann also warns of the dangers of placing excessive emphasis on load optimisation. His study of wind turbine costs [23] shows that although the tower material costs comprise over half (56%) of the material costs of the support structure. when the combined costs of materials and various finishing operations are compared, the tower accounts for only about one third (37%). Although it is not possible to optimise the costs of the project with stress-limited optimisation alone, optimisation is not possible without stress analysis. Other costs such as transport and installation are investigated by Bormann [23].

Figure 8.6 shows six different tower shapes by plotting the variation of outside radius with dimensionless distance up the tower. A, B. D and E are arbitrary geometric shapes. C is a scaled version of the optimised. free-standing tower described later in Section 8.3.1.4. The last tower shape F is a scaled version of the double-tapered towers used for the Carter 300 kW wind turbines.

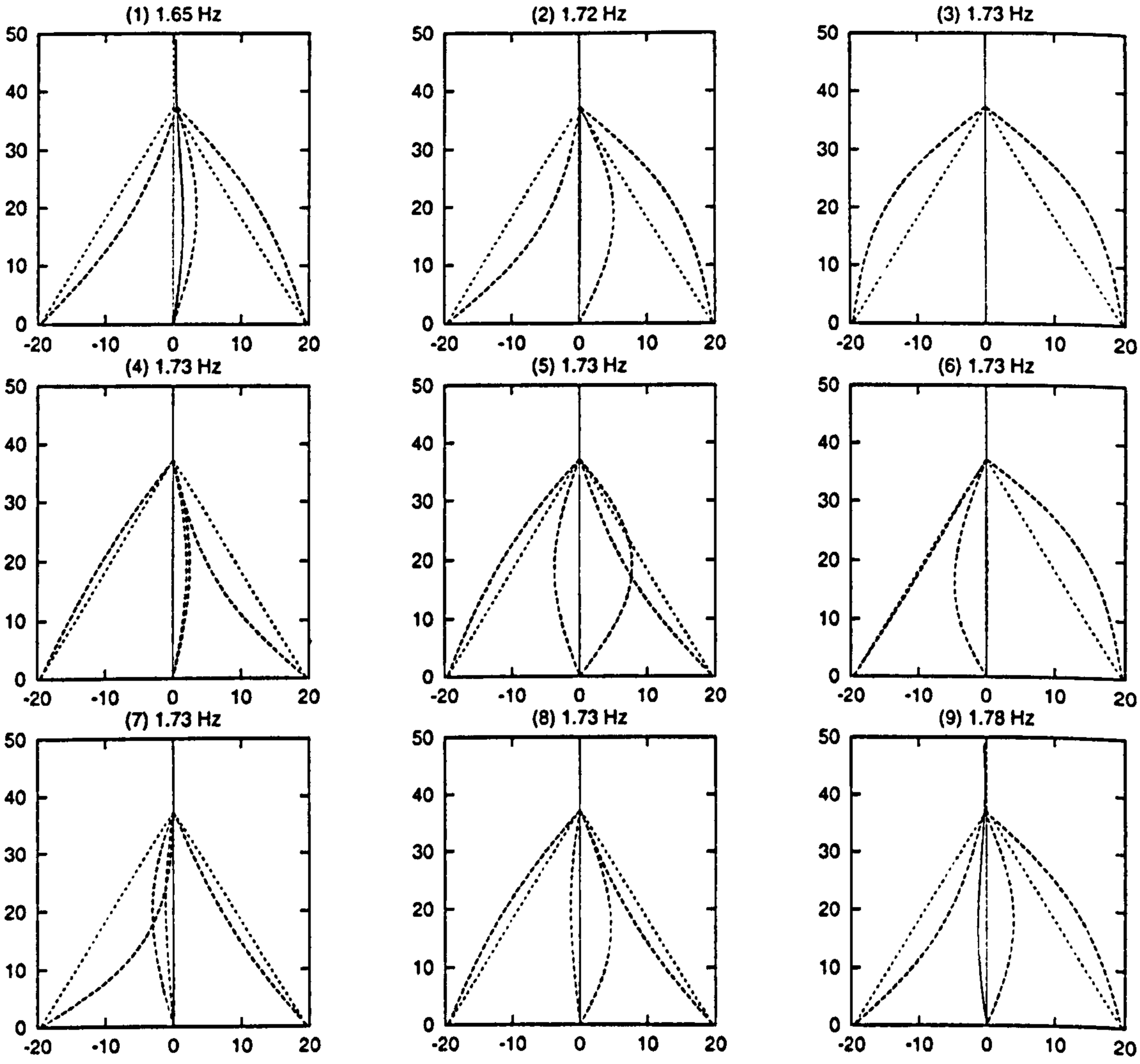

Figure 8.5: The mode shapes predicted by ANSYS 5.0 Finite Element analysis. In all cases the initial strain in the guy cables, ϵ_{ic}, is 0.0009 and the base of the tower is hinged. Using Equation 8.1, the frequency of vibration of the guy cables alone is 1.73 Hz. The first and ninth plots show the combined first lateral harmonic tower mode and fundamental guy cable mode for the structure. Plots 2–8 show modes involving vibration of the guy cables only. All modes are listed in order of increasing frequency. The differences in frequency between particular modes for plots 3–8 are all less than 0.0001 Hz. The first two modes of vibration of the whole structure are not shown here and comprise the fundamental lateral vibrations of the tower alone in orthogonal (x–z and y–z) planes.

In order to compare performance, several parameters are maintained constant for all towers.

- The total mass of the structure (including guy cables if there are any) is 15000 kg.
- The head load (F_{nh}) is 100000 N for static stress calculation (it is the only load on the structure apart from gravity).
- The wall thickness, t of the tower is constant at 0.015 m.
- The height, H of the tower is 49 m.
- The initial strain, ϵ_{ic} in the guys is 0.0005.
- The ratio to the tower height, of the height to the point on the tower to which the guy cables are attached λ_{ct} is 0.76.
- The ratio to the tower height, of the displacement of the guy cable anchor points from the base of the tower λ_{cg} is 0.4.
- The nacelle mass (M_n) and moment of inertia (J_{nt}) are 4780 kg and 15200 kg m^2.
- The number of nodal points is 101 and the number of points in each spline section is 21.
- The base is built in ($k_{Bf} = 1 \times 10^{12}$ N m rad^{-1}).

Other design parameters are taken from the parameter set for the Carter 300 kW machine (Appendix H).

Table 8.1: List of symbols used to identify curves on Figures in Sections 8.3 and 8.3.1.3.

▯	A	cylindrical, parallel-sided, free-standing tower
⏢	B	conical, free-standing tower
⏢	C	optimised, free-standing tower
⩚	D	cylindrical, parallel-sided, guyed tower
⩚	E	conical, guyed tower
⩚	F	double-tapered, guyed tower

The stiffness of a particular tower design can be assessed in two ways:

1. the static load necessary for unit deflection of the tower (stiffness = $\frac{dF_{nh}}{dv(H)}$):
2. the frequency of vibrations of the tower (stiffness $\propto \sqrt{f_{1B}}$).

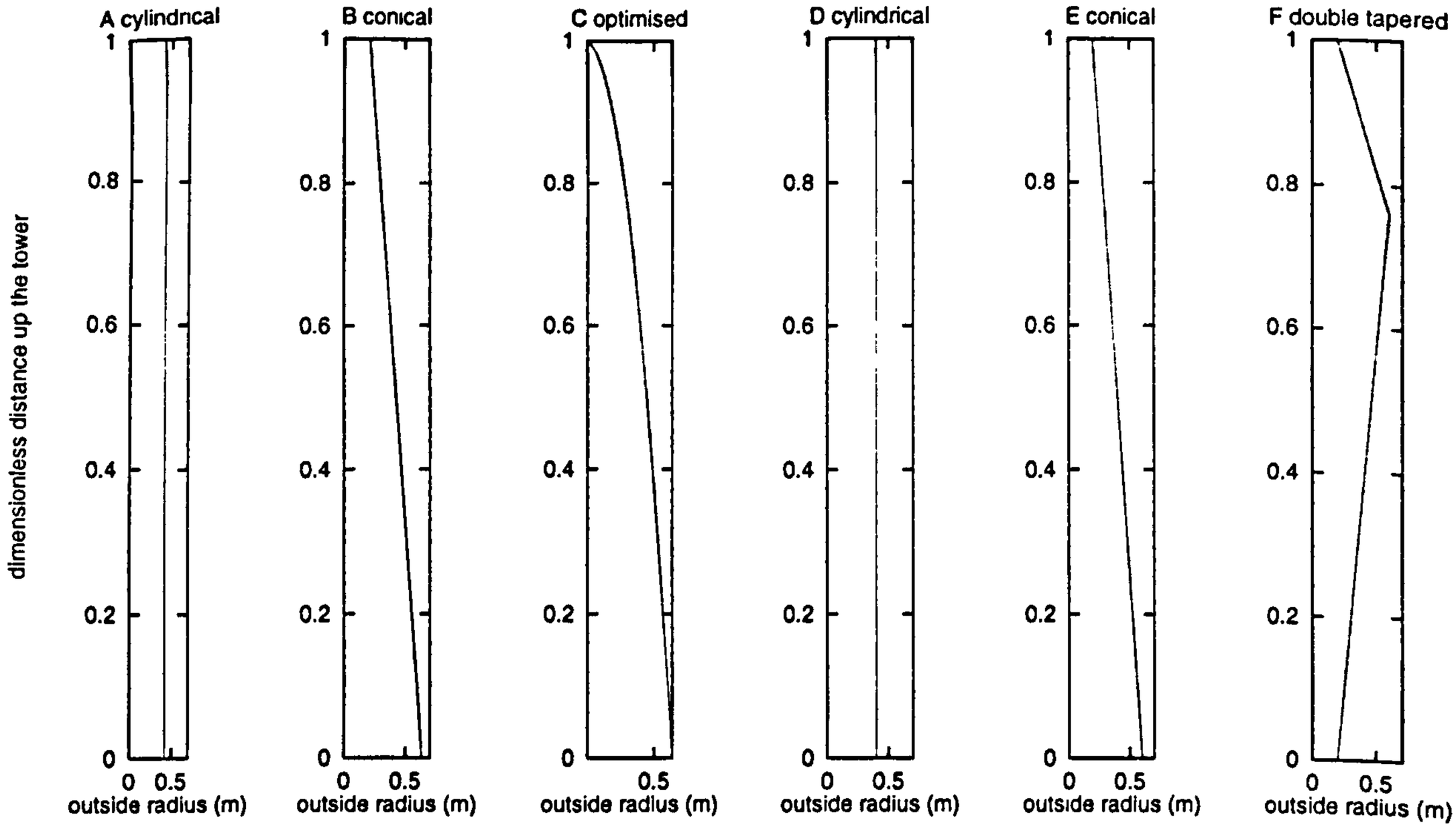

Figure 8.6: The six tower designs to be compared. The first three (A–C) are free-standing and the last three (D–F) are guyed. The wall thickness is 0.015 m. The overall mass of the structure is 15000 kg. Symbols used to denote the six shapes A–F are listed in Table 8.1.

Figure 8.8 shows how unguyed towers are far less stiff than guyed towers of the same overall mass. Cylindrical towers are least stiff but as mentioned in Section 8.3.1.1, standard gauge cylindrical tubes may be cheaper than a complicated, fabricated tower. The stiffness of the conical tower is significantly greater. This is the choice usually made for large, commercial machines. A further improvement can be seen if the tower shape is optimised with respect to maximum stress (Section 8.3.1.4). Guyed towers are significantly stiffer but the conical tower is actually less stiff for the same mass than the cylindrical tower. The Carter 300 kW machines have double-tapered towers. Of the variants compared here, the example of this geometry is the most stiff.

The same trends can also be seen in Figure 8.11 where guyed towers are significantly stiffer than free-standing towers. The fundamental frequencies of guyed towers are significantly higher than free-standing towers.

The stress distribution over the height of the tower under a constant static load (Figure 8.9) is very much affected by the shape of the tower. Stresses in the free-standing, cylindrical tower reach the highest values. Conical, free-standing towers have a much more even distribution of stress with height. The optimised tower has been designed so that the stress is the same everywhere under a constant horizontal head load (F_{nh}). There are large variations with height of the maximum stress in cylindrical and conical guyed towers. The conical, guyed tower has a maximum stress greater than either of the best free-standing towers. Of the guyed towers considered, the double-tapered tower used in the Carter 300 kW machines shows both the lowest maximum stress value and the least variation of stress with

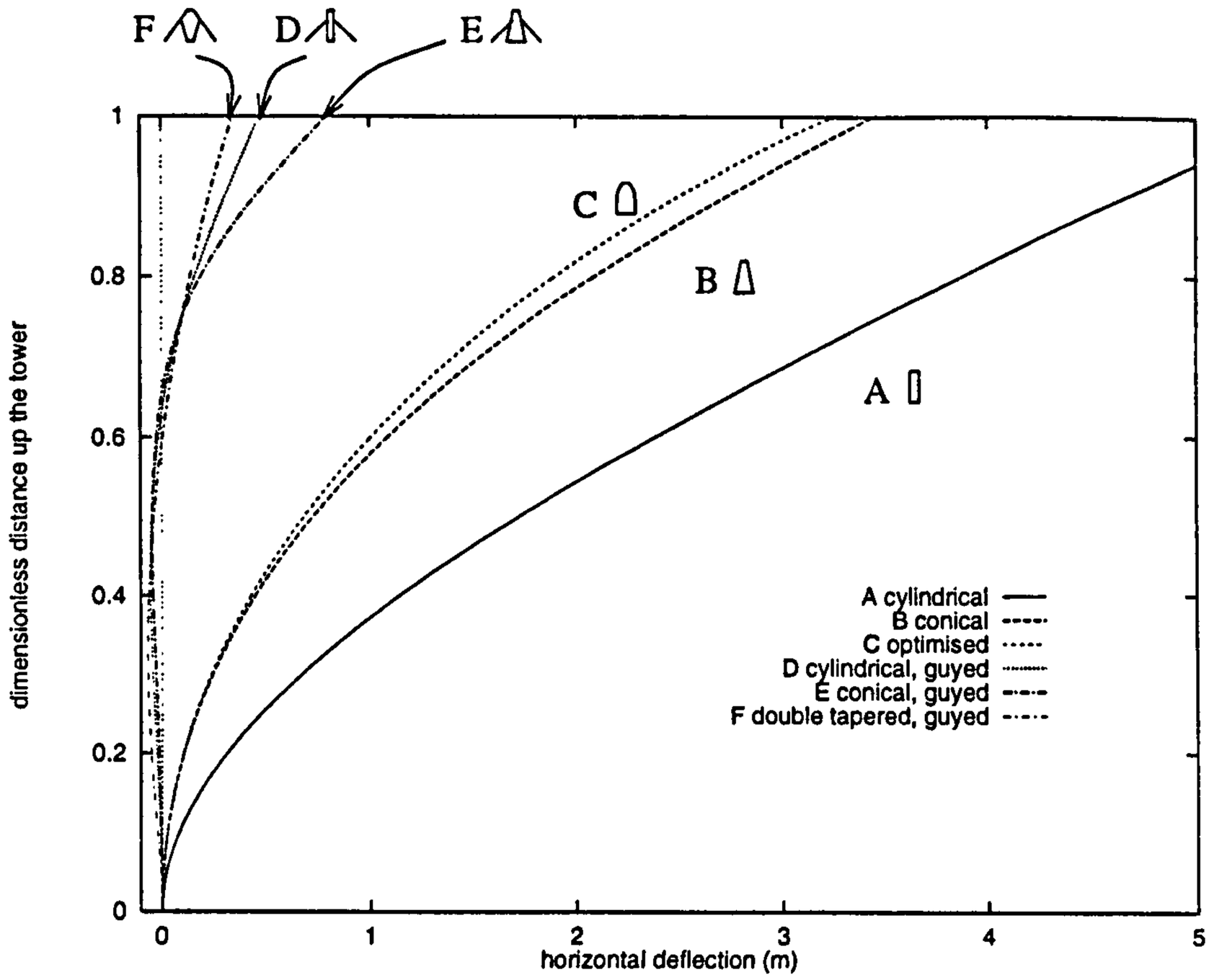

Figure 8.7: The static deflection of each of the towers (A–F in Figure 8.6) under a constant horizontal thrust at hub height of $F_{nh} = 100000$ N.

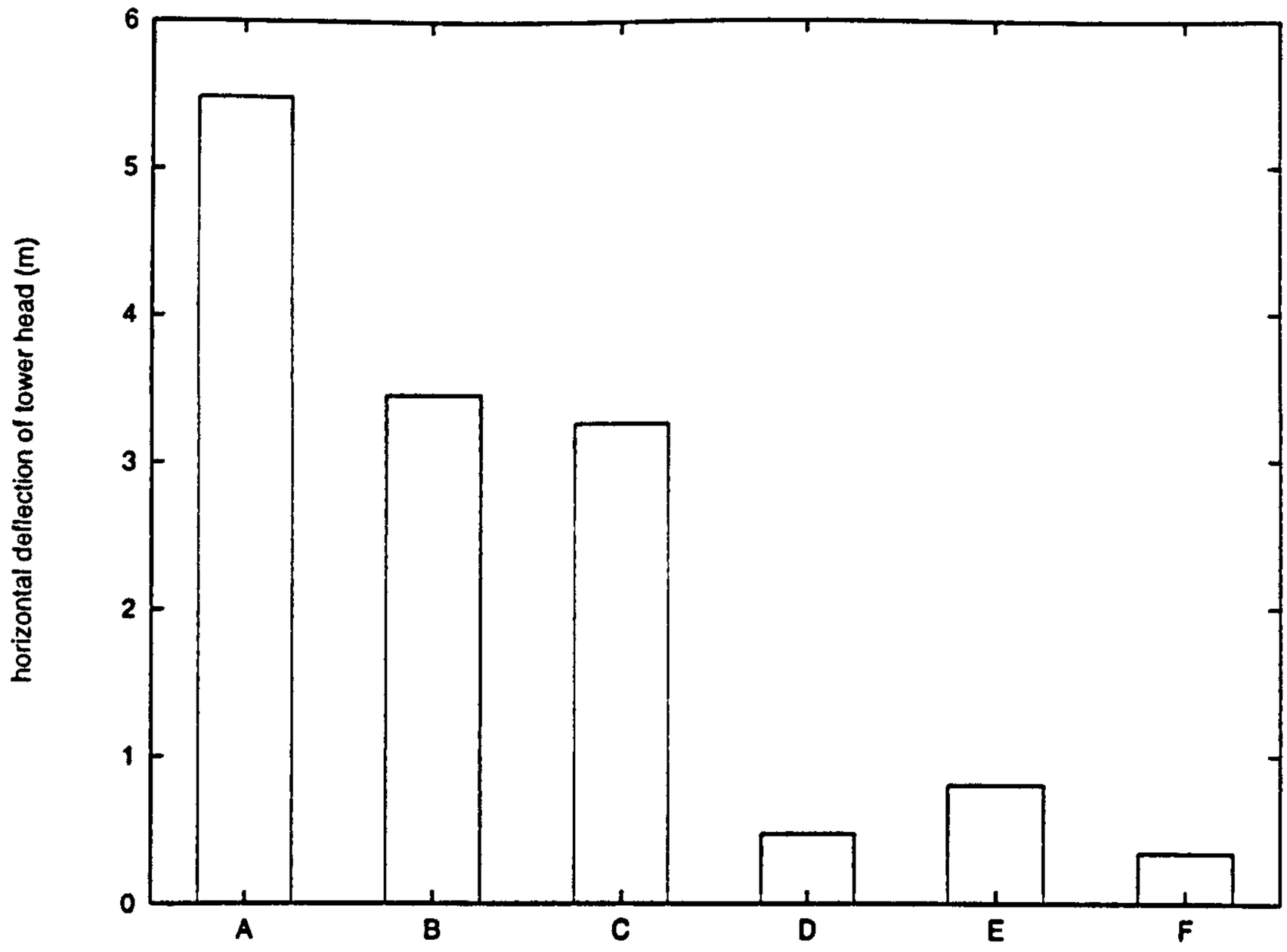

Figure 8.8: Comparing the deflection of the tower head of each of the six towers (A–F in Figure 8.6) under a constant horizontal thrust at hub height of F_{nh} = 100000 N. Head deflections have been obtained from the same data used to produce Figure 8.7.

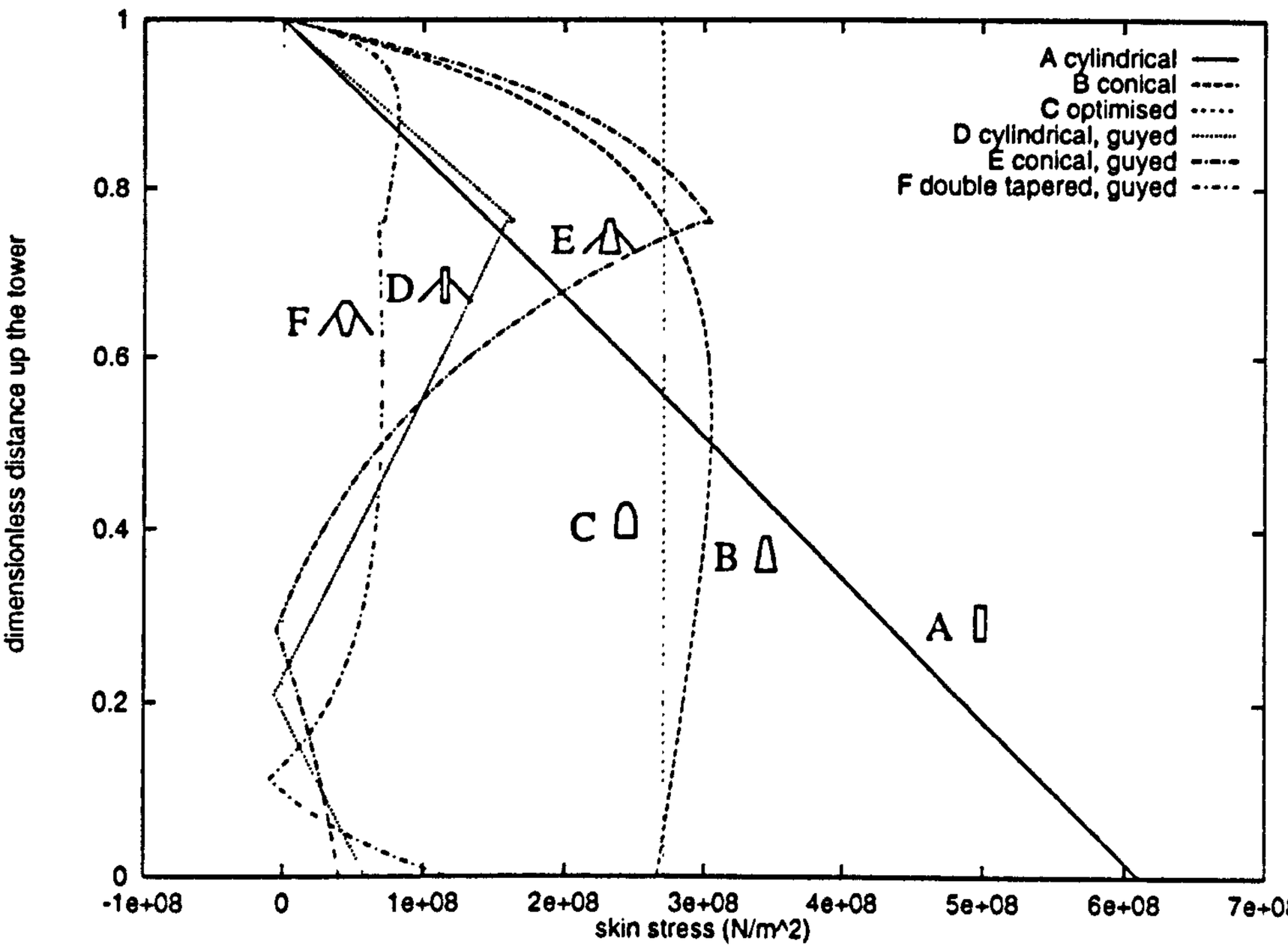

Figure 8.9: The skin stress distribution in each of the towers (A–F in Figure 8.6) under a constant horizontal thrust at hub height of F_{nh} = 100000 N. Skin stress is defined in Section 8.3.1, Equation 8.9.

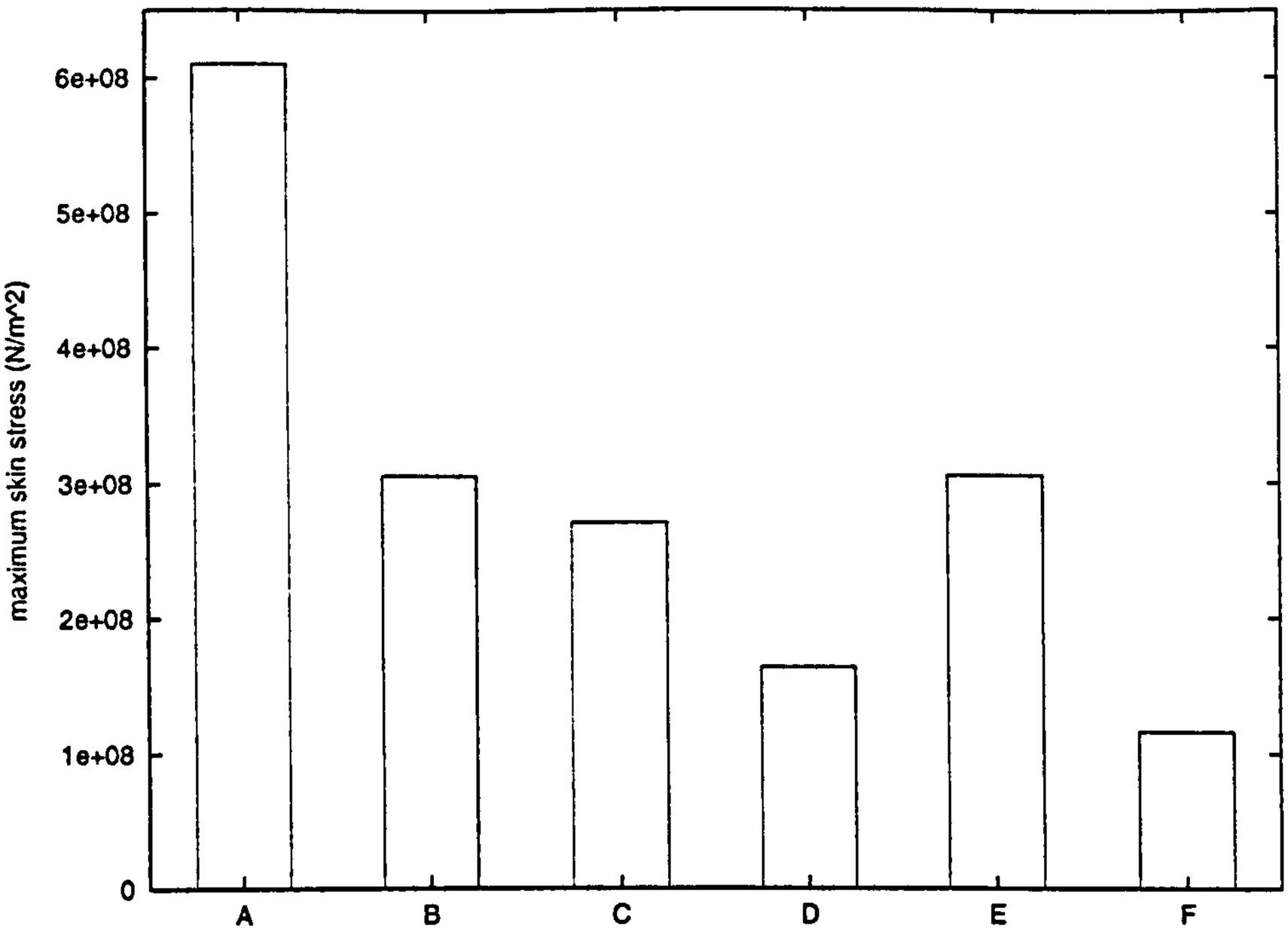

Figure 8.10: Comparing the maximum skin stress in each of the six towers (A–F in Figure 8.6) under a constant horizontal thrust at hub height of F_{nh} = 100000 N. Maximum stress values have been obtained from the same data used to produce Figure 8.10.

height.

In Figures 8.9 and 8.10, the stress distribution for an optimised, free-standing tower has been obtained by first optimising the tower outside radius for a wall thickness of 0.015 m and then scaling the outside radius distribution to find the scale factor for which the overall mass of the tower is 15000 kg.

Tower designs of the same mass have been compared in this introductory section. Since mass is proportional to total tower cost, it is more useful to optimise the tower with respect to some set of constraints in order to minimise the mass. This is the subject of the remaining sections in this chapter.

8.3.1 Stress-Limited Optimisation

8.3.1.1 Varying Tower Wall Thickness

Under a given set of load conditions, a tower design may be optimised so that the maximum stress is just equal to the product of the ultimate stress of the material used σ_u and a safety factor. The load conditions may be specified by a certification body or may be the designer's choice of extreme conditions which the machine must withstand. It is important that all loads are defined and their origins understood.

Here the principles of optimisation are illustrated for a set of extreme loads corresponding to a wind turbine generating 300 kW electrical power in a wind speed of 21.5 m s^{-1}. Only the wall thickness is changed in order to minimise the tower's mass. For small wind turbines.

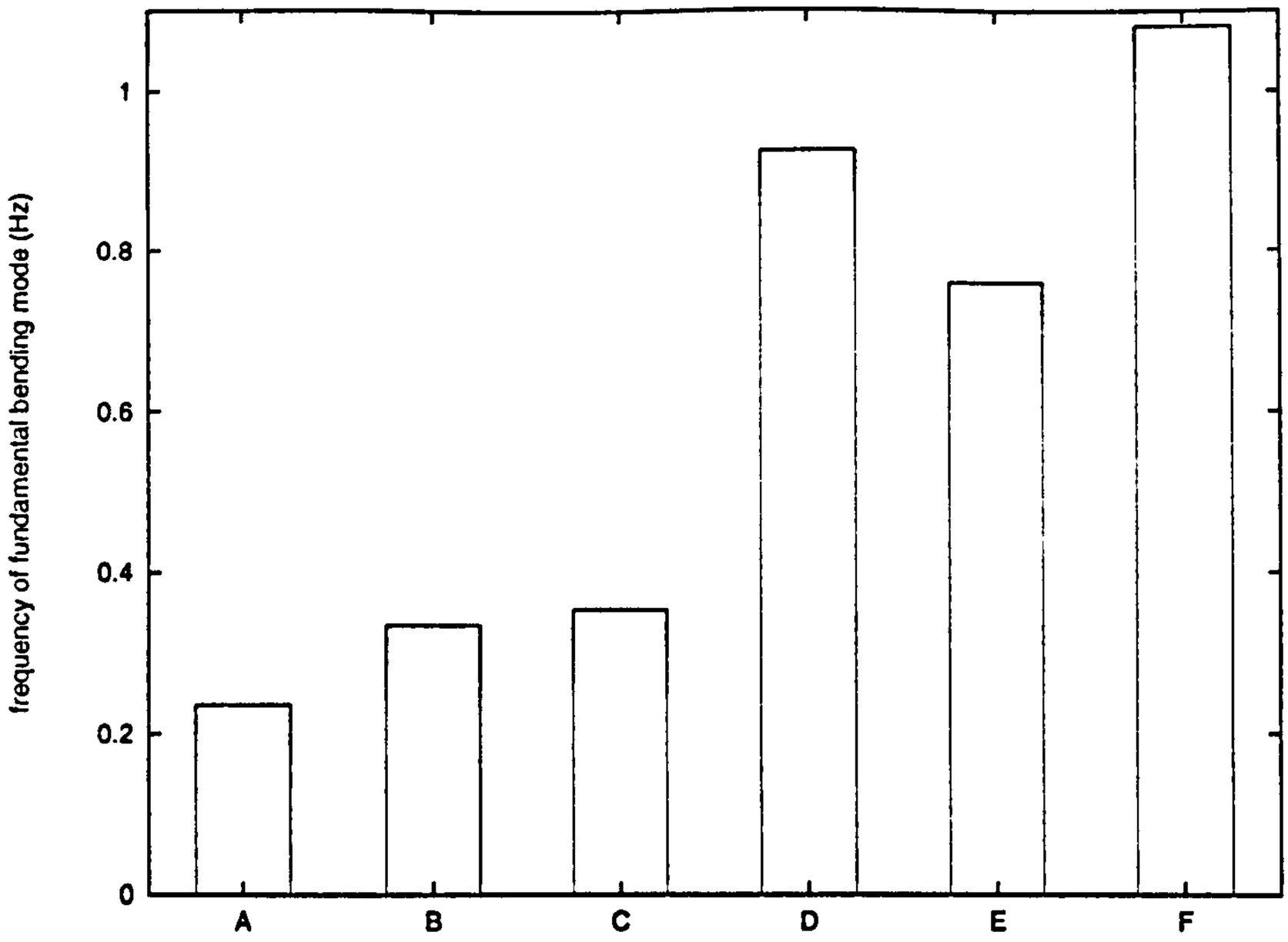

Figure 8.11: The frequency of the fundamental lateral (bending) mode of each of the six towers (A–F in Figure 8.6).

cost of manufacture may dictate the choice of tower shape. Although a more complicated shape may be optimal, straight, cylindrical towers are often chosen because the diameter required is readily available as standard gauge. Fabrication of the optimal tower is likely to be more expensive. In all cases the wall thickness is constant throughout the tower's height.

Equation 8.5 (see for example Meriam's book on statics [32]) gives the stress σ at a distance y from the neutral axis for bending (y measured in the plane of bending). The applied bending moment at that position along the beam is M and the second moment of area of the cross section is I. By rearranging Equation 8.5 to make σ the subject, it can be shown that the maximum stress due to pure bending will be in the outermost annulus of material (σ_B in Equation 8.6).

$$\frac{\sigma}{y} = \frac{M}{I} \tag{8.5}$$

$$\sigma_B = \left(\frac{M_t}{I_{xt}}\right) r_o \tag{8.6}$$

Equation 2.6 can be substituted into Equation 8.6 to give Equations 8.7 and 8.8.

$$\sigma_B = \left(\frac{E_t I_{xt} \frac{d^2v}{dx^2}}{I_{xt}}\right) r_o \tag{8.7}$$

$$\sigma_B = E_t r_o \frac{d^2v}{dx^2} \tag{8.8}$$

The total tensile stress at the edge of the tower cross section will be referred to in this thesis as *the skin stress* and is the sum of the stress due to pure bending and any axial tension (Equation 8.9). The stress distribution over the cross section will be symmetrical about the neutral axis for bending. The maximum tensile stress will be furthest from the centre of curvature (see Figure 8.12) and the maximum compressive stress will be nearest the centre of curvature.

$$\sigma_T = \left| E_t r_o \frac{d^2 v}{dx^2} \right| - \frac{C}{A_{xt}} \tag{8.9}$$

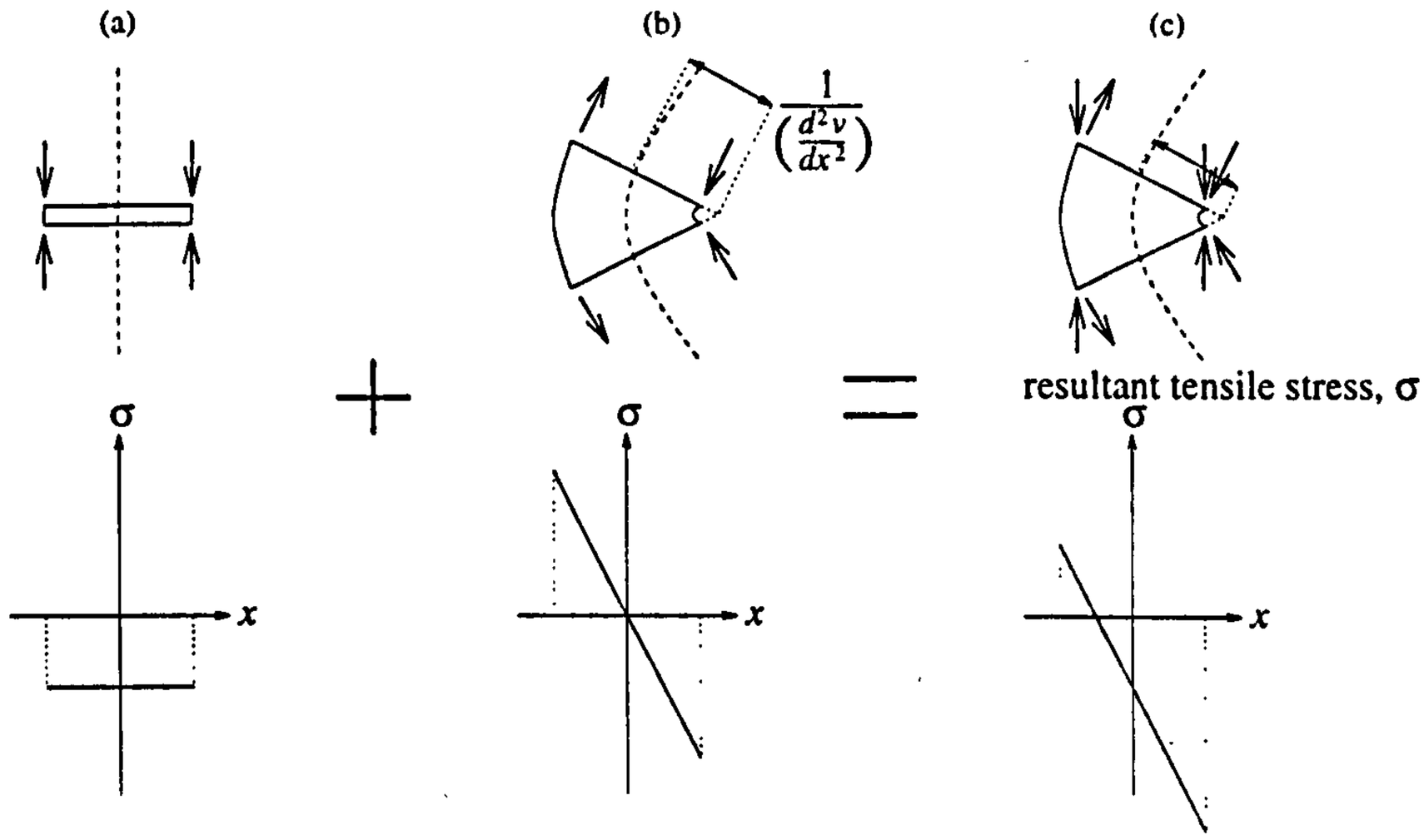

Figure 8.12: (a) the stress distributions across a horizontal line through a tower subject to compressive loads and (b) across a line perpendicular to neutral stress axis for a tower subject to pure bending. (c) the maximum tensile stress in the same cross section under loading combined with axial compression is reduced.

The second derivative of tower deflection in Equation 8.9 is output from the computer model of the static analysis of bending. From this, the distribution of skin stress up the tower can be found using Equation 8.9.

The ultimate load condition is taken here as the load at which the maximum tensile stress in the structure is equal to the yield stress of the material multiplied by some factor of safety. The load condition could equally have been defined in terms of compressive stresses. In fact, it may be that compressive stresses are more important since, because the tower is compressed by its own weight and by the pretension in the guys, compressive stresses will be larger than tensile stresses. If the compressive stress for yield σ_y is the same as the tensile stress for yield, then it is the maximum compressive stress which limits the ultimate loads carried by the structure. It may also be that because of local geometry, stresses are higher than average for the structure leading to local buckling which may be the limiting factor. To use compressive stress as the limiting factor does not preclude use of the same method demonstrated here since maximum compressive stress (Equation 8.10 is calculated

in a similar way to tensile stress (see Figure 8.12). The analysis of compressive stresses is therefore not repeated here.

$$\sigma_C = \left| E_t r_o \frac{d^2 v}{dx^2} \right| + \frac{C}{A_{xt}} \tag{8.10}$$

.The longitudinal deflection model (Section 2.4) is used to calculate a distribution of axial compression forces. From these forces additional stresses can be calculated which are constant across any particular tower cross section. Here, C is used to denote the axial force in the tower due to these axial loads. The most significant loads are the tower's weight and the axial compression due to pre-tension in the guys. For C, compression is positive. These additional stresses reduce the tensile stresses in the structure due to bending alone (see Equation 8.9). Because in the longitudinal deflection model, compressive forces are treated as positive, the term for longitudinal stress is subtracted from the term for skin stress due to bending.

8.3.1.2 Search Method

The static models (Chapter 2) of tower bending (Section 2.3) and tower longitudinal deflection (Section 2.4) allow the maximum stress in the structure to be found for a particular load regime. The regime corresponds to extreme conditions determined by the designer and any international standards the design adheres to. The wind turbine may or may not be generating power and may be orientated in any direction with respect to the oncoming wind. It represents the most extreme conditions that it is judged the machine should withstand. It consists of six head loads (forces and torques) and six loads distributed along the height of the tower as illustrated in Figure 5.1. By varying the design of the structure, one can be found for which the maximum stress is equal to the ultimate stress of the material chosen (usually the yield stress). This criterion may also include a safety factor. For example, the maximum stress calculated may be constrained to be only half the ultimate stress of the material.

A search method used is the Van Wijngaarden, Dekker, Brent [31] method. The search function changes the tower wall thickness until the maximum skin stress is equal to a critical value. This value is the product of the ultimate tensile stress of the material and some safety factor. The skin stress is calculated using Equation 8.9.

The search is likely to fail if the function is discontinuous. In this case, a discontinuity occurs when the guys become suddenly slack if the tower is too flexible below the point of attachment or if vertical loads are too large.

8.3.1.3 Comparing Tower Designs

Figures 8.14 and 8.15 show the variation of tower mass and wall thickness with outside radius. Three tower design approaches are compared.

1. the outside radius at the base ($r_o(0)$) of a conical. free-standing tower is varied:

2. the outside radius at the base ($r_o(0)$) of a conical. guyed tower is varied:

3. the outside radius at the point of attachment of the guys to the tower ($r_o(\lambda_{ct}H)$) of a double-tapered, guyed tower is varied and the base outside radius is held constant at 0.269 m.

The general shapes are illustrated in Figure 8.13. The base is either fixed rigidly to the base fixing or freely hinged.

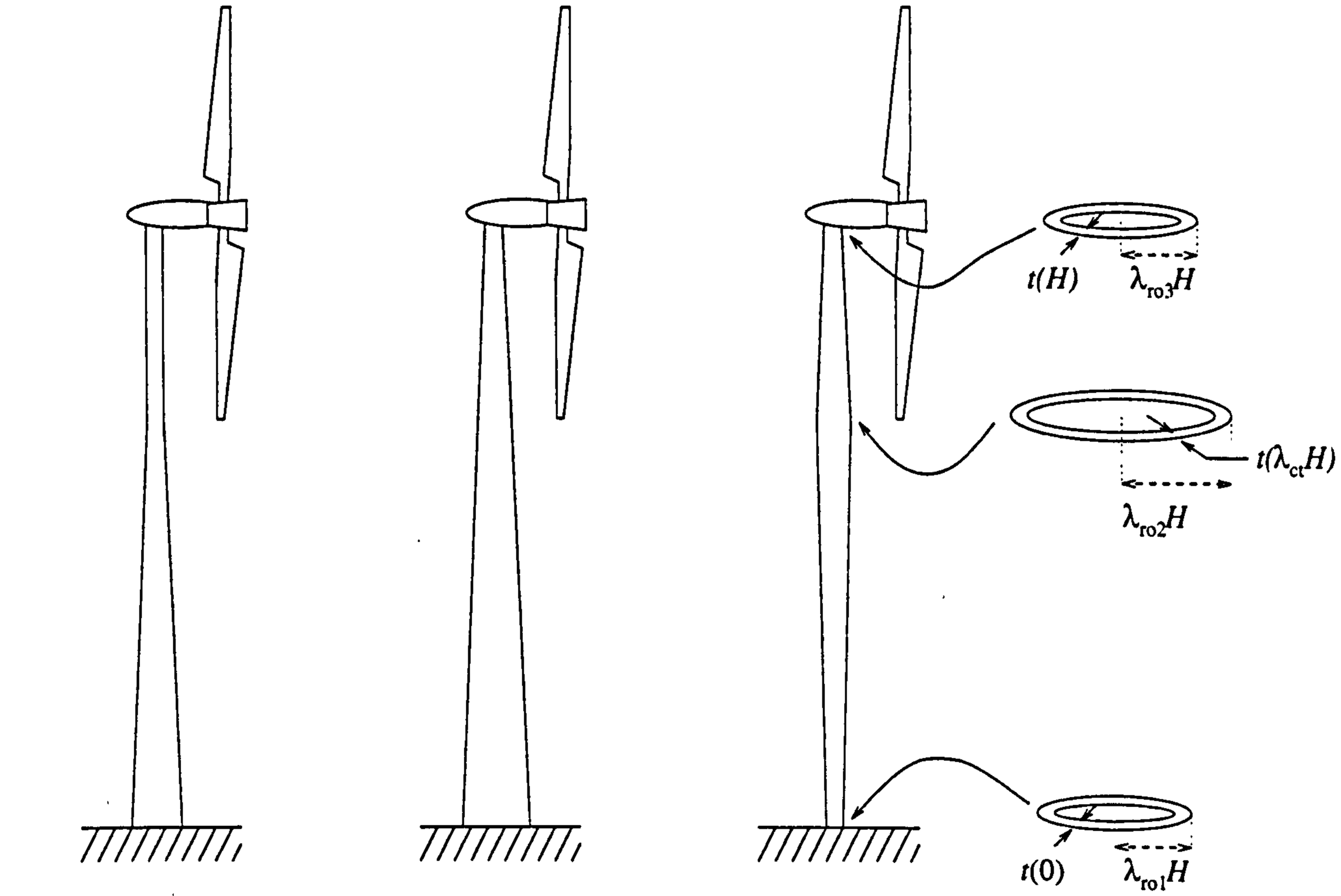

(a) double tapered tower (concave)

(b) conical tower

(c) double tapered tower of the kind used for Carter 300 kW wind turbines

Figure 8.13: By increasing the outside radius of the tower at the base, a general, double-tapered tower changes from being (a) concave through being (b) conical to being (c) convex. The two tower variants from which tower designs are optimised are conical and double-tapered ((b) and (c)).

In all cases other design parameters are held constant. The additional design parameters used are for a Carter 300 kW wind turbine. For example, the outside radius of the top of the tower is 0.270 m, the tower height is 49 m, the guy cables are attached at a height of 37.24 m. the rated power of the machine is 300 kW and the swept area is 444 m^2.

The load conditions used were the thrust due to the powertrain generating 300 kW power in a windspeed of 21.5 ms^{-1} (103 kN). The vertical forces are due to gravity acting on the nacelle and tower and, most significantly, the axial compression in the lower portion of the

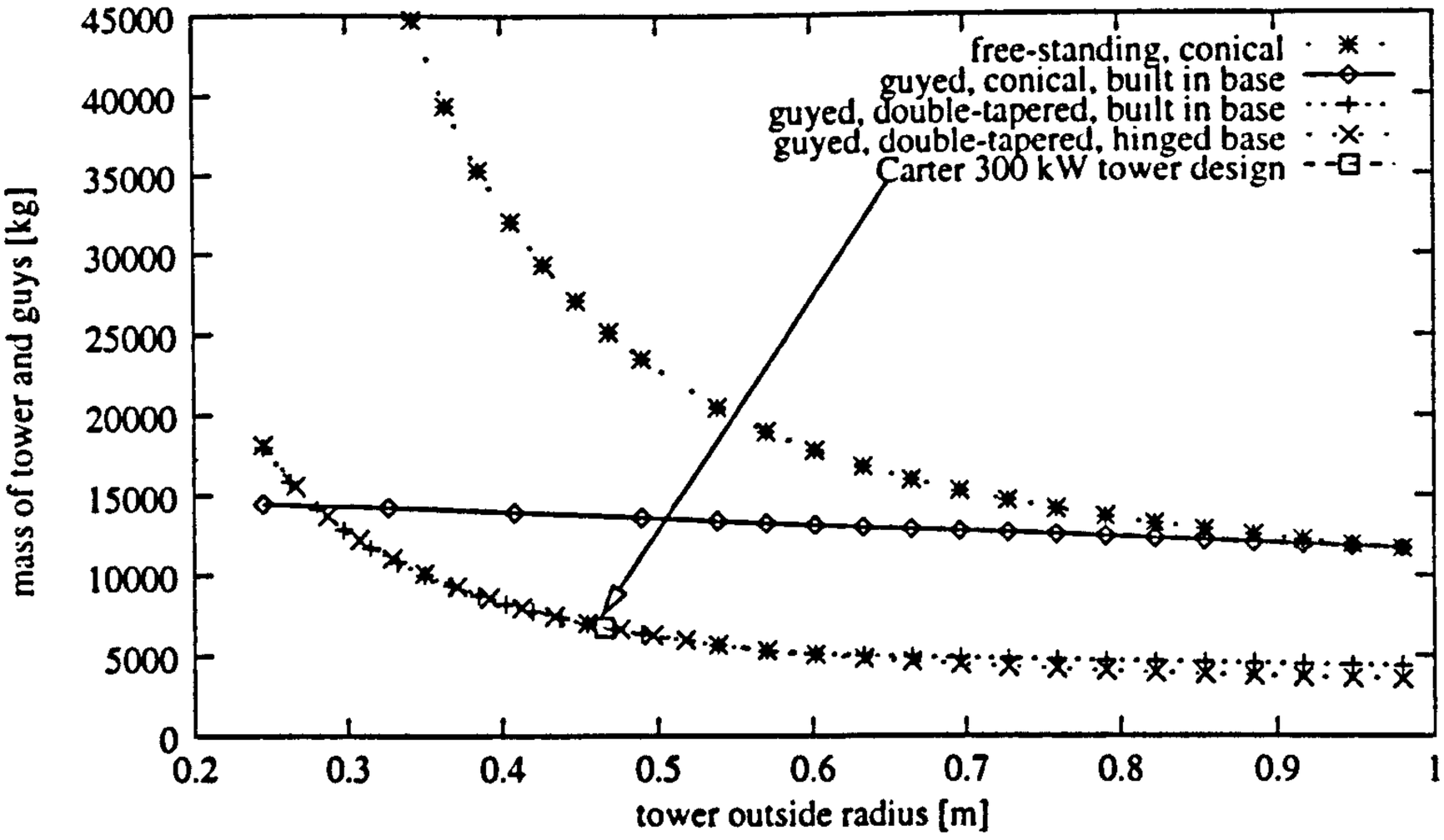

Figure 8.14: The relationship between the overall mass of the structural support system and the outside radius of the tower either at the base for conical towers or at the point of attachment of the guys to the tower for double-tapered towers. Three tower geometries are considered. For each point on each curve, the wall thickness of the tower is varied until the maximum skin stress in the tower is equal to the ultimate tensile stress of the material multiplied by a safety factor.

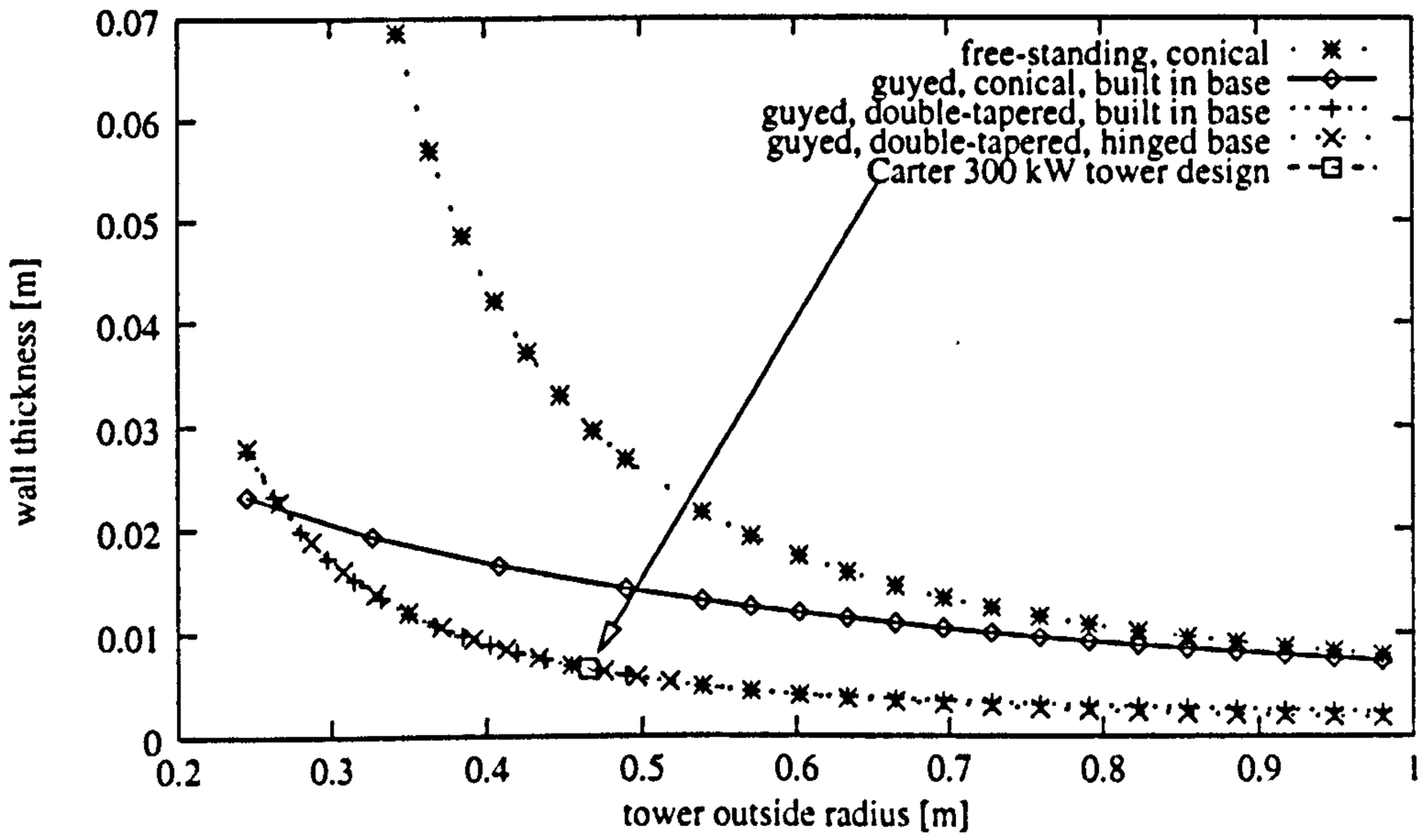

Figure 8.15: The relationship between wall thickness and outside radius for the same situations as in Figure 8.14.

tower due to the pre-stressed guy cables. For the material used, the ultimate stress was $\sigma_u = 282$ MPa. This value has been arrived at somewhat arbitrarily. It was known neither what ultimate load conditions the Carter 300 kW wind turbine was designed to withstand nor what the ultimate tensile strength was of the material used (galvanised steel) nor what safety factor was used. But applying the given load condition, the maximum stress in the structure was found to be 282 MPa. Using this figure subsequently allows results to be compared with existing Carter 300 kW tower design (a point for the Carter machine is plotted on both Figures 8.14 and 8.15).

The position and magnitude of the maximum stress in the tower are greatly influenced by the chosen extreme load conditions. It may be that a situation of very high wind speed when the machine is not generating is important. It may be that the yaw rate of the nacelle is limited and so there is a maximum value for gyroscopic loads. The extreme load condition must be determined by the designer before stress-limited optimisation of the tower mass.

In Figure 8.14, the curve for free-standing, conical towers falls below that for guyed, conical towers. This is because of the extra mass of the guys which must be included for the latter. If the wall thicknesses are compared (Figure 8.15), the curves do not cross but almost meet. This suggests that for steeply coned towers, including guys gives little load-bearing advantage.

Curves representing guyed towers cross (both Figure 8.14 and Figure 8.15) where the conical and double-tapered groups of towers are equivalent. To the left of this crossing point, the double-tapered tower is in fact concave (the slope of the tower sides below the point of attachment of the guys to the tower is greater than the tower slope above). To the right, the tower is convex as is the tower of the Carter 300 kW design (the guy attachment point is the widest point on the tower). Figure 8.13 demonstrates the difference between concave and convex, double-tapered tower geometries.

The position of maximum skin stress would be expected to be at the base of a conical, free-standing tower but in fact, if the extent of coning is sufficient, the maximum skin stress is above the base (see Figures 8.16 and 8.17).

Table 8.2: The gravity and the initial strain both affect the lateral stiffness parameter and the axial load on the tower from the guy cables. Quoted are the final values after assembly of the guy cables and consequent vertical deflection of the tower (Figure 2.10).

gravity (kg m s^2)	initial strain (ϵ_{ic})	lateral stiffness (k_{Bc} N m^{-1})	axial compression (F_{cv} N)
0.00	0.000	0.67×10^6	0.0
0.00	0.001	1.3×10^6	0.42×10^6
9.81	0.001	1.3×10^6	0.41×10^6

Table 8.2 shows the effect on the guy stiffness parameter k_{Bc} and the axial load on the tower F_{cv} from the guy cables of different values of gravity and initial strain ϵ_{ic}. If both gravity and initial strain are zero. there are no vertical forces on the tower. there is no vertical deformation of the tower and the axial compression is also zero. Figure 2.10 shows

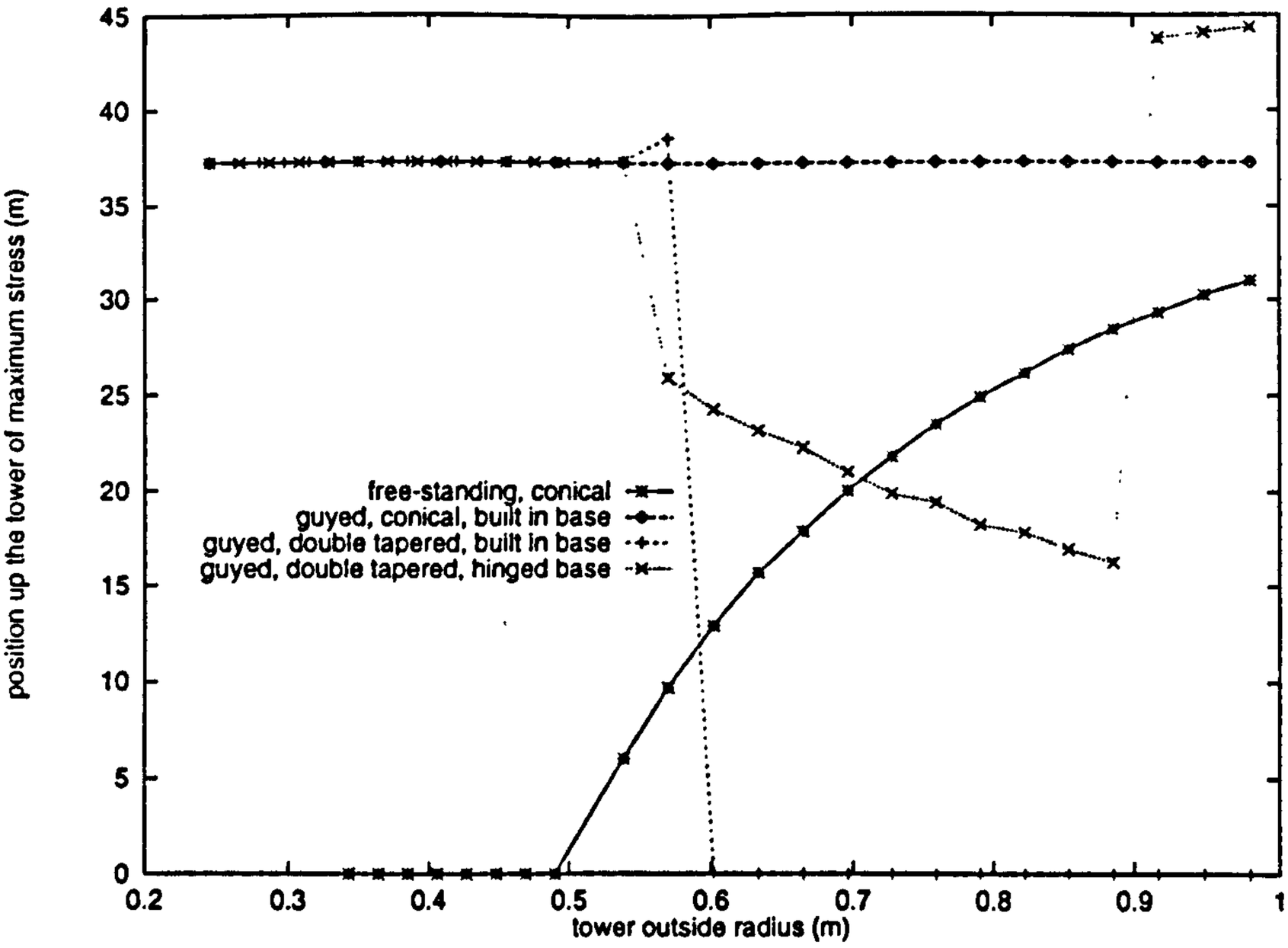

Figure 8.16: The relationship between the position of the maximum skin stress up the tower and the outside radius of the tower for the same situations as in Figures 8.14 and 8.15 above.

the steps which comprise the calculation of the two parameters k_{Bc} and F_{cv} before any static analysis is undertaken. If the initial strain in the guy cables is increased, the tower deforms vertically and both k_{Bc} and F_{cv} are slightly less than if the cables were rigidly fixed to a point $\lambda_{ct}H$ above the tower base. If gravity loads are added, k_{Bc} and F_{cv} are further decreased by 0.007% and 2%. The latter can be seen in the third line of Table 8.2.

Stress distribution curves plotted using Equation 8.9 are more complicated when the tower is guyed. They are made up of two components. If gravity, external loads, f_v and the initial strain in the guy cables, ϵ_{ic} are all set to zero, there are no vertical loads on the tower and the distribution of skin stresses is due only to the bending moment distribution (Equation 8.8). This is the first curve plotted in Figures 8.18. A tower with a built in base has a finite skin stress at the base (it is positive because of the definition of skin stress due to bending moments in Equation 8.8). A tower with a hinged base has zero skin stress there. Because in Equation 8.9 the skin stress is dependent on the magnitude of the bending moment, the first curve ((a) skin stress due to bending moment only) is always positive. $\sigma_T > 0.0$ in both cases.

If the initial strain in the guy cables ϵ_{ic} is not zero, the stress distributions for the lower portion of the tower are translated to the left and additional stresses added. If gravity loads are added, the stresses are increased throughout the tower.

The addition of guys to a coned tower changes the position of maximum skin stress (Figure 8.16 and Figure 8.19). This position is the point of attachment of the guy cables for narrow tower bases. Above a certain tower base radius (0.55 m in Figure 8.16), this maximum stress point changes. In the case of a built in tower, the point rises between about

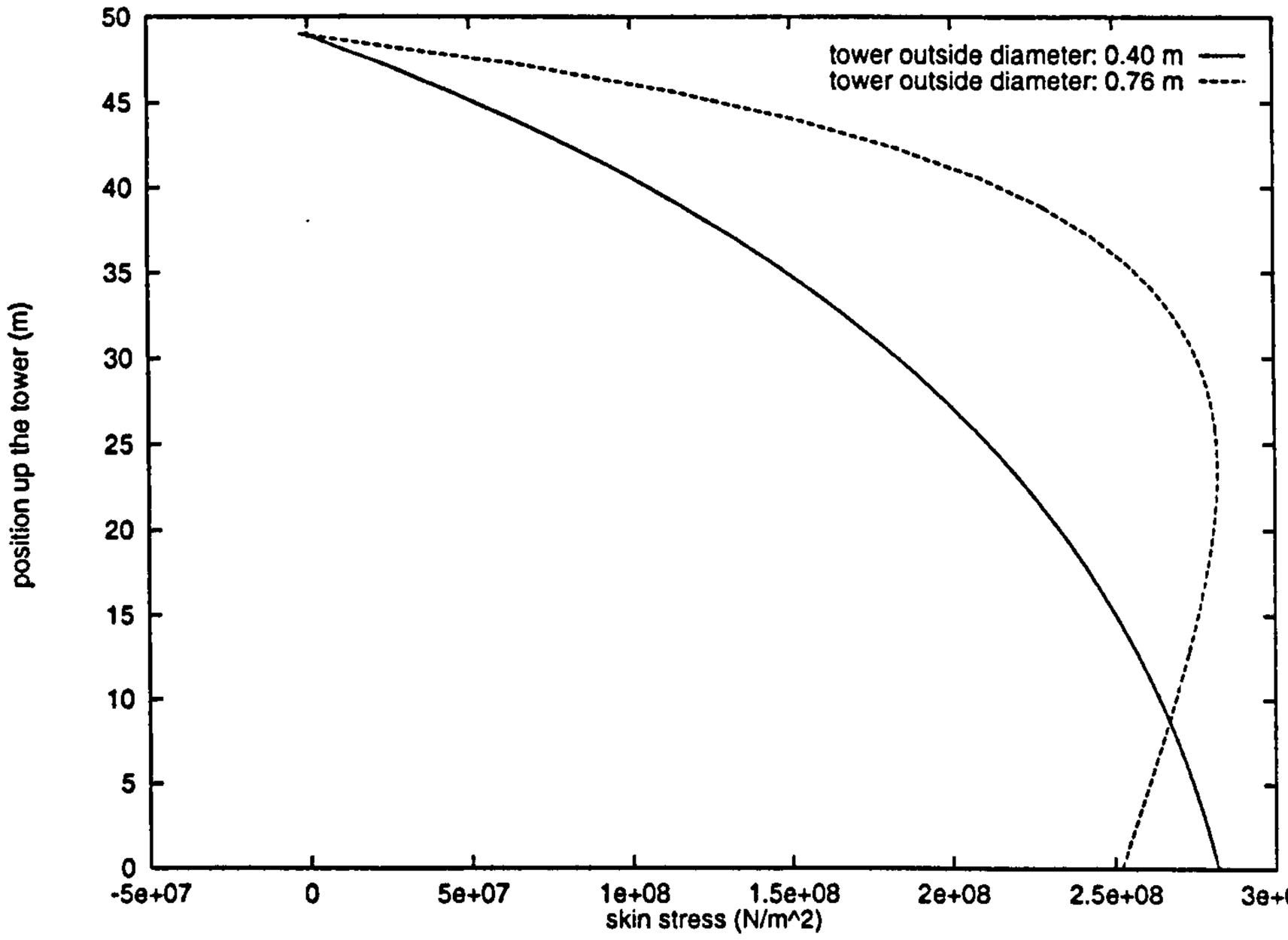

Figure 8.17: The skin stress distributions in two free-standing, coned tower designs. For the first, the base outside radius was set at 0.41 m and the tower wall thickness was found to be 0.042 m in order that the maximum skin stress should be 282 MPa. The position of the maximum skin stress is at the base. For the second, the base outside radius was set at 0.76 m and the tower wall thickness was found to be 0.012 m. The position of the maximum skin stress is at 23.5 m up the tower.

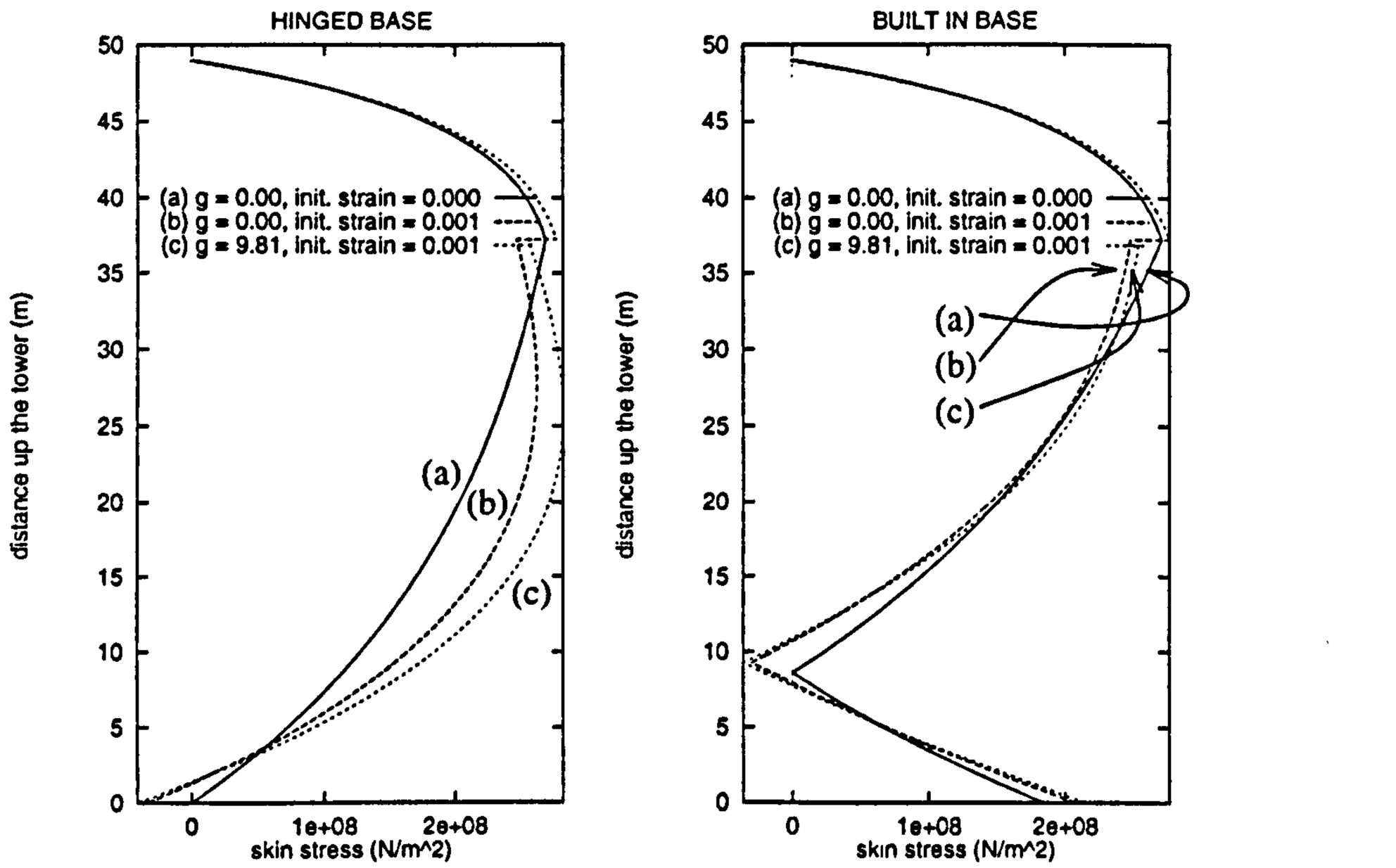

Figure 8.18: Skin stress distributions in a double-tapered, guyed tower with either a hinged or a built in base. Three different combinations of guy cable initial strain, ϵ_{ic} and gravity acceleration measured in $m\ s^{-2}$ are compared. The values are listed in the keys. Equation 8.9 is used to calculate the skin stress at points up the tower. The load case is $F_{nh} = 10{,}000\ N$ for all curves. The values of the lateral stiffness and the axial compression due to the guys are given in Table 8.2.

5.5 m and 5.9 m and jumps to the base. The reason for this discontinuous behaviour can be seen by looking at the distributions of stress with vertical position up the tower (Figure 8.19). The base carries high stress because it is built in and carries a large bending moment reaction (Equations 2.9 and 2.27). The position of the point of maximum stress will either be at the base or at a point between the point of attachment of the guys to the tower and the tower top.

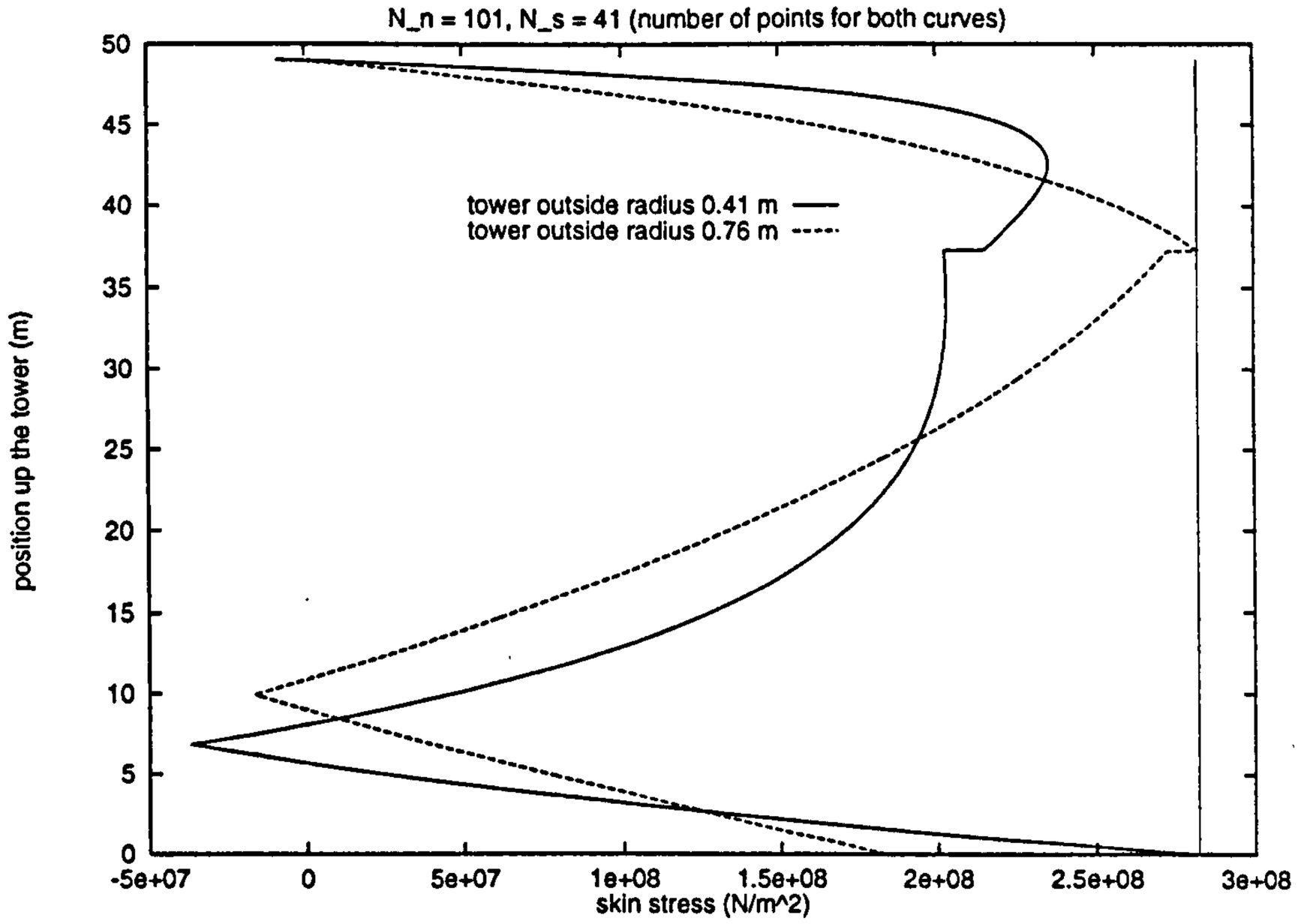

Figure 8.19: The skin stress distributions for two double-tapered, guyed towers with bases rigidly built into the foundation. For the first, the outside radius of the tower at the point of attachment of the guys to the tower was set at 0.41 m and the tower wall thickness was found to be 0.0089 m, skin stress maximum at the base. For the second, the outside radius was set at 0.76 m and the tower wall thickness was found to be 0.0031 m, maximum skin stress at 37.2 m (guy cable attachment point).

Guying a tower allows the possibility of making the base connection a free hinge. Maintenance is then possible simply by lowering the entire structure to the ground. If one guy snaps, though, it would be disastrous. A halfway configuration is for the tower to be free-standing when the wind turbine is shut down. Guys are necessary to support the wind turbine when generating. This is a strategy proposed for the new 6–10 kW wind turbine launched by Farm Power, the specialist agricultural division of Micon on 28th August 1997. It is not the design of the prototype launched but one of the options considered for later development.

The stress at the base of a simply supported tower is low because the bending moment there must be zero. If the tower base radius is greater than a certain value (0.55 m in this case). the position of the maximum stress in the tower is somewhere between the base and the point of attachment of the cables to the tower (see Figure 8.16). This discontinuity can

also be explained by looking at Figure 8.20.

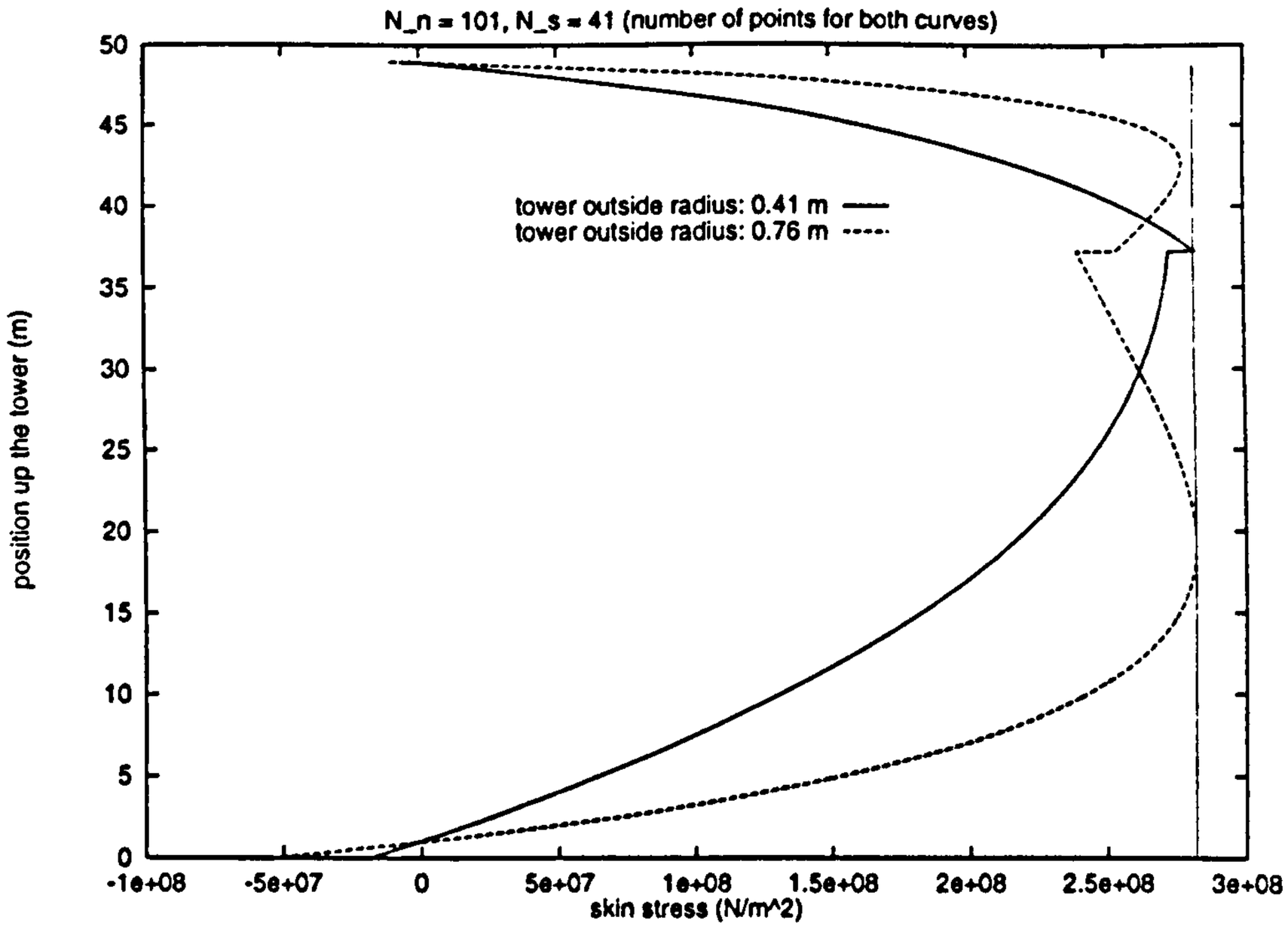

Figure 8.20: The skin stress distributions for two double-tapered, guyed towers with bases freely hinged. For the first, the outside radius of the tower at the point of attachment of the guys to the tower was set at 0.41 m and the tower wall thickness was found to be 0.0087 m, maximum skin stress at 37.2 m. For the second, the outside radius was set at 0.76 m and the tower wall thickness was found to be 0.0027 m, maximum skin stress at 19.4 m up the tower.

8.3.1.4 Varying Outside Radius

It is also possible to optimise the load-bearing ability of the tower by altering the outside radius of the tower at every point up the tower. As already mentioned in Section 8.3.1, this may increase cost of manufacture unacceptably but towers should be optimised before being cost is compared with towers of standard gauge. The method for optimising outside radius described here is only applicable to free-standing towers.

If there are no vertical loads on the tower (no guy cables. negligible weight). the bending moment distribution is unaffected by deflection and so can be calculated in advance (Section 2.3). The outside radius can be calculated by rearranging Equation 8.11. The skin stress, σ_T is equal to the ultimate stress, σ_u. The terms for the cross sectional area and second moment of area of a ring are expanded. Terms in which the wall thickness is raised to a power higher than one are neglected. In this way. Equation 8.12 has been derived. The radius predicted in this way is very close to the radius necessary for the stress $\sigma_T = \sigma_u$. Using the line search method [31]. the radius is calculated to the required accuracy.

$$\sigma_T = \frac{r_o}{I_{xt}} |M_t(x)| - \frac{C(x)}{A_{xt}} \tag{8.11}$$

$$r_o(x) \approx \frac{1}{2\sigma_u} \left(\frac{-C(x)}{2\pi t_t} + \sqrt{\frac{C(x)^2}{2\pi t_t} + \frac{4\sigma_u M_t(x)}{\pi t_t}} \right) \tag{8.12}$$

In order to ensure that skin stress is indeed equal to σ_u everywhere up the tower (Figure 8.22), the following three steps are carried out:

1. static analyses of tower bending and also of tower longitudinal deflection;
2. the process of radius optimisation described here for each vertical position up the tower;
3. bending and longitudinal analyses.

The radius variation is not dramatically different from the initial conical tower shape.

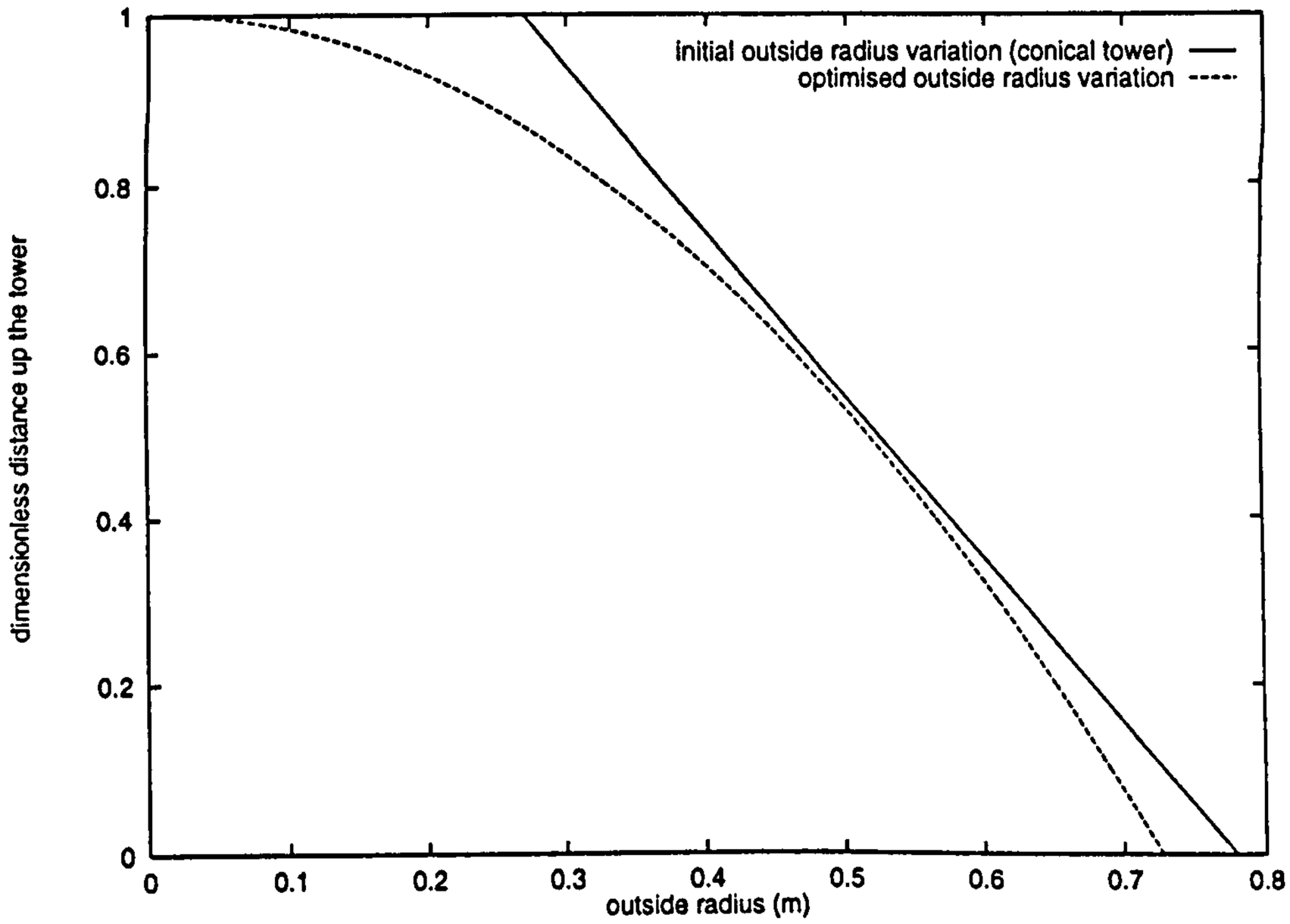

Figure 8.21: Variations of tower outside radius with vertical distance up the tower. Initially. the tower is conical, after optimisation the sides are curved. Initial design parameters come from the set for the Carter 300 kW machine with wall thickness set to 0.0110 m, tower base outside radius set to 0.780 m, tower top outside radius remains 0.270 m. This optimisation reduces the mass of the whole tower and guys from 13700 kg to 12700 kg.

This method of tower mass optimisation is not applicable for guyed towers. This is because the technique described in Section 8.3.1.4 is based on the assumption that the stress distribution is dependent only on the loading and is unaffected by the deflection of the tower.

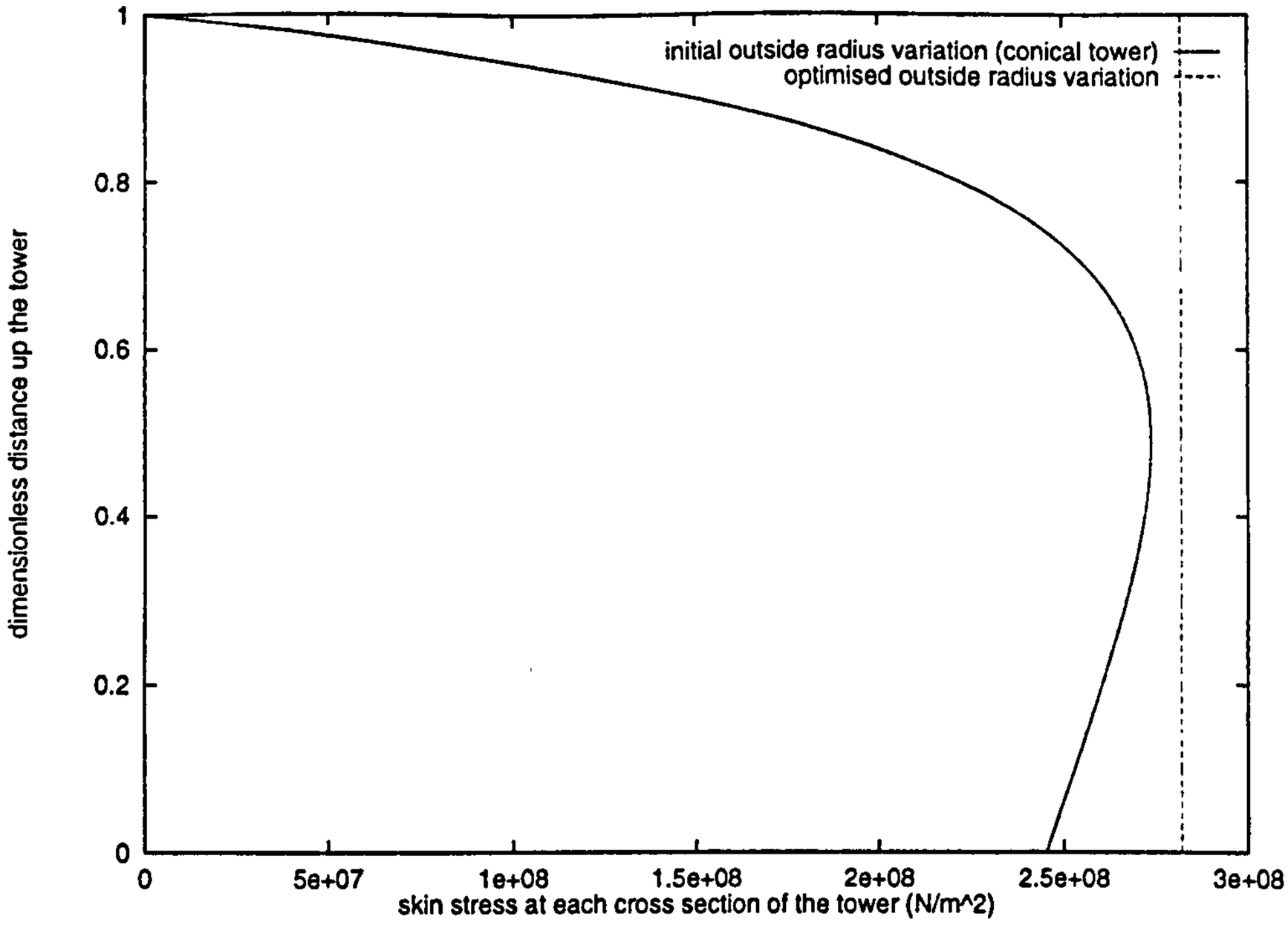

Figure 8.22: Variations of skin stress in the tower for the two cases described in the caption for Figure 8.21 above. In the optimised tower, the stress is equal to the ultimate stress for the material at all positions up the tower.

When axial loads are included, the deflection of the tower gives rise to bending moments (Section 2.3) which give rise to additional components of the stress distribution. Secondly, the stress may change continuously from positive to negative values due to the combined effect of tower bending and axial loads (for example, see Figure 8.18). In these situations, it is not possible to ensure that the stress is σ_u everywhere and a more complicated set of rules must be developed to optimise the stress distribution.

8.3.1.5 The Perfect Tower for Static Load Bearing

For the purposes of supporting a particular load regime, a perfect tower can be designed. Given sophisticated enough search routines, the outside and inside diameters of the tower at every point up the tower can be optimised. This can be simultaneous with optimisation of the geometry of the guy cables. In a perfect tower design, the product of the skin stress and the safety factor will be equal to the ultimate stress at every point up the tower height. Potentially, actuators in each guy could alter the tension to maintain optimum static load-bearing capability and also optimum dynamic characteristics.

In order to reach the optimum design, the geometric parameters must be altered so that at points of high stress, cross sectional areas or diameters are larger than in areas of lower stress. This is the same mechanism by which natural structures such as trees and bones are optimised and has been explored by Mattheck [67].

8.3.1.6 Dynamic and Static Stability

Having shown that the tower designs withstand specific, extreme load conditions, the dynamic characteristics must also be investigated.

As the outside diameter of the tower is increased and the wall thickness decreases, the first and second natural frequencies increase (Figure 8.23). The frequencies of free-standing, conical towers are all significantly lower than guyed structures (< 50% for fundamental frequencies). Making the base freely hinged reduces the stress carried by the tower (see Figure 8.14) but also decreases the natural frequencies (particularly the second frequency) for any new design, a Campbell diagram (Figure 1.1) should be plotted to investigate interference between forcing and response frequencies.

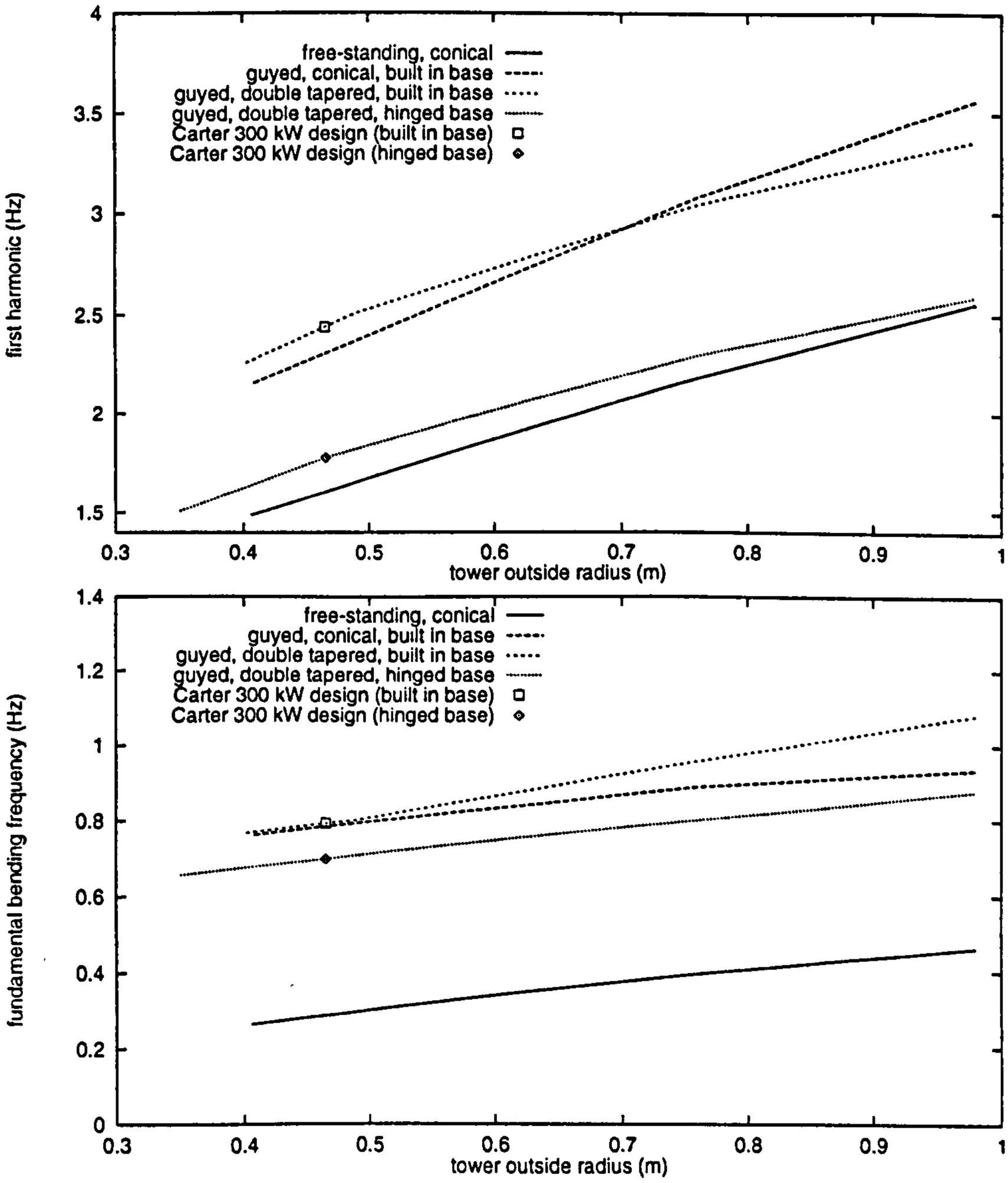

Figure 8.23: The first and second modal frequencies have been calculated for different tower designs whose wall thickness parameters have been minimised for the same extreme load conditions used to obtain data for Figures 8.14 and 8.15.

Optimisation of the tower design (similar to static load-limited optimisation) can be achieved with respect to dynamic response. A particular resonant frequency may be required or the structure may merely be required to be soft or stiff. The design can then be modified until this is achieved. The modal characteristics are of particular importance where dual or variable speed operation is desired.

The ultimate load-bearing capability is likely to be more important. Most flexible would be a search method having access to many design parameters and seeking both a set of load-bearing criteria and a set of dynamic criteria.

The loads at which the tower buckles elastically must also be determined. Figure 8.24 shows the maximum values of tower head vertical forces to avoid buckling. Forces arise from the weight of the nacelle and any deviation from the horizontal of the powertrain thrust. In practice however, these loads are likely to be orders of magnitude lower than the loads critical for buckling.

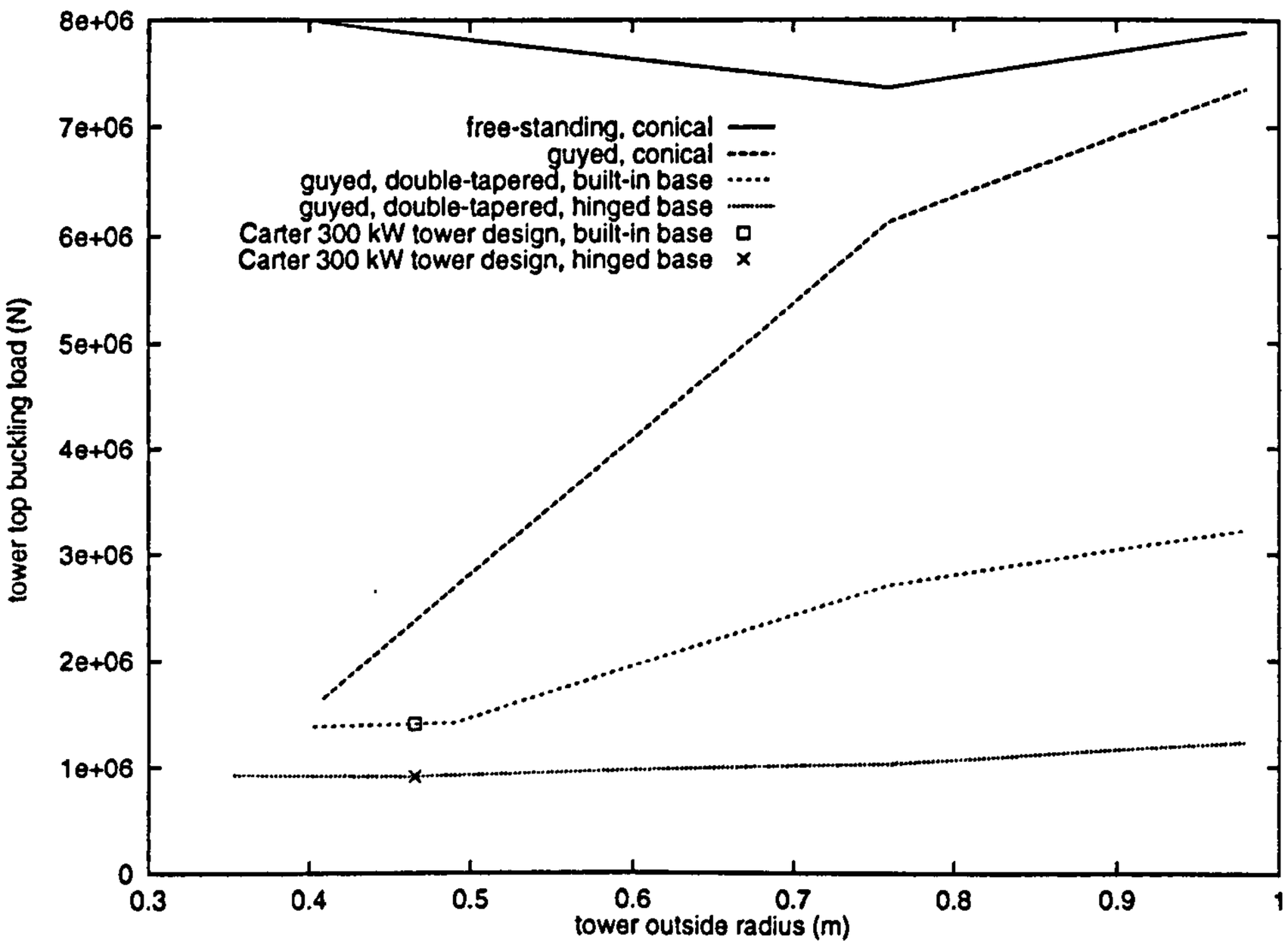

Figure 8.24: The ultimate elastic buckling loads have been calculated for the same tower designs from which modal data were obtained for Figure 8.23. The loads represent the maximum vertical head load which the tower can support.

The tower is more likely to buckle under extremes of guy tension (see Figure 8.25). The assembled guy load for the Carter 300 kW machine is plotted on the same graph (< 30% the smallest critical load). This load may increase during operation because of increased guy tension due to large lateral loads on the tower, or due to vibration of the guys. Such additional loads should be calculated by the designer for any of these expected circumstances.

The buckling loads of all double-tapered towers are significantly lower than for conical towers. Minima on the relevant curves suggest that there is a conflict between the narrowing of the wall thickness which tends to decrease the buckling load and the widening of the

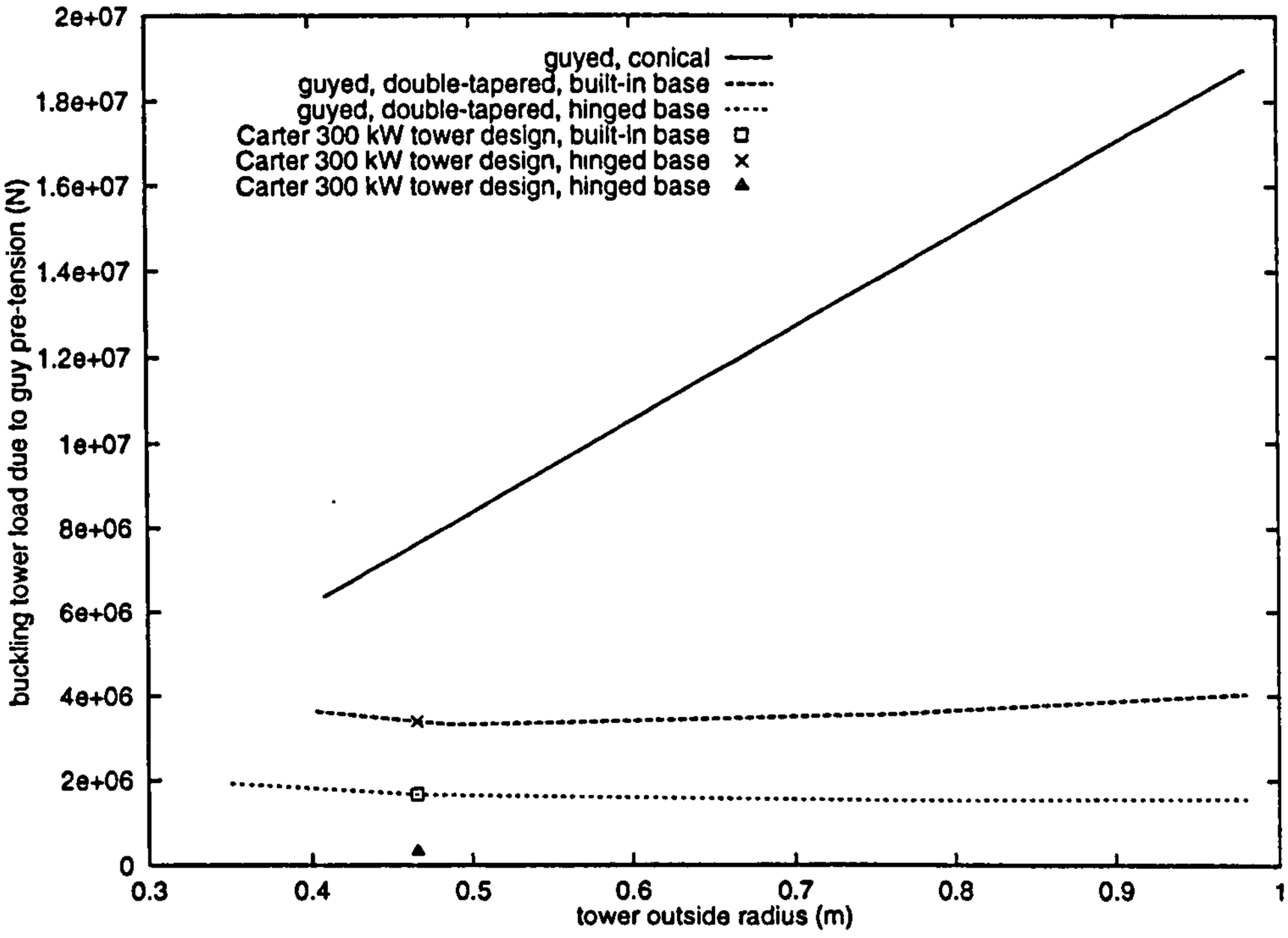

Figure 8.25: The ultimate elastic buckling loads have been calculated for the same tower designs from which modal data were obtained for Figure 8.23. The loads represent the maximum vertical load passed to the tower from the guys. The parameter varied is the initial strain in the guys at assembly. Some reduction in the initial vertical load occurs as the tower deforms vertically after assembly of the guys.

outside diameter which tends to increase it.

8.3.1.7 Summary of Stress-Limited Optimisation

As stated at the beginning of Section 8.3, it is more useful to compare towers in which the maximum stress is the same for a particular set of loads than to compare towers of the same mass. In this final section, a selection of the same six tower shapes as in Figure 8.6 are compared. The set of conditions and parameters which is held constant is listed below.

- The maximum tensile stress in the structure is 282×10^6 N m^{-2}.
- The head load (F_{nh}) is 100000 N (it is the only load on the structure apart from gravity).
- The height, H of the tower is 49 m.
- The initial strain, ϵ_{ic} in the guys is 0.0005.
- The ratio to the tower height of the height to the point on the tower to which the guy cables are attached, λ_{ct} is 0.76.
- The ratio to the tower height of the displacement of the guy cable anchor points from the base of the tower, λ_{cg} is 0.4.
- The nacelle mass (M_n) and moment of inertia (J_{nt}) are 4780 kg and 15200 kg m^2.
- The number of nodal points is 101 and the number of points in each spline section is 21.
- In the case of guyed towers, the base is freely hinged ($k_{Bf} = 0$ N m rad^{-1}).

Other design parameters are taken from the parameter set for the Carter 300 kW machine (Appendix H).

The maximum tensile stress in each of the six towers is constrained to be 282×10^6 N m^{-2} (Figure 8.27). This is acheived by varying the wall thickness (Table 8.3). The outside radii of the towers have been chosen so as to give approximately the same wall thickness values. From Figures 8.26 and 8.28, the stiffness of each of the towers can be compared. The guyed towers are all stiffer than the free-standing one although they are lighter (Figure 8.29). The double-tapered tower is not as stiff as the other guyed towers even though the maximum tensile stress carried is the same. The double-tapered tower is also the lightest and therefore the cheapest in terms of material costs.

With more sophisticated search routines, it should be possible to hold both the maximum static stress and the fundamental frequency of vibration constant. It would then be expected that deflections of the various towers under identical load conditions would also be similar. The designs could then be compared to see which was lightest and therefore cheapest in terms of material costs.

Table 8.3: Geometrical parameters for the six tower designs compared in this section. If the tower is cylindrical or conical, the outside radius at the point of attachment of the guys to the tower is calculated from the other two outside radii given. The outside radius of the third tower design is optimised for the given wall thickness.

tower shape	base outside radius (m)	outside radius at point of attachment of guy cables (m)	outside radius at tower top (m)	skin thickness (m)
A	1.0	–	1.0	0.00561
B	1.0	–	0.50	0.00566
C	–	–	–	0.00560
D	0.50	–	0.50	0.00546
E	0.90	–	0.40	0.00501
F	0.31	0.5	0.25	0.00554

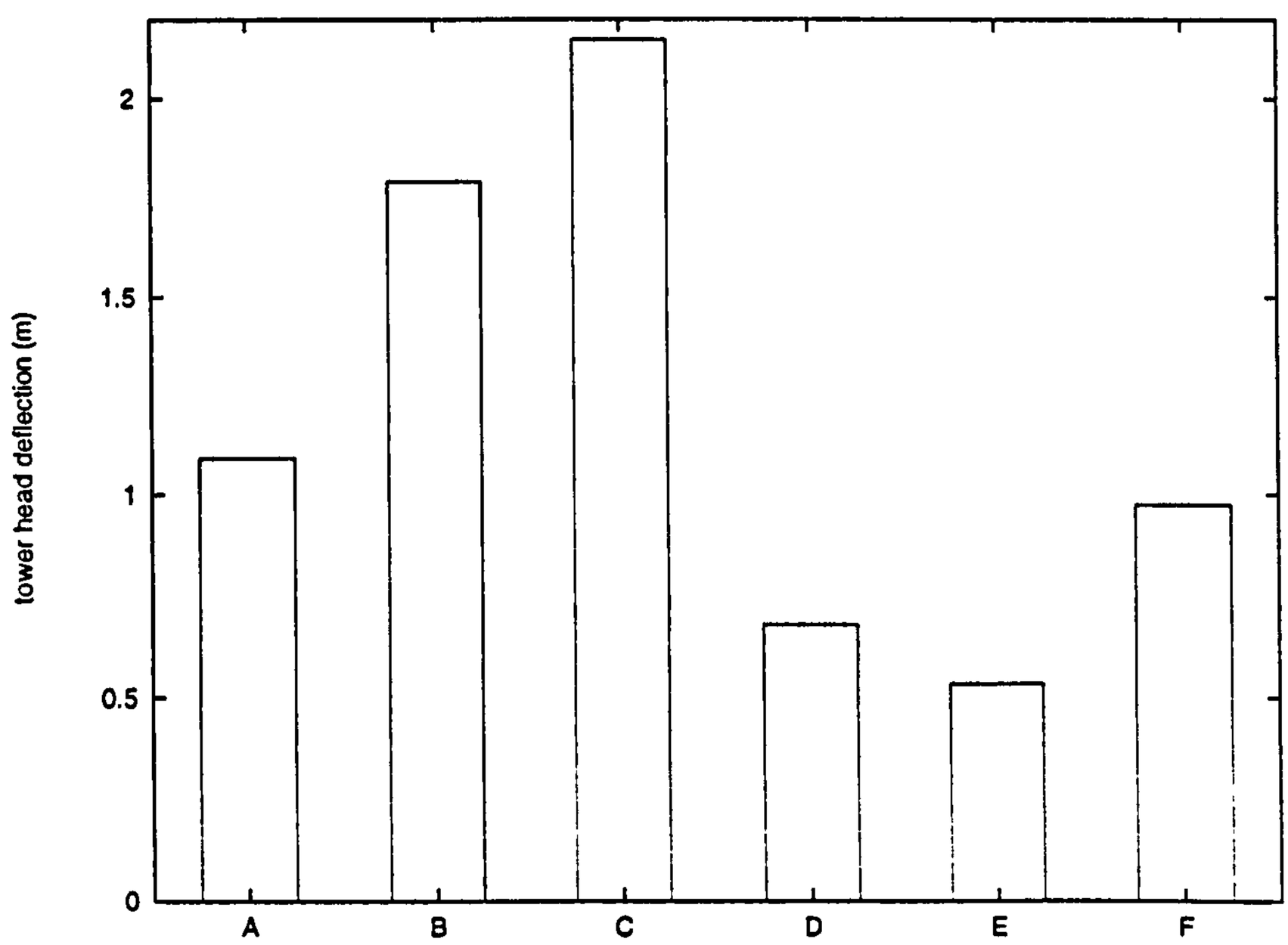

Figure 8.26: Comparing the deflection of the tower head of each of the six towers (the shapes are similar to A–F in Figure 8.6) under a constant horizontal thrust at hub height of F_{nh} = 100000 N. Tower deflection shapes are similar to the six illustrated in Figure 8.7.

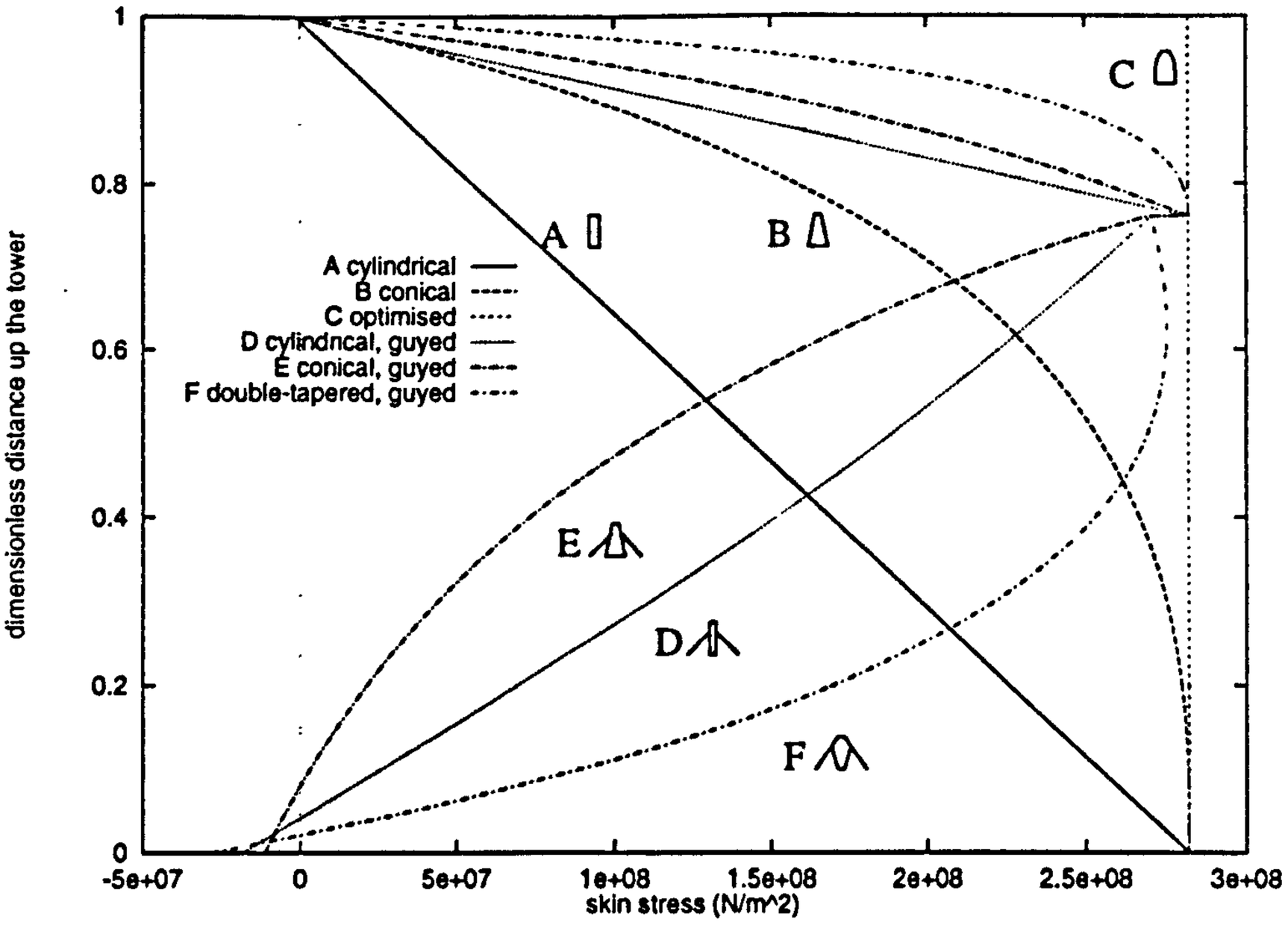

Figure 8.27: The skin stress distribution in each of the towers (A–F in Figure 8.6) under a constant horizontal thrust at hub height of F_{nh} = 100000 N. Skin stress is defined in Section 8.3.1, Equation 8.9. Tower wall thickness parameters are optimised so that the maximum tensile stress is 282×10^6 N m^{-2}.

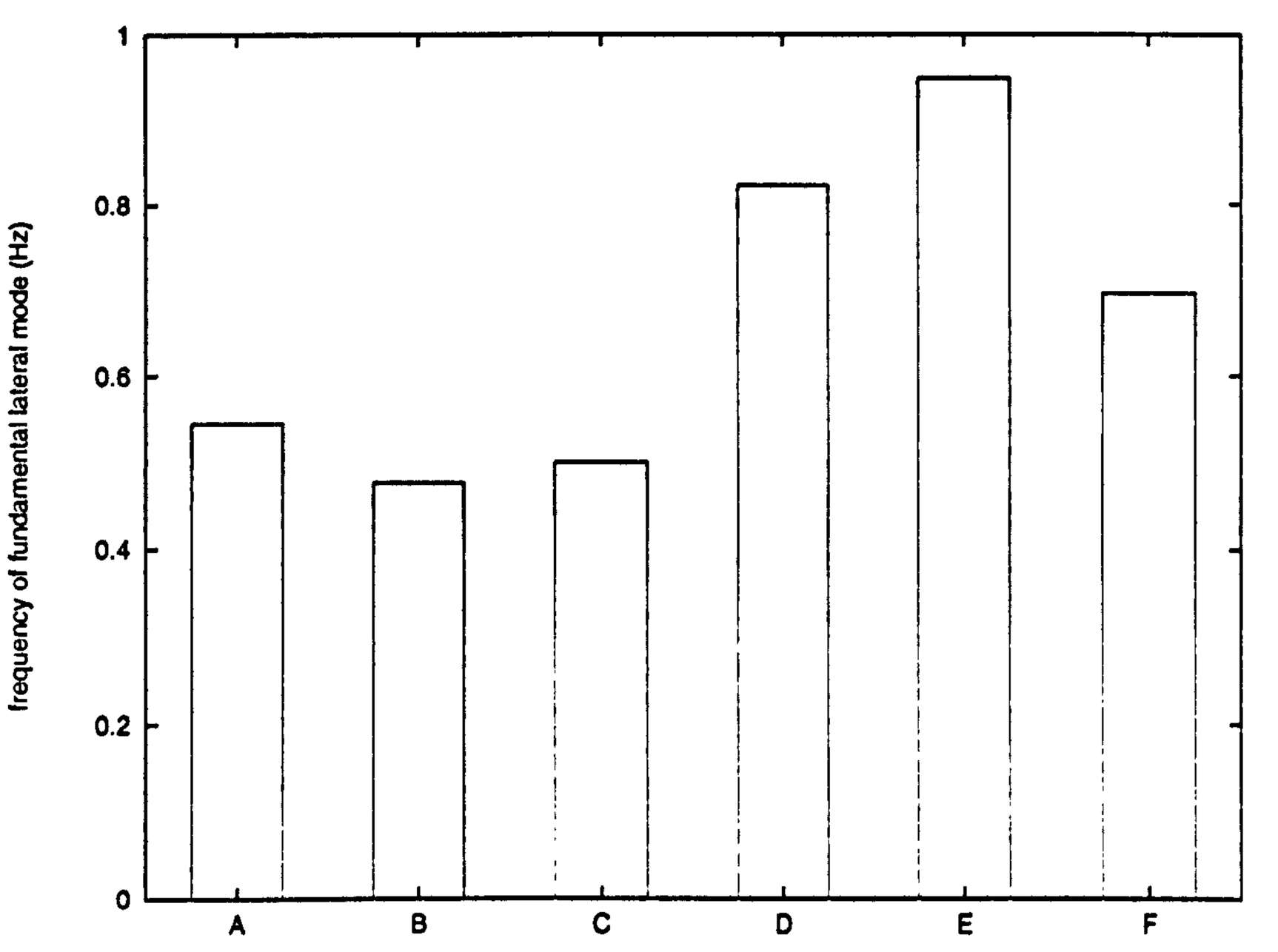

Figure 8.28: The frequency of the fundamental lateral (bending) mode of each of the six towers (the shapes are similar to A–F in Figure 8.6).

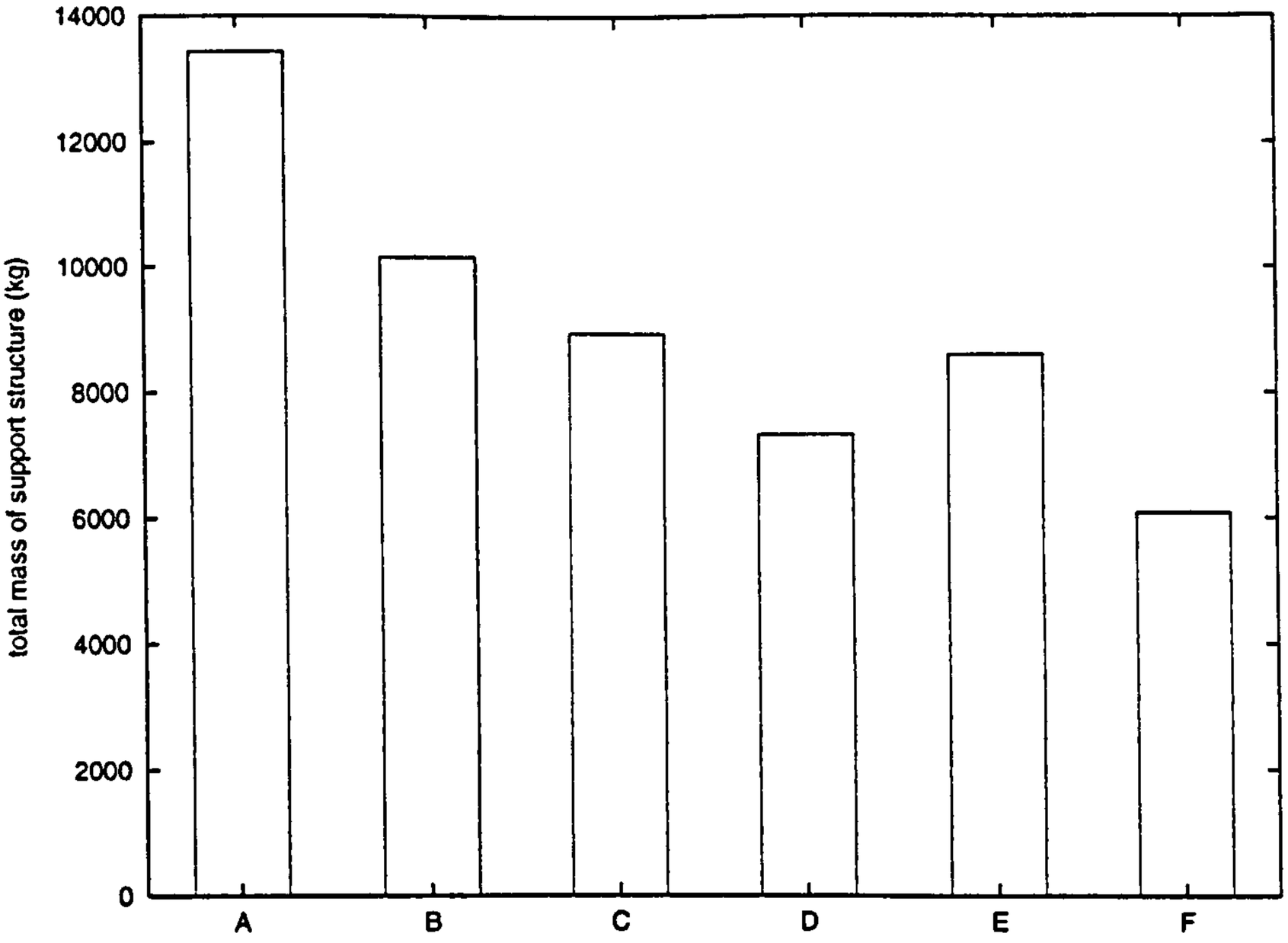

Figure 8.29: The total mass of the structural support system (including tower and guys, where present). The shapes of the six towers are similar to A–F in Figure 8.6.

8.3.2 Conclusions

Static analysis of the whole structure subject to a particular extreme load condition is important in order to identify highly-stressed regions. Using this analysis, the tower design can be optimised using an appropriate search method so that the geometry gives a minimum overall mass for a particular maximum stress under a specific extreme load condition.

Such optimised tower designs tend to decrease in mass with increasing outside base diameter for conical towers and with increasing outside diameter at guy attachment height for double-tapered towers. Also increasing with outside diameter are the first and second natural frequencies of the tower. There are also changes in the critical vertical loads for elastic buckling of the tower.

New designs should be tested statically and dynamically under expected extreme load conditions.

Chapter 9

Conclusions

9.1 Applications and Developments

Amongst commercial wind turbines currently available, machines with lightweight structural supports are rare. The Carter 300 kW wind turbine is an example of an extremely compact, lightweight and flexible design. One factor which helps it acheive this is that the tower is supported by four guy cables attached to four additional concrete foundations near the base.

For such machines, structural analysis is even more important than for stiffer contemporaries. Large deflections could mean collisions between blades and tower. Large stresses could give rise to yield, fracture, fatigue or buckling. If the resonant frequency of the tower is lower than the forcing frequencies (1P and 2P for a two bladed rotor), then resonance will be excited at all times during which the machine is disconnected from the mains electricity grid and the rotor speed free-wheels between the 1P and zero. It is important that aerodynamic and structural damping reduce the amplitude of vibrations on these occasions but also that the natural frequencies of the tower are accurately known. The damage due to fatigue will therefore be minimised by such a comprehensive knowledge of the harmonic behaviour of the structure.

It is also important to the designer to have tools available that allow rapid comparisons of many design options. The simplest techniques are fastest and also most transparent, enabling the relationship between various parameters and the desired behaviour of the machine to be gauged.

The approach adopted for modelling wind turbine towers has been to use the simplest techniques and where necessary to develop them. This has meant that, as the analyst and programmer, I have seen the connections between various elements of the models. Increases in complexity have only been made when necessary.

The combination of Rayleigh's and Stodola's methods together with the static analysis tool which combines direct solutions of the equations of static equilibrium with cubic spline interpolation between a course grid of nodal points is unique. The accuracy is comparable not only to direct, classical methods where models are sufficiently simplified but is also close to the results of Finite Element analysis of a beam representation of the structure

The goal of transparency is achieved because the effect of any changes in the set of design parameters (Appendix H) is apparent from the position in the Rayleigh formula

(Equation 4.8) of the energy term(s) associated with that parameter (see Appendix D for a complete list of Rayleigh energy terms). For instance, increasing the axial load on the tower (F_{cv}) is likely to decrease the frequency of bending vibrations because from Equation D.2, the numerator in Equation D.1 will be reduced. Alternatively, increasing the yaw moment of inertia of the nacelle will decrease the frequency of torsional vibrations provided there is stiff coupling between the tower and nacelle because from Equation D.9, the denominator in Equation D.7 will be increased.

Because the problem is defined specifically for wind turbines, solutions will in general be simpler and faster to obtain than by using a general Finite Element Analysis package. This has been born out by experience of using both modelling techniques. For objective comparisons between the methods described here and a Finite Element Analysis method, it is necessary to find out the number of unknowns, the number of mathematical operations and the amount of data which it is necessary for the computer to store at any one time for each method and for equivalent levels of accuracy. This could constitute an additional piece of research.

The techniques allow any function to be used to describe the variation with height of the mass and stiffness of the structure even if the variation is non-linear and discontinuous.

Estimation of mode shapes and frequencies using Rayleigh's and Stodola's methods is via an iterative technique making use of a method of static analysis which finds deflections in one step. This contrasts with other techniques of modal analysis which involve some method of generating a matrix which represents a linear combination of mass and stiffness matrices for the structure. The eigenvalues and eigenfunctions are then found from this matrix. Calculating eigenvalues is more general and allows additional complexity to be included that could not be included in a Rayleigh/ Stodola method but is more complex to program and less transparent to the user.

An advantage of the Rayleigh/ Stodola method over both Finite Element methods and eigenvalue methods is the small number of discrete parameters which define the structure. Although the list in Appendix H may appear long, the number of parameters which can usefully be controled by the designer is relatively small. The generation of a model and its solution to predict static deflections, buckling loads or eigenvalues is all automatic allowing the optimisation and comparisons of the kind reported in Chapters 7 and 8.

Comparisons of predictions obtained using the Rayleigh/ Stodola method with measurements from real machines have also shown good agreement. The method measuring 'static' deflection (during constant thrust due to constant electrical power generation) and lateral fundamental frequency directly from video recordings is also unique. The method is non-invasive and doesn't disrupt normal installation of the wind turbine although particular events such as an emergency shut down give clear excitation of the fundamental lateral mode. The method could be improved by measuring the position automatically from images recorded digitally. The method is also cheap and portable and so can be used on many different machines for purposes of comparison.

Acceleration measurements have been inconclusive but improvements to the experimental method are possible. For both methods, data could be analysed more completely using wavelet transforms to observe changes with time of the response spectrum of the structure.

It has been demonstrated that the method of modal analysis can be applied to a structure

with any initial combination of applied static loads but that loads applied in the same direction as deflections have no effect on frequencies of vibration. This has been important in the extension of the method to analyse the vibration of the rotating blades.

The numbers of nodal and inter-nodal spline points used in the model are important. For modal analysis, the spacing between nodes must be the same above and below the point of attachment of the guy cables to the tower for greatest accuracy. For analysis of tower buckling, it is the number of nodal points rather than the total number of points which is important. The more points the greater the accuracy but there is a trade off with computation time.

9.1.1 The Design of Wind Turbine Towers

By changing the shape of a free-standing tower, the mass can be optimised. Comparisons between different tower design approaches have been interesting.

For a free-standing, cylindrical, tubular tower, the position of the maximum stress due to tower bending alone will be at the base. If a conical tower with a wide base is used, the maximum stress will occur at a point in the tower above the base. This may be important to avoid concentrating stress at the base where flanges and bolts are used to connect the tower to the foundation. Figure 9.1 is derived from Figure 8.16 and shows the variation of the position of the maximum stress in the tower wall with the outside radius of the tower base. This variation has been projected onto the conical shape of the tower. To optimise the mass of the tower as well as move the position of the maximum stress up from the base, a curved profile can be used. This analysis must be repeated using all required sets of design loads. The design loads used in this thesis were only due to tower head thrust during normal operation.

Using guys to support the tower allows the mass of the tower to be reduced with no reduction in strength. The position of the maximum stress due to tower bending will often be above the base. The base can be hinged to enable easier installation and maintenance in which case the stress due to bending at the base is zero. There are shear stresses at the base. Cylindrical and double-tapered, guyed towers are lighter for the same requirements than conical, guyed towers.

Stiffness affects both deflections and frequencies of vibration. Optimisation of the support structure with respect to modal characteristics is also possible but has not been implimented here. Ultimately, the structure can be optimised with respect to many design requirements simultaneously but this requires more complicated search methods than have been implimented in this research.

There is also an important trade off controlling the geometry of the guy cables but this has not been quantified here. If the axial tension in the lower portion is to be reduced without changing the lateral stiffness of the system of guy cables. the angle between the guy cables and the ground must be decreased. Ultimately. a situation can be imagined in which the guy cables radiate horizontally from the tower and are secured to some large foundations at the same height as their point of attachment to the tower. In this situation there would be no axial compression in the tower due to the cables. The only practical approach to this ultimate case is to decrease the angle the guy cables make with the ground by increasing the

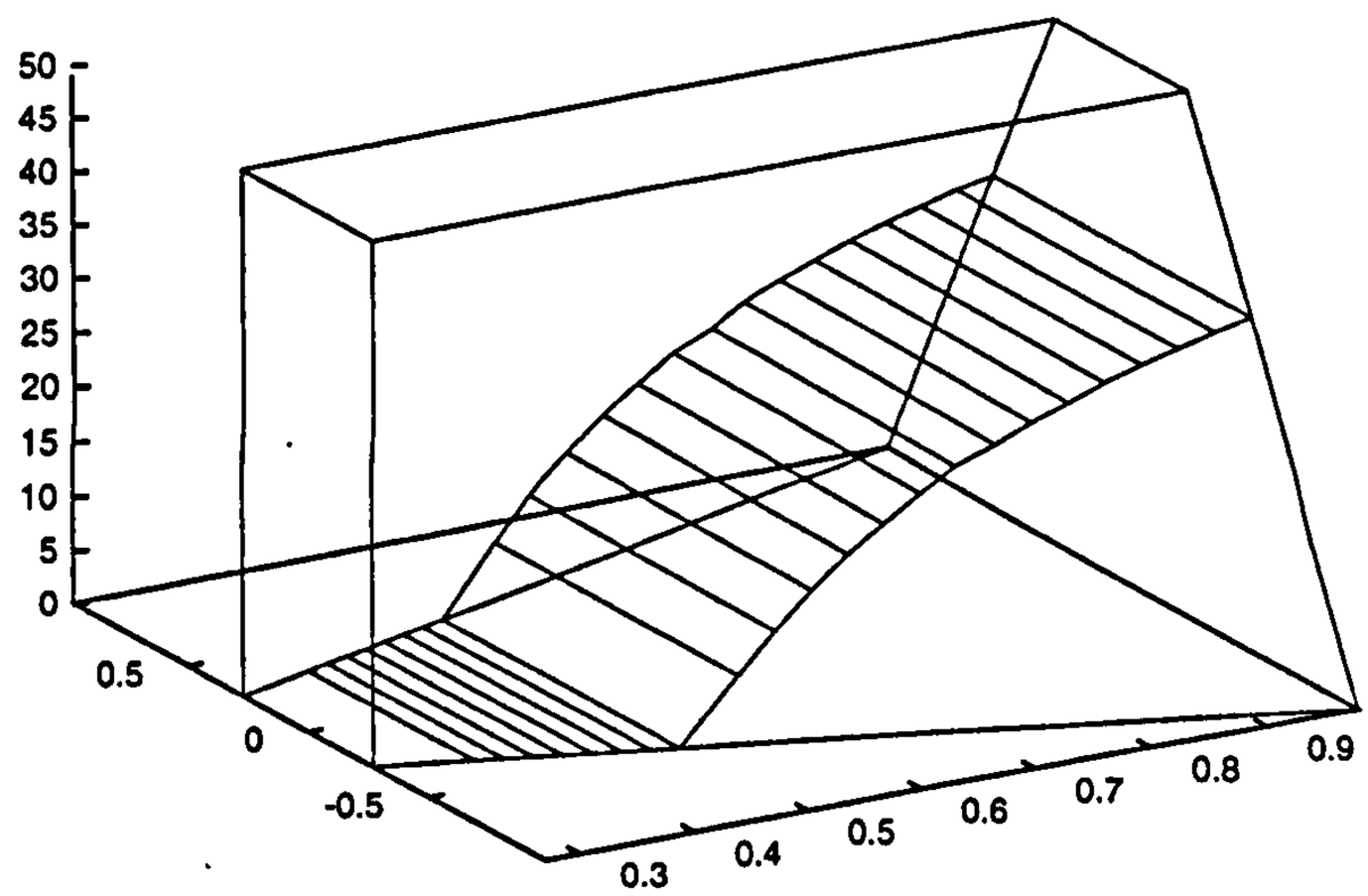

Figure 9.1: The variation of the position of the maximum stress in the tower wall with the outside radius of the tower base. All towers have been optimised by altering the wall thickness of the tower skin so that the maximum stress is 282 MPa. The outside radius of the tower top is 0.270 m and the applied load is 103 kN in all cases. Two examples of stress distributions with height are shown in Figure 8.17.

distance between the tower base foundation and the foundations of the guy cables. This is limited by the maximum amount of land area that the structure can be tolerated to occupy.

9.1.2 Modelling Rotor Vibrations

As mentioned in Section 4.2.2, it is important to understand vibrations of the rotor but this is made complicated:

- by the rotation of the blades which may be constant if the wind turbine is grid-connected but varies when the machine is free-wheeling (not generating electricity) or if variable speed operation is intended;
- by the damping or excitation due to the turbulent flow of air over the moving blades.

The techniques of Floquet analysis (for example, John Dugundji's review of analysis methods for rotating systems [68], Johnson's Helicopter Theory [69] or Peters and Hohenemser [70]) and aeroelastics (for example Bisplinghoff and Ashley's book [47] or Kiessling's derivation of the equations of motion using symbolic processing [48]) have been developed to consider these two developments. Kaiser and Gasch [21] show that aerodynamic damping and stiffness matrices can be calculated approximately before the analysis and used subsequently in Finite Element Analysis.

Resonance of the rotor alone has been examined using the techniques of tower analysis described here (see Section 4.7.4) either when stationary or rotating at constant angular speed. Alternatively, the same techniques could have been used to model the rotor as additional structural components attached rigidly to the tower top. This would give a good indication of the way in which the parked rotor would modify the tower vibration modes. With some small changes to the computer software, two and three-bladed rotors could have been analysed in this way.

The techniques developed here do not model any coupling between torsional and lateral deflections because towers are usually symmetrical and prismatic. Rotor blades are neither. The *flutter* modes mentioned in Section 2.2.1 should therefore be predicted but cannot at present using this code. Such additional information is likely to change the results substantially.

The models described here do not include any coupling between rotor and tower for the reasons described in Sections 4.2.1 and 4.2.2. Floquet methods allow blade/ tower coupling by simultaneously analysing the stationary and rotating reference frames.

Specifically, both the gyroscopic coupling between the blade torsional modes and tower fore aft modes and the coupling between blade torsional modes and nacelle yaw should be investigated. Unlike the situations illustrated in Section 4.2.1. Figure 4.3, neither can be eliminated by a simple hinged teeter bearing but could. if necessary. be eliminated by a more complicated connection between the rotor and low speed shaft. These coupling situations only arise at certain rotor azimuth angles. These are horizontal rotor for the former and vertical rotor for the latter. The rotor is perpendicular to the positions illustrated in Figure 4.3. Therefore, any coupling is only likely to be significant when the rotor is parked and is less significant for three bladed rotors than for two bladed rotors.

9.1.3 Non-Linear Static Analysis

1. For the models described in Chapter 2 it is assumed that all structural stiffnesses are constant with deflection and time. This is not always the case. As shown in Section 4.7.3, the models of the guy cables developed include the discontinuities which occur when cables slacken.

2. Also, if vertical loads (such as F_{cv}) vary linearly with deflection, their contributions to the resultant bending moment on the free body (Figure 2.20) will vary parabolically with deflection (Section 2.3).

3. Also any of the stiffnesses may actually vary non-linearly with deflection as do the guy cables under large initial strains (Figure 4.20).

4. For large deflections of the structure, a lot of the assumptions in Section 2.1 must be re-evaluated. Rosenthal and Skop in 1980 [14] validated a model of a guyed structure against the known deflections of an *elastica* and found that it could predict large deflections successfully. They also included both longitudinal (axial) and three-dimensional lateral deflections in the same analysis which would be possible with slight adjustments of the *structural spline method.*

5. Finally, material parameters such as Young's Modulus may not be constant. To study deflections of the structure subject to loads which give rise to stresses in excess of the yield stress of the material, the static model must be capable of dealing with non-linear stiffnesses.

In situations such as the five listed above, loads can be applied to the structure progressively. Three possible changes can be made to the existing static analysis models.

1. If stiffnesses such as that due to the guy cables (k_{Bc}) are piecewise linear, loads can be applied in stages so that the incremental deflection at each stage is calculated with a different value of the stiffness. The total deflection is the sum of all the incremental deflections calculated. This is similar to the strategy employed by Poskitt [13].

2. If there are regions over which stiffnesses are linear, the same approach as in (1) above can be adopted but where changes of stiffness are rapid, load increments must be small.

3. Where stiffnesses are non-linear, the loads must be applied in small increments and equilibrium of all loads on the structure calculated between each increment.

9.1.4 Non-Linear Dynamic Analysis

Modal analysis is useful for estimating the dynamic behaviour of the structure. In order to predict the fatigue life of parts of the machine. for instance, a much more detailed prediction of the dynamic behaviour of the whole system is necessary.

In addition to the effects listed above which necessitate the use of a non-linear static model. a dynamic model is subject to time-dependent and velocity-dependent loads such as

friction and damping. To include these effects, a non-linear model is necessary. One approach to non-linear structural analysis is to increase time in small steps, calculating, at each point, the position of the whole system by assuming that all static and inertia (*d'Alembert* [71]) loads are in equilibrium. To include damping, the *structural spline method* of static analysis which takes applied loads as input and estimates structural deflections could be used.

Errors build up considerably during time-integration. Figure 9.3 shows that very small time steps are necessary to prevent numerical instabilities introducing unwanted behaviour into a very simple system. With time steps of 0.01 s (150 per period), the dynamic behaviour predicted is similar to the solution of the differential equation. With time steps of 0.15 s (10 per period), the system is predicted to be dynamically unstable, whereas the direct analytical solution shows that oscillations die away. The period of oscillations predicted is similar in all cases.

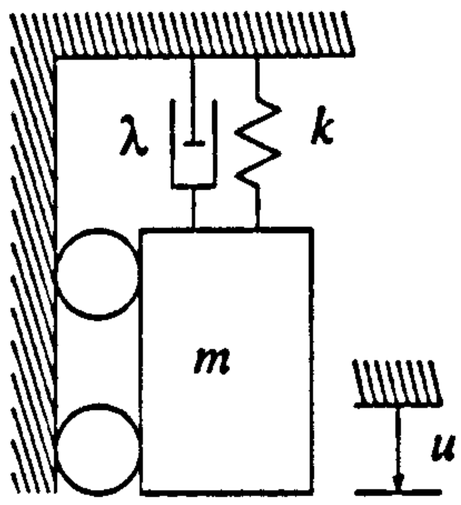

Figure 9.2: A second order linear system with damping.

The time taken to obtain accurate solutions would be increased still further if more comprehensive static models were developed which involved iteration towards static equilibrium. This is illustrated by the static model of longitudinal deflections. Section 2.4 describes how the code for static analysis is called twice, once to find the deflection of the point of attachment of the guys and a second time having estimated a linear stiffness parameter equivalent to the guy cables. In fact the restoring forces due to the guys do not vary linearly with deflections. More accurate models of the guys have already been developed. In the software, other functions call these models in order to linearise the behaviour of the guys. It would be easy to use the non-linear functions directly but static equilibrium could only be estimated by an iterative process. Iterative code may be necessary for static analysis for other reasons too. Finite element packages include algorithms for taking short cuts to acheive static equilibrium or to perform numerical time integrations.

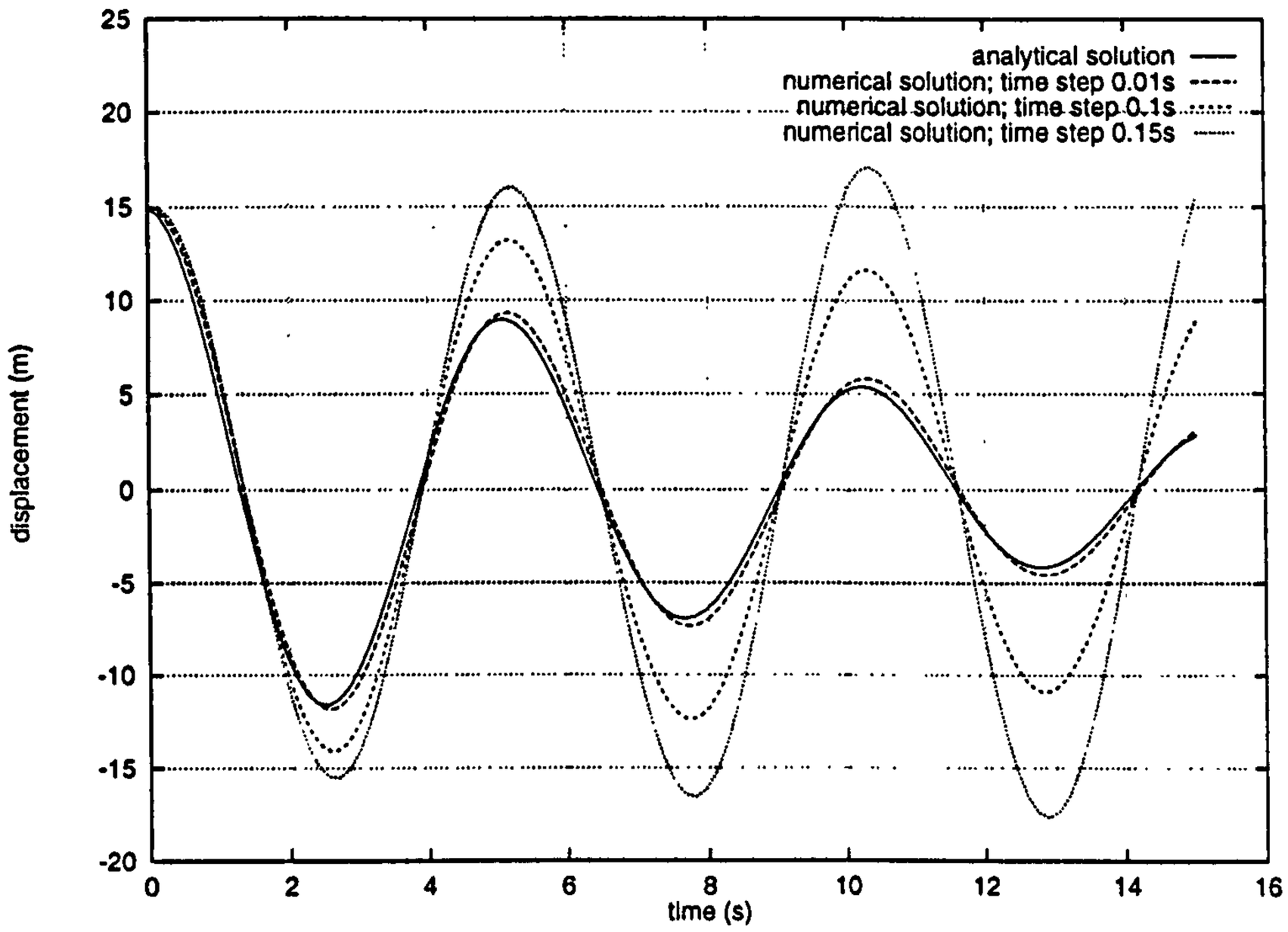

Figure 9.3: A comparison between the displacement of the mass illustrated in Figure 9.2 estimated by numerical time integration and the transient response expected from solution of the equations of motion. Three numerical approximations are shown, their different time step sizes are given in the legend.

Appendix A

Torsional and Longitudinal Static Deflections

A.1 Longitudinal Deflections

Having obtained an array of compressive forces at heights x up the tower, Equation 4.1 is integrated to find the vertical deflections, u. Similar methods can be used to calculate torsional deflection angles, θ (Section A.2) and can be used for lateral deflections, v if there are no vertical loads such as the compression in the lower part of the tower due to the guys and the weight forces of the tower and nacelle.

The forces applied externally to the tower element are in equilibrium (Figure A.1). The unknown forces are due to elastic deformation of the system of guy cables, F_{cv} (see Section 2.2.3) and the base fixing, F_{fv} (Section 2.2.2). Equation A.1 shows the equilibrium of these forces (Figure A.1 (b)).

$$F_{fv} + F_{cv} + F_{nv} + \int_0^H f_v dX = 0 \tag{A.1}$$

An array of vertical forces per unit length is applied at increasing heights. At each height, the force density is constant over the horizontal cross sections of the tower. A free body consisting of the part of the tower below x is considered (see Equation A.2). Equilibrium of loads on this body gives the internal force $C_t(x)$ (for which compression is positive) at a height, x. Macauley's method [72] allows the inclusion of concentrated forces (such as the reaction of the guys) applied above the tower base. Dividing by $E_t A_{xt}$ gives the material strain $\epsilon = \frac{du}{dx}$. Integrating this expression with respect to tower height gives the vertical deflection of the tower $(u(x))$.

$$\frac{du}{dx} = \frac{C_t}{E_t A_{xt}} = \frac{1}{E_t A_{xt}} \left(-F_{fv} - \int_0^x f_v dX - F_{cv} \right) \tag{A.2}$$

For the purposes of numerical solution. the array u of deflections at each of the tower points is made up of the sum of $N_c + 1$ arrays (Equation A.3) where N_c is the number of sets of guy cables. The array u_t is simply calculated using Equations A.1 and A.2 excluding forces due to the guys ($F_{cv} = 0$).

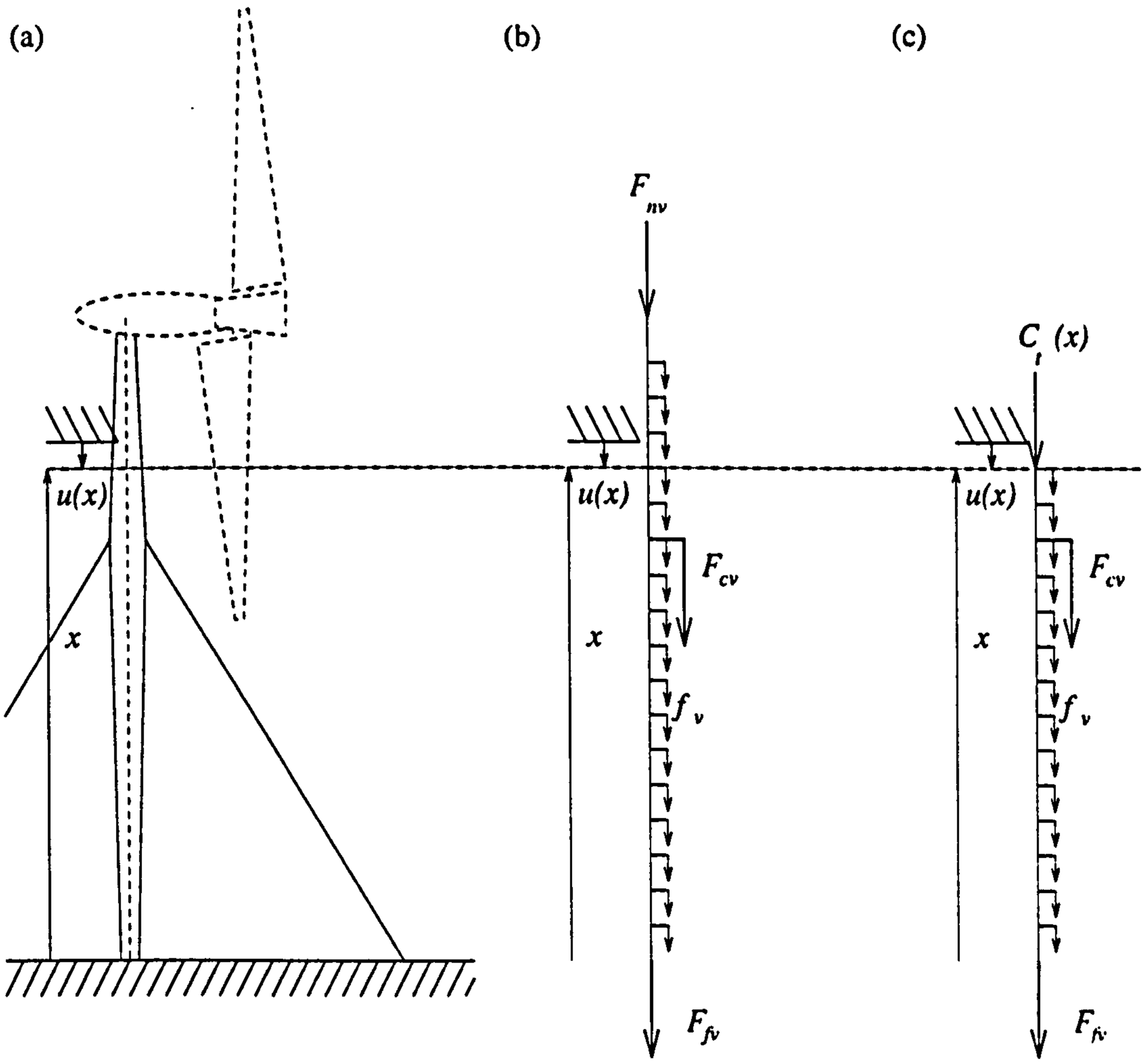

Figure A.1: (a) The vertical forces on a wind turbine tower. (b) The equilibrium between externally applied vertical forces and the base reaction vertical force (F_{fv}). (c) The equilibrium between the compressive force $C_t(x)$ in the tower, vertical forces applied to a free body *consisting of that section of the tower below the point of interest (height, x), and the base reaction vertical force (F_{fv}).*

$$u = u_t + \sum_{i=1}^{N_c} F_{icv} U_{ic} + C_I \tag{A.3}$$

$$\text{where:} U_{ic} = \frac{u - u_t}{F_{cv}} \tag{A.4}$$

For each set of guy cables, an additional array (U_{ic}) is derived of values of 'tower deflection/ cable reaction force' ($\frac{u-u_t}{F_{cv}}$). The guy reactions are initially unknown but are calculated in the course of the analysis. Additionally, the deflection of the base of the tower is unknown because of the integration of strains $u(x) = \int_0^H \frac{du}{dx} dx + u(0)$. The unknowns can be found by solving a set of at least two simultaneous equations.

From now on, the analysis will be demonstrated for towers with just one set of four guy cables at a height of $\lambda_{ct} H$. Instead of U_{ic}, the array of deflections due to the guy cables is denoted U_c.

The array, U_c is calculated from an array C_{tc} of compressive forces in the tower if the only force applied externally is a guy force $F_{cv} = 1$ N (Equation A.5). All that is needed after the analysis is completed, to recover the true deflection of the tower is to multiply this array by the guy reaction and add it to the array of tower deflections u_t (Equation A.3). The cable reaction is the sum of vertical components of the cable tension at the height of attachment of the cables.

$$C_{tc} = \begin{cases} 1 & (0 < x < \lambda_{ct} H) \\ 0 & (0 < x < \lambda_{ct} H) \end{cases} \tag{A.5}$$

$$U_c = \int_0^x \frac{C_{tc}}{E_t A_{xt}} dX \tag{A.6}$$

Section 2.2.2 above defines the complete set of tower base elastic stiffness parameters.

The deflection of the tower base must be due to the vertical elastic deformation of the base fixing under the sum of all applied loads.

$$F_{fv} = -F_{cv} - F_{nv} - \int_0^H f_v dX = -(u_t(0) + F_{cv} U_c(0) + C_I) k_{Cf} \tag{A.7}$$

The deflection of the tower at the point of attachment of the guy cables must be due to the lateral elastic deformation of the guy cables under the applied loading.

$$F_{cv} = -(u_t(\lambda_{ct} H) + F_{cv} U_c(\lambda_{ct} H) + C_I) k_{Cc} \tag{A.8}$$

In Equations A.7 and A.8, the only parameters not known before the analysis are F_{cv} and C_I. Since there are two equations and two unknowns. a solution is obtained using matrix algebra. It is straightforward to extend this example to find the deflection of a tower with more than one set of guy cables by generating an additional equation with the introduction of each additional unknown cable force.

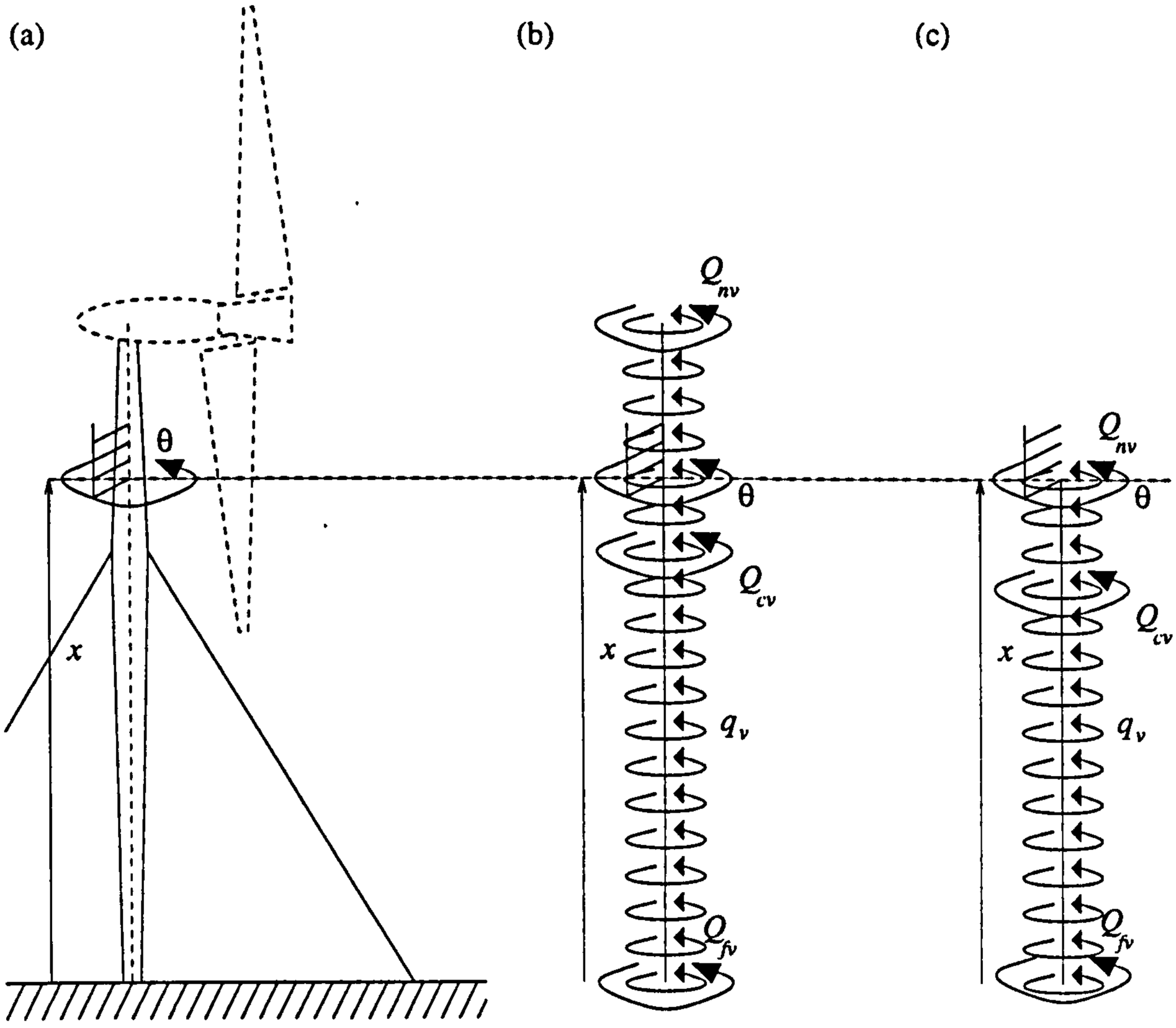

Figure A.2: (a) The torques on a wind turbine tower about vertical axes. (b) The equilibrium between torques applied externally and the base reaction torque (Q_{fv}). (c) The equilibrium between the torque $Q_t(x)$ in the tower, torques applied to a free body *consisting of that section of the tower below the point of interest (height, x) and the base reaction torque, Q_{fv}.*

A.2 Torsional Deflections

Equations A.1 to A.8 are rewritten below for the analysis of torsional deflections.

The equilibrium of torques applied externally with the base reaction:

$$Q_{fv} + Q_{cv} + Q_{nv} + \int_0^H q_v dX = 0 \tag{A.9}$$

The elastic equation giving the twist, $\frac{d\theta}{dx}$:

$$\frac{d\theta}{dx} = \frac{Q_t}{G_t J_{xt}} = \frac{1}{E_t A_{xt}} \left(-Q_{fv} - \int_0^x q_v dX - Q_{cv} \right) \tag{A.10}$$

The composition of the array of twist angles θ for a structure with more than one set of guy cables:

$$\theta = \theta_t + \sum_{i=1}^{N_c} Q_{icv} \Theta_{ic} + C_I \tag{A.11}$$

$$\text{where:} \Theta_{ic} = \frac{\theta - \theta_t}{Q_{icv}} \tag{A.12}$$

Obtaining the array of 'twist angle per unit guy torque' $\frac{\theta - \theta_t}{Q_{cv}}$ by integration:

$$Q_{tc} = \begin{cases} 1 & (0 < x < \lambda_{ct} H) \\ 0 & (0 < x < \lambda_{ct} H) \end{cases} \tag{A.13}$$

$$\Theta_c = \int_0^x \frac{Q_{tc}}{G_t J_{xt}} dX \tag{A.14}$$

The elastic equations for the guy cables and the foundation (Section 2.2.2):

$$Q_{fv} = -Q_{cv} - Q_{nv} - \int_0^H q_v dx = -(\theta_t(0) + Q_{cv}\theta_c(0) + C_I) k_{Tf} \tag{A.15}$$

$$Q_{cv} = -(\theta_t(\lambda_{ct} H) + Q_{cv}\theta_c(\lambda_{ct} H) + C_I) k_{Tc} \tag{A.16}$$

In addition, the yaw stiffness parameter k_{Yn} allows variable flexibility between the top of the tower and the nacelle. The angle of twist of the top of the tower is $\theta(H)$. The angle of twist θ_n of the nacelle is given in Equation A.17.

$$\theta_n = \theta(H) + \frac{Q_{nv}}{k_{Yn}} \tag{A.17}$$

Appendix B

Guy Reactions

In this appendix, the relationship between deflection and restoring load is investigated for each of the three classes of deflection. The processes are described by which equivalent stiffness parameters are derived for use in the static and modal analysis software. The results are compared with approximations based on simplified geometries and also with finite element models of the guy cables.

For the models described in Chapters 2, 3 and 4, the stiffness parameters (k_{Bc}, k_{Cc} and k_{Tc}) are derived numerically by calculating the restoring load (F_{ch}, F_{cv} or Q_{cv}) which arises from a small deflection ($v(\lambda_{ct}H)$, $u(\lambda_{ct}H)$ or $\theta(\lambda_{ct}H)$) of the point of attachment of the guy cables to the tower (in this appendix, the *guy point*). By taking two, small, negative deflections and two, small, positive deflections an array of five loads and five deflections is obtained ($\{ -\delta \quad -\frac{1}{2}\delta \quad 0 \quad \frac{1}{2}\delta \quad \delta \}$). The limits of this array ($[-\delta, \quad \delta]$) depend on the class of deflections considered. The load array is differentiated numerically with respect to the deflection array to find the stiffness parameter using one of Equations B.1, B.2 or B.3. For the differentiation, quadratic curves are constructed between consecutive triplets of points and where there are two values of the gradient at one point, the average is calculated.

$$k_{Bc} = -\left.\frac{dF_{ch}}{dv_c}\right|_{v_c=0} \quad \text{where } v_c = v(\lambda_{ct}H) \tag{B.1}$$

$$k_{Cc} = -\left.\frac{dF_{cn}}{du_c}\right|_{u_c=0} \quad \text{where } u_c = u(\lambda_{ct}H) \tag{B.2}$$

$$k_{Tc} = -\left.\frac{dQ_{cv}}{d\theta_c}\right|_{\theta_c=0} \quad \text{where } \theta_c = \theta(\lambda_{ct}H) \tag{B.3}$$

B.1 Calculating the Restoring Loads

The restoring loads, F_{ch}, F_{cv} and Q_{ch} are derived by calculating the length of each cable after deflection of the guy point (v horizontally, u vertically and angle θ about a vertical axis). Although the vertical dip of the guy point and consequently the rotation of the tower at the guy point about a horizontal axis is considered, the restoring torque (Q_{ch}) about a horizontal axis is neglected. The dip of the guy point due to lateral deflection of the tower

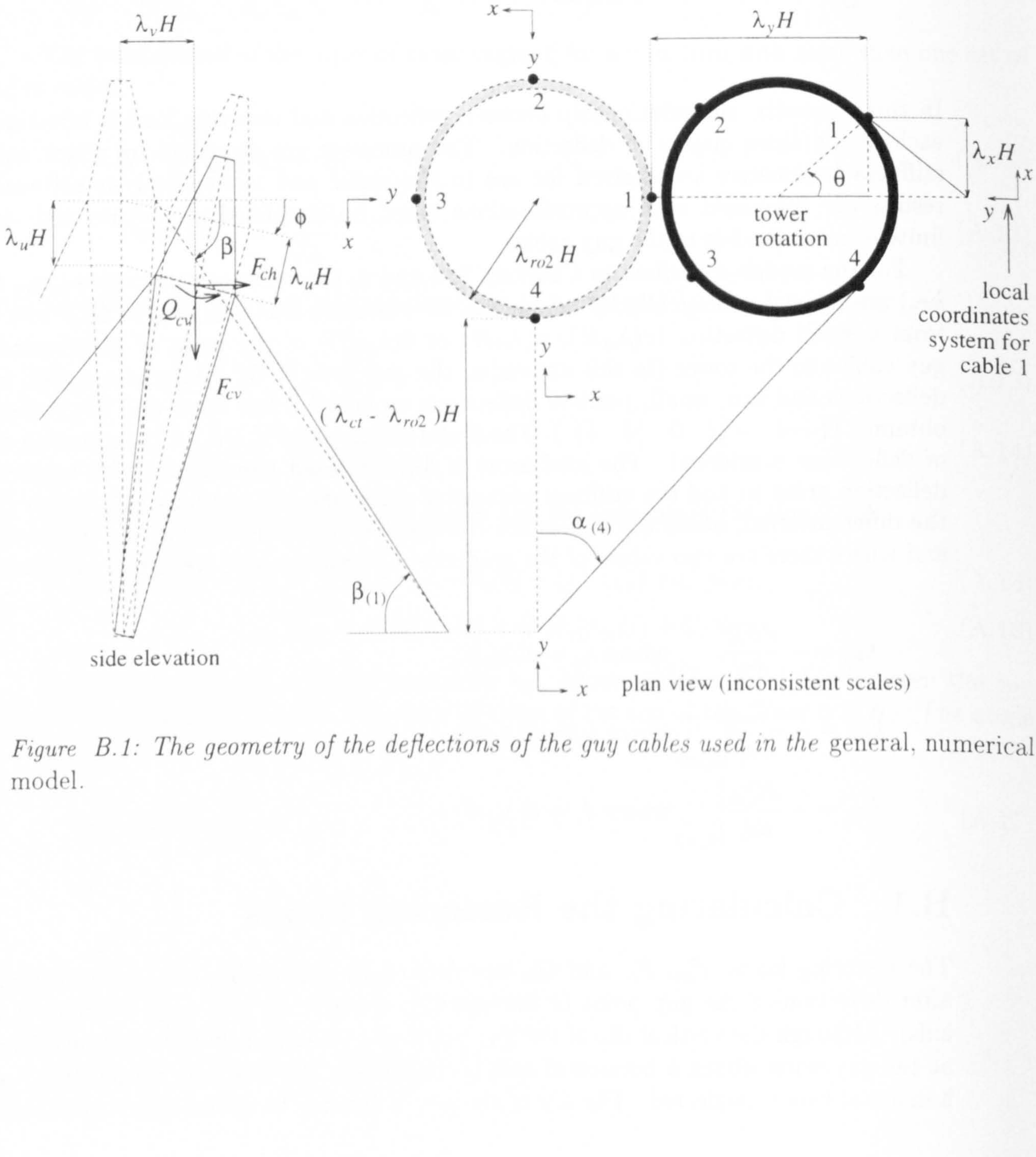

Figure B.1: The geometry of the deflections of the guy cables used in the general, numerical model.

is calculated assuming that the straight line distance between the tower base and the guy point is $\lambda_{ct}H$. This ignors the curvature of the tower due to bending distributed along its length. It is thus a conservative estimate of the vertical dip of the guy point. Figure B.1 shows that this dip is $v\sin(\phi)$ at the tower centreline (where $v = \lambda_v H$).

A local coordinates system is used for each guy cable. The cables are numbered 1–4 from the cable which is shortest after deflection of the tower as shown in Figure B.1. Equations B.4 to B.15 illustrate the expressions used to calculate the reaction force on the guy point for cable 1. Similar equations are derived for cables 2–4 and combined using equations B.16 to B.18 to give the restoring loads, F_{ch}, F_{cv} and Q_{ch}.

$$\lambda_{x(1)} = \lambda_{ro2}\sin\theta \tag{B.4}$$

$$\lambda_{y(1)} = \lambda_{cg} - \lambda_{ro2}\cos\theta - \lambda_v \tag{B.5}$$

$$\phi = \tan^{-1}\left(\frac{\lambda_{ct} - \lambda_u - \sqrt{(\lambda_{ct} - \lambda_u)^2 - \lambda_v^2}}{\lambda_v}\right) \tag{B.6}$$

$$\lambda_{z(1)} = \sqrt{(\lambda_{ct} - \lambda_u)^2 - \lambda_v^2} - \lambda_{ro2}\cos\theta\sin\phi \tag{B.7}$$

$$\lambda_{(1)} = \sqrt{\lambda_{x(1)}^2 + \lambda_{y(1)}^2 + \lambda_{z(1)}^2} \tag{B.8}$$

$$\beta_{(1)} = \tan^{-1}\left(\frac{\lambda_{z(1)}}{\sqrt{\lambda_{y(1)}^2 + \lambda_{x(1)}^2}}\right) \tag{B.9}$$

$$\alpha_{(1)} = \tan^{-1}\left(\frac{\lambda_{x(1)}}{\lambda_{y(1)}}\right) \tag{B.10}$$

as long as the cable has not gone slack:

$$\epsilon_c = \log\left(\frac{\lambda_{(1)}}{\lambda_n}\right) \tag{B.11}$$

$$A_{xc(1)} = (1 - \nu_c\epsilon_c)^2 A_{xc0} \tag{B.12}$$

$$F_{x(1)} = -E_c A_{xc(1)}\epsilon_c \cos(\beta_{(1)})\sin(\alpha_{(1)}) \tag{B.13}$$

$$F_{y(1)} = -E_c A_{xc(1)}\epsilon_c \cos(\beta_{(1)})\cos(\alpha_{(1)}) \tag{B.14}$$

$$F_{z(1)} = E_c A_{xc(1)}\epsilon_c \sin(\beta_{(1)}) \tag{B.15}$$

$$F_{ch} = -F_{y(1)} - F_{x(2)} + F_{y(3)} + F_{x(4)} \tag{B.16}$$

$$F_{cv} = F_{z(1)} + F_{z(2)} + F_{z(3)} + F_{z(4)} \tag{B.17}$$

$$Q_{cv} = H\left(\lambda_{ro2}\sum_{i=1}^{4}\left(F_{x(i)}\cos\theta + F_{y(i)}\sin\theta\right) + (F_{x(1)} - F_{y(2)} - F_{x(3)} + F_{y(4)})\lambda_v\right) \tag{B.18}$$

where:

$\lambda_{x(1)}$ is the dimensionless (relative to the total tower height) component of the cable's new length parallel to the local x axis

$\lambda_{y(1)}$ is the dimensionless (relative to the total tower height) component of the cable's new length parallel to the local y axis

$\lambda_{z(1)}$ is the dimensionless (relative to the total tower height) component of the cable's new length parallel to the local z axis

$\lambda_{(1)}$ is the dimensionless new length of the cable

λ_v is the dimensionless horizontal deflection of the guy point ($v = \lambda_v H$)

λ_u is the dimensionless vertical deflection of the guy point ($u = \lambda_u H$)

θ is the rotation of the guy point about a vertical axis

ϕ is the rotation of the guy point about a horizontal axis

$\beta_{(1)}$ is the new angle of the cable to the horizontal

$\alpha_{(1)}$ is the angular deflection of the projection of the cable onto a horizontal plane

A_{xc0} is the initial cross sectional area of the cable

$A_{xc(1)}$ is the cross sectional area of the cable adjusted using the poissons ratio (ν_c) for the material [25]

$F_{x(1)}$ the horizontal component of the tension in the cable parallel to the x axis

$F_{y(1)}$ the horizontal component of the tension in the cable parallel to the y axis

$F_{z(1)}$ the vertical component of the tension in the cable

This *general, numerical method* calculates true strain (Equation B.11) and true stress (by adjusting the cross sectional area of the guys in Equation B.12) as opposed to nominal stress and nominal strain [25]. This would enable large deformations of the cables to be more accurately modelled.

A method of modelling cables which may be slack as well as taut is proposed by Peyrot and Goulois [29] but the forces on the tower due to the cables when slack are negligible in comparison with the forces due to the taut cables. As long as the initial strain in the cables is large enough, they should not become slack during vibrations. An example of the cable tension of an existing wind turbine design, the Carter 300 kW machine has an initial cable tension of 80kN equivalent to an initial strain of 0.11%.

B.2 Approximate Equations for the Stiffness Parameters

B.2.1 Lateral Stiffness Parameter

The numerical method described in this appendix for linearising the load/ deflection curves for the system of guy cables gives an almost identical result to an expression obtained directly, assuming small lateral deflections (see Equation B.20). The approximate geometry of the

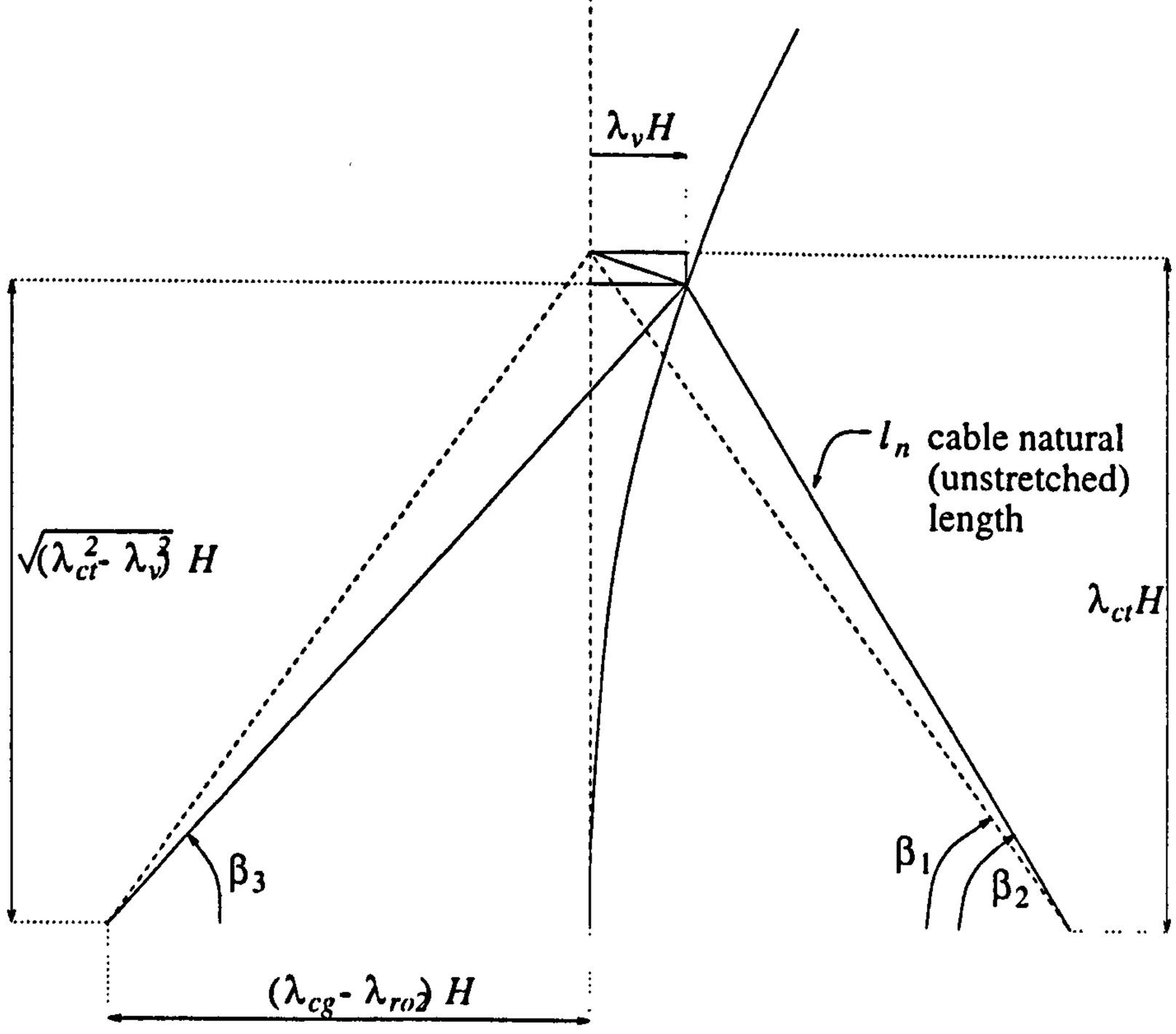

Figure B.2: Lateral stiffness parameter. *The geometry of the tower and guy cables from which an expression can be obtained for k_{Bc} (the equivalent lateral stiffness parameter of the system of cables).*

cables is illustrated in Figure B.2. The angle between a guy and the horizontal is assumed to be unchanged by the deflection of the guy point ($\beta = \beta_1$).

$$F_{ch} \approx -\frac{E_c A_{xc0}}{\lambda_{cn}} \cos(\beta_1) \left(\sqrt{\lambda_{cg}^2 - 2\lambda_{cg}\lambda_v + \lambda_{ct}^2} - \sqrt{\lambda_{cg}^2 + 2\lambda_{cg}\lambda_v + \lambda_{ct}^2} \right) \tag{B.19}$$

$$k_{Bc} = \frac{E_c A_{xc0}}{\lambda_{cn} H} \cos(\beta_1) \lambda_{cg} \left(\frac{1}{\sqrt{\lambda_{cg}^2 - 2\lambda_{cg}\lambda_v + \lambda_{ct}^2}} + \frac{1}{\sqrt{\lambda_{cg}^2 - 2\lambda_{cg}\lambda_v + \lambda_{ct}^2}} \right) \tag{B.20}$$

Figure B.3 compares the restoring force, F_{ch} calculated using Equation B.19 with the restoring force calculated using Equations B.4 to B.16. For small positive or negative deflections, the two methods are similar. Likewise, comparisons between the lateral stiffness parameter calculated using both methods are made in Figure B.4.

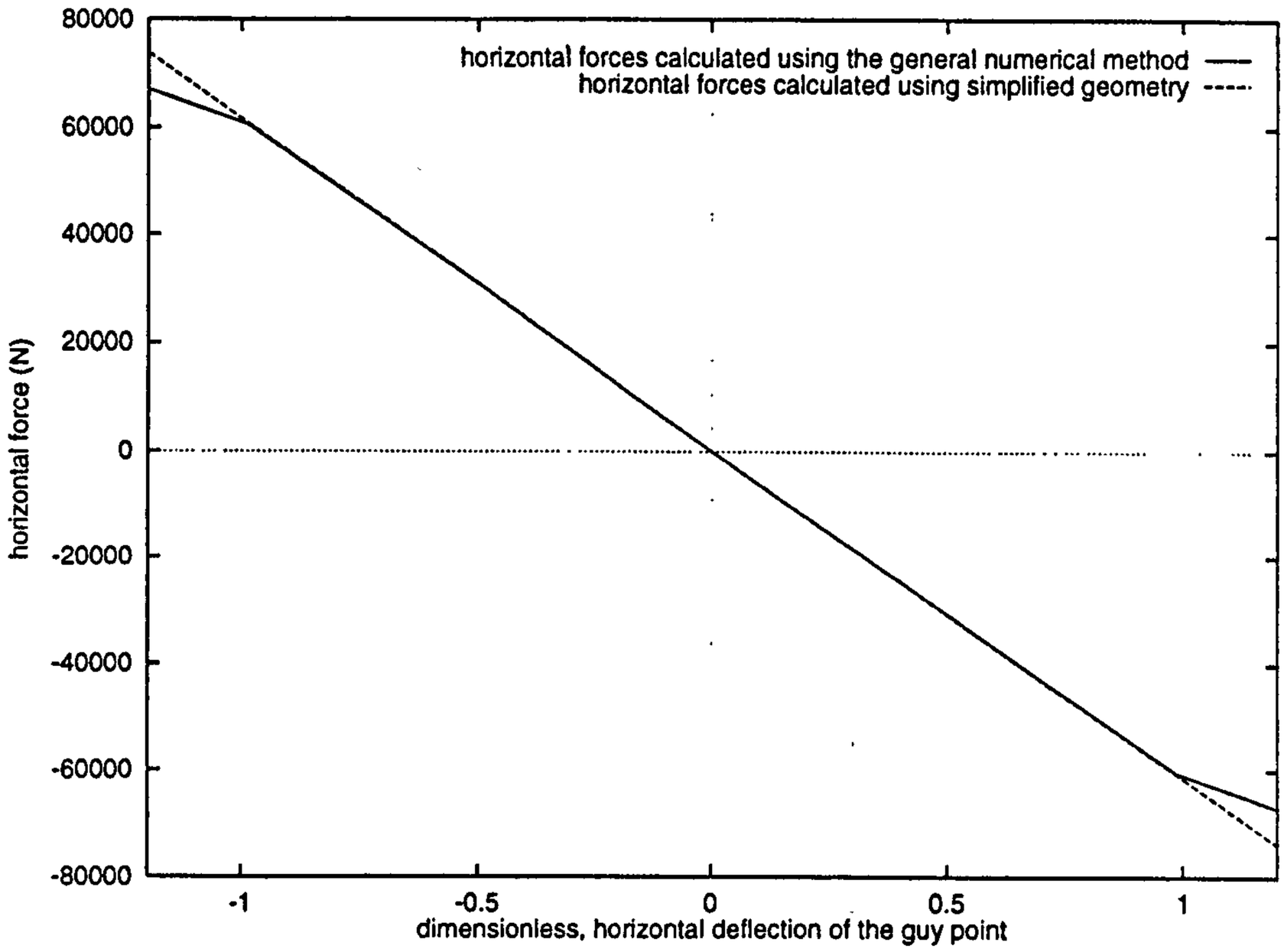

Figure B.3: Comparisons between horizontal restoring forces F_{ch} calculated using Equations B.4 to B.16 and those calculated using Equation B.19. The horizontal deflection of the guy point is dimensionless. The reference value is the deflection at which one of the guys goes slack (Equation B.21).

Two discontinuities can be seen on Figure B.3. They are due one of the cables going slack. The horizontal scale is the ratio of the true deflection to the deflection at which one of these discontinuities occurs. Using Pythagoras' theorem for the situation where one of the cables is just about to go slack, Equation B.21 is obtained. The horizontal scale is obtained from the true horizontal deflections using Equation B.22.

$$\lambda_{cv0} = \lambda_{cg} - \lambda_{ro2} - \sqrt{\lambda_{cn}^2 - \lambda_{ct}^2} \tag{B.21}$$

$$\text{horizontal scale} = \frac{v}{\lambda_{cv0} H} \tag{B.22}$$

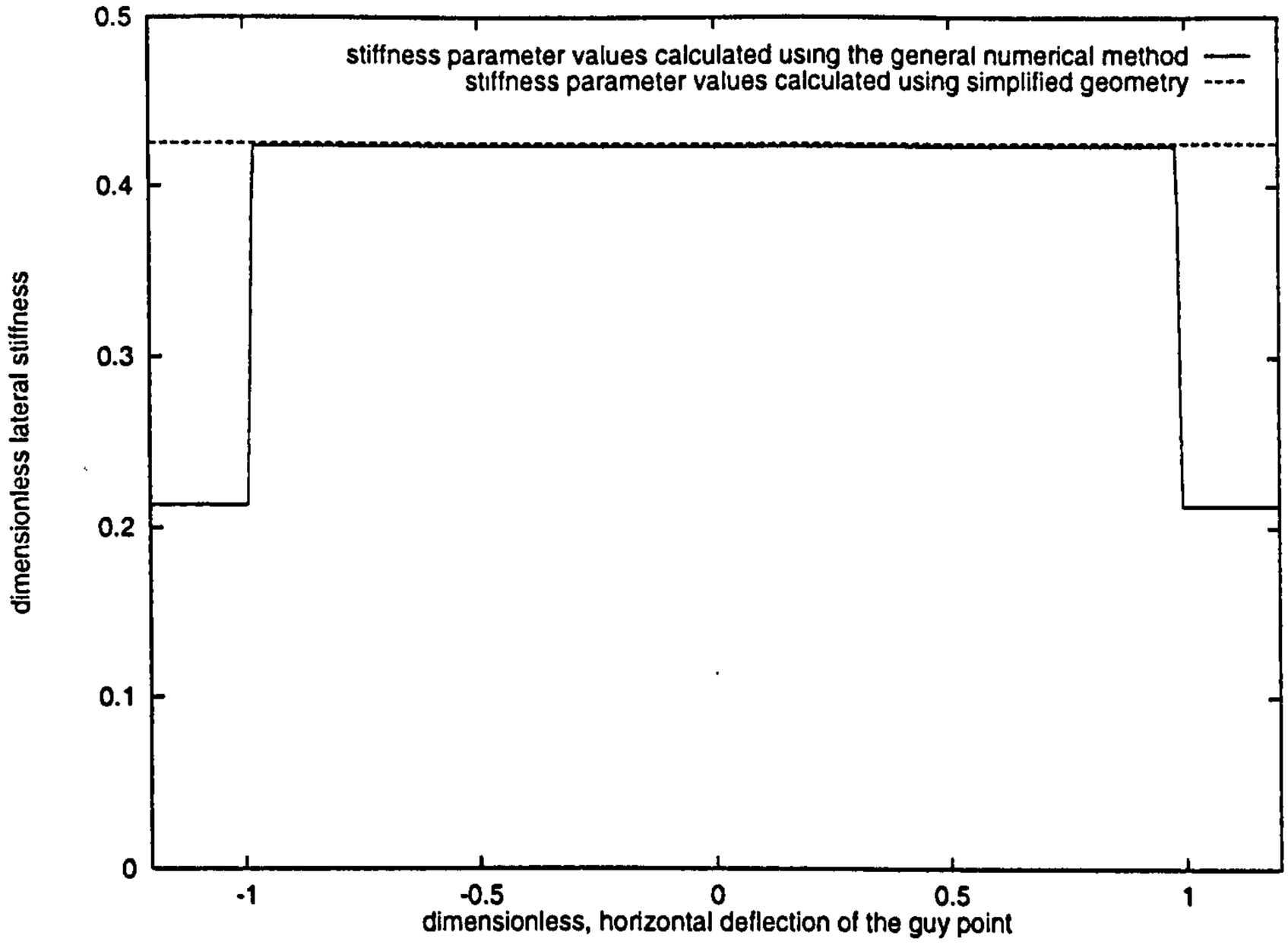

Figure B.4: Comparisons between values of the lateral stiffness parameter calculated using Equations B.4 to B.16 and those calculated using Equation B.20. Lateral stiffess values plotted are dimensionless. The scale factor is $\frac{E_c A_{xc}}{\lambda_{cn} H}$. *The same dimensionless horizontal deflection parameter is used as was used in Figure B.3. The initial strain parameter* (ϵ_{ic}) *used is 0.0005 and the scale factor for stiffness values is* $2.72 \times 10^7\ N\ m^{-1}$.

Equation B.20 shows that there is an elastic component and a geometric component to the lateral elastic parameter. The elastic component is $\frac{E_c A_{xc0}}{\lambda_{cn} H}$.

B.3 Longitudinal Stiffness Parameter

Figure B.5 shows four different simplifications of the geometry of the tower and cables when the tower undergoes longitudinal deformation. The axial force (downwards is positive) on the tower at the guy point, F_{cv} is given by the four alternative Equations B.23 to B.26. Because of initial tension in the cables, there is an initial axial compression in the undeflected tower. The deflection of the cable attachment point at which the cables go slack is u_{c0} or. alternatively $\lambda_{cu0} H$. It is calculated using Equation 5.9 in Section 5.1.1.2.

Figure B.5 (1) assumes no change in geometry of the guy cables so that the length of the cables after vertical deflection of the point of attachment to the tower decreases by $\frac{u}{\sin \beta_1}$ where β_1 is the angle made by the guy cables to the ground before the deflection.

$$F_{cv} = \frac{4 E_c A_{xc}}{\lambda_{cn}} (\lambda_{cu0} - \lambda_u) \tag{B.23}$$

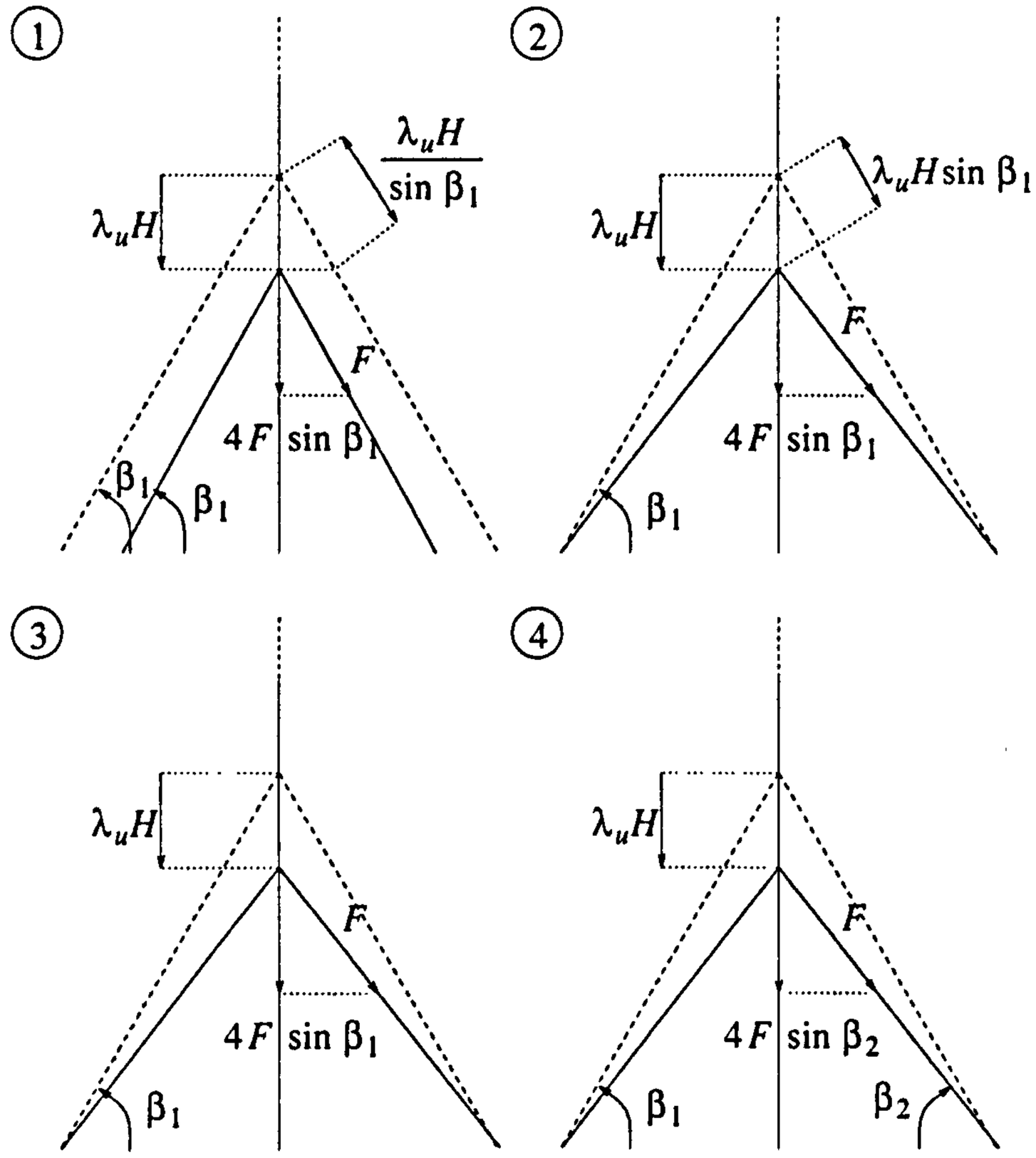

Figure B.5: Longitudinal stiffness parameter. *The geometry of the tower and guy cables from which an expression can be obtained for k_{Cc} (the equivalent longitudinal stiffness parameter of the system of cables).*

Figure B.5 (2) assumes that the change in geometry of the guy cables is small. The vertical deflection of the point of attachment to the tower can be resolved along the original angle β_1 of the cables and the same angle can be used to resolve the forces vertically. From Figure B.6, it can be seen that this approximation (Figure B.6 (c)) is more accurate than the previous (Figure B.6 (c)).

$$F_{cv} = \frac{4E_c A_{xc}}{\lambda_{cn}} \sin^2 \beta_1 \left(\lambda_{cu0} - \lambda_u\right) \tag{B.24}$$

Figure B.5 (3) shows how the new length of each cable is calculated but forces are resolved vertically using the original angle β_1. Figure B.5 (4) shows how the new angle β_2 can be found by trigonometry and used to resolve the tensions in each cable vertically.

$$F_{cv} = \frac{4E_c A_{xc}}{\lambda_{cn}} \sin \beta_1 \left(\sqrt{(\lambda_{ct} - \lambda_u)^2 + (\lambda_{cg} - \lambda_{ro2})^2} - \lambda_{cn}\right) \tag{B.25}$$

$$F_{cv} = \frac{4E_c A_{xc}}{\lambda_{cn}} \left(\lambda_{ct} - \lambda_u\right) \left(1 - \frac{\lambda_{cn}}{\sqrt{(\lambda_{ct} - \lambda_u)^2 + (\lambda_{cg} - \lambda_{ro2})^2}}\right) \tag{B.26}$$

There is a marked increase in accuracy between the methods which attempt to estimate the strain by taking components of the vertical deflection parallel to the guys (Equations B.23 and B.24) and those which calculate the new lengths of the cables which are used to calculate the strain (Equations B.25 and B.26). This is demonstrated in Figure B.6 where curves (d) and (e) are much closer to the curve (a) calculated using the *general numerical method* than curves (b) and (c). As in the case of lateral tower deformations, the equivalent stiffness parameter is the value of $\frac{dF_{cv}}{du}$ when the tower and cables are in static equilibrium.

From Equation B.24, Equation B.27 is derived. Although the differences in forces (F_{cv}) are significant (Figure B.6), the differences in stiffness between that calculated using Equation B.27 and that calculated using the *general, numerical method* (Equations B.4 to B.17) are insignificant.

$$k_{Cc} = \frac{4E_c A_{xc}}{\lambda_{cn} H} \sin^2 \beta_1 \tag{B.27}$$

B.4 Torsional Stiffness Parameter

From Figure B.9, it can be seen that the restoring torque due to the guys does not vary linearly with tower deflection angle. For linear modal analysis. the equivalent stiffness parameter used is $\frac{dQ_c}{d\theta}\Big|_{\theta=0}$ at the point of attachment of the cables to the tower. This is constant only for small anglular deflections.

An approximate expression for the torque on the tower about a vertical axis is given by Equation B.28. It can be obtained from the simplified geometry of small deformations illustrated in Figure B.8. This can be differentiated to find the stiffness parameter. k_{Tc} at the point of zero deformation (Equation B.29). Comparisons are made between the results of this equation and the numerical differentiation of the force deflection relationships given by Equations B.4 to B.18 in Figure B.10.

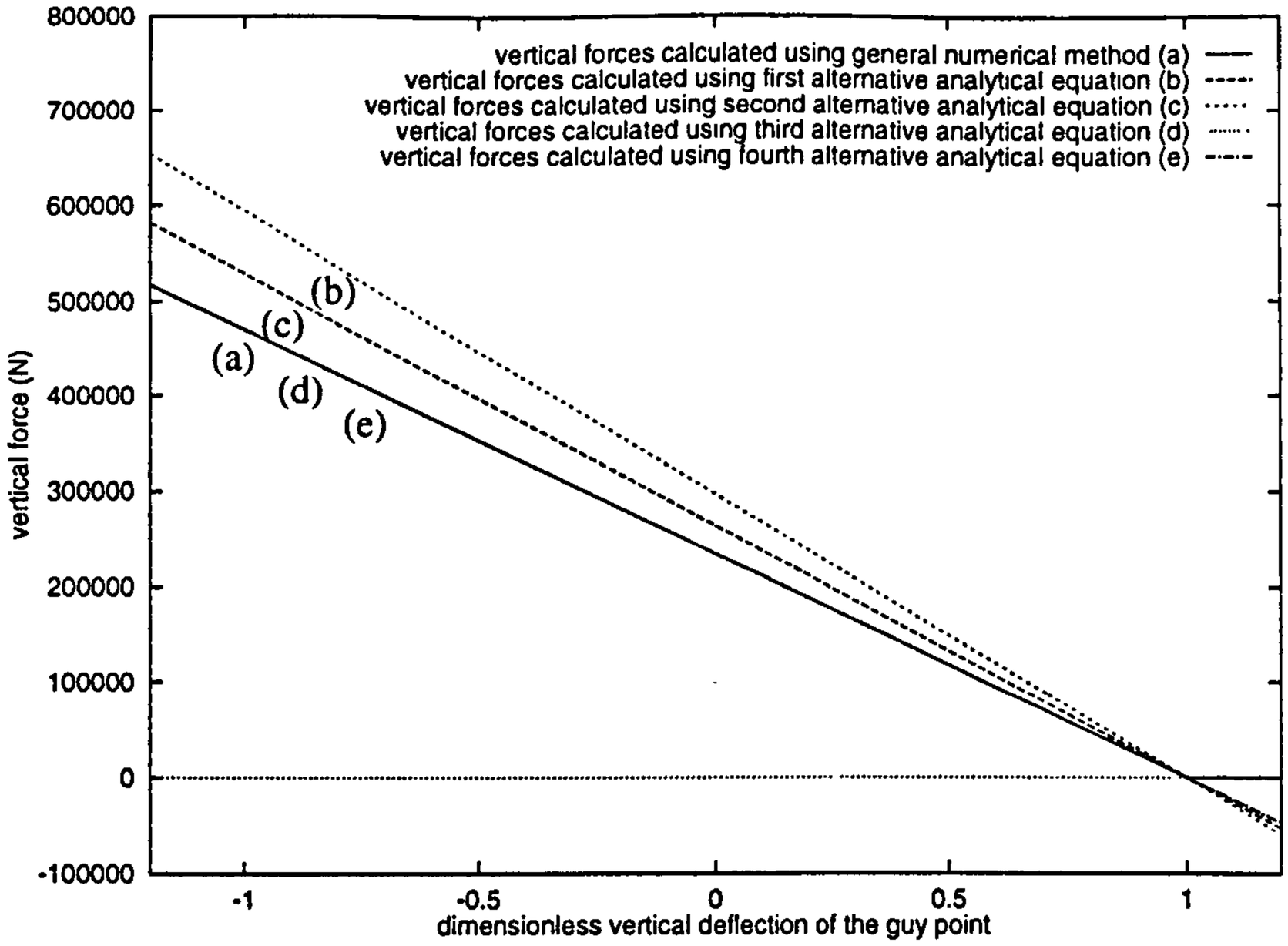

Figure B.6: Comparisons between vertical restoring forces F_{cv} calculated using Equations B.4 to B.17 and those calculated using Equations B.23 to B.26. The vertical deflection of the guy point is dimensionless. The reference deflection is calculated using Equation 5.9 ($\lambda_u = \lambda_{cu0}$).

$$Q_{cv} = \frac{4E_c A_{xc} H}{\lambda_{cn}} \lambda_{ro2} \sin(\theta + \alpha) \cos\beta_1 \times \left(\sqrt{(\lambda_{cg} - \lambda_{ro2}\cos\theta)^2 + (\lambda_{ro2}\sin\theta)^2 + \lambda_{ct}^2} - 1 \right) \tag{B.28}$$

$$k_{Tc}|_{\theta=0} = \frac{dQ_{cv}}{d\theta}$$

$$\Rightarrow k_{Tc}|_{\theta=0} = 4E_c A_{xc} \lambda_{ro2} H \cos\beta_1 \left(\frac{\cos(\theta)}{\lambda_{cn}} \sqrt{-2\lambda_{cg}\lambda_{ro2}\cos(\theta) + \lambda_{cg}^2 + \lambda_{ro2}^2 + \lambda_{ct}^2} + \frac{\lambda_{cg}\lambda_{ro2}\sin^2(\theta)}{\lambda_{cn}\sqrt{-2\lambda_{cg}\lambda_{ro2}\cos(\theta) + \lambda_{cg}^2 + \lambda_{ro2}^2 + \lambda_{ct}^2}} - \cos(\theta) \right) \tag{B.29}$$

B.5 Comparison with a Finite Element Model

The *general, numerical model* of the guys used in this thesis has been compared with a model generated for the ANSYS Finite Element Analysis [49] program. The Finite Element model consisted of four chains of 40 link elements joined to a common ring whose height above the base was the same as for the wind turbine. By loading the guys at this height and constraining the movement of the ring in the ways illustrated in Figure B.11. data for

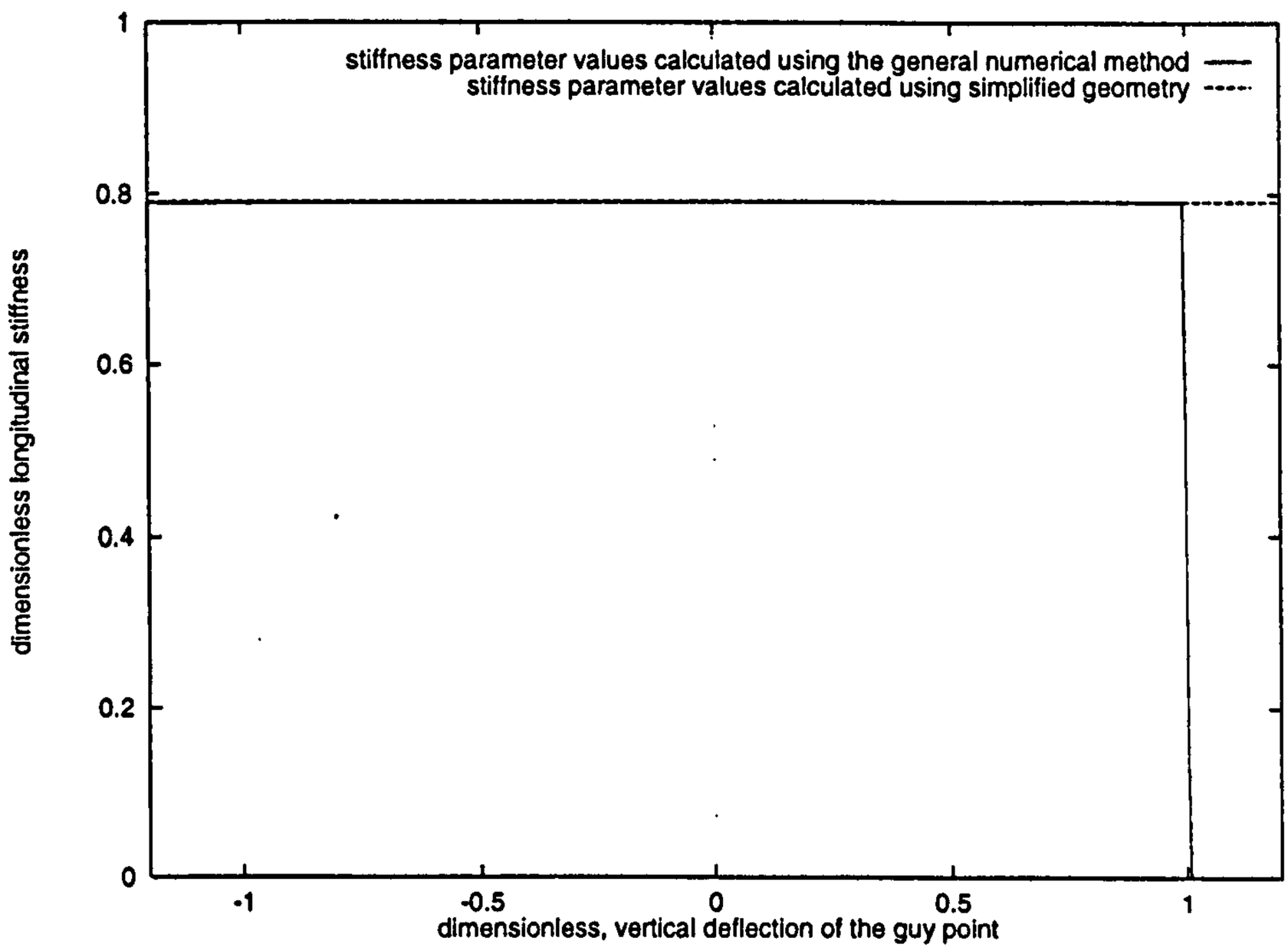

Figure B.7: Comparisons between values of the longitudinal stiffness parameter calculated using Equations B.4 to B.17 and those calculated using Equation B.27. Longitudinal stiffess values plotted are dimensionless. The scale factor is $\frac{4E_cA_{xc}}{\lambda_{cn}H}$. *The same dimensionless vertical deflection parameter is used as was used in Figure B.6. The initial strain parameter* (ϵ_{ic}) *used is 0.0005 and the scale factor for stiffness values is* $1.09 \times 10^8\ N\ m^{-1}$.

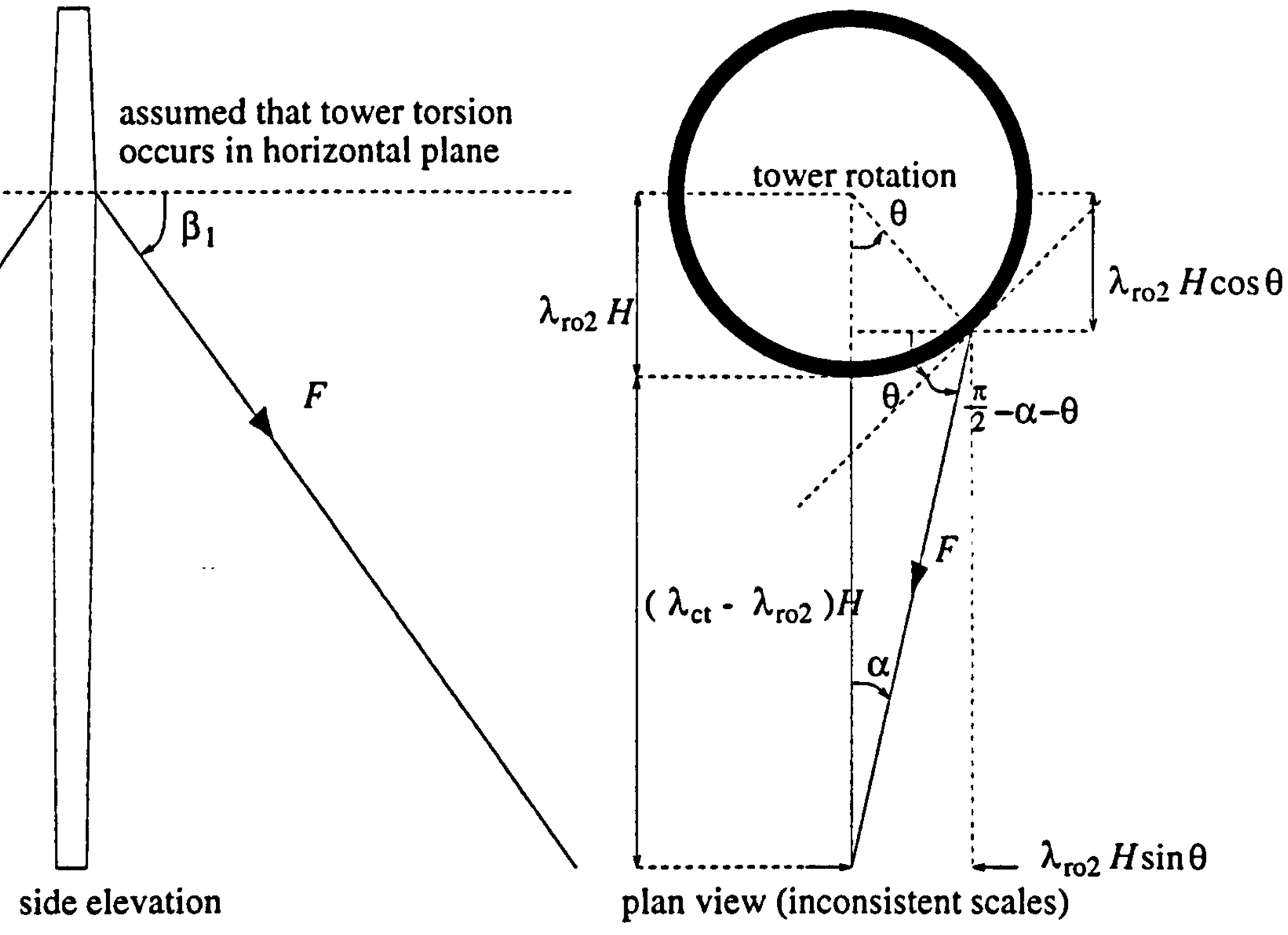

Figure B.8: Torsional stiffness parameter. *The geometry of the tower and guy cables from which an expression can be obtained for k_{Tc} (the equivalent torsional stiffness parameter of the system of cables).*

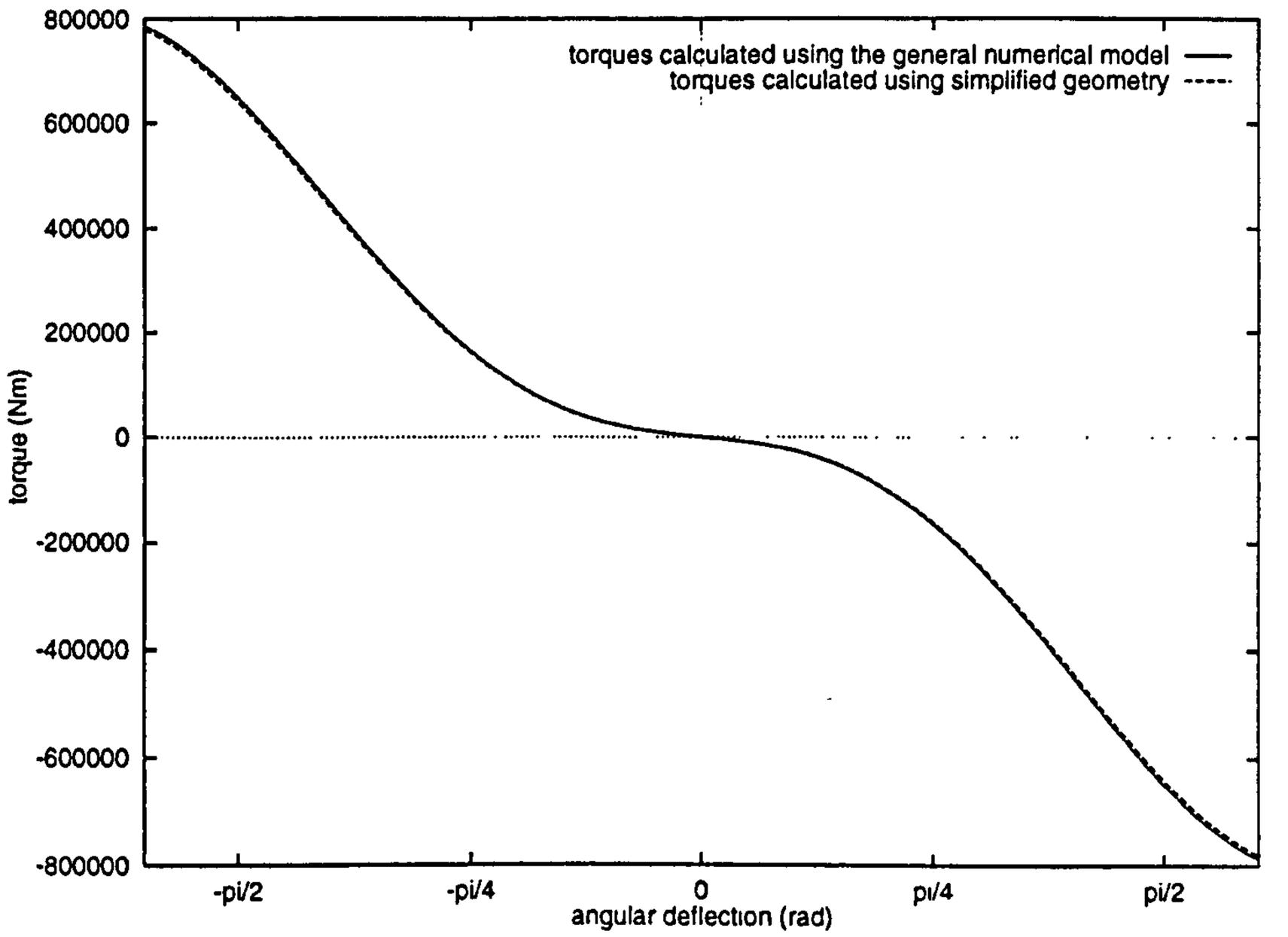

Figure B.9: Comparisons between torques, Q_{cv} calculated using Equations B.4 to B.18 and those calculated using Equation B.28. The initial strain parameter (ϵ_{ic}) used is 0.0005.

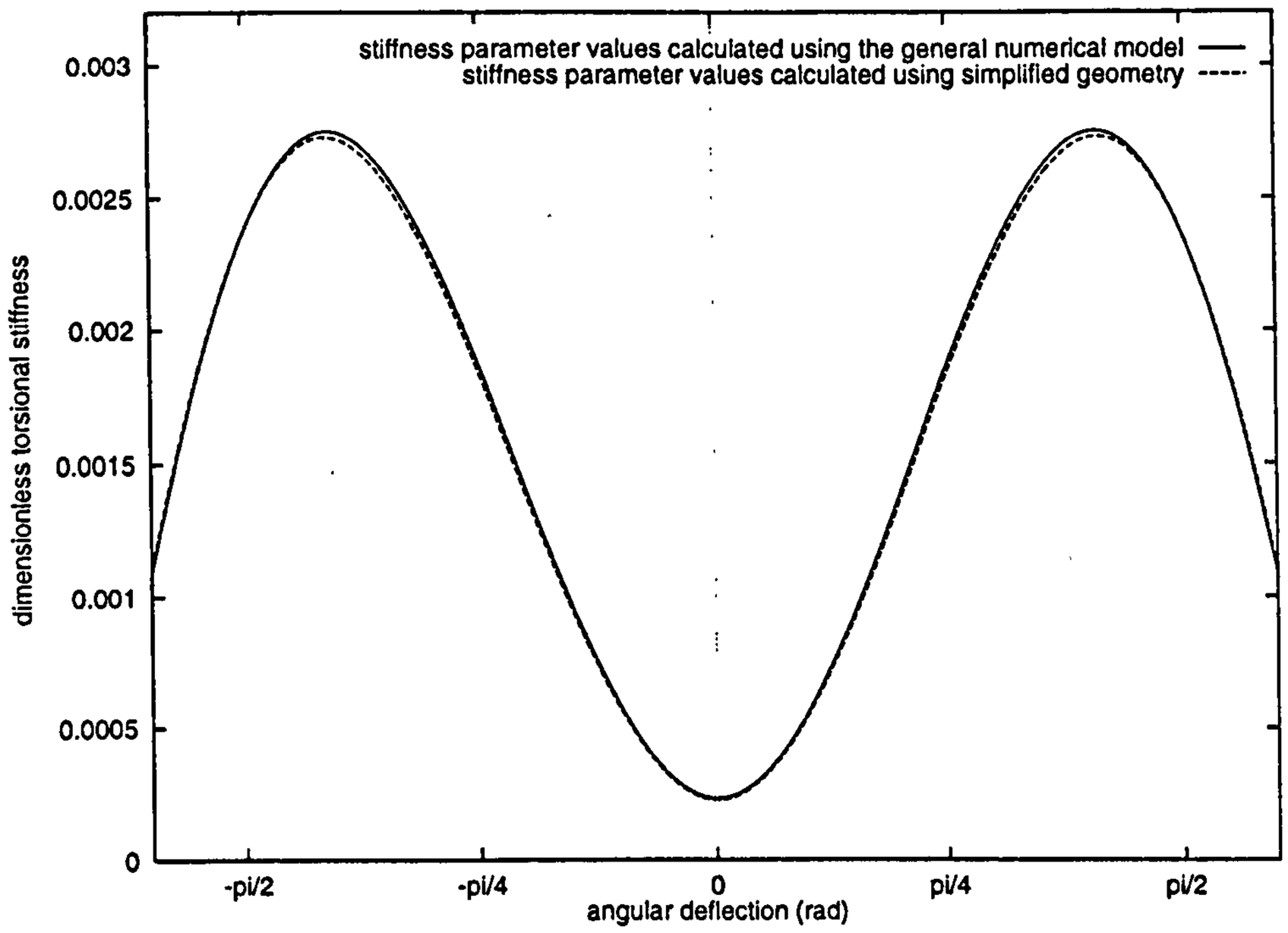

Figure B.10: Comparisons between values of the torsional stiffness parameter calculated using Equations B.4 to B.18 and those calculated using Equation B.29. Torsional stiffness values are dimensionless. The scale factor is $4E_cA_{xc}\lambda_{ro2}H$. *For an initial strain* (ϵ_{ic}) *of 0.0005, the scale factor for stiffness values is* $2.46 \times 10^8\ N\ m\ rad^{-1}$.

Figures B.12 and B.13 were obtained. Differences between the Finite Element and *general, numerical models* are listed below.

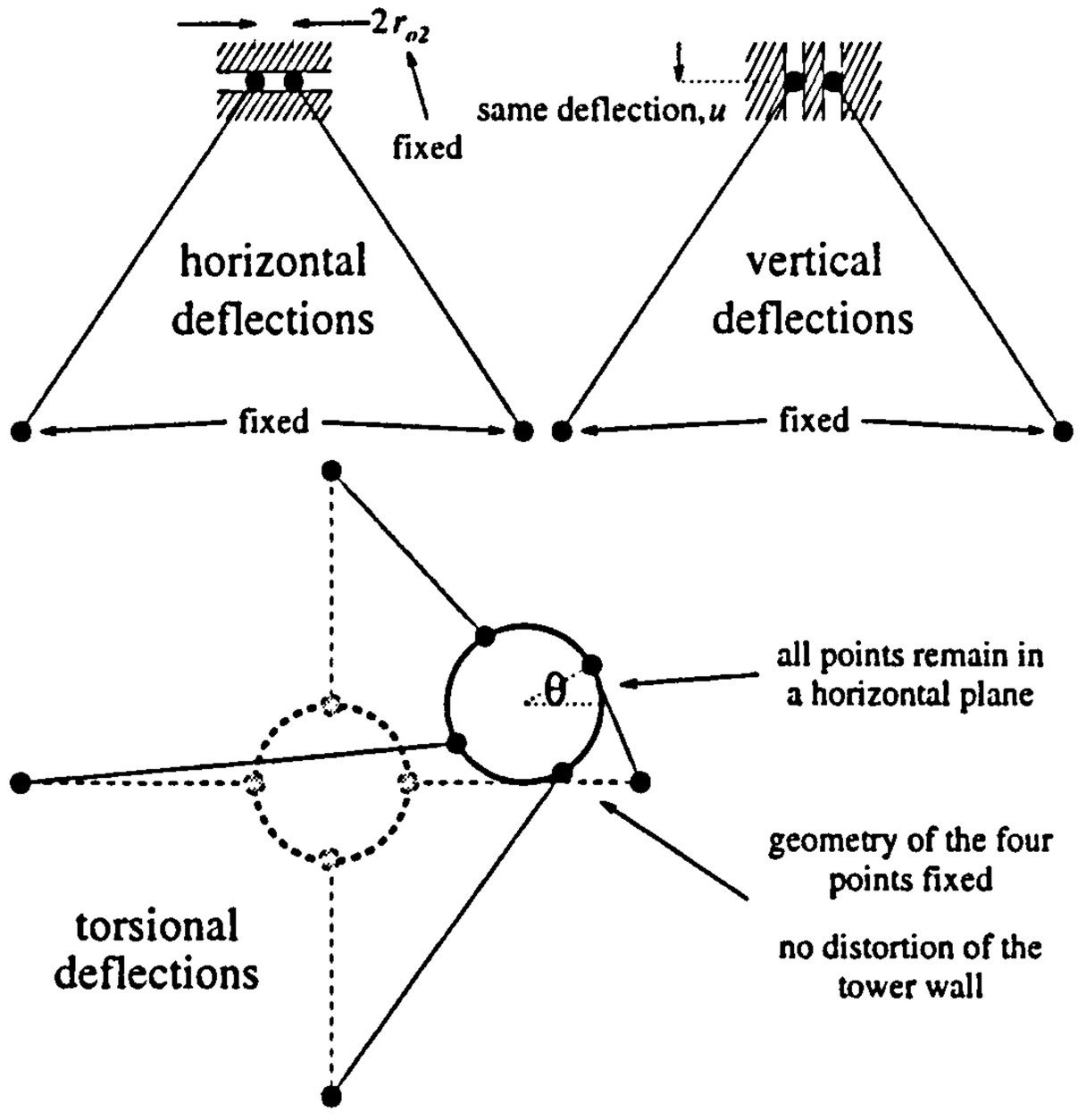

Figure B.11: The geometric constraints imposed on the Finite Element models of the four guys for comparisons with load/ deflection curves calculated using the general, numerical model *of the guys. The model of torsional deflections allows both torsion and horizontal deflection of the tower.*

- Gravity acts on all elements of the ANSYS model. The *general, numerical model* uses only one element whose mass is not considered, so gravity has no effect.
- Expressions for the true stress and true strain in the cables are used in the *general numerical model*, ANSYS uses nominal stress and nominal strain.
- For the ANSYS model, vertical motion of this single point is constrained along a single line, horizontal motion along a plane of constant height. The dip of the tower due to lateral deflections is modelled approximately in the *general, numerical model.*

Importantly, the gradients of the curves shown in Figures B.12 and B.13 as sample comparisons are the same for Finite Element and *general, numerical* models. From these curves, the stiffness parameter equivalent to deflection in each direction is estimated and used throughout static or modal analysis.

For the ANSYS model of torsional deflections, it has not been possible to formulate correctly the equations necessary to constrain the four guy cable attachment points to remain rigid with respect to one another.

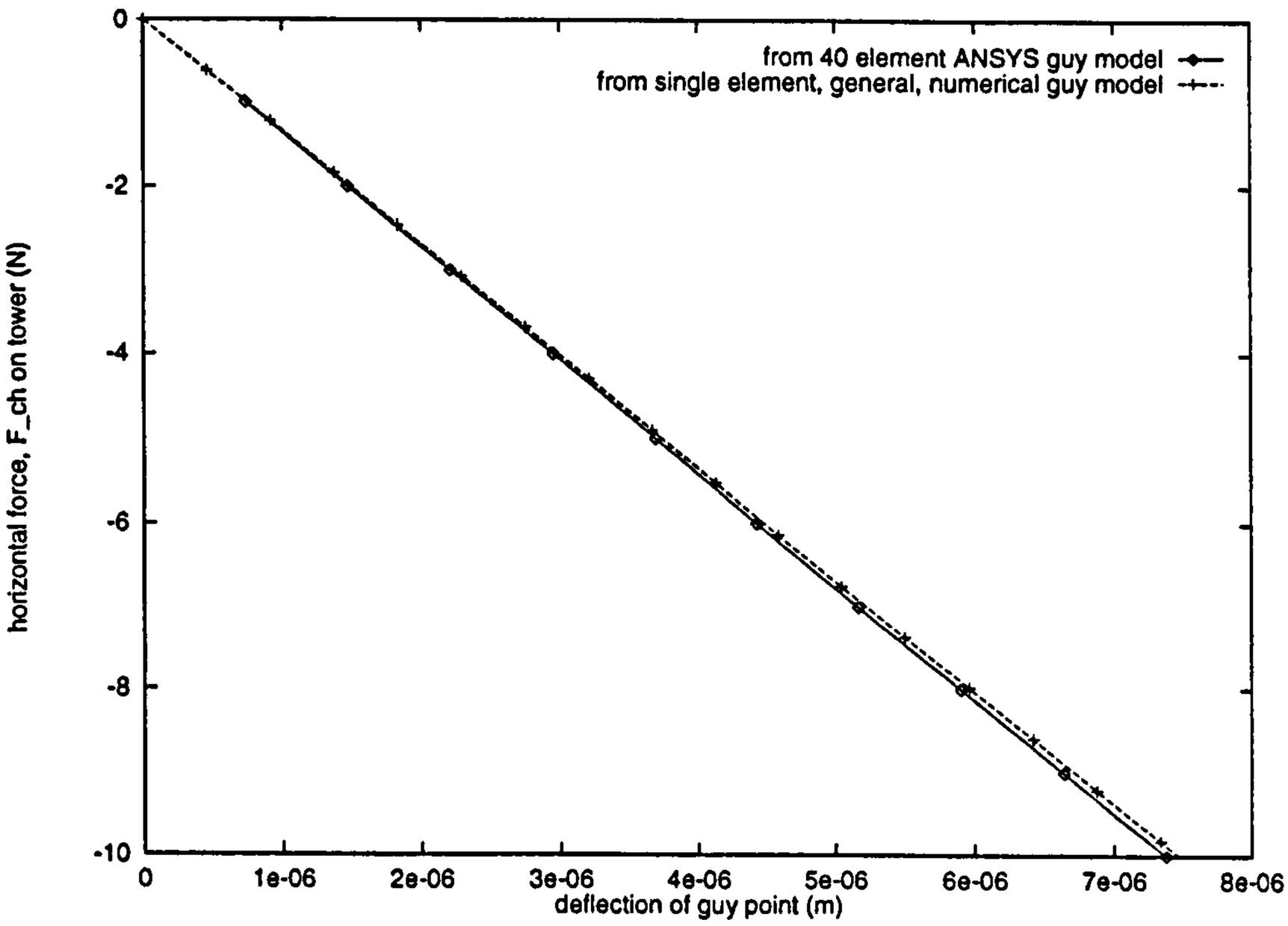

Figure B.12: Comparison between results from an ANSYS model of horizontal deflections of the point of attachment of the guy cables to the tower (Figure B.11) and from the general numerical model. *The effect of gravity on the distributed mass of the cables is included in the ANSYS model.*

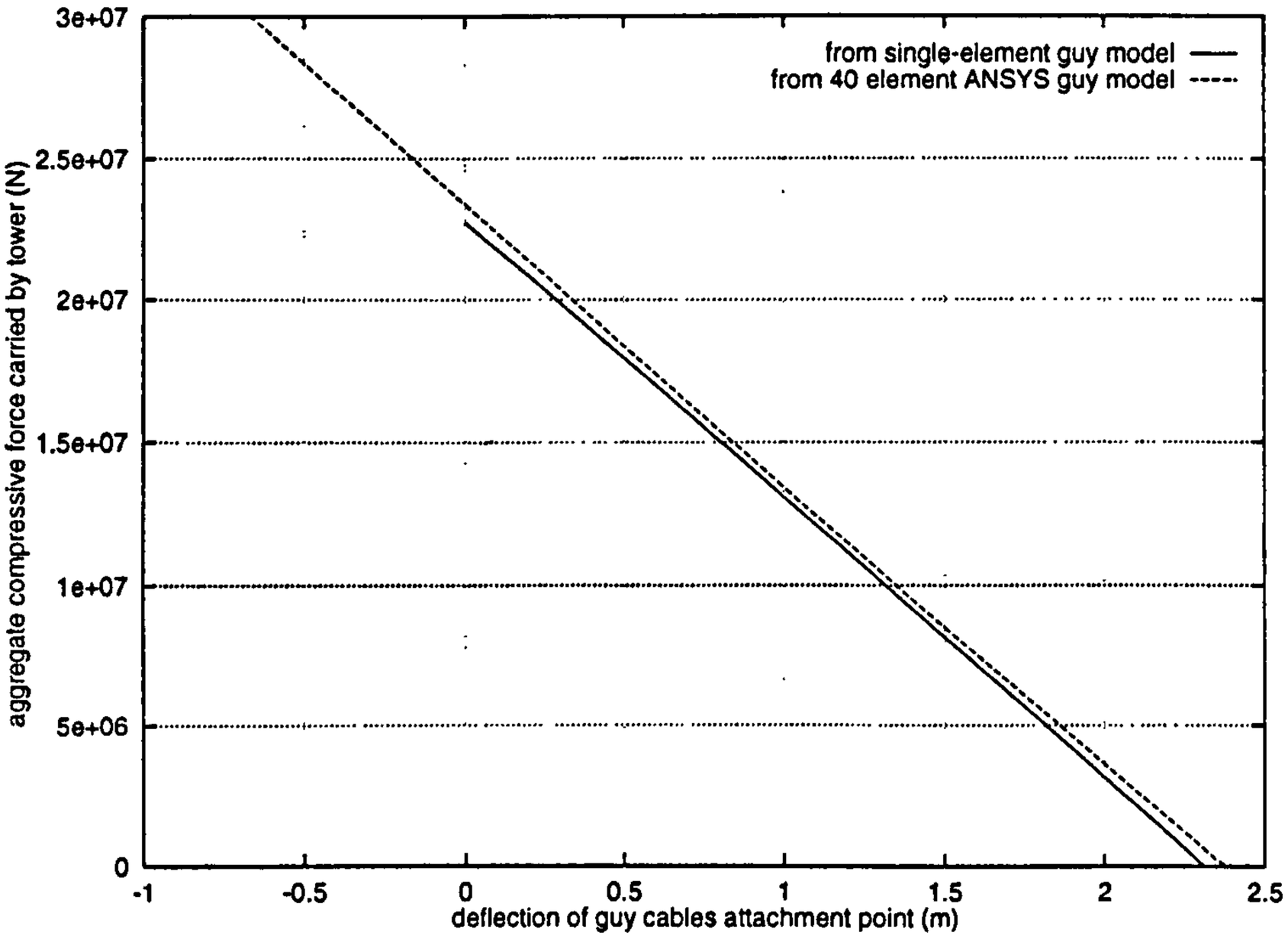

Figure B.13: Comparison between results from an ANSYS model of vertical deflections of the point of attachment of the guy cables to the tower (Figure B.11) and from the general numerical model. *The effect of gravity on the distributed mass of the cables is included in the ANSYS model.*

Appendix C

Solution of the Biharmonic Equation for a Continuous Beam

Figure C.1 shows the shear forces, S and the bending moments, M on an element of a vibrating beam. The sign convention is for displacements and forces to the right to be positive. Bending about a centre of curvature to the right is also positive. By consideration of equilibrium of this general element, *Equation C.3 can be derived. The fourth order. partial* differential equation is a biharmonic, also called 'Euler's Equation'.

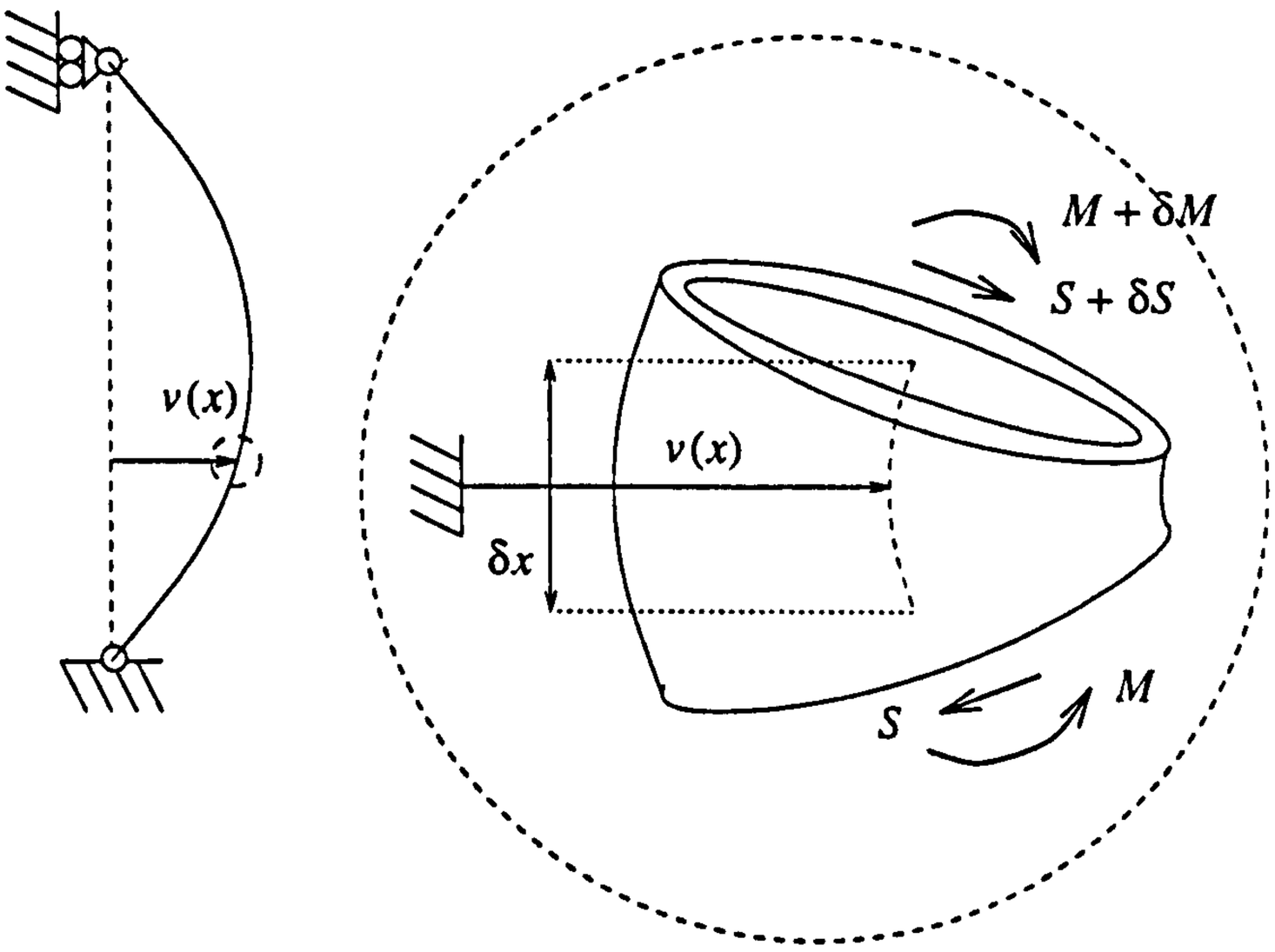

Figure C.1: The equation of motion of a simply supported beam is derived by considering the equilibrium of forces on a small element of the height. The sign convention is maintained for positive deflections, gradients, second derivatives, shear forces and bending moments.

The equilibrium of forces on the element illustrated in Figure C.1 gives a relationship between the net shear force on an element and its acceleration:

$$\rho_t A_{xt} \frac{\partial^2 v}{\partial t^2} \delta x = \frac{\partial S}{\partial x} \delta x \tag{C.1}$$

Using the theory of beam bending [32], the shear stress, S over the tower cross section can be related to the bending moment at that height. Using the formula for the elasic Young's modulus of the material and integrating stresses over the cross sectional area, the bending moment can be related to the flexural rigidity of the beam at that height ($E_t(x)I_{xt}(x)$). These two relationships are summarised in Equation C.2.

$$S = \frac{\partial M}{\partial x} = E_t I_{xt} \frac{\partial^3 v}{\partial x^3} \tag{C.2}$$

Equation C.2 is differentiated and substituted into Equation C.1 to give Equation C.3. If, instead of measuring the height, x in metres, dimensionless heights X are related to the height of the tower ($X = \frac{x}{H}$), Equation C.3 can be rearranged to give Equation C.4.

$$\rho_t A_{xt} \frac{\partial^2 v}{\partial t^2} = E_t I_{xt} \frac{\partial^4 v}{\partial x^4} \tag{C.3}$$

$$\frac{\partial^2 v}{\partial t^2} = \frac{E_t I_{xt}}{\rho_t A_{xt} H^4} \frac{\partial^4 v}{\partial X^4} \tag{C.4}$$

The solution of Equation C.4 is a function of both time and distance, $v(X,t)$. By assuming that it is a separable function, with a harmonic time dependence, $v(X)cos\,(\omega_{nB}t)$, the acceleration of the beam (on the left hand side of Equation C.4) can be rewritten as the product of the modal amplitude of vibrations and the square of the angular frequency (Equation C.5).

$$v\omega_{nB}^2 = \frac{E_t I_{xt}}{\rho_t A_{xt} H^4} \frac{d^4 v}{dX^4} \tag{C.5}$$

$$v = \frac{1}{C_{\omega iB}^4} \frac{d^4 v}{dX^4} \tag{C.6}$$

where:

$$C_{\omega iB} = \sqrt[4]{\frac{\rho_t A_{xt} H^4 \omega_{nB}^2}{E_t I_{xt}}} \tag{C.7}$$

Equation C.6 shows that the fourth order partial differential equation (Equation C.4) has been reduced to a fourth order ordinary differential equation (Equation C.6) with the particular coefficient, $C_{\omega iB}$ defined in Equation C.7. The general solution to such a differential equation is Equation C.8. Once again, the dimensionless height, X is used.

$$v = C_1 e^{C_{\omega iB} X} + C_2 e^{-C_{\omega iB} X} + C_3 \sin(C_{\omega iB} X) + C_4 \cos(C_{\omega iB} X) \tag{C.8}$$

By differentiating Equation C.8 three times. the boundary conditions for the bottom and top of the tower can be expressed as four simultaneous equations with four unknowns (C_1. C_2, C_3 and C_4). The Glossary includes definitions of various boundary conditions in terms of

v, $\frac{dv}{dx}$, $\frac{d^2v}{dx^2}$ and $\frac{d^3v}{dx^3}$. These four simultaneous equations can be rewritten as a matrix equation. The example given by Equation C.9, is for a beam with both ends built in.

$$\begin{bmatrix} 1 & 1 & 0 & 1 \\ 1 & -1 & 1 & 0 \\ e^{C_{\omega iB}} & e^{-C_{\omega iB}} & \sin C_{\omega iB} & \cos(C_{\omega iB}) \\ e^{C_{\omega iB}} & -e^{-C_{\omega iB}} & \cos C_{\omega iB} & -\sin C_{\omega iB} \end{bmatrix} \begin{bmatrix} C_1 \\ C_2 \\ C_3 \\ C_4 \end{bmatrix} = \begin{bmatrix} 0 \\ 0 \\ 0 \\ 0 \end{bmatrix} \tag{C.9}$$

Since the right hand side of Equation C.9 is **0**, $C_{\omega iB}$ is found by the following steps:

1. equating the determinant of the matrix of boundary conditions with zero to find $C_{\omega iB}$,

2. substituting $C_{\omega iB}$ into the matrix,

3. then finding the eigenvector $\{C_1 C_2 C_3 C_4\}$ of the same matrix whose eigenvalue is zero.

To find $C_{\omega iB}$ for which the determinant is zero, a numerical search routine is used.

When these five values ($C_{\omega iB}$, C_1, C_2, C_3 and C_4) are substituted into Equation C.8, the equation of the tower mode shape is obtained.

Figure C.2 shows the eigenfunctions of Equation C.6 and Table C.1 lists values of the coefficient, $C_{\omega iB}$ and the constants used in Equation C.8.

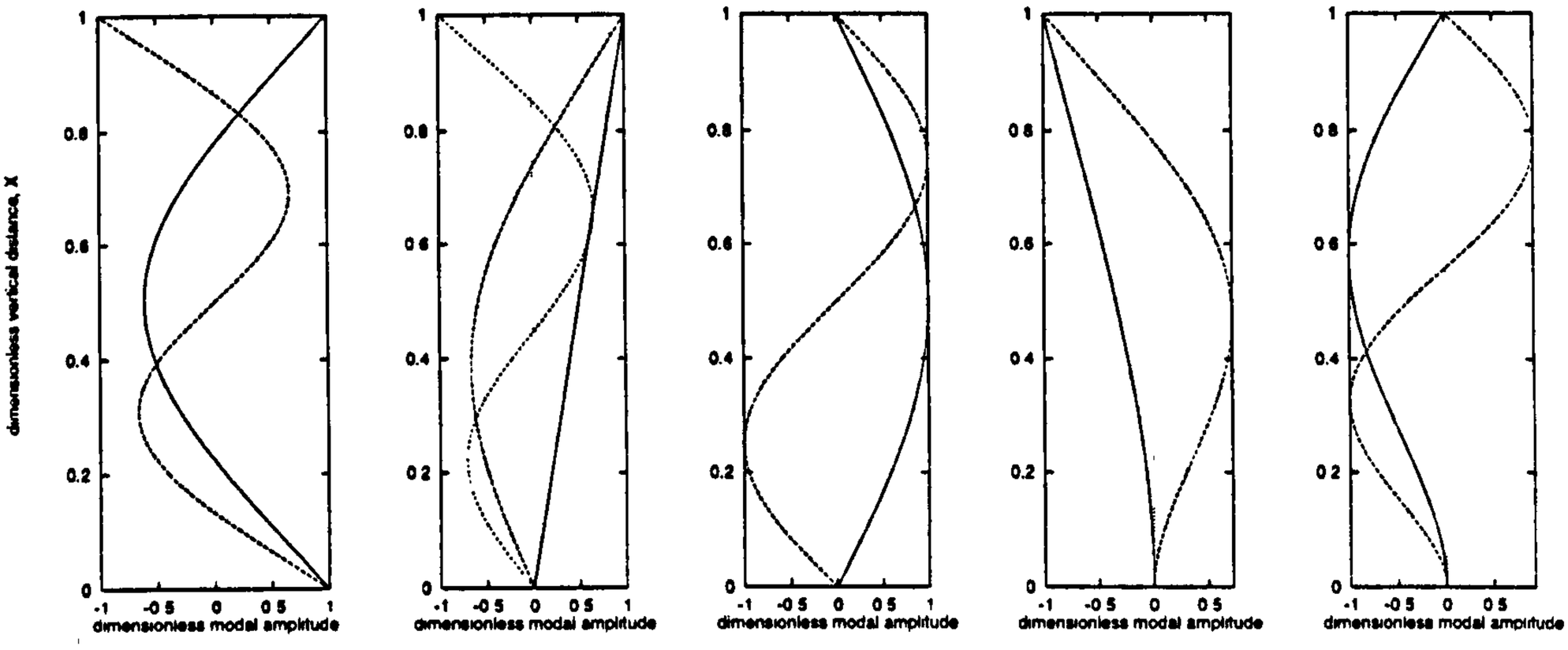

Figure C.2: The eigenfunctions of Equation C.6 plotted with a dimensionless vertical scale, X.

Table C.1: The values of the coefficient $C_{\omega iB}$ used in Equation C.6 and the constants used in the general form (Equation C.8) of the solution of Equation C.6.

mode, i	boundary conditions		$C_{\omega iB}$	C_1	C_2	C_3	C_4
1	free	free	22.29	0.005	0.58	-0.57	0.58
2	free	free	61.68	0.005	0.58	-0.57	0.58
1	hinged	free	0.0	0	0	0	0
2	hinged	free	15.42	0	0	-1	0
3	hinged	free	49.96	0	0	-1	0
1	hinged	hinged	9.870	0	0	1	0
2	hinged	hinged	39.48	0	0	1	0
1	built in	free	3.516	-0.088	-0.57	-0.48	0.66
2	built in	free	22.03	-0.0053	0.58	0.58	-0.57
1	built in	hinged	15.42	0.0002	-0.58	-0.58	0.58
2	built in	hinged	49.96	0	-0.58	-0.58	0.58

Appendix D

Complete List of Rayleigh Energy Expressions

In this Appendix, the energy expression used in the formula for Rayleigh's approximation for the fundamental natural frequency (Equation 4.8) is given for all components of the model.

D.1 Bending Vibrations

$$\omega_{R1B} = \sqrt{\frac{V_{Bt} + V_{Bf} + V_{Bc}}{\frac{T_{Bn}+T_{Bt}}{\omega^2_{R1B}}}} \tag{D.1}$$

D.1.1 The Tower

$$V_{Bt} = \int_0^H \frac{1}{2} E_t I_{xt} \left(\frac{d^2v}{dx^2}\right)^2 dx - \int_0^{\lambda_{ct}H} \frac{1}{2} F_{cv} \left(\frac{dv}{dx}\right)^2 dx \tag{D.2}$$

$$\frac{T_{Bt}}{\omega_{R1B}} = \omega^2_{R1B} \left(\int_0^H \frac{1}{2} \rho_t A_{xt} \left(v\left(x\right)\right)^2 dx + \int_0^H \frac{1}{2} \rho_t I_{xt} \left(\left.\frac{dv}{dx}\right|_x\right)^2 dx \right) \tag{D.3}$$

D.1.2 The Guy Cables

$$V_{Bc} = \frac{1}{2} k_{Bc} v\left(\lambda_{ct} H\right)^2 \tag{D.4}$$

D.1.3 The Nacelle

$$\frac{T_{Bn}}{\omega_{R1B}} = \omega^2_{R1B} \left(\frac{1}{2} M_n v(H)^2 + \frac{1}{2} J_{tn} \left.\frac{dv}{dx}\right|^2_{x=H} \right)$$

or:

$$\frac{T_{Bn}}{\omega_{R1B}} = \omega^2_{R1B} \left(\frac{1}{2} M_n v(H)^2 + \frac{1}{2} J_{rn} \left.\frac{dv}{dx}\right|^2_{x=H} \right) \tag{D.5}$$

D.1.4 The Base and Foundation

$$V_{Bf} = \frac{1}{2}k_{Bf}\left.\frac{dv}{dx}\right|_{x=0}^{2} + \frac{1}{2}k_{Lf}v(0)^2 \tag{D.6}$$

D.2 Torsional Vibrations

$$\omega_{R1T} = \sqrt{\frac{V_{Tt} + V_{Tf} + V_{Tc}}{\frac{T_{Tn}+T_{Tt}}{\omega^2_{R1T}}}} \tag{D.7}$$

D.2.1 The Tower

$$V_{Tt} = \int_0^H \frac{1}{2}G_t J_{xt}\left(\frac{d\theta}{dx}\right)^2 dx \tag{D.8}$$

$$\frac{T_{Tt}}{\omega_{R1T}} = \omega^2_{R1T}\int_0^H \frac{1}{2}\rho_t J_{xt}\theta\,(x)^2\,dx \tag{D.9}$$

D.2.2 The Guy Cables

$$V_{Tc} = \frac{1}{2}k_{Tc}\theta\,(\lambda_{ct}H)^2 \tag{D.10}$$

D.2.3 The Nacelle

$$\frac{T_{Tn}}{\omega_{R1T}} = \omega^2_{R1T}\left(\frac{1}{2}J_{ny}\theta_n^2\right) \tag{D.11}$$

$$V_{Tn} = \frac{1}{2}k_{Yn}\left(\theta_n - \theta(H)\right)^2 \tag{D.12}$$

The angle of twist of the nacelle, θ_n includes any additional rotation of the nacelle due to the compliance of the nacelle/ tower coupling (see Appendix A.2, Equation A.17).

D.2.4 The Base and Foundation

$$V_{Tf} = \frac{1}{2}k_{Tf}\theta(0)^2 \tag{D.13}$$

D.3 Longitudinal Vibrations

$$\omega_{R1C} = \sqrt{\frac{V_{Ct} + V_{Cf} + V_{Cc} + V_{Cn} - V_{C0}}{\frac{T_{Cn}+T_{Ct}}{\omega^2_{R1C}}}} \tag{D.14}$$

Where V_{C0} is the total potential energy stored in the system at static equilibrium.

D.3.1 The Tower

$$V_{Ct} = \int_0^H \frac{1}{2} E_t A_{xt} \left(\frac{du}{dx}\right)^2 - \rho_t A_{xt} g u(x) dx \tag{D.15}$$

$$\frac{T_{Ct}}{\omega_{R1C}} = \omega_{R1C}^2 \left(\int_0^H \frac{1}{2} \rho_t A_{xt} \left(u(x) - u_0(x)\right)^2 dx\right) \tag{D.16}$$

(D.17)

Where g is the acceleration due to gravity.

D.3.2 The Guy Cables

$$V_{Cc} = \frac{1}{2} k_{Cc} \left(u_{c0} - u\left(\lambda_{ct} H\right)\right)^2 \tag{D.18}$$

Provided that $u_{c0} > u(\lambda_{ct} H)$, otherwise, $V_{Cc} = 0$.

D.3.3 The Nacelle

$$\frac{T_{Cn}}{\omega_{R1C}} = \omega_{R1C}^2 \left(\frac{1}{2} M_n \left(u(H) - u_0(x)\right)^2\right) \tag{D.19}$$

$$V_{Cn} = -M_n g u(H) \tag{D.20}$$

Where g is the acceleration due to gravity.

D.3.4 The Base and Foundation

$$V_{Cf} = \frac{1}{2} k_{Cf} u(0)^2 \tag{D.21}$$

Appendix E

Complete List of Stodola Inertia Loads

All loads (forces, force densities, torques and torque densities) are listed as applied to the appropriate static model. Although, they are given in Sections 4.4.1 and 4.4.2 as functions of time, only the time magnitudes (maximum over time) are listed here. These values all correspond to the loads at the time when the deflection of the tower is zero everywhere (Figure 4.8). This corresponds to the loads at times $t = n\pi\omega$ (see Equations 4.28 and 4.30) where n is 0 or a positive integer and ω is the appropriate angular frequency of the class of vibrations begin considered (such as ω_{1B} or ω_{2T}). In the combined *Rayleigh/ Stodola* method, the values of these angular frequencies are the current Rayleigh estimates (ω_{R1B} or ω_{R2T}). The fundamental frequencies are used here to illustrate the inertia loads.

E.1 Bending Vibrations

E.1.1 The Tower

$$f_h = -\rho_t A_{xt} \omega_{1B}^2 v(x) \tag{E.1}$$

$$f_v = \rho_t A_{xt} g \tag{E.2}$$

$$q_h = -\rho_t I_{xt} \omega_{1B}^2 \left.\frac{dv}{dx}\right|_x \tag{E.3}$$

Where g is the acceleration due to gravity.

E.1.2 The Nacelle

$$F_{nh} = -M_n \omega_{1B}^2 v(H) \tag{E.4}$$

$$F_{nv} = M_n g \tag{E.5}$$

$$Q_{nh} = -J_{rn} \omega_{1B}^2 \left.\frac{dv}{dx}\right|_H$$

or:

$$Q_{nh} = -J_{tn}\omega_{1B}^2 \left.\frac{dv}{dx}\right|_H \tag{E.6}$$

E.2 Torsional Vibrations

E.2.1 The Tower

$$q_v = -\rho_t J_{xt}\omega_{1T}^2\theta(x) \tag{E.7}$$

E.2.2 The Nacelle

$$Q_{nv} = -J_{ny}\omega_{1T}^2\theta(H) \tag{E.8}$$

E.3 Longitudinal Vibrations

E.3.1 The Tower

$$f_v = \rho_t A_{xt}\left(g - (u(x) - u_0(x))\,\omega_{1C}^2\right) \tag{E.9}$$

E.3.2 The Nacelle

$$F_{nv} = M_n\left(g - (u(H) - u_0(H))\,\omega_{1C}^2\right) \tag{E.10}$$

Appendix F

Tower Buckling

Tower buckling is a static instability. Euler theory predicts the lateral deflection of the tower due to vertical (axial) loads. Solution is only possible for simple sets of boundary conditions and applied loads. The *general, numerical model* described here includes the effects of axial loads. If axial loads are increased, buckling will occur and the deflected shape output from the model will be a buckling mode shape. In order to find the critical load regime, an initial estimate must be made. Euler's formula (Equation 3.6) can be used for this. The two situations dealt with are towers with multiple sets of guys at different heights (Figure 3.5) and towers with different base rigidity values.

This section offers more practical detail on the method of effective length than given in the initial description in Section 3.1.1.

F.1 The Method of Effective Length

F.1.1 Multiple Sets of Guys

The Carter wind turbines use towers guyed at one height by four cables. Most of the models have been developed for this configuration. Figure 3.5 shows a wind turbine tower with three sets of guy cables attached to the tower at different heights. An example of such a configuration is the Aerowatt (now Vergnet) UM70 10 kW wind turbine (Figure 3.1 shows such a wind turbine after buckling of the tower). Throughout Appendix F.1, the term *sections* of the tower refers to the portions of the tower's length between:

1. the base and the first set of guys,

2. each subsequent set of guys and

3. the last set and the nacelle.

This is a different use of the term *tower sections* than was used in Section 2.2.1 and subsequently in the body of the thesis where it referred to the physical tubular sub-sections of the tower.

The particular boundary conditions for a section of the tower can be modelled by choosing an effective height for that section and using Equation 3.6 to calculate the Euler load. The

factor $\lambda_e = \frac{H_{(eff)}}{H}$ is used to modify the physical height. λ_e will depend either on the height of the nearest neighbouring tower sections or on some other boundary condition. Taking the value of λ_{ea} due to the nearest section above the section of interest as an example:-

- λ_{ea} is 2 if the upper end of the section is free;
- λ_{ea} is 1 if the upper end of the section is hinged or there is a section above which is the same length or larger;
- λ_{ea} is 0.7 if the upper end of the section is built in or there is a section above which is very short.

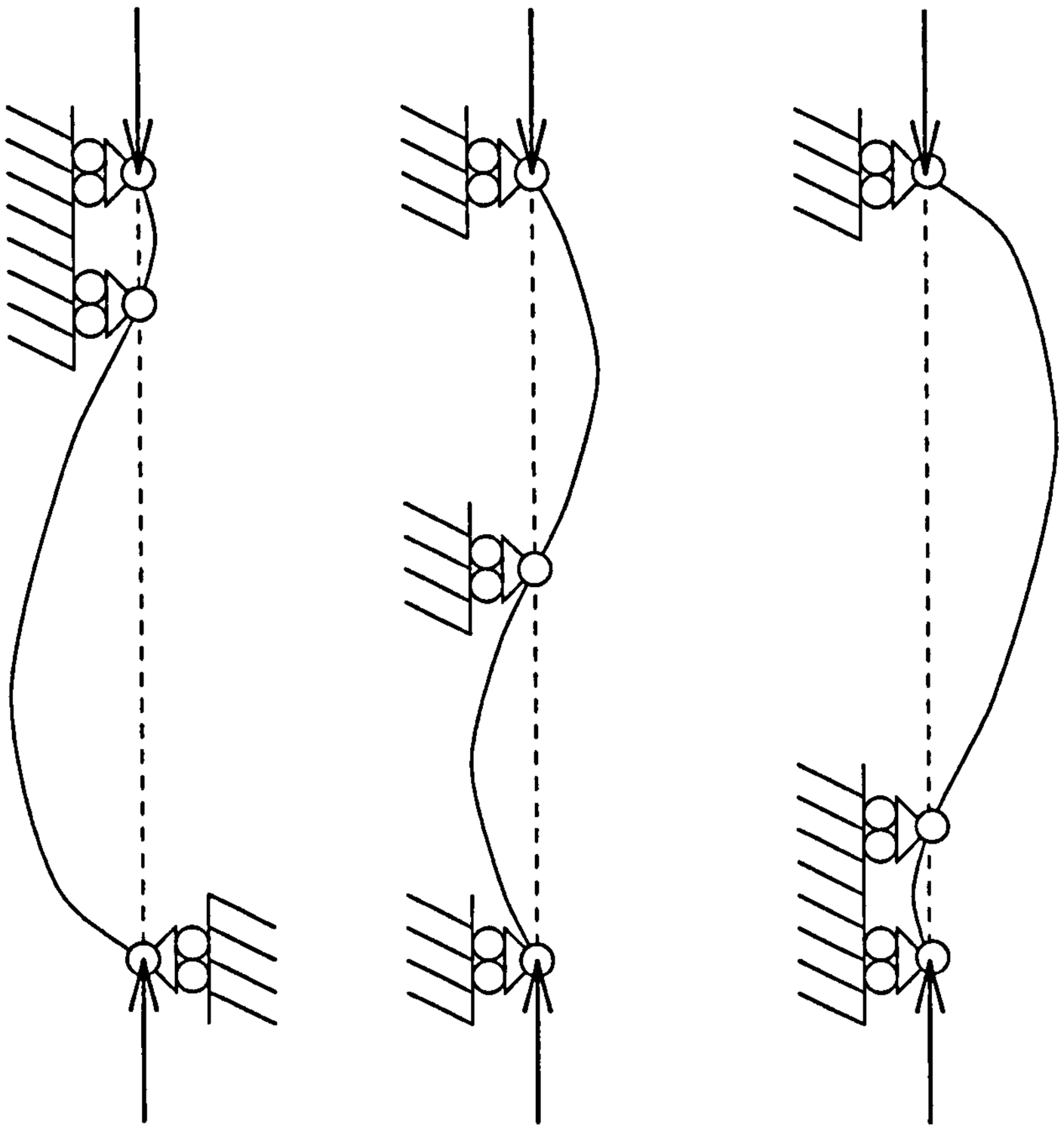

Figure F.1: Three sections of a simply supported strut. If the nearest section above the section of interest is very short, the section of interest is effectively built in at the upper end and its effective length is shorter than its physical length. If the nearest section above the section of interest is very long, the section of interest is unlikely to buckle first so estimating a value for its effective length is unimportant. In an attempt to model this behaviour mathematically. Equations F.1 and F.2 have been postulated. The shape is shown in Figure F.2).

For a simply supported strut with a large number of sections each simply supported, only the two nearest neighbouring sections are used to calculate λ_e which will vary as shown in Figure F.2. This curve is a conservative approximation because effective lengths are likely to be longer than those predicted with it. It is a Weibull function (Equations F.1 and F.2). H

is the height of the section of interest. H_a is the height of the section just above the section of interest ($\lambda_{ea} = H/H_a$). The height of the section just below the section of interest is H_b ($\lambda_{eb} = H/H_b$). The effective height can then be calculated using: $\lambda_e = \lambda_{ea}\lambda_{eb}$.

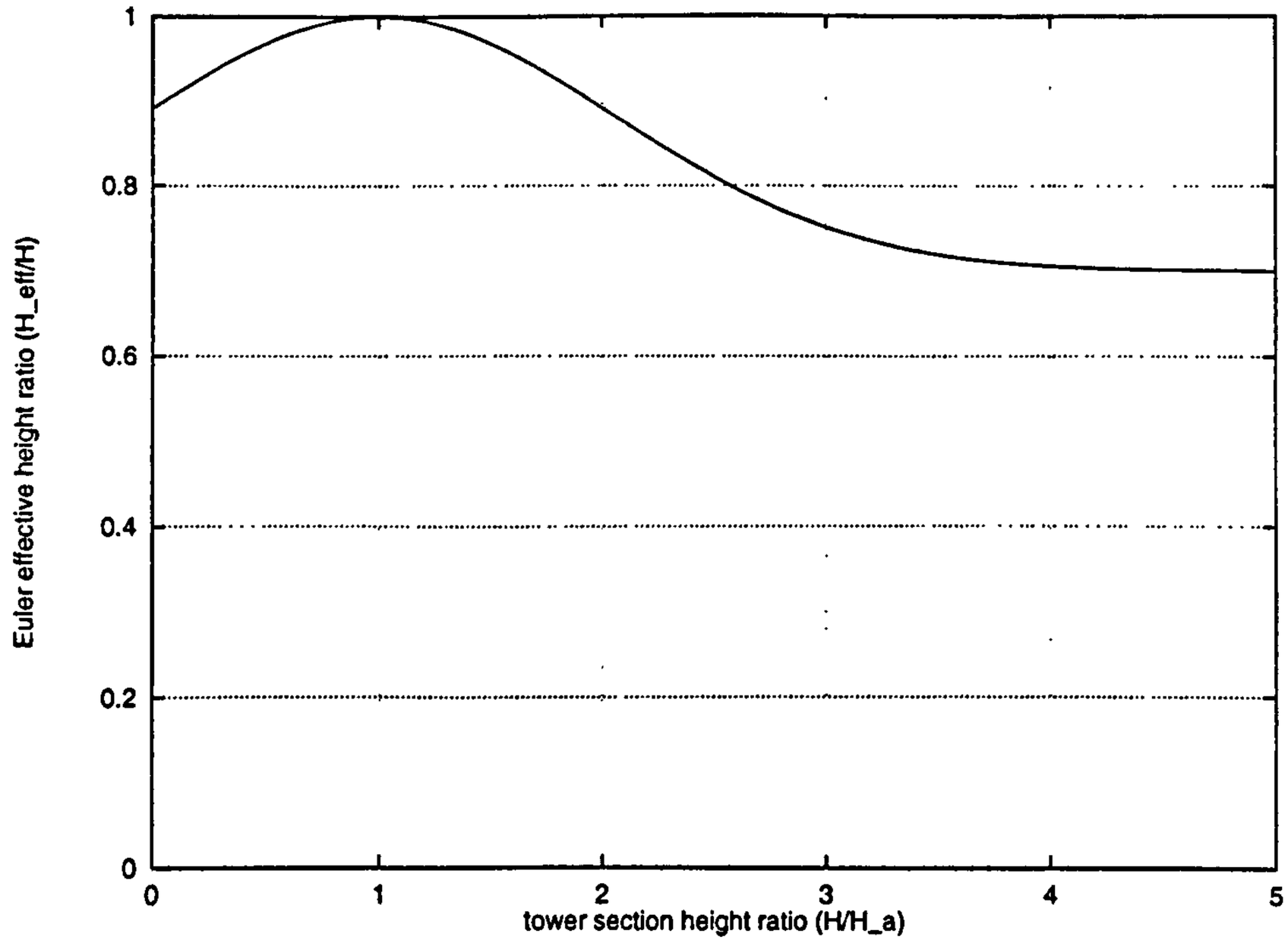

Figure F.2: The variation of the effective height ratio, λ_e with the ratio of physical heights of the section of interest to one of its two nearest neighbours (Equation F.1 with $\lambda_{e(\min)} = 0.7$, $\lambda_{e(\mathrm{dif})} = 0.3$ and $A = 1.5$).

$$\lambda_{ea} = \lambda_{e(\min)} + \lambda_{e(\mathrm{dif})} e^{-\left(\left(\frac{H}{H_a}-1\right)\frac{1}{A}\right)^2} \tag{F.1}$$

$$\lambda_{eb} = \lambda_{e(\min)} + \lambda_{e(\mathrm{dif})} e^{-\left(\left(\frac{H}{H_b}-1\right)\frac{1}{A}\right)^2} \tag{F.2}$$

F.1.2 Base Boundary Condition

The base condition can either be hinged ($\lambda_{eb} = 1.0$) or built in ($\lambda_{eb} = 0.7$). By investigating the effect on the buckling load of different values of the base torsional stiffness parameter k_{Bf}, a function approximately relating λ_{eb} to k_{Bf} can be derived. Two types of function have been fitted to data ($H_{(\mathrm{eff})}$ calculated at different values of k_{Bf}):

1. a Weibull function (Equation F.3) and
2. an inverse tangent function (Equation F.4).

The data is obtained:

1. by non-Euler buckling analysis using the *structural spline* method and a directed search method (Section 3.2.1),

2. by using Equation 3.6 to calculate the effective length of the tower,

3. by dividing by the physical length of the tower (H in the case of buckling due to F_{nv}; $\lambda_{ct}H$ in the case of buckling due to initial guy tension, ϵ_{ic}) to get values of λ_{eb}.

The data in Figure F.3 has been obtained for buckling of the lower section of the tower due to initial tension in the guys. The variation shown in Figure F.3 is similar to the variation of deflection gradient in Figure 5.2.

$$\lambda_{eb} = \lambda_{e(\min)} + \lambda_{e(\mathrm{dif})} e^{-\left(\frac{k_{Bf}}{10^A}\right)^B} \tag{F.3}$$

$$\lambda_{eb} = \lambda_{e(\min)} + \lambda_{e(\mathrm{dif})} \left(\frac{1}{\pi}\tan^{-1}\left(B\left(A - \log_{10}(k_{Bf})\right)\right) + 0.5\right) \tag{F.4}$$

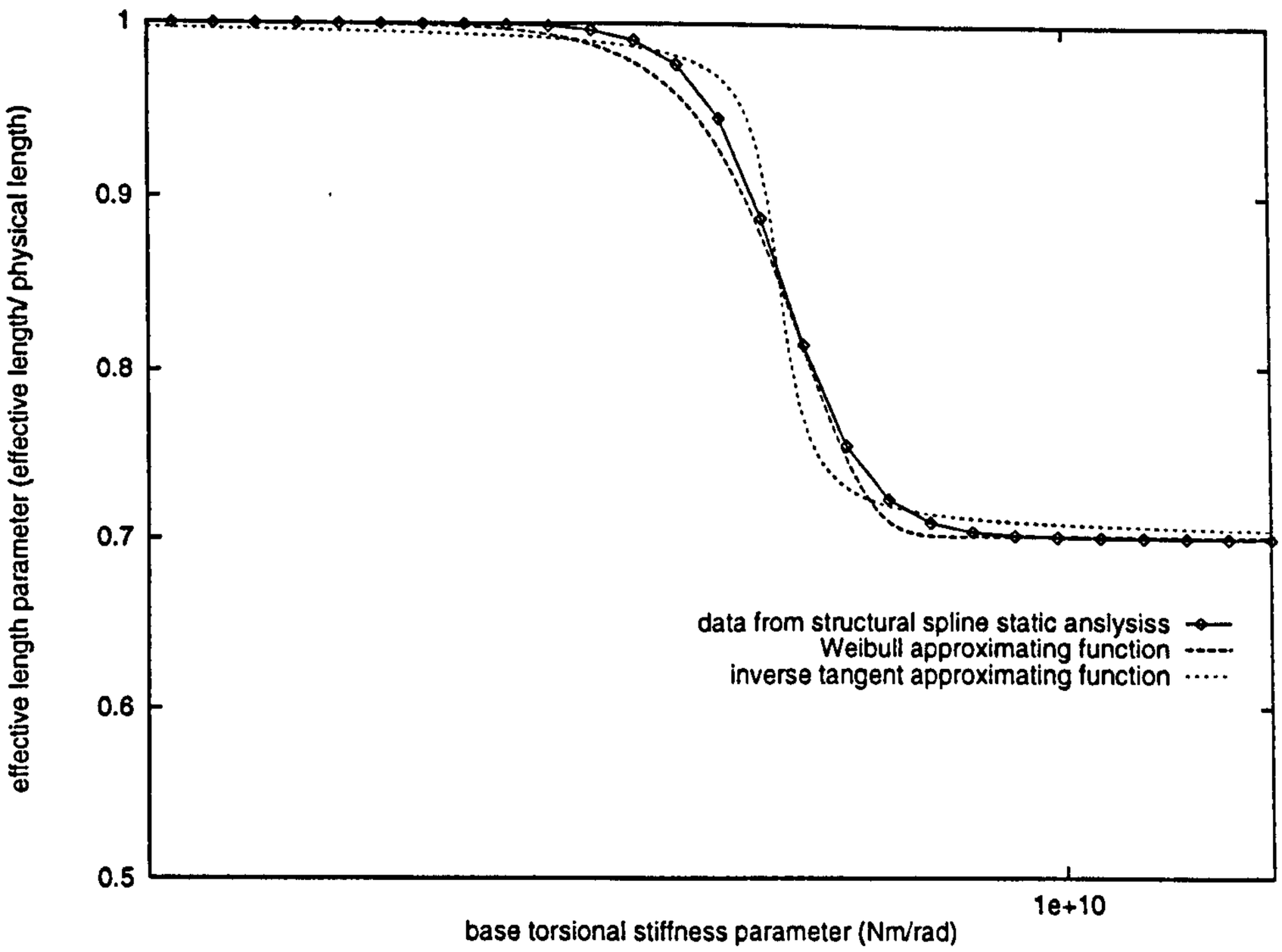

Figure F.3: The variation of the effective height ratio, λ_{eb} with the base torsional stiffness parameter, k_{Bf}. The tower was constrained at the point of attachment of the guys as if hinged there by setting the guy Young's modulus parameter to $E_c = 1 \times 10^{15}$ and setting uniform tower properties. Number of nodal points $N_n = 91$. number of spline interpolation points $N_s = 51$. The two curves fitted to the data are Equation F.3 and Equation F.4. Parameters for Equation F.3: $\lambda_{e(\mathrm{dif})} = 0.3$, $\lambda_{e(\min)} = 0.7$, $A = 7.45$ and $B = \frac{2}{3}$. Parameters for Equation F.4: $\lambda_{e(\mathrm{dif})} = 0.3$, $\lambda_{e(\min)} = 0.7$, $A = 7.21$ and $B = 5$.

For both functions (Equation F.3 and F.4), parameter A affects the horizontal translation of the function. In the case of Equation F.4 the point at which $k_{Bf} = 10^A$ is a point

of rotational symmetry of the curve if plotted using a logarithmic scale for the horizontal axis. Equation F.3 has no rotational symmetry on these axes. The data also appears to have rotational symmetry if plotted with a logarithmic horizontal scale. In both functions, parameter B affects the gradient of the function. If B is larger, the function is steeper and the transition from $\lambda_{eb} = 1.0$ to $\lambda_{eb} = 0.7$ occurs within a smaller range of values of k_{Bf}. The four parameters have been obtained here by trial and error. Better fits between approximating functions and data could be obtained if a non-linear χ^2 minimisation algorithm were used such as the Levenberg/ Marquardt method [31].

Appendix G

Details of Experimental Method

G.1 Positioning Accelerometers to Distinguish Mode Classes

To distinguish between torsional and lateral modes, two accelerometers are attached to the tower on opposite sides. The time series are subtracted. Figure G.1 shows this configuration of accelerometers.

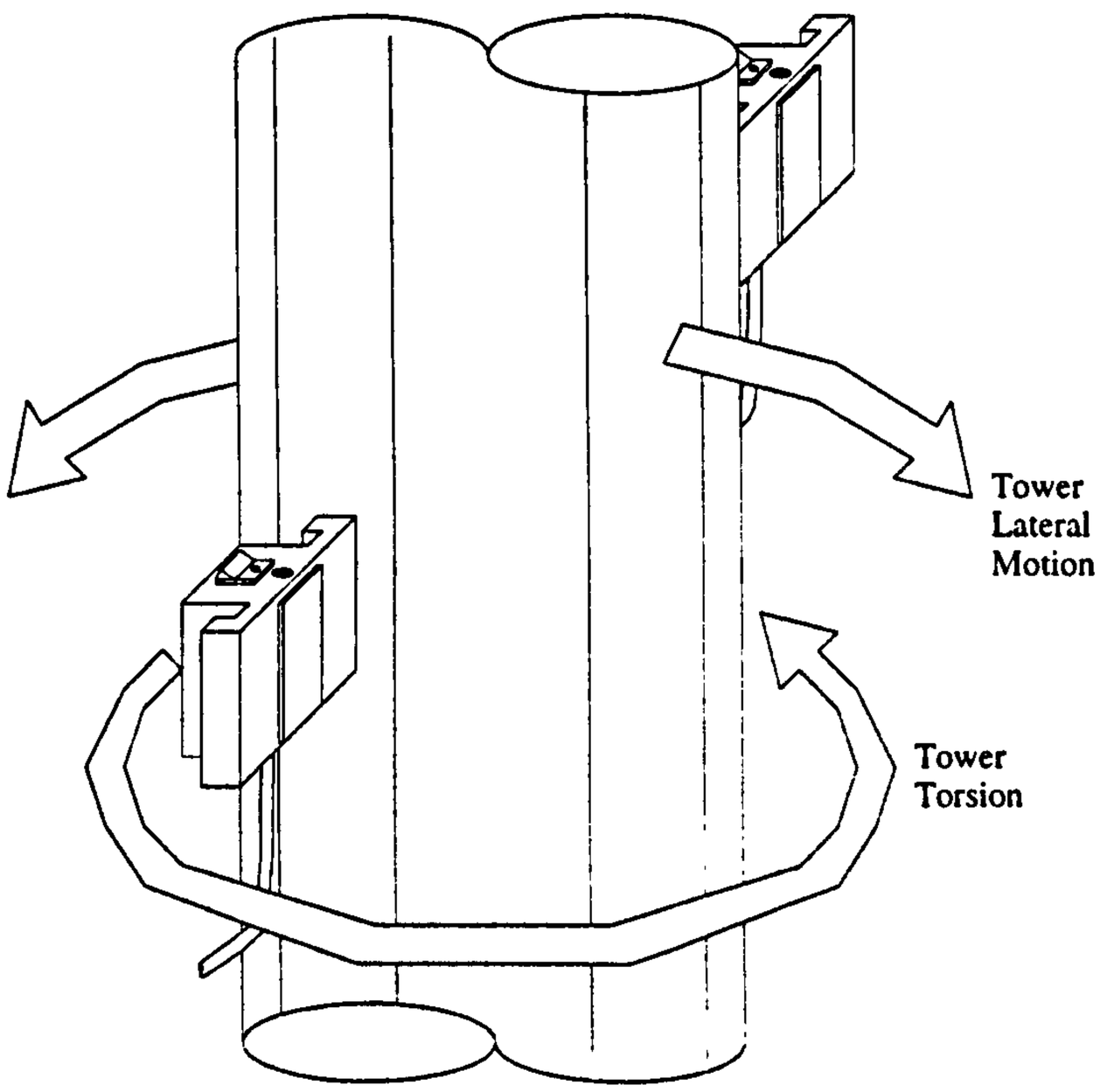

Figure G.1: The configuration of the accelerometers in order to distinguish torsional from lateral vibrations.

If both accelerometers are moving simultaneously, a particular spectral peak will be low when time series are subtracted and high when they are added. Figure G.2 shows three accelerometer configurations. Using the equations listed alongside, spectra could be obtained

for torsional, longitudinal or lateral tower vibrations. To detect a torsional mode the spectral peak will be low if time series are added and high if time series are subtracted.

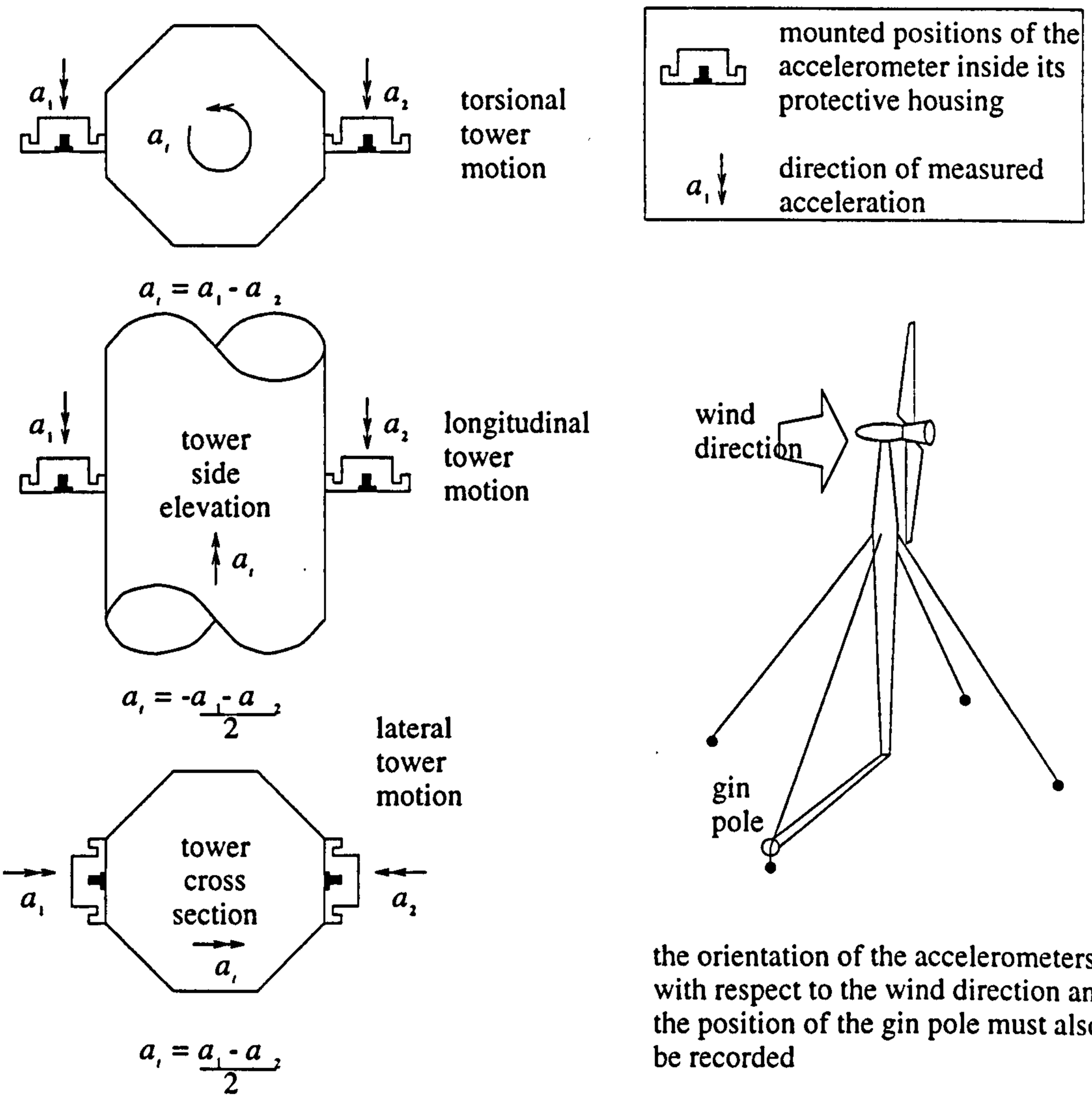

Figure G.2: Three different accelerometer configurations for distinguishing torsional, longitudinal and lateral tower vibrations.

Because signals are subtracted, absolute accelerations must be measured identically by each accelerometer. The zero errors and multiplying factors calculated from measurements of the output voltage under controlled conditions of acceleration and excitation voltage are derived in the form of a calibration plane for each accelerometer (see Section G.2.2 below). Thus systematic errors in the two sets of measurements can be reduced.

G.2 The Accelerometers

G.2.1 Protection

The accelerometers used (Setra 141a) are externally excited devices. They must be protected carefully from damaging excitation signals. A Zener diode connected in parallel with the excitation terminals (see Figure G.3) not only prevents reverse polarity excitation which could destroy the device immediately but also excitation in excess of 10 V. The safe maximum excitation is 18V. A strong enclosure provides mechanical protection for the accelerometer and houses the protective circuitry (see Figure G.4).

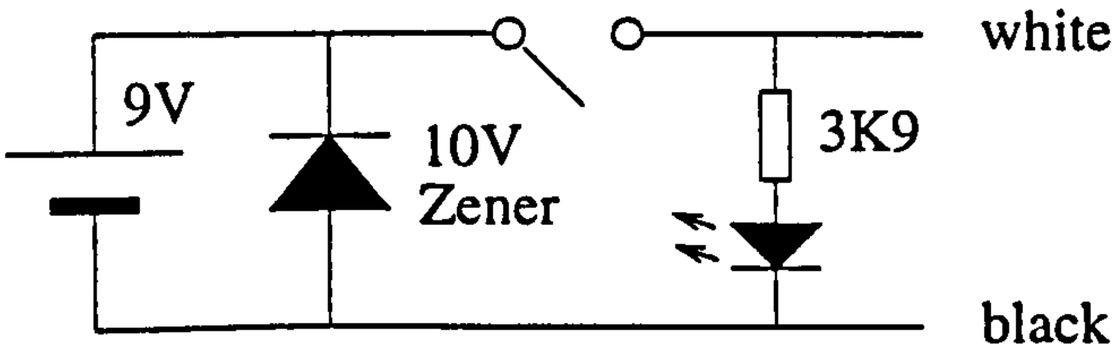

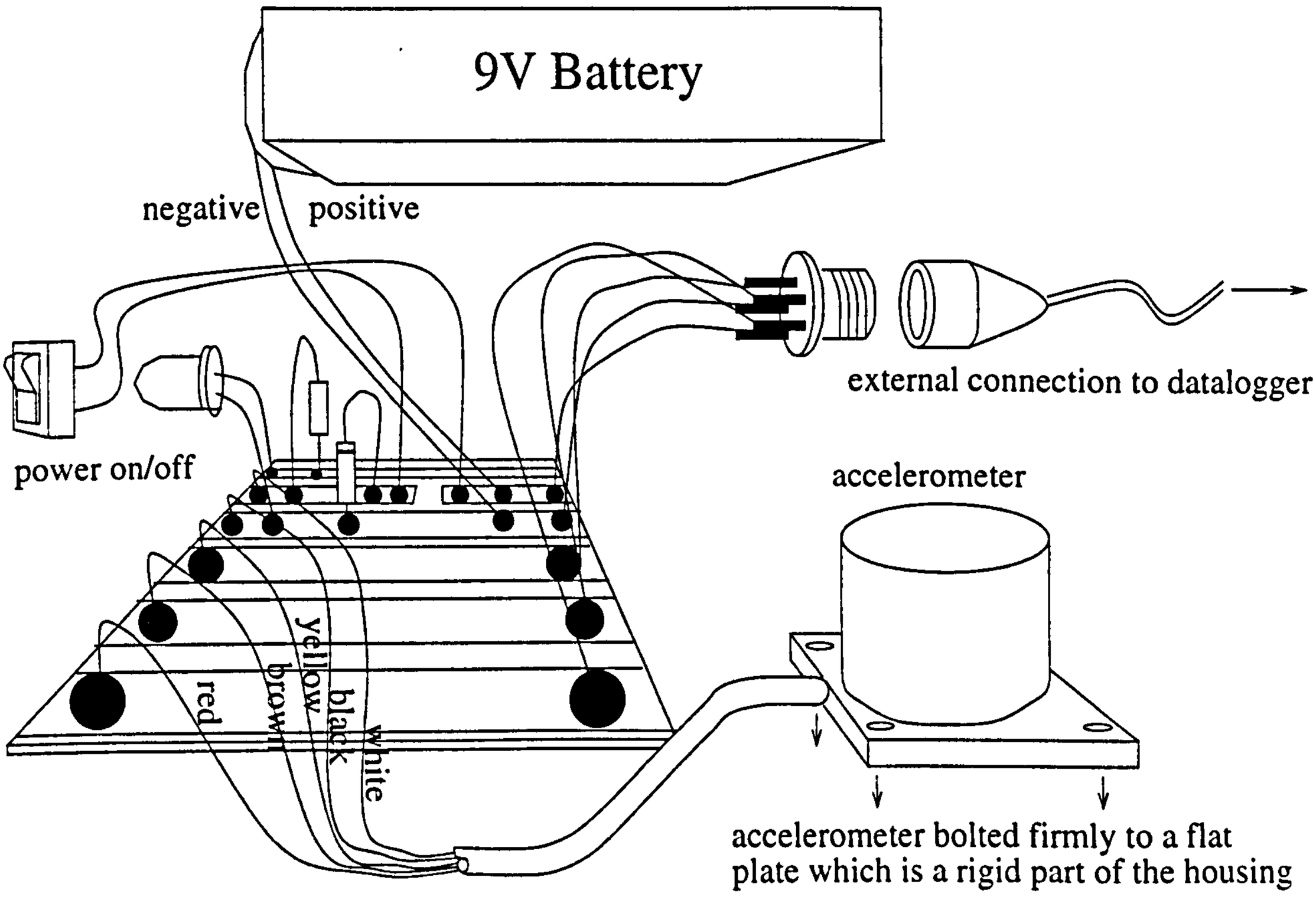

Figure G.3: The circuit diagram and interior layout of the accelerometer housing fabricated for protection of the instrument.

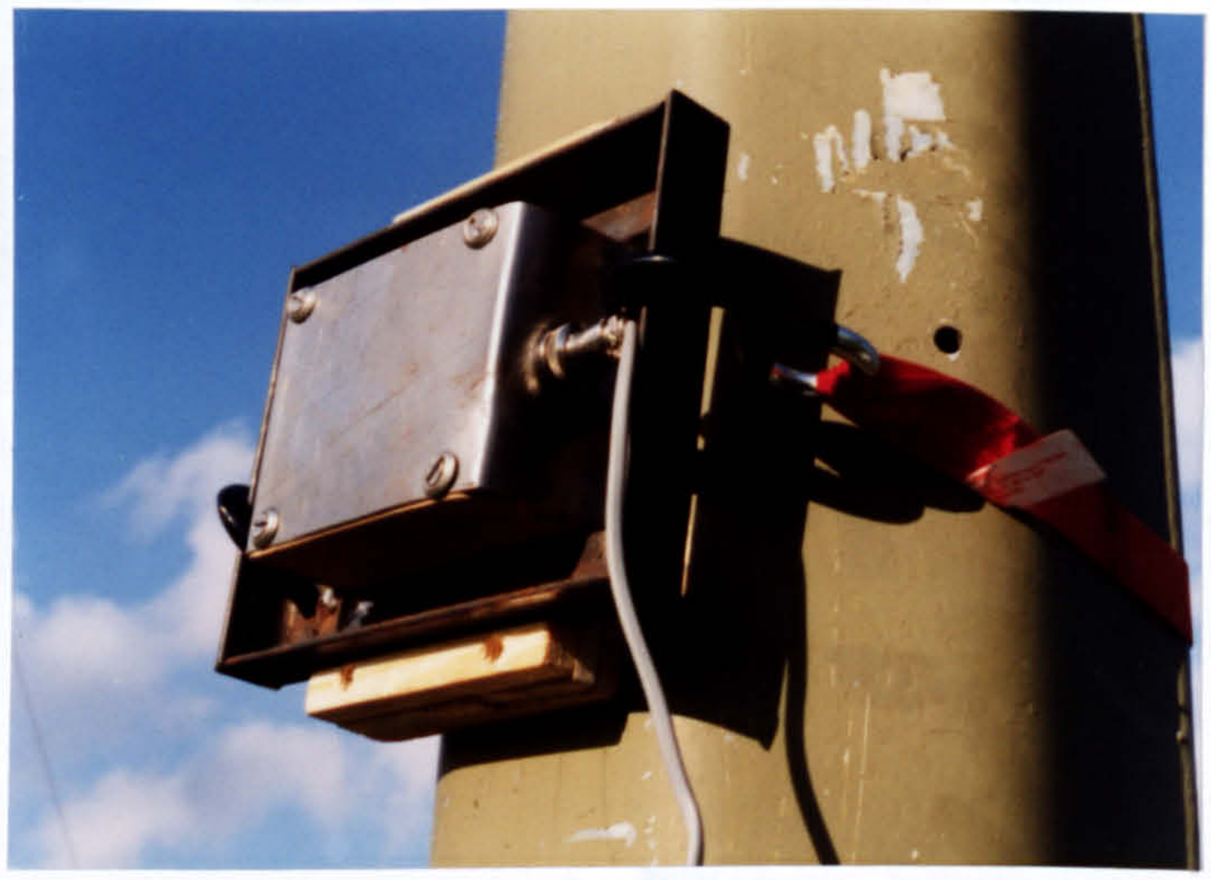

Figure G.4: The accelerometer housing strapped to the tower of a 25 kW Carter wind turbine.

G.2.2 Calibration

Accelerometer excitation is from a 9V alkaline battery inside the accelerometer housing. Factory calibration was at 10 V excitation and the response variation with excitation voltage is almost linear. The manufacturer's calibration curves (for accelerometer 1 [73] and accelerometer 2 [74]) are shown in Figure G.5 below.

In order to find the relationship between measured output voltage and excitation voltage, the readings have been noted at constant acceleration (the acceleration due to gravity) for different excitation voltages. The relationship in each case is linear. Repeatablility of the results was very high. The significant errors in the calibration experiment were due to the accuracy of the voltmeters (±1 mV for the accelerometer output and ±100 mV for the excitation).

G.2.3 Calibration Planes

From these results, the equation of the calibration plane for each accelerometer is estimated using least squares regression to derive the parameters, m_1, m_2 and c for the general equation of a plane (Equation G.1). A MATLAB [59] linear regression function was available to find the plane best fitting the data. Plane parameters are listed for the two accelerometers in Table G.1. The errors for this method are depicted in Figure G.8.

$$a = m_1 V_e + m_2 V_o + c \tag{G.1}$$

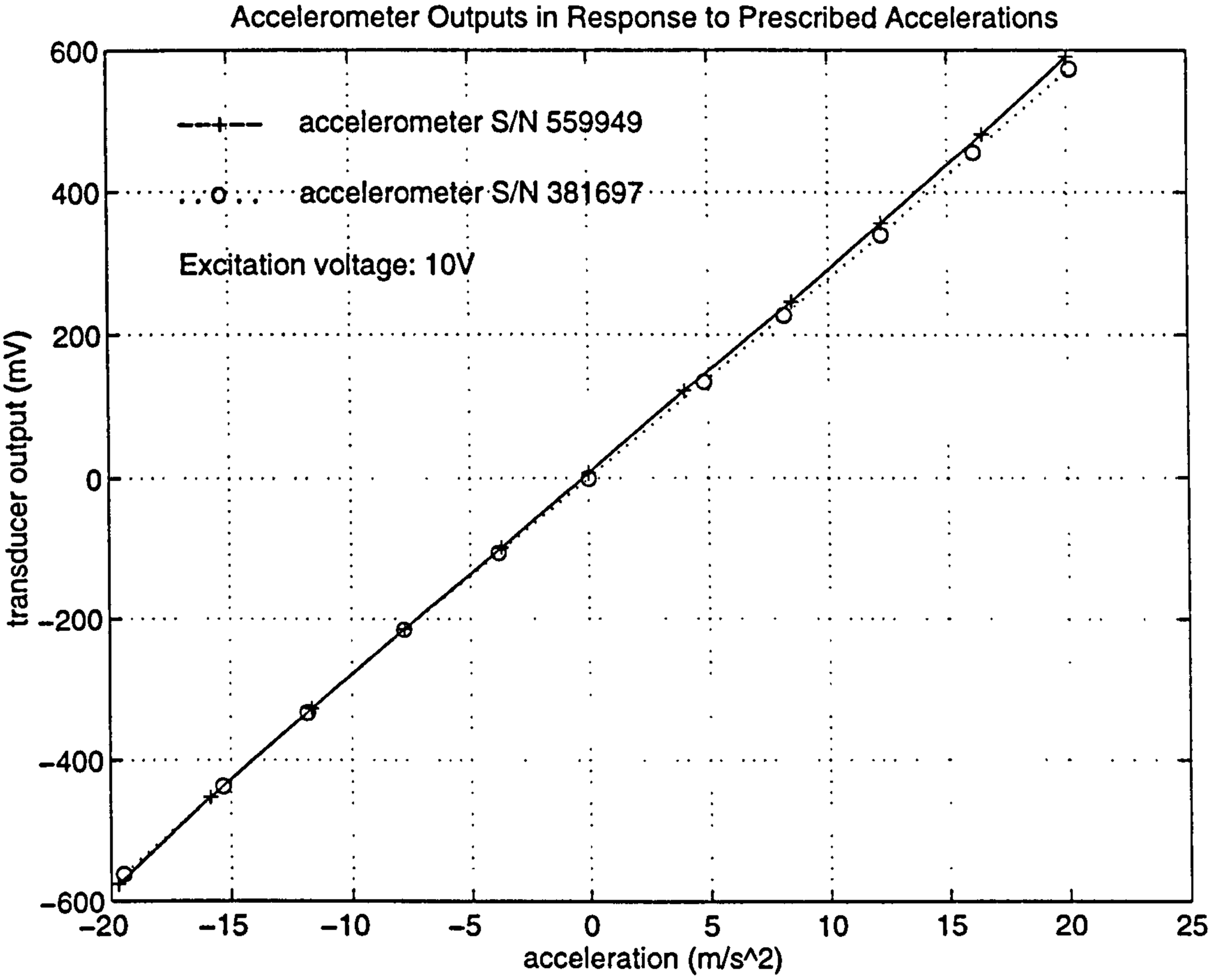

Figure G.5: The calibration curve for the accelerometer response. Information supplied by the manufacturer.

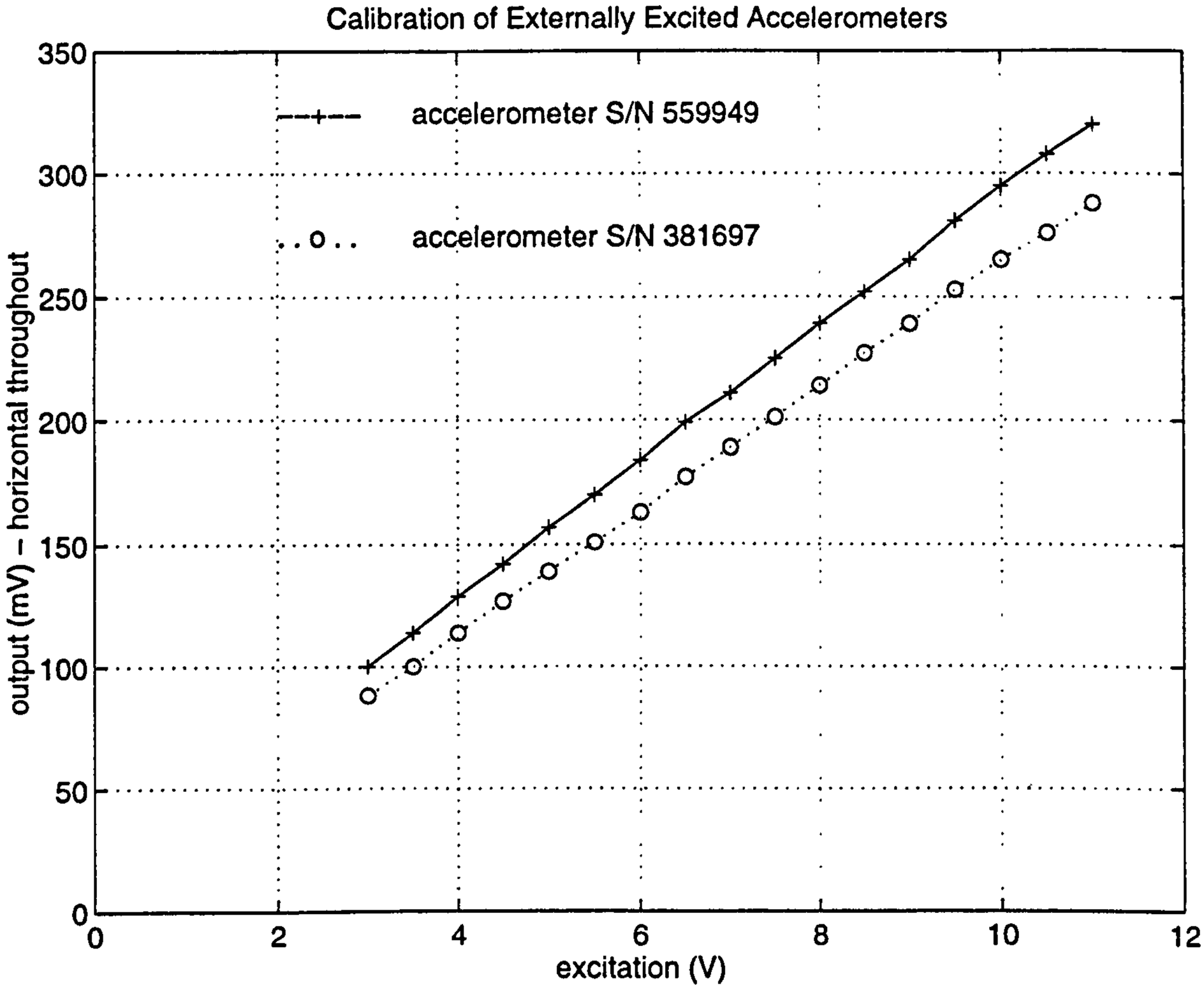

Figure G.6: The excitation curves for the two accelerometers showing the output voltage (mV) for constant acceleration conditions in terms of the excitation voltage (V). Calibrated in AMSET laboratory, 6th June 1996.

where:-

a = real acceleration of accelerometer
m_1 = first gradient parameter
V_e = excitation voltage
m_2 = second gradient parameter
V_o = measured output voltage
c = constant parameter (absolute zero error)

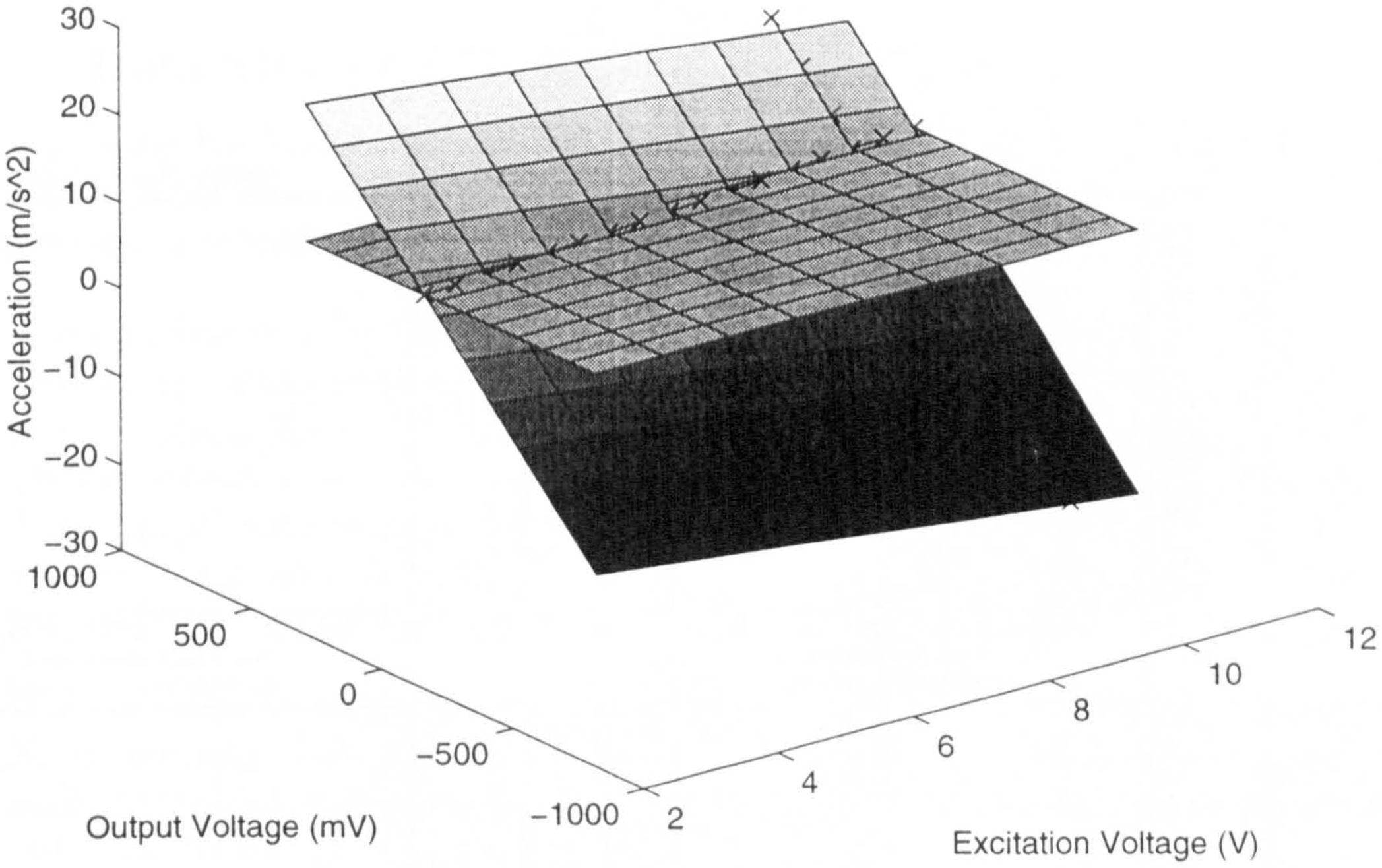

Figure G.7: The calibration plane for accelerometer S/N 381697. The crosses mark the points measured experimentally. The equation of the plane is defined by the parameters, m_1 = -0.901 m s^{-2} V^{-1}, m_2 = 0.0353 m s^{-2} mV^{-1} and c = 9.09 m s^{-2}. A horizontal plane at an acceleration of 9.4765 m s^{-2} has also been superimposed to represent the constant laboratory conditions of the calibration.

To identify modal frequencies of the structure, the relative magnitudes of the spectral peaks are compared. It is not important to know absolute accelerations. However, to distinguish torsional from lateral motion, data from one accelerometer must be subtracted from data from the other. For this, absolute values must be accurate to within ± 10% (see Appendix G, Section G.1). Figure G.8 suggests that errors are generally less than ±5% and that for accelerations not near to zero, errors are often less than ±1%. The calibration planes allow the absolute acceleration to be calculated for a reading on one of the accelerometers from knowledge of the excitation and output voltages.

Table G.1: Table of % errors calculated using Equation G.1 to predict accelerations and expressing the absolute error as a fraction of the real accelerations. Linear regression was used to calculate the parameters for Equation G.1.

calibration plane parameters	accelerometer S/N 559949	accelerometer S/N 381697
m_1	-0.970	-0.901
m_2	0.0356	0.0353
c	9.55	9.09

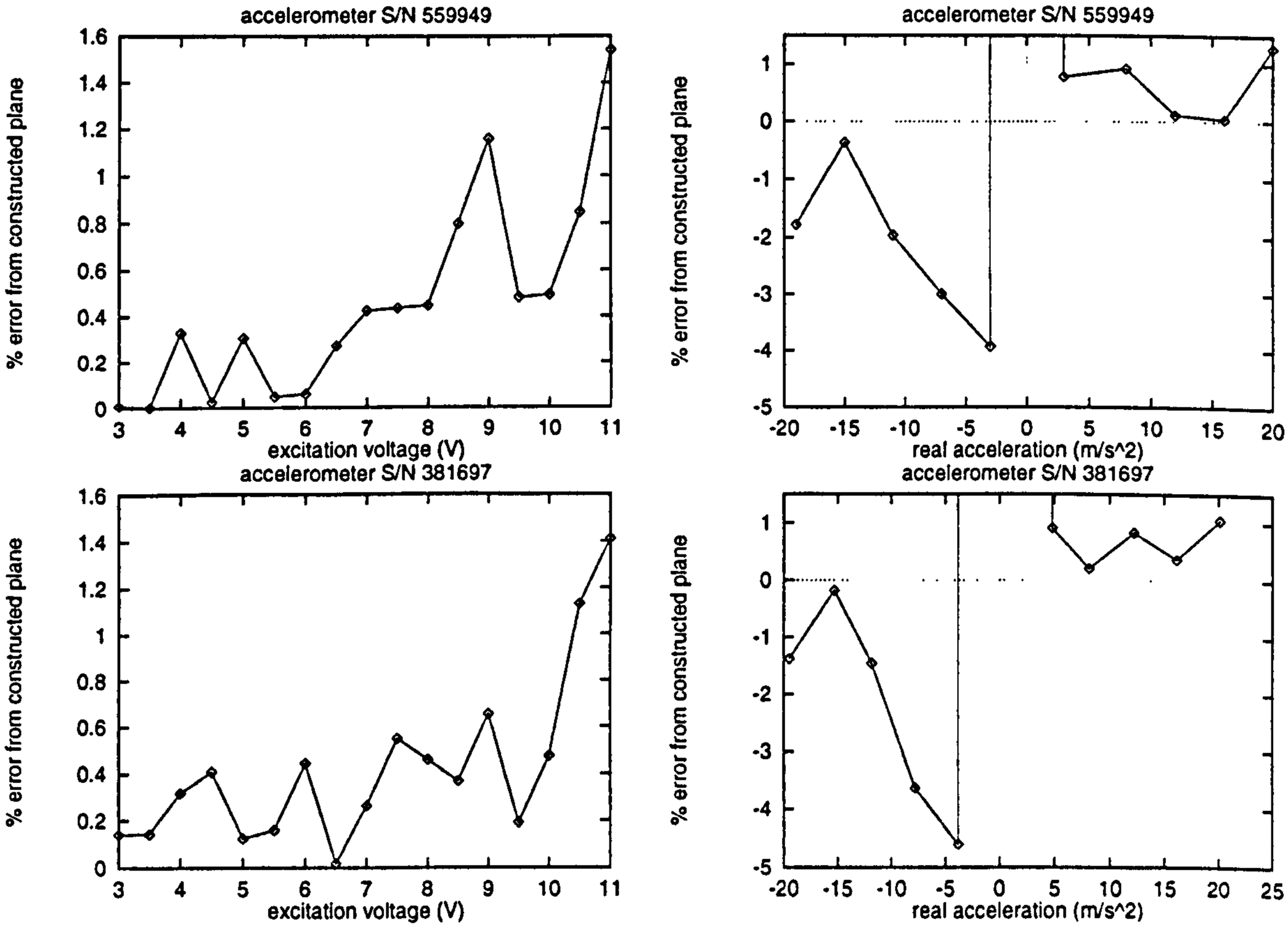

Figure G.8: The calibration plane for accelerometer S/N 381697. The crosses mark the points measured experimentally. The equation of the plane is defined by the parameters. m_1 = -0.901 m s^{-2} V^{-1}, m_2 = 0.0353 m s^{-2} mV^{-1} and c = 9.09 m s^{-2}. A horizontal plane at an acceleration of 9.4765 m s^{-2} has also been superimposed to represent the constant laboratory conditions of the calibration.

G.3 The Data Logger

The CR10 Campbell Data Logger is programmed from a separate computer. Specific IBM PC compatible software is available for writing programs or, alternatively, programs can be written using a text editor and compiled. The clocks are synchronised using a serial RS232 interface. Every time the power is disconnected from the CR10, the clock is reset and all data stored in input, intermediate and final storage RAM are lost. Following each data-logging session, data must either be sent to the computer or stored on non-volatile memory such as an EEPROM storage Card. When power is turned on and the logger connected to the computer, the CR10 clock can be synchronised to the computer's permanent clock. The compiled program is then downloaded and immediately takes control of the activity of the CR10.

G.3.1 Data Storage Limitations

The data logger has limited final storage memory (see Tables G.3 and G.2). Two programs have been written for controlling the CR10. At the beginning of a campaign of data, the date and time is recorded.

1. Accelerations from two input channels are recorded at a frequency of 64 per second. This is the fastest sampling rate at which the CR10 can process the data for storage in the internal RAM. The software allows the channels to be monitored in real time. This enables the operator to check that all signals are being processed and logged. This type of program has also been used to validate the data collection system (see Section G.4.2) by collecting and processing data about known accelerations. High or low resolution data entries may be used. An example program is listed in G.4 below.

2. Data are sent at a sample rate of 275 Hz directly to a Card Storage Module (CSM). No monitoring of the data is possible. Up.to 30 minutes of data may be stored at this sample rate. Three campaigns of 10 minutes each are recorded. Low resolution entries only may be used.

Table G.2: Storage space necessary for different measurements.

type of measurement	number of bytes
time (hour/minute)	4
time (seconds)	2
low resolution acceleration measurement	2
high resolution acceleration measurement	4

The first option requires that the computer is connected to the CR10 all the time. Data are stored in the internal RAM of the CR10 (final storage area). As soon as this space is full, more data are stored and the oldest data already stored are erased. This means that the

Table G.3: Storage available in the Campbell CR10 data logger.

storage area	total space available for data (in bytes)
input	112
intermediate	256
final	59 816
PROM memory card	2 000 000

data retrieved are only those recorded up until the time that a retreive command is issued by the computer.

The second option allows data to be collected during a particular time window. The exact time window is unimportant if the weather conditions and other factors are fairly constant. The CR10 may be programmed and then disconnected from the computer. Data will be recorded without fail as long as the accelerometer and the CR10 both have power. When the internal clock reaches a prescribed time, data is sent to the memory card for a prescribed length of time and then data collection stops. The extra storage can either be used to collect data at high speed to eliminate 'aliasing' of the signals (Section 6.3.1.3) or to store longer windows of measurements (Section 6.3.1.4). Although the sample rate can be as high as 750 Hz, this is not necessary if a low-pass filter is used to exclude all signals except the low frequency vibrations of interest as discussed in Section 6.3.1.3.

G.3.2 Sample Rate Limitations

There is also a maximum practical sampling rate for the data logger. Each measurement is made by making an internal connection between the analogue input to the internal circuitry of the logger for a finite period of time, integrating the variations with respect to time and then dividing by the time interval to obtain an average measurement which is stored. This integration limits the maximum sample rate for a 'burst' measurement (where data are sent immediately to the Storage Card) to 750 Hz.

G.4 Validation of the Complete Data Collection System

G.4.1 Validation with Known, Static Acceleration Inputs

In order to validate the whole data collection system, measurements were made both with a separate Digital Voltage Meter (D.V.M.) and using the internal digital to analogue converters in the CR10. Six situations were recorded with different alignments of the accelerometers relative to the direction of the acceleration due to gravity. The results are summarised in Tables G.5 and G.6. Although care was taken to ensure correct alignment of the accelerometers using a spirit level, some misalignment may have been responsible for the large errors.

Table G.4: A listing of the CR10 program for logging accelerations at two channels (1) to monitor the signals and (2) to validate the data acquisition system (see Section G.4.2 below).

```
;{CR10}
*Table 1 Program
  01: 0.015625  Execution Interval (seconds)

1:  Do (P86)
 1: 10          Set Output Flag High

2:  Real Time (P77)
 1: 0011        Hour/Minute,Seconds

3:  Volts (SE) (P1)
 1: 1           Reps
 2: 35          2500 mV 50 Hz Rejection Range
 3: 1           In Chan
 4: 1           Loc [ accelmtr1 ]
 5: 1.0         Mult
 6: -10         Offset

4:  Volts (SE) (P1)
 1: 1           Reps
 2: 35          2500 mV 50 Hz Rejection Range
 3: 2           In Chan
 4: 2           Loc [ accelmtr2 ]
 5: 1.0         Mult
 6: 20          Offset

5:  Sample (P70)
 1: 1           Reps
 2: 1           Loc [ accelmtr1 ]

6:  Sample (P70)
 1: 1           Reps
 2: 2           Loc [ accelmtr2 ]

7:  Do (P86)
 1: 0           Go to end of Program Table

End Program
```

Table G.5: Table of results of static validation of accelerometer S/N 559949 and data collection system.

accelerometer serial number	559949					
orientation	voltage (from DVM)		voltage (from Campbell logger)		Acceleration predicted from calibration plane ($m\ s^{-2}$)	% error (as a fraction of 9.81 $m\ s^{-2}$)
closed circuit excitation voltage (V)	8.15	± 1.0	8.15	± 0.2	.	.
vertical (0^0)	8.0	± 1.0	7.7	± 0.3	1.77	18.0
vertical (90^0)	8.0	± 1.0	7.7	± 0.2	1.77	18.0
vertical (180^0)	11.0	± 0.5	11.5	± 0.2	1.87	19.0
vertical (270^0)	11.0	± 0.5	11.5	± 0.2	1.87	19.0
horizontal (upright)	239.0	± 1.0	242.2	± 0.2	9.71	1.0
horizontal (upside down)	-221.0	± 1.0	-221.7	± 0.2	-6.10	38.0

The spirit level only ensured alignment in one plane. As summarised in Figure G.8, errors in the calibration of the accelerometers were small.

Random errors were estimated from fluctuations in the displayed readings. These are due to inaccuracy of accelerometer alignment and variations in the DVM circuitry.

From Tables G.5 and G.6, it can be seen that the differences between DVM measurements and measurements stored in the data logger's internal RAM are negligible. From Figure G.8, it can be seen that the calibration curves predict accelerations to within ±5%. It is not known why there are large errors in the measured signals from the accelerometers. However, this anomaly does not affect the validity of frequency measurements except in the case where torsional and lateral modes are to be distinguished from one another by subtracting signals from the two accelerometers.

G.4.2 Measuring Known Accelerations

Measurements have been made of the accelerations of a system consisting of a mass on the end of a spring (see Figure G.9). To impliment this, the accelerometer housing was suspended

Table G.6: Table of results of static validation of accelerometer S/N 381697 and data collection system.

accelerometer serial number	381697					
orientation	voltage (from DVM)		voltage (from Campbell logger)		Acceleration predicted from calibration plane ($m\ s^{-2}$)	% error (as a fraction of 9.81 $m\ s^{-2}$)
closed circuit excitation voltage (V)	8.23	± 1.0	8.23	± 0.2	.	.
vertical (0^0)	-20.0	± 1.0	-20.4	± 0.2	1.34	14.0
vertical (90^0)	-20.0	± 1.0	-20.4	± 0.2	1.34	14.0
vertical (180^0)	-17.0	± 1.0	-16.5	± 0.2	1.48	15.0
vertical (270^0)	-17.0	± 1.0	-16.5	± 0.2	1.48	15.0
horizontal (upright)	208.0	± 1.0	212.2	± 0.3	9.60	2.0
horizontal (upside down)	-247.0	± 1.0	-251.2	± 0.2	-6.86	30.0

on a spring of known stiffness and accelerations measured at a rate of 64 per second over a period of 4 minutes. The frequency of vibration is given by Equation G.4. The data were collected by the CR10 logger and stored continuously in the final storage area. After approximately five minutes, the data were retrieved and stored in comma delimited ASCII format on the hard disc of the computer. A MATLAB procedure similar to that described above (see Section 6.3.1.3 above) for Fourier analysis was used to obtain a frequency power spectrum (see Figure G.11).

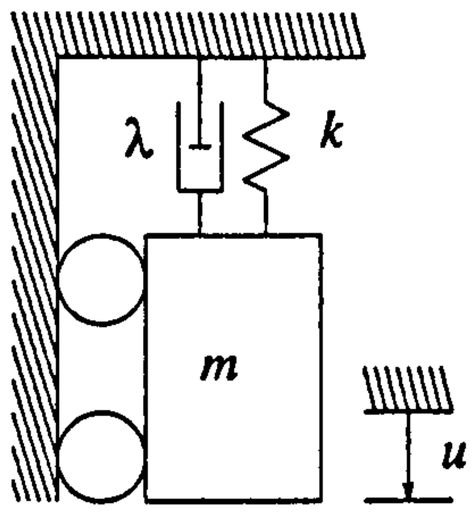

Figure G.9: The spring/ mass/ damper system whose frequency was measured to validate the data acquisition system. Gravity constantly acts vertically downwards on the mass. The damping due to air resistance and heat dissipation in the spring is small and neglected in Equation G.2.

$$u = u_g + u_a \cos\left(\sqrt{\frac{k}{m}}t\right) \tag{G.2}$$

$$\ddot{u} = -u_a \frac{k}{m} \cos(\left(\sqrt{\frac{k}{m}}t\right) \tag{G.3}$$

$$f = \frac{1}{2\pi}\sqrt{\frac{k}{m}} \tag{G.4}$$

Where, in Equations G.2 to G.4:

where:

u = deflection of mass (m)

u_a = amplitude of mass movements (m)

u_g = static deflection of mass due to gravity (m)

$\ddot{u}$ = acceleration of mass (m s^{-2})

f = natural frequency of system (Hz)

t = time from release of mass

Initially, the deflection was $u_a + u_g$.

From Equation G.3, the acceleration of the mass at any time can be compared with the theoretical predictions (see Figure G.10). The theory does not include any damping due to the air or dissipation of energy in the spring. Comparisons are therefore most accurate near the beginning of the experiment when the amplitude is largest. From Equation G.4, the frequency of vibrations can be predicted and compared with the peak on the power density spectrum generated from the measured data.

Figure G.10: Comparison between accelerations measured and predicted with Equation G.3.

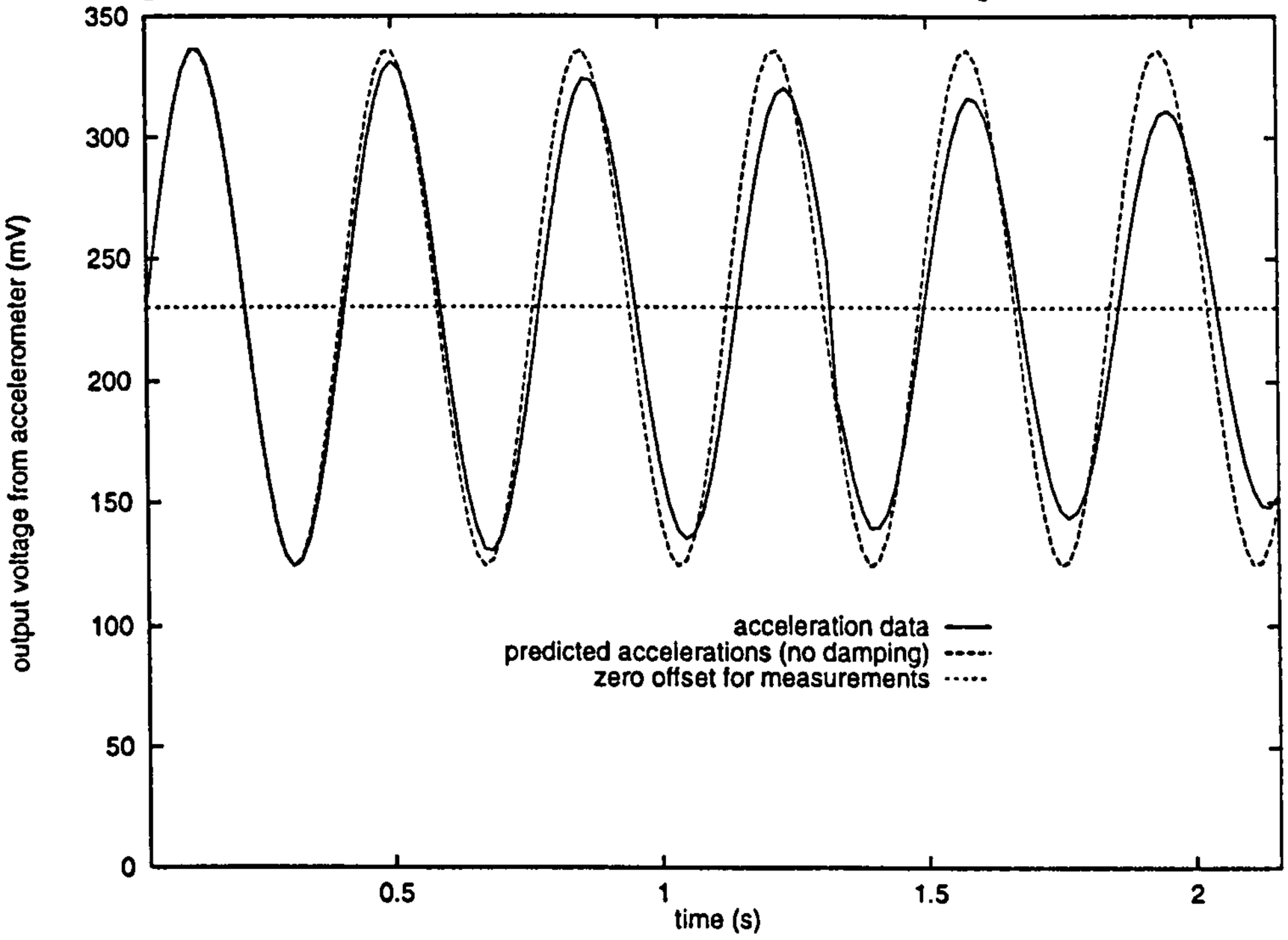

The mass of the accelerometer housing is 1.325 kg. The stiffness of the spring is 402.9 N m^{-1}. As can be seen from Figure G.11, there is a distinct peak near the expected natural frequency of the system of 2.78 Hz.

For the measured accelerations in Figure G.10, the offset is 8.77 m s^{-2} and the amplitude is 4.49 m s^{-2}. The offset exists because, when undisturbed and horizontal, the accelerometer measures the acceleration due to gravity. It was the measurement of the acceleration due to gravity which was being attempted when data were collected for Tables G.5 and G.6. Because the accelerometer was not exactly horizontal, this offset acceleration cannot be predicted and so has been calculated retrospectively in order to align the curves compared in Figure G.10. The amplitude of vibrations was 15 mm which corresponds to an acceleration amplitude of 4.56 m s^{-2} demonstrating the accuracy of the accelerometer. Both accelerations ($\pm$1.6% error) and frequencies ($\pm$0.3% error) can be measured with precision.

G.4.3 Filtering Acceleration Data

In order to avoid aliasing of frequencies, the cables from the accelerometers were connected to low pass filters and from there to the data collection system. The voltage characteristics

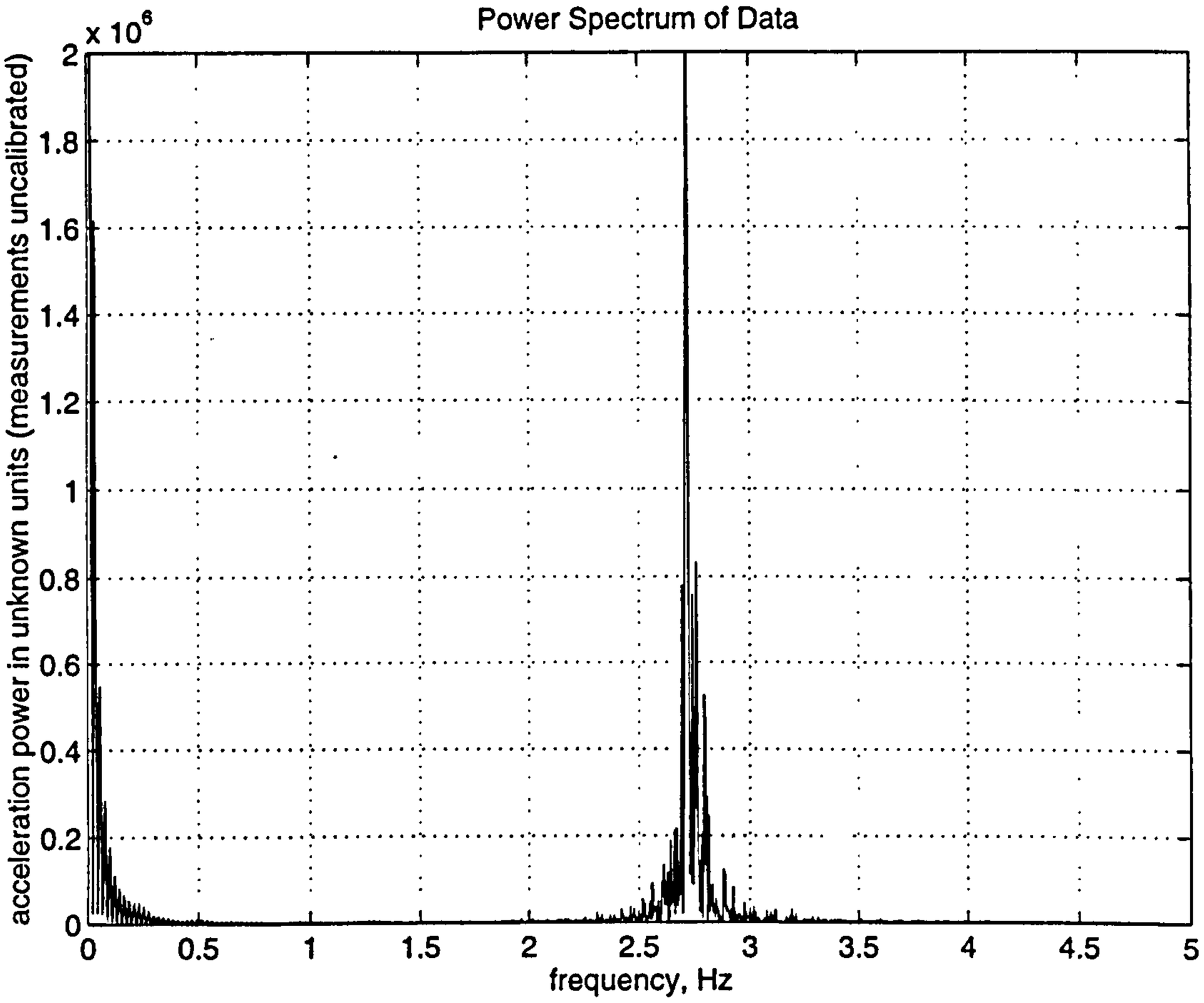

Figure G.11: The power spectrum calculated from data measured from the spring/ mass system.

of the filters were recorded by measuring the attenuation of a 0.2 V sinusoidal waveform passed through the filter. See Figure G.12 for an example of this.

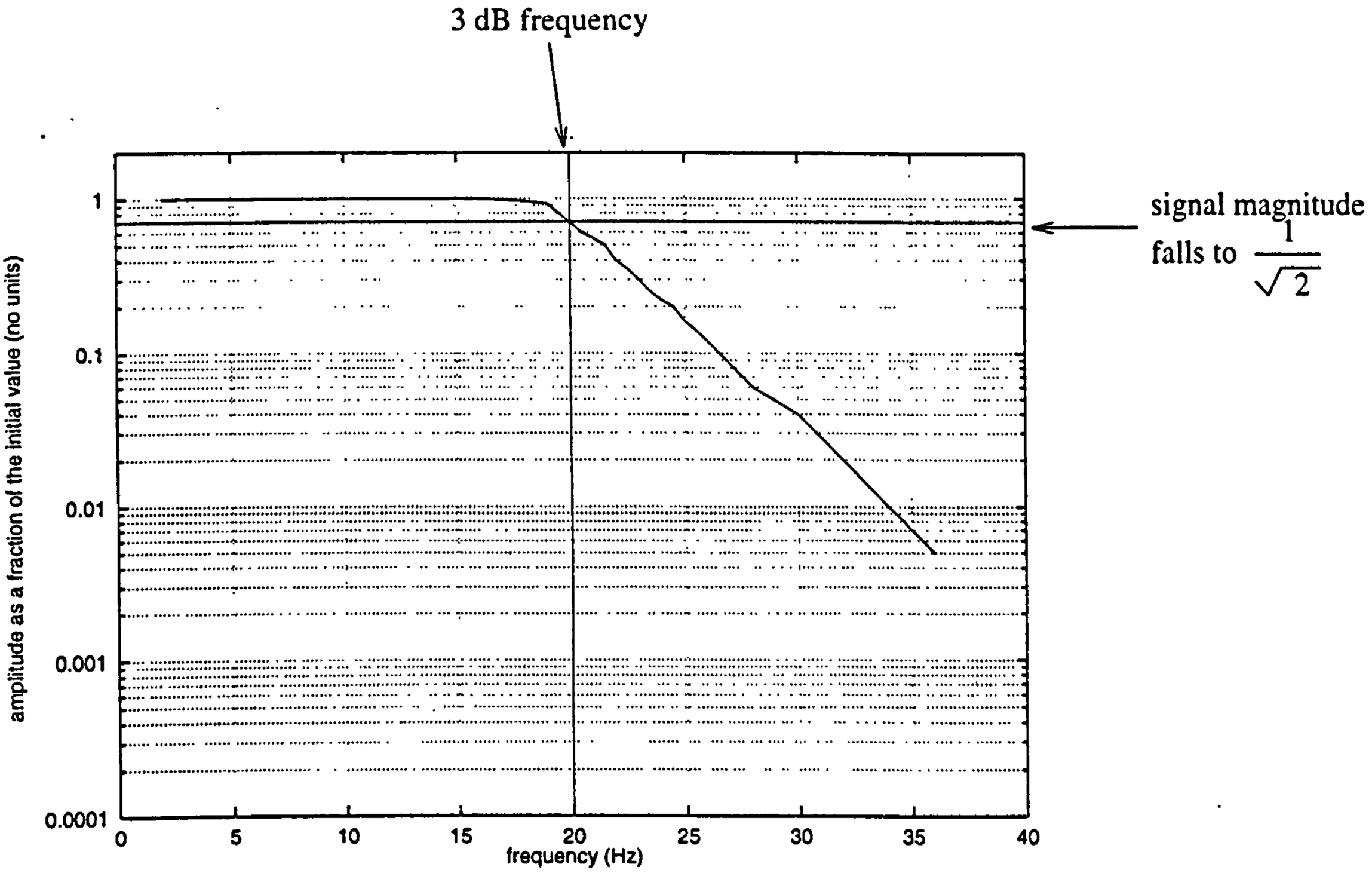

Figure G.12: The voltage characteristic of a bench-top, mains-supplied, low-pass filter. Amplitudes are displayed in dimensionless units by dividing the voltage by the initial value (0.2 V).

The filters required 240 V mains. This was available at the base of the 25 kW machine at West Beacon farm but not at Great Orton airfield or Faccombe estate. Data were therefore not filtered at these latter two locations. Portable filters have now been constructed integral with the accelerometer protection circuitry. Two independent 12 V power supplies are required for the full-wave filter circuits which are based on operational amplifiers.

Appendix H

Descriptions of Three Commercial Wind Turbine Towers

In order to model real structures, certain key parameters must be known. These define the structure in a way that is recognised by the software. The most direct way to define a parameter list is in a data file. In the case of MATLAB [59] script files, this conveniently separates the data definition from any processing commands. In the case of a compiled program (using for instance 'C' as the programming language[75]), data can be changed by changing the data file without the need to re-compile all the source code. The most important parameters are illustrated in Figure H.1.

Three different designs for the structural support system of a wind turbine have been subject to experimental measurements. The parameters necessary to define the *structural spline* model proposed here are listed in Table H.1.

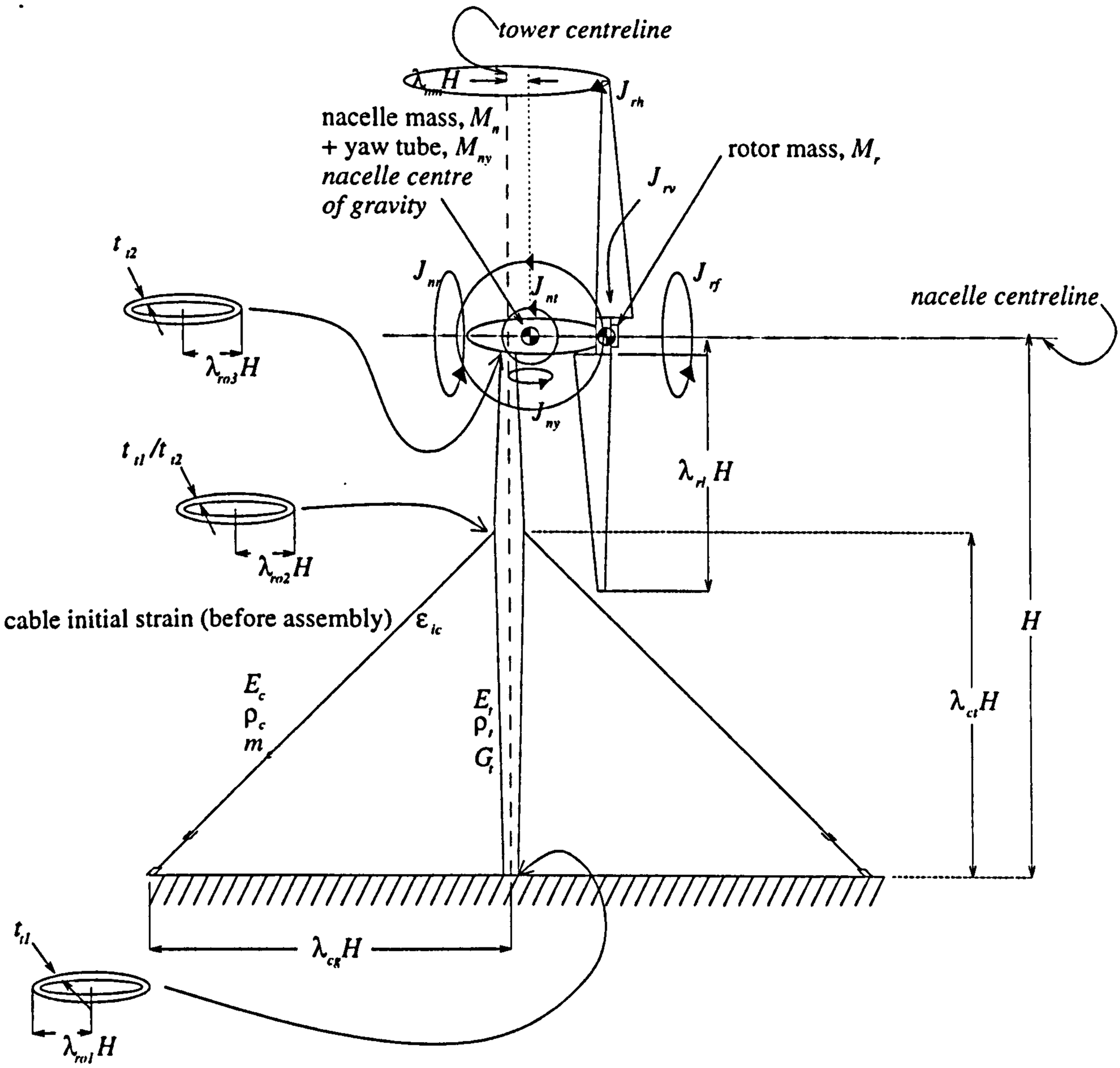

Figure H.1: The main parameters used by the model.

Table H.1: Lists of the design parameters measured from the three different designs of structural support system which were subject to experimental measurements.

	Location of an example of tower design		
	Great Orton Airfield	Faccombe Estates	West Beacon Farm
the acceleration due to gravity	9.81	9.81	9.81
density of stranded guy cable	5437	5437	5437
diameter of guy cable	0.0339	0.0339	0.013
initial strain in guy cables	0.0005	0.0005	0.0005
tower height	49	38.69	23.25
radius of hub	0.89	0.89	0.43
cable anchor displacement ratio	0.400	0.510	0.404
guy cable attachment point ratio	0.760	0.696	0.660
nacelle centre of gravity displacement ratio	0.020	0.020	0.030
length of single rotor	0.2449	0.2449	9.224×10^{-2}
dimensionless average external radius of tower (bottom)	6.33×10^{-3}	9.12×10^{-3}	4.796×10^{-3}
dimensionless average external radius of tower (middle)	9.50×10^{-3}	12.0×10^{-3}	7.518×10^{-3}
dimensionless average external radius of tower (top)	5.49×10^{-3}	6.95×10^{-3}	8.925×10^{-3}
tower aspect ratio factor (for wind loading)	1.00	1.00	1.00
bending about built in base axis (N m/rad)	1×10^{12}	1×10^{12}	1×10^{12}
compression (N/m)	1×10^{12}	1×10^{12}	1×10^{12}
in lateral directions (N/m)	1×10^{12}	1×10^{12}	1×10^{12}
torsion (N m/rad)	1×10^{12}	1×10^{12}	1×10^{12}
yaw coupling between top of tower and nacelle	1×10^{12}	1×10^{12}	1×10^{12}
the Poisson's ratio of the cables	0.33	0.33	0.33

Table H.2: Lists of the design parameters measured from the three different designs of structural support system which were subject to experimental measurements.

density of air	1.00	1.00	1.00
cable material density	7800	7800	7800
tower material density	7800	7800	7800
tower shear modulus	79×10^9	79×10^9	79×10^9
temperature (Kelvin) at which thermal expansion coefficient was measured	273	273	273
coefficient of thermal expansion for guys	1×10^4	1×10^4	1×10^4
tower drag coefficient	0.9	0.9	0.9
wall thickness of sections of tower below the guys	6.5396×10^{-3}	6.69×10^{-3}	4.5×10^{-3}
wall thickness of sections of tower above the guys	6.5396×10^{-3}	6.69×10^{-3}	4.5×10^{-3}
cable Young's modulus	210×10^9	210×10^9	210×10^9
tower Young's modulus	210×10^9	210×10^9	210×10^9

Glossary and List of Symbols

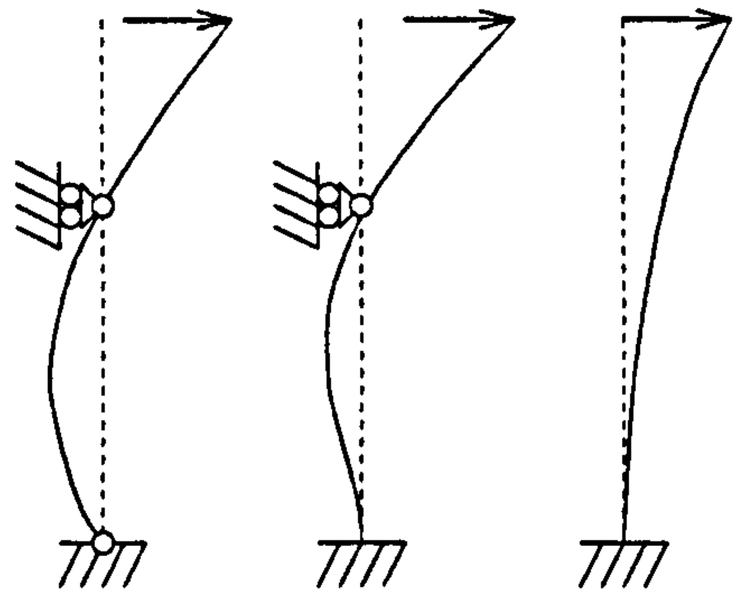

Columns with different ideal support conditions: simply supported, built in *at the base and* cantilevered. *Hinged supports are on rollers so that no axial load is passed to the column.*

aspect ratio The ratio of length to width is called the aspect ratio; long, slender objects have higher aspect ratios than short, thick objects.

free support The tower is not anchored at the point of interest. This support is equivalent to the boundary conditions $\frac{d^2v}{dx^2} = 0$ and $\frac{d^3v}{dx^3} = 0$ (see the illustration at the beginning of this glossary and the statics textbook by Meriam and Kraige [32]).

simply supported The base of the tower is freely hinged and the other support passes no axial load to the tower. This support is equivalent to the boundary conditions $v = 0$ and $\frac{d^2v}{dx^2} = 0$ (see the illustration at the beginning of this glossary and [32]).

hinged The term is used to described one support. *simply supported* applies to the whole beam and implies no axial load is passed to the beam by the sypports. Describing a support as hinged just implies that no bending moment is passed to the beam.

built in support The base of the tower is rigidly fixed. The tower is also called a cantilever beam (see the illustration at the beginning of this glossary). This support is equivalent to the boundary conditions $v = 0$ and $\frac{dv}{dx} = 0$ (see the illustration at the beginning of this glossary and [32]). This type of support is also called *encastré.*

free body In order to calculate internal stresses in a structure, a free body is postulated which consists of the structure cut at some point. The internal loads at that point

are those required to bring the 'free body' into static equilibrium. In the case of a beam, bending moments can be calculated by considering just the section of beam above or below the point of interest. The free body chosen is the one which makes the equilibrium calculation easier. In the case of bending moments, it has been the section of the tower below the point of interest which has been considered as a free body throughout this thesis (see Figure 2.20 in Section 2.3 and [32]).

LU decomposition Using LU decomposition of a square matrix, its inverse can be found and the system of linear simultaneous equations can be solved with a small number of operations. The matrix **L** is a lower triangular matrix and **U** is an upper triangular matrix such that $\mathbf{LU} = \mathbf{A}$ where **A** is the original square matrix (see [31]).

Rayleigh frequency Where a frequency has been calculated (for any arbitrary deflection shape) using Rayleigh's method, it is called the Rayleigh frequency in this thesis.

simple harmonic motion Where energy is conserved and there is no damping, a system undergoes simple harmonic motion such that the variation of the deflection of any point in the system with time is sinusoidal and all points move simultaneously.

longitudinal/ compressive Longitudinal deflections and vibrations are vertical deflections or vibrations. 'Compressive' is used as a reminder that the convention used here is that compressive loads in the structure and deflections u downwards are positive.

lateral/ transverse/ bending Lateral deflections are horizontal deflections. Bending vibrations are so-called as a reminder that the convention here is that the tower deflects in pure bending.

roll The nacelle rolls when it rotates about a horizontal axis through the hub and parallel to the low speed shaft. The roll moment of inertia, J_{nr} is the moment of inertia about the roll axis.

tilt The nacelle tilts when it rotates about a horizontal axis parallel to the plane of the rotor (the tilt axis). The upwind and downwind ends of the nacelle move in opposite directions. The tilt moment of inertia, J_{nt} is the moment of inertia about the tilt axis.

yaw The nacelle yaws when it rotates about a vertical axis through the tower. This is the normal mechanism for aligning the rotor with the oncoming wind. The yaw moment of inertia, J_{ny} is the moment of inertia about the yaw axis.

The subscripts that have been commonly used in this thesis are listed here with some examples of their use.

	some of the subscripts used indicate quantities associated with:-
1	first natural frequency, fundamental vibration
2	second natural frequency, first harmonic
B	lateral (Bending) vibrations
a	the section above the section of interest
b	the section below the section of interest
C	longitudinal (Compressive) vibrations
c	cables
(crit)	critical value
(eff)	effective value
(eq)	equivalent or combined value
e	critical for Euler buckling of a slender strut
f	base (foundation) or front
F	Fast Fourier Transform
h	horizontal (applies to loads only and occurs last in a sequence of subscripts)
i	inner tower radius or integer number of mode
o	outer tower radius
n	nacelle or node
R	Rayleigh frequency
r	rotors or radius
t	tower
T	Torsional vibrations
v	vertical (applies to loads only and occurs last in a sequence of subscripts)
x	cross section
m	mass of a component or modal deflection shape

other subscripts occur in one symbol only and are included in the following list ...

	examples of subscripted quantities	units
ϵ_{ic}	initial strain in guy cables (the design parameter for computer code)	
λ_{cn}	cable natural length ratio (the parameter used in the text to simplify equations)	
λ_{At}	tower Aspect ratio (height/ diameter)	
λ_{cg}	cable ground anchor length ratio	
λ_{mn}	nacelle centre of mass displacement ratio	
	tower centreline	
λ_{ri1}, λ_{ri2} ...		
λ_{ro1}, λ_{ro2} ...	inner and outer tower radius ratios at various heights	
λ_{ct}	tower cable attachment length ratio	
ω_{1T}	fundamental rotational frequency of torsional vibrations	rad s^{-1}
ω_{R1T}	fundamental Rayleigh estimate of the above	rad s^{-1}
ρ_c, ρ_t	density of materials	kg m^{-3}

	examples of subscripted quantities (continued)	units
θ_n	the total angle of twist of the nacelle	rad
A_{xc}, A_{xt}	areas of cross section	m^2
E_c, E_t	Young's modulus of materials	N m^{-2}
f_{3C}	third harmonic frequency of longitudinal vibrations	Hz
F_{nv}	vertical force on the tower due to the nacelle	N
g	acceleration due to gravity	m s^{-2}
G_t	shear modulus of the tower	N m^{-2}
H	tower height	m
I_{xt}	second moment of area of tower	m^4
J_{xt}	polar second moment of area of tower	m^4
J_{nr}, J_{nt}, J_{ny}, J_{rf}, J_{rh}, J_{rv}	moments of inertia of the nacelle (roll, yaw and tilt) and rotor (front, horizontal and vertical)	kg m^2
k_{Bf}, k_{Tf}	Bending and Torsional base fixing stiffness parameters	N m rad^{-1}
k_{Lf}, k_{Cf}	Lateral and Compressive base fixing stiffness parameters	N m^{-1}
k_{Cc}	equivalent stiffness for longitudinal vibrations due to the cable set	N m^{-1}
k_{Bc}	equivalent stiffness for Bending vibrations due to the cable set	N m^{-1}
K_c	thermal expansion constant of the cables	K^{-1}
L_r	length of a single rotor	m
m_c	mass per unit length of the cable	kg m^{-1}
M_n, M_r	total masses of the nacelle and rotor	kg
M_{ny}	mass of the yaw tube	kg
N_t	number of points up the tower (for example: for integration)	
N_n	number of nodal points up the tower for bending integration)	
N_s	number of points on a spline between consecutive nodes for the calculation of intermediate values	
r_o	tower outside radius	m
t_t	tower skin thickness	m
f_h, f_v	forces distributed up the tower (per unit length)	N m^{-1}
X	dimensionless distance up the tower (relative to tower height: $X = \frac{x}{H}$)	
x	distance up the tower	m

References

[1] Mark Johnston. Prediction of available wind resource at a potential wind farm site. Technical Report WE003/94, Anthony Marmont Sustainable Energy Technology Centre, 1994. Series Editor: John Twidell.

[2] N.G. Mortensen, L. Landberg, I. Troen, and E.L. Peterson. The wind atlas analysis and application program (WA^{s}P). Technical report, Risoe National Laboratory, Denmark, 1993.

[3] P.H. Geraets, R.S. Haines, and M.A. Wastling. Light can be tough. In *19th British Wind Energy Association Annual Conference* [76].

[4] G.A.M. van Kuik, J.C. Jong, and R.W. Sherwin. The ultimate wind turbine: A minimum cost and maintenance turbine. In *Proceedings of the European Wind Energy Association Conference and Exhibition*, Goteburg, May 1996.

[5] Dr. Ing. Andreas Reuter and Cand. Ing. Alexander Bormann. New concepts and optimal design of steel towers for large wind turbines. In *Proceedings of the European Wind Energy Association Conference and Exhibition*, Goteburg, May 1996.

[6] M. Kühn. Soft or stiff a fundamental question for designers of offshore wind energy converters. In *Proc. European Wind Energy Conference*, Dublin, October 1997.

[7] Bundesverband Windenergie e.V. Windkraftanlagen 1997 marktübersicht. Technical report, Bundesverband Windenergie, Natruper Strasse 70, D49090, Osnabrück, Germany. 1997. ISBN: 3-9804399-8-4.

[8] Helge Glück. Windkraftanlagen markt: Typen, technik, preise. Technical report. Winkra-Recom, Leisewitzstrasse 37, D30175 Hannover. Germany, 1996. ISBN: 3-9804393-0-5.

[9] Paul Gipe. *Wind Energy Comes of Age.* John Wiley and Sons, Inc., 1995.

[10] D. Corbet. Viability of a wind farm in an area of low wind speed. In *16th British Wind Energy Association Annual Conference*, Stirling. 1994. Mechanical Engineering Publications Ltd.

[11] P. Jamieson. Common fallacies in wind turbine design. In *19th British Wind Energy Association Annual Conference* [76].

[12] J.G. Warren. Report on the modal survey of the 60 m LS-1. Technical report, Department of Energy, April 1991. Agreement E/5A/CON/5051/1388 by the Wind Energy Group.

[13] Trevor John Poskitt and Robert Kenneth Livesley. Structual analysis of guyed masts. In *Proceedings of the Institution of Civil Engineers*, volume 24, pages 373–386. March 1963.

[14] Felix Rosenthal and Richard A. Skop. Guyed towers under arbitrary loads. *Journal of the Structural Division*, 106(ST3):679–692, March 1980.

[15] Richard J. McCaffrey and Alois J. Hartmann. Dynamics of guyed towers. *Journal of the Structural Division*, 98(ST6):1309–1323, June 1972.

[16] J.W.S. Rayleigh. *The Theory of Sound.* Dover Publications, 1945 (First Published 1894).

[17] A. Stodola. *Steam and Gas Turbines.* McGraw-Hill, 1927. translated from the 6th German ed. by Louis C. Loewenstein.

[18] W.A. Henniger, J.A. Hoffman, and D.R. Williamson. *Wind Energy System Coupled Dynamics Analysis (MOSTAS): User's Manual.* Paragon Pacific, Inc., January 1977. Number PPI-1014-8 and PPI-1014-9.

[19] K.R.V. Kaza and D.C. Janetzke. MOSTAS computer code evaluation for dynamic analysis of two-bladed wind turbines. *Journal of Energy*, 4(4):162–169, 1980.

[20] D.C. Quarton and A.D. Garrad. Symbolic computing for the analysis of wind turbine dynamics. *Journal of Sound and Vibration*, September 1985. I.Mech.E.

[21] K. Kaiser and R. Gasch. The influence of aerodynamic damping and stiffness on the vibrational behaviour of windturbines. In *Proceedings of the Institute of Mechanical Engineers*, Oxford, 1996.

[22] D.C. Quarton. Monitoring and analysis of a Carter 200/300 wind turbine. Technical report, Energy Technology Support Unit, February 1997. Final Report on Contract W/24/00350/REP by Garrad Hassan and Partners Ltd.

[23] Alexander Bormann. Turmkonzepte und optimierter Entwurf von Türmen für Windenergie Großanlagen. Technical report, Institut für Luft- und Raumfahrt der T.U. Berlin in Kooperation mit C.A.L. Apparatebau Leipzig, April 1996. student research project.

[24] S.P. Timoshenko. *Strength of Materials.* volume 1. Van Nostrand Reinhold Company. 1958.

[25] Michael F. Ashby and David R.H. Jones. *Engineering Materials 1.* Pergamon Press. Oxford, 1980.

[26] R.W. Thresher, W.E. Holley, C.E. Smith, N. Jafarey, and S.-R. Lin. Modeling the response of wind turbines to atmospheric turbulence. Technical report, Oregon State University, Mechanical Engineering Department, August 1981. U.S. Department of Energy report number DOE/ET/23144-81/2 (DE83000334).

[27] Richard A. Skop. Cable spring constants for guyed tower analysis. *Journal of the Structural Division*, 105(ST7):1307–1318, July 1979.

[28] R.A. Skop and G.J. O'Hara. The Method of Imaginary Reactions. *Marine Technology Society Journal*, 4(1):21–30, January 1970.

[29] A.H. Peyrot and A.M. Goulois. Analysis of cable structures. *Computers and Structures*, 10:805–813, 1979.

[30] N. Ben Kahla. Dynamics of a single guy cable. *Computers and Structures*, 0181(1):1197–1211, 1995.

[31] William H. Press, Saul A. Teukolsky, William T. Vetterling, and Brian P. Flannery. *Numerical Recipes in C.* Cambridge University Press, 1992.

[32] J.L. Meriam and L.G. Kraige. *Engineering Mechanics*, volume 1. John Wiley and Sons, Inc., third edition, 1993.

[33] R.P. Brent. *Algorithms for Minimization without Derivatives*, chapter 3, 4. Prentice-Hall International, Englewood Cliffs, New Jersey, 1973.

[34] J.P. Den Hartog. *Mechanical Vibrations.* McGraw-Hill, 1956.

[35] Ray W. Clough and Joseph Penzien. *Dynamics of Structures.* McGraw-Hill International Book Company, 1982. ISBN: 0-07-011392-0.

[36] British Standards Association. *Steel, Concrete and Composite Bridges*, bs5400, part 10 edition. Code of Practice for Fatigue.

[37] N.W.M. Bishop, Z. Hu, R. Wang, and D. Quarton. Methods for the rapid evaluation of fatigue damage on the Howden HWP330 wind turbine. In *15th British Wind Energy Association Annual Conference*, York, 1993. Mechanical Engineering Publications Ltd.

[38] A. D. Garrad and U. Hassan. The dynamic response of wind turbines for fatigue life and extreme load prediction. In *Proceedings of the European Wind Energy Association Conference and Exhibition*, Rome, October 1986.

[39] H.H. Rosenbrock. Vibration and stability problems in large horizontal axis wind turbines having hinged blades. Technical report, E.R.A., Leatherhead. England. 1955. Report number C/T 113.

[40] Stephen P. Timoshenko. D.H. Young. and Jr. William Weaver. *Vibration Problems in Engineering.* John Wiley and Sons, Inc., fourth edition, 1974.

[41] I.G. Rosen. Spline-based Rayleigh-Ritz methods for the approximation of the natural modes of vibration for flexible beams with tip bodies. *Quarterly of Applied Mathematics*, 44(1):169–185, April 1986.

[42] Robert Schmidt. Accurate fundamental frequencies of vibrating beams via a Ritz-Rayleigh-Sturm-Liouville approach. *The Journal of the Industrial Mathematics Society.* 39(1):37–46, 1989.

[43] S. Wang. A unified timoshenko beam B-spline Rayleigh-Ritz method for vibration and buckling analysis of thick and thin beams and plates. *International Journal for Numerical Methods in Engineering*, 40(3):472–491, February 1997.

[44] T. Niblett. The normal modes of beams by a Lanczos-Stodola method. *Journal of Sound and Vibration*, 91(2):247–253, 1983.

[45] N. Nakahira, K. Ozawa, and T. Mizusawa. Vibration of beams with varying cross-sections by the Stodola-Newmark method. *Computers and Structures*, 43(5):999–1004, June 1992.

[46] Paul Gipe. *Wind Energy Comes of Age*, pages 176–184. John Wiley and Sons, Inc., 1995.

[47] R.L. Bisplinghoff and H. Ashley. *Principles of Aeroelasticity.* John Wiley and Sons, Inc., New York, 1962.

[48] F. Kiessling. Computer-aided derivation of equations of motion for rotary-wing aeroelastic problems. In *13th Congress of the International Council of Aeronautical Sciences/ A.I.A.A. Aircraft Systems and Technology Conference*, Seattle, Washington, 1982.

[49] Swanson Analysis Systems Inc., P.O. Box 65, Johnson Rd., Houston, PA 15342-0065. *ANSYS User's Manual for Revision 5.0*, December 1992.

[50] L.S. Timothy. Simplified modeling for wind turbine modal analysis using NASTRAN. In *NASA Conference Publication 2034*, November 1977. US Department of Energy Publication CONF-771148, 'Wind Turbine Structural Dynamics'.

[51] D.W. Lobitz. NASTRAN-based software for the structural dynamic analysis of vertical and horizontal axis wind turbines. In *Proceedings of the European Wind Energy Association Conference and Exhibition*, Hamburg, October 1984.

[52] The MacNeal-Schwendler Corp., Los Angeles, California. *MSC/ NASTRAN user's manual*, 1981.

[53] M.H. Patel and A.O. Garrad. The development of a finite element method for the dynamic analysis of wind turbines. In *12th British Wind Energy Association Annual Conference*, Norwich, 1990. Mechanical Engineering Publications Ltd.

[54] N. El Chazly. Wind turbine tower structural and dynamic analysis using the finite element method. In *15th British Wind Energy Association Annual Conference.* Mechanical Engineering Publications Ltd., 1993.

[55] K. McLernon, N. Gibson, and P. Geraets. Development of a blade test facility and the testing of the flexible blade assembly for the new MS4-600 wind turbine. In *19th British Wind Energy Association Annual Conference* [76].

[56] John Twidell and Tony Weir. *Renewable Energy Resources.* E. and F.N. Spon, Chapman and Hall, 2–6 Boundary Row, London SE1 8HN, U.K., 1986. ISBN: 0-419-12010-6.

[57] B.S. Massey. *Mechanics of Fluids.* Chapman and Hall Ltd., 11 New Fetter Lane, London EC4P 4EE, U.K., sixth edition, 1990. ISBN: 0-412-34280-4.

[58] Henry Stark and Franz B. Tuteur. *Modern Electrical Communications - Theory and Systems.* Prentice/ Hall International, Inc., 1979.

[59] The MathWorks Inc. *MATLAB Users Guide for UNIX Workstations.* The MathWorks Inc.,, Cochituate Place, 24 Prime Way, Natick, Mass. 01760, August 1992.

[60] Samuel D. Stearns. *Digital Signal Analysis.* Hayden, New York, 1975.

[61] D. G. Childers, editor. *Modern Spectral Analysis.* I.E.E.E. Press, New York, 1978.

[62] M.B. Priestley. *Spectral Analysis and Time Series.* Academic Press Inc. (London) Ltd., Dept. of Mathematics, University of Manchester Institute of Science and Technology, 1981. Volume 1: Univariate Series.

[63] G.M. Chapman and J. Turnbull. Introducing undergraduates to modal analysis using a structured laboratory package. In G. J. Macnulty and P. B. Round, editors, *6th British Conference on Teaching Vibration and Noise*, Sheffield, July 1988. ISBN: 0-86339-182-6.

[64] Thomas G. Carne. Guy cable design and damping for vertical axis wind turbines. Technical report, Sandia National Laboratories, Albuquerque, New Mexico 87185 and Livermore, California 94550, 1981. prepared for the U.S. Department of Energy under contract DE-AC04-76DP00789.

[65] R.M. Goodall and S.A. Austin. Modelling, placing and controlling active elements in strutural engineering design. *Control Engineering Practice*, 2(5):743–753, 1994.

[66] Lansford C. Bell and Daniel M. Brown. Guyed tower optimisation. *Computers and Structures*, 6(6):447–450, December 1975.

[67] Claus Mattheck. *Design in der Natur.* Vogel Verlag, Freiburg, 1992.

[68] J. Dugundji and J.H. Wendell. Some analysis methods for rotating systems with periodic coefficients. In *A.I.A.A. Journal*, volume 21, pages 890–897, June 1983.

[69] W. Johnson. *Helicopter Theory.* Princeton University Press. Princeton, New Jersey. 1980.

[70] D.A. Peters and K.H. Hohenemser. Application of the Floquet transition matrix to problems of lifting rotor stability. *Journal of the American Helicopter Society*, 14(2):25–33, 1971.

[71] J.L. Meriam and L.G. Kraige. *Engineering Mechanics*, volume 2. John Wiley and Sons, Inc., third edition, 1993.

[72] W.T. Marshall and H.M. Nelson. *Structures.* Pitman Publishing, 1969.

[73] Techni Measure; 59 Alcester Road; Studley; Warwickshire. Tel:(052785) 4103. published calibration data supplied by manufacturer. Setra Calibration Certificate, October 1995. Part Number:141100-SP; Serial Number: 559949.

[74] Techni Measure; 59 Alcester Road; Studley; Warwickshire. Tel:(052785) 4103. published calibration data supplied by manufacturer. Setra Calibration Certificate, May 1993. Part Number:141100-10; Serial Number:381697.

[75] Brian W. Kernigham and Dennis M. Ritchie. *The C Programming Language.* Prentice-Hall International, second edition, 1988.

[76] K. Kaiser. Aerodynamic damping for flexible structures. In *19th British Wind Energy Association Annual Conference*, Edinburgh, July 1997. Mechanical Engineering Publications Ltd.